POLISH ANATOMICAL SOCIETY

FOLIA MORPHOLOGICA

Vol. 83　　*2024*　　*No. 1*

V M
VIA MEDICA

VIA MEDICA

R E V I E W   A R T I C L E

Anatomical review of internal jugular vein cannulation

Natalie Kosnik, Taylor Kowalski, Lorraine Lorenz, Mercedes Valacer,
Sumathilatha Sakthi-Velavan

Division of Biomedical Sciences, Marian University College of Osteopathic Medicine, Indianapolis, IN, United States

The internal jugular veins (IJV) are the primary venous outflow channels of the head and neck. The IJV is of clinical interest since it is often used for central venous access. This literature aims at presenting an overview of the anatomical variations, morphometrics based on various imaging modalities, cadaveric and surgical findings, and the clinical anatomy of IJV cannulation. Additionally, the anatomical basis of complications, techniques to avoid complications, and cannulation in special instances are also included in the review.

The review was performed by a detailed literature search and review of relevant articles. A total of 141 articles were included and organized into anatomical variations, morphometrics, and clinical anatomy of IJV cannulation.

The IJV is next to important structures such as the arteries, nerve plexus, and pleura, which puts them at risk of injury during cannulation. Anatomical variations such as duplications, fenestrations, agenesis, tributaries, and valves, may lead to an increased failure rate and complications during the procedure, if unnoticed. The morphometrics of IJV, such as the cross-sectional area, diameter, and distance from the skin-to-cavo-atrial junction may assist in choosing the appropriate cannulation techniques and hence reduce the incidence of complications. Age, gender, and side-related differences explained variations in the IJV-common carotid artery relationship, cross-sectional area, and diameter. Accurate knowledge of anatomical variations in special considerations such as paediatrics and obesity may help prevent complications and facilitate successful cannulation. (Folia Morphol 2024; 83, 1: 1–19)

Keywords: internal jugular vein, anatomical variations, morphometrics, cannulation, imaging, landmarks

INTRODUCTION

The internal jugular vein (IJV) is the main venous drainage of the head and neck and is the continuation of the sigmoid sinus [92]. It travels down the neck through the carotid sheath, along with the common carotid artery (CCA), the internal carotid artery (ICA), the vagus nerve, and the deep cervical lymph nodes [82]. The IJV joins with the subclavian vein posterior to the sternal end of the clavicle and forms the brachiocephalic vein [83]. The IJV typically runs anterolaterally to the ICA and CCA before joining the subclavian vein [135]. Deviations from the normal anatomy due to embryological dysgenesis cause a variety of clinically significant anatomical variations. The IJV serves as

a major surgical landmark for structures such as the spinal accessory nerve (SAN), the carotid artery, and cervical lymph nodes [33]. Hence, the altered anatomy of the IJV is of significance as the landmark may be misinterpreted if not identified correctly.

Besides anatomical variations, dimensions of IJV are of significant clinical interest; hence, various imaging modalities are used to measure IJV dimensions. Colour Doppler ultrasonography (USG), magnetic resonance imaging (MRI), and computed tomography (CT) are the most common non-invasive techniques used to measure dimensions, identify variations, and diagnose pathologies [113, 141]. Variables such as head positioning and respiratory changes are known to alter the dimensions [117]. In addition, age, population demographics, and external compression may account for the varying measurements reported in the literature [63, 117, 141]. Some of the commonly reported dimensions include cross-sectional area (CSA) and diameter of the IJV. The CSA is significant since a low CSA may indicate stenosis or an underlying pathology [63]. Variations in CSA at different cervical levels, head rotations, and positions provide options that are most favourable for successful IJV cannulation [19, 49, 66, 95].

The dimensions and anatomical relationships alter through the normal aging process, differ between genders, and are influenced by pathologies such as increased body mass index (BMI) [40, 44, 70, 74, 75, 81, 99, 106, 123]. It is important to be aware of these possible changes in varying patient populations, especially in IJV cannulation. Traditionally, the anatomical landmark technique was utilized to perform cannulation of the IJV [21, 67, 115]. However, considering the highly variable nature of the IJV, the USG-guided procedure has added benefits [17].

There are numerous cadaveric and clinical reports on anatomical variations, dimensions, relations, age-related differences, and the anatomical aspects of IJV cannulation and stenosis. Currently, there is not a comprehensive review of the IJV available. The aim of this study was to review the anatomic variations of the IJV with special reference to the clinical anatomy of IJV cannulation, including special considerations in paediatrics and obese patients.

MATERIALS AND METHODS

The aim of this research was to perform a narrative review of the IJVs. The literature search was conducted using the databases, PubMed and Google Scholar.

Table 1. Summary of search results

Manuscript section	Sub-section	Number of resources
Anatomical variations	Agenesis	10
	Hypoplasia	5
	Duplication	20
	Valves	6
	Tributaries	6
	Congenital fistulas	9
	Arterio-venous relation	4
Morphometrics	CSA	21
	Diameter	5
	Variations in CSA and diameter	13
	Distance between skin and atrio-caval junction	5
IJV cannulation	Clinical anatomy of IJV cannulation and cannulation techniques	12
	Complications	24
Special considerations	Body mass index	11
	Paediatrics	7

CSA — cross-sectional area; IJV — internal jugular vein (subsections are listed in the order they appear in the manuscript. Some references are included in more than one section listed in the table)

The Medical Subject Headings (MeSH) terms used were Jugular Veins/Abnormalities and Jugular Veins/Diagnostic Imaging. The keywords internal jugular vein, anatomical variations, morphometrics, cannulation, imaging, and landmarks were used. Several cross-references were utilized and compared to identify the most up-to-date information. The references utilized for this review ranged from imaging studies, case reports, cadaveric studies, literature reviews, and textbooks. There were no exclusions based on publication date.

RESULTS

The electronic search yielded a total of 3237 results. The authors analysed the results and selected 141 articles as relevant to this review. These references were grouped into categories of anatomic variations, morphometrics, differences in the IJV based on sex and age, and special considerations such as IJV cannulation in paediatric and obese patients. A summary of the resources used is outlined (Table 1).

DISCUSSION

Cadaveric, surgical, and radiological findings helped understand the anatomy of IJVs. Due to their non-invasive approach, colour Doppler USG and MRI are commonly used [141]. The benefits of USG include its ability to provide real-time images of structure and display the haemodynamics, while drawbacks

are primarily due to the accuracy and reproducibility of USG being dependent on the skill of the operator [141]. A disadvantage of both USG and MRI is that they require the operator to apply external pressure to vessels with a probe or collar, which could lead to inaccurate measurements of IJV characteristics, such as shape, thickness, diameter, CSA, and flow [53, 113, 117, 141]. Advantages of MRI and magnetic resonance venography (MRV) include the ability to view structural abnormalities, quantify venous blood flow compared to arterial flow, track progression of diseases over time, and provide images used by interventionalists when planning for treatment [141]. A CT scan can be used to non-invasively assess IJV's relation to surrounding structures, dimensions, and detect abnormalities not revealed by USG [70, 113]. There is no gold standard for the diagnosis of IJV pathologies, but a combination of various imaging modalities and criteria are commonly used to assess these conditions [141].

ANATOMICAL VARIATIONS

Embryologically, the IJV develops from the right and left cardinal veins at 8 weeks of gestation [83]. Developmental abnormalities may result in a variety of anatomical variations, which range from complete agenesis to duplication [120]. In a study of 1197 patients, there were 40 total variations found, which included bifurcation (4), duplication (14), fenestration (16), trifurcation (1), and posterior tributary (5) [83].

Agenesis

Congenital agenesis or complete absence of the IJV is a rare condition, and only 8 cases have been reported in the literature. It may result from abnormally formed channels lined by quiescent endothelium [59]. Four cases of agenesis of the right IJV were detected during attempted cannulations and all of them were cannulated into the left IJV or the axillary vein [4, 61, 79, 96]. A 55-year-old patient showed right IJV agenesis, and a detailed study on venous anatomy revealed left IJV phlebectasia and collateral channel that drained the right IJV into the left IJV [43]. The venous return may also be taken over by the external jugular vein (EJV) [120]. A case of left IJV agenesis was incidentally found in a 62-year-old male during neck dissection for oral carcinoma, and the neck collaterals and EJV were enlarged [10]. Besides failed and complicated cannulation, there is a spectrum of symptoms with agenesis of the IJV [96]. In a case of

right IJV agenesis, the left IJV wall was thickened as a compensatory mechanism that resulted in a rare complication of IJV thrombosis [59]. Due to inadequate drainage from the cranium into the neck, cerebral venous insufficiency has been implicated in patients with IJV agenesis [4]. The agenesis of IJV may be associated with malformations in the intracranial venous system [24]. A summary of the cases with IJV agenesis is listed (Table 2).

Hypoplasia

Hypoplasia of IJV indicates a narrowing of its lumen. Hypoplasia possibly occurs due to truncal venous malformations arising from developmental arrest in a late embryonic stage [65]. Typically, the IJV is double the size of the CCA, measuring 9.1–10.2 mm in diameter [71]. There is no standard dimension of IJV that indicates it to be hypoplastic; however, it was either difficult or impossible to cannulate when the IJV diameter was less than half its normal size [11]. In an USG-based study, 8.7% of the 104 uremic patients had an IJV diameter measuring under 5 mm [71]. In a study, 9.5% (47 of 493) patients were found to have IJV diameter less than 7 mm; 14.9% of them had failure of IJV cannulation while 8.5% had complicated cannulation [77] In a cadaveric study, three out of 93 dissections showed a narrowing of the IJV with an increase in ipsilateral EJV magnitude [11]. A paediatric study found the IJV to be hypoplastic in 4% of individuals, and this group measured under 5 mm and 3 mm in children and infants, respectively [5]. Due to considerable difficulty with cannulating a hypoplastic IJV, pre-cannulation imaging and cannulating a different vein may be beneficial.

Duplication

Duplication and fenestration comprise the commonly reported variations and are found in 0.4% of cases [92]. The terms duplication, bifurcation, and fenestrations are often confused. A duplication is defined as a split in the IJV, with each branch having its own attachment to the subclavian vein [33, 132]. If the IJV splits at or superior to the omohyoid muscle, that is considered a bifurcation [83]. However, if the IJV splits inferior to the omohyoid muscle, it is considered a duplication [83]. Fenestration is defined as a split in the IJV that reunites before merging with the subclavian vein [132]. There are three embryonic hypotheses considered for IJV duplication: the vascular hypothesis, the neuronal hypothesis, and the bony

Table 2. Agenesis of the internal jugular vein

Study	Age and gender	Side of agenesis	Mode of discovery	Clinical scenario	Salient features
Miller, 2011 [79]	12 years; not reported	Right	Ultrasound, Doppler imaging	Recognized during pre-cannulation ultrasound	Left IJV was enlarged and was the of same diameter as the left CCA
Kayiran et al., 2015 [59]	17 years; female	Right	CT, Doppler USG, and dynamic MRI indicated absence of right IJV	Diagnosed when investigated for painless left sided mass	Enlarged left IJV presented as a mass in the neck
Alagöz et al., 2015 [4]	66 years; female	Right	Ultrasound indicated the absence of the right IJV, confirmed with colour Doppler	Identified during attempted cannulation for acute respiratory failure	None reported
Tejada et al., 2015 [114]	16 years; not reported	Right	Ultrasound	Identified during attempted cannulation for laparotomy	Enlarged collaterals (thyro-lingual-facial trunk and middle thyroid vein)
Rewari et al., 2015 [96]	65 years; male	Right	Ultrasound	Failed right IJV cannulation	None reported
Kong et al., 2017 [61]	43 years; female	Right	Ultrasound, Doppler imaging, CT	Recognized during pre-cannulation ultrasound	None reported
Filograna et al., 2019 [43]	52 years; male	Right	Non-contrast CT	Recognized during staging of colon carcinoma	Collateral venous circulation that drained from the right anterior IJV and right retromandibular vein into the left IJV
Aroor et al., 2020 [10]	62 years; male	Left	CT, confirmed with histopathology	Misdiagnosed as IJV thrombosis while investigated for oral carcinoma	Enlarged neck collateral veins

CCA — common carotid artery; CT — computed tomography; IJV — internal jugular vein; USG — ultrasound; MRI — magnetic resonance imaging

hypothesis [92]. The vascular hypothesis argues that the persistence of two venous channels during the process of IJV development forms the duplication. The neuronal hypothesis argues that the SAN is trapped in the venous capillary plexuses during development, which can lead to an anterior and posterior portion of the IJV. The bony hypothesis contributes the embryogenesis of this variation to duplication of the jugular foramen [86]. The vascular theory of duplication is the most widely accepted of these hypotheses [48].

A review of 22 cases from cadaveric, surgical, and radiological reports classified three morphological patterns of duplication: type A, type B, and type C [86]. Type A duplication, found in 15 of the 22 cases, had the IJV split superior to the lower border of the posterior belly of the digastric; the two veins then rejoined at the omohyoid central tendon, and the SAN ran in between them. This description has been referred to as a fenestration [33, 122], partial duplication [98], or incomplete duplication [110]. In 295 patients, who underwent surgical neck dissections, only 2 cases were reported to have fenestration [33]. An incidental finding of a fenestrated IJV was noted in another patient admitted following a motor vehicle accident [12].

Type B duplication, found in 2 of the 22 cases, was the true or complete duplication in which the IJV split superior to the digastric and continued inferiorly to drain into the subclavian separately [86]. This type was associated with difficulty preserving the vein during neck dissections [86]. Type C duplication, found in 5 of the 22 cases, had the IJV split at a lower level around the hyoid bone, and the veins drained separately into the subclavian vein. In all 5 cases, the lateral of the two veins was partly outside the carotid sheath [86].

Type C duplications caused the most difficulty in surgery and imaging interpretation. A rare case of bilateral type C duplication was associated with a bulbous jugulo-vertebro-subclavian venous sinus [39]. A rare case of bilateral duplication had both vessels draining separately into the subclavian vein on the right, while they drained into the jugulo-vertebro-subclavian sinus on the left [39].

The SAN is superficial to the IJV, divides the deep and superficial cervical lymph node, and needs to be considered in IJV duplications [35]. In a meta-analysis of 1491 hemi-necks dissection, the relationship between the SAN and an IJV duplication was classified into four types [35]. Type 1 (79.7%) had the SAN superficial to the duplicated IJV; type 2 (16.6%) had the SAN posterior to the split vein; type 3 (0.7%) had the SAN between the split veins; type 4, which was never reported, had the nerve pass around the

branches of the vein [35]. Another study showed that in 2 of the 3 patients, SAN bisected the fenestration, while one SAN ran medial to the fenestration [33]. Surgeons must consider the variant relationship and determine the location of the SAN in relation to the variant IJV preoperatively by USG to avoid damage to the SAN during neck dissections [1, 3].

Duplication has not been reported to have physiological implications, but there are certain clinical implications such as phlebectasias and aneurysms. An aneurysm is a vessel dilation that involves degeneration of all layers of the venous wall, while phlebectasia involves thinning of tunica media [6, 15]. Duplications were found to be associated with phlebectasia in 46% of cases [86, 116]. IJV phlebectasia is a fusiform, soft, non-pulsating swelling of the vein which increases in size during the Valsalva manoeuvre [57]. Aneurysms were commonly reported at a vessel bifurcation, as there is a weakening at the proximal and distal end of the split [118]. There are two proposed hypotheses for these pathologies: turbulent flow at the bifurcation [118], or an incomplete formation of the tunica media [34]. The right jugular bulb is positioned superiorly to the left jugular bulb, which can be a predisposing factor to phlebectasia [56]. Phlebectasia could complicate choosing an appropriate vein for free-flap reconstructions [86]. This can be avoided by a preoperative diagnosis using venography, arteriography, and USG [110].

Valves

The IJV has a single valve located near the inferior jugular bulb, and it regulates the transmission of intrapleural pressure to the brain [52]. However, conflicting reports on the presence and competency of the IJV have been reported in the literature. Dissection and USG-based clinical studies on 75 cadavers and 75 adult patients found the valves bilaterally in 84% and 60%, respectively [68] while an USG-based study on 120 children showed bilateral valves in 74% of cases [36]. Almost 80% of cases with unilateral valves were found to have valves on the right IJV [36, 68]. Anatomical studies showed a higher incidence of valves than imaging since the thinness of valves allowed a better direct visualization due to the thinness of valve leaflets [36]. Cadaveric findings showed bicuspid valves in 98.5% while USG-based studies reported only 42% [36, 68]. Another study using colour Doppler showed two-leaflet valves in 75%, single-leaflet in 14%, and three-leaflet in 11% of the

462 IJVs examined [126]. Besides the valve thinness, difficulty in accessing the lower left IJV due to its position behind the clavicle probably caused these differential findings.

The IJV valve was found at an average distance of 28 mm and 9.2 mm from the jugulo-subclavian junction in adults and children, respectively [36]. However, an atypical location of the valve in the mid-neck far from the clavicle was found during an IJV cannulation [80]. The IJV valvular motion is likely a protective factor against cerebral venous engorgement; it was noted that 90% of the valves were incompetent and 29 out of 41 competent valves were bicuspid, and the researchers proposed that incompetent valves seemed to be a normal phenomenon [126]. In contrast to this finding, a recent study that explored the valve competency using hydrostatic pressure technique and found them to be competent in all the 25 living subjects and 93% of the 30 cadavers examined in the study [108]. Damage to the IJV valves at cannulation may destroy the leaflets and secondarily lead to an increased cerebrospinal pressure; hence it is important for clinicians to be aware of the valvular anatomical variants [52]. A real-time USG may be helpful in avoiding damage to a high positioned valve or a valve with abnormal cusps.

Tributaries

The typical tributaries of the IJV, the inferior petrosal sinus, the facial, lingual, pharyngeal, and superior and middle thyroid veins enter the IJV anteriorly; hence, surgical approach is easier from posterior to anterior because the posterior triangle has no tributaries of the IJV [130]. However, rare instances of posterior tributaries have been reported. A case showed a posterior tributary that joined with the IJV from the medial aspect of the sternocleidomastoid (SCM) and in another case, the tributary arose from under the SCM and drained into the lower third of the IJV [83]. In another case, the EJV was found to drain into the IJV instead of the subclavian vein, hence grouped as a posterior tributary [8]. In two instances, posterior tributaries of IJV were found during surgical dissection, one of which coursed deep to the posterior belly of the digastric, and another that coursed above the inferior belly of omohyoid [37]. Although the author called it an additional tributary, the description mimics a duplicated IJV. A lateral tributary was reported during a neck dissection, and it was found to drain into the lower part of the right

IJV [78]. In a cadaveric case report, a vein, 4 mm in diameter, formed from the junction of the common facial vein and IJV ran parallel to the IJV for 3 cm and then rejoined with the IJV [85]. It is imperative that variant tributaries are considered while performing surgical and interventional radiology procedures in this region.

Congenital arterio-venous fistulas

Congenital arterio-venous fistulas of IJV are vascular malformations that involve abnormal communication between IJV and a carotid artery [20]. It may result due to arrested venous development and abnormal arterio-venous differentiation during embryogenesis [41]. Acquired fistulas are usually traumatic in origin and often a complication of IJV cannulation [41]. Fistulas demonstrate progressive growth, which then may present clinically as localized swelling, bruit, or a pulsating mass or with neurological symptoms and often warrant treatment by embolization [20, 50]. Reported cases of an external carotid artery (ECA) and IJV fistula included a 15-year-old-female and a 2-year-old male who presented with a pulsatile swelling in the neck [2, 20], and a 27-year-old-male with neurological manifestations besides a neck swelling [50]. A fistula between the ICA and IJV was reported in a 64-year-old female with a pulsating swelling and bruit [131]. Lagos also reported a fistula between the ICA/IJV in a 7-year-old patient who presented with status epilepticus [64]. Two cases of spontaneous IJV-CCA fistulas were reported and they were likely related to collagen vascular diseases [94, 103]. A case of fetal IJV-carotid fistula was diagnosed during 27 weeks of gestation, in which case the fistula was accompanied by tricuspid regurgitation and pericardial effusion due to high flow through the fistula, but the report did not specify if it was IJV-ECA or ICA or CCA fistula [51]. An IJV fistula should be recognized before attempting IJV cannulation to avoid an arterial injury during the procedure.

Arterio-venous relations

Several studies have found anatomical variations in the relationship between IJV and CCA in 9.4–29% of patients [93]. A study on 120 healthy adults showed that the IJV is mostly anterolateral to the CCA; it was lateral to the CCA in approximately 6% and anterior to the CCA in approximately 15% of sides [92]. Another study on 100 adults also found an anterolateral IJV as the most common positioning; while an anterior

IJV was found in 15% on the right, the frequency was higher (28%) on the left side [88] a lateral IJV was less common than the earlier study (4% on the right and 1% on the left). Another study found that the IJV was commonly located lateral to the CCA (85.2%) with anterior next (12.5%) [70]. This study did not include an anterolateral classification which explains why the findings were different from other studies. Anterior IJV is the most dangerous location since it puts the CCA at risk of injury and USG-guided cannulation may help prevent this complication.

Age-related differences

The relationship of the IJV to CCA was shown to vary with age. Two studies on neonates found the lateral IJV as the most common position [81, 124]. Two paediatric studies found the IJV to be anterolateral to the CCA when the head position was 30° contralateral rotation and neutral [40, 99]. Another study on paediatrics found the majority of IJV to be anterolateral or anterior to CCA, with position changing after insertion of a laryngeal mask airway [84]. A study including both neonates and paediatrics found that the IJV was lateral to CCA in 51.3% and anterolateral in 42.9% with a head rotation of 45° contralaterally [123]. Thus, neonates have a more lateral IJV in relationship to the CCA, which progresses to an anterolateral position in paediatrics. However, since these studies all have varying head rotations, it could also be argued that lesser degrees of head rotation (30° contralateral and less) favour an anterolateral IJV relationship to the CCA, whereas a larger rotation of 45° contralateral head rotation may push the IJV into a slightly more lateral position with respect to the CCA. A study on age-related differences in the IJV-CCA relation showed that the subset with anterolateral IJV (87.9%), had a mean age of 41.6 years while the lateral IJV (10.3%), had a mean age of 59.4 years [106]. Knowledge of relatively more common lateral IJV in older individuals is clinically useful information while attempting IJV cannulation.

MORPHOMETRICS

The dimensions of IJV are variable since it is a compliant structure, and its measurements can change with the positioning of the patient, respiration, and cardiac function [63, 117]. Since IJVs are the primary extracranial venous drainage pathways, variations or changes in dimensions will likely have an impact on the drainage of the cerebrospinal nervous system [141].

Cross sectional area

The cross sectional area (CSA) is a commonly measured dimension of the IJV. A larger CSA is the target for the IJV cannulation [112]. Additionally, a significant change in IJV CSA could underlie an elevated BMI [63]. Due to venous structures having rapid responses to changes in blood pressure, an increase in IJV CSA suggests an increase in venous blood pressure which corresponds to impaired venous flow and sometimes an increased intrathoracic pressure [74]. Hence, several studies have aimed at finding the normal ranges of IJV CSA in various populations and age groups.

The findings obtained from several studies that used radiological modalities to measure the IJV CSA are shown (Table 3). USG typically measured the CSA at the middle segment of the IJV at the level of the thyroid gland and facial vein [141]. This middle segment is commonly referred to as J2, as compared to the inferior (J1) and superior (J3) portions [141]. The table shows a wide difference between the CSA values provided by each imaging modality and is likely due to several reasons: IJV dimensions are highly variable due to the individual's cardiac function, heart rate, volume status, respiratory function, and posture [117]. Therefore, it is important to take into consideration the positioning of the patients while images were obtained. Aging, as described in further detail below, is associated with an increase in CSA. Notably, the studies that used MRI-imaged individuals of an older age group than those imaged in the CT studies. Other demographics, such as country of origin, play a role in dimensions, as well [63]. Most MRI analytical software, such as time-of-flight, differs from that of CT and likely contributed to the difference [63]. Both MRI and USG require external compression, thereby altering IJV dimensions [117, 141]. The CSA tends to increase moving caudally, making the level of measurement another important aspect differentiating published results [18]. Given the variability of normal CSA values, a recent study used an interesting technique by using each IJV as its own internal control to measure the level of stenosis in the vessel with MRV [117].

Diameter

The diameter of the IJV is of similar significance as the CSA; interestingly, the IJV is not a perfect circle and hence has varying diameters in different planes. A summary of findings from several studies is shown (Table 3). The CT-based studies determined the maximal diameter while USG measured the anteroposterior, transverse, or lateral diameters [32, 87, 113]. The average diameter obtained from USG showed a smaller average than CT, which was likely related to compression of the IJV during the procedure. A cadaveric study found a similar average diameter to those by USG [45]. Besides knowing the normal range of IJV diameter, this dimension has a clinically significant correlation to right atrial pressure (RAP). An USG-based study on 72 adults found that IJV anteroposterior diameter showed a significant positive correlation with RAP [125]. The mean maximum IJV diameter for RAP < 10 mmHg was 7 ± 3 mm, and for RAP ≥ 10 mmHg, it was 10 ± 2 mm [125]. Additionally, a correlation between the RAP and respiratory variations in IJV diameter was noted; the variations of 14% and 40% were noted for RAP ≥ 10 mmHg and RAP < 10 mmHg, respectively [125]. This is a new area of correlation and needs further research.

Variations in cross-sectional area and diameter
Side differences

The right and left IJVs are often asymmetrical due to asymmetries in the drainage of blood through the dural venous sinuses, favouring the right transverse sinus and IJV over the left [100]. Lim et al. [70] found that the mean right IJV diameter was 14.1 mm compared to the mean left IJV diameter of 11.74 mm. Other studies that measured the IJV diameters found a similar difference [45, 70, 88, 113]. Beggs et al. [18] found a mean difference in CSA of 15.64 mm^2 at the C2-C3 level and 26.31 mm^2 at the C7-T1 levels, and the right IJV was larger than the left at both levels. Other studies on CSA concurred with these findings [63, 113, 137]. The overall larger size of the right IJV is likely why it is favoured to be used in cannulation over the left IJV.

Differences in cervical levels

Differences in dimensions of IJV have been noted at various cervical levels. Magnano et al. [74] measured average CSA values larger at the lower cervical levels as compared to upper cervical levels. Higher CSA at lower cervical levels was likely due to increased flow into the lower portion of IJV [18, 63, 74]. There was also more variability noted in the CSA at lower cervical levels [63], which was postulated to be due to breathing artifacts. Research findings support the IJV having a conical structure with an increasing area at

7

a lower level [18, 46, 63, 74], and therefore recommend cannulation to be attempted at lower levels of the IJV where there is a larger CSA to target. However, a recent study supported a rhomboid shape of the IJV and found that the middle IJV (level of cricoid) was larger than the upper and lower IJV and therefore rec-

Table 3. Dimensions of the internal jugular vein

Imaging modality	Study	Average CSA [mm²]	Diameter [mm]	Patient's position	Average age [years]	Population demographics
USG	Clenaghan et al., 2005 [32]	n/a	R 13.5 (Lat)	Su	22–57 (range)	Ireland 10 M/10 F
			R 15.5 (Lat)	10° T		
			R 15.5 (Lat)	15° T		
			R 16.4 (Lat)	20° T		
			R 16.7 (Lat)	25° T		
			R 16.7 (Lat)	30° T		
	Kim et al., 2008 [60]	R 11.2 ± 0.8	n/a	Su	27.6 ± 1.9	South Korea 20 M/0 F
		R 16.6 ± 6.70		15° T		
		R 3.80 ± 2.30		15° RT		
		R 14.0 ± 6.40		50° PLR		
	Sayin et al., 2008 [102]	R 2.9 ± 2.2 (0–1 y) R 4.3 ± 1.8 (1–2 y) R 5.4 ± 3.4 (2–6 y) R 5 ± 2.6 (6–15 y)	R 5.2 (0–1 y) R 6.6 (1–2 y) R 7.5 (2–6 y) R 7.2 (6–15 y)	Su, cricoid cartilage level	2.7	Turkey
		n/a	R 5.3 (0–1 y) R 6.4 (1–2 y) R 7.0 (2–6 y) R 7.6 (6–15 y)	Su, sterno-clavicular junction level		
		R 2.5 ± 1.2 (0–1 y) R 4.5 ± 2.2 (1–2) R 5.9 ± 4.1 (2–6 y) R 6.2 ± 3.7 (6–15 y)	n/a	T, cricoid cartilage		
	Bellazzini et al., 2009 [19]	R 9.0 ± 5.6	n/a	Su, 20–30° CLR	37 ± 11	United States 23 M/29 F
		R 12.6 ± 6.9		T, 20–30° CLR		
		R 15.8 ± 6.5		Su, V, 20–30° CLR		
		R 17.0 ± 7.9		T, V, 20–30° CLR		
	Ozbek et al., 2013 [87]	R 10.8 ± 0.6	R 13.6 ± 0.4 (Tr) R 9.7 ± 0.3 (AP)	Su, 15–20° T, neutral head positioning	37.8 ± 13.3	Turkey 25 M/14 F
		R 12.7 ± 0.7	R 14.4 ± 0.4 (Tr) R 10.9 ± 0.3 (AP)	Su, 15–20° T, < 30° CLR		
		R 14.2 ± 0.8	R 15.0 ± 0.4 (Tr) R 10.9 ± 0.3 (AP)	Su, 15–20° T, > 30° CLR		
		R 8.7 ± 0.6	R 12.9 ± 0.5 (Tr) R 7.9 ± 0.3 (AP)	Su, 15–20° T, < 30° ILR		
	Parmar et al., 2013 [88]	n/a	R 13.23 ± 2.52 L 10.25 ± 2.29	15° T, 45° CLR	27.12 ± 4.41	India 50 M/50 F
	Ciuti et al., 2013 [31]	R 4.2 ± 4.0	n/a	Su	27	Italy 12 M/13 F
		R 0.70 ± 0.60		Si		
	Seong et al., 2016 [104]	R 10.6 ± 3.60	n/a	Su	28.15 ± 2.85	South Korea 26 M/15 F
		R 13.4 ± 4.50		Su, V		
		R 12.6 ± 4.10		Su, EDC		
		R 14.1 ± 4.70		Su, V, EDC		
	López Álvarez et al., 2017 [72]	n/a	5.9 ± 2.3 (AP)	Su, 10–15° CLR	5.5 ± 5.2	Spain 70 M/55F

→

Table 3. cont. Dimensions of the internal jugular vein

Imaging modality	Study	Average CSA [mm²]	Diameter [mm]	Patient's position	Average age [years]	Population demographics
MRI	Laganà et al., 2016 [63]	R 63.26 ± 31.51 L 53.52 ± 25.58	n/a	Su	31.22 ± 9.29	Italy 13 M/23 F
	Magnano et al., 2016 [74]	R 68.7 ± 53.7 L 49.3 ± 37.5	n/a	Su; C7/T1 level	43 ± 17.5	United States 63 M/130 F
		R 55.4 ± 38.0 L 42.1 ± 30.6		Su; C5/C6 level		
		R 52.5 ± 28.2 L 38.8 ± 23.5		Su; C4 level		
		R 39.2 ± 24.1 L 27.5 ± 18.0		Su; C2/C3 level		
	Pelizzari et al., 2018 [90]	R 46.6 (median) L 24.4 (median)	n/a	Su	30.9 ± 9.0	Finland 1 M/8 F
CT	Lim et al., 2006 [70]	n/a	R 14.1 L 11.74	Su	Adults	Australia
	Tartière et al., 2009 [113]	R 181 ± 111 L 120 ± 81	R 17 ± 5 L 14 ± 5	Su	60 ± 15	France 132 M/58 F
	Yoon et al., 2013 [137]	R 165 ± 81 L 119 ± 57	R 16.7 ± 3.8 (Tr) R 12.6 ± 3.7 (AP) L 13.7 ± 3.5 (Tr) L 11.1 ± 2.6 (AP)	Su	48 ± 14	South Korea 34 M/46 F
	Jeon et al., 2020 [54]	R 124.3 L 89.1	R 14.3 L 12.0	Su; Upper (Hyoid)	65 (median)	South Korea 160 M/153 F
		R 190.8 L 127.0	R 17.6 L 14.4	Su; Middle (Cricoid)		
		R 183.1 L 94.5	R 16.5 L 11.8	Su; Lower (T1)		
Autopsy dissection	Furukawa et al., 2010 [45]	n/a	R 13.4 L 9.4	n/a	54.4	Japan 18 M/12 F

CSA — cross-sectional area; USG — ultrasonography; MRI — magnetic resonance imaging; CT — computed tomography; R — right IJV; L — left IJV; Lat — lateral; AP — anteroposterior; Tr — transverse; Su — supine; Si — sitting; T — Trendelenburg; RT — reverse Trendelenburg; V — Valsalva; M — male; F — female; PLR — passive leg raising; CLR — contralateral rotation; ILR — ipsilateral rotation; EDC — external digital compression; IJV — internal jugular vein; n/a — not available

ommended cannulation near the level of the cricoid cartilage, which may also help to avoid unnecessary complications, such as pneumothorax [54]. However, this retrospective study did not account for variables such as patients' physiological state or underlying diseases; hence further prospective research is needed to confirm the findings.

Age-related differences

Studies have shown differences in IJV dimensions with age. A significantly larger CSA (at mid-cervical levels) was associated with increasing age [54] and the difference was primarily observed in patients over 40 years of age [74]. The difference was likely due to a lower velocity and lower outflow volume in the IJV and reduced atrial emptying [30]. Another study on 462 IJVs of patients in the 21–92 years age group reported a similar difference, but it was not statisti-cally significant [126]. It is important to remember that while the larger CSA with increasing age may favour IJV cannulation, other cardiac factors such as lower blood flow and increased RAP may influence the procedure.

Gender differences

A study using 2-dimensional MRV found the CSA of IJV in males to be larger than in females, with this difference being even more obvious on the right side and in older males [74]. The findings are consistent with other studies on IJV dimensions like any other blood vessel in the body [126]. On the other hand, a CT-based study showed a larger CSA in males compared to females, which was not statistically significant [54]. A possible explanation for this difference is due to the difference between the type of imaging used in these two studies.

Distance between skin and atrio-caval junction

A study on 100 patients using USG-guided catheterization revealed that the mean distance from the skin puncture (or access) sites to the superior vena cavo-atrial junction was 18.3 cm and 16 cm for the left and right IJV cannulation, respectively [7]. The mean distance was 1.7 cm higher in males than in females for the right IJV approach (p < 0.1) [7]. A prospective study on 239 patients correlated catheter tip position and catheter length with the patients' recorded heights and found that most catheters having their tips in superior vena cava (SVC) had a length described by the following formula (where 'H' is patient height in centimetres): from the right IJV, (H/10) cm for right IJV cannulation [91]. However, Andrews et al. [7] found gender to be a better predictor of the access site to cavo-atrial junction distance rather than height.

The depth of IJV from the skin influences the cannulation technique and dimensions of the catheter used for cannulation. The right IJV runs more superficially to the skin compared to the left IJV since the mean skin to IJV distance was found to be 17.4 mm on the right compared to 18.7 mm on the left [53]. Parmer et al. [88] concurred with this finding; however, the average thickness on the right side measured 9.75 mm, and the left measured 10.3 mm. Another study yielded the mean depths on the right and left as 14 and 14.5 mm when measured in the transverse plane from the skin [70]. The differences are possibly due to differences in study techniques and the population studied.

INTERNAL JUGULAR VEIN CANNULATION

Cannulation of the IJV is performed for administering medications, fluids, and monitoring pressures, and in cardiac surgery patients for haemodynamic monitoring and measuring cardiac filling pressures [27, 115]. The goal is to have a successful first attempt at cannulation because increased attempts increase the risk of complications [115]. It is important to remember the normal and variant anatomy of the IJV and surrounding structures to prevent complications such as arterial puncture or haemothorax [22].

Clinical anatomy of IJV cannulation

The IJV is preferred for central venous cannulation due to the easily accessible external landmarks such as the carotid artery, decreased risk of pneumothorax in comparison to subclavian vein access, easier management of bleeding, relatively fewer chances of a mispositioned catheter, and higher chances of cannulation under USG-guidance [97]. Besides, the IJV is preferred during emergency venous access because cardiopulmonary resuscitation can still be performed [97]. The right IJV is preferred because it has a larger CSA than the left and is in a straight line with the innominate veins and SVC, which allows for improved placement of the catheter [22, 42]. The right IJV is mostly chosen because of its accessibility and safety for right-handed anaesthesiologists [44]. Also, the right-sided approach avoids injury to the thoracic duct, which is a possibility with left IJV cannulation [22, 53].

Cannulation techniques

Internal jugular vein cannulation can be done by the landmark technique or the USG technique, but it is important to be comfortable utilizing the landmark technique in cases when USG is not available [115].

Currently, three techniques are used for IJV cannulation: central, anterior, and posterior (Fig. 1). The location of the carotid artery is felt by palpation in the space between the trachea and SCM, and then the IJV is found lateral to the carotid pulse [22]. The central//middle approach utilizes Sedillot's triangle, which is a triangle formed by the sternal and clavicular heads of the SCM, and the needle is inserted at the apex of the triangle [97]. The puncture site is the same as the alternative technique described earlier. In the anterior approach, the needle is inserted along the medial border of SCM, 2–3 finger breadths superior to the clavicle. This approach accesses the IJV at a slightly higher level than the low approach described earlier; in the posterior approach, the needle is inserted along the lateral border of the SCM, halfway between the mastoid process and the clavicle [97]. Some authors used the terms anterior and central interchangeably [22, 23]. Two studies used the point where the EJV crosses over the SCM, at a point just lateral to the SCM, around one-third of the distance between the clavicle and mastoid process for the posterior approach [22, 76].

A randomized study of 104 patients compared the central approach with the posterior approach and reported more complications such as interruption of blood flow with the posterior approach [76]. The central or middle approach was the preferred approach in other studies [16, 140]. The posterior approach was recommended for patients with scoliosis and pathologies of the lower neck when the
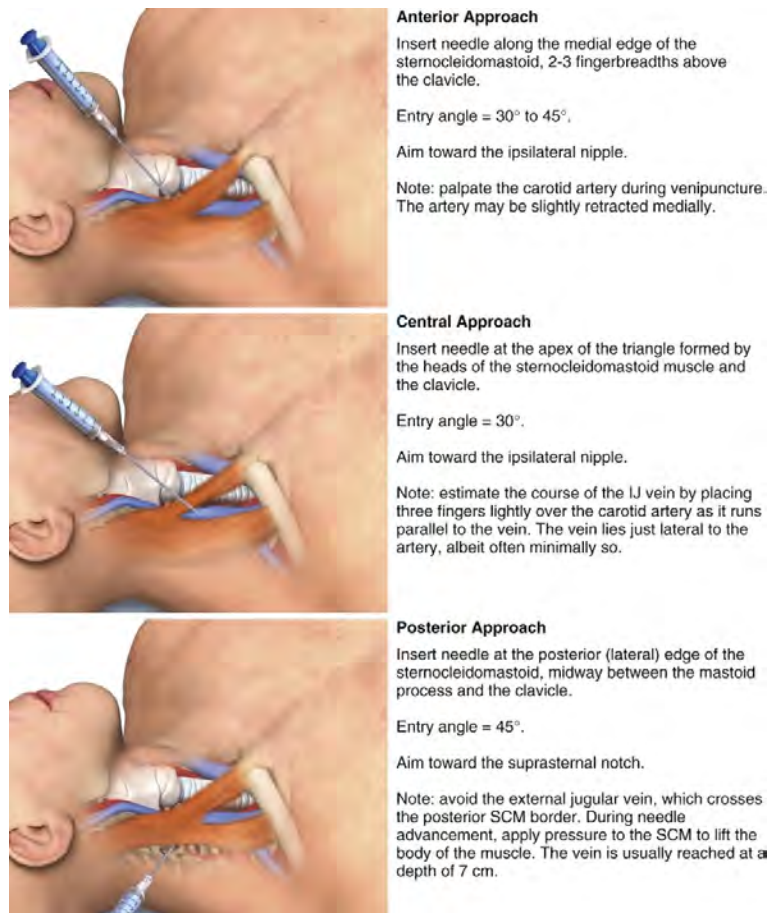
Anterior Approach

Insert needle along the medial edge of the sternocleidomastoid, 2-3 fingerbreadths above the clavicle.

Entry angle = 30° to 45°.

Aim toward the ipsilateral nipple.

Note: palpate the carotid artery during venipuncture. The artery may be slightly retracted medially.

Central Approach

Insert needle at the apex of the triangle formed by the heads of the sternocleidomastoid muscle and the clavicle.

Entry angle = 30°.

Aim toward the ipsilateral nipple.

Note: estimate the course of the IJ vein by placing three fingers lightly over the carotid artery as it runs parallel to the vein. The vein lies just lateral to the artery, albeit often minimally so.

Posterior Approach

Insert needle at the posterior (lateral) edge of the sternocleidomastoid, midway between the mastoid process and the clavicle.

Entry angle = 45°.

Aim toward the suprasternal notch.

Note: avoid the external jugular vein, which crosses the posterior SCM border. During needle advancement, apply pressure to the SCM to lift the body of the muscle. The vein is usually reached at a depth of 7 cm.

Figure 1. Approaches to the internal jugular vein; IJ — internal jugular; SCM — sternocleidomastoid [97]. (Reprinted from Roberts and Hedges' Clinical Procedures in Emergency Medicine and Acute Care, Seventh Edition, Salim R. Rezaie, E.C. Coffey, Christopher R. McNeil, Central Venous Catheterization and Central Venous Pressure Monitoring, 405–438.e3., 2019, with permission from Elsevier).

central approach could not be performed [29, 76]. On the contrary, Babu et al. [13] recommended the posterior approach due to fewer attempts required to successfully cannulate since 80% of the cannulations were successful on the first attempt compared to 57% with the anterior approach. Since the posterior approach involved needle insertion higher up in the neck, allowing a longer vein length, the study reported fewer cases of haemothorax, pneumothorax, and arterial puncture [13]. In obese, critically ill, or short-necked patients, the posterior approach is preferred to prevent complications [29].

Complications

When performing IJV cannulation, it is important to be aware of the complications associated with the procedure as well as variations in each patient that may complicate the procedure. A study evaluated the structures near the IJV that are susceptible to transfixion during IJV cannulation [26]. When using USG-guided cannulation, it is possible to puncture the posterior wall of the vein because low-pressure veins can collapse [26]. When carotid artery puncture results in a haematoma, finding the IJV can be difficult because of the compression caused by arterial leakage and pseudo-aneurysms [9, 73]. Near the puncture site of the IJV, at the level of the cricoid cartilage, the upper trunk of the brachial plexus is posterior to the IJV, so utilizing the posterior approach for IJV cannulation may result in injury to the upper trunk of the brachial plexus [89].

The catheter tip may be positioned incorrectly, which is more common on the left IJV because the left brachiocephalic vein is longer and has more tributaries [127, 133]. Abnormal positioning of the catheter tip may predispose to thrombosis, infection, vessel or cardiac perforation, and valvular injury [109]. An angle of a tip to vessel wall greater than 40° was found to be more likely to lead to SVC wall perforation, which was shown in a laboratory [111].
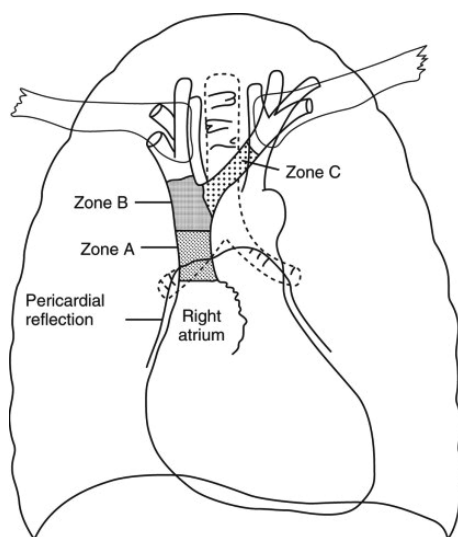
Figure 2. Stylized anatomical figure dividing the great veins and upper right atrium (RA) into three zones (A–C), representing different areas of significance for placement of central venous catheter (CVCs); Zone A — upper RA and lower superior vena cava (SVC); Zone B — upper SVC and junction of left and right innominate veins; Zone C — left innominate vein [111]. (Reprinted from British Journal of Anaesthesia, Vol. 96, Stonelake PA, Bodenham AR. The carina as a radiological landmark for central venous catheter tip position, 335–340, 2006, with permission from Elsevier).

Techniques to reduce complications and increase success rate

An understanding of the normal anatomy of the IJV and its relations is essential to prevent injury to surrounding structures, and an experienced clinician can help aid successful cannulation. Recognition of anatomical variations such as agenesis and duplication may help minimise the complications due to multiple failed attempts. Anatomical variations of the size and positions of the IJVs should be assessed when using the landmark technique or USG to reduce complications [14, 97]. IJV cannulation using the landmark technique in a patient with an absent IJV may be related to a higher incidence of complications such as arterial puncture and pneumothorax [96]. Detecting variations before the procedure was recommended to allow a preoperative discussion between the patient and surgeon on alternative cannulation sites and monitoring strategies [61]. Although a meta-analysis reported that real-time USG-guided IJV placement was not beneficial, USG imaging prior to IJV insertion was found to lower cannulation failure and injury to the carotid artery [107].

To avoid mechanical complications and ensure accurate monitoring of CVP, it is important to ensure that the tip of the catheter lies in the SVC (at its junction with the right atrium), in line with its long axis, right above the pericardial reflection, and the angle of the catheter to vessel wall should be less than 40 degrees [62]. As a surface marking, the atrio-caval junction corresponds to the level of sternal angle [16]. A study explored the radiological landmark to confirm the catheter tip position after cannulation since it should always lie above the pericardial reflection [111]. The upper limit of the pericardial reflection is below the carina, and the tip position varies based on left and right-sided cannulation [111]. Radiologically, zone A corresponds to the lower SVC, and upper right atrium, zone B, the area around the junction of the left and right innominate veins and the upper SVC, and zone C represents the left innominate vein proximal to the SVC (Fig. 2) [111]. The study concluded that right-sided central venous catheters should be sited above the carina and left-sided should be sited in the SVC with the tip at a shallow angle to the vessel wall [111].

Many studies have identified an increase in IJV CSA with contralateral head rotation, making this a useful manoeuvre during cannulation [19, 49, 87, 97]. An USG-based study found that the right IJV CSA decreased from 14.2 mm^2 to 8.7 mm^2 when transitioning from a > 30° contralateral rotation to < 30° ipsilateral rotation [87]. Rotating the patient's head also alters the location of the IJV's relation to the carotid artery, yielding a 95% to 57.5% decrease in CCA overlap with this rotation [87]. While a decreased overlapping is preferred for cannulation, it was determined that a greater CSA was more important in performing successful cannulation under optimum conditions [87]. An USG-guided simulation on volunteers showed the risk of injury to CCA was lower with less than 45° contralateral head rotation [69].

The Trendelenburg position or head-down tilt is recommended in central venous cannulation, as it increases CSA due to greater central blood volume and venous return, causing distention of the vessel [134]. In this position, the patient's supine body is placed at an angle to the horizontal with the lower extremities at an elevation compared to the head [55]. A 15° head-down tilt increased IJV CSA compared to neutral positioning, reverse Trendelenburg positioning, and passive leg elevation (Table 3) [60]. Increased tilt over 15° increases CSA further but has been shown to increase intracranial pressure [32]. Therefore, IJV cannulation is recommended to be performed at

a Trendelenburg position of 5° to 10° with 45° contralateral head rotation, allowing a significant increase in IJV CSA without a significant displacement of the IJV location [49].

Passive leg raising while maintaining the torso in a horizontal plane, has also been shown to increase IJV CSA. One study in mechanically ventilated patients showed that both Trendelenburg position and passive leg raising significantly increased right IJV CSA, 26% and 23%, respectively, as well as both vertical and transverse diameters of the IJV [47]. If Trendelenburg position is contraindicated or not possible, passive leg raising may be considered during cannulation [47, 60].

Special considerations
IJV cannulation in obese patients

A BMI over 30 kg/m^2 is considered true obesity, and these patients are often at risk of difficult cannulation [105]. The thick subcutaneous layer is likely to hide surface landmarks and requires more pressure and acute angulation to insert the needle [38]. An MRV-based study on 193 individuals showed that elevated BMI correlated with an increased IJV CSA at lower cervical levels, especially at C7/T1, while no such correlation was observed at upper cervical levels [75]. The larger IJV CSA measurements seen with high BMI patients were likely due to these patients having an increased intrathoracic pressure leading to the IJV enlargement [74].

There is a higher incidence of successful cannulation by the posterior approach (97%) in the higher weight group/obese patients compared to the anterior approach (75%), and there is a significant decrease in arterial puncture using the posterior approach (3.1%) in comparison to the anterior approach (16.6%) [29]. The study did not find a significant difference in procedure difficulty or complication rates between weight groups or approaches [29].

Although USG showed a greater incidence of CCA and IJV overlapping in obese patients compared to non-obese patients (which was especially significant at 30° or greater of head rotation), there was no statistically significant difference seen between the two groups regarding CCA puncture during the cannulation attempts under USG guidance [44, 69, 119]. USG guidance and head rotation less than 30° for central venous cannulation in obese patients may help avoid or quickly address any complications of the procedure and minimise overlapping of the IJV and CCA [25, 44, 69, 121, 137].

While the Trendelenburg position is helpful in non-obese patients, the outcome may be detrimental in obese patients. It is hypothesized that placing an obese patient in the Trendelenburg position exacerbates the risk of procedural complications due to an increase in pressure, compression, and stretch on the patient from weight [139]. Therefore, Trendelenburg positioning is not recommended in obese patients during cannulation.

IJV cannulation in paediatrics

Several studies in infants and children found that USG-guided cannulation was superior to the anatomical landmark method [28, 101, 128, 129]. The USG-guided cannulation was associated with increased success rates, fewer attempts at cannulation, fewer arterial punctures [28, 128]. In infants and paediatric populations, USG-guided cannulation seems to be the most effective and efficient.

Internal jugular vein cannulation is technically challenging in infants, especially when using the traditional landmarks technique [136]. In a new landmark technique, the carotid artery was marked at the level of the cricoid cartilage, as well as the apex of the triangle formed by the clavicle and two heads of the SCM then the needle was inserted between the marks, towards the ipsilateral nipple [136]. If the first attempt was not successful, the needle was inserted more laterally for the second attempt, and if that attempt was unsuccessful, then the needle was inserted more medially [136]. Results found the new landmark technique to reduce complications such as carotid artery puncture, the duration of the procedure was shorter, and this new technique had an overall higher success rate [136].

A clinically relevant correlation between a patient's height and depth of catheter placement was found by researchers if the patient's height was between 40 and 140 cm [138]. This study used an anterior approach to insert the catheter in the right IJV and then confirmed placement with transoesophageal echocardiography [138]. The final equation that was produced is as follows: optimal depth (cm) = 1.7 + (0.7 × height) [138]. This finding is very clinically relevant and helps in planning catheter insertion in children.

The vertebral artery (VA) was at risk of transfixation in paediatric patients based on the extent of overlap of VA with IJV; assessed by the width of VA, the distance between the VA and IJV/skin [58]. Thirteen

percent of patients were at high risk, and hence the VA should be found by USG before cannulation [58].

CONCLUSIONS

Anatomic variations in the IJV are to be looked for when utilizing the IJV for central venous access and can be assessed by imaging modalities to view the IJV. The CSA and diameter of the IJV are variable per patient and can be changed based on patient position and breathing patterns. The dimensions and position of the IJV in relation to the CCA change with aging, with neonates having a more lateral position and paediatrics and adults having a more anterolateral position. A detailed understanding of the neck anatomy surrounding the IJV, complications associated with IJV cannulation, and the best approach and imaging modality aid in successful cannulation. While cannulation can be done by the landmark technique or the USG-guided technique, it is important to be comfortable utilizing the landmark technique in cases when USG is not available. Special considerations such as high BMI and age must be assessed before cannulation to employ techniques to increase successful cannulation rates and avoid complications.

REFERENCES

1. Abakay MA, Şimşek BM, Olgun B, et al. Ultrasonic identification of internal jugular vein fenestration. Surg Radiol Anat. 2019; 41(9): 1079–1081, doi: 10.1007/s00276-019-02226-7, indexed in Pubmed: 30919043.
2. Ahmad S, Suleman FE. Rare cause of a neck mass: successful balloon embolisation of a congenital external carotid artery-internal jugular vein fistula. Pediatr Surg Int. 2011; 27(12): 1375–1376, doi: 10.1007/s00383-011-2918-0, indexed in Pubmed: 21590480.
3. Alaani A, Webster K, Pracy JP. Duplication of internal jugular vein and relation to the spinal accessory nerve. Br J Oral Maxillofac Surg. 2005; 43(6): 528–531, doi: 10.1016/j.bjoms.2005.03.013, indexed in Pubmed: 15896889.
4. Alagöz A, Tunç M, Sazak H, et al. Absence of the Right Internal Jugular Vein During Ultrasound-Guided Cannulation. Turk J Anaesthesiol Reanim. 2015; 43(3): 212–214, doi: 10.5152/TJAR.2015.82713, indexed in Pubmed: 27366499.
5. Alderson PJ, Burrows FA, Stemp LI, et al. Use of ultrasound to evaluate internal jugular vein anatomy and to facilitate central venous cannulation in paediatric patients. Br J Anaesth. 1993; 70(2): 145–148, doi: 10.1093/bja/70.2.145, indexed in Pubmed: 8435256.
6. Alshehri WM, Alothmani SK, Alshamrani AM, et al. Internal jugular vein aneurysm: a case report. J Surg Case Rep. 2019; 2019(5): rjz159, doi: 10.1093/jscr/rjz159, indexed in Pubmed: 31139340.
7. Andrews RT, Bova DA, Venbrux AC. How much guidewire is too much? Direct measurement of the distance from subclavian and internal jugular vein access sites to the superior vena cava-atrial junction during central venous catheter placement. Crit Care Med. 2000; 28(1): 138–142, doi: 10.1097/00003246-200001000-00023, indexed in Pubmed: 10667513.
8. Anehosur V, Rajendiran S, Jayade GR, et al. An unusual observation during neck dissection. J Maxillofac Oral Surg. 2016; 15(Suppl 2): 306–308, doi: 10.1007/s12663-015-0839-5, indexed in Pubmed: 27408458.
9. Armstrong PJ, Sutherland R, Scott DH. The effect of position and different manoeuvres on internal jugular vein diameter size. Acta Anaesthesiol Scand. 1994; 38(3): 229–231, doi: 10.1111/j.1399-6576.1994.tb03879.x, indexed in Pubmed: 8023661.
10. Aroor R, Serigar V, Amulya TM, et al. Absence of internal jugular vein flow: a diagnostic dilemma. Indian J Surg Oncol. 2020; 11(Suppl 1): 109–111, doi: 10.1007/s13193-020-01091-w, indexed in Pubmed: 33088143.
11. Asouhidou I, Natsis K, Asteri T, et al. Anatomical variation of left internal jugular vein: clinical significance for an anaesthesiologist. Eur J Anaesthesiol. 2008; 25(4): 314–318, doi: 10.1017/S0265021508003700, indexed in Pubmed: 18289445.
12. Atalar MH, Altuntaş EE, Koşar MI, et al. Multidetector CT findings of an extraordinary fenestration of the internal jugular vein. Diagn Interv Radiol. 2012; 18(2): 164–166, doi: 10.4261/1305-3825.DIR.4474-11.1, indexed in Pubmed: 22020950.
13. Babu BVM, Rao AK, Srikanth B. Comparision of posterior and anterior approaches for internal jugular venous cannulation–a prospective & randomised controlled study. Int J Sci Study. 2014; 2(2): 35–38.
14. Bailey PL, Whitaker EE, Palmer LS, et al. The accuracy of the central landmark used for central venous catheterization of the internal jugular vein. Anesth Analg. 2006; 102(5): 1327–1332, doi: 10.1213/01.ane.0000202467.10465.12, indexed in Pubmed: 16632804.
15. Baker JB, Ingraham CR, Fine GC, et al. Pediatric jugular vein aneurysm (phlebectasia): report of two cases and review of the literature. Radiol Case Rep. 2017; 12(2): 391–395, doi: 10.1016/j.radcr.2016.12.003, indexed in Pubmed: 28491195.
16. Bannon MP, Heller SF, Rivera M. Anatomic considerations for central venous cannulation. Risk Manag Healthc Policy. 2011; 4: 27–39, doi: 10.2147/RMHP.S10383, indexed in Pubmed: 22312225.
17. Batllori M, Urra M, Uriarte E, et al. Randomized comparison of three transducer orientation approaches for ultrasound guided internal jugular venous cannulation. Br J Anaesth. 2016; 116(3): 370–376, doi: 10.1093/bja/aev399, indexed in Pubmed: 26705350.
18. Beggs CB, Magnano C, Belov P, et al. Internal jugular vein cross-sectional area and cerebrospinal fluid pulsatility in

the aqueduct of sylvius: a comparative study between healthy subjects and multiple sclerosis patients. PLoS One. 2016; 11(5): e0153960, doi: 10.1371/journal.pone.0153960, indexed in Pubmed: 27135831.

19. Bellazzini MA, Rankin PM, Gangnon RE, et al. Ultrasound validation of maneuvers to increase internal jugular vein cross-sectional area and decrease compressibility. Am J Emerg Med. 2009; 27(4): 454–459, doi: 10.1016/j.ajem.2008.03.034, indexed in Pubmed: 19555617.

20. Bellosta R, Vescovi M, Attisani L, et al. Endovascular treatment of congenital external carotid-jugular fistula: case report and review of the literature. Vasc Endovascular Surg. 2017; 51(5): 316–319, doi: 10.1177/1538574417702777, indexed in Pubmed: 28399714.

21. Bold RJ, Winchester DJ, Madary AR, et al. Prospective, randomized trial of Doppler-assisted subclavian vein catheterization. Arch Surg. 1998; 133(10): 1089–1093, doi: 10.1001/archsurg.133.10.1089, indexed in Pubmed: 9790206.

22. Boon JM, van Schoor AN, Abrahams PH, et al. Central venous catheterization--an anatomical review of a clinical skill. Part 2. Internal jugular vein via the supraclavicular approach. Clin Anat. 2008; 21(1): 15–22, doi: 10.1002/ca.20563, indexed in Pubmed: 18058904.

23. Botha R, van Schoor AN, Boon JM, et al. Anatomical considerations of the anterior approach for central venous catheter placement. Clin Anat. 2006; 19(2): 101–105, doi: 10.1002/ca.20240, indexed in Pubmed: 16302239.

24. Boukobza M, Enjolras O, Guichard JP, et al. Cerebral developmental venous anomalies associated with head and neck venous malformations. AJNR Am J Neuroradiol. 1996; 17(5): 987–994, indexed in Pubmed: 8733978.

25. Brusasco C, Corradi F, Zattoni PL, et al. Ultrasound-guided central venous cannulation in bariatric patients. Obes Surg. 2009; 19(10): 1365–1370, doi: 10.1007/s11695-009-9902-y, indexed in Pubmed: 19554381.

26. Chandra M, Start S, Roberts D, et al. Arterial vessels behind the right internal jugular vein with relevance to central venous catheterisation. J Intensive Care Soc. 2015; 16(3): 202–207, doi: 10.1177/1751143714567434, indexed in Pubmed: 28979411.

27. Chennakeshavallu GN, Gadhinglajkar S, Sreedhar R, et al. Comparison of three ultrasound views for internal jugular venous cannulation in patients undergoing cardiac surgery: a randomized trial. J Med Ultrasound. 2021; 29(3): 176–180, doi: 10.4103/JMU.JMU_135_20, indexed in Pubmed: 34729326.

28. Chuan WX, Wei W, Yu Li. A randomized-controlled study of ultrasound prelocation vs anatomical landmark-guided cannulation of the internal jugular vein in infants and children. Paediatr Anaesth. 2005; 15(9): 733–738, doi: 10.1111/j.1460-9592.2004.01547.x, indexed in Pubmed: 16101703.

29. Chudhari LS, Karmarkar US, Dixit RT, et al. Comparison of two different approaches for internal jugular vein cannulation in surgical patients. J Postgrad Med. 1998; 44(3): 57–62, indexed in Pubmed: 10703572.

30. Chung CP, Lin YJ, Chao AC, et al. Jugular venous hemodynamic changes with aging. Ultrasound Med Biol. 2010; 36(11): 1776–1782, doi: 10.1016/j.ultrasmedbio.2010.07.006, indexed in Pubmed: 20800950.

31. Ciuti G, Righi D, Forzoni L, et al. Differences between internal jugular vein and vertebral vein flow examined in real time with the use of multigate ultrasound color Doppler. AJNR Am J Neuroradiol. 2013; 34(10): 2000–2004, doi: 10.3174/ajnr.A3557, indexed in Pubmed: 23721896.

32. Clenaghan S, McLaughlin RE, Martyn C, et al. Relationship between Trendelenburg tilt and internal jugular vein diameter. Emerg Med J. 2005; 22(12): 867–868, doi: 10.1136/emj.2004.019257, indexed in Pubmed: 16299195.

33. Contrera KJ, Aygun N, Ward BK, et al. Internal jugular vein duplication and fenestration: Case series and literature review. Laryngoscope. 2016; 126(7): 1585–1588, doi: 10.1002/lary.25743, indexed in Pubmed: 26498831.

34. Cvetko E. Unilateral fenestration of the internal jugular vein: a case report. Surg Radiol Anat. 2015; 37(7): 875–877, doi: 10.1007/s00276-015-1431-x, indexed in Pubmed: 25875636.

35. da Silva Correia AG, Alves JN, da Mota Santos SA, et al. Anatomical variations in the relationship between the spinal accessory nerve and internal jugular vein: a systematic review and meta-analysis. Int J Oral Maxillofac Surg. 2023; 52(1): 13–18, doi: 10.1016/j.ijom.2022.03.008, indexed in Pubmed: 35367117.

36. Darge K, Brandis U, Zieger B, et al. Internal jugular venous valves in children: high-resolution US findings. Eur Radiol. 2001; 11(4): 655–658, doi: 10.1007/s003300000646, indexed in Pubmed: 11354763.

37. Deepak CA, Sarvadnya JJ, Sabitha KS. Variant anatomy of internal jugular vein branching. Ann Maxillofac Surg. 2015; 5(2): 284–286, doi: 10.4103/2231-0746.175751, indexed in Pubmed: 26981491.

38. Downey LA, Blaine KP, Sliwa J, et al. Positive end-expiratory pressure to increase internal jugular vein size is poorly tolerated in obese anesthetized adults. Anesth Analg. 2014; 119(3): 619–621, doi: 10.1213/ANE.0000000000000347, indexed in Pubmed: 25137000.

39. Downie SA, Schalop L, Mazurek JN, et al. Bilateral duplicated internal jugular veins: case study and literature review. Clin Anat. 2007; 20(3): 260–266, doi: 10.1002/ca.20366, indexed in Pubmed: 16838288.

40. Du Y, Wang J, Jin L, et al. Ultrasonographic assessment of anatomic relationship between the internal jugular vein and the common carotid artery in infants and children after ETT or LMA insertion: a prospective observational study. Front Pediatr. 2020; 8: 605762, doi: 10.3389/fped.2020.605762, indexed in Pubmed: 33194931.

41. El-Shahawy MA, Khilnani H. Carotid-jugular arteriovenous fistula: a complication of temporary hemodialysis catheter. Am J Nephrol. 1995; 15(4): 332–336, doi: 10.1159/000168859, indexed in Pubmed: 7573193.

42. English IC, Frew RM, Pigott JF, et al. Percutaneous cannulation of the internal jugular vein. Thorax. 1969; 24(4): 496–497, doi: 10.1136/thx.24.4.496, indexed in Pubmed: 5795652.

43. Filograna L, Calcagni A, Rossi G, et al. Internal jugular vein agenesis: a rare vascular abnormality and incidental finding. A case of internal jugular vein agenesis in a 52-years old male. Radiol Case Rep. 2019; 14(4): 452–455, doi: 10.1016/j.radcr.2019.01.008, indexed in Pubmed: 30733847.

44. Fujiki M, Guta CG, Lemmens HJM, et al. Is it more difficult to cannulate the right internal jugular vein in morbidly

obese patients than in nonobese patients? Obes Surg. 2008; 18(9): 1157–1159, doi: 10.1007/s11695-008-9590-z, indexed in Pubmed: 18574645.

45. Furukawa S, Nakagawa T, Sakaguchi I, et al. The diameter of the internal jugular vein studied by autopsy. Rom J Leg Med. 2010; 18(2): 125–128, doi: 10.4323/rjlm.2010.125.

46. Giordano CR, Murtagh KR, Mills J, et al. Locating the optimal internal jugular target site for central venous line placement. J Clin Anesth. 2016; 33: 198–202, doi: 10.1016/j.jclinane.2016.03.070, indexed in Pubmed: 27555164.

47. Gok F, Sarkilar G, Kilicaslan A, et al. Comparison of the effect of the Trendelenburg and passive leg raising positions on internal jugular vein size in critically ill patients. Int J Clin Exp Med. 2015; 8(10): 19037–19043, indexed in Pubmed: 26770530.

48. Hashimoto Y, Otsuki N, Morimoto K, et al. Four cases of spinal accessory nerve passing through the fenestrated internal jugular vein. Surg Radiol Anat. 2012; 34(4): 373–375, doi: 10.1007/s00276-011-0875-x, indexed in Pubmed: 21938454.

49. Hernández-Garate YA, Elizondo-Omaña RE, Casas-Murillo CA, et al. Trendelenburg (Head-Down tilt) and head rotation: Ultrasonographic effects on the internal jugular vein for catheterization safety. Clin Anat. 2022; 35(7): 883–890, doi: 10.1002/ca.23884, indexed in Pubmed: 35411564.

50. Horiuchi M, Kamo T, Sugihara H, et al. An adult case of congenital external carotid-jugular arteriovenous fistula with reversible circulatory insufficiency in the cerebellum and lower brain stem. AJNR Am J Neuroradiol. 2001; 22(2): 273–276, indexed in Pubmed: 11156768.

51. Hu J, Zeng Xi, Yuan X. Fetal carotid-jugular fistula: A case report. Medicine (Baltimore). 2019; 98(28): e16250, doi: 10.1097/MD.0000000000016250, indexed in Pubmed: 31305405.

52. Imai M, Hanaoka Y, Kemmotsu O. Valve injury: a new complication of internal jugular vein cannulation. Anesth Analg. 1994; 78(6): 1041–1046, indexed in Pubmed: 8198256.

53. Ishizuka M, Nagata H, Takagi K, et al. Right internal jugular vein is recommended for central venous catheterization. J Invest Surg. 2010; 23(2): 110–114, doi: 10.3109/08941930903469342, indexed in Pubmed: 20497014.

54. Jeon JC, Choi WIk, Lee JHo, et al. Anatomical morphology analysis of internal jugular veins and factors affecting internal jugular vein size. Medicina (Kaunas). 2020; 56(3): 135, doi: 10.3390/medicina56030135, indexed in Pubmed: 32197519.

55. Johnson S, Henderson SO. Myth: the Trendelenburg position improves circulation in cases of shock. CJEM. 2004; 6(1): 48–49, doi: 10.1017/s1481803500008915, indexed in Pubmed: 17433146.

56. Kandiah R, Mohamad I. The louder the bigger: A case of jugular phlebectasia in a child. Malays Fam Physician. 2019; 14(3): 77–79, indexed in Pubmed: 32175047.

57. Kapre M, Mangalgiri AS. Clinical importance of duplication of internal jugular vein. Indian J Otolaryngol Head Neck Surg. 2012; 64(4): 386–388, doi: 10.1007/s12070-011-0410-8, indexed in Pubmed: 24294586.

58. Kayashima K, Ueki M, Kinoshita Y. Ultrasonic analysis of the anatomical relationships between vertebral arteries and internal jugular veins in children. Paediatr Anaesth. 2012; 22(9): 854–858, doi: 10.1111/j.1460-9592.2012.03816.x, indexed in Pubmed: 22340889.

59. Kayiran O, Calli C, Emre A, et al. Congenital agenesis of the internal jugular vein: an extremely rare anomaly. Case Rep Surg. 2015; 2015: 637067, doi: 10.1155/2015/637067, indexed in Pubmed: 25821625.

60. Kim JT, Kim HS, Lim YJ, et al. The influence of passive leg elevation on the cross-sectional area of the internal jugular vein and the subclavian vein in awake adults. Anaesth Intensive Care. 2008; 36(1): 65–68, doi: 10.1177/0310057X0803600111, indexed in Pubmed: 18326134.

61. Kong VKf, Jian CJ, Ji R, et al. Management of an incidental finding of right internal jugular vein agenesis. Hong Kong Med J. 2017; 23(4): 414–415, doi: 10.12809/hkmj166086, indexed in Pubmed: 28775223.

62. Kujur R, Rao MS, Mrinal M. How correct is the correct length for central venous catheter insertion. Indian J Crit Care Med. 2009; 13(3): 159–162, doi: 10.4103/0972-5229.58543, indexed in Pubmed: 20040815.

63. Laganà MM, Pelizzari L, Scaccianoce E, et al. Assessment of internal jugular vein size in healthy subjects with magnetic resonance and semiautomatic processing. Behav Neurol. 2016; 2016: 9717210, doi: 10.1155/2016/9717210, indexed in Pubmed: 27034585.

64. Lagos JC, Riley HD. Congenital intracranial vascular malformations in children. Arch Dis Child. 1971; 46(247): 285–290, doi: 10.1136/adc.46.247.285, indexed in Pubmed: 5314563.

65. Lee AB, Laredo J, Neville R. Embryological background of truncular venous malformation in the extracranial venous pathways as the cause of chronic cerebro spinal venous insufficiency. Int Angiol. 2010; 29(2): 95–108, indexed in Pubmed: 20351665.

66. Lee SC, Han SS, Shin SY, et al. Relationship between positive end-expiratory pressure and internal jugular vein cross-sectional area. Acta Anaesthesiol Scand. 2012; 56(7): 840–845, doi: 10.1111/j.1399-6576.2011.02638.x, indexed in Pubmed: 22288836.

67. Lefrant JY, Cuvillon P, Bénézet JF, et al. Pulsed Doppler ultrasonography guidance for catheterization of the subclavian vein: a randomized study. Anesthesiology. 1998; 88(5): 1195–1201, doi: 10.1097/00000542-199805000-00009, indexed in Pubmed: 9605678.

68. Lepori D, Capasso P, Fournier D, et al. High-resolution ultrasound evaluation of internal jugular venous valves. Eur Radiol. 1999; 9(6): 1222–1226, doi: 10.1007/s003300050822, indexed in Pubmed: 10415266.

69. Lieberman JA, Williams KA, Rosenberg AL. Optimal head rotation for internal jugular vein cannulation when relying on external landmarks. Anesth Analg. 2004; 99(4): 982–988, doi: 10.1213/01.ANE.0000132908.77111.CA, indexed in Pubmed: 15385337.

70. Lim CL, Keshava SN, Lea M. Anatomical variations of the internal jugular veins and their relationship to the carotid arteries: a CT evaluation. Australas Radiol. 2006; 50(4): 314–318, doi: 10.1111/j.1440-1673.2006.01589.x, indexed in Pubmed: 16884415.

71. Lin BS, Kong CW, Tarng DC, et al. Anatomical variation of the internal jugular vein and its impact on temporary haemodialysis vascular access: an ultrasonographic survey in uraemic patients. Nephrol Dial Transplant. 1998; 13(1): 134–138, doi: 10.1093/ndt/13.1.134, indexed in Pubmed: 9481729.

72. López Álvarez JM, Pérez Quevedo O, Santana Cabrera L, et al. Vascular ultrasound in pediatrics: estimation of depth and diameter of jugular and femoral vessels. J Ultrasound. 2017; 20(4): 285–292, doi: 10.1007/s40477-017-0272-3, indexed in Pubmed: 29204232.

73. Luckraz H. Venous pseudo-aneurysm as a late complication of short-term central venous catheterisation. Cardiovasc Ultrasound. 2003; 1: 6, doi: 10.1186/1476-7120-1-6, indexed in Pubmed: 12780937.

74. Magnano C, Belov P, Krawiecki J, et al. Internal jugular vein cross-sectional area enlargement is associated with aging in healthy individuals. PLoS One. 2016; 11(2): e0149532, doi: 10.1371/journal.pone.0149532, indexed in Pubmed: 26895434.

75. Magnano C, Belov P, Krawiecki J, et al. Internal jugular vein narrowing and body mass index in healthy individuals and multiple sclerosis patients. Veins Lymphatics. 2014; 3(3), doi: 10.4081/vl.2014.4632.

76. Mathur M, D'Souza AVL, Prasad D, et al. A comparative study of central versus posterior approach for internal jugular hemodialysis catheter insertion. Indian J Nephrol. 2015; 25(5): 265–268, doi: 10.4103/0971-4065.151356, indexed in Pubmed: 26628790.

77. Mey U, Glasmacher A, Hahn C, et al. Evaluation of an ultrasound-guided technique for central venous access via the internal jugular vein in 493 patients. Support Care Cancer. 2003; 11(3): 148–155, doi: 10.1007/s00520-002-0399-3, indexed in Pubmed: 12618924.

78. Micozkadioglu S, Erkan A. Internal jugular vein anomaly: A lateral branch of the internal jugular vein in the neck. EJENTAS. 2011; 12(1): 77–79, doi: 10.1016/j.ejenta.2011.04.010.

79. Miller BR. Absence of a right internal jugular vein detected by ultrasound imaging. Paediatr Anaesth. 2011; 21(1): 91, doi: 10.1111/j.1460-9592.2010.03472.x, indexed in Pubmed: 21155934.

80. Mitsuda S, Motoyasu A, Tokumine J, et al. Atypical venous valve of the internal jugular vein. J Cardiothorac Vasc Anesth. 2018; 32(1): e30–e31, doi: 10.1053/j.jvca.2017.10.033, indexed in Pubmed: 29203300.

81. Montes-Tapia F, Rodríguez-Taméz A, Hernandez-Garduño A, et al. Vascular assessment of the right internal jugular vein in low birth weight newborns. J Matern Fetal Neonatal Med. 2013; 26(15): 1510–1513, doi: 10.3109/14767058.2013.789853, indexed in Pubmed: 23528221.

82. Moore KL, Persaud TVN, Torchia MG. Before We are Born E-Book: Essentials of Embryology and Birth Defects with STUDENT CONSULT Online Access:. Elsevier Health Sciences 2015.

83. Mumtaz S, Singh M. Surgical review of the anatomical variations of the internal jugular vein: an update for head and neck surgeons. Ann R Coll Surg Engl. 2019; 101(1): 2–6, doi: 10.1308/rcsann.2018.0185, indexed in Pubmed: 30322289.

84. Nagaraja RG, Wilson M, Wilson G, et al. The anatomic relationship between the internal jugular vein and the carotid artery in children after laryngeal mask insertion. An ultrasonographic study. Paediatr Anaesth. 2011; 21(1): 62–64, doi: 10.1111/j.1460-9592.2010.03459.x, indexed in Pubmed: 21155928.

85. Nayak SB. Jug handle tributary of internal jugular vein: a potentially dangerous venous variation. J Craniofac Surg. 2019; 30(1): e7–e8, doi: 10.1097/SCS.0000000000004826, indexed in Pubmed: 30277954.

86. Nayak SB. Split internal jugular vein: surgical and radiological implications. Br J Oral Maxillofac Surg. 2017; 55(8): 870–871, doi: 10.1016/j.bjoms.2017.08.002, indexed in Pubmed: 28843969.

87. Ozbek S, Apiliogullari S, Kıvrak AS, et al. Relationship between the right internal jugular vein and carotid artery at ipsilateral head rotation. Ren Fail. 2013; 35(5): 761–765, doi: 10.3109/0886022X.2013.789970, indexed in Pubmed: 23650892.

88. Parmar S, Parikh S, Mehta H. Anatomical variations of the internal jugular vein in relation to carotid artery: an ultrasound study. Int J Med Sci Public Health. 2013; 2(2): 223, doi: 10.5455/ijmsph.2013.2.215-220.

89. Paschall RM, Mandel S. Brachial plexus injury from percutaneous cannulation of the internal jugular vein. Ann Emerg Med. 1983; 12(1): 58–60, doi: 10.1016/s0196-0644(83)80141-3, indexed in Pubmed: 6849530.

90. Pelizzari L, Laganà MM, Jakimovski D, et al. Neck vessel cross-sectional area measured with MRI: scan-rescan reproducibility for longitudinal evaluations. J Neuroimaging. 2018; 28(1): 48–56, doi: 10.1111/jon.12488, indexed in Pubmed: 29205670.

91. Peres PW. Positioning central venous catheters — a prospective survey. Anaesth Intensive Care. 1990; 18(4): 536–539, doi: 10.1177/0310057X9001800422, indexed in Pubmed: 2268022.

92. Prades JM, Timoshenko A, Dumollard JM, et al. High duplication of the internal jugular vein: clinical incidence in the adult and surgical consequences, a report of three clinical cases. Surg Radiol Anat. 2002; 24(2): 129–132, doi: 10.1007/s00276-002-0020-y, indexed in Pubmed: 12197023.

93. Prasad S, Kumar J, Reddy C, et al. Ultrasonographic study of anatomical characteristics of internal jugular vein in relation to common carotid artery. J Dr NTR Univ Health Sci. 2014; 3(2): 97, doi: 10.4103/2277-8632.134847.

94. Puca AE, Pignatelli F. An adult case of idiopathic internal carotid-internal jugular vein arteriovenous fistula. Ann Vasc Surg. 2015; 29(4): 842.e5–842.e7, doi: 10.1016/j.avsg.2014.12.030, indexed in Pubmed: 25749610.

95. Quiroga-Garza A, Fernandez-Rodarte B, Alvarez-Villalobos N, et al. Anatomical changes of the internal jugular vein with Trendelenburg position: A systematic review and meta-analysis. FASEB J. 2021: 35.

96. Rewari V, Chandran R, Ramachandran R, et al. Absent internal jugular vein: Another case for ultrasound guided vascular access. Indian J Crit Care Med. 2015; 19(1): 53–54, doi: 10.4103/0972-5229.148652, indexed in Pubmed: 25624653.

97. Roberts JR. Roberts and Hedges' Clinical Procedures in Emergency Medicine and Acute Care, Salim R. Rezaie, E.C. Coffey, Christopher R. McNeil, Central Venous Catheterization and Central Venous Pressure Monitoring. Seventh Edition, Elsevier 2019.

98. Rossi A, Tortori-Donati P. Internal jugular vein phlebectasia and duplication: case report with magnetic resonance angiography features. Pediatr Radiol. 2001; 31(2): 134, doi: 10.1007/s002470000350, indexed in Pubmed: 11214685.

99. Roth B, Marciniak B, Engelhardt T, et al. Anatomic relationship between the internal jugular vein and the carotid artery in preschool children--an ultrasonographic study. Paediatr Anaesth. 2008; 18(8): 752–756, doi: 10.1111/j.1460-9592.2008.02635.x, indexed in Pubmed: 18613933.

100. Saiki K, Tsurumoto T, Okamoto K, et al. Relation between bilateral differences in internal jugular vein caliber and flow patterns of dural venous sinuses. Anat Sci Int. 2013; 88(3): 141–150, doi: 10.1007/s12565-013-0176-z, indexed in Pubmed: 23572397.

101. Samerchua A, Kongwatmai K, Boonsri S, et al. A Comparison of the external anatomical landmark and the radiological landmark for obtaining the optimal depth of a right internal jugular venous catheter in pediatric cardiac patients. Paediatr Anaesth. 2020; 30(4): 490–497, doi: 10.1111/pan.13836, indexed in Pubmed: 32011044.

102. Sayin MM, Mercan A, Koner O, et al. Internal jugular vein diameter in pediatric patients: are the J-shaped guidewire diameters bigger than internal jugular vein? An evaluation with ultrasound. Paediatr Anaesth. 2008; 18(8): 745–751, doi: 10.1111/j.1460-9592.2008.02631.x, indexed in Pubmed: 18544148.

103. Schievink WI, Piepgras DG, Nichols DA. Spontaneous carotid-jugular fistula and carotid dissection in a patient with multiple intracranial arachnoid cysts and hemifacial atrophy: a generalized connective tissue disorder? Case report. J Neurosurg. 1995; 83(3): 546–549, doi: 10.3171/jns.1995.83.3.0546, indexed in Pubmed: 7666235.

104. Seong H, Kang B, Kim G. Comparison of internal jugular vein dilation between Valsalva maneuver and proximal internal jugular vein compression. Clin Exp Emerg Med. 2016; 3(4): 193–196, doi: 10.15441/ceem.15.098, indexed in Pubmed: 28168225.

105. Shenkman Z, Shir Y, Brodsky JB. Perioperative management of the obese patient. Br J Anaesth. 1993; 70(3): 349–359, doi: 10.1093/bja/70.3.349, indexed in Pubmed: 8471381.

106. Shoja MM, Ardalan MR, Tubbs RS, et al. The relationship between the internal jugular vein and common carotid artery in the carotid sheath: the effects of age, gender and side. Ann Anat. 2008; 190(4): 339–343, doi: 10.1016/j.aanat.2008.04.002, indexed in Pubmed: 18595678.

107. Sigaut S, Skhiri A, Stany I, et al. Ultrasound guided internal jugular vein access in children and infant: a meta-analysis of published studies. Paediatr Anaesth. 2009; 19(12): 1199–1206, doi: 10.1111/j.1460-9592.2009.03171.x, indexed in Pubmed: 19863734.

108. Silva MA, Deen KI, Fernando DJS, et al. The internal jugular vein valve may have a significant role in the prevention of venous reflux: evidence from live and cadaveric human subjects. Clin Physiol Funct Imaging. 2002; 22(3): 202––205, doi: 10.1046/j.1475-097x.2002.00418.x, indexed in Pubmed: 12076346.

109. Sivasubramaniam S, Hiremath M. Central Venous Catheters: Do we need to Review Practice on Positioning? J Intensive Care Soc. 2008; 9(3): 228–231, doi: 10.1177/175114370800900307.

110. Som PM, Shugar JM, Sacher M, et al. Internal jugular vein phlebectasia and duplication: CT features. J Comput Assist Tomogr. 1985; 9(2): 390–392, doi: 10.1097/00004728-198503000-00035, indexed in Pubmed: 3973172.

111. Stonelake PA, Bodenham AR. The carina as a radiological landmark for central venous catheter tip position. Br J Anaesth. 2006; 96(3): 335–340, doi: 10.1093/bja/aei310, indexed in Pubmed: 16415318.

112. Suarez T, Baerwald JP, Kraus C. Central venous access: the effects of approach, position, and head rotation on internal jugular vein cross-sectional area. Anesth Analg. 2002; 95(6): 1519–1524, doi: 10.1097/00000539-200212000-00010, indexed in Pubmed: 12456410.

113. Tartière D, Seguin P, Juhel C, et al. Estimation of the diameter and cross-sectional area of the internal jugular veins in adult patients. Crit Care. 2009; 13(6): R197, doi: 10.1186/cc8200, indexed in Pubmed: 20003190.

114. Tejada S, Hernando J, Carrió M, et al. Absence of a right internal yugular vein, an ultrasound finding. Rev Esp Anestesiol Reanim. 2015; 62(1): 56–57, doi: 10.1016/j.redar.2014.01.009, indexed in Pubmed: 24612590.

115. Tempe DK, Virmani S, Agarwal J, et al. The success rate and safety of internal jugular vein cannulation using anatomical landmark technique in patients undergoing cardiothoracic surgery. Ann Card Anaesth. 2013; 16(1): 16–20, doi: 10.4103/0971-9784.105364, indexed in Pubmed: 23287081.

116. Thakur J, Sharma D, Mohindroo N. Double Fenestration of the Internal Jugular Vein: A Rare Anatomic Variant. Ear, Nose Throat J. 2019; 91(10): 420–427, doi: 10.1177/014556131209101004.

117. Torres C, Hogan M, Patro S, et al. Extracranial Venous abnormalities: A true pathological finding in patients with multiple sclerosis or an anatomical variant? Eur Radiol. 2017; 27(1): 239–246, doi: 10.1007/s00330-016-4314-6, indexed in Pubmed: 27011374.

118. Towbin AJ, Kanal E. A review of two cases of fenestrated internal jugular veins as seen by CT angiography. AJNR Am J Neuroradiol. 2004; 25(8): 1433–1434, indexed in Pubmed: 15466347.

119. Troianos CA, Kuwik RJ, Pasqual JR, et al. Internal jugular vein and carotid artery anatomic relation as determined by ultrasonography. Anesthesiology. 1996; 85(1): 43–48, doi: 10.1097/00000542-199607000-00007, indexed in Pubmed: 8694381.

120. Tubbs RS, Shoja MM, Loukas M. Bergman's Comprehensive Encyclopedia of Human Anatomic Variation. John Wiley & Sons, Incorporated, Hoboken, USA 2016.

121. Turker G, Kaya FN, Gurbet A, et al. Internal jugular vein cannulation: an ultrasound-guided technique versus a landmark-guided technique. Clinics (Sao Paulo). 2009; 64(10): 989–992, doi: 10.1590/S1807-59322009001000009, indexed in Pubmed: 19841706.

122. Uecker FC, Wüstenberg E, Zahnert T. [High duplication of an internal jugular vein]. Laryngorhinootologie. 2007; 86(8): 592–594, doi: 10.1055/s-2006-945094, indexed in Pubmed: 17219335.

123. Uzumcugil F, Ekinci S. Ultrasound-guided anatomical evaluation of right internal jugular vein in children aged 0-2 years: A prospective observational study. Paediatr Anaesth. 2020; 30(8): 934–940, doi: 10.1111/pan.13961, indexed in Pubmed: 32618403.

124. Uzumcugil F, Yilbas AA, Akca B. Ultrasound-guided anatomical evaluation and percutaneous cannulation of the right internal jugular vein in infants <4000 g. J Vasc Access. 2020; 21(1): 92–97, doi: 10.1177/1129729819845620, indexed in Pubmed: 31081445.

125. Vaidya GN, Ghafghazi S. Correlation of internal jugular and subclavian vein diameter variation on bedside ultrasound with invasive right heart catheterization. Indian Heart J. 2021; 73(2): 231–235, doi: 10.1016/j.ihj.2021.01.024, indexed in Pubmed: 33865526.

126. Valecchi D, Bacci D, Gulisano M, et al. Internal jugular vein valves: an assessment of prevalence, morphology and competence by color Doppler echography in 240 healthy subjects. Ital J Anat Embryol. 2010; 115(3): 185–189, indexed in Pubmed: 21287973.

127. van Haeften TW, van Pampus EC, Boot H, et al. Cardiac tamponade from misplaced central venous line in pericardiophrenic vein. Arch Intern Med. 1988; 148(7): 1649–1650, doi: 10.1001/archinte.148.7.1649, indexed in Pubmed: 3382311.

128. Verghese ST, McGill WA, Patel RI, et al. Ultrasound-guided internal jugular venous cannulation in infants: a prospective comparison with the traditional palpation method. Anesthesiology. 1999; 91(1): 71–77, doi: 10.1097/00000542-199907000-00013, indexed in Pubmed: 10422930.

129. Verghese ST, McGill WA, Patel RI, et al. Comparison of three techniques for internal jugular vein cannulation in infants. Paediatr Anaesth. 2000; 10(5): 505–511, doi: 10.1046/j.1460-9592.2000.00554.x, indexed in Pubmed: 11012954.

130. Vinchurkar K, Patil R. Aberrant posterolateral tributary to IJV. IP Indian J Anat Surg Head Neck Brain. 2019; 4(2): 38–39, doi: 10.18231/2581-5229.2018.0010.

131. Wang M, Fan W, Mungur R, et al. Endovascular treatment of congenital internal carotid-jugular fistula. Front Neurol. 2018; 9: 1118, doi: 10.3389/fneur.2018.01118, indexed in Pubmed: 30619070.

132. Wang X, Peng L, Guo H, et al. Internal jugular vein fenestration and duplication: anatomical findings, prevalence, and literature review. Front Surg. 2020; 7: 593367, doi: 10.3389/fsurg.2020.593367, indexed in Pubmed: 33282909.

133. Weeden D, Abel M. Malposition of a central venous catheter. Br J Anaesth. 1982; 54(1): 109, doi: 10.1093/bja/54.1.109, indexed in Pubmed: 7055520.

134. Welch M. Patient positioning for surgery and anesthesia. In: Joyce A, Wahr M. FAHA, editor, UpToDate 2022.

135. Werner JD, Siskin GP, Mandato K, et al. Review of venous anatomy for venographic interpretation in chronic cerebrospinal venous insufficiency. J Vasc Interv Radiol. 2011; 22(12): 1681–1691, doi: 10.1016/j.jvir.2011.08.018, indexed in Pubmed: 21975259.

136. Xiao W, Yan F, Ji H, et al. A randomized study of a new landmark-guided vs traditional para-carotid approach in internal jugular venous cannulation in infants. Paediatr Anaesth. 2009; 19(5): 481–486, doi: 10.1111/j.1460-9592.2009.02989.x, indexed in Pubmed: 19453580.

137. Yoon HK, Lee HK, Jeon YT, et al. Clinical significance of the cross-sectional area of the internal jugular vein. J Cardiothorac Vasc Anesth. 2013; 27(4): 685–689, doi: 10.1053/j.jvca.2012.10.007, indexed in Pubmed: 23642889.

138. Yoon SZ, Shin TJ, Kim HS, et al. Depth of a central venous catheter tip: length of insertion guideline for pediatric patients. Acta Anaesthesiol Scand. 2006; 50(3): 355–357, doi: 10.1111/j.1399-6576.2006.00951.x, indexed in Pubmed: 16480470.

139. Zillioux JM, Krupski TL. Patient positioning during minimally invasive surgery: what is current best practice? Robot Surg. 2017; 4: 69–76, doi: 10.2147/RSRR.S115239, indexed in Pubmed: 30697565.

140. Zimmerman JJ. Fuhrman and Zimmerman's Pediatric Critical Care. Sixth ed 2021.

141. Zivadinov R, Bastianello S, Dake MD, et al. Recommendations for multimodal noninvasive and invasive screening for detection of extracranial venous abnormalities indicative of chronic cerebrospinal venous insufficiency: a position statement of the International Society for Neurovascular Disease. J Vasc Interv Radiol. 2014; 25(11): 1785–94.e17, doi: 10.1016/j.jvir.2014.07.024, indexed in Pubmed: 25255703.

VIA MEDICA

REVIEW ARTICLE

Lung segments from anatomy to surgery

Jakub Wąsik[1], R. Shane Tubbs[2–7], Nicol Zielinska[1], Piotr Karauda[1], Łukasz Olewnik[1]

[1]Department of Anatomical Dissection and Donation, Medical University of Lodz, Poland
[2]Department of Neurosurgery, Tulane University School of Medicine, New Orleans, LA, United States
[3]Department of Neurosurgery and Ochsner Neuroscience Institute, Ochsner Health System, New Orleans, LA, United States
[4]Department of Anatomical Sciences, St. George's University, Grenada, West Indies
[5]Department of Structural and Cellular Biology, Tulane University School of Medicine, New Orleans, LA, United States
[6]Department of Surgery, Tulane University School of Medicine, New Orleans, LA, United States
[7]University of Queensland, Brisbane, Australia

Bronchopulmonary segments are of increasing interest to clinicians because surgical procedures are emerging that maintain as much pulmonary function as possible. The conventional textbook borders between these segments, their many anatomical variations, and their numerous lymphatic or blood vessels, make them challenging for surgeons, especially thoracic surgeons. Fortunately, because imaging techniques such as three-dimensional-computed tomography are developing further, we can see the anatomical structure of the lungs in detail. Moreover, segmentectomy is now seen as an alternative to a more radical lobectomy, especially for lung cancer. This review explores the connection between the anatomical structure of the lungs, especially their segments, and surgical procedures. Further research on minimally invasive surgical procedures is timely as we can diagnose lung cancer and other diseases ever earlier. In this article, we will look at the latest trends in thoracic surgery. Importantly, we propose a classification of lung segments in reference to surgery difficulties due to their anatomy. (Folia Morphol 2024; 83, 1: 20–34)

Keywords: bronchopulmonary segment, lungs, diagnosis, thoracic surgery, anatomy, systematic review, segmentectomy, cancer

INTRODUCTION

In the structure of the lungs we can distinguish specific divisions into lobes, which in turn are divided into bronchopulmonary segments. The right lung has three lobes comprising 10 bronchopulmonary segments. The left lung is divided into two lobes, which also comprise 8–10 segments. Each segment has its own bronchus and is supplied by segmental branches of the pulmonary artery. Their main function is to deliver oxygen to the distal parts of the lungs [52].

Lung anatomy is highly variable, starting with the division into the bronchial tree, in which a cardiac bronchus or tracheal bronchus can be observed [21]. The pulmonary fissures and even the lobes also vary [1, 6]. Finally, the segments are variable; for instance, there can be an additional segment [48].

Pulmonary segments are important in the clinic, starting with computed tomography (CT) imaging showing changes in the lungs. Identifying segments on this basis can be difficult owing to the intersegmental planes of the lungs that divide the lobes into seg-

ments [93], so they are marked in various ways such as by inflation-deflation or applying contrast. One of the most common procedures in thoracic surgery is segmentectomy, in which a specific segment is excised [85]. This is often performed to treat benign lesions or cancer [56]. It can be performed by videotoracoscopy or robot or by open access. Each of these methods has advantages and disadvantages [58].

The main purpose of the present review is to explain how lung anatomy and its variability, especially in the segments, affect surgical procedures such as segmentectomy. Due to the division of the lung segments in the literature based on the bronchus that supplies it, we will make another division of the bronchopulmonary segments. It will be based on intersegmental planes and may facilitate the assessment of the difficulties of the surgery. As lung cancer is still a major challenge in oncology, particular emphasis is placed on minimally invasive procedures such as segmentectomy rather than the more radical lobectomy. This article will contain much information on the topic. We will also refer to one of the newer and less well known surgical procedures, subsegmentectomy.

CONTROVERSY ABOUT DIVISION

It is worth noting how recently the nomenclature relating to segmentation of the lobes of the lungs was adopted. The current account of segmentation was introduced by Jackson and Huber in 1943 [30]. They did not fully agree with the terminology proposed by other researchers because the names of individual segments did not quite correspond to their anatomical orientation in space. Additionally, they observed anatomical variations in the lung fissures, which will be discussed later. Therefore, they concluded that the lungs should be divided according to the bronchial distribution [30].

However, this did not end the discussion about division because, as Boyden [7] observed in 1953, there was still no consistency in marking segment numbers, particularly in relation to the bronchial tree (although he noted that some medical textbooks such as Gray had already adopted the terminology proposed by Jackson and Huber [30]). His objection concerned, *inter alia,* the nomenclature of the B7 and B8 bronchi, especially the omission of the B7 bronchus on the left side of the lung on the basis of comparative anatomy and the rarity of its lesions [7]. Boyden [7] also wished to adhere to the terminology

adopted by Jackson and Huber [30] until the matter was discussed by an international committee [7]. A year later, Kassay [34] commented on this discussion, supporting Boyden's suggestions, and mentioned the subsuperior bronchus, which we will also look at later in view of its clinical implications.

ANATOMY

To begin with, a definition of "the bronchopulmonary segment" is worthwhile. The bronchopulmonary segment is a pyramid-shaped part of a lobe with its base facing towards the pleural surface and its apex facing the root of the lung [52, 77]. Each segment is named after the tertiary bronchus that supplies it, which originates from the secondary lobar bronchus [52].

The three lobes of the right lung are divided into 10 bronchopulmonary segments. The two lobes of the left lung are also divided into 8–10 segments. Each segment is supplied by branches of the left and right pulmonary arteries, which supply the left and right segments, respectively [52]. These branches are further divided into smaller segmental and sub-segmental vessels. The pulmonary artery divides below the aortic arch at the level of the tracheal spur [33].

The segmental and subsegmental pulmonary arteries are generally parallel to the segmental and subsegmental bronchi and are named according to the bronchopulmonary segments they supply [33]. Thus, when a segment is marked as S4, we designate its artery as A4. The same convention is used for veins and bronchi.

At this point, a more precise description of the division into segments is needed [30, 33, 51, 52, 60, 77]. There are three segments in the superior lobe of the right lung, apical (S1), posterior (S2) and anterior (S3), two in the middle lobe, lateral (S4) and medial (S5), and five in the inferior lobe, superior (S6), medial-basal (S7), anterior-basal (S8), lateral-basal (S9) and posterior-basal (S10) [52, 77]. The superior and inferior lobes of the left lung are each divided into five segments. The following are distinguished in the superior lobe: apical (S1), posterior (S2), anterior (S3), superior lingula (S4) and inferior lingula (S5). In the inferior lobe we distinguish: superior (S6), medial basal (S7), anterior basal (S8), lateral basal (S9) and posterior basal (S10) (Figs. 1, 2) [52, 77].

The quoted number of left lung segments (8–10) varies [30, 52, 60] because the medial (S7) and anterior basal (S8) segments are combined into an anter-
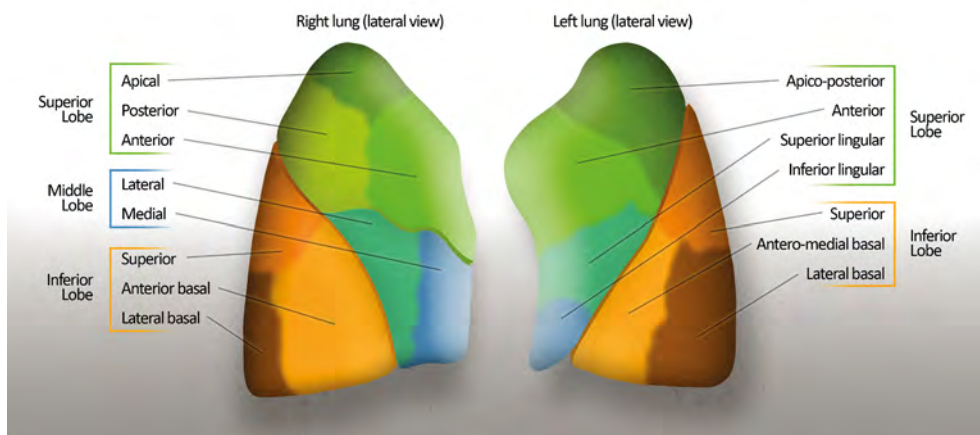
Figure 1. Lateral view of lung segments.
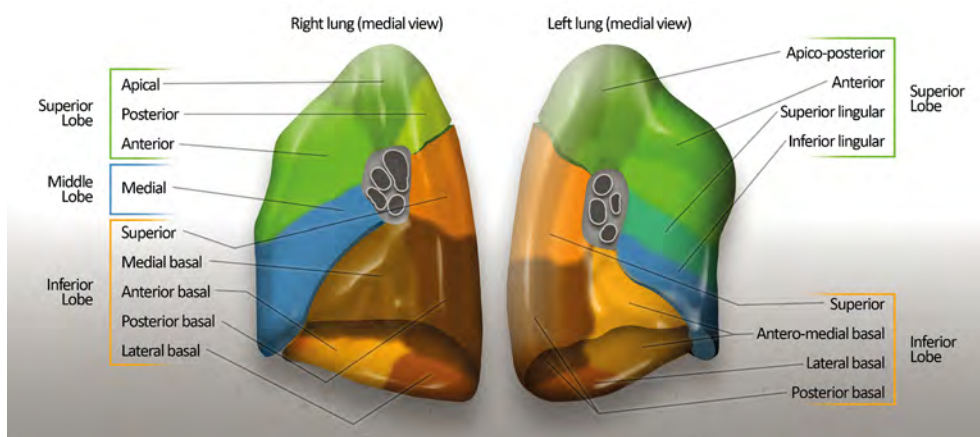
Figure 2. Medial view of lung segments.

omedial segment (S7+S8), while the apical (S1) and posterior (S2) segments together give the apicoposterior segment (S1+S2) [51]. This occurs because the anterior and medial segments originate from a single branch of the lower lobe bronchus [77].

ANATOMICAL VARIATION

The division of the bronchial tree is key to the division of the lungs into segments. Ghaye et al. [21] studied bronchial abnormalities in patients undergoing imaging tests and found that an accessory cardiac bronchus occurred in 14 of 17,500 patients (0.08%). The accessory cardiac bronchus results from an abnormal evolution of the heart bud during the first week of embryo development [4]. Anatomically speaking, it arises from the inner wall of the right main or intermediate bronchus [79].

Another anatomical variant described by Ghaye et al. [21] is the tracheal bronchus, which occurred in 35 patients out of the 17,500 tested (0.2%). Although the name suggests an origin from the trachea, the study showed that most tracheal bronchi originated from distal bronchi (68.6%) and only a few from the trachea (22.9%). The tracheal bronchus is the result of additional tracheal outgrowth early in development [3]. Knowledge of the structure of the lung, in particular its vascularization and the anatomical variations of the fissures, lobes and hilum structures, has important clinical implications. For example, the apical segment can be supplied by two branches of the segmental artery of the lower right lobe [33]. Additional lobes or fissures can cause radiographs to be misinterpreted [63].

Martín-Ruiz et al. [49] studied anatomical variations of the lungs by dissecting the lungs of 17 cadavers and examining bronchoscopies of 50 hospital patients. Only 37.31% of lung pairs showed no variability [49]. In this study, the right lower lobe

Table 1. Comparison of the frequencies of complete, incomplete and absent fissures in lungs based on autopsies

Study	Right lung, frequency %						Left lung, frequency %		
	Oblique fissure			Horizontal fissure			Oblique fissure		
	Complete	Incomplete	Absent	Complete	Incomplete	Absent	Complete	Incomplete	Absent
West et al. (2021) [84]	64.2	35.8	–	22.2	66.7	11.1	81.5	16.0	2.5
Bostanci et al. (2020) [6]	–	68.4	–	–	84.5	4.3	–	63.0	–
Sudikshya et al. (2018) [38]	69.6	30.4	–	52.2	34.8	13.0	48.2	51.9	–
George et al. (2014) [19]	–	3.1	–	–	35.4	3.07	–	15.1	–

showed the highest percentage variability; the middle and left lower lobes showed the lowest. A dissection study by Bostanci et al. [6] also revealed that 77% of lungs had anatomical variations in their fissures (though neither lung had accessory or absent lobes) [6]. Gonlugur et al. [23] conducted bronchoscopies on a large number of patients (1880 male and 670 female) over 8 years to identify major variations of the tracheobronchial tree. The most common variation was a bifurcate pattern in the upper lobe of the right lung, and an additional bronchus after the lingular division in the left. However, these variants were not frequent; only 67 patients (2.6% of the population studied) showed major variations.

The azygos lobe is interesting. It is not an additional lobe, but a part of the upper lobe of the right lung; it does not have its own bronchus and does not correspond to any specific bronchopulmonary segment [1]. It is made up of the arch of the azygos vein, which creates a depression that can be called a fissure in this lobe [50, 77]. Its frequency is low [6, 50, 77], so it can be perceived as a different anatomical structure with or within the lung on CT images, even by some medical residents [2]. Interestingly, as suggested in the extensive study by Yurasakpong et al. [91], it could be associated with genetic factors (such as Turner's syndrome) and/or cardiopulmonary malformation. Because of this anomaly, the apical segment lies on the medial or mediastinal side of the depression [6]. It is usually diagnosed by chance during a chest X-ray or CT [81]. It is also found in children, but has not been implicated in recurrent infections [81]. There are descriptions of the azygos lobe in the literature that also refer to surgery.

The first case we will describe was presented by Akhtar et al. [1]. A 55-year-old male presented with a complaint of dry cough and dyspnoea and chest X-ray and chest CT were performed. The azygos lobe was visible on radiograms thanks to the azygos fis-

sure [1, 50]. This lobe is important in surgery because the azygos vein and its mesenteriole can cover the sympathetic chain [43, 71].

The second case was presented by Gill et al. [22]. During a thoracoscopic sympathectomy, an azygos lobe was spotted in a patient with hyperhidrosis. Care was taken not to injure the azygos vein, otherwise the surgery would have been converted to a thoracotomy [22].

There are also descriptions of a left azygos lobe in the literature, but it is extremely rare [41, 73].

Table 1 shows how many anatomical variants there can be of just one element, i.e. the pulmonary fissure [6, 19, 38, 84].

SURGICAL PROCEDURES

Computed tomography is used to visualize the lung segments. However, as previously mentioned, the automatic formation of images of segments based on CT can be hampered by dissimilarities in pulmonary fissures or disease [63]. Using imaging methods such as CT, it is difficult to distinguish each lung segment by tracking the course of the intersegmental planes of the lungs [93], which divide the lobes into segments. Intersegmental veins also run through these planes [77].

In surgical procedures, inflation-deflation is used to distinguish a segment, using the difference in ventilation between the target and other segments [93]. In this method, the bronchus connected to the segment we want to excise is ligated, while the rest of the lung is inflated by forcing air into the bronchi [31]. This enables us to distinguish visually between the uninflated segment and the rest. Another method, the opposite of inflation-deflation, was presented by Kamiyoshihara et al. [31]. It involves introducing air through a butterfly needle into the selected segmental bronchus, which expands the segment [32, 45]; air is forced into the distal part of the bronchus while the proximal part is constricted [31].

The above-mentioned methods are limited, because if the intersegmental planes are separated by electrocoagulation, air can escape from the intersegmental space and the inflated lung collapses [66]. This of course complicates the procedure because the inflation and deflation line must then be reestablished. Another limitation is the difficulty of locating this plane in emphysema patients [11, 32]. Lung diseases such as emphysema and interstitial pneumonia [56] can lead to pre-indications for surgical procedures such as segmentectomy, which we will focus on later.

One of the newer methods for separating a bronchopulmonary segment is ligation of the target segmental artery, as presented by Zhao et al. [93]. The segmental artery is ligated with a stapler block, and then unilateral ventilation is performed and this artery is cut. The visual changes are observed. The target segment darkens owing to ischaemia and therefore also hypoxia, while the rest of the lungs remain pink [93].

Gao and Liu [18] proposed the designation of arteriopulmonary segments instead of bronchial segments because in most cases studied (90%) the segmental bronchi were accompanied by segmental arteries visible on CT imaging (by administering contrast intravenously [18]). All this could be distinguished owing to the segmented arrangement of the arteries that formed arteriopulmonary segments with visible gaps between them. Moreover, these segments were visible from any viewpoint, anterior, lateral or posterior [18].

The abovementioned intersegmental plane is significant for segmentectomy. If there is only one plane to identify, then segment resection is considered technically simple; however, if there are two or more, it is more challenging for the entire operating team, especially the thoracic surgeon [72]. Intersegmental veins serve as anatomical landmarks for preparing the middle part of the intersegmental plane [56]. In contrast, the demarcation line on the lung surface helps when the peripheral part of the intersegmental plane is prepared [16, 56]. The demarcation line is created on the basis of the previously mentioned difference between segment deflation and inflation, and it is marked by electrocoagulation so the activity does not have to be repeated [37]. For an upper lobe segmentectomy, the middle plane is identified first and then the peripheral one [70].

Anatomical variations of the bronchi are worth mentioning, specifically their influence on treatment. Deviations of bronchial divisions from the norm most often concern the lobes and segmental bronchi [21]. One example of bronchial variation is a displaced left apicoposterior bronchus (B1+2) described by Yanagiya et al. [88]. Left lung segmentectomy (S1+S2) was performed on a male patient with a ground-glass nodule. Of course, chest CT with three-dimensional (3D) imaging was very helpful in this procedure. The bronchial abnormality arose at the back of the left main pulmonary artery, so the bronchus had to be accessed from the posterior side [88].

Maki et al. [48] observed an additional bronchi (B*) in 129 (24.0%) patients undergoing CT imaging. Martín-Ruiz et al. [49] (previously mentioned in the context of anatomical variations of the lungs) provided quantitative information about B*: it occurred in 19.4% of cases, mainly on the right side (most in the right lower lobe, then the right upper lobe). Similar results were obtained by Nagashima et al. [54] from 3D-CT images of patients with changes in the respiratory system or mediastinum before surgery. A subsuperior segmental bronchus was detected in 55 (20.4%) cases [54].

Liu et al. [47] distinguished three types of subsuperior segmental bronchus according to the direction. The first is a posterior bronchus between B6 and B10 (known as the narrow sense of a subsuperior segmental bronchus), observed in 10.5% of patients. The second is a lateral one between B6 and B9 (4.6%) and the third is anterior, between B6 and B8 (1.8%). This bronchus is also associated with a change in the intersegmental plane [47].

If there is a B*, how is it connected to the segment? An additional segment called the subsuperior segment (S*) can be distinguished between S6 and S8-S10, coexisting with the accessory bronchus and having its own vascularization [47, 54]. There is very little literature about S*.

Shimizu et al. [69] described two patients who underwent segmentectomy. The first had two nodules in the S9 and S* segments of the right lung. By applying traction on B* they found an additional segmental artery (A*). The surgeon made a decision about S* segmentectomy with S9 wedge resection on the basis of CT images and tumour location. The second patient had a pulmonary hamartoma at the boundary of the S6 and S* segments. In this case, it was decided to perform a bisegmentectomy. In both cases, the presence of B* and A* had to be taken into account (although there was no additional vein to collect blood from this segment, nor were lymph

vessels mentioned). Sometimes, if the tumour is on the border between two segments, as in the second case, bisegmentectomy should be considered to ensure an appropriate surgical margin [69].

In another case report by Liu et al. [44], the patient had a nodule in S* of the left lower lung. There were anatomical similarities to the earlier case in that the segment had its own bronchus and artery. In this case, removing the nodule by wedge resection would have been difficult, so a segmentectomy was performed. The independent S* resection was intended to ensure more functional reserve. A uniportal VATS was used to minimise muscle and intercostal nerve injury.

Both of these cases can be considered very important for S* segmentectomy. Shimizu et al. [69] were the first to perform the procedure using four ports, while Liu et al. [44] were the first to perform it using a single port. Most importantly, as the authors [69] of the first case report noted, such operations are technically possible. On the other hand, Maki et al. [48] noted that single segmentectomy of S* using pulmonary veins to distinguish the intersegmental planes would be difficult because there are multiple intersegmental veins and S* is a small segment. Interestingly, a subsuperior bronchus, especially in the right lung, had already been described by Kassay [34], who added that it merits an update of the nomenclature.

Other variations concern the previously-mentioned lung fissures. These variations have clinical implications as patients with an incomplete fissure are more likely to experience postoperative air leakage following a lobectomy, which can necessitate a sleeve lobectomy [74]. Sleeve lobectomy is performed if a tumour arises at the origin of a lobar bronchus; it focuses on removing the lobe of the lung with part of the main bronchus [14]. It is not difficult to guess that this location makes resection of the part of the lung affected by the tumour the only possibility, if complete pneumonectomy is to be avoided [14].

We mentioned earlier that 3D-CT using intravenous contrast is needed to visualise the course of the pulmonary vessels. However, the surgeon cannot rely on radiographic images alone; they have a margin of error. Therefore, it is also important to determine the intersegmental plane in the target lung in a different form or as a supplement to inflation-deflation. To determine the segment, indocyanine green (ICG) is administered; it binds to lipoprotein $\alpha 1$ in the blood [17] and fluoresces.

There are different ways to implement this. One is transbronchial administration with an ultrathin bronchoscope [17, 80], followed by airflow to accelerate diffusion. Before the ICG is administered, the target segmental blood vessels and bronchi are separated [90], so the target segment has no blood supply and is therefore non-fluorescent. Another way is to administer the ICG intravenously [53]. An infrared camera is used to observe the coloured segments, which assume a light green colour [80]. The diode emits at 760–805 nm wavelength [17, 53], which is captured by ICG bound to the plasma protein; reflected light with a similar wavelength (830 nm) is then captured by the camera [53]. This method of ICG fluorescence imaging is widely used, not only in segmentectomy, because it has side effects and is simple [17]. The intersegmental planes can be identified quickly in the vast majority (88–95.6%) of cases; the contrast fluorescence is maximum after 20–30 s [53, 64, 90]. In most cases the intersegmental plane disappears within 2 min [64, 90], which should be enough time for the surgeon to mark it by electrocoagulation [37].

It is important not to give too much ICG. As noted by Wada et al. [80], if a nontarget segment has an excess of the solution, dots appear on the referred segment, precluding separation of the intersegmental plane [80]. Another limitation on this method is the variable thickness of the pleura [80], or diseases such as pulmonary emphysema [64].

Zhang et al. [92] reported a new method, evaluated by both *in vivo* research and surgery, for determining interstitial planes by administering methylene blue into the target segmental bronchus using a syringe with an intravenous needle, causing that segment to turn blue [92]. This is an interesting discovery but it has limitations. In the *in vivo* study the blue colour lasted at least 30 min, but the authors [92] did not specify how long it remained during the operation; they only mentioned that the mean was 3 min [92].

SEGMENTECTOMY

One of the most common procedures in thoracic surgery is segmentectomy, involving resection of a given lung segment [85]. The essence of this procedure is to isolate and divide the segmental bronchus, and then excise it along with the peripheral lung parenchyma [89]. Not only the segmental bronchi are excised, but also arteries and intrasegmental veins, with possible preservation of intersegmental veins [85]. In most cases, the surgery begins with ligation of

Table 2. Comparison of histological diagnoses in patients undergoing segmentectomy

	Suzuki et al. [72]	Yamashita et al. [87]	Hwang et al. [29]	Cao et al. [8]
N	552	90	100	809
Squamous cell carcinoma	38 (6.9%)	11 (12%)	15 (15%)	182 (22.5%)
Adenocarcinoma	483 (87.5%)	74 (82%)	80 (80%)	529 (65.4%)
Large cell carcinoma	1 (0.2%)	–	–	–
Non-small carcinoma	30 (5.4%)	–	–	–
Others	–	5 (6%)	5 (5%)	98 (12.1%)

Note: In Yamashita et al. [87], adenocarcinoma *in situ* and minimally invasive adenocarcinoma were also included with adenocarcinoma.

Table 3. Types of segmentectomy

	Pischik and Kovalenko, 2018 [64]	Gossot et al., 2016 [24]	Hwang et al., 2015 [29]	Yamashita el al., 2012 [87]	Ojanguren et al., 2016 [61]
Right lung	40%	41.7%	43.0%	51.1%	47.3%
S1	5.6%	0.4%	–	6.7%	–
S2	8.9%	0.4%	5.0%	6.7%	–
S3	2.2%	1.7%	5.0%	7.8%	0.6%
S6	10%	9.8%	17.0%	10%	10.3%
S7	–	–	1.0%	–	–
S8	1.1%	0.4%	3.0%	2.2%	0.6%
S1+S2	6.7%	17.4%	–	1.1%	23.0%
S9+S10	1.1%	0.9%	–	2.2%	0.6%
Left lung	60%	58.3%	57.0%	48.9%	52.7%
S2	1.1%	0.4%	–	–	0.6%
S3	2.2%	–	–	2.2%	–
S4	–	–	–	1.1%	–
S6	7.8%	14.5%	9.0%	7.8%	13.9%
S8	–	0.9%	–	3.3%	–
S10	1.1%	–	1.0%	–	–
S1+S2	15.6%	7.7%	–	3.3%	7.8%
S9+S10	–	2.1%	–	1.1%	3.6%

the segmental pulmonary vein, and then, depending on the segment, ligation of the bronchus or artery [89]. Segmental bronchi are separated by surgical staplers [11] or ligated with a silk thread [36]. There are several indications for this treatment. It is performed for metastases or benign lesions, and it is an option for early-stage lung cancers such as non-small cell lung cancer, or for patients who are not typed for standard lobectomy [40, 56]. Another indication, although definitely less common, is lung infection [5]. Along with wedge resections, it is one of the most frequently used methods for sublobar resection [36]. Among the most frequently excised segments are those in the superior lobe of the right lung [24, 40]. Table 2 summarizes the histological diagnoses

in patients who underwent segmentectomy, [8, 29, 72, 87] and Table 3 gives the statistics of the types of segmentectomy [24, 29, 61, 64, 87].

For segmentectomy, a chest CT scan is necessary to visualise the veins and arteries [11, 36, 66]. The patient receives intravenous contrast, which shows the courses of blood vessels, making it possible to reconstruct those courses on the images [70]. Three-dimensional tomography has the advantage over two-dimensional because the surgeon can view the image from all sides and freely zoom in and out. This is essential for locating structures, including pathological ones such as a nodule deep in the lung parenchyma on the border between two segments [85]. In such cases, 3D-CT angiography can help to

determine the vascularization of the lung very accurately, along with the tiny arteries around the tumour [55]. It can also assist with imaging during surgery with the C-arm [11].

The C-arm is a great convenience for the surgeon since the lung volume can change because of inflation or collapse. It also allows the location of the tumour to be monitored continuously and its distance assessed. This shows the importance of cooperation between radiologists and surgeons, because radiographic images facilitate the ligation and dissection of segmental vessels and reveal changes [11, 55].

The technical aspects of the procedure should also be discussed, focusing not only on lung cancers or anatomical variations. Segmentectomy is performed under general anaesthesia with double-lumen endotracheal tube intubation [24, 29]. There are several methods of surgical access to the lung segment. Video-assisted thoracic surgery (VATS) can be used, during which the patient lies in the lateral decubitus position, and the working port is performed 4–7 cm in the fourth or fifth intercostal space [24, 32]. The number of access ports is usually 1–4 [56]. Thus, additional ports of smaller diameter can be made, for example in the seventh intercostal space in the anterior axillary line, or the eighth/ninth intercostal space in the posterior axillary line [13, 32]. During the operation with a single-port system, additional ports can be made if the surgeon encounters problems such as difficult access to nodules or pleural adhesions [45]. An endoscope is inserted through one port, which acts as an extension of the surgeon's eye and is necessary throughout the operation. It allows the operation to be previewed on the screen [87]. Before the surgeon starts working on the segment, a preliminary examination is needed to exclude conditions that preclude surgery such as pleural cancer [13].

A more automated variation of VATS is a robotic operation [83] in which the surgeon controls the robotic arms with the surgical instruments using foot pedals and a console [78]. Robot arms mimic the movements of human shoulders and wrists, but have the obvious advantage of filtering out physiological tremor [62]. Although studies show that this is the most expensive treatment option because of the cost of robotic-specific supplies, the hospitalization cost is reduced because the median length of stay is shorter than with VATS and open approaches [15, 58].

Another method is segmentectomy with an open approach [67]. As the name suggests, axillary thoracotomy or posterolateral thoracotomy is performed in this case, with possible muscle sparing [9, 15]. The duration of surgery is shorter than with VATS or the robotic technique, but the median hospital stay is the longest [15, 58].

Since the procedures are aimed at minimising invasiveness, we ask whether, in relation to anaesthesia, new methods are also tested for the benefit of the patient or the medical staff. The literature throws some light on this. Liu et al. [45] recently reported on the possibility of using nonintubated uniportal thoracoscopic segmentectomy instead of intubation for patients with early lung cancer, which could reduce the number of surgical complications resulting from endotracheal intubation. However, as they point out, it is a newly-developed method with risks, such as hypoxia or hypercapnia in patients with impaired respiratory function. These methods without intubation had been proposed earlier; in 2014, a similar method was presented by Hung et al. [28], also using intravenous fentanyl as premedication. The difference lay in the surgical access; a method with three ports was used. Both studies mention the possibility of reflex cough during manipulations around the hilum of the lungs, which can be prevented by a vagal nerve block. The nonintubated method was also described by Liu et al. [46], who noted the importance of studies on the long-term prognosis for patients undergoing such surgery.

It is important to remember lymph drainage in the lungs, including drainage through the intersegmental veins. If these are associated with the tumour their removal should be considered because tumour cells could migrate through the lymphatic vessels [66]. There can be lymph nodes at the beginning of a segmental bronchus, so they must be cleared of lymph and evaluated by a surgeon [24].

Topol and Masłoń [75] observed that a small percentage (5.2%) of lymphatic vessels in their cadaveric study crossed the borders of bronchopulmonary segments. A small proportion of these vessels (7.4%) also run to lymph nodes in another region, so adjacent segments should be carefully observed because of the possibility of metastasis. Watanabe et al. [82] found that patients with non-small cell lung cancer with mediastinal lymph node metastasis (pN2) were more likely to develop upper mediastinal metastases in upper segment lesions than the basal segment. They were also more likely to develop metastases to the pericardium if there was metastasis to the

superior mediastinum [82]. Lin et al. [42] conducted similar studies on adenocarcinoma. They showed that patients with basal segment tumours had a lower probability of freedom from recurrence than those with upper segment tumours [42].

It was mentioned earlier that segmentectomy is an option for patients who do not qualify for lobectomy, which is undoubtedly more extensive surgery. The two methods should be compared to see the potential advantages and disadvantages of segmentecotmy. Compared to lobectomy, performed routinely in lung cancer patients [5], segmentectomy entails slightly more blood loss during surgery, as well as air leakage. However, this difference is not large; the median was 44.5 vs. 50 mL [72] in a study by Suzuki et al. [72] on comparable groups of patients who underwent lobectomy (n = 554) and segmentectomy (n = 552). Another study also reported low intraoperative blood loss in segmentectomy, the median being 60 mL [24]. Segmentectomy also had a shorter mean operation time than lobectomy for stage I of the TNM (tumour, node and metastasis) classification in non-small cell lung cancer, which had a significant impact on the older patients who underwent surgery [40]. There were greater decreases in forced vital capacity, forced expiratory volume in 1 s and maximum voluntary ventilation in patients undergoing lobectomy than segmentectomy (1 year after surgery), although, as in lobectomy, there was a significant decrease in diffusion capacity for carbon monoxide (DLCO) [39]. The risk of complications does not differ significantly from that in lobectomy, the most common ones being bronchopneumonia, prolonged air leak, and atrial fibrillation [5]. Segmentectomy is also associated with low postoperative mortality [5, 24, 40, 72, 87]. To prevent air leakage, continuous over-and-over suturing should be instituted; and to prevent later leakage, sealing materials such as polyglycolic acid felt can be used [32, 37].

Possible complications can also arise from variant anatomy: incorrect division of the intersegmental vein, or the accidental cutting of one of the veins supplying the bronchopulmonary segment, can cause postoperative haemoptysis [27, 85, 86]. Another example is confusion of the variant lingular segmental artery with an anterior segmental artery during a left upper or anterior segmentectomy [85].

The abovementioned anatomical variations show how important anatomical knowledge is for performing a segmentectomy procedure. Cooperation by the patient is also important; he should return regularly for postoperative check-ups, having a chest X-ray and CT scan to ensure that the tumour has been completely resected and there is no recurrence [29].

Is segmentectomy similar for each segment, or are some segments easier or more difficult to access operatively; and if there are differences, where do they come from? The literature indicates that there is no simple answer. Suzuki et al. [72] and Oizumi et al. [59] defined a simple segmentectomy as one that takes place along one intersegmental plane, or has been described in the literature; it concerns the S6 segment of the right lung and the S5-S6 segments of the left lung. More studies focusing on this division including both simple and difficult segmentectomies would be worthwhile because, as Oizumi et al. [59] noted, many factors are involved in the technical difficulty including the angles of the preparation surface, the number of cases described, and the location of the bronchial pulmonary artery within the segment. A similar impression can be obtained from, for example, Yotsukura et al. [90], who described simple segmentectomy with reference to left S1+2 and S3, left S4+5, S6, or basilar segments. It is worth describing the technique of the operation with reference to the abovementioned superior segment. Yang et al. [89] describe the resection beginning with mobilization of the inferior pulmonary vein to identify a vein from the target segment, followed by division of a venous branch with a linear stapler. The artery is then ligated so that the lung parenchyma can be divided.

There is no doubt that segmentectomy is one of the more demanding procedures because of the sizes of the structures involved, and their fleshiness and delicacy. The surgeon aims to minimise the impairment of lung function, so the operation is performed with the use of a camera, which can also be a disadvantage if to the image cannot be seen physically but only by previewing it on screen. For a difficult segmentectomy, the criterion could be, for example, segment size. For instance, S9 and S10 are rather small segments, so creating an intersegmental plane for them can be technically difficult [48].

In a segmentectomy to treat cancer, the surgical margins should be extending at least 2 cm outside the lesion or should be 2 cm greater than the tumour size [72, 85, 86]. For this to be possible, the size of the segment should be taken into account. Ueda et al. [76] showed that the right medial-basal (S7) is smallest and the left apicoposterior segment

Table 4. Division of the bronchopulmonary segments surgery procedures

	Present study		Suzuki et al., 2019 [72]		Handa et al., 2019 [25]		Oizumi et al., 2011 [59]	
	Right lung	Left lung	Right lung	Left lung	Right lung	Left lung	Right lung	Left lung
Simple	S4-S6	S5, S6	S6	S4-S6	S6	S1-S6	S6	S5, S6
Difficult	S1-S3, S7-S10	S1-S4, S7-S10	S1-S5, S7-S10	S1-S3, S7-S10	S1-S5, S7-S10	S7-S10	S1-S5, S7-S10	S1-S4, S7-S10
Classification method	Intersegmental plane		Intersegmental plane		Intersegmental plane and surgical procedures		Intersegmental plane and literature reports	

(S1+S2) largest, which bears on the possibility of segmentectomy of any given segment. This report is very important for anticipating the success of a segmentectomy. However, it has disadvantages, considering that if there is a tumour in S1 or S2, only a S1+S2 bisegmentectomy should be performed. Ueda et al. [76] was cited by Kawakita et al. [37], who reported a successful S7 segmentectomy in a patient with a metastasis in this segment. They noticed that S7 segmentectomy is rare because this segment is so small. Sarsam et al. [65] estimated the volume of the S6 segment from vein, artery and bronchus areas based on CT image reconstruction; the vein gave the largest segmental volume, while the bronchus gave the smallest. This study shows that segment volume and intersegmental planes can differ depending on the reference point adopted [65].

HOW TO DIVIDE A BRONCHOPULMONARY SEGMENT FROM ANATOMY TO SURGERY?

Due to the different operational divisions of all segments into the simple and difficult ones in the above-mentioned literature, we propose division of the segments based on their anatomy. The criterion is the number of intersegmental planes surrounding the segment. It is related to the necessity to mark segments in the case of surgical procedures with the use of intersegmental planes. The segment that is easier to operate on is cut by 1 intersegmental plane, while the more difficult segment is cut by 2 or more. As to S2 in right lung, there are two intersegmental planes — one is a plane between S1 and S2, and the other is a plane between S2 and S3. We believe that this is an objective classification that can be used in operational practice (Table 4) [25, 59, 72].

The division is similar to that in Suzuki et al. [72]; however, they did not distinguish between the S4-S5 split in the left lung, but wrote it as a lingular segment. With reference to their study [72] and Oizumi

et al. [59] wonders why marking S4-S5 segments of the right lung as difficult. From an anatomical point of view, pulmonary vein anomalies such as right middle lobe pulmonary vein may be a challenge for right lung S4 and S5 segmentectomy [68]. The presence of the phrenic nerve near the hilum of the lung is also an important element [20]. But we have not found a clear answer in the literature why they are omitted. The example of how they are omitted is no data in Table 3 for S4 and S5 segmentectomy in the right lung. This can be also explained by the small mean volume in the case of S4, but in the case of S5 it is similar to S6 [12]. The intersegmental planes, not the volume, may be the more important factor. This is shown by an example of a larger mean volume of S4 than S5 in the left lung, yet it is S4 that is considered more difficult in surgery [57].

An interesting division was proposed by Handa et al. [25], who assigned the segmentectomy to the left upper division segment to this simple one. Also in their study, the S4-S5 division in the left lung was not distinguished. This division seems important to us because in the case of the S4 of the left lung, there are two intersegmental planes — between the S3 and S4 and between S4 and S5.

Based on the literature, we believe that separate S4 and S5 segmentectomies of the right lung should also be considered, which are technically possible, but more often performed as S4+S5 bisegmentectomies [20].

SUBSEGMENTECTOMY

An extended segmentectomy can be performed to secure the resection margins, based on incising the adjacent fragments in a non-anatomical way or cutting the adjacent subsegment [66]. This brings us to subsegmentectomy, much less commonly mentioned in the literature than segmentectomy, but meriting a separate section in this review. Since segmental bronchi are divided into lobar bronchi, we

can also add subsegments to them. For example, we can distinguish subsegments S6a, S6b, S6c in the S6 segment of the left lung [35]. A subsegmentectomy is performed for small tumours or when, for example, a tumour is near the pulmonary hilum [35]. The procedure is similar to segmentectomy. It begins with preoperative 3D lung reconstruction using CT after administration of iodinated contrast medium to visualise veins and arteries [26, 35]. The procedure is then performed under general anaesthesia. For lung access, the surgeon can for example perform a single-port thoracoscopy with a 3.5–4.0 cm incision (or 3–5 cm, depending on the operator's decisions and accounts in the literature) at the midaxillary line over the fourth or fifth intercostal space [10, 26]. Anatomically, it achieves the same function as dividing blood vessels and bronchi and then preparating them [26].

Chang et al. [10] compared single-port VATS segmentectomy with single-port VATS subsegmentectomy and showed that subsegmentectomy could have advantages over the former method in selected cases. The operation time was similar in both groups, though slightly shorter for subsegmentectomy (the authors stated that there was a larger proportion of infectious diseases in the segmentectomy group). A greater difference could be seen in another parameter: there was less intraoperative blood loss during subsegmentectomy (median 25.3 vs. 81.4 mL). This is in line with the results of Kato et al. [35], where the median was 19 mL for subsegmentectomy. In a more recent study by the same author [36], who compared segmentectomy and subsegmentectomy patients, there were two statistically significant differences. First, the median time of surgery for the first procedure was longer by 11 min (178 vs. 167 min). Second, the median bleeding from segmentectomy was 40 mL greater (53 vs. 13 mL). These results encourage further development of minimally invasive surgical procedures [10, 35, 36].

CONCLUSIONS

To sum up, lung segments are anatomically variable, for example in the bronchial tree and vascularization or lymph drainage. Despite this known variability, there are no current supplements to them in surgical procedures, as the example of the subsuperior segment shows. Medics must depend on future research focusing on bronchopulmonary segment surgery that will allow the duration of procedures to be reduced and preserve lung functionality. We tried to organize the collected data in the literature on the division of segmentectomy into simple and difficult. We have made an anatomical division which is also used in other clinical studies so we believe that it is possible to extend the surgery to other bronchopulmonary segments.

Ethical approval and consent to participate

The cadavers belonged to the Department of Anatomical Dissection and Donation, Medical University of Lodz.

Conflict of interest: None declared

REFERENCES

1. Akhtar J, Lal A, Martin KB, et al. Azygos lobe: A rare cause of right paratracheal opacity. Respir Med Case Rep. 2018; 23: 136–137, doi: 10.1016/j.rmcr.2018.02.001, indexed in Pubmed: 29719800.
2. Al-Mnayyis A, Al-Alami Z, Altamimi N, et al. Azygos lobe: prevalence of an anatomical variant and its recognition among postgraduate physicians. Diagnostics (Basel). 2020; 10(7), doi: 10.3390/diagnostics10070470, indexed in Pubmed: 32664403.
3. Barat M, Konrad HR. Tracheal bronchus. Am J Otolaryngol. 1987; 8(2): 118–122, doi: 10.1016/s0196-0709(87)80034-0, indexed in Pubmed: 3592078.
4. Barreiro TJ, Gemmel D. Accessory cardiac bronchus. Lung. 2014; 192(5): 821–822, doi: 10.1007/s00408-014-9617-2, indexed in Pubmed: 25001980.
5. Bédat B, Abdelnour-Berchtold E, Perneger T, et al. Comparison of postoperative complications between segmentectomy and lobectomy by video-assisted thoracic surgery: a multicenter study. J Cardiothorac Surg. 2019; 14(1): 189, doi: 10.1186/s13019-019-1021-9, indexed in Pubmed: 31699121.
6. Bostanci K, Ozyurtkan MO, Polat MO, et al. Variations in pulmonary fissural anatomy: a medicolegal autopsy study of 256 cases. ANZ J Surg. 2020; 90(4): 608–611, doi: 10.1111/ans.15553, indexed in Pubmed: 31709740.
7. Boyden EA. A critique of the international nomenclature on bronchopulmonary segments. Dis Chest. 1953; 23(3): 266–269, doi: 10.1378/chest.23.3.266, indexed in Pubmed: 13033655.
8. Cao J, Yuan P, Wang Y, et al. Survival rates after lobectomy, segmentectomy, and wedge resection for non-small cell lung cancer. Ann Thorac Surg. 2018; 105(5): 1483–1491, doi: 10.1016/j.athoracsur.2018.01.032, indexed in Pubmed: 29462591.
9. Carr SR, Schuchert MJ, Pennathur A, et al. Impact of tumor size on outcomes after anatomic lung resection for stage 1A non-small cell lung cancer based on the current staging system. J Thorac Cardiovasc Surg. 2012; 143(2): 390–397, doi: 10.1016/j.jtcvs.2011.10.023, indexed in Pubmed: 22169444.
10. Chang CC, Yen YT, Lin CY, et al. Single-port video-assisted thoracoscopic surgery subsegmentectomy: The learning curve and initial outcome. Asian J Surg. 2020; 43(5):

625–632, doi: 10.1016/j.asjsur.2019.09.009, indexed in Pubmed: 31672480.

11. Chang SS, Okamoto T, Tokunaga Y, et al. Intraoperative computed tomography navigation during thoracoscopic segmentectomy for small-sized lung tumors. Semin Thorac Cardiovasc Surg. 2018; 30(1): 96–101, doi: 10.1053/j.semtcvs.2017.08.005, indexed in Pubmed: 28935510.

12. Daimon T, Fujimoto K, Tanaka K, et al. Volume of pulmonary lobes and segments in chronic obstructive pulmonary diseases calculated using newly developed three-dimensional software. Jpn J Radiol. 2009; 27(3): 115–122, doi: 10.1007/s11604-008-0307-y, indexed in Pubmed: 19412678.

13. D'Amico TA. Thoracoscopic segmentectomy: technical considerations and outcomes. Ann Thorac Surg. 2008; 85(2): S716–S718, doi: 10.1016/j.athoracsur.2007.11.050, indexed in Pubmed: 18222203.

14. De Leyn P, Rots W, Deneffe G, et al. Sleeve lobectomy for non-small cell lung cancer. Acta Chir Belg. 2003; 103(6): 570–576, doi: 10.1080/00015458.2003.11679493, indexed in Pubmed: 14743560.

15. Deen SA, Wilson JL, Wilshire CL, et al. Defining the cost of care for lobectomy and segmentectomy: a comparison of open, video-assisted thoracoscopic, and robotic approaches. Ann Thorac Surg. 2014; 97(3): 1000–1007, doi: 10.1016/j.athoracsur.2013.11.021, indexed in Pubmed: 24480259.

16. Endoh M, Oizumi H, Kato H, et al. How to demarcate intersegmental plane with resected-segments inflation method using the slip knot technique in thoracoscopic anatomic segmentectomy. J Vis Surg. 2017; 3: 100, doi: 10.21037/jovs.2017.06.11, indexed in Pubmed: 29078662.

17. Funai K, Kawase A, Shimizu K, et al. Fluorescence navigation with indocyanine green for identification of intersegmental planes using a photodynamic eye camera. J Thorac Dis. 2020; 12(9): 4817–4824, doi: 10.21037/jtd-20-1448, indexed in Pubmed: 33145054.

18. Gao H, Liu C. Demarcation of arteriopulmonary segments: a novel and effective method for the identification of pulmonary segments. J Int Med Res. 2021; 49(5): 3000605211014383, doi: 10.1177/03000605211014383, indexed in Pubmed: 33990153.

19. George BM, Nayak SB, Marpalli S. Morphological variations of the lungs: a study conducted on Indian cadavers. Anat Cell Biol. 2014; 47(4): 253–258, doi: 10.5115/acb.2014.47.4.253, indexed in Pubmed: 25548723.

20. Gharagozloo F, Meyer M. The technique of robotic anatomic pulmonary segmentectomy I: right sided segments. Mini-invasive Surgery. 2020; 2020, doi: 10.20517/2574-1225.2020.53.

21. Ghaye B, Szapiro D, Fanchamps JM, et al. Congenital bronchial abnormalities revisited. Radiographics. 2001; 21(1): 105–119, doi: 10.1148/radiographics.21.1.g01ja06105, indexed in Pubmed: 11158647.

22. Gill AJ, Cavanagh SP, Gough MJ. The azygos lobe: an anatomical variant encountered during thoracoscopic sympathectomy. Eur J Vasc Endovasc Surg. 2004; 28(2): 223–224, doi: 10.1016/j.ejvs.2004.02.011, indexed in Pubmed: 15234706.

23. Gonlugur U, Efeoglu T, Kaptanoglu M, et al. Major anatomical variations of the tracheobronchial tree: broncho-scopic observation. Anat Sci Int. 2005; 80(2): 111–115, doi: 10.1111/j.1447-073x.2005.00104.x, indexed in Pubmed: 15960317.

24. Gossot D, Lutz J, Grigoroiu M, et al. Thoracoscopic anatomic segmentectomies for lung cancer: technical aspects. J Vis Surg. 2016; 2: 171, doi: 10.21037/jovs.2016.10.04, indexed in Pubmed: 29078556.

25. Handa Y, Tsutani Y, Mimae T, et al. Surgical outcomes of complex versus simple segmentectomy for stage i non-small cell lung cancer. Ann Thorac Surg. 2019; 107(4): 1032–1039, doi: 10.1016/j.athoracsur.2018.11.018, indexed in Pubmed: 30550801.

26. Hong R, Chen C, Zheng W, et al. "Split" combined subsegmentectomy: A case series. Thorac Cancer. 2022; 13(3): 423–429, doi: 10.1111/1759-7714.14275, indexed in Pubmed: 34907669.

27. Hu CG, Yang XT, Zhao M, et al. Three-Dimensional computed tomography bronchography and angiography-guided thoracoscopic segmentectomy for pulmonary nodules. Surg Innov. 2022; 29(3): 343–352, doi: 10.1177/15533506211044389, indexed in Pubmed: 34559004.

28. Hung MH, Hsu HH, Chan KC, et al. Non-intubated thoracoscopic surgery using internal intercostal nerve block, vagal block and targeted sedation. Eur J Cardiothorac Surg. 2014; 46(4): 620–625, doi: 10.1093/ejcts/ezu054, indexed in Pubmed: 24585550.

29. Hwang Y, Kang CH, Kim HS, et al. Comparison of thoracoscopic segmentectomy and thoracoscopic lobectomy on the patients with non-small cell lung cancer: a propensity score matching study. Eur J Cardiothorac Surg. 2015; 48(2): 273–278, doi: 10.1093/ejcts/ezu422, indexed in Pubmed: 25406426.

30. Jackson C, Huber J. Correlated applied anatomy of the bronchial tree and lungs with a system of nomenclature. Dis Chest. 1943; 9(4): 319–326, doi: 10.1378/chest.9.4.319.

31. Kamiyoshihara M, Kakegawa S, Morishita Y. Convenient and improved method to distinguish the intersegmental plane in pulmonary segmentectomy using a butterfly needle. Ann Thorac Surg. 2007; 83(5): 1913–1914, doi: 10.1016/j.athoracsur.2006.06.052, indexed in Pubmed: 17462440.

32. Kamiyoshihara M, Kakegawa S, Ibe T, et al. Butterfly-needle video-assisted thoracoscopic segmentectomy: a retrospective review and technique in detail. Innovations (Phila). 2009; 4(6): 326–330, doi: 10.1097/IMI.0b013e3181c488bb, indexed in Pubmed: 22437229.

33. Kandathil A, Chamarthy M. Pulmonary vascular anatomy & anatomical variants. Cardiovasc Diagn Ther. 2018; 8(3): 201–207, doi: 10.21037/cdt.2018.01.04, indexed in Pubmed: 30057869.

34. Kassay D. Remarks on the international nomenclature of bronchopulmonary segments. Dis Chest. 1954; 26(5): 610–611, doi: 10.1016/s0096-0217(15)32487-0, indexed in Pubmed: 13210171.

35. Kato H, Oizumi H, Inoue T, et al. Port-access thoracoscopic anatomical lung subsegmentectomy. Interact Cardiovasc Thorac Surg. 2013; 16(6): 824–829, doi: 10.1093/icvts/ivt037, indexed in Pubmed: 23427315.

36. Kato H, Oizumi H, Suzuki J, et al. Roles and outcomes of thoracoscopic anatomic lung subsegmentectomy for lung cancer. Interact Cardiovasc Thorac Surg. 2022; 34(1): 81–90, doi: 10.1093/icvts/ivab221, indexed in Pubmed: 34999803.

37. Kawakita N, Toba H, Sakiyama S, et al. A case of thoracoscopic medial basal segmentectomy. Int J Surg Case Rep. 2019; 55: 15–17, doi: 10.1016/j.ijscr.2018.12.004, indexed in Pubmed: 30660053.

38. Kc S, Shrestha P, Shah AK, et al. Variations in human pulmonary fissures and lobes: a study conducted in nepalese cadavers. Anat Cell Biol. 2018; 51(2): 85–92, doi: 10.5115/acb.2018.51.2.85, indexed in Pubmed: 29984052.

39. Keenan RJ, Landreneau RJ, Maley RH, et al. Segmental resection spares pulmonary function in patients with stage I lung cancer. Ann Thorac Surg. 2004; 78(1): 228–233, doi: 10.1016/j.athoracsur.2004.01.024, indexed in Pubmed: 15223434.

40. Kilic A, Schuchert MJ, Pettiford BL, et al. Anatomic segmentectomy for stage I non-small cell lung cancer in the elderly. Ann Thorac Surg. 2009; 87(6): 1662–1667, doi: 10.1016/j.athoracsur.2009.02.097, indexed in Pubmed: 19463574.

41. Lesser MB. Left azygos lobe. Report of a case. Dis Chest. 1964; 46: 95–96, doi: 10.1378/chest.46.1.95, indexed in Pubmed: 14195416.

42. Lin YH, Hung JJ, Yeh YC, et al. Prognostic significance of basal versus superior segment in patients with completely resected lung adenocarcinoma in the lower lobe. Thorac Cancer. 2019; 10(2): 312–320, doi: 10.1111/1759-7714.12957, indexed in Pubmed: 30601596.

43. Lindner HH, Saunders JB. Newer concepts of anatomy of the lungs; advantages to surgeons, internists, bronchoscopist and radiologists. Calif Med. 1952; 76(2): 74–76, indexed in Pubmed: 14905286.

44. Liu G, Hu H, Dong P, et al. Modified left subsuperior segmentectomy via 2-cm uniportal video-assisted thoracoscopic surgery. Surg Today. 2021; 51(1): 172–175, doi: 10.1007/s00595-020-02009-3, indexed in Pubmed: 32328737.

45. Liu HY, Chiang XH, Hung MH, et al. Nonintubated uniportal thoracoscopic segmentectomy for lung cancer. J Formos Med Assoc. 2020; 119(9): 1396–1404, doi: 10.1016/j.jfma.2020.03.021, indexed in Pubmed: 32303399.

46. Liu J, Cui F, Pompeo E, et al. The impact of non-intubated versus intubated anaesthesia on early outcomes of video-assisted thoracoscopic anatomical resection in non-small-cell lung cancer: a propensity score matching analysis. Eur J Cardiothorac Surg. 2016; 50(5): 920–925, doi: 10.1093/ejcts/ezw160, indexed in Pubmed: 27165771.

47. Liu Y, Qiu B, Zhang S, et al. A simplified model for determining the cutting plane during thoracoscopic anatomical partial lobectomy of the right lower lobe. Transl Lung Cancer Res. 2021; 10(7): 3203–3212, doi: 10.21037/tlcr-21-525, indexed in Pubmed: 34430358.

48. Maki R, Miyajima M, Ogura K, et al. Anatomy of the left subsuperior segment for segmentectomy. Surg Today. 2022; 52(7): 1054–1062, doi: 10.1007/s00595-021-02417-z, indexed in Pubmed: 34812942.

49. Martín-Ruiz S, Gutiérrez-Collar C, Forcén Vicente De Vera E, et al. The bronchial segmentation and its anatomical variations. A clinical-anatomic and bronchoscopy study. Ann Anat. 2021; 235: 151677, doi: 10.1016/j.aanat.2021.151677, indexed in Pubmed: 33515691.

50. Mata J, Cáceres J, Alegret X, et al. Imaging of the azygos lobe: normal anatomy and variations. AJR Am J Roentgenol. 1991; 156(5): 931–937, doi: 10.2214/ajr.156.5.2017954, indexed in Pubmed: 2017954.

51. Mehran RJ. Fundamental and Practical Aspects of Airway Anatomy: From Glottis to Segmental Bronchus. Thorac Surg Clin. 2018; 28(2): 117–125, doi: 10.1016/j.thorsurg.2018.02.003, indexed in Pubmed: 29627044.

52. Moore KL, Dalley AF, Agur A. Clinically oriented anatomy (8th ed.). Lippincott Williams and Wilkins. 2017.

53. Mun M, Okumura S, Nakao M, et al. Indocyanine green fluorescence-navigated thoracoscopic anatomical segmentectomy. J Vis Surg. 2017; 3: 80, doi: 10.21037/jovs.2017.05.06, indexed in Pubmed: 29078643.

54. Nagashima T, Shimizu K, Ohtaki Y, et al. Analysis of variation in bronchovascular pattern of the right middle and lower lobes of the lung using three-dimensional CT angiography and bronchography. Gen Thorac Cardiovasc Surg. 2017; 65(6): 343–349, doi: 10.1007/s11748-017-0754-4, indexed in Pubmed: 28197816.

55. Nakamoto K, Omori Ki, Nezu K, et al. Lung Cancer Project Group of West-Seto Inland Sea, Japan. Superselective segmentectomy for deep and small pulmonary nodules under the guidance of three-dimensional reconstructed computed tomographic angiography. Ann Thorac Surg. 2010; 89(3): 877–883, doi: 10.1016/j.athoracsur.2009.11.037, indexed in Pubmed: 20172147.

56. Nakazawa S, Shimizu K, Mogi A, et al. VATS segmentectomy: past, present, and future. Gen Thorac Cardiovasc Surg. 2018; 66(2): 81–90, doi: 10.1007/s11748-017-0878-6, indexed in Pubmed: 29255967.

57. Nakazawa S, Yajima T, Numajiri K, et al. Superior lingular S segmentectomy. Ann Thorac Surg. 2022; 113(2): e141––e144, doi: 10.1016/j.athoracsur.2021.04.050, indexed in Pubmed: 33945813.

58. Novellis P, Bottoni E, Voulaz E, et al. Robotic surgery, video-assisted thoracic surgery, and open surgery for early stage lung cancer: comparison of costs and outcomes at a single institute. J Thorac Dis. 2018; 10(2): 790–798, doi: 10.21037/jtd.2018.01.123, indexed in Pubmed: 29607150.

59. Oizumi H, Kanauchi N, Kato H, et al. Anatomic thoracoscopic pulmonary segmentectomy under 3-dimensional multidetector computed tomography simulation: a report of 52 consecutive cases. J Thorac Cardiovasc Surg. 2011; 141(3): 678–682, doi: 10.1016/j.jtcvs.2010.08.027, indexed in Pubmed: 20884021.

60. Oizumi H, Kato H, Endoh M, et al. Techniques to define segmental anatomy during segmentectomy. Ann Cardiothorac Surg. 2014; 3(2): 170–175, doi: 10.3978/j.issn.2225-319X.2014.02.03, indexed in Pubmed: 24790841.

61. Ojanguren A, Gossot D, Seguin-Givelet A. Division of the intersegmental plane during thoracoscopic segmentectomy: is stapling an issue? J Thorac Dis. 2016; 8(8): 2158–2164, doi: 10.21037/jtd.2016.07.47, indexed in Pubmed: 27621872.

62. Pardolesi A, Park B, Petrella F, et al. Robotic anatomic segmentectomy of the lung: technical aspects and initial results. Ann Thorac Surg. 2012; 94(3): 929–934,

doi: 10.1016/j.athoracsur.2012.04.086, indexed in Pubmed: 22748642.

63. Park J, Yun J, Kim N, et al. Fully automated lung lobe segmentation in volumetric chest CT with 3D U-Net: Validation with Intra- and extra-datasets. J Digit Imaging. 2020; 33(1): 221–230, doi: 10.1007/s10278-019-00223-1, indexed in Pubmed: 31152273.

64. Pischik VG, Kovalenko A. The role of indocyanine green fluorescence for intersegmental plane identification during video-assisted thoracoscopic surgery segmentectomies. J Thorac Dis. 2018; 10(Suppl 31): S3704–S3711, doi: 10.21037/jtd.2018.04.84, indexed in Pubmed: 30505555.

65. Sarsam M, Glorion M, de Wolf J, et al. The role of three-dimensional reconstructions in understanding the intersegmental plane: an anatomical study of segment 6. Eur J Cardiothorac Surg. 2020; 58(4): 763–767, doi: 10.1093/ejcts/ezaa123, indexed in Pubmed: 32359060.

66. Sato M, Murayama T, Nakajima J. Concepts and techniques: how to determine and identify the appropriate target segment in anatomical pulmonary segmentectomy? J Thorac Dis. 2019; 11(3): 972–986, doi: 10.21037/jtd.2019.02.83, indexed in Pubmed: 31019788.

67. Schuchert MJ, Pettiford BL, Pennathur A, et al. Anatomic segmentectomy for stage I non-small-cell lung cancer: comparison of video-assisted thoracic surgery versus open approach. J Thorac Cardiovasc Surg. 2009; 138(6): 1318–13125.e1, doi: 10.1016/j.jtcvs.2009.08.028, indexed in Pubmed: 19931665.

68. Shi Y, Mi S, Shi Y, et al. Evaluation of pulmonary vein anatomy using 256-slice computed tomography. Turk J Med Sci. 2017; 47(5): 1526–1534, doi: 10.3906/sag-1506-84, indexed in Pubmed: 29151328.

69. Shimizu K, Mogi A, Yajima T, et al. Thoracoscopic subsuperior segment segmentectomy. Ann Thorac Surg. 2017; 104(5): e407–e410, doi: 10.1016/j.athoracsur.2017.07.007, indexed in Pubmed: 29054241.

70. Shimizu K, Nakazawa S, Nagashima T, et al. 3D-CT anatomy for VATS segmentectomy. J Vis Surg. 2017; 3: 88, doi: 10.21037/jovs.2017.05.10, indexed in Pubmed: 29078650.

71. Sieunarine K, May J, White GH, et al. Anomalous azygos vein: a potential danger during endoscopic thoracic sympathectomy. Aust N Z J Surg. 1997; 67(8): 578–579, doi: 10.1111/j.1445-2197.1997.tb02046.x, indexed in Pubmed: 9287933.

72. Suzuki K, Saji H, Aokage K, et al. West Japan Oncology Group, Japan Clinical Oncology Group. Comparison of pulmonary segmentectomy and lobectomy: Safety results of a randomized trial. J Thorac Cardiovasc Surg. 2019; 158(3): 895–907, doi: 10.1016/j.jtcvs.2019.03.090, indexed in Pubmed: 31078312.

73. Takasugi JE, Godwin JD. Left azygos lobe. Radiology. 1989; 171(1): 133–134, doi: 10.1148/radiology.171.1.2928516.

74. Taverne Y, Kleinrensink GJ, de Rooij P. Perioperative Identification of an Accessory Fissure of the Right Lung. Case Rep Pulmonol. 2015; 2015: 954769, doi: 10.1155/2015/954769, indexed in Pubmed: 26185701.

75. Topol M, Masłoń A. Some variations in lymphatic drainage of selected bronchopulmonary segments in human lungs. Ann Anat. 2009; 191(6): 568–574, doi: 10.1016/j.aanat.2009.08.008, indexed in Pubmed: 19800774.

76. Ueda K, Tanaka T, Hayashi M, et al. What proportion of lung cancers can be operated by segmentectomy? A computed-tomography-based simulation. Eur J Cardiothorac Surg. 2012; 41(2): 341–345, doi: 10.1016/j.ejcts.2011.05.034, indexed in Pubmed: 21703862.

77. Ugalde P, Camargo Jd, Deslauriers J. Lobes, fissures, and bronchopulmonary segments. Thorac Surg Clin. 2007; 17(4): 587–599, doi: 10.1016/j.thorsurg.2006.12.008, indexed in Pubmed: 18271171.

78. Veronesi G, Novellis P, Perroni G. Overview of the outcomes of robotic segmentectomy and lobectomy. J Thorac Dis. 2021; 13(10): 6155–6162, doi: 10.21037/jtd-20-1752, indexed in Pubmed: 34795966.

79. Volpe A, Bozzetto S, Baraldi E, et al. Accessory-lobed accessory cardiac bronchus: Presentation and treatment in a pediatric patient. Pediatr Pulmonol. 2017; 52(10): E85–E87, doi: 10.1002/ppul.23776, indexed in Pubmed: 28834413.

80. Wada H, Yamamoto T, Morimoto J, et al. Near-Infrared-Guided pulmonary segmentectomy after endobronchial indocyanine green injection. Ann Thorac Surg. 2020; 109(2): 396–403, doi: 10.1016/j.athoracsur.2019.08.083, indexed in Pubmed: 31586621.

81. Wang L, Zhao F, Liu H, et al. Clinical characteristics of 50 children with azygos lobe: a retrospective study. Eur J Pediatr. 2021; 180(8): 2687–2691, doi: 10.1007/s00431-021-04133-9, indexed in Pubmed: 34086104.

82. Watanabe Si, Suzuki K, Asamura H. Superior and basal segment lung cancers in the lower lobe have different lymph node metastatic pathways and prognosis. Ann Thorac Surg. 2008; 85(3): 1026–1031, doi: 10.1016/j.athoracsur.2007.10.076, indexed in Pubmed: 18291191.

83. Wei B, Cerfolio RJ. Robotic lobectomy and segmentectomy: technical details and results. Surg Clin North Am. 2017; 97(4): 771–782, doi: 10.1016/j.suc.2017.03.008, indexed in Pubmed: 28728715.

84. West CT, Slim N, Steele D, et al. Are textbook lungs really normal? A cadaveric study on the anatomical and clinical importance of variations in the major lung fissures, and the incomplete right horizontal fissure. Clin Anat. 2021; 34(3): 387–396, doi: 10.1002/ca.23661, indexed in Pubmed: 32713079.

85. Wu WB, Xu XF, Wen W, et al. Three-dimensional computed tomography bronchography and angiography in the preoperative evaluation of thoracoscopic segmentectomy and subsegmentectomy. J Thorac Dis. 2016; 8(Suppl 9): S710–S715, doi: 10.21037/jtd.2016.09.43, indexed in Pubmed: 28066674.

86. Wu YJ, Shi QT, Zhang Y, et al. Thoracoscopic segmentectomy and lobectomy assisted by three-dimensional computed-tomography bronchography and angiography for the treatment of primary lung cancer. World J Clin Cases. 2021; 9(34): 10494–10506, doi: 10.12998/wjcc.v9.i34.10494, indexed in Pubmed: 35004981.

87. Yamashita Si, Tokuishi K, Anami K, et al. Thoracoscopic segmentectomy for T1 classification of non-small cell lung cancer: a single center experience. Eur J Cardiothorac Surg. 2012; 42(1): 83–88, doi: 10.1093/ejcts/ezr254, indexed in Pubmed: 22228839.

88. Yanagiya M, Yamaguchi H, Hiyama N, et al. Left apicoposterior segmentectomy for lung cancer with displaced segmental bronchus: a case report. J Cardiothorac Surg.

2020; 15(1): 274, doi: 10.1186/s13019-020-01328-3, indexed in Pubmed: 32993707.

89. Yang CFJ, Fitch ZW, Balderson SS, et al. Anatomic thoracoscopic segmentectomy for early-stage lung cancer. J Vis Surg. 2017; 3: 123, doi: 10.21037/jovs.2017.08.19, indexed in Pubmed: 29078683.

90. Yotsukura M, Okubo Yu, Yoshida Y, et al. Indocyanine green imaging for pulmonary segmentectomy. JTCVS Tech. 2021; 6: 151–158, doi: 10.1016/j.xjtc.2020.12.005, indexed in Pubmed: 34318180.

91. Yurasakpong L, Yammine K, Limpanuparb T, et al. The prevalence of the azygos lobe: A meta-analysis of 1,033,083 subjects. Clin Anat. 2021; 34(6): 872–883, doi: 10.1002/ca.23737, indexed in Pubmed: 33908686.

92. Zhang Z, Liao Y, Ai Bo, et al. Methylene blue staining: a new technique for identifying intersegmental planes in anatomic segmentectomy. Ann Thorac Surg. 2015; 99(1): 238–242, doi: 10.1016/j.athoracsur.2014.07.071, indexed in Pubmed: 25440279.

93. Zhao Y, Xuan Y, Song J, et al. A novel technique for identification of the segments based on pulmonary artery plane combined with oxygen diffusing discrepancy. J Thorac Dis. 2019; 11(12): 5427–5432, doi: 10.21037/jtd.2019.11.42, indexed in Pubmed: 32030261.

Morphometry of the heart orifices and morphometry and topography of the coronary ostia in the goat

Karolina Barszcz[1] , Olga Szaluś-Jordanow[2] , Michał Buczyński[3], Michał Czopowicz[4] , Agata Moroz-Fik[4] , Marcin Mickiewicz[4] , Wojciech Mądry[3], Jarosław Kaba[4]

[1]Department of Morphological Sciences, Institute of Veterinary Medicine,
Warsaw University of Life Sciences — SGGW, Warsaw, Poland
[2]Department of Small Animal Diseases with Clinic, Institute of Veterinary Medicine,
Warsaw University of Life Sciences — SGGW, Warsaw, Poland
[3]Department of Cardiac and General Pediatric Surgery, Medical University of Warsaw, Warsaw, Poland
[4]Division of Veterinary Epidemiology and Economics, Institute of Veterinary Medicine,
Warsaw University of Life Sciences — SGGW, Warsaw, Poland

Background: The coronary vessels have been described in various species of domestic and wild ruminants. However, no studies on the detailed morphology and morphometry of heart orifices and coronary ostia in the Polish goat are available.
Materials and methods: The study was carried out on 112 female, adult dairy goats belonging to Polish Fawn Improved and Polish White Improved breed, closely related to French Alpine and Saanen, respectively.
Results: In all examined individuals, all heart orifices and heart valves were of normal structure. There was no significant difference between diameter of the aortic and pulmonary orifice. The right atrioventricular opening was significantly wider than the left atrioventricular opening. The dimension of the left coronary ostium ranged from 1.0 to 5.5 mm with the arithmetic mean (± standard deviation [SD]) of 4.3 ± 0.8 mm. The dimension of the right coronary ostium ranged from 0.5 to 5.0 mm with the arithmetic mean (± SD) of 2.8 ± 0.7 mm. Both coronary artery ostia were located under the sinotubular junction. Out of 112 examined goats, 39 (34.8%) had variations in the structure of the coronary ostia such as the lack of main trunk or the presence of additional coronary ostia. They were observed in one (in 34/39 goats) or both coronary arteries (5/39 goats).
Conclusions: In goats, the dimensions of aortic and pulmonary orifices are similar while the right atrioventricular opening outsizes the left one. On the other hand, the left coronary ostium is wider than the right one. Morphological variations in the coronary ostia occur in approximately one third of goats, more often in the right than in the left ostium. (Folia Morphol 2024; 83, 1: 35–43)
Keywords: aortic orifice, pulmonary orifice, left atrioventricular ostium, right atrioventricular ostium, coronary ostia, heart, goat

Address for correspondence: Dr. Karolina Barszcz, Department of Morphological Sciences, Institute of Veterinary Medicine, Warsaw University of Life Sciences — SGGW, ul. Nowoursynowska 159c, 02–776 Warszawa, Poland, e-mail: karolina_barszcz@sggw.edu.pl

INTRODUCTION

Heart vascularization is a common topic of anatomical studies both in human and veterinary medicine [5, 8, 19, 21, 35, 40–43, 50, 58]. A detailed analysis of the coronary vessels has been performed in domestic and wild ruminants including goats [10], sheep [12, 40], roe deer [20], and European bison [9, 29]. Proper myocardial perfusion is, however, related not only to the architecture of the branches of the main vascular trunks but also to the topography, morphology, and dimensions of the coronary ostia [28].

In human medicine, the assessment of the morphology of heart valves and their anatomical elements, including coronary vessels, is an element of diagnostic process of various diseases and preparation for surgical procedures — coronary angiography, catheterization, and angioplasty [24, 32, 44, 52]. In veterinary medicine, it is performed mostly in animals species which serve as an experimental model for humans in biomedical research in the field of comparative anatomy of the cardiovascular system [6, 7, 13, 16–18, 33, 46, 51, 53, 54]. One of such species is the goat [48, 59]. The available studies lack detailed morphological and morphometric descriptions of the heart valves and the coronary ostia in the domestic goat.

The aim of this study was to determine the dimensions of the heart orifice and coronary ostia and assess their location in aortic sinuses in goats.

MATERIALS AND METHODS

The study was carried out on 112 female, adult dairy goats belonging to Polish Fawn Improved and Polish White Improved breed. These breeds are closely related to French Alpine and Saanen, respectively.

The hearts were collected by the veterinarians (the authors of this manuscript) during diagnostic autopsies carried out immediately after euthanasia. The goats were euthanized due to severe and irreversible clinical signs of caprine arthritis-encephalitis, mainly carpal arthritis. According to Polish law, tests on tissues obtained post-mortem do not require the approval of the Ethics Committee (regulation of the Parliament of the Republic of Poland) [39]. The terminology used in the manuscript was based on the prevailing veterinary nomenclature [36].

Morphologic and morphometric studies

The hearts were rinsed and placed in a hypertonic 0.9% saline solution to remove blood. Next, the pericardial sac was removed and the main vessels were cut out. The hearts were weighed on a laboratory scale (AXIS AD2000, Poland) and examined for signs of hypertrophy of the walls and interventricular septum, possible thickening or fibrosis of the mitral or pulmonary valves, endocardium and myocardium.

In the first stage, morphometry of aortic orifice, pulmonary trunk orifice, left atrioventricular opening, and right atrioventricular opening was performed using Hegar dilators (SPE-MED, Poland) and valve sizers (Trifecta™ Valve Series Sizer Set, Abbott, Abbott Park, IL, USA). Measurements were taken with the precision of 1 mm.

The ascending aorta was cut above the aortic valve commissures. Afterwards, a longitudinal section was made between the aortic valve leaflets to visualize the left coronary ostium and the right coronary ostium. The sinotubular junction was used to determine the location of the ostia in the respective aortic sinuses of the semilunar leaflets (Fig. 1). Then, morphometry of the left coronary artery ostium and right coronary artery ostium was performed with the use of Hegar dilators (SPE-MED, Leszno, Poland). Measurements were taken with the precision of 0.5 mm.

Coronary ostia were visually inspected for the following morphological variations: additional coronary ostium or ostia in the area of the coronary ostium or outside the area of the coronary artery.

Statistical analysis

Categorical variables were expressed as counts and percentages. The 95% confidence intervals (CI 95%) for proportions were calculated using Wilson's score method and the difference in proportions along with CI 95% was calculated using Newcombe's method [2]. Numerical variables were presented as the arithmetic mean, standard deviation (SD), and range. The dimensions of the ostia were compared using the paired-sample t-test (contralateral ostia) or the unpaired-sample t-test (unpaired groups). The homogeneity of variances was confirmed by an insignificant Brown-Forsythe test. The magnitude of the differences was expressed with the mean difference with CI 95%. The correlation between the diameters of the ostia and the heart's weight was investigated using the Pearson's linear correlation coefficient (r) with CI 95% calculated according to Altman et al. [2]. Strength of correlation was classified as follows: r = 0.00 to 0.19 — very weak, 0.20 to 0.49 — weak, 0.50 to 0.69 — moderate, 0.70 to 0.89 — strong, and 0.90 to 1.00 — very strong [1].
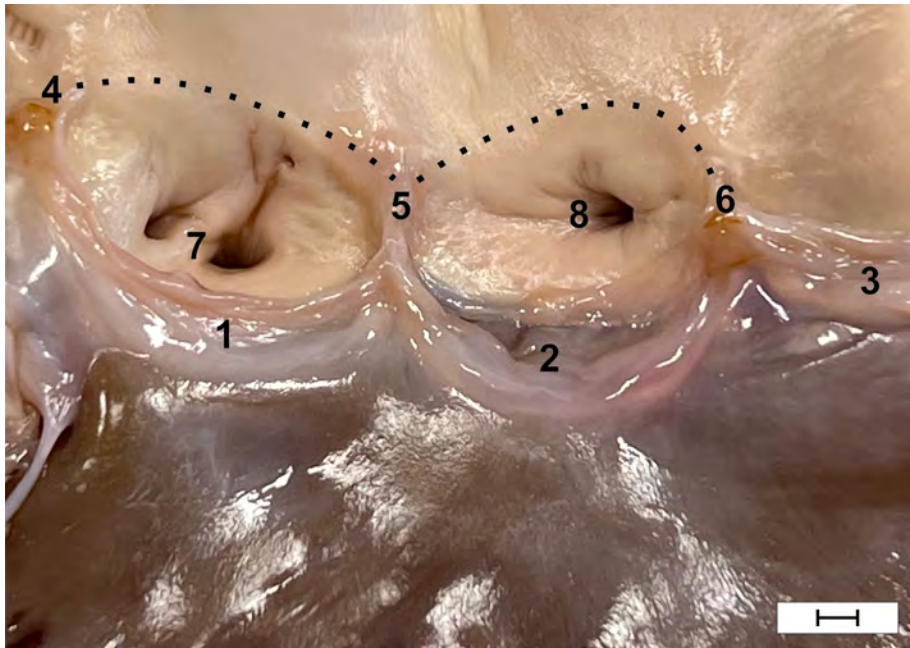
Figure 1. Location of the coronary ostia. The sinotubular junction (dotted lines); 1 — the left semilunar leaflet; 2 — the right semilunar leaflet; 3 — the septal semilunar leaflet; 4 — the left aortic valve commissure; 5 — the intermediary aortic valve commissure; 6 — the right aortic valve commissure; 7 — the left coronary ostium; 8 — the right coronary ostium. Scale bar: 2 mm.

All statistical tests were two-sided and a significance level (α) was set at 0.05. Statistical analysis was performed in TIBCO Statistica 13.3 (TIBCO Software Inc., Palo Alto, CA, USA).

RESULTS

The heart weight ranged from 43 to 450 g with the arithmetic mean ($\pm$ SD) of 230.5 $\pm$ 60.0 g. In all studied goats, the aortic valve consisted of the three semilunar leaflets: left, right, and septal, that respectively delimited the left coronary, right coronary, and the non-coronary aortic sinuses. The diameter of the aortic orifice ranged from 10 to 23 mm with the arithmetic mean ($\pm$ SD) of 16.4 $\pm$ 2.1 mm (Fig. 2A). On the wall of the aorta, the right and left coronary ostia were observed in the respective aortic sinus. In all examined individuals, the coronary ostia were located under the sinotubular junction (Fig. 1). Variations in the structure of the coronary ostia were observed in 39/112 goats (34.8%, CI 95%: 26.6%–44.0%). In 34/39 goats (87.2%) morphological variations were observed in only one coronary artery — in 11 goats in the left and in 23 goats in the right. In the remaining 5 goats morphological variations were present in both coronary arteries. They were related to the structure of the left and right coronary ostia, or the presence of additional coronary ostia.

Morphological variations of the left coronary artery were found in 16/112 goats (14.3%, CI 95%: 9.0%–22.0%) and were as follows:

— In 11/16 goats (68.8%), two well-defined openings (paraconal interventricular branch and the left circumflex branch) were noted in the area of the left coronary ostium. The close proximity of these structures indicated that these individuals lacked the main left trunk (Fig. 3).

— In 5/16 goats (31.2%), an additional coronary ostium was found outside the area of the left coronary artery. It was located in the aortic sinus of the left semilunar leaflet on the side of the intermediary aortic valve commissure or the left aortic valve commissure (Fig. 4).

Morphometric studies of the left coronary ostium were carried out in 101/112 goats (90.2%) in which the common left trunk was present. The dimension of the left coronary ostium ranged from 1.0 to 5.5 mm with the arithmetic mean ($\pm$ SD) of 4.3 $\pm$ 0.8 mm (Fig. 2B).

The following morphological variations in the right coronary artery were observed in 28/112 goats (25.0%; CI 95%: 17.9%–33.8%):

— in 20/28 goats (71.4%), an additional coronary ostium was noted outside the area of the right coronary artery. It was located in the aortic sinus
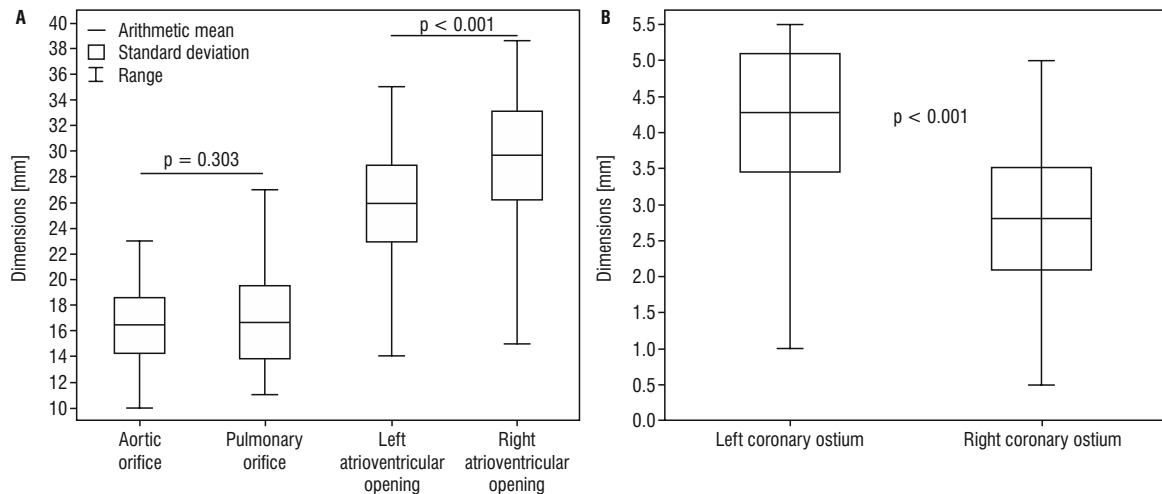
Figure 2. Measurements: **A.** Of heart orifice; **B.** Of coronary ostia.
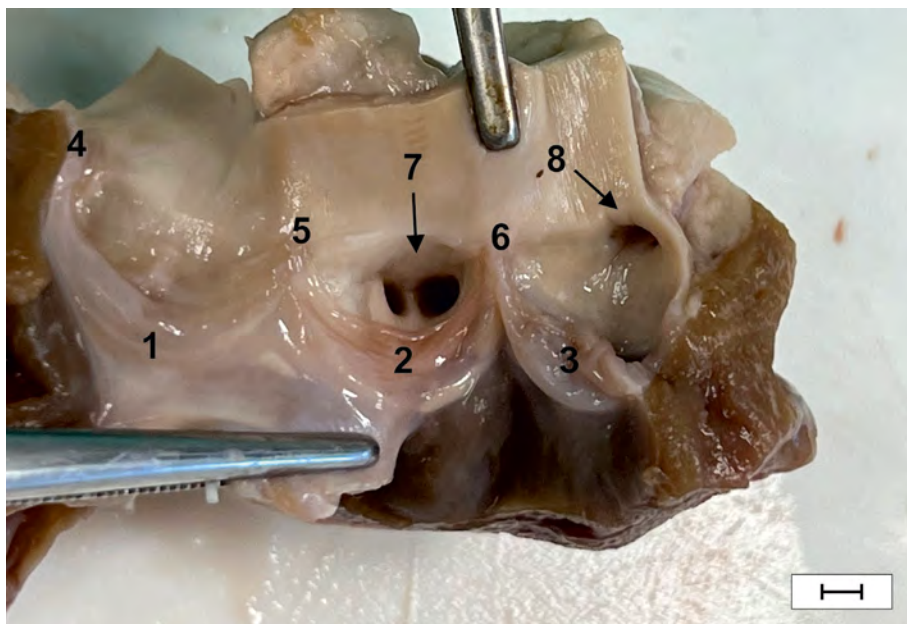
Figure 3. Overview of the aortic valve; 1 — the septal semilunar leaflet; 2 — the left semilunar leaflet; 3 — the right semilunar leaflet; 4 — the right aortic valve commissure; 5 — the left aortic valve commissure; 6 — the intermediary aortic valve commissure; 7 — lack of the main trunk of the left coronary artery; 8 — the right coronary ostium. Scale bar: 3 mm.

of the right semilunar leaflet on the side of the intermediary aortic valve commissure (Fig. 5B);
— in 8/28 goats (28.6%), two additional coronary ostia were found outside the outline of the right coronary ostium. They were located in the aortic sinus of the right semilunar leaflet on the side of the intermediary aortic valve commissure (Fig. 5A).

The dimension of the right coronary ostium ranged from 0.5 to 5.0 mm with the arithmetic mean (± SD) of 2.8 ± 0.7 mm (Fig. 2B). The morphological variations were significantly more common in the right than the left coronary ostium (difference in proportion of 10.7%, CI 95%: 0.4%–20.8%).

The pulmonary valve consisted of the three semilunar leaflets: left, right, and intermediate. The dimension of the pulmonary orifice ranged from 11 to 27 mm with the arithmetic mean (± SD) of 16.7 ± 2.9 mm (Fig. 2A).

The bicuspid valve was composed of the parietal and septal cusp. The dimension of the left atrioventricular opening ranged from 14 to 35 mm with the arithmetic mean (± SD) of 25.9 ± 3.0 mm (Fig. 2A).
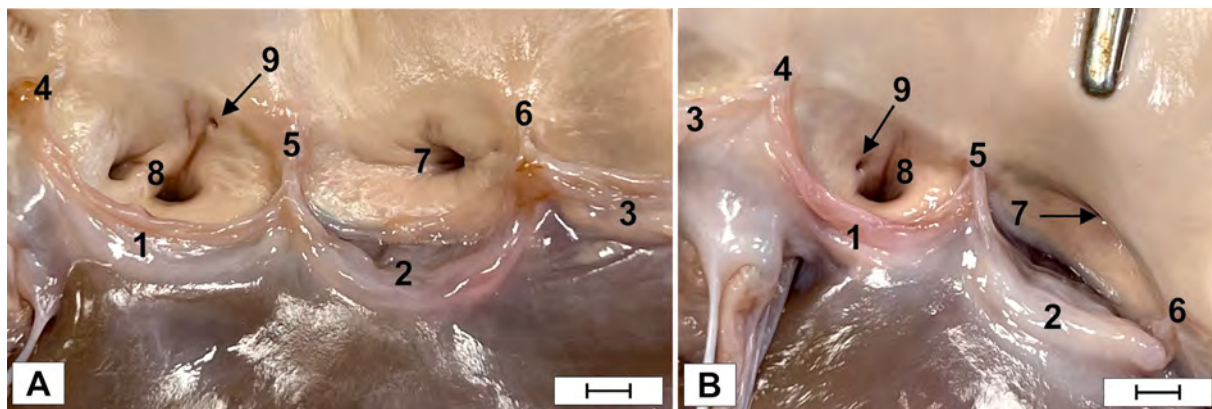
Figure 4. Overview of the aortic valve. **A, B.** The additional coronary ostia in the left aortic sinus; 1 — the left semilunar leaflet; 2 — the right semilunar leaflet; 3 — the septal semilunar leaflet; 4 — left aortic valve commissure; 5 — the intermediary aortic valve commissure; 6 — right aortic valve commissure; 7 — the right coronary ostium; 8 — the left coronary ostium; 9 — the additional coronary ostium. Scale bar: 3 mm.
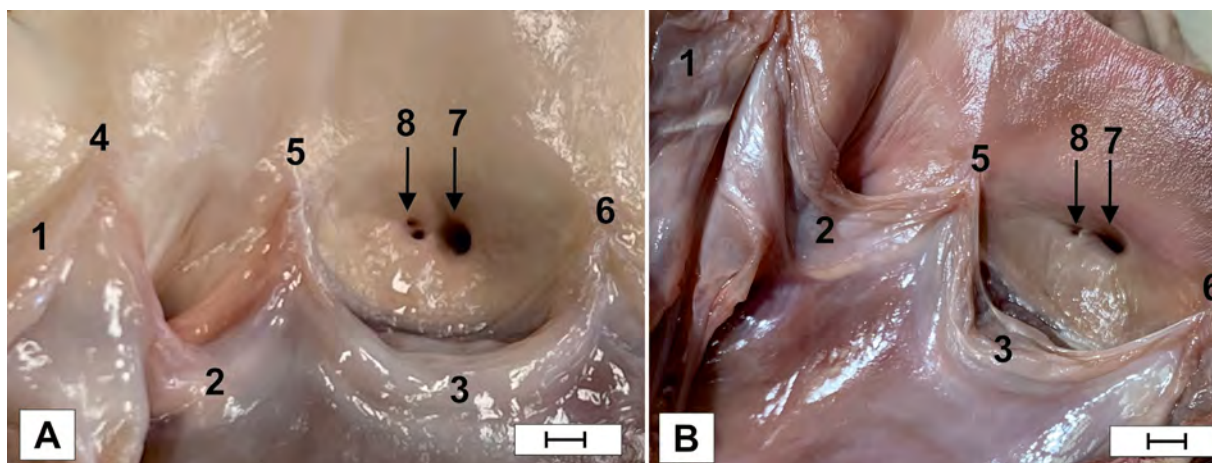
Figure 5. Overview of the aortic valve. **A, B.** The additional coronary ostia in the right aortic sinus; 1 — the septal semilunar leaflet; 2 — the right semilunar leaflet; 3 — the left semilunar leaflet; 4 — left aortic valve commissure; 5 — the intermediary aortic valve commissure; 6 — right aortic valve commissure; 7 — the right coronary ostium; 8 — the additional coronary ostium. Scale bar: 3 mm.

The tricuspid valve consisted of three cusps: parietal, septal, and angular. The dimension of the right atrioventricular opening ranged from 15 to 39 mm with the arithmetic mean (± SD) of 29.7 ± 3.5 mm (Fig. 2A).

There was no significant difference in the dimension between the aortic and pulmonary orifice (the mean difference of –0.2 mm, CI 95%: –0.7 to 0.2 mm; p = 0.303). The right atrioventricular opening was significantly wider than the left atrioventricular opening (the mean difference of 3.8 mm, CI 95%: 3.3–4.3 mm; p < 0.001) (Fig. 2A) and the left coronary ostium was significantly wider than the right coronary ostium (the mean difference of 1.5 mm, CI 95%: 1.3–1.6 mm; p < 0.001) (Fig. 2B).

All the heart dimensions were significantly positively correlated with the heart weight (p < 0.001). The correlation was moderate in the case of the left atrioventricular opening (r = 0.60, CI 95%: 0.47–0.71) and the right atrioventricular opening (r = 0.57, CI 95%: 0.43–0.68) and weak in the case of the pulmonary orifice (r = 0.48, CI 95%: 0.32–0.61), aortic orifice (r = 0.38, CI 95%: 0.21–0.53) as well as the left (r = 0.41, CI 95%: 0.23–0.56), and right coronary ostium (r = 0.31, CI 95%: 0.13–0.47).

There was no significant difference between the dimension of the right coronary ostium in goat in which the right additional ostium was absent (n = 84; 2.8 ± 0.7 mm, range 0.5–5.0 mm) or present (n = 28; 2.9 ± 0.6 mm, range 2.0–4.5 mm; p = 0.469).

Neither was there any significant difference between the dimension of the left coronary ostium in goat in which the left accessory ostium was present (n = 5; 4.0 ± 0.4 mm, range 3.5–4.5 mm) or absent (n = 96; 4.3 ± 0.8 mm, range 1.0–5.5 mm; p = 0.145).

Ethics approval and consent to participate

Parliament of the Republic of Poland: Ustawa z dnia 15 stycznia 2015 r. o ochronie zwierząt wykorzystywanych do celów naukowych lub edukacyjnych. Dz.U. 2015 r. poz. 266. www.dziennikustaw.gov.pl/du/2015/266/D2015000026601.pdf.

DISCUSSION

Publications in the field of human medicine present detailed results of morphometry of the heart orifices, leaflets of the heart valves, and the diameter of the ostia and trunks of the coronary arteries. Based on these studies, surgeries are performed to replace entire valves or their parts, as well as diagnostic and repair procedures on the coronary arteries [4, 14, 15, 26, 30–32, 37, 45, 49, 56]. A substantial development in veterinary cardiology has taken place in recent years. However, only a few morphometric studies on animal hearts have been published. These include European bison [9], cat [6, 7], cattle [22, 23], chicken [11], hamster [13, 17, 18], donkey [38], and dog [3]. This is particularly important in the case of species that are used as biomedical models [55]. The similarity in the size of organs between goats and humans has caused an increase in the usage of these animals; instead of dogs, as a model in cardiological studies. Moreover, societal expectations, emotional connections, and growing costs, have contributed to this [27, 57].

In all examined goats, the coronary arteries were located in the area of the aortic sinus of the semilunar leaflet, left and right, respectively, just below the sinotubular junction. A similar situation was noted in the European bison [9]. For both ruminant species, the sinotubular junction is a well-defined structure. It protrudes towards the lumen of the aorta, which determines the location of the coronary ostia [9]. Therefore, the method proposed by Loukas et al. [30] was used.

To determine the location of the coronary ostia, the authors also use the intercommissural line, which allows for the specification of three types of location — on the intercommissural line, below the intercommissural line, and above the intercommissural line.

The method proposed by Cavalcanti et al. [15] is widely used in human and veterinary medicine [6, 15, 40, 41]. According to this method, it was frequently found that in humans, both coronary ostia were below the intercommissural lines (42% for the left coronary artery, 60% for the right coronary artery). The location of the ostia on the intercommissural lines was observed the least frequently: 18% for the left coronary artery and 12% for the right coronary artery [15].

Observations by Islam et al. [22] also showed differences in the location of the coronary ostia. The authors emphasized that the right coronary ostium in the bovine heart was located above the intercommissural line.

Studies on the location of the coronary ostia were also carried out in domestic cats. Most often, both coronary ostia were located on the intercommissural line — in the case of the left coronary artery in 42 (65%) cats, and the case of the right coronary artery in 43 (66%) cats. Least often, coronary ostia were located above the intercommissural lines — in 6 (9%) subjects for the left coronary artery and 9 (14%) for the right coronary artery [6].

In various animal species, the authors conducted morphological observations regarding the symmetry of the location of the coronary ostia. Pereira et al. [40, 41] described the symmetrical position of the coronary ostia in 45 out of 70 horses, 42 out of 58 sheep, and 16 out of 60 pigs. In the case of the domestic cat, a similar situation was described in 50 out of 65 cats studied [6].

Morphometric observations of the coronary ostia were carried out in subjects with no variations in the structure of the main ostium. In all examined goats, the left coronary artery ostium was larger — the arithmetic mean (± SD) of 4.3 ± 0.8 mm than the right one — the arithmetic mean (± SD) of 2.8 ± 0.7 mm. Similar morphometric ratios were obtained in European bison, in which the left coronary ostium was significantly larger than the right coronary ostium. It was longer by 4.5 mm, and wider by 1.6 mm. Its area was on average 31.6 mm² larger than the right coronary ostium [9]. In the case of the Bactrian camel, the mean diameter of the left coronary artery was 16.98 mm and the right one was 11.08 mm [58]. Research by Ozgel et al. [38] in donkeys also showed that the diameter of the left coronary artery (0.9–1.0 mm) was larger than the diameter of the right coronary artery (0.1–0.3 mm).

In the crab-eating macaque the diameters of the left and right coronary artery were 1.2–2.5 mm (mean 1.8 mm) and 0.7–1.2 mm (mean 0.9 mm), respectively [54]. Similar results were obtained in the green monkey and crab-eating macaque by Nikolic et al. [34] — the average diameter of the left coronary artery was 1.65 ± 0.39, and that of the right one 0.94 ± 0.15 mm.

In the case of the domestic cat, the surface area of the main coronary ostia was measured. In all subjects, the surface area of the left coronary artery (0.54–2.64 mm^2) was greater than the area of the right coronary artery (0.12–1.37 mm^2) [7].

Similar morphometric relationships have been described in human medicine for the coronary ostia. In most of the examined hearts, the ostium of the left coronary artery was larger than the ostium of the right one. This is confirmed by the results obtained by Cavalcanti et al. [15], Kaur et al. [25], Sirikonda and Sreelatha [47].

One third of goats examined in our study had variations related to the structure of the left or right coronary ostia or the presence of additional coronary ostia. Variations were usually observed in only one coronary artery. In veterinary medicine, few publications have described the occurrence of variants of the coronary ostia and additional ones. In the research conducted on the European bison, the morphological varieties of the coronary ostia or the presence of additional coronary ostia were described in 18 out of 27 examined bison (67%). Both in goats and European bison, they more often affected the right coronary artery [9]. In the case of the right coronary artery, similarly to the European bison, the presence of an additional coronary ostia close to the intermediary aortic valve commissure was most often observed. Observations by Pereira et al. [40, 41] showed the presence of additional coronary ostia in 8.6% of horses, 18.6% of sheep [40], and 10% of swine [41]. Studies were also carried out on carnivores. Of the 65 domestic cats examined, 13 (20%) had variations related to the morphology of the coronary ostia or the presence of additional coronary ostia. They were observed both in the left and right coronary arteries [6]. The presence of additional coronary ostia was also found in more than 5% of Syrian hamsters tested [13, 17, 18]. Studies conducted on the vascularization of the heart of green monkeys and crab-eating macaques showed the presence of the third coronary artery [34].

In 10% examined goats, two independent ostia (left circumflex branch and paraconal interventricular branch) were observed instead of the main trunk of the left coronary artery. A similar variation was noted in 5 out of 27 European bison examined (19%) [9]. It was much less frequently reported in carnivores — in 1 out of 20 examined dogs (5%) [35] and 2 out of 65 cats (3%) [6].

It is noteworthy that diseases associated with disorders of the heart's vessels in animals have not been studied in detail. In many cases, it is difficult to assess whether the varied number of coronary vessels can be treated as the independence of larger branches of the main arteries. It should be assumed that their effect on the vascularization of the heart depends on the depth of the variety, i.e. whether it involves the ostium itself or the further course of the vessel.

The analysis of anatomical variations can contribute to obtaining an actual image of the inside of the human and animal body, which is crucial in everyday clinical practice. Deviations from the most common arrangement of specific anatomical structures are common and constitute the actual norm [60].

CONCLUSIONS

The dimensions of aortic and pulmonary orifices are similar while the right atrioventricular opening outsizes the left one. On the other hand, the left coronary ostium is wider than the right one. Morphological variations in the coronary ostia in goats are common and occur in approximately one third of goats, more often in the right than in the left ostium.

Conflict of interest: None declared

REFERENCES

1. Akoglu H. User's guide to correlation coefficients. Turk J Emerg Med. 2018; 18(3): 91–93, doi: 10.1016/j.tjem.2018.08.001, indexed in Pubmed: 30191186.
2. Altman D, Machin D, Bryant T, Gardner M. Statistics with Confidence: Confidence Intervals and Statistical Guidelines, 2nd ed. BMJ Books, Bristol 2000.
3. Alves JR, Wafae N, Beu CC, et al. Morphometric study of the tricuspid valve in dogs. Anat Histol Embryol. 2008; 37(6): 427–429, doi: 10.1111/j.1439-0264.2008.00872.x, indexed in Pubmed: 18798836.
4. Anderson RH, Razavi R, Taylor AM. Cardiac anatomy revisited. J Anat. 2004; 205(3): 159–177, doi: 10.1111/j.0021-8782.2004.00330.x, indexed in Pubmed: 15379923.
5. Barszcz K, Kupczyńska M, Klećkowska-Nawrot J, et al. Arterial coronary circulation in cats. Med Weter. 2014; 70(6): 373–377.

6. Barszcz K, Kupczyńska M, Klećkowska-Nawrot J, et al. Morphology of coronary ostia in domestic shorthair cat. Anat Histol Embryol. 2016; 45(2): 81–87, doi: 10.1111/ahe.12174, indexed in Pubmed: 25639274.

7. Barszcz K, Kupczyńska M, Polguj M, et al. Morphometry of the coronary ostia and the structure of coronary arteries in the shorthair domestic cat. PLoS One. 2017; 12(10): e0186177, doi: 10.1371/journal.pone.0186177, indexed in Pubmed: 29020103.

8. Barszcz K, Kupczyńska M, Wąsowicz M, et al. Patterns of the arterial vascularization of the dog's heart. Med Weter. 2013; 69(9): 531–534.

9. Barszcz K, Polguj M, Klećkowska-Nawrot J, et al. Morphometry and topography of the coronary ostia in the European bison. Folia Morphol. 2020; 79(1): 105–112, doi: 10.5603/FM.a2019.0041, indexed in Pubmed: 30973638.

10. Barszcz K, Szaluś-Jordanow O, Czopowicz M, et al. Topography of coronary arteries and their ramifications in the goat. Biologia. 2019; 74(6): 683–689, doi: 10.2478/s11756-019-00208-z.

11. Bartyzel BJ, Charuta A, Barszcz K, et al. Morphology of the aortic valve of Gallus gallus f. domestica. Bull Vet Inst Pulawy. 2009; 53(1): 147–151.

12. Besoluk K, Tipirdamaz S. Comparative macroanatomic investigations of the venous drainage of the heart in Akkaraman sheep and Angora goats. Anat Histol Embryol. 2001; 30(4): 249–252, doi: 10.1046/j.1439-0264.2001.00327.x, indexed in Pubmed: 11534331.

13. Cardo M, Fernández B, Durán AC, et al. Anomalous origin of the left coronary artery from the dorsal aortic sinus and its relationship with aortic valve morphology in Syrian hamsters. J Comp Pathol. 1995; 112(4): 373–380, doi: 10.1016/s0021-9975(05)80018-0, indexed in Pubmed: 7593759.

14. Cartier R, Ranga A, Mongrain R. Aortic root reconstruction: from principles to numerical modeling. Can J Cardiol. 2005; 21(12): 1071–1076, indexed in Pubmed: 16234892.

15. Cavalcanti JS, de Melo NC, de Vasconcelos RS. Morphometric and topographic study of coronary ostia. Arq Bras Cardiol. 2003; 81(4): 359–362, doi: 10.1590/s0066-782x2003001200003, indexed in Pubmed: 14666278.

16. Crick SJ, Sheppard MN, Ho SY, et al. Anatomy of the pig heart: comparisons with normal human cardiac structure. J Anat. 1998; 1(Part 1): 105–119, doi: 10.1046/j.1469-7580.1998.19310105.x, indexed in Pubmed: 9758141.

17. Durán AC, Arqué JM, Fernández B, et al. Separate origin of the main components of the left coronary artery in Syrian hamsters (Mesocricetus auratus). J Vet Med A Physiol Pathol Clin Med. 2007; 54(6): 297–301, doi: 10.1111/j.1439-0442.2007.00928.x, indexed in Pubmed: 17650149.

18. Durán AC, Fernández MC, Fernández B, et al. Number of coronary ostia in Syrian hamsters (Mesocricetus auratus) with normal and anomalous coronary arteries. Anat Histol Embryol. 2007; 36(6): 460–465, doi: 10.1111/j.1439-0264.2007.00788.x, indexed in Pubmed: 18021357.

19. Erdoğan S, Lima M, Pérez W. Inner ventricular structures and valves of the heart in white rhinoceros (Ceratotherium simum). Anat Sci Int. 2014; 89(1): 46–52, doi: 10.1007/s12565-013-0199-5, indexed in Pubmed: 23979858.

20. Frackowiak H, Jasiczak K, Pluta K, et al. Coronary arteries of the roe deer (Capreolus capreolus; Linnaeus 1758) heart. Pol J Vet Sci. 2007; 10(2): 105–108, indexed in Pubmed: 17882934.

21. Ghazi SR, Tadjalli M. Coronary arterial anatomy of the one-humped camel (Camelus dromedarius). Vet Res Commun. 1993; 17(3): 163–170, doi: 10.1007/BF01839161, indexed in Pubmed: 8284892.

22. Islam MN, Khan ZI, Khan SR, et al. Morphometry of the intercommissural distances and other structures of the aortic valve of bovine heart. Mymensingh Med J. 2006; 15(2): 153–158, doi: 10.3329/mmj.v15i2.35, indexed in Pubmed: 16878096.

23. Islam MN, Khan M, Khan SR, et al. Gross anatomy of the aortic valve of indigenous cattle (bos indicus) of Bangladesh. Bangl J Vet Med. 1970; 4(1): 31–37, doi: 10.3329/bjvm.v4i1.1522.

24. Jyothi SR, Dakshayani KR. Morphometric study of coronary ostia in human cadavers by dissection method. Indian J Clin Anat Physiol. 2017; 4(2): 130–132, doi: 10.18231/2394-2126.2017.0033.

25. Kaur D, Singh K, Nair N, et al. Morphology and morphometry of coronary ostia in South Indian adult human cadaveric hearts. Int J Biol Med Res. 2012; 3: 2169–2171.

26. Kawase I, Ozaki S, Yamashita H, et al. Aortic valve reconstruction of unicuspid aortic valve by tricuspidization using autologous pericardium. Ann Thorac Surg. 2012; 94(4): 1180–1184, doi: 10.1016/j.athoracsur.2012.05.016, indexed in Pubmed: 22771488.

27. Kim WG, Cho SR, Sung SH, et al. A chronic heart failure model by coronary artery ligation in the goat. Int J Artif Organs. 2003; 26(10): 929–934, doi: 10.1177/039139880302601010, indexed in Pubmed: 14636010.

28. Kulkarni P, Paranjpe V. Topography, morphology and morphometry of coronary ostia – cadaveric study. Eur J Anat. 2015; 19(2): 165–170.

29. Kupczyńska M, Barszcz K, Olbrych K, et al. Coronary arteries of the European bison (Bison bonasus). Acta Vet Scand. 2015; 57(1): 82, doi: 10.1186/s13028-015-0173-4, indexed in Pubmed: 26608615.

30. Loukas M, Bilinsky E, Bilinsky S, et al. The anatomy of the aortic root. Clin Anat. 2014; 27(5): 748–756, doi: 10.1002/ca.22295, indexed in Pubmed: 24000000.

31. Misfeld M, Sievers HH. Heart valve macro- and microstructure. Philos Trans R Soc Lond B Biol Sci. 2007; 362(1484): 1421–1436, doi: 10.1098/rstb.2007.2125, indexed in Pubmed: 17581807.

32. Nasr AY, El Tahlawi M. Anatomical and radiological angiographic study of the coronary ostia in the adult human hearts and their clinical significance. Anat Cell Biol. 2018; 51(3): 164–173, doi: 10.5115/acb.2018.51.3.164, indexed in Pubmed: 30310708.

33. Nie Xm, Zhou Yj, Xie Y, et al. [Effect of stent coated with diallyl trisulfide on endothelial structure and function after coronary injury: experiment with dogs]. Zhonghua Yi Xue Za Zhi. 2006; 86(16): 1125–1128, indexed in Pubmed: 16796841.

34. Nikolić V, Teofilovski-Parapid G, Stanković G, et al. Third coronary artery in monkey heart. Acta Vet Hung. 2004; 52(3): 253–257, doi: 10.1556/AVet.52.2004.3.1, indexed in Pubmed: 15379440.

35. Noestelthaller A, Probst A, König HE. Branching patterns of the left main coronary artery in the dog demonstrated by the use of corrosion casting technique. Anat Histol Embryol. 2007; 36(1): 33–37, doi: 10.1111/j.1439-0264.2006.00711.x, indexed in Pubmed: 17266665.

36. Nomina Anatomica Veterinaria sixth edition. Prepared by the International Committee on Veterinary Gross Anatomical Nomenclature (I.C.V.G.A.N.) Published by the Editorial Committee Hanover (Germany), Ghent (Belgium), Columbia, MO (U.S.A.), Rio de Janeiro (Brazil). 2017 With permission of the World Association of Veterinary Anatomists (W.A.V.A.).

37. Oliveira D, Srinivasan J, Espino D, et al. Geometric description for the anatomy of the mitral valve: a review. J Anat. 2020; 237(2): 209–224, doi: 10.1111/joa.13196, indexed in Pubmed: 32242929.

38. Ozgel O, Haligur AC, Dursun N, et al. The macroanatomy of coronary arteries in donkeys (Equus asinus L.). Anat Histol Embryol. 2004; 33(5): 278–283, doi: 10.1111/j.1439-0264.2004.00548.x, indexed in Pubmed: 15352880.

39. Parliament of the Republic of Poland: Ustawa z dnia 15 stycznia 2015 r. o ochronie zwierząt wykorzystywanych do celów naukowych lub edukacyjnych. Dz.U. 2015 r. poz. 266. www.dziennikustaw.gov.pl/du/2015/266/D2015000026601.pdf.

40. Pereira VP, Prates BM, Seyfert CE, et al. Morphological importance of coronary ostia in sheep and swine. Anat Histol Embryol. 2022; 51(3): 339–346, doi: 10.1111/ahe.12793, indexed in Pubmed: 35165926.

41. Pereira VP, Seyfert CE, Santos JML, et al. Morphological importance of coronary ostia in equine. Anat Histol Embryol. 2022; 51(5): 658–665, doi: 10.1111/ahe.12844, indexed in Pubmed: 35894158.

42. Pérez W, Katz H, Lima M. Gross heart anatomy of Arctocephalus australis (Zimmerman, 1783). Anat Sci Int. 2008; 83(1): 6–10, doi: 10.1111/j.1447-073X.2007.00189.x, indexed in Pubmed: 18402082.

43. Rajendra RS, Brady AG, Parks VL, et al. The normal and abnormal owl monkey (Aotus sp.) heart: looking at cardiomyopathy changes with echocardiography and electrocardiography. J Med Primatol. 2010; 39(3): 143–150, doi: 10.1111/j.1600-0684.2010.00403.x, indexed in Pubmed: 20149027.

44. Ramlawi B, Ramchandani M, Reardon MJ. Surgical approaches to aortic valve replacement and repair-insights and challenges. Interv Cardiol. 2014; 9(1): 32–36, doi: 10.15420/icr.2011.9.1.32, indexed in Pubmed: 29588775.

45. Ruvolo G, Fattouch K. Aortic valve-sparing root replacement from inside the aorta using three Dacron skirts preserving the native Valsalva sinuses geometry and stabilizing the annulus. Interact Cardiovasc Thorac Surg. 2009; 8(2): 179–181, doi: 10.1510/icvts.2008.184200, indexed in Pubmed: 19019850.

46. Sahni D, Kaur GD, Jit H, et al. Anatomy & distribution of coronary arteries in pig in comparison with man. Indian J Med Res. 2008; 127(6): 564–570, indexed in Pubmed: 18765875.

47. Sirikonda P, Sreelatha S. Measurements and location of coronary ostia. Int J Biol Med Res. 2012; 3(4): 2489–2496.

48. Shiraishi Y, Yambe T, Yoshizawa M, et al. Examination of mitral regurgitation with a goat heart model for the development of intelligent artificial papillary muscle. Annu Int Conf IEEE Eng Med Biol Soc. 2012; 2012: 6649–6652, doi: 10.1109/EMBC.2012.6347519, indexed in Pubmed: 23367454.

49. Skwarek M, Hreczecha J, Dudziak M, et al. The morphology of the right atrioventricular valve in the adult human heart. Folia Morphol. 2006; 65(3): 200–208, indexed in Pubmed: 16988916.

50. Smodlaka H, Henry RW, Schumacher J, et al. Macroscopic anatomy of the heart of the ringed seal (Phoca hispida). Anat Histol Embryol. 2008; 37(1): 30–35, doi: 10.1111/j.1439-0264.2007.00791.x, indexed in Pubmed: 18197897.

51. Szaluś-Jordanow O, Bonecka J, Pankowski F, et al. Postmortem imaging in goats using computed tomography with air as a negative contrast agent. PLoS One. 2019; 14(4): e0215758, doi: 10.1371/journal.pone.0215758, indexed in Pubmed: 31013296.

52. Tatsuishi W, Nakano K, Kubota S, et al. Identification of coronary artery orifice to prevent coronary complications in bioprosthetic and transcatheter aortic valve replacement. Circ J. 2015; 79(10): 2157–2161, doi: 10.1253/circj.CJ-15-0415, indexed in Pubmed: 26227280.

53. Teofilovski-Parapid G, Kreclović G. Coronary artery distribution in Macaca fascicularis (Cynomolgus). Lab Anim. 1998; 32(2): 200–205, doi: 10.1258/002367798780600007, indexed in Pubmed: 9587903.

54. Teofilovski-Parapid G, Nikolić V, Ranković A, et al. [Coronary arteries in the Macaca fascicularis monkey]. Srp Arh Celok Lek. 1993; 121(8-12): 117–119, indexed in Pubmed: 7725149.

55. Uiterwijk M, van der Valk DC, van Vliet R, et al. Pulmonary valve tissue engineering strategies in large animal models. PLoS One. 2021; 16(10): e0258046, doi: 10.1371/journal.pone.0258046, indexed in Pubmed: 34610023.

56. Warraich HJ, Matyal R, Bergman R, et al. Impact of aortic valve replacement for aortic stenosis on dynamic mitral annular motion and geometry. Am J Cardiol. 2013; 112(9): 1445–1449, doi: 10.1016/j.amjcard.2013.06.013, indexed in Pubmed: 23891429.

57. Xiao-bing L, Zhou Cb, Chen JM, et al. A fetal goat model of cardiopulmonary bypass with cardioplegic arrest and hemodynamic assessment. J Thorac Cardiovasc Surg. 2011; 142(6): 1562–1566, doi: 10.1016/j.jtcvs.2011.06.022, indexed in Pubmed: 21783208.

58. Yuan G, Ma J, Ye W, et al. Macroanatomy of coronary arteries in Bactrian camel (Camelus bactrianus). Vet Res Commun. 2009; 33(4): 367–377, doi: 10.1007/s11259-008-9185-0, indexed in Pubmed: 19011985.

59. Zhang Y, Wang YT, Shan ZL, et al. Role of inflammation in the initiation and maintenance of atrial fibrillation and the protective effect of atorvastatin in a goat model of aseptic pericarditis. Mol Med Rep. 2015; 11(4): 2615–2623, doi: 10.3892/mmr.2014.3116, indexed in Pubmed: 25524260.

60. Żytkowski A, Tubbs R, Iwanaga J, et al. Anatomical normality and variability: Historical perspective and methodological considerations. Trans Res Anat. 2021; 23: 100105, doi: 10.1016/j.tria.2020.100105.

ORIGINAL ARTICLE

Analysis of the regional anatomy of the retro-oesophageal right subclavian artery and surrounding structures

Shigeyuki Esumi*, Yoshihiro Kumagai*, Yoshikazu Koba, Takaichi Fukuda

Department of Anatomy and Neurobiology, Graduate School of Medical Sciences, Kumamoto University, Kumamoto, Japan

Background: The retro-oesophageal right subclavian artery (RRSA) is a congenital anomalous branching of the arch of the aorta. Because its incidence is very low, it has not been fully understood how the RRSA develops during embryogenesis, and thus accumulation of observed findings in newly found cases is important to elucidate the aetiology of the RRSA.

Materials and methods: We encountered a case of the RRSA during the course of gross anatomy dissection for medical students.

Results: The main findings in the present observations are that (a) the RRSA arose from the right side wall of the arch of the aorta as its last branch; (b) the detected RRSA was directed to the right and upward between the oesophagus and vertebral column; (c) the right vertebral artery branched from the RRSA and entered the sixth cervical foramen transversarium; (d) the suprema intercostal artery branched from the costocervical trunk on both sides and its distal branches were distributed to the first and second intercostal spaces; and (e) both sides of bronchial arteries originated from the thoracic aorta.

Conclusions: The present study gives further information about the morphological details of the RRSA leading to better understanding of its developmental process. (Folia Morphol 2024; 83, 1: 44–52)

Key words: gross anatomy, arteria lusoria, bronchial artery, dorsal aorta, non-recurrent laryngeal nerve

INTRODUCTION

Aberrant right subclavian artery (ARSA), also named the arteria lusoria, is an embryologically derived rare variations of aortic arch branching that arises directly from the aortic arch as fourth branch. The reported incidence of ARSA ranges from 0.2% to 1.6% in Japanese [2, 9, 10, 13, 14, 23, 26] and 0.2% to 4.4% of population in other countries [1, 3–5, 7, 11, 12, 15, 19–22, 24, 25, 27, 28]. The retro-oesophageal right subclavian artery (RRSA) is one of the variations of ARSA. RRSA, is an embryological variation that can be detected as the terminal branch of the arch of the aorta passing dorsal to the oesophagus and taking a course toward the right axilla as the usual subclavian artery. The RRSA has been thought to be part of the right dorsal aorta that is normally eliminated by birth. It has been reported that ~80% of ARSA crosses behind the oesophagus [3, 12] as RRSA. Here we report

a case of RRSA encountered in student dissection at Kumamoto University School of Medicine during the period from 2018 to 2022. According to previous studies, the general idea about the origin of RRSA is that it develops from the regression of the embryotic fourth aortic arch and a portion of the right dorsal aorta cranial to the seventh intersegmental artery, accompanied with the persistence of the normally regressed segment of the right dorsal aorta caudal to the seventh intersegmental artery. However, the pattern of elimination and persistence of the components of the aortic arch complex is not always the same, showing some inconformity with the influential idea [13]. Thus, the traditional view of the process of RRSA development should be reconsidered based upon detailed observations and analysis of the regional anatomy including branches of RRSA and surrounding structures. Because the incidence of RRSA is very low, it is worth examining how morphological details of the newly found case in the present study can be related to findings in previous observations. Moreover, close observations of this anomaly can give useful knowledge for certain clinical applications such as possible defect of the right recurrent nerve that often accompanies the RRSA and thus requires careful manipulations of cervical structures during surgery.

MATERIALS AND METHODS

The RRSA was found in a donated cadaver of a 62-year-old Japanese male, who had died from kidney cancer, during routine medical student gross anatomy dissection at Kumamoto University School of Medicine. The incidence was 0.7% (1/141 bodies studied from 2018 to 2022). The cadaver was injected with 10% formalin solution from the radial artery by gravity flow and preserved in 30% alcohol. This anomalous case was observed carefully and sketched in detail, and three-dimensional photographs were taken. The protocol for this study did not include any specific issue needed to be approved by Ethics Committee of Kumamoto University Graduate School of Medical Sciences, and the study conformed to the provisions of the Declaration of Helsinki in 1995 (as revised in Fortaleza 2013).

RESULTS

The origin of the RRSA

The RRSA arose from the right side of the most distal part of the arch of the aorta as its fourth branch, following bifurcations of the right common carotid,

left common carotid, and left subclavian artery (Figs. 1–6). The RRSA emerged from the arch of the aorta at the level of the third thoracic vertebra. The diameter of the RRSA in its proximal part and that of the left subclavian artery were 2 cm and 1 cm, respectively (Figs. 3, 4). The RRSA was initially directed to the right and upward, passing through the space between the oesophagus and the vertebral column of the level from the second to the third thoracic vertebrae. Thereafter, the RRSA extended to the right side of the oesophagus (Figs. 5, 6). There was no Kommerell diverticulum that was previously described in the proximal part of RRSA [10, 29]. We considered this case as Adachi's G-type [2].

Branches of the RRSA

The right vertebral artery and the right costocervical trunk were branches of the RRSA in the present case. The right vertebral artery entered the cervical foramen transversarium of the sixth cervical vertebra, whereas the left vertebral artery arising from the left subclavian artery entered the fifth cervical foramen transversarium (Figs. 3, 4). Both of the thyrocervical trunk and the internal thoracic artery branched off from the RRSA just before it passed through the scalene space (Fig. 4). The right dorsal scapular artery branched from the RRSA at the position deep to the scalenus anterior muscle. The artery then passed under the C7 nerve root, became located dorsal to the C5–C6 nerve root (superior trunk of the brachial plexus), and reached the position medial to the border of the levator scapulae and serratus anterior muscles before entering the deep muscle layer (Figs. 2, 4). The suprascapular artery branched from the RRSA in the so-called third part of the subclavian artery at the inferior edge of the first costa (Fig. 2). This artery passed anterior to the C5–C6 nerve root and posterior to a thin branch accompanying the superior trunk, then it entered the suprascapular notch. The RRSA followed the expected path as a right axillary artery.

The highest posterior intercostal artery arising from the thoracic aorta

The suprema intercostal artery branched from the costocervical trunk on both sides and bifurcated into the first and second intercostal arteries. The third and fourth posterior intercostal arteries arose from the thoracic aorta as a common trunk of the highest posterior intercostal artery on both sides (Figs. 3, 4).
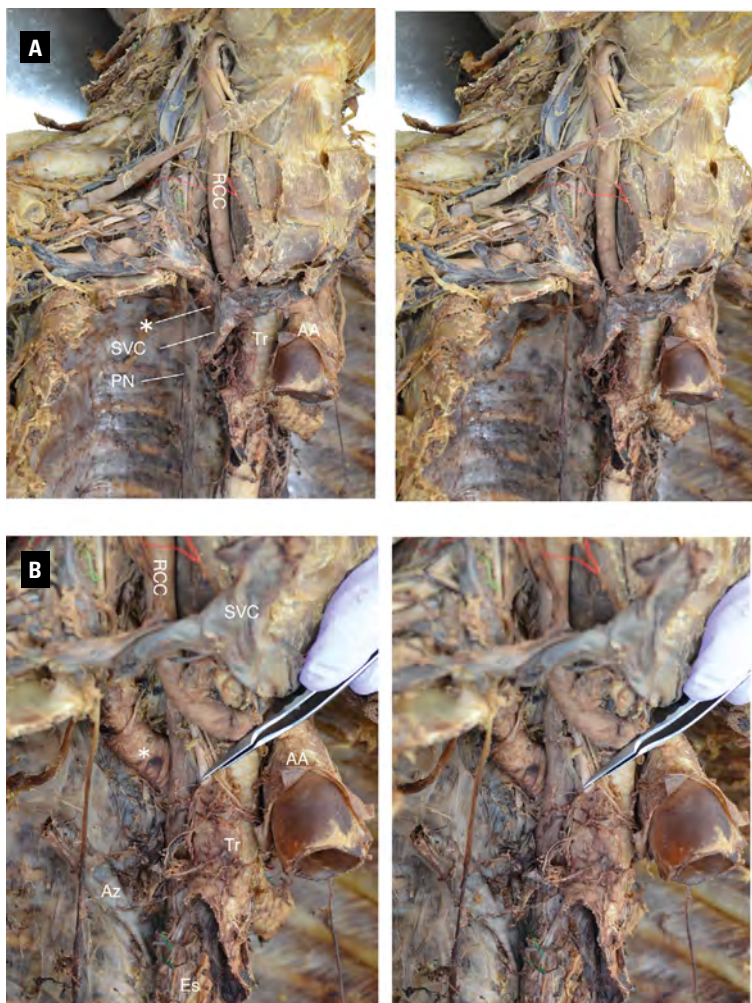
Figure 1. Cross-vision stereophotographs of a case of retro-oesophageal right subclavian artery; **A.** Right anterior view of cervix and mediastinum with retro-oesophageal right subclavian artery (asterisk); **B.** The superior vena cava is pulled above, and the right vagus nerve is held by tweezer; AA — arch of aorta; Az — azygos vein; Es — oesophagus; PN — phrenic nerve; RCC — right common carotid artery; SVC — superior vena cava; Tr — trachea.

The right bronchial artery arising from the thoracic aorta

The bronchial arteries branched from the right anterior part of the thoracic aorta, located distal to the RRSA branching point, at the level of the fourth thoracic vertebra. It then extended toward the anterior hilum of the lung, along with the right main bronchus. Another bronchial artery that was also directed to the hilum of the right lung originated from the caudal common trunk that arose from the anterior surface of the thoracic aorta at the position 3.5 cm distal to the bifurcation of the first bronchial artery. Then, this caudal common trunk bifurcated into two branches (rostral and caudal). The rostral branch further divided into two distal branches, which were directed toward to the hilum of the left lung, taking the course along the ventral and dorsal walls of the left main bronchus.

The caudal branch of the common trunk also bifurcated into two distal branches. The rostral bronchial artery that above mentioned extended to the right direction, passing between the left main bronchus and the oesophagus and further along the dorsal wall of the right main bronchus. It finally reached the hilum of the right lung. The other branch descended anteriorly and passed through the oesophageal hiatus. Finally, it connected with a branch of the left gastric artery.

The thoracic duct

The thoracic duct ascended between the thoracic aorta and the azygos vein, passed dorsal to the RRSA and ventral to the left vertebral artery/vein (Figs. 3, 4). Finally, it reached the left venous angle by passing through the usual route between the left common carotid artery and the left subclavian artery.
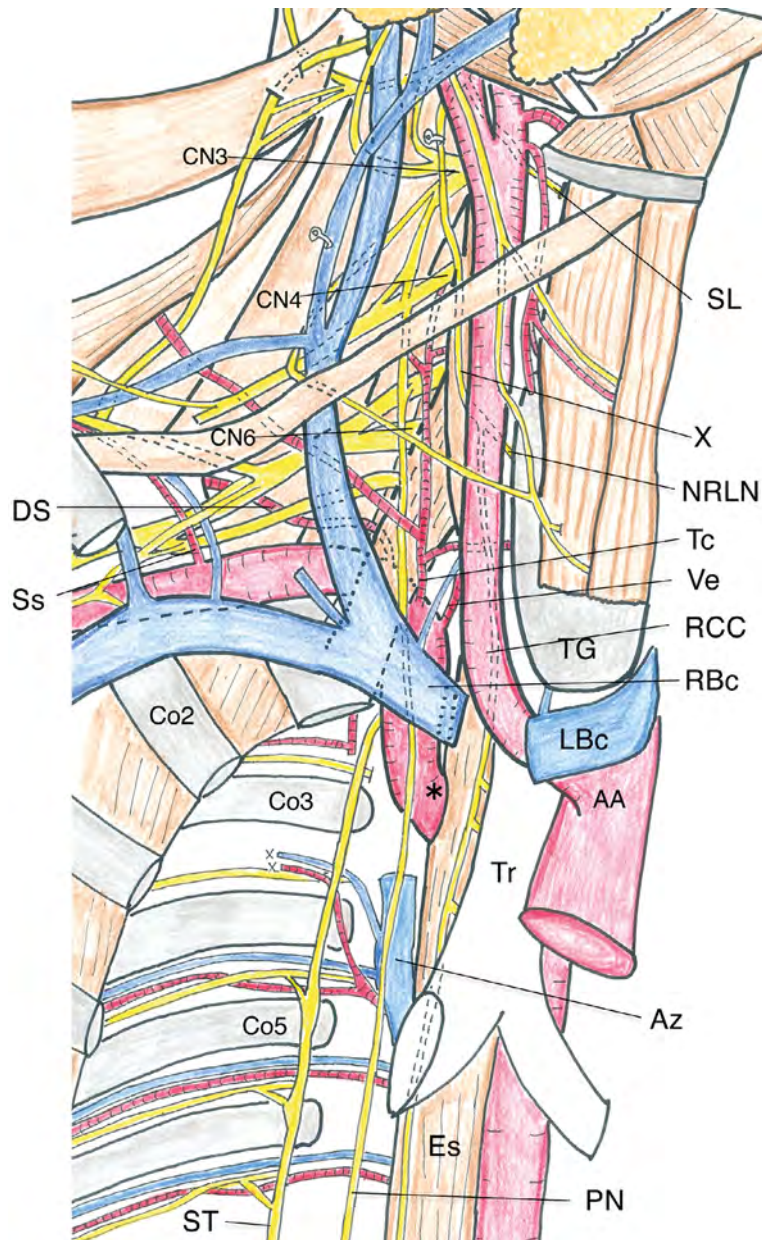
Figure 2. A schematic drawing of the retro-oesophageal right subclavian artery (asterisk) and branches of the arch of the aorta after removal of lungs and heart; AA — arch of aorta; Az — azygos vein; CN — cervical nerve; Co — costa; DS — dorsal scapular artery; Es — oesophagus; LBc — left brachiocephalic vein; NRLN — non-recurrent laryngeal nerve; PN — phrenic nerve; RBc — right brachiocephalic vein; RCC — right common carotid artery; SL — superior laryngeal nerve; Ss — suprascapular artery; ST — sympathetic trunk; Tc — thyrocervical trunk; TG — thyroid gland; Tr — trachea; Ve — vertebral artery; X — vagus nerve.

Non-recurrent laryngeal nerve

The recurrent laryngeal nerve is a branch of the vagus nerve. The right recurrent laryngeal nerve loops under the subclavian artery and supplies to larynx. Non-recurrent laryngeal inferior nerve (NRLN) is a very rare anatomic variation that originates from the vagus nerve and directly provides the branch to the larynx. It has been reported that the NRLN is related to vascular anomalies of the branches of the arch

of aorta. The right vagus nerve descended with the right common carotid artery and branched directly into the larynx without recurrence (NRLN) in RRSA [8, 17, 18, 30]. In the normal developmental process, the persistence of right fourth aortic arch leads to the recurrence of the laryngeal nerve of this level. In contrast, the laryngeal branch of the vagus nerve becomes directly connected to the larynx when the right fourth aortic arch disappears in RRSA [8, 17, 18,

47
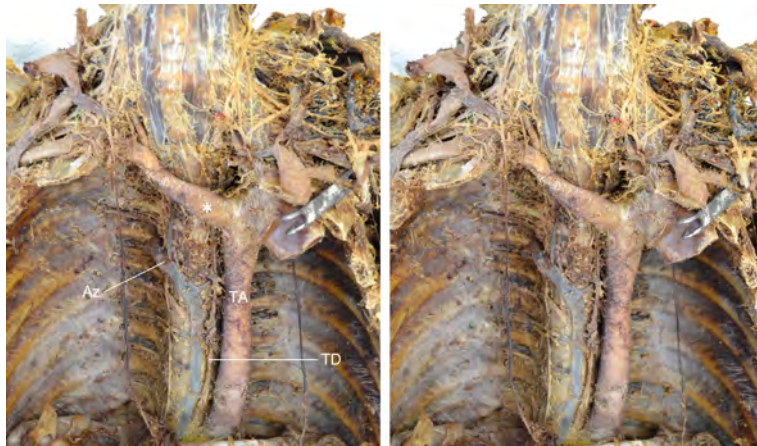
Figure 3. Cross-vision stereophotograph showing the overview of the retro-oesophageal right subclavian artery (RRSA) (asterisk). The arch of the aorta is pulled to the left for observation of the whole RRSA. Lungs, oesophagus, heart, and trachea were removed; Az — azygos vein; TA — thoracic aorta; TD — thoracic duct.
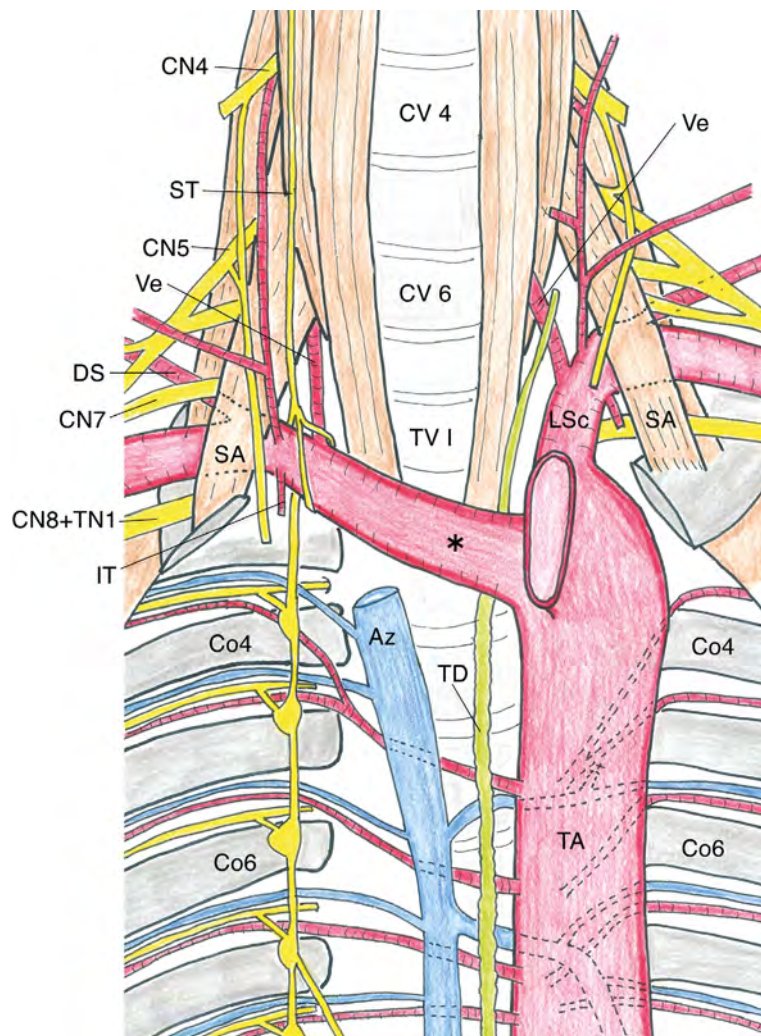
Figure 4. A schematic drawing of the whole retro-oesophageal right subclavian artery (asterisk) arising from the arch of the aorta as its last branch. Lungs, oesophagus, heart, and trachea were removed for demonstration; Az — azygos vein; CN — cervical nerve; Co — costa; CV — cervical vertebra; DS — dorsal scapular artery; IT — internal thoracic artery; LSc — left subclavian artery; SA — scalenus anterior; ST — sympathetic trunk; TA — thoracic aorta; TD — thoracic duct; TN — thoracic nerve; TV — thoracic vertebra; Ve — vertebral artery.

Figure 5. Cross-vision stereophotograph of left and right bronchial arteries (dot) arising from the thoracic aorta in the present case having the retro-oesophageal right subclavian artery. Three lines drawn to the white dot represents bronchial arteries; AA — arch of aorta; Es — oe-sophagus; SVC — superior vena cava; TG — thyroid gland; Tr — trachea; X — vagus nerve.

30]. In this case, the right vagus nerve branched into the NRLN at the level of the sixth cervical vertebra (Figs. 1, 7). On the left side of the present material, a typical recurrent laryngeal nerve was observed. Our observations are consistent to previous finding and support the hypothesis.

DISCUSSION

This study describes the morphology of the RRSA and its associated structures. Because RRSA is a rare anomaly, accumulation of findings in newly found cases will lead to better understanding of the process of forming RRSA. Previous studies have suggested that the proximal part of the RRSA is the persistent of the distal part of the right dorsal aorta, whereas the fourth aortic arch of the right side, which usually remains in the proximal part of the right subclavian artery, is eliminated during the genesis of the RRSA. However, the fourth right aortic arch persists in some RRSA cases [13]. This variability is associated with the morphological variation of the right vertebral artery in two ways: one is the position of branching from the parent artery and the other is the level of the cervical foramen transversarium to which the right vertebral artery is introduced. In the present case, the right vertebral artery arose from the right subclavian artery and entered the foramen at the sixth cervical vertebra as in usual cases. In the previous study focusing this issue [13], three out of five RRSA cases also showed the same pattern (Case No. 2, 3, 4). In these three cases, both the fourth aortic arch and part of right dorsal aorta cranial to the seventh intersegmental artery are thought to be eliminated during the developmental process, and this is in conformity with

the traditional view of the process of RRSA genesis. However, in Case No. 1 and 5 of the same study, the right vertebral artery arose from not RRSA but the right common carotid artery [13]. Moreover, the right vertebral artery entered the foramen at the fourth cervical vertebra in both cases; the foramen of the fifth vertebra was also targeted in Case No. 5. The patterns in these two cases can be interpreted as the result of the persistence of the fourth aortic arch and some cranial portion of the right dorsal aorta, which violates the traditional view. The vasculature morphology in the present case corresponds to the pattern in Case No. 2, 3, 4 mentioned above. The observation in another study also revealed a similar pattern regarding the right vertebral artery arising from the RRSA [23]. Because the number of the bodies analysed is rather small, it is uncertain whether disappearance of the fourth aortic arch, as suggested by the present case, is the dominant form of the RRSA. Judging from the previous observations of multiple cases in which the fourth aortic arch persists, it can at least be said that the theory regarding the mechanism of generating the RRSA needs to be modified to explain heterogeneous vasculature patterns in a consistent manner, which might also give perspective to understand the morphogenesis of aortic arches and related arteries in both normal and variant cases.

Because information about the morphology of bronchial arteries in RRSA is limited in previous studies of RRSA, we concentrated on them in this report. It has been reported that 97% of left bronchial arteries originate from the thoracic aorta, whereas the right posterior intercostal artery supplies 89% of the right bronchial artery [6, 16]. In the study of the RRSA,
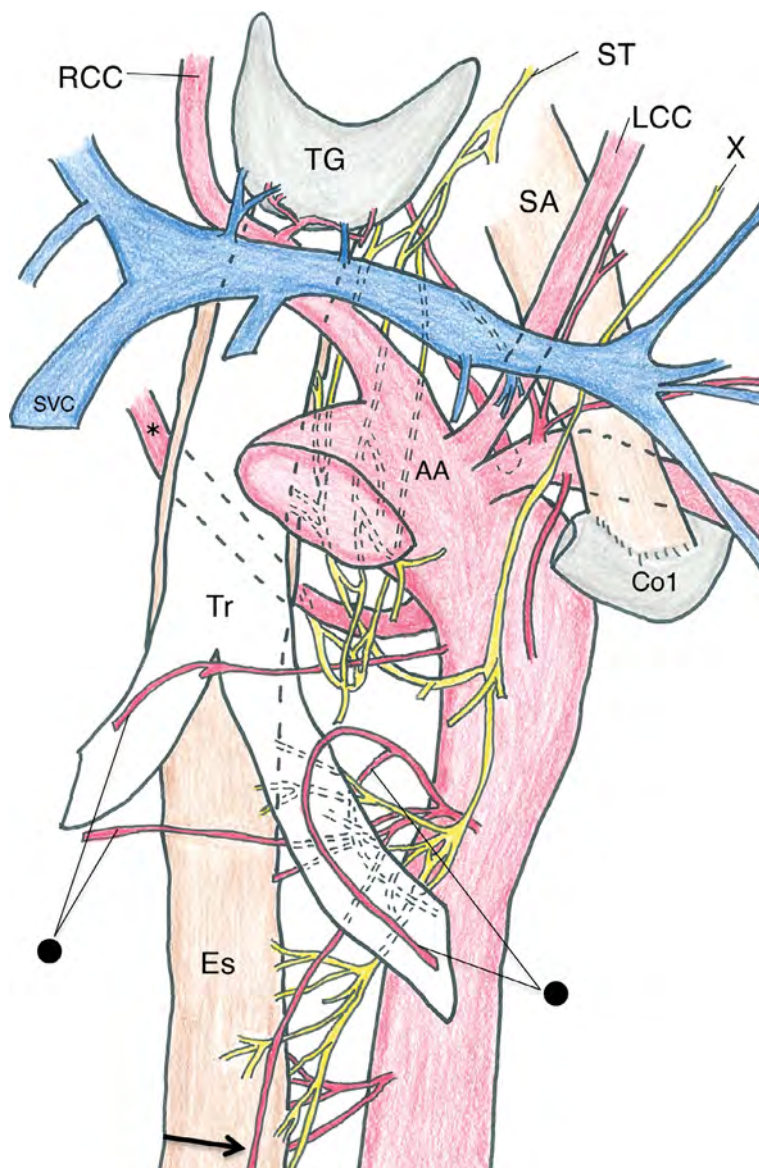
Figure 6. A schematic drawing of right and left bronchial arteries (dots), cervical structure and mediastinum in this retro-oesophageal right subclavian artery (asterisk) case. One of the two right bronchial arteries branches from the thoracic aorta. Another right bronchial artery is bifurcated from a trunk that is branched from the thoracic aorta and gives rise to two left bronchial arteries. Arrow represents the branch that is anastomosed with the branches of the left gastric artery; AA — arch of aorta; Co — costa; Es — oesophagus; LCC — left common carotid artery; RCC — right common carotid artery; SA — scalenus anterior; ST — sympathetic trunk; SVC — superior vena cava; TG — thyroid gland; Tr — trachea; X — vagus nerve.

the right posterior intercostal artery was the origin of the right bronchial artery in four out of five cases, whereas the RRSA was the origin of the right bronchial artery in the remaining one case [13]. It was postulated there that branching of the bronchial artery, which can be the visceral branch of the aorta, from the RRSA is compatible with the traditional view that the most proximal part of the RRSA is derived from the dorsal aorta of the right side. It should be noted here that the origin of the right bronchial artery in the present case was neither the posterior intercostal

artery nor the RRSA: the right bronchus was targeted by two branches of the thoracic aorta.

CONCLUSIONS

Our report suggests that there is a variability regarding the vascular pattern in structures surrounding the RRSA that can become the origin of the right bronchial artery. This also suggests the necessity of further study to reconsider the mechanism of RRSA development by accumulating findings in this anomaly in future studies.

Figure 7. A case of non-recurrent laryngeal nerve on the right side; **A.** Right non-recurrent laryngeal nerve is shown by arrow; **B.** Left recurrent laryngeal nerve (arrow), held by tweezer, is taking a usual course passing dorsal beneath the aortic arch; AA — arch of aorta; RCC — right common carotid artery; RCC — right common carotid artery; TG — thyroid gland.

REFERENCES

1. Abhaichand RK, Louvard Y, Gobeil JF, et al. The problem of arteria lusoria in right transradial coronary angiography and angioplasty. Catheter Cardiovasc Interv. 2001; 54(2): 196–201, doi: 10.1002/ccd.1266, indexed in Pubmed: 11590683.

2. Adachi B. Das Arteriensystem der Japaner, Bd.1. Maruzen, Kyoto 1928: 35–41.

3. Alghamdi MA, Al-Eitan LN, Elsy B, et al. Aberrant right subclavian artery in a cadaver: a case report of an aortic arch anomaly. Folia Morphol. 2021; 80(3): 726–729, doi: 10.5603/FM.a2020.0081, indexed in Pubmed: 32748949.

4. De Luca L, Bergman JJ, Tytgat GN, et al. EUS imaging of the arteria lusoria: case series and review. Gastrointest Endosc. 2000; 52(5): 670–673, doi: 10.1067/mge.2000.109808, indexed in Pubmed: 11060196.

5. Dong S, Alarhayem AQ, Meier G, et al. Contemporary management and natural history of aberrant right subclavian artery. J Vasc Surg. 2022; 75(4): 1343–1348.e2, doi: 10.1016/j.jvs.2021.11.051, indexed in Pubmed: 34838611.

6. Fei QL, Zhou YY, Yuan YX, et al. An applied anatomical study of bronchial artery. Surg Radiol Anat. 2018; 40(1): 55–61, doi: 10.1007/s00276-017-1918-8, indexed in Pubmed: 28942519.

7. Haesemeyer SW, Gavant ML. Imaging of acute traumatic aortic tear in patients with an aberrant right subclavian artery. Am J Roentgenol. 1999; 172(1): 117–120, doi: 10.2214/ajr.172.1.9888750, indexed in Pubmed: 9888750.

8. Henry BM, Sanna S, Graves MJ, et al. The non-recurrent laryngeal nerve: a meta-analysis and clinical considerations. Peer J. 2017; 5: e3012, doi: 10.7717/peerj.3012, indexed in Pubmed: 28344898.

9. Iimura A, Oguchi T, Tou M, et al. The retroesophageal right subclavian artery - A case report and review. Okajimas Folia Anat Jpn. 2017; 94(3): 75–80, doi: 10.2535/ofaj.94.75, indexed in Pubmed: 29681591.

10. Ito T, Itoh A, Kiyoshima D, et al. Anatomical characteristics of two cases of aberrant right subclavian artery. Anat Sci Int. 2022; 97(4): 423–427, doi: 10.1007/s12565-022-00658-7, indexed in Pubmed: 35316514.

11. Jahangeer S, Bashir M, Harky A, et al. Aberrant subclavian: new face of an old disease. J Vis Surg. 2018; 4: 108, doi: 10.21037/jovs.2018.05.11, indexed in Pubmed: 29963397.

12. Kau T, Sinzig M, Gasser J, et al. Aortic development and anomalies. Semin Intervent Radiol. 2007; 24(2): 141–152, doi: 10.1055/s-2007-980040, indexed in Pubmed: 21326792.

13. Kawai K, Honma S, Kumagai Y, et al. A schematic diagram showing the various components of the embryonic aortic arch complex in the retroesophageal right subclavian artery. Anat Sci Int. 2011; 86(3): 135–145, doi: 10.1007/s12565-010-0101-7, indexed in Pubmed: 21246420.

14. Kawashima T, Sasaki H. Topological changes of the human autonomic cardiac nervous system in individuals with a retroesophageal right subclavian artery: two case reports

and a brief review. Anat Embryol (Berl). 2005; 210(4): 327–334, doi: 10.1007/s00429-005-0052-2, indexed in Pubmed: 16222543.

15. Kelly MD. Endoscopy and the aberrant right subclavian artery. Am Surg. 2007; 73(12): 1259–1261, indexed in Pubmed: 18186385.

16. Kodama K. Bronchial artery. In: Anatomic Variations in Japanese. In: Sato T, Akita K (eds) (in Japanese). University of Tokyo Press, Tokyo 2000: 237–239 .

17. Lee JY, Won DY, Oh SH, et al. Three concurrent variations of the aberrant right subclavian artery, the non-recurrent laryngeal nerve and the right thoracic duct. Folia Morphol. 2016; 75(4): 560–564, doi: 10.5603/FM.a2016.0025, indexed in Pubmed: 27830894.

18. Lu Y, Deng C, Lan N, et al. The nonrecurrent laryngeal nerve without abnormal subclavian artery: report of two cases and review of the literature. Ear Nose Throat J. 2021 [Epub ahead of print]: 1455613211056547, doi: 10.1177/01455613211056547, indexed in Pubmed: 34935547.

19. Mirande MH, Durhman MR, Smith HF. Anatomic investigation of two cases of aberrant right subclavian artery syndrome, including the effects on external vascular dimensions. Diagnostics (Basel). 2020; 10(8), doi: 10.3390/diagnostics10080592, indexed in Pubmed: 32823848.

20. Natsis K, Didagelos M, Gkiouliava A, et al. The aberrant right subclavian artery: cadaveric study and literature review. Surg Radiol Anat. 2017; 39(5): 559–565, doi: 10.1007/s00276-016-1796-5, indexed in Pubmed: 27999944.

21. Natsis KI, Tsitouridis IA, Didagelos MV, et al. Anatomical variations in the branches of the human aortic arch in 633 angiographies: clinical significance and literature review. Surg Radiol Anat. 2009; 31(5): 319–323, doi: 10.1007/s00276-008-0442-2, indexed in Pubmed: 19034377.

22. Nie B, Zhou Yj, Li Gz, et al. Clinical study of arterial anatomic variations for transradial coronary procedure in Chinese population. Chin Med J (Engl). 2009; 122(18): 2097–2102, indexed in Pubmed: 19781291.

23. Okamoto K, Wakebe T, Saiki K, et al. A case of retroesophageal right subclavian artery, with special reference to the second intercostal artery, retroesophageal right vertebral artery, and thoracic duct. Anat Sci Int. 2013; 88(4): 234–238, doi: 10.1007/s12565-013-0178-x, indexed in Pubmed: 23677877.

24. Ostrowski P, Bonczar M, Przybycień W, et al. An aberrant right subclavian artery in a 63-year-old male cadaver. Folia Morphol. 2023; 82(3): 726–731, doi: 10.5603/FM.a2022.0085, indexed in Pubmed: 36178279.

25. Polguj M, Chrzanowski Ł, Kasprzak JD, et al. The aberrant right subclavian artery (arteria lusoria): the morphological and clinical aspects of one of the most important variations--a systematic study of 141 reports. Scientific World J. 2014; 2014: 292734, doi: 10.1155/2014/292734, indexed in Pubmed: 25105156.

26. Saito T, Tamatsukuri Y, Hitosugi T, et al. Three cases of retroesophageal right subclavian artery. J Nippon Med Sch. 2005; 72(6): 375–382, doi: 10.1272/jnms.72.375, indexed in Pubmed: 16415518.

27. Sangam MR, Anasuya K. Arch of aorta with bi-carotid trunk, left subclavian artery, and retroesophageal right subclavian artery. Folia Morphol. 2010; 69(3): 184–186, indexed in Pubmed: 21154291.

28. Tallarita T, Rogers RT, Bower TC, et al. Characterization and surgical management of aberrant subclavian arteries. J Vasc Surg. 2023; 77(4): 1006–1015, doi: 10.1016/j.jvs.2022.12.018, indexed in Pubmed: 36565775.

29. van Son JA, Konstantinov IE, Burckhard F. Kommerell and Kommerell's diverticulum. Tex Heart Inst J. 2002; 29(2): 109–112, indexed in Pubmed: 12075866.

30. Wang Yu, Ji Q, Li D, et al. Preoperative CT diagnosis of right nonrecurrent inferior laryngeal nerve. Head Neck. 2011; 33(2): 232–238, doi: 10.1002/hed.21434, indexed in Pubmed: 20848443.

The inferior gluteal artery anatomy: a detailed analysis with implications for plastic and reconstructive surgery

Kamil Gabryszuk[1], Michał Bonczar[2, 3], Patryk Ostrowski[2, 3], Jakub Gliwa[2, 3],
Alicia del Carmen Yika[2], Tomasz Iskra[2], Michał Kłosiński[2], Wadim Wojciechowski[4],
Jerzy Walocha[2, 3], Mateusz Koziej[2, 3]

[1]Chiroplastica — The Lower Silesian Centre of Hand Surgery and Aesthetic Medicine, Wroclaw, Poland
[2]Department of Anatomy, Jagiellonian University Medical College, Krakow, Poland
[3]Youthoria, Youth Research Organization, Krakow, Poland
[4]Department of Radiology, Jagiellonian University Medical College, Krakow, Poland

Background: *The inferior gluteal artery (IGA) is a large terminal branch of the anterior division of the internal iliac artery (ADIIA). There is a significant lack of data regarding the variable anatomy of the IGA.*

Materials and methods: *A retrospective study was conducted to establish anatomical variations, their prevalence and morphometrical data on IGA and its branches. The results of 75 consecutive patients who underwent pelvic computed tomography angiography were analysed.*

Results: *The origin variation of each IGA was deeply analysed. Four origin variations have been observed. The most common type O1 occurred in 86 of the studied cases (62.3%). The median IGA length was set to be 68.50 mm (lower quartile [LQ]: 54.29; higher quartile [HQ]: 86.06). The median distance from the origin of the ADIIA to the origin of the IGA was set to be 38.22 mm (LQ: 20.22; HQ: 55.97). The median origin diameter of the IGA was established at 4.69 mm (LQ: 4.13; HQ: 5.45).*

Conclusions: *The present study thoroughly analysed the complete anatomy of the IGA and the branches of the ADIIA. A novel classification system for the origin of the IGA was created, where the most prevalent origin was from the ADIIA (type 1; 62.3%). Furthermore, the morphometric properties (such as the diameter and length) of the branches of the ADIIA were analysed. This data may be incredibly useful for physicians performing operations in the pelvis, such as interventional intraarterial procedures or various gynaecological surgeries.* (Folia Morphol 2024; 83, 1: 53–65)

Keywords: inferior gluteal artery, plastic surgery, uterine artery, anatomy, surgery

Address for correspondence: Dr. Mateusz Koziej, Department of Anatomy, Jagiellonian University Medical College, ul. Mikołaja Kopernika 12,
33–332 Kraków, Poland, e-mail: mateuszkoziej01@gmail.com

Figure 1. Inferior gluteal artery and its close anatomical area; 1 — inferior gluteal artery; 2 — inferior gluteal vein; 3 — inferior gluteal nerve; 4 — superior gluteal artery; 5 — sacrotuberous ligament; 6 — ischial tuberosity; 7 — gluteus maximus muscle; 8 — piriformis muscle; 9 — gluteus medius muscle.

INTRODUCTION

The inferior gluteal artery (IGA) (Fig. 1) is a large terminal branch of the anterior division of the internal iliac artery (ADIIA). It courses posteriorly between the sacral nerves (typically S2 and S3) and exits the pelvis through the inferior section of the greater sciatic foramen, below the piriformis muscle. The IGA supplies the skin and muscles of the buttocks (through muscular branches to the piriformis, obturator internus, and gluteus maximus muscles), as well as the posterior surface of the thigh. Furthermore, it gives off a companion branch to the sciatic nerve, as well as contributing branches to the trochanteric and cruciate anastomoses [15].

There is a significant lack of data regarding the variable anatomy of the IGA. The arterial anatomy of the pelvis is known for being highly variable, making it a difficult area to operate in [12, 16, 26, 27]. The origin of the IGA has not been sufficiently studied in the past, even though its highly relevant in emboliza-tion procedures for pseudoaneurysms [13]. Therefore, in the present study, a novel classification system of the different origin types of the IGA was created.

The other branches of the ADIIA are also subjects for embolization procedures, especially the uterine artery. Uterine artery embolization can be performed to prevent or treat bleeding associated with various obstetric conditions, such as postpartum haemor-rhage or ectopic pregnancy [9]. Furthermore, uterine fibroids, the most common pelvic tumours in women, acquire their blood supply almost exclusively from the uterine artery [17, 24, 25]. Embolization of uterine arteries reduces the blood supply to the uterus and, with that, reduces the size of fibroids, resulting in decreased pain and dysmenorrhea [14]. Therefore, the morphometric properties of the IGA and the branches of the ADIIA were also analysed.

It is hoped that the results of the present study may give new insights into the complex anatomy of the IGA and the ADIIA, which can ultimately lead to a greater understanding of the vascular anatomy of the pelvis.

MATERIALS AND METHODS

Bioethical Committee

The research protocol was submitted for eval-uation and approved by the Bioethical Commit-

tee of Jagiellonian University, Krakow, Poland (1072.6120.254.2022). Further stages of the study were carried out in accordance with the approved guidelines.

Study group

A retrospective study was conducted to establish anatomical variations, their prevalence and morpho-metrical data on IGA and its branches. The results of 75 consecutive patients who underwent pelvic computed tomography angiography (CTA) were analysed. The CTAs were performed in the Department of Radiology of the Jagiellonian University Medical College, Cracow, Poland, between 2017 and 2022. The results of each patient were analysed bilaterally at the Department of Anatomy of the Jagiellonian University Medical College, Krakow, Poland, in August 2022. A total of 150 IGAs were initially evaluated. Exclusion criteria were set as follows: (1) pelvic or abdominal trauma affecting the course of the IGA and/or its initial branches, (2) significant artifacts that prevented accurate and precise imaging and/or measurement of the IGA and/or its initial branches, (3) low quality and illegible images and (4) significant lack of filling the whole arterial system with contrast. Defects, which met the exclusion criteria but included only one side of the CTA, without interference with the contralateral side, did not disqualify the whole CTA but only the affected side. Therefore, of the initial 150, a total of 12 IGAs were excluded due to significant artifacts (n = 5) or a lack of contrast filling (n = 7) in order to minimise possible bias. Finally, 138 IGA of 69 patients met the required criteria.

Acquisition of results

All pelvic CTA were performed on a 128-slice scanner CT (Philips Ingenuity CT, Philips Healthcare). The main CTA imaging parameters were as follows: collimation/increment: 0.625/0.3 mm; tube current: 120 mAs; field of view: 210 mm; matrix size: 512 × 512. All of the patients received intravenous administration of contrast material at a dose of 1 mL/kg (standard dose). A non-ionic contrast medium (CM) containing 350 mg of iodine per mL was used (Jowersol 741 mg/mL, Optiray®, Guerbet, France). CT data acquisition was triggered using a real-time bolus-tracking technique (Philips Healthcare) with the region of interest placed in the ascending aorta. The CM was intravenously injected using a power injector

at a flow rate of 5 mL/s. This was immediately followed by the injection of 40 mL of saline solution at the same flow rate. Following injection of CM and saline, image acquisition was automatically started with a 2 s delay when the attenuation trigger value reached a threshold of 120 Hounsfield units (HU). Scanning was performed in the caudocranial direction.

The CTAs were analysed on a dedicated workstation at the Anatomical Department of Jagiellonian University Medical College, Krakow, Poland. To ensure the highest possible quality of the visualizations and measurements and minimize potential bias, Materialise Mimics Medical version 21.0 software (Materialise NV, Leuven, Belgium) software was used. Three-dimensional (3D) reconstructions of each scan were developed, employing a set of settings, severally adjusted to each scan. A volume rendering opacity range oscillated from 25 to 80 HU for the lower limit and up to 3070 HU for a higher limit. The range was individually adjusted to each TT after a visual investigation.

Evaluation and measurements

At the beginning of each evaluation, the authors ensured that each IGA, its branches, and its close anatomical area were fully visualized. Subsequently, each branch of the IGA was identified by following its course. The origin of the IGA and a set of its branches was evaluated with their arrangement and were descriptively noted. Subsequently, a set of measurements was conducted on each IGA and its close anatomical area by two independent researchers, and a mean was established taking into account both results. All measurements were rounded to two decimal places. The following measurements were taken: (1) IGA length [mm]; (2) distance from the origin of the ADIIA to the origin of the IGA [mm]; (3) Distance from the origin of the IIA to the origin of the IGA [mm]; (4) Distance from the origin of the superior gluteal artery (SGA) to the origin of the IGA [mm]; (5) Distance from the origin of the posterior division of the internal iliac artery (PDIIA) to the origin of the IGA [mm]; (6) IGA origin diameter [mm]; (7) IGA origin area [mm^2]; (8) IGA origin angle; (9) Obturator artery origin diameter [mm]; (10) Obturator artery origin area [mm^2]; (11) Umbilical artery origin diameter [mm]; (12) Umbilical artery origin area [mm^2]; (13) Uterine artery origin diameter [mm]; (14) Uterine artery origin area [mm^2]; (15) Vaginal artery

Table 1. Qualitative results of the data analysis

Category	N	Percentage
Patients' sex		
Females	78	56.5%
Males	60	43.5%
Patients' side		
Left	71	51.4%
Right	67	48.6%
Origin type		
Type O1 (ADIIA)	86	62.3%
Type O2 (IIA)	33	23.9%
Type O3 (SGA)	10	7.2%
Type O4 (PDIIA)	9	6.5%

IGA — inferior gluteal artery; ADIIA — anterior division of the internal iliac artery; IIA — internal iliac artery; SGA — superior gluteal artery; PDIIA — posterior division of the internal iliac artery. The four types of origin are established as follows: (1) Type O1 — IGA branches off directly from the ADIIA; (2) Type O2 — IGA branches off directly from the IIA; (3) Type O3 — IGA branches off directly from the SGA; (4) Type O4 — IGA branches off directly from the PDIIA

origin diameter [mm]; (16) Vaginal artery origin area [mm^2]; (17) Middle anorectal artery origin diameter [mm]. (18) Middle anorectal artery origin area [mm^2]; (19) Internal pudendal artery origin diameter [mm]; (20) Internal pudendal l artery origin area [mm^2]; (21) Inferior vesical origin diameter [mm]; (22) Inferior vesical origin area [mm^2]; (23) Distance between the origin of the obturator artery and the origin of the IGA [mm]; (24) Distance between the origin of the umbilical artery and the origin of the IGA [mm]; (25) Distance between the origin of the uterine artery and the origin of the IGA [mm]; (26) Distance between the origin of the vaginal artery and the origin of the IGA [mm]; (27) Distance between the origin of the middle anorectal artery and the origin of the IGA [mm]; (28) Distance between the origin of the internal pudendal artery and the origin of the IGA [mm]; (29) Distance between the origin of the inferior vesical artery and the origin of the IGA [mm]. In addition, a set of individual patient parameters such as age and sex were observed.

Statistical analysis

Statistical analysis was performed with SATISTICA v13.1 (StatSoft Inc., Tulsa, OK, USA). The frequencies and percentages presented qualitative features. The Shapiro-Wilk test was used to assess the normal distribution. Quantitative characteristics were presented by medians and higher and lower quartiles (HQ, LQ), as well as means and standard deviation (SD), depending on the verified normality of the data. Statistical significance was defined as $p < 0.05$. U Mann-Whitney and Wilcoxon signed-rank tests were used to establish potential differences between groups. Spearman's rank correlation coefficient was used to determine possible correlations between the parameters.

RESULTS

Qualitative results

All subsequent results are presented in relation to the number of IGA instead of number of patients. A total of 138 IGA were analysed. Of these, 78 (56.5%) were from women and 60 (43.5%) were from men. The origin variation of each IGA was deeply analysed. Four origin variations have been observed. Therefore, in response to the literature lacks, a classification method of the IGA origin was set and consists of four main types. Those four main types were set as follows: (1) Type O1 — IGA branches off directly from the ADIIA; (2) Type O2 — IGA branches off directly from the IIA; (3) Type O3 — IGA branches off directly from the SGA; (4) Type O4 — IGA branches off directly from the PDIIA. The most common Type O1 occurred in 86 (62.3%) of the studied cases. All the statistics mentioned above, and more detailed ones can be found in Table 1. Origin types are illustrated on Figure 2.

Measurements analysis

The median IGA length was set to be 68.50 mm (LQ: 54.29; HQ: 86.06). The median distance from the origin of the ADIIA to the origin of the IGA was set to be 38.22 mm (LQ: 20.22; HQ: 55.97). The median origin diameter of the IGA was established at 4.69 mm (LQ: 4.13; HQ: 5.45). The median origin area of the IGA was found to be 15.16 mm (LQ: 11.00; HQ: 18.84). The detailed results of each category can be found in Table 2.

Sexual dimorphism

Separate statistical analysis has been performed, with respect to the sex of the patient. The results statistically significantly ($p < 0.05$) differed between sexes in four categories. Those results are gathered in Table 3.

Correlations

Potential associations between each category and patient's age was demonstrated. Three categories statistically significantly correlate with patient's age. The
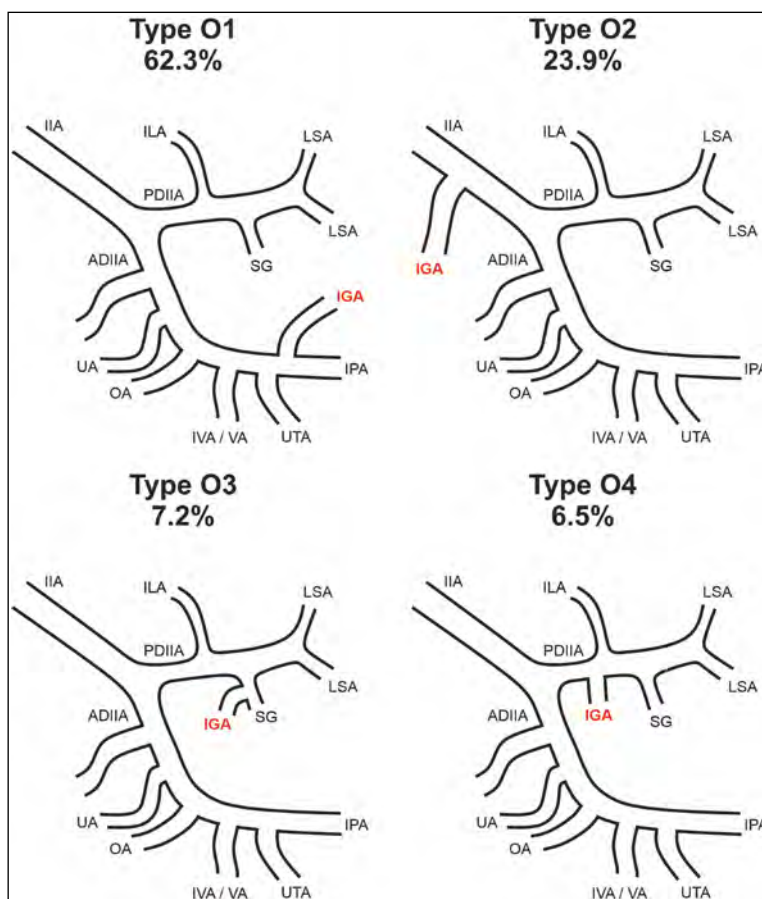
Figure 2. Origin types of the inferior gluteal artery (IGA); IIA — internal iliac artery; PDIIA — posterior division of the internal iliac artery; ADIIA — anterior division of the internal iliac artery; ILA — iliolumbar artery; SG — superior gluteal artery; LSA — lateral sacral arteries; UA — umbilical artery; OA — obturator artery; IVA — inferior vesicular artery; VA — vaginal artery; UTA — uterine artery; IPA — internal pudendal artery.

R values obtained in the correlation analysis between the groups can be found in Table 4. Highlighted in red are those in which the p-value was less than 0.05.

Side differences

Subsequently, potential differences in the measured parameters, occurrence of origin types and cooccurrence of types with respect to the patient's side have been analysed. The detailed results can be found in Table 5.

DISCUSSION

The present study is the first to thoroughly analyse the anatomy of the IGA using CTA. With the data gathered from the acquired imaging studies, a novel classification system of the origin of the said artery was created. Our classification system consists of four different types: type 1 represents the most frequent origin pattern, namely, the IGA originating directly from the ADIIA (O1: 62.3%). Next, type 2 presents the IGA originating directly from the IIA before it bifurcates into its anterior and posterior trunks (O2: 23.9%). Type 3 represents the IGA arising from the superior gluteal artery (O3: 7.2%). Lastly, type 4 describes the IGA as originating from the PDIIA (O4: 6.5%). This is the most in-depth analysis performed concerning the origin of the IGA in the available literature. Our data shows that the IGA originates most frequently from the ADIIA, fitting the description provided by the major anatomical textbooks [15]. However, our results show also that the IGA is subject to a relatively high degree of variability.

Although rare, aneurysms of IGA may occur. Kuzuya et al. [13] presented a case report about a 78-year-old patient presenting with painful swelling in the right buttock. There was no history of trauma or infection, and the patient was undergoing antiplatelet therapy. Arteriography demonstrated a pseudoaneurysm arising from the right IGA. The

Table 2. Results of the measurements

Category	Median	LQ	HQ	Minimum	Maximum	Mean	SD
IGA length [mm]	68.50	54.29	86.06	4.26	149.31	71.53	27.43
Distance from the origin of the ADIIA to the origin of the IGA [mm]	38.22	20.22	55.97	6.91	92.48	39.77	23.06
Distance from the origin of the IIA to the origin of the IGA [mm]	63.67	46.74	74.20	13.19	90.10	59.37	18.76
Distance from the origin of the SGA to the origin of the IGA [mm]	37.94	36.17	41.99	14.65	53.30	38.04	10.48
Distance from the origin of the PDIIA to the origin of the IGA [mm]	37.49	19.17	44.55	14.78	53.79	33.87	14.56
IGA origin diameter [mm]	4.69	4.13	5.45	1.83	11.41	4.80	1.08
IGA origin area [mm^2]	15.16	11.00	18.84	2.41	36.17	15.59	5.77
IGA origin angle	123.29	86.12	142.27	14.46	178.01	112.78	39.66
Obturator artery origin diameter [mm]	3.13	2.65	3.76	1.42	5.89	3.23	0.87
Obturator artery origin area [mm^2]	7.00	4.66	8.64	1.18	15.44	7.00	3.16
Umbilical artery origin diameter [mm]	2.84	2.49	3.52	1.40	5.30	2.94	0.78
Umbilical artery origin area [mm^2]	5.66	3.85	9.08	1.21	15.02	6.23	3.10
Uterine artery origin diameter [mm]	3.18	2.45	3.89	1.87	4.70	3.19	0.88
Uterine artery origin area [mm^2]	6.30	4.07	8.37	2.10	16.87	6.84	3.57
Vaginal artery origin diameter [mm]	2.67	2.63	3.33	1.90	3.64	2.79	0.56
Vaginal artery origin area [mm^2]	4.95	4.66	6.83	2.59	9.85	5.66	2.32
Middle anorectal artery origin diameter [mm]	3.05	2.63	3.43	1.76	4.60	3.05	0.69
Middle anorectal artery origin area [mm^2]	5.93	4.69	7.95	1.51	15.32	6.73	3.18
Internal pudendal artery origin diameter [mm]	3.20	2.70	3.85	1.60	6.35	3.28	0.86
Internal pudendal l artery origin area [mm^2]	6.74	4.67	9.13	1.30	30.95	7.15	3.64
Inferior vesical origin diameter [mm]	1.84	1.75	2.31	1.14	3.37	2.08	0.83
Inferior vesical origin area [mm^2]	2.92	1.86	6.18	1.67	8.56	4.02	3.17
Distance between the origin of the obturator artery and the origin of the IGA [mm]	21.34	9.25	41.88	0.00	77.00	26.53	20.19
Distance between the origin of the umbilical artery and the origin of the IGA [mm]	24.42	11.36	39.85	0.00	74.54	28.18	19.99
Distance between the origin of the uterine artery and the origin of the IGA [mm]	28.09	21.34	31.38	8.29	49.52	26.79	10.85
Distance between the origin of the vaginal artery and the origin of the IGA [mm]	38.21	29.89	40.67	3.06	56.52	33.67	19.64
Distance between the origin of the middle anorectal artery and the origin of the IGA [mm]	59.96	32.25	73.90	0.00	103.62	51.35	27.05
Distance between the origin of the internal pudendal artery and the origin of the IGA [mm]	0.00	0.00	12.99	0.00	44.69	7.80	12.91
Distance between the origin of the inferior vesical artery and the origin of the IGA [mm]	54.16	54.01	54.30	54.01	54.30	54.16	0.21

LQ — lower quartile; HQ — higher quartile; SD — standard deviation; IGA — inferior gluteal artery; ADIIA — anterior division of the internal iliac artery; IIA — internal iliac artery; SGA — superior gluteal artery; PDIIA — posterior division of the internal iliac artery

treatment consisted of a transluminal coil embolization by ultrasound-guided direct puncture of the IGA. The catheter was successfully advanced to the proximal side of the pseudoaneurysm and occluded with two coils. This proves the importance of having adequate knowledge about the anatomy of the IGA.

The IGA perforator flap has been used in both reconstructions of the gluteal region, but also breast reconstructive procedures [1, 11]. Because of the clinical significance of this vessel, its anatomy has been extensively researched in the past. Georgantopoulou et al. [4] analysed the microvascular anatomy of the SGA and IGA perforator flaps. In the study, it was stated that the location of the IGA perforators was less definite and varied considerably. Interestingly, Vigato et al. [23] stated that the gluteal region was

Table 3. Results of the measurements concerning the sex

Category	Sex	Median	LQ	HQ	Minimum	Maximum	Mean	SD	P
IGA length [mm]	Female	73.13	57.10	88.88	14.35	149.31	73.12	28.29	0.38
	Male	67.67	51.42	81.27	4.26	145.60	69.49	26.38	
Distance from the origin of the ADIIA to the origin of the IGA [mm]	Female	41.37	25.42	55.97	6.91	92.48	42.74	22.18	0.12
	Male	24.29	15.31	59.48	8.51	85.70	35.31	23.96	
Distance from the origin of the IIA to the origin of the IGA [mm]	Female	56.29	44.37	68.99	13.19	87.94	56.69	19.53	0.46
	Male	64.83	47.65	76.53	21.06	90.10	62.05	18.19	
Distance from the origin of the SGA to the origin of the IGA [mm]	Female	37.40	31.17	41.63	14.65	49.28	35.25	11.75	0.34
	Male	39.62	36.81	47.65	36.36	53.30	42.23	7.79	
Distance from the origin of the PDIIA to the origin of the IGA [mm]	Female	23.34	14.78	37.48	14.78	37.48	25.20	11.46	0.14
	Male	44.01	37.50	45.08	14.99	53.79	39.07	14.66	
IGA origin diameter [mm]	Female	4.48	3.92	5.26	1.83	6.73	4.61	0.93	0.01
	Male	4.94	4.37	5.59	3.20	11.41	5.07	1.22	
IGA origin area [mm²]	Female	14.57	10.60	18.04	2.41	30.50	15.18	5.83	0.25
	Male	15.32	11.95	18.99	6.46	36.17	16.15	5.68	
IGA origin angle	Female	106.74	68.48	134.06	14.46	178.01	105.15	41.98	0.03
	Male	132.26	119.63	146.18	40.40	166.62	127.64	30.48	
Obturator artery origin diameter [mm]	Female	3.01	2.56	3.50	1.42	5.89	3.07	0.87	0.00
	Male	3.58	3.11	4.17	1.50	5.18	3.50	0.80	
Obturator artery origin area [mm²]	Female	6.32	4.50	7.74	1.18	15.44	6.44	3.06	0.01
	Male	8.28	5.85	9.23	1.50	15.37	7.98	3.14	
Umbilical artery origin diameter [mm]	Female	2.85	2.49	3.60	1.40	5.30	3.00	0.82	0.52
	Male	2.82	2.25	3.00	1.61	3.95	2.75	0.64	
Umbilical artery origin area [mm²]	Female	5.85	3.96	9.48	1.21	15.02	6.53	3.31	0.46
	Male	5.47	3.74	6.57	1.38	9.87	5.33	2.23	
Uterine artery origin diameter [mm]	Female	3.18	2.45	3.89	1.87	4.70	3.19	0.88	–
	Male	–	–	–	–	–	–	–	
Uterine artery origin area [mm²]	Female	6.30	4.07	8.37	2.10	16.87	6.84	3.57	–
	Male	–	–	–	–	–	–	–	
Vaginal artery origin diameter [mm]	Female	2.67	2.63	3.33	1.90	3.64	2.79	0.56	–
	Male	–	–	–	–	–	–	–	
Vaginal artery origin area [mm²]	Female	4.95	4.66	6.83	2.59	9.85	5.66	2.32	–
	Male	–	–	–	–	–	–	–	
Middle anorectal artery origin diameter [mm]	Female	3.05	2.63	3.46	1.76	4.60	3.06	0.76	0.93
	Male	3.06	2.61	3.32	2.44	3.69	3.01	0.44	
Middle anorectal artery origin area [mm²]	Female	5.93	4.69	8.27	1.51	15.32	6.78	3.45	0.92
	Male	6.47	5.05	7.94	3.05	10.45	6.55	2.29	
Internal pudendal artery origin diameter [mm]	Female	3.02	2.48	3.80	1.60	5.42	3.21	0.95	0.15
	Male	3.36	2.95	3.85	2.02	6.35	3.38	0.73	
Internal pudendal I artery origin area [mm²]	Female	6.30	4.18	9.04	1.30	14.34	6.72	3.29	0.11
	Male	7.11	5.70	9.13	2.83	30.95	7.78	4.05	
Inferior vesical origin diameter [mm]	Female	–	–	–	–	–	–	–	–
	Male	2.08	1.80	2.84	1.75	3.37	2.32	0.74	
Inferior vesical origin area [mm²]	Female	–	–	–	–	–	–	–	–
	Male	2.92	1.86	6.18	1.67	8.56	4.02	3.17	

→

Table 3. cont. Results of the measurements concerning the sex

Category	Sex	Median	LQ	HQ	Minimum	Maximum	Mean	SD	P
Distance between the origin of the obturator artery and the origin of the IGA [mm]	Female	24.07	9.25	42.32	0.00	77.00	27.83	20.65	0.57
	Male	16.87	9.22	41.88	0.00	58.89	23.87	19.37	
Distance between the origin of the umbilical artery and the origin of the IGA [mm]	Female	26.00	11.51	39.85	5.44	74.54	28.79	19.06	0.59
	Male	19.71	8.17	43.91	0.00	71.94	26.44	23.23	
Distance between the origin of the uterine artery and the origin of the IGA [mm]	Female	28.09	21.34	31.38	8.29	49.52	26.79	10.85	–
	Male	–	–	–	–	–	–	–	
Distance between the origin of the vaginal artery and the origin of the IGA [mm]	Female	38.21	29.89	40.67	3.06	56.52	33.67	19.64	–
	Male	–	–	–	–	–	–	–	
Distance between the origin of the middle Anorectal artery and the origin of the IGA [mm]	Female	60.54	35.91	73.90	6.78	90.28	52.99	23.47	0.64
	Male	46.11	14.11	74.62	0.00	103.62	46.66	37.02	
Distance between the origin of the internal pudendal artery and the origin of the IGA [mm]	Female	0.00	0.00	6.89	0.00	44.69	6.15	11.79	0.19
	Male	0.00	0.00	20.54	0.00	43.29	10.63	14.42	
Distance between the origin of the inferior vesical artery and the origin of the IGA [mm]	Female	–	–	–	–	–	–	–	–
	Male	54.16	54.01	54.30	54.01	54.30	54.16	0.21	

LQ — lower quartile; HQ — higher quartile; SD — standard deviation; IGA — inferior gluteal artery; ADIIA — anterior division of the internal iliac artery; IIA — internal iliac artery; SGA — superior gluteal artery; PDIIA — posterior division of the internal iliac artery

vascularized by perforators of multiple source arteries, not only from the IGA and SGA. Furthermore, in another anatomical and radiological study conducted by Song et al. [20] on the anatomy of the IGA and SGA, the IGA was found to be absent in 13.5% of cases. We did not note this happening in our analysis.

Surgeons should always be aware of detailed anatomical knowledge about the IGA and its close area should when performing augmentation gluteoplasty with a dermal fat flap [8, 21]. The key to performing gluteal augmentation safely and minimising risk and complications is to truly know the anatomy of the gluteal area [8].

The relation and course of the IGA to the sciatic nerve and the sacrospinous ligament have also been extensively discussed in the literature. Gabrielli et al. [3] stated that the IGA was found medial to the sciatic nerve in the majority of the cases (77.5%), and in the rest of the cases (22.5%), the main trunk of the artery or one of its branches perforated the said nerve. The anatomy of the pelvic arteries adjacent to the sacrospinous ligament was discussed in a study conducted by Thompson et al. [22]. In the study, the IGA was found behind the sciatic nerve and the sacrospinous ligament when originating from either the ADIIA or PDIIA. When it was leaving the pelvis, the artery passed posterior to the upper edge of the said ligament and followed the inferior portion of the sciatic nerve out of the greater sciatic foramen.

Knowledge about this region is particularly important when putting sutures through the sacrospinous ligament during various obstetric and gynaecological surgeries in the pelvis.

The IGA contributes to the blood supply of the hip through the anastomosis with the medial femoral circumflex artery. This phenomenon has been extensively described by Grose et al. [5] in a cadaveric study consisting of eight fresh-frozen cadaver pelvis specimens. They concluded that the medial circumflex artery receives a direct blood supply from the IGA immediately before passing beneath the hip capsule. A precise understanding of the vascular anatomy of this region may help to clarify the development of avascular necrosis after hip trauma.

Having extensive knowledge regarding the arterial anatomy of the pelvis may be of immense importance during numerous pelvic operations, especially interventional intraarterial procedures [10]. Embolization of the uterine artery can be performed to prevent or treat haemorrhage associated with numerous obstetric conditions, such as postpartum bleeding or ectopic pregnancy [9]. Postpartum haemorrhage accounts for up to 25% of maternal deaths worldwide [19], and the main treatment option is said to be embolization of the uterine artery. However, embolization of the said vessel may be challenging due to its variable anatomy. Therefore, Ostrowski et al. [16] analysed the complete anatomy of this artery

Table 4. Correlations between the measured parameters of the inferior gluteal artery (IGA) and patient's age

Category	Age	IGA length [mm]
IGA length [mm]	–0.08	1.00
Distance from the origin of the ADIIA to the origin of the IGA [mm]	0.32	–0.37
Distance from the origin of the IIA to the origin of the IGA [mm]	0.09	–0.01
Distance from the origin of the SGA to the origin of the IGA [mm]	0.46	–0.30
Distance from the origin of the PDIIA to the origin of the IGA [mm]	0.34	–0.33
IGA origin diameter [mm]	0.02	–0.04
IGA origin area [mm²]	0.04	0.07
IGA origin angle	–0.06	–0.27
Obturator artery origin diameter [mm]	–0.08	–0.36
Obturator artery origin area [mm²]	–0.07	–0.31
Umbilical artery origin diameter [mm]	0.02	–0.19
Umbilical artery origin area [mm²]	0.02	–0.15
Uterine artery origin diameter [mm]	–0.32	0.08
Uterine artery origin area [mm²]	–0.29	0.16
Vaginal artery origin diameter [mm]	–0.32	0.00
Vaginal artery origin area [mm²]	–0.29	–0.05
Middle anorectal artery origin diameter [mm]	–0.22	–0.05
Middle anorectal artery origin area [mm²]	–0.09	0.03
Internal pudendal artery origin diameter [mm]	–0.08	–0.15
Internal pudendal l artery origin area [mm²]	–0.05	–0.06
Inferior vesical origin diameter [mm]	0.67	0.70
Inferior vesical origin area [mm²]	0.95	0.80
Distance between the origin of the obturator artery and the origin of the IGA [mm]	0.28	–0.33
Distance between the origin of the umbilical artery and the origin of the IGA [mm]	0.21	–0.45
Distance between the origin of the uterine artery and the origin of the IGA [mm]	0.25	0.44
Distance between the origin of the vaginal artery and the origin of the IGA [mm]	0.97	–0.10
Distance between the origin of the middle anorectal artery and the origin of the IGA [mm]	0.13	0.70
Distance between the origin of the internal pudendal artery and the origin of the IGA [mm]	–0.01	0.04

Highlighted in red are those in which the p-value was less than 0.05. IGA — inferior gluteal artery; ADIIA — anterior division of the internal iliac artery; IIA — internal iliac artery; SGA — superior gluteal artery; PDIIA — posterior division of the internal iliac artery. R — Spearman's rank correlation coefficient

in a meta-analysis consisting of over 2000 subjects. In the study, it was stated that the knowledge about the morphometric values of the uterine artery (UTA) specifically its diameter is of great importance when choosing an appropriately-sized catheter for embolization procedures. The meta-analysis showed that the mean diameter of the uterine artery was 2.74 mm. Our study presents a slightly higher median diameter of 3.18 mm. Another branch of the ADIIA, the middle anorectal artery, is also highly variable. The said artery is also important to interventional radiologists who might embolize this vessel as a treatment for rectal bleeding [6]. Pichon et al. [18] presented two successful cases of this technique, where the aetiology of the bleeding was trauma to the rectum. We found the external diameter of the middle anorectal artery to be 3.05 mm, which is considerably higher than what was reported in other studies in the literature [2, 7].

Limitations of the study

The present study undoubtedly has some limitations. Although the size of the study group used in the current paper is the largest among imaging studies regarding IGA, larger population-based research is still warranted to discern the true prevalence of its variants. Furthermore, radiological imaging only allows one to evaluate haemodynamically efficient arteries. Therefore, this can be a relatively large source of bias when assessing anatomical variations of the IGA and other arterial entities. The particular branches

Table 5. Comparison between patient's side

Occurrence of IGA origin type with respect to the patient's side

Category	Left side	Right side
Type 01 (ADIIA)	42 (59.2%)	44 (65.7%)
Type 02 (IIA)	22 (31.0%)	11 (16.4%)
Type 03 (SGA)	3 (4.2%)	7 (10.4%)
Type 04 (PDIIA)	4 (5.6%)	5 (7.5%)

Cooccurrence of SGA origin types

Cooccurrence		Origin type on the right side			
		Type 01 (ADIIA)	Type 02 (IIA)	Type 03 (SGA)	Type 04 (PDIIA)
Origin type on the left side	Type 01 (ADIIA)	31 (46.3%)	2 (3.0%)	5 (7.5%)	3 (4.5%)
	Type 02 (IIA)	11 (16.4%)	9 (13.4%)	0 (0.0%)	1 (1.5%)
	Type 03 (SGA)	1 (1.5%)	0 (0.0%)	2 (3.0%)	0 (0.0%)
	Type 04 (PDIIA)	1 (1.5%)	0 (0.00%)	0 (0.0%)	1 (1.5%)

Comparison of selected parameters with respect to the patient's side

Category	Side	Median	LQ	HQ	Minimum	Maximum	Mean	SD	P
IGA length [mm]	Left	71.53	57.10	81.66	14.35	149.31	72.47	26.08	0.75
	Right	66.52	52.37	88.57	4.26	145.60	70.55	28.94	
Distance from the origin of the ADIIA to the origin of the IGA [mm]	Left	30.57	18.63	55.66	6.91	92.48	38.07	23.35	0.50
	Right	39.69	22.41	60.38	8.44	85.70	41.35	22.94	
Distance from the origin of the IIA to the origin of the IGA [mm]	Left	65.74	49.35	73.18	21.06	90.10	61.54	17.39	0.48
	Right	59.10	39.58	77.84	13.19	81.81	55.22	21.39	
Distance from the origin of the SGA to the origin of the IGA [mm]	Left	39.08	36.17	41.99	36.17	41.99	39.08	4.12	0.90
	Right	37.94	33.77	45.46	14.65	53.30	37.78	11.77	
Distance from the origin of the PDIIA to the origin of the IGA [mm]	Left	44.55	29.40	49.44	14.78	53.79	39.42	17.00	0.31
	Right	30.41	19.17	37.49	14.99	37.50	28.33	11.12	

LQ — lower quartile; HQ — higher quartile; SD — standard deviation; IGA — inferior gluteal artery; PDIIA — posterior division of the internal iliac artery; ADIIA — anterior division of the internal iliac artery; IIA — internal iliac artery; SGA — superior gluteal artery

of the IGA and their anastomosis with surrounding vascular structures should be further investigated in the future due to their potential clinical significance in endovascular and orthopaedic procedures.

CONCLUSIONS

The present study thoroughly analysed the complete anatomy of the IGA and the branches of the ADIIA. A novel classification system for the origin of the IGA was created, where the most prevalent origin was from the ADIIA (type 1; 62.3%). Furthermore, the morphometric properties (such as the diameter and length) of the branches of the ADIIA were analysed. This data may be incredibly useful for physicians performing operations in the pelvis, such as interventional intraarterial procedures or various gynaecological surgeries.

REFERENCES

1. Boustred AM, Nahai F. Inferior gluteal free flap breast reconstruction. Clin Plast Surg. 1998; 25(2): 275–282, indexed in Pubmed: 9627785.
2. DiDio LJ, Diaz-Franco C, Schemainda R, et al. Morphology of the middle rectal arteries. A study of 30 cadaveric dissections. Surg Radiol Anat. 1986; 8(4): 229–236, doi: 10.1007/BF02425072, indexed in Pubmed: 3107146.
3. Gabrielli C, Olave E, Sarmento A, et al. Abnormal extrapelvic course of the inferior gluteal artery. Surg Radiol Anat. 1997; 19(3): 139–142, doi: 10.1007/BF01627962, indexed in Pubmed: 9381313.
4. Georgantopoulou A, Papadodima S, Vlachodimitropoulos D, et al. The microvascular anatomy of superior and inferior gluteal artery perforator (SGAP and IGAP) flaps: a fresh cadaveric study and clinical implications. Aesthetic Plast Surg. 2014; 38(6): 1156–1163, doi: 10.1007/s00266-014-0398-z, indexed in Pubmed: 25209531.
5. Grose AW, Gardner MJ, Sussmann PS, et al. The surgical anatomy of the blood supply to the femoral head: de-

scription of the anastomosis between the medial femoral circumflex and inferior gluteal arteries at the hip. J Bone Joint Surg Br. 2008; 90(10): 1298–1303, doi: 10.1302/0 301-620X.90B10.20983, indexed in Pubmed: 18827238.

6. Heinze T, Fletcher J, Miskovic D, et al. The middle rectal artery: revisited anatomy and surgical implications of a neglected blood vessel. Dis Colon Rectum. 2023; 66(3): 477–485, doi: 10.1097/DCR.0000000000002531, indexed in Pubmed: 36630321.

7. Jones OM, Smeulders N, Wiseman O, et al. Lateral ligaments of the rectum: an anatomical study. Br J Surg. 1999; 86(4): 487–489, doi: 10.1046/j.1365-2168.1999.01080.x, indexed in Pubmed: 10215819.

8. Kalaaji A, Dreyer S, Vadseth L, et al. Gluteal augmentation with fat: retrospective safety study and literature review. Aesthet Surg J. 2019; 39(3): 292–305, doi: 10.1093/asj/sjy153, indexed in Pubmed: 29931270.

9. Katz MD, Sugay SB, Walker DK, et al. Beyond hemostasis: spectrum of gynecologic and obstetric indications for transcatheter embolization. Radiographics. 2012; 32(6): 1713–1731, doi: 10.1148/rg.326125524, indexed in Pubmed: 23065166.

10. Kędzia A, Dudek K, Ziajkiewicz M, et al. The morphometrical and topographical evaluation of the superior gluteal nerve in the prenatal period. PLoS One. 2022; 17(8): e0273397, doi: 10.1371/journal.pone.0273397, indexed in Pubmed: 36018841.

11. Koshima I, Moriguchi T, Soeda S, et al. The gluteal perforator-based flap for repair of sacral pressure sores. Plast Reconstr Surg. 1993; 91(4): 678–683, doi: 10.1097/00006534-199304000-00017, indexed in Pubmed: 8446721.

12. Kozioł T, Chaba W, Janda P, et al. A three-headed piriformis muscle: an anatomical case study and narrative review of literature. Folia Morphol. 2023; 82(4): 969–974, doi: 10.5603/FM.a2022.0108, indexed in Pubmed: 36573364.

13. Kuzuya A, Fujimoto K, Iyomasa S, et al. Transluminal coil embolization of an inferior gluteal artery aneurysm by ultrasound-guided direct puncture of the target vessel. Eur J Vasc Endovasc Surg. 2005; 30(2): 130–132, doi: 10.1016/j.ejvs.2005.03.006, indexed in Pubmed: 15890542.

14. Liapis K, Tasis N, Tsouknidas I, et al. Anatomic variations of the uterine artery. Review of the literature and their clinical significance. Turk J Obstet Gynecol. 2020; 17(1): 58–62, doi: 10.4274/tjod.galenos.2020.33427, indexed in Pubmed: 32341832.

15. Moore KL, Dalley AF, Agur A. Clinically oriented anatomy (8th ed). Lippincott Williams and Wilkins 2017.

16. Ostrowski P, Bonczar M, Michalczak M, et al. The anatomy of the uterine artery: A meta-analysis with implications for gynecological procedures. Clin Anat. 2023; 36(3): 457–464, doi: 10.1002/ca.23983, indexed in Pubmed: 36448185.

17. Pelage JP, Jacob D, Fazel A, et al. Midterm results of uterine artery embolization for symptomatic adenomyosis: initial experience. Radiology. 2005; 234(3): 948–953, doi: 10.1148/radiol.2343031697, indexed in Pubmed: 15681687.

18. Pichon N, François B, Pichon-Lefièvre F, et al. Embolization of rectal arteries: an alternative treatment for hemorrhagic shock induced by traumatic intrarectal hemorrhage. Cardiovasc Intervent Radiol. 2005; 28(4): 515–517, doi: 10.1007/s00270-004-0168-4, indexed in Pubmed: 16010510.

19. Rand T, Patel R, Magerle W, et al. CIRSE standards of practice on gynaecological and obstetric haemorrhage. CVIR Endovasc. 2020; 3(1): 85, doi: 10.1186/s42155-020-00174-7, indexed in Pubmed: 33245432.

20. Song WC, Bae SM, Han SH, et al. Anatomical and radiological study of the superior and inferior gluteal arteries in the gluteus maximus muscle for musculocutaneous flap in Koreans. J Plast Reconstr Aesthet Surg. 2006; 59(9): 935–941, doi: 10.1016/j.bjps.2005.11.028, indexed in Pubmed: 16920585.

21. Sozer SO, Agullo FJ, Palladino H. Autologous augmentation gluteoplasty with a dermal fat flap. Aesthet Surg J. 2008; 28(1): 70–76, doi: 10.1016/j.asj.2007.10.003, indexed in Pubmed: 19083509.

22. Thompson JR, Gibb JS, Genadry R, et al. Anatomy of pelvic arteries adjacent to the sacrospinous ligament: importance of the coccygeal branch of the inferior gluteal artery. Obstet Gynecol. 1999; 94(6): 973–977, doi: 10.1016/s0029-7844(99)00418-4, indexed in Pubmed: 10576185.

23. Vigato E, De Antoni E, Tiengo C, et al. Radiological anatomy of the perforators of the gluteal region: The "radiosome" based anatomy. Microsurgery. 2018; 38(1): 76–84, doi: 10.1002/micr.30214, indexed in Pubmed: 28767166.

24. Walocha JA, Litwin JA, Bereza T, et al. Vascular architecture of human uterine cervix visualized by corrosion casting and scanning electron microscopy. Hum Reprod. 2012; 27(3): 727–732, doi: 10.1093/humrep/der458, indexed in Pubmed: 22252085.

25. Walocha JA, Miodoński AJ, Szczepański W, et al. Two types of vascularisation of intramural uterine leiomyomata revealed by corrosion casting and immunohistochemical study. Folia Morphol. 2004; 63(1): 37–41, indexed in Pubmed: 15039897.

26. Zarzecki MP, Ostrowski P, Wałęga P, et al. The middle anorectal artery: A systematic review and meta-analysis of 880 patients/1905 pelvic sides. Clin Anat. 2022; 35(7): 934–945, doi: 10.1002/ca.23898, indexed in Pubmed: 35474241.

27. Żytkowski A, Tubbs R, Iwanaga J, et al. Anatomical normality and variability: Historical perspective and methodological considerations. Transl Res Anat. 2021; 23: 100105, doi: 10.1016/j.tria.2020.100105.

Figure 3. Anterior view of the analysed computer tomography angiography. Some of the arteries were shortened and/or excluded in order to provide clearest possible view; CIA — common iliac artery; IIA — internal iliac artery; EIA — external iliac artery; OA — obturator artery; UA — umbilical artery; IGA — inferior gluteal artery; MRA — middle rectal artery; IVA — inferior vesical artery.
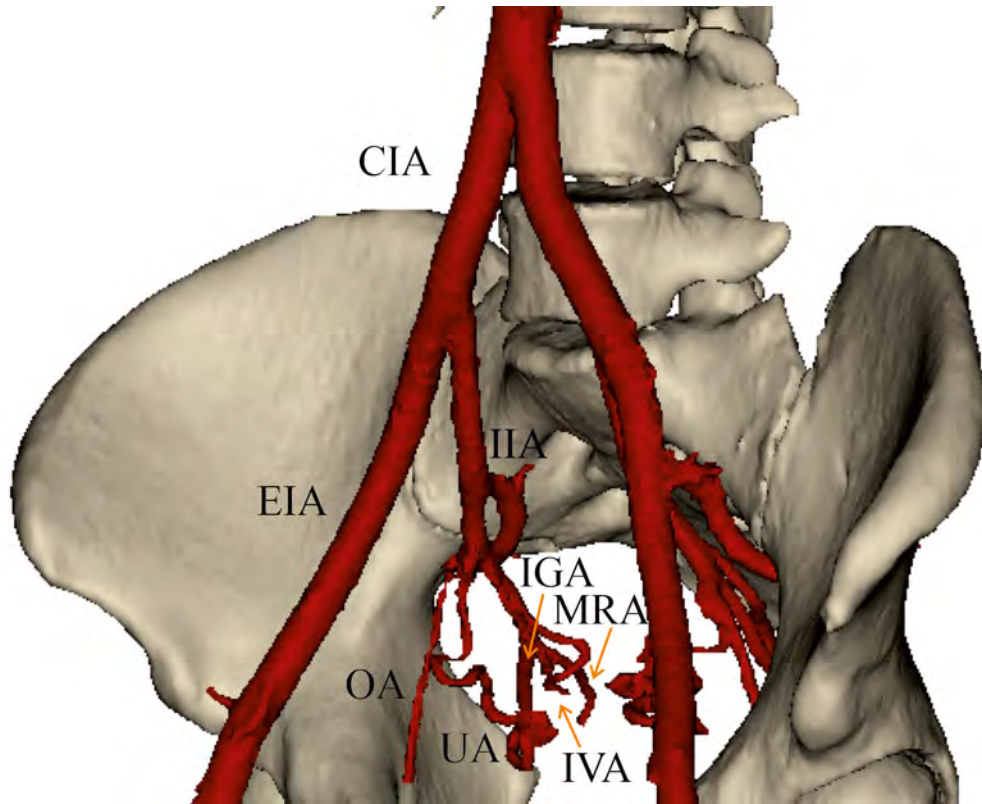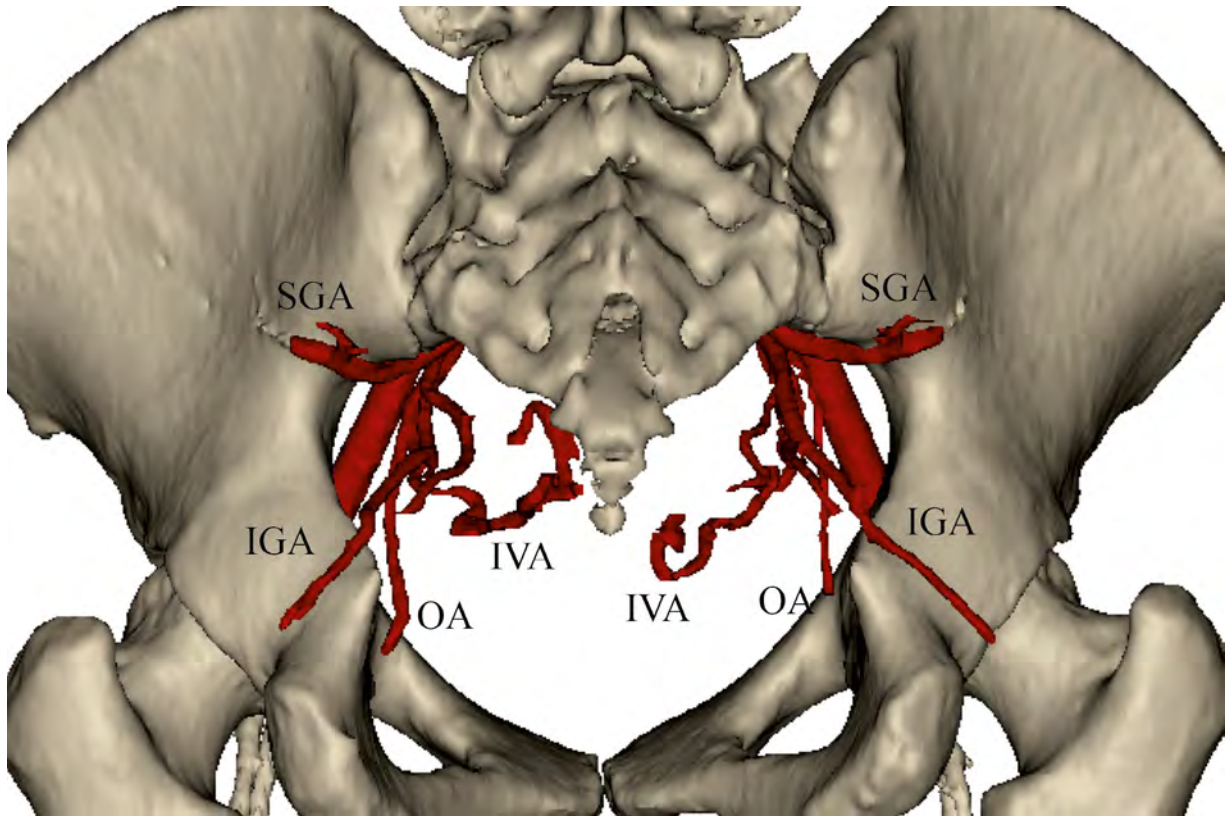
Figure 4. Posterior view of the analysed computer tomography angiography. Some of the arteries were shortened and/or excluded in order to provide clearest possible view; IGA — inferior gluteal artery; SGA — superior gluteal artery; OA — obturator artery; IVA — inferior vesical artery.

ORIGINAL ARTICLE

The relationship between the auriculotemporal nerve and middle meningeal artery in a sample of the South African population

Sherelle Moodley[1] , Sundika Ishwarkumar[2], Pamela Pillay[1]

[1]University of KwaZulu-Natal, Durban, South Africa
[2]University of Johannesburg, Johannesburg, South Africa

Background: The interaction between the auriculotemporal nerve and the middle meningeal artery within the infratemporal fossa is vital in the spread of perineural tumours. Knowledge of their morphological and morphometric variations is critical to surgeons approaching the infratemporal fossa. There is a paucity of literature on the relationship between the auriculotemporal nerve and middle meningeal artery in a South African population. Hence, the aim of this study was to document the morphology and morphometry of the auriculotemporal nerve and its relationship to the middle meningeal artery within a South African cohort.

Materials and methods: The infratemporal fossae of 32 cadaveric specimens were dissected and the auriculotemporal nerves and middle meningeal arteries were analysed, together with their variations.

Results: Nine out of 32 specimens displayed one-root, 14/32 two-root, 7/32 three-root, and 2/32 four-root auriculotemporal nerves. Eighteen auriculotemporal nerves originated from the mandibular nerve, while the rest had at least one communication to the inferior alveolar nerve. The mean distance between the first and second roots of the auriculotemporal nerve was 4.69 mm. There were V-shaped formations found in 23 auriculotemporal nerves. However, the middle meningeal artery only passed through 13/23 V-shapes. The maxillary artery was of a deep course in relation to the lateral pterygoid muscle in 19/32 and superficial in 13/32 of the sample. There were 15 accessory middle meningeal arteries present in 14/32 specimens. The accessory middle meningeal arteries often arose from the middle meningeal artery (46.67%).

Conclusions: The results of this study show a high possibility of variations of the auriculotemporal nerve and middle meningeal artery in the South African population. The variations and interactions should be considered during surgical procedures. (Folia Morphol 2024; 83, 1: 66–71)

Keywords: infratemporal fossa, mandibular nerve, maxillary artery, meningeal arteries, neoplasms

Address for correspondence: Dr. Pamela Pillay, School of Laboratory Medicine and Medical Sciences, College of Health Sciences, University of KwaZulu-Natal, Westville Campus, Private Bag X54001, Durban, 4000, South Africa, e-mail: soobramoneypa@ukzn.ac.za

INTRODUCTION

The auriculotemporal nerve (ATN) may be involved in parotid gland cancers and the resultant perineural tumour spread along the nerve may extend cranially to the foramen ovale, through which the mandibular branch of the trigeminal nerve passes [5, 19]. The progression of a tumour along the ATN can compromise tissues in the infratemporal fossa, cause trigeminal nerve palsy, and displace or obliterate vascular structures [17, 21]. The interaction between nerves and vessels is critical in the spread of perineural tumours, and the close association between the ATN and the middle meningeal artery [22] may cause additional complications [17]. As a result, medical practitioners must understand the morphology of the ATN and its relationship to the middle meningeal artery (MMA), as well as the anatomy of the infratemporal fossa, to appropriately identify the neurovasculature and limit the risk of complications during procedures to the infratemporal fossa. However, the relationship between the ATN and MMA has not been investigated in a South African population.

The auriculotemporal, inferior alveolar, and lingual nerves are the cutaneous branches of the posterior division of the mandibular nerve [8, 18]. The ATN has been reported to arise as two roots within the infratemporal fossa, forming a buttonhole to encircle the MMA before re-joining to form its main trunk [8, 18]. Some aural structures, the temporomandibular joint, the posterior portion of the temple, and the parotid gland, are innervated by the ATN [8, 10, 18].

The MMA is the maxillary artery's largest branch, and originates within the infratemporal fossa as the third branch from the first segment of the maxillary artery [11, 18]. The MMA coursed cranially through the buttonhole of the ATN and entered the cranium via foramen spinosum, supplying the dura mater [11, 18]. The infratemporal fossa may contain an accessory MMA, which arises from either the MMA or the maxillary artery, depending on the anatomical relationship between the maxillary artery and the lateral pterygoid muscle [1, 4, 11, 18].

While standard anatomical text stipulates the usual morphology of the ATN and its relationship to the MMA, many authors have discovered variations in this regard [3, 5, 7, 9, 13, 20]. Hence, the present study aimed to document the morphological and morphometrical anatomy of the ATN, the relationship between the MMA and the ATN, as well as their variations (if any) in a South African sample.

MATERIALS AND METHODS

The study used 16 formalin-fixed South African cadavers dissected bilaterally (n = 32) at the Department of Clinical Anatomy, University of KwaZulu-Natal. The Biomedical Research Ethics Committee at the University of KwaZulu-Natal granted ethical permission for this study (BREC/00002919/2021). The dissection procedures followed those of Dias et al. [7], Komarnitki et al. [13], and Loukas et al. [14].

This study used all available adult cadavers with no visible injury to the mandibular ramus or contents of the infratemporal fossa. The cadavers were placed in a supine position and dissected to expose the infratemporal fossa and its contents. The skin and superficial tissue overlying the zygomatic arch, parotid gland and duct, and mandibular ramus was removed. Thereafter, the zygomatic arch and mandibular ramus was cleaned and dissected using a bone saw to expose the contents of the infratemporal fossa [13]. The lateral and medial pterygoid muscles were dissected to reveal the deep contents of the infratemporal fossa, *viz.* the mandibular nerve and the MMA. Tracing the inferior alveolar nerve superiorly to the foramen ovale assisted in identifying the trunk of the mandibular nerve [14]. The roots of the ATN were cleaned and traced from the most inferior root to facilitate proper identification of the ATN's variations. The MMA was also cleaned and traced from its origin to the foramen ovale. The maxillary artery was identified, and the part from which the MMA originated was recorded. Variations in the ATN's roots and its relationship with the MMA were documented, as well as the presence of the accessory middle meningeal artery (aMMA). The distance between the roots of the ATN was measured three times for accuracy using a digital vernier calliper. The descriptions and data were entered on a Microsoft Excel 2016 spreadsheet for analysis.

The data were statistically analysed using the R Project for Statistical Computing software (version 3.6.3 of the R Core Team). Data were analysed using descriptive statistics, and parameters were found to be statistically significant with p-values less than 0.05.

RESULTS

The results of this study is shown in Table 1.

Demographics

The specimens used in the study were of South African White (87.50%) and Black (12.50%) descent. The cadavers were of an older cohort (72.4 ± 11.9

Table 1. Quantity and description of ATN, MMA, and aMMA discovered in the bilateral dissection of infratemporal fossae in a South African population (n = 32)

One-root ATN (%)	Two-root ATN (%)	Three-root ATN (%)	Four-root ATN (%)	Buttonhole formations (%)	V-shape formations (%)	aMMA present (%)	Maxillary artery deep to LPM (%)	Maxillary artery superficial to LPM (%)
9 (28.13%)	14 (43.75%)	7 (21.88%)	2 (6.25%)	1 (3.13%)	22 (68.75%)	14 (43.75%)	19 (59.38%)	13 (40.63%)

aMMA — accessory middle meningeal artery; ATN — auriculotemporal nerve; LPM — lateral pterygoid muscle
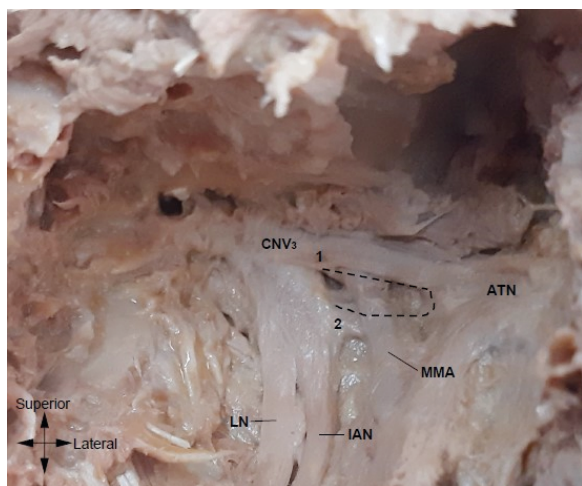

Figure 1. A two-root auriculotemporal nerve (ATN) and middle meningeal artery (MMA) within the infratemporal fossa. The first root of the nerve joins with the second root, forming a V shape (black dashed line). The MMA coursed through the V shape; 1 — first root of ATN, 2 — second root of ATN; CNV$_3$ — mandibular nerve; LN — lingual nerve; IAN — inferior alveolar nerve.

years) and there was equal distribution regarding the sex of the specimens.

Morphology of the ATN

One-root ATN. Eight of the nine one-root ATN specimens originated from the mandibular nerve, while the remaining one originated from the inferior alveolar nerve.

Two-root ATN. Seven of the 14 two-root specimens displayed both roots originating from the mandibular nerve. The remaining specimens showed the first root originating from the mandibular nerve and the second from the inferior alveolar nerve. All specimens with a two-root ATN had a V-shape formation, but the MMA was only found to pass through eight (Fig. 1).

Three-root ATN. Seven specimens had three-root ATN (Table 1). However, only three specimens were discovered with all roots originating from mandibular nerve. The first root of the remaining four specimens originated from the mandibular nerve and the two

inferior roots from the inferior alveolar nerve. All specimens had a V-shape formation; however, the MMA only passed through four.

Four-root ATN. Only two specimens displayed four-root ATN with their first root from the mandibular nerve, and their third and fourth roots originating from the inferior alveolar nerve. However, in one specimen, the second root originated from the mandibular nerve, while another originated from the inferior alveolar nerve. Both specimens exhibited V-shaped formations, but only one had the MMA passing through.

Morphometry of the ATN

The mean distances measured between the roots of the ATN are shown in Table 2. The mean distance between the first and second roots of the ATN was found to be the largest, while the distances between the third and fourth roots were the smallest.

Relationship between the ATN's roots and the MMA or maxillary artery

The observations of the relationship between the ATN and MMA are depicted in Table 3. However, it is noted that particular specimens were also related to the maxillary artery.

In a two-root specimen, the second root of the ATN was superficial to both the MMA and maxillary artery. Two specimens had their second roots deep to the maxillary artery and were, therefore, unrelated to the MMA. The second root of another specimen, which originated from the mandibular nerve, split into a buttonhole but did not contain any vasculature.

The second root in a three-root specimen was superficial to the maxillary artery and anterior to the MMA. Furthermore, the second root of the ATN in two specimens was closely related to the maxillary artery — one was deep to the maxillary artery, and another was inferior. The third roots of four specimens were also closely related to the maxillary artery — two were superficial, one was deep, and one inferior to the maxillary artery.

Table 2. Mean distances measured between the first and second, second and third, and third and fourth roots of the auriculotemporal nerve (ATN) [mm]

	One-root ATN	Two-root ATN		Three-root ATN			Four-root ATN				Total
	First root	First root	Second root	First root	Second root	Third root	First root	Second root	Third root	Fourth root	
Superficial to MMA	9	13	1	6	2	–	2	–	–	–	33
Deep to MMA	–	1	10	–	1	3	–	2	2	1	20
Anterior to MMA	–	–	1	1	1	1	–	–	–	1	5

MMA — middle meningeal artery

Table 3. Relationship between roots of the one-, two-, three-, and four-root auriculotemporal nerve and the middle meningeal artery in dissected infratemporal fossae

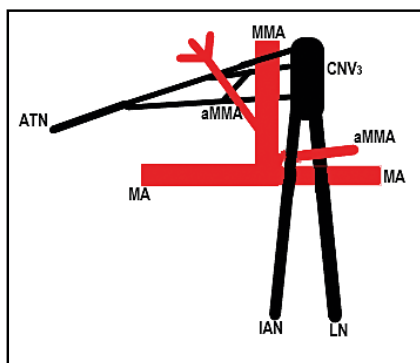|	Measurement [mm] Mean ± SD
Distance between the first and second roots	4.69 ± 5.24
Distance between the second and third roots	3.63 ± 3.89
Distance between the third and fourth roots	2.67 ± 2.06

SD — standard deviation

Figure 2. Schematic representation of the three-root auriculotemporal nerve (ATN) variant. The second root bifurcated — upper part joined first root and lower part joined third root. Middle meningeal artery (MMA) passed through V-shape created between the first and second roots; MA — maxillary artery; aMMA — accessory middle meningeal artery; CNV₃ — mandibular nerve; IAN — inferior alveolar nerve; LN — lingual nerve.

Course of the maxillary artery

The maxillary artery often coursed deep to the lateral pterygoid muscle in the studied sample (Table 1). Of the 19 deep course specimens, the maxillary arteries coursed through a loop formed in the inferior alveolar nerve in six specimens.

Presence of the aMMA

The aMMA was present in 14 (43.75%) specimens (Table 1). A double aMMA was found in one specimen, which coursed superiorly, superficial to the ATN, and trifurcated (Fig. 2). Hence, 15 aMMA was encountered in this study.

DISCUSSION

The ATN has been described to originate as two roots from the mandibular nerve, forming a button-hole to enclose the MMA [8, 18]. However, many studies have discovered that the ATN can arise from as few as one to as many as five roots [12, 16]. The two-root ATN is the most prevalent in the American, Turkish, Polish, New Zealand, Indian, and Thai populations [2, 6, 7, 9, 12, 16]. This correlated with the present study, as a prevalence of 43.75% was documented. Furthermore, the ATN can originate from the inferior alveolar and mandibular nerves [6, 7, 12], which was shown to be true in the present study. This study demonstrated that the first root of the ATN originated from the mandibular nerve and the inferior roots from the inferior alveolar nerve. This corroborated with Komarnitki et al. [12], Dias et al. [7], and Chanasong et al. [6] who found that the inferior alveolar nerve contributes to the main trunk of the ATN. Although, Quadros et al. [16] discovered that the inferior alveolar nerve was a point of origin of all the ATN in their population. The inferior alveolar nerve's contribution to the ATN could explain unexpected ATN neuralgia resulting from an inferior alveolar nerve block [15].

The morphometric distance measured between the roots of the auriculotemporal nerve suggested that the distance between the inferior roots is smaller than that of the superior roots. The mean distance between all the roots of the ATN was 4.42 mm in the present study, while Baumel et al. [2] and Gulekon et al. [9] found that the distance between the roots of the auriculotemporal nerve was 3.92 mm and 4.12, respectively. The difference in measurements amongst the various populations may suggest that morphometric distances may be affected by ethnicity.

Previous research has described the relationship between the roots of the ATN and the MMA as either superficial or deep to the artery [2, 7, 9, 16]. The present study further included a description of the roots being anterior to the artery. However, this study also demonstrated that the superior roots are usually superficial to the MMA, whereas the inferior roots are deep. These results corroborated with Baumel et al. [2] and Gulekon et al. [9]. Furthermore, the anatomical relationship of the three-root ATN to the MMA in a South African population is similar to that of the American population — the superior two roots are superficial to the MMA, and the inferior root is deep [2]. Contrarily, the first root in the Turkish population was superficial to the MMA, while the lower two were deep [9], while the Indian population showed one root being deep and two superficial to the MMA [16]. As a result, there is a great deal of variation in the relationship between the ATN roots and the MMA.

In agreement with previous literary reports, the typical buttonhole formation was not discovered in the present South African population [2, 7, 12]. The most common interval formed by the roots of the ATN in this study was a V-shape, as found in previous studies [2, 7, 12]. Although the V-shape was found in 22/32 of the selected sample, the MMA was only enclosed in 14 (63.64%). Dias et al. [7] and Chanasong et al. [6] found the MMA enclosed in 52.00% and 69.86% of their specimens, respectively. The findings of this study support previous research stating that the buttonhole is seldom present and that the MMA does not always pass through the ATN [2, 7, 12].

Although Baumel and Beard [1] concluded that the aMMA is commonly present, it was only found in 43.75% in the present study. Similarly, Chanasong et al. [6] discovered an aMMA in 21.91% of their sample. The aMMA may also arise in equal parts from the MMA and the maxillary artery [1]. However, Chanasong et al. [6] discovered that the aMMA arose more frequently from the MMA (75.00%). This study also found the aMMA frequently originating from the MMA (53.33%) in the South African population. Baumel and Beard [1] suggested that the course of the maxillary artery in relation to the lateral pterygoid muscle determined the origin of the aMMA. When the maxillary artery was superficial to the lateral pterygoid muscle, the aMMA arose from the MMA. However, the aMMA arose from the maxillary artery when the maxillary artery coursed deep to the lateral pterygoid muscle [1]. This relationship was also demonstrated in the current study.

CONCLUSIONS

This study examined the relationship between the MMA and the ATN in a South African population and added pivotal information on the contents of the infratemporal fossa in a South African population which may be beneficial to anatomists and surgeons. The findings of this study indicated several variations in the morphology of the ATN and its relationship to the MMA, which are similar to those found in population groups previously studied. The results of this study further highlighted that the variations of the ATN and the MMA are not concisely documented in standard anatomical literature.

Limitations and recommendations

Due to the limited sample size, no significant differences could be found between the individuals' sexes, sides, and ethnicities. However, the findings of this study may aid future research in discovering ethnic differences. Hence, the recommendation made for future studies is to utilise a bigger sample size to determine if there are significant differences in laterality, age, sex, and population groups. Due to the paucity of literature on the ATN and MMA, ethnic differences have not been previously established. This study, therefore, adds to the existing literature by discovering the morphology of the ATN and MMA in a South African population which may be useful for future studies examining population differences.

Ethical approval

This study was performed in line with the principles of the Declaration of Helsinki. The Biomedical Research Ethics Committee of the University of KwaZulu-Natal (BREC/00002919/2021) granted ethical approval for this study.

Acknowledgements

Conflict of interest: None declared

REFERENCES

1. Baumel JJ, Beard DY. The accessory meningeal artery of man. J Anat. 1961; 95(Pt 3): 386–402, indexed in Pubmed: 13688000.
2. Baumel JJ, Vanderheiden JP, McElenney JE. The auriculotemporal nerve of man. Am J Anat. 1971; 130(4):

431–440, doi: 10.1002/aja.1001300405, indexed in Pubmed: 5581228.

3. Bhardwaj N, Sahni P, Singhvi A, et al. Case report. Anomalous bilateral communication between the inferior alveolar nerve and the auriculotemporal nerve: a rare variation. Malaysian J Med Sci. 2014; 21(5): 71–74, indexed in Pubmed: 98622818.

4. Bonasia S, Smajda S, Ciccio G, et al. Middle meningeal artery: anatomy and variations. AJNR Am J Neuroradiol. 2020; 41(10): 1777–1785, doi: 10.3174/ajnr.A6739, indexed in Pubmed: 32883667.

5. Chan M, Dmytriw AA, Bartlett E, et al. Imaging of auriculotemporal nerve perineural spread. Ecancermedicalscience. 2013; 7(374): 1–5, doi: 10.3332/ecancer.2013.374, indexed in Pubmed: 24282445.

6. Chanasong R, Kiti-ngoen K, Khaodaeng C, et al. Anatomical variation of the auriculotemporal nerve in thai cadavers. Int J Morphol. 2020; 38(6): 1657–1661, doi: 10.4067/s0717-95022020000601657.

7. Dias GJ, Koh JMC, Cornwall J. The origin of the auriculotemporal nerve and its relationship to the middle meningeal artery. Anat Sci Int. 2015; 90(4): 216–221, doi: 10.1007/s12565-014-0247-9, indexed in Pubmed: 24973088.

8. Ellis H, Lawson A. The Cranial Nerves. 2013 2013/11/20 In: Anatomy for Anaesthetists [Internet]. Wiley-Blackwell. 9th [243-91]. https://doi.org/10.1002/9781118375945.ch6 (cited 2021/06/23).

9. Gülekon N, Anil A, Poyraz A, et al. Variations in the anatomy of the auriculotemporal nerve. Clin Anat. 2005; 18(1): 15–22, doi: 10.1002/ca.20068, indexed in Pubmed: 15597375.

10. Janis JE, Hatef DA, Ducic I, et al. Anatomy of the auriculotemporal nerve: variations in its relationship to the superficial temporal artery and implications for the treatment of migraine headaches. Plast Reconstr Surg. 2010; 125(5): 1422–1428, doi: 10.1097/PRS.0b013e3181d4fb05, indexed in Pubmed: 20440161.

11. Joo W, Funaki T, Yoshioka F, et al. Microsurgical anatomy of the infratemporal fossa. Clin Anat. 2013; 26(4): 455–469, doi: 10.1002/ca.22202, indexed in Pubmed: 23355316.

12. Komarnitki I, Andrzejczak-Sobocińska A, Tomczyk J, et al. Clinical anatomy of the auriculotemporal nerve in the area of the infratemporal fossa. Folia Morphol. 2012; 71(3): 187–193, indexed in Pubmed: 22936556.

13. Komarnitki I, Tomczyk J, Ciszek B, et al. Proposed classification of auriculotemporal nerve, based on the root system. PLoS One. 2015; 10(4): e0123120, doi: 10.1371/journal.pone.0123120, indexed in Pubmed: 25856464.

14. Loukas M, Benninger B, Tubbs RS. Gray's Clinical Photographic Dissector of the Human Body, 2 Edition- South Asia Edition-E-Book. Elsevier Health Sciences 2019: 484.

15. Ngeow WC, Chai WL. Numbness of the ear following inferior alveolar nerve block: the forgotten complication. Br Dent J. 2009; 207(1): 19–21, doi: 10.1038/sj.bdj.2009.559, indexed in Pubmed: 19590550.

16. Quadros LS, Jaison J, Bhat N, et al. Auriculotemporal nerve: a study on its roots. Online J Health Allied Sci. 2016: 15.

17. Schmalfuss IM, Tart RP, Mukherji S, et al. Perineural tumor spread along the auriculotemporal nerve. AJNR Am J Neuroradiol. 2002; 23(2): 303–311, indexed in Pubmed: 11847060.

18. Standring S, Anand N, Birch R, Collins P, Crossman AR, Gleeson M. Gray's Anatomy: the anatomical basis of clinical practice. 41st ed. Elsevier, Edinburgh 2016: 1584.

19. Thompson JD, Avey GD, Wieland AM, et al. Auriculotemporal Nerve Involvement in Parotid Bed Malignancy. Ann Otol Rhinol Laryngol. 2019; 128(7): 647–653, doi: 10.1177/0003489419837574, indexed in Pubmed: 30894024.

20. Thotakura B, Sharmila SR, Vaithianathan G, et al. Variations in the posterior division branches of the mandibular nerve in human cadavers. Singapore Med J. 2013; 54(3): 149–151, doi: 10.11622/smedj.2013051, indexed in Pubmed: 23546028.

21. Tiwari R. Surgical landmarks of the infratemporal fossa. J Craniomaxillofac Surg. 1998; 26(2): 84–86, doi: 10.1016/s1010-5182(98)80044-9, indexed in Pubmed: 9617670.

22. Ukoha UU, Umeasalugo KE, Udemezue OO, et al. Anthropometric measurement of infraorbital foramen in south-east and south-south Nigeria. Natl J Med Res. 2014; 4(3): 225–227.

VIA MEDICA

ORIGINAL ARTICLE

Biodegradable nanofiber coated human umbilical cord as nerve scaffold for sciatic nerve regeneration in albino Wistar rats

Balasundari Ramesh[1], Jaikanth Chandrasekaran[1], Kotturathu Mammen Cherian[1], Adegbenro Omotuyi John Fakoya[2]

[1]Frontier Lifeline Pvt Ltd., Chennai, India
[2]Louisiana State University, Health Sciences Centre, Shreveport, United States

Background: Human umbilical cord (hUC) is encompassed by a mucoid connective tissue called Wharton's jelly (WJ), made of hyaluronic acid, collagen, and stromal cells to support the blood vessels of hUC. This study was aimed to determine the in vitro neuronal differentiation of WJ-derived mesenchymal stem cells (WJMSCs), and in vivo axonal regeneration potential of nanofiber coated human Wharton's jelly as a neuronal graft after sciatic nerve injury in immunosuppressed albino Wistar rats.

Materials and methods: Wharton's jelly-derived mesenchymal stem cells could be differentiated to neuron-like cells by inducing with neuronic supplementing media. The test animal's axotomized nerves were implanted with trimmed human umbilical cord devoid of vascularity and nanocoated with electro-spun poly-l-lactic acid nanofibers. The control animals were bridged with native sciatic nerve reversed and sutured. Post-surgical functional recovery was studied by walking track, pinprick, muscle weight, and sweating quantification. At the end of the 4th week, the animals were euthanized, and magnetoneurography was performed. The explanted grafts were quantified by immunohistochemistry for immuno-rejection, neural scarring, neural adhesion axon regeneration, fibre diameter, myelin thickness, and G-ratio. The sciatic function index values were similar by walking track analysis for both the test and control groups.

Results: The animals had functional and sensation recovery by the end of 2 weeks. No mortality, signs of inflammation, and acute immune rejection were observed post-surgery.

Conclusions: The hUCWJ devoid of vascular elements can be a perfect peripheral nerve graft, and we hypothesis that the cryopreserved hUC could be an ideal resource for axonal regeneration in the future. (Folia Morphol 2024; 83, 1: 72–82)

Keywords: umbilical cord, Wharton's jelly, mesenchymal stem cells, nanofiber, sciatic nerve, axonal regeneration

Address for correspondence: Prof. Adegbenro Omotuyi John Fakoya, Department of Cellular Biology and Anatomy, Louisiana State University, Health Sciences Centre, 1501 Kings Highway P.O. Box 33932, 71103 Shreveport, United States, e-mail: adegbenro.fakoya@lsuhs.edu

INTRODUCTION

Traumatic peripheral nerve injury is a global problem and can cause devastating functional disabilities [11]. Several hundred thousand cases of peripheral nerve injury occur each year, results from stretch-related injuries, lacerations, or compressive trauma. The affected limb displays painful neuropathy symptoms, such as hyperalgesia, pain-related gait, and swelling. Ascending spinal pathways subsequently distribute nociceptive pain to multiple cortical, limbic structures and hypothalamus [15]. Current treatment modalities for peripheral nerve injuries involve end-to-end suturing of uninjured nerve ends for minor injuries and the use of autologous nerve grafts and neural prosthesis for significant damages. The application of nerve grafts for peripheral nerve repair is associated with donor site morbidity, the need for multiple surgeries, limited tissue availability, and inadequate functional reinnervation [28]. Allografts and cell suspension from the fetal central nervous system as the most effective neuro graft and have been substantially studied for their ability to develop and integrate within the host organism. However, ethical, social, and political issues act as a barrier to the application of fetal tissues [3, 13].

The unique morphologic properties of the human umbilical cord make them productive and the alternate source for mesenchymal stem cells (UC-MSCs), primarily as compared with umbilical cord blood [4, 16]. The UC-MSCs secretes different cytokines, chemokines, and growth factors known neurogenic cytokines, such as neurotrophin 3, endothelial growth factor, and midkine, may be a potential MSC source for neural stem cell therapies. The extracellular matrix of human umbilical cords (hUC) is rich in collagen IV and V, hyaluronan, and sulfated glycosaminoglycans [14, 21].

In the present basic research, we investigated the *in vitro* differentiation of human umbilical cord mesenchymal stem cells (hUC-MSCs) to neuron-like cells. The differentiated cells were verified for positive expression of neuronal markers by a reverse transcriptase-polymerase chain reaction and immunocytochemistry. Furthermore, an attempt was made to use human umbilical cord devoid of blood vessels as a neural graft to replace axotomized sciatic nerve in albino Wistar rats to restore impaired motor or sensory functions.

MATERIALS AND METHODS

The study was conducted after proper approval from various committees, including the Animal ethical committee and the stem cell ethics committee (IC-SCR). All the animals involved in this research were treated humanely, and experiments were conducted as per the guidelines of the Committees for the purpose of Control and Supervision of Experiments on Animals (CPCSEA).

The animals were purchased from Tamil Nadu Veterinary and Animal Science University. The experimental grafts were recovered from animals after euthanasia was done by certified veterinary technician. The euthanasia was done by using a pre-euthanasia anaesthetic (Telazol or PreMix 0.5 mL/10 pounds) to render the animal unconscious before injecting the euthanasian drug (Sodium Pentobarbital 117 mg//pound). The control animals involved in the research were maintained till natural death in the small animal facility in Frontier Mediville. There were no criteria needed for euthanizing animals prior to the planned end of the experiment.

For the collection of the amniotic membrane and cord blood, a written informed consent was administered to the patients or their parents. The patients were prescreened for HBsAg, HIV I and II, HCV, CMV, and venereal diseases. The study was conducted after a proper approval from various committees, which includes animal ethical committee and stem cell ethics committee (IC-SCR).

In vitro studies: neuronic differentiation of Wharton's jelly-derived mesenchymal stem cells (WJMSCS)

Derivation of poly-l-lactic acid (PLLA) nanofibers. PLLA nanofibers were derived by dissolving PLLA pellets in 1,1,1,3,3,3 hexafluoroisopropanol (HFIP, Sigma Aldrich 105228) and electrospun at a flow rate of 12–14 μL/min, with an applied voltage of 10–18 kV and 15 cm from a 4.5% (w/v) polymer solution [26]. The nanofibers can be directly coated on cell culture plates for *in vitro* experience and hUCs prior to *in vivo* experiments.

The hUCs were collected in Hanks balanced salt solution (HBSS, Himedia-TS1003) with antibiotic solution (Himedia A002A) from C-section delivery and transported to the laboratory with chilled packs within 6 hours. The hUCs were washed well with normal saline (0.9% W/V) and antibiotics to remove the residual blood from the veins and artery. Further, the hUCs were dissected free from vascularity. The dissected tissues, approximately 50 mg were minced using sterile method into small fragments 1–2 mm. The

minced tissue was also digested with 0.5 mg/mL collagenase (Sigma, C9722) and 0.2 mg/mL hyaluronidase (Sigma H3506) for 2 hours at 37°C. After enzymatic digestion, cold Dulbecco's phosphate buffered saline (DPBS, Himedia-TS1006) was added to cease the enzymatic activity. Further, the digested Wharton's jelly was washed by centrifuging twice with DPBS at 1500 rpm. The pellet along tissue debris was plated in the PLLA nanofiber coated plates with Dulbecco's modified eagle's media (DMEM with 4500 mg/mL glucose) and 2 mM l-glutamine (GIBCO-119950), supplemented with 10% fetal bovine serum (FBS, GIBCO-26140079). After 48 hours, the floating cells and debris were removed. The 2/3 confluent flask with adherent fibroblast cells was passaged using TrypLE Select (GIBCO). The Passage 2 cells were characterized using immunocytochemistry and flow cytometry [24].

Characterisation of Wharton's jelly cells

Immunocytochemistry. The cells were fixed with 4% paraformaldehyde in phosphate-buffered saline pH 7.4 for 15 min at room temperature, followed by permeabilization with 0.25% Triton X and were incubated for 1 hour with primary antibodies: anti CD73 (Abcam ab54217), anti CD90 (Abcam ab23894), anti-CD (Abcam ab44967), anti CD44 (Abcam ab9124), anti CD34 (Abcam ab8536), anti CD45 (Abcam ab40763). The primary monoclonal antibodies were added to the six-well culture plates as 1/100 dilution in 5% bovine serum albumin (BSA, Himedia, TC 194). After that, the cells were washed with DPBS and incubated with fluorescein isothiocyanate (FITC, Abcam ab5765) or phycoerythrin (PE, Abcam ab97024) conjugated secondary antibody at room temperature for 1 hour. The nucleus was stained using 4',6-diamidino-2-phenylindole 300 nm in Distilled water as per manufactures protocol (DAPI, Sigma D9542). The immune-stained cells were observed under fluorescent microscope (Olympus), and images were captured.

Flow cytometry. The cultured WJMSCs were detached with 0.25% trypsin and 0.2% EDTA, further blocked with 1% BSA in DPBS and incubated with Abcam primary antibody (20 μg/mL in 1% BSA) at 4°C overnight. Cells were washed twice with DPBS and incubated with the fluorophore (FITC or PE) conjugated secondary antibody at room temperature for 30 min. The cells were fixed with 2% paraformaldehyde and approximately 10^6 cells were subjected to flow cytometry by FACS Calibur (Becton-Dickinson) [24, 25].

Induction of WJMSCS to neuronic differentiation

The WJMSCs at cell culture passage five were used for differentiation experiments. Briefly, WJMSCs were induced to neuronic lineage differentiation by serum-free neurocult media (stem cell technologies). Control cultures were maintained in DMEM media supplemented with 10% FBS. The cells were replenished with new medium every alternate day and cultured for 3 weeks in the medium. The cultures were maintained in triplicates, and significant change in cell morphology was noted. At the end of the 3rd week, the cells were fixed for immunocytochemistry [7].

***In vivo* small animal experiment**

Surgical procedure. Sciatic nerve injury and graft implantation of biological nerve graft were conducted as described earlier methods [27, 34]. Albino Wistar rats 12 Nos male (6 Nos for umbilical grafts + 6 Nos for control autografts) approximately weighing 200 ± 20 g were used for axonal regeneration studies. Wistar rats were anesthetized intraperitoneally by using ketamine (75 mg/kg) and xylazine (20 mg/kg). The left hind limb sciatic nerve was exposed through a gluteal muscle incision, and about 1 cm sciatic nerve was transected at the mid-thigh level. The umbilical cord graft was trimmed with stereomicroscope following sterile protocols to remove the blood vessels and to match the size (length and width) of rat sciatic nerves. The test group rat axotomized nerve was bridged by suturing with human umbilical cord. These animals were administered with hydrocortisone (50 mg/kg) to prevent immune rejection as human umbilical cords were transplanted in rats. The control group axotomized sciatic nerve was reversed and sutured. Behaviour analysis was performed every week post-surgery to study the functional recovery of test and control rats by walking track analysis, pin-prick test, muscle weight, and sweating quantification. At the end of the 4th week, the animals were euthanized, and magnetoneurography (MNG) was performed in the umbilical cord grafted sciatic nerve, autografted sciatic nerve, and control native sciatic nerve from right hind limb. The explanted grafts were quantified by immunohistochemistry for immune-rejection, neural scarring, neural adhesion, axon regeneration, fibre diameter, myelin thickness, and G-ratio [8].

Functional tests were performed before the injury, immediately after transplantation, and after that weekly for 12 weeks after transplantation. Locomotor

activity was evaluated to assess the animal's loco-motor function using the walking track analysis as described below.

Walking track analysis

The most commonly used method of evaluation of the function of target organs after nerve injury in the rat is walking track analysis [2, 10]. The sciatic function index (SFI), is calculated using three measures of hind leg footprints acquired by walking track analysis: the 1–5 toe spread (TS), the 2–4 intermediate toe spread (ITS) and the print length (PL). The SFI was measured at a weekly interval between the 1st and 8th postoperative weeks. Triple measures were performed for each print and represented statistically. SFI = 0 was considered normal, whereas SFI = 100 was considered to indicate full damage. N is the values for normal rat, and E is for experimental rat.

$$SFI = -38.3 \times \left(\frac{EPL - NPL}{NPL} \right) + 109.5 \times \left(\frac{ETS - NTS}{NTS} \right) + 13.3 \times \left(\frac{EIT - NIT}{NIT} \right) - 8.8$$

Pin-prick test

The pin-prick test (PP) was used for sensitivity repair recovery. The test consisted of the pin-prick with a forceps of the animal-operated hind limb to evaluate the sensory recovery. The animal was pin-pricked from the toes to the knee until limb withdrawal was observed. Sensory recovery was graded on a scale from 0 to 3. Where grade 0 — represent the lack of response to pain stimulus, grade 1 — represents the limb withdrawal on stimuli above the ankle, grade II — withdrawal below the ankle, in the heel region, and grade III — limb withdrawal after the application of stimuli in the metatarsal region.

Toe spread test

Toe spread test was used for motor recovery evaluation. It is because the non-operated, normal rat extends and spreads the toes when it is hung by the tail. As in sensory recovery, motor recovery was graded on a scale from 0 to 3, where grade 0 — digital movement absence, grade I — any movement, grade II — toe spread, and grade III — toe extension and abduction.

Sweating quantification

The sweating of paws reflects autonomic nerve activity. Reinnervation of albino Wistar rat's hind paws sweats glands after peripheral nerve injury can be quantified by counting active sweat glands after induction by pilocarpine.

The albino Wistar rats were anesthetized with ketamine and xylazine as above. The implanted left hind paw was cleaned with distilled water and dried using nitrogen gas, and pilocarpine (80 mg/kg) was administered through *intra peritoneum* (*i.p.*) route. The sweat droplets were collected for 2–3 min after injection. After collection, micropipettes were centrifuged for oil and sweat separation, and the aqueous layer was quantified to measure the sweat volume.

Magento neurography

Magento neurography endpoint measurements were carried out 4, 8, and 12 weeks following the ex vivo MNG technique following the protocol described by Cudlip et al. (2002) [9]. The animals were anesthetized with urethane i.p. 12.5% (1 mL/100 g). The sciatic nerve was exposed from its origin in the lumbar spine to distal to the trifurcation at knee level to acquire a segment of maximum length. To prevent axon leakage, the proximal part and the three branches of the sciatic nerve were ligated with a 6-0 suture and were transected proximally and distally to the knots, respectively. The MNG recording chamber was filled with ringers lactate buffer containing glucose, 1 g/L, at 21 ± 0.1°C. The sciatic nerve was guided through the recording sensor coils and the stimulation cuff and stretched to *in vivo* length by clamping the two sutures in the recording chamber. The distal nerve end was stimulated with a biphasic constant current pulse of 50 μs delivered by two separate stimulus units (Digitimer DS3), connected in parallel. To guarantee supramaximal stimulation, the stimulator was finally set to 1.4 times the strength of the lowest current that produced a maximal signal. Every time the stimulation cuff changed position; this stimulus strength was redetermined. Both the right (control — normal nerve) and left (Test 6 Nos for Umbilical cord and 6 for native nerve graft surgery) sciatic nerve were measured. In the recording setting of the right nerve, the stimulation cuff cathode was positioned 10 mm distal to the suture line. Sensor 1 and sensor 2 were placed 4 mm and 14 mm proximal to the suture line, respectively. Only axons with fibres regenerating across the lesion were stimulated and recorded by applying distal stimulation and proximal recording. For the contralateral (unoperated) nerve, similar recording settings were used, and an imaginary suture line was created at the same distance
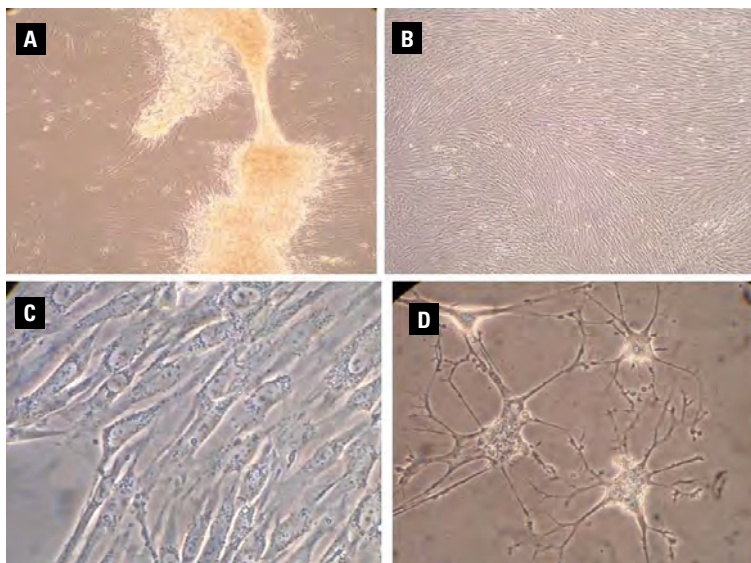
Figure 1. Expansion and differentiation of umbilical cord derived stem cells, **A.** Primary culture of collagenase digested umbilical cord stem cells; **B.** Passaged mesenchymal stem cells (×40); **C.** P4 umbilical cord mesenchymal stem cells control undifferentiated cells (×400); **D.** Umbilical cord mesenchymal stem cells differentiated to neuron like cells (×400).

from the distal nerve end as present in the repaired nerve. [29].

Muscle weight

After explanting the sciatic nerves for MNG measurement, the gastrocnemius muscles were simultaneously dissected and detached from their origin, insertion and weighed immediately. Muscle weight was expressed as the ratio of the left (operated) over the right (control) muscle weight.

Histological and immunohistochemical studies

At sacrifice 4 weeks later, the nerves were histologically evaluated for traumatic neuroma formation, Wallerian degeneration, perineural scar formation, and morphometric analysis. The distal sections were analysed for the differences in total fascicular area, myelinated fibres per nerve, fibre density, myelin area per nerve, myelinated fibre diameter, axon diameter, myelin thickness, or G-ratio.

The nerve impulse conduction speed was calculated using G ratio, a value representing the division of the axon's diameter by the nerve fibre diameter. According to Torch et al. (1989) [31], G ratio between 0.6 and 0.79 was considered normal in nerve conduction. G ratio below 0.6 implies dense myelinization, while the values above 0.79 evinces poor myelinization and conduction abnormality quantification of Nissl-stained sensory neurons was performed according to the empirical method of Coggeshall et al.

(1984) [8]. Briefly, nucleolar profiles (clearly visible nucleus with one or more nucleoli) were counted at 400× in every 10 sections starting with a randomly chosen part I. The calculations were multiplied by 10 and a correction factor to convert the nucleolar counts into neuronal numbers. This factor consisted of the nucleolar profile per 100 neurons after comparison of a randomly chosen section and the section adjacent to it. To study the dynamics of the lesion process, chromatolytic, eccentric, and pyknotic cells were quantified.

Statistical comparison

The Shapiro-Wilk was used for normality assessment. ANOVA was used for normally distributed data and SFI data. Friedman's test was used for intragroup comparison, and the Kruskal-Wallis test was used for intergroup comparison. The significance level was set at 5%.

RESULTS

Wharton's jelly (WJ) is one of the sources of immuno-privileged stem cells and derived from extraembryonic mesoderm as neuro system. Hence, we attempted to study WJ as neural graft for regeneration of peripheral nerve injury. We approve that the human WJ cells correspond phenotypically and functionally to MSCs. Accordingly, the cells were plastic adherent with fibroblastic morphology (Fig. 1). Using flow cytometry analysis and immune-cytochemistry, we
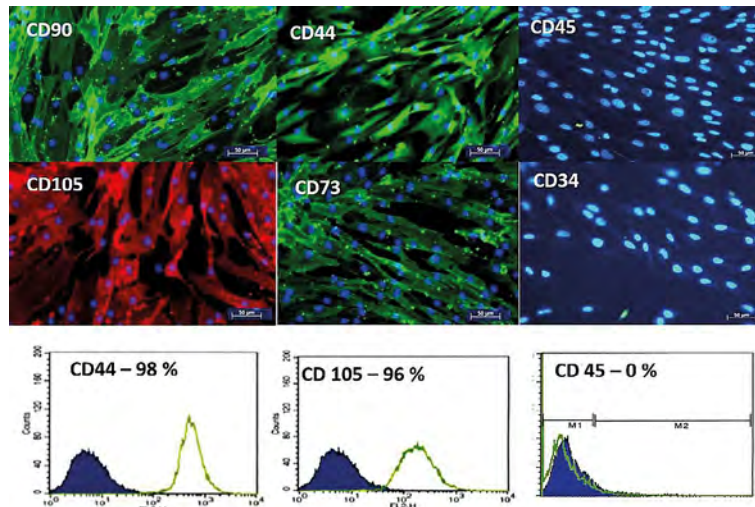
Figure 2. Immunohistochemistry and flowcytometry; immunocytochemistry and flowcytometry analysis of stem cells isolated from Wharton's jelly; red colour — tetramethyl rhodamine; green colour — fluorescein isothiocyanate; blue colour — 4'6-diamidino phenylindole stain for nucleus.
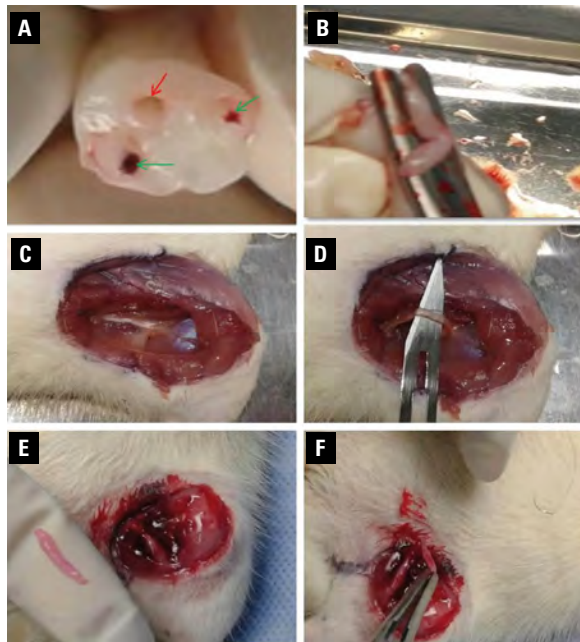

Figure 3. Sciatic nerve animal experiments, *in vivo* animal experiments; **A.** Cross section view of human umbilical cord showing one umbilical vein (red colour arrow) and two arteries (green arrows); **B.** Dissection of umbilical portion devoid of vascular elements; **C.** Exposure of left sciatic nerve; **D.** Separation of left sciatic nerve; **E.** Trimming the umbilical cord to the size of nerve; **F.** Suturing the umbilical cord portion to the cut end of the nerve.
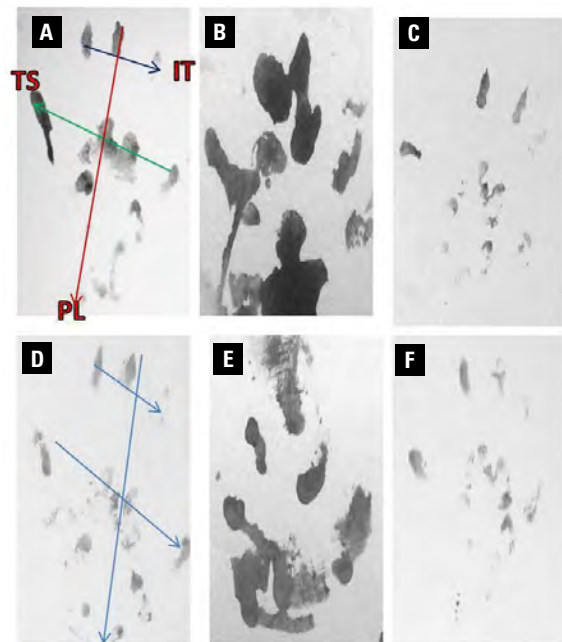
$$SFI = -38.3 \times \left(\frac{EPL - NPL}{NPL} \right) + 109.5 \times \left(\frac{ETS - NTS}{NTS} \right) + 13.3 \times \left(\frac{EIT - NIT}{NIT} \right) - 8.8$$

Figure 4. Walking track analysis; Walking track analysis image, **A, B, C.** Control mice before autografting, 2 week post grafting, 4 week post grafting; **D, E, F.** Test rat before Wharton jelly grafting, 2 week post grafting, 4 weeks post grafting; IT — intermediate toe spread; TS — toe spread; PL — print length.

found that mesenchymal stem cells (MSC) isolated from WJ revealed the high cell surface expression of MSC markers CD105, CD90, CD73, CD44, and absence for haematopoietic cells (Fig. 2).

The *in vivo* animal experiments were successfully carried out (Fig. 3). The SFI values were standard by walking track analysis for both the test and control groups (Fig. 4). The test and control animals were
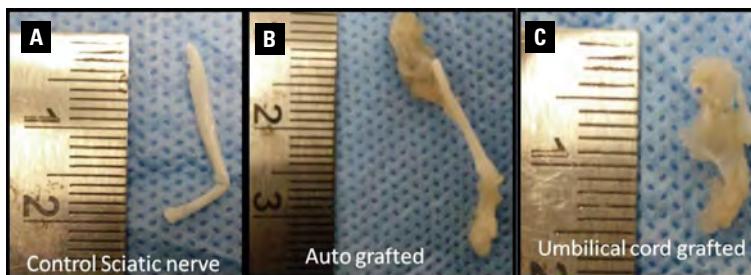
Figure 5. Explanted nerves; formaldehyde fixed explanted nerves after 2 months of implantation, **A.** Control sciatic nerve; **B.** Autografted control nerve; **C.** Umbilical cord grafted portion.
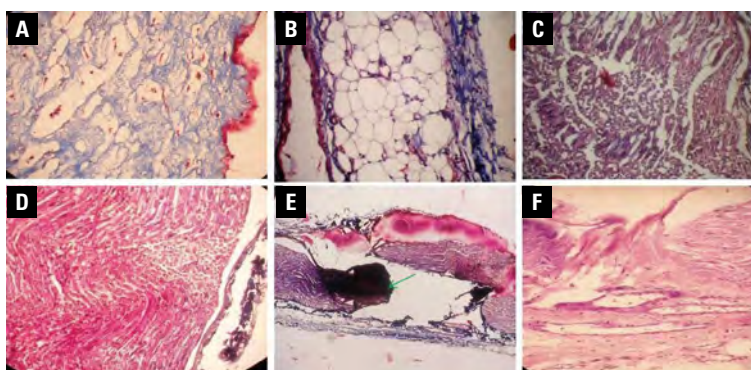

Figure 6. Histopathological Trichome staining for explanted nerves; **A.** Control umbilical cord prior to implantation; **B.** One month explanted rejected tissue; **C.** Two months old explanted umbilical cord tissue; **D.** Control sciatic nerve; **E.** Autografted sciatic nerve showing the axonal growth cone at site of axotomy (green arrow); **F.** Two months old autografted nerve at the site of axotomy.
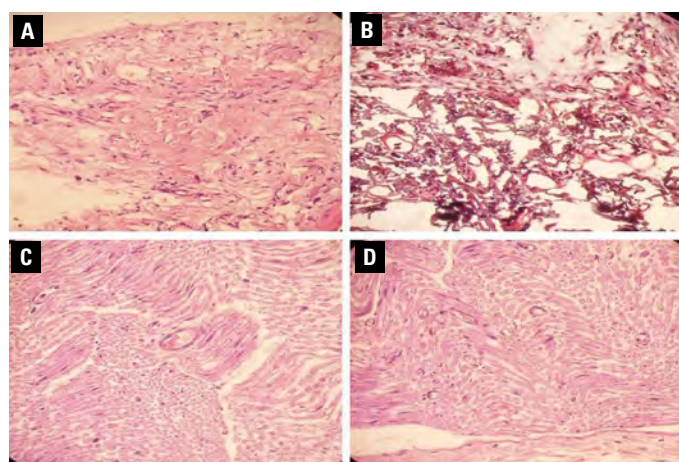
Figure 7. Immunohistochemistry for infiltration of CD25 activated T cells; **A.** Control umbilical cord — negative for CD25; **B.** Explanted umbilical cord positive for CD25; **C.** Control native sciatic nerve — negative for CD25; **D.** Immunostained sciatic nerve explanted control — negative for CD25.

able to recover their sensation on the grafted legs by the end of 2 weeks. No mortality, signs of inflammations, and graft rejection were observed in Wistar rats during the surgical experiment and post-surgery (Fig. 5). There was no evidence of fibrosis and neural scarring in both groups. Walking track analysis generated a significant value (p = 0.523), which implied similar healing and regeneration between the positive control and treated group (Fig. 6). The immuno-histochemistry for T antigen CD25 (Fig. 7) in explanted grafts indicates that WJ grafts are less immunogenic, although there was minimal infiltration of CD25 cells.

Table 1. Functional evaluation for control and test animals

S.No.	Functional evaluation	1st week		2nd week		3rd week		4th week	
		Control rats	Test rats	Control rats	Test rats	Control rats	Test rats	Control rats	Test rats
1	Pin-prick test	Grade I	Grade 0	Grade I	Grade 0	Grade II	Grade I	Grade III	Grade II
1	Toe spread test	Grade 0	Grade 0	Grade I	Grade 0	Grade I	Grade I	Grade II	Grade II
3	Sweating quantification [μL]	9.75 ± 1.7	7 ± 1.4	11 ± 1.8	8.25 ± 1.2	14.25 ± 0.9	11 ± 1.8	16 ± 1.4	12.25 ± 2.0

Table 2. Action potential of sciatic nerve evaluation using a magnetoneurography system (MNG)

MNG	1st week		2nd week		3rd week		4th week	
	Control rats	Test rats	Control rats	Test rats	Control rats	Test rats	Control rats	Test rats
LATN1 [ms]	0.12 ± 0.09	0.8 ± 0.18	0.17 ± 0.16	0.11 ± 0.12	0.22 ± 0.08	0.15 ± 0.14	0.28 ± 0.15	0.23 ± 0.12
LATN2 [ms]	0.18 ± 0.06	0.9 ± 0.10	0.26 ± 0.12	0.18 ± 0.15	0.30 ± 0.16	0.23 ± 0.14	0.36 ± 0.10	0.43 ± 0.12
CVN1 [m/s]	62 ± 26.75	55 ± 28.05	65 ± 32.1	58 ± 25.3	70.25 ± 28.13	63 ± 18.2	85 ± 23.3	69 ± 35.8
CVN2 [m/s]	46 ± 24.3	33 ± 16.8	54.31 ± 23.5	39.64 ± 28.5	66.32 ± 22.06	43.28 ± 26.71	79.24 ± 17.8	52.21 ± 22.7
AMPN1 [mV]	1.12 ± 0.32	0.83 ± 0.46	1.38 ± 0.26	0.9 ± 0.54	1.57 ± 0.48	1.39 ± 0.36	1.8 ± 0.43	1.43 ± 0.34
AMPN2 [mV]	0.52 ± 0.28	0.31 ± 0.35	0.68 ± 0.33	0.43 ± 0.26	0.74 ± 0.49	0.61 ± 0.47	0.86 ± 0.34	0.77 ± 0.29

AMPN1 — initial nerve action potentials amplitudes; AMPN2 — final nerve action potential amplitudes; LATN1 — initial nerve action potentials latencies; LATN2 — final nerve action potential latencies; CVN1 — initial nerve action potential conduction velocities; CVN2 — final nerve action potentials conduction velocities; ms — millisecond; m/s — meters per second; mV — millivolt

The infiltration could be due to cross-species (human to rats) transplantation of graft. Moreover, no statistical difference in G-ratio was found between the autograft and WJ grafted group.

The functional nerve recovery was assessed by the rats walking track analysis. As the walking footprints are shown in Figure 4, the sciatic nerve injury treated group showed recovery. The SFI value varies from 100 to 0. The value 0 indicates normal function, and 100 means complete loss of function. The SFI value of treated group suggests functional recovery. Further, no significant difference exists between the autograft and test animal group. The interpersonal correlation in measurement was high after the 3rd week. Inadequate definition of footprints was noted in the first 2 weeks. The functional recovery results by pin-prick test, toe spread test, and sweating quantifications indicate that by the end of the 4th week, the test rats transplanted with umbilical cord have grade II recovery. In contrast, the autografted controls had better sensitivity (Table 1). MNG values were recorded for the first 4 weeks, and the values were noted (Table 2). The initial and final nerve action potentials were significant and showed gradual improvements from 1st week to 4th week. There was no significant difference in muscle weight between control and test animals. Trichome staining and microscopic analysis revealed

that cross-section of an intra-muscular nerve bundle and blood vessel formation are seen in treated sciatic nerve when compared to cross-section of normal sciatic nerve. In the case of a longitudinal section of treated sciatic nerve, demarcation was observed between native sutured nerve and WJ (Fig. 6).

DISCUSSION

Clinical literature reports that less than 25% of nerve repair patients recover complete voluntary motor function and less than 3% recover full normal sensation [29]. The clinical results of these procedures have served as the impetus to continue the search for alternative methods of repairing peripheral nerve injuries. One such alternative is the use of various "nerve conduits" which may replace the need for nerve grafting. This is a novel attempt of using human umbilical cord Wharton's jelly (hUC-WJ), which is discarded as medical waste as a biological nerve graft for peripheral nerve injury. This experiment is to validate the efficacy of using the human cord as a nerve graft, as it is the natural reservoir of immune privileged stem cells in WJ. The immunomodulatory effects of hUC-MSCs are mediated by multiple factors. The hUC-MSCs could reduce or block MHC class II expressions on vascular endothelial cell surface in cardiac allografts and decrease proinflammatory cy-

tokines interleukin 2 and interferon gamma, enhance anti-inflammatory cytokines, such as interleukin 10 and transforming growth factor betta1 expression *in vivo*. The soluble factors secreted by hUC-MSC have immunoregulatory effects as well [22]. For more than a decade there are several attempts exploring the use of umbilical cord as a graft for clinical application. In 1995, Angelo et al. [1] had conducted a large animal experiment using lamb autologous umbilical cord veins and arteries for femoral artery reconstructive surgeries. The preliminary results suggest that umbilical vessels could be used as vascular autograft provided with the immediate care of vasoactive graft during the perioperative period. Chen et al. (2012) [6] hypothesize that the hUC may be an adequate novel substitute for the reconstruction of the extrahepatic bile duct.

Wharton's jelly tissue is the combination of stromal microenvironment and hUC-MSCs, which could be appropriate for treating traumatic brain injury than hUC-MSCs cell suspension. Transplanting the human WJ tissue on the surface of the injured brain of Sprague Dawley rats developed significant protection with improved histologic and functional outcomes after traumatic brain injury [5]. Decellularized human umbilical arteries seeded with human umbilical vein endothelial cells preserved the extracellular matrix and retained function *in vivo* for up to 8 weeks in nude rats. These properties suggest the potential use of decellularized umbilical arteries as small-diameter vascular grafts [12]. Recent research with decellularized WJ as three-dimensional (3D) tissue engineered graft that can be used as osteogenic or chondrogenic grafts. The decellularized WJ graft experiments in murine calvarial defect model with green fluorescent protein labelled osteocytes indicates that this matrix can be used as a 3D porous, bioactive, and biocompatible scaffold for tissue engineering and regenerative medicine applications [17, 18]. Moreover, recent surgical advances make use of cryopreserved autologous umbilical cords as shunt conduits in neonatal cardiac surgery clinical trial (ClinicalTrials.gov; Identifier: NCT02766998).

In our experiment, WJ sutured to the sciatic nerve transection showed functional recovery of rat model at the site of nerve injury. Axonal regeneration was observed during the explant after 4 weeks of surgery. Functional recovery was evidenced by walking track analysis and histopathological studies. Walking track analysis is a quantitative method of analysing

functional recovery of peripheral nerve in the rats. The performance of hind limbs after nerve injuries are analysed by examining footprints, known as the SFI [32]. In our studies the performance and analysis infers the explanted tissue analysis shows similar healing between auto grafted and treated group. To add on histopathology evaluation had sections of developing axons and neoangiogenic vessels. Axonal regeneration may be aided due to the presence of MSCs in WJ. The WJ-derived MSCs avoid ethical issues involved in embryonic stem cell research and being immune-privileged, which makes them an advantageous cell type for allogeneic transplantation [23, 30]. The *in vitro* culture studies proved that these MSCs are plastic adherent cells positive for markers CD105, CD90, CD73, CD44 and could be differentiated to neuron-like cells. WJ-MSCs have the ability to differentiate into WJ-Schwann cells like cells (WJ-SCLCs) that effectively enhance the outgrowth of neurites *in vitro*. In addition, implantation of WJ-SCLCs-laden acellular nerve grafts isolated and decellularized from male Sprague–Dawley rats were superior to acellular nerve grafts alone in inducing functional recovery after sciatic nerve injury [7]. A novel method using lyophilization and enzymes to prepare acellular nerve scaffold was effective in removal of cells, myelin and maintain the integrity and mechanical properties of nerve fibre than the traditional methods. The combination of hUC-MSCs with acellular nerve scaffold promotes repair and regeneration of the sciatic nerve Sprague–Dawley animal model [20, 22]. In another similar studies tonsils derived mesenchymal stem cells (T-MSCs) were differentiated to Schwann cells (SC) *in vitro*. T-MSCs were able to express SC-specific markers, support of neurite outgrowth, and formation of myelin sheaths. Moreover, T-MSC-SC transplantation produced functional improvements in a mouse model of sciatic nerve mild injury [19].

Wharton's jelly-MSCs may serve as a valuable source of SCs for use in transplantation, and human WJ-SCLCs may be effective for promoting the regeneration of peripheral nerves. Topical administration of human WJ-MSC bound to a delivery agent such as hydrogel may even provide sustained therapeutic effects with localized delivery of cells to the affected area [33]. For proper development of therapeutic approaches, it is essential to elucidate the possible mechanism by which stem cells play a pivotal role in aiding in functional recovery after peripheral nerve injury. We hypothesis that the

therapeutic benefits such as angiogenesis, neurogenesis, synaptogenesis, cell fusion, and reduction of apoptosis could be achieved in the zone of the injury by implanting human umbilical cord. The elevation of neuronal-specific genes and varying levels of neural and astrocyte-specific proteins could be confirmed by immunolabelling after explantation of the graft. We envisage further elucidation of these ongoing investigations in the hope of using hUC WJ as nerve graft that will meet the complete clinical requirements.

Limitation of the study

It was challenging to suture the nanocoated umbilical cord with native rat sciatic nerve as it was very tiny. We should have used gelatine glue instead of suturing. However, the outcome of this experiment was excellent. All the experimental rats resumed the functional recovery, no immunorejection was observed.

CONCLUSIONS

In conclusion, we emphasize that the *in vivo* animal experimentation of the human umbilical cord WJ devoid of vascular elements, allantoic duct, and amniotic epithelium can be a perfect neuro graft for peripheral nerve injuries. WJ is a natural reservoir of immune-privileged stem cells, which share properties of adult and embryonic stem cells should be a boon in nerve remodelling. Moreover, the presence of hyaluronic acid, collagen and growth factors guide the neurogenesis. The nerve repair and reconstruction data from animal experiments can be translated to clinical practice followed by clinical trials. However, some factors such as cognitive capacity and coping, which are known to influence outcome following nerve repair, are challenging to study in animal models. Furthermore, the molecular and cellular mechanism of neurogenesis needs to be analysed using an immune deficient animal model. Future concurrent research is necessary to elucidate the use of cryopreserved umbilical cords as neural grafts as it has been a recent practice to bank umbilical cords along with cord blood.

Acknowledgements

Conflict of interest: None declared

REFERENCES

1. Angelo AV, Hovaguimian H, Arntson E, et al. Use of autologous umbilical artery and vein for vascular reconstruction in the newborn. J Thorac Cardiovasc Surg. 1995; 109(5): 854–857, doi: 10.1016/S0022-5223(95)70308-X, indexed in Pubmed: 7739244.

2. Bain JR, Mackinnon SE, Hunter DA. Functional evaluation of complete sciatic, peroneal, and posterior tibial nerve lesions in the rat. Plast Reconstr Surg. 1989; 83(1): 129–138, doi: 10.1097/00006534-198901000-00024, indexed in Pubmed: 2909054.

3. Barker RA, Barrett J, Mason SL, et al. Fetal dopaminergic transplantation trials and the future of neural grafting in Parkinson's disease. Lancet Neurol. 2013; 12(1): 84–91, doi: 10.1016/S1474-4422(12)70295-8, indexed in Pubmed: 23237903.

4. Campagnoli C, Roberts IA, Kumar S, et al. Identification of mesenchymal stem/progenitor cells in human first-trimester fetal blood, liver, and bone marrow. Blood. 2001; 98(8): 2396–2402, doi: 10.1182/blood.v98.8.2396, indexed in Pubmed: 11588036.

5. Cheng T, Yang Bo, Li D, et al. Wharton's jelly transplantation improves neurologic function in a rat model of traumatic brain injury. Cell Mol Neurobiol. 2015; 35(5): 641–649, doi: 10.1007/s10571-015-0159-9, indexed in Pubmed: 25638565.

6. Cheng Y, Lin Y, Xiong X, et al. The human umbilical cord: A novel substitute for reconstruction of the extrahepatic bile duct. J Med Hypotheses Ideas. 2012; 6(1): 7–11, doi: 10.1016/j.jmhi.2012.03.001.

7. Choi SJ, Park SY, Shin YHo, et al. Mesenchymal stem cells derived from wharton's jelly can differentiate into schwann cell-like cells and promote peripheral nerve regeneration in acellular nerve grafts. Tissue Eng Regen Med. 2021; 18(3): 467–478, doi: 10.1007/s13770-020-00329-6, indexed in Pubmed: 33515168.

8. Coggeshall RE, Chung K, Greenwood D, et al. An empirical method for converting nucleolar counts to neuronal numbers. J Neurosci Methods. 1984; 12(2): 125–132, doi: 10.1016/0165-0270(84)90011-6, indexed in Pubmed: 6527551.

9. Cudlip SA, Howe FA, Griffiths JR, et al. Magnetic resonance neurography of peripheral nerve following experimental crush injury, and correlation with functional deficit. J Neurosurg. 2002; 96(4): 755–759, doi: 10.3171/jns.2002.96.4.0755, indexed in Pubmed: 11990818.

10. de Medinaceli L, Freed WJ, Wyatt RJ. An index of the functional condition of rat sciatic nerve based on measurements made from walking tracks. Exp Neurol. 1982; 77(3): 634–643, doi: 10.1016/0014-4886(82)90234-5, indexed in Pubmed: 7117467.

11. Dvir T, Timko BP, Kohane DS, et al. Nanotechnological strategies for engineering complex tissues. Nat Nanotechnol. 2011; 6(1): 13–22, doi: 10.1038/nnano.2010.246, indexed in Pubmed: 21151110.

12. Gui L, Muto A, Chan SA, et al. Development of decellularized human umbilical arteries as small-diameter vascular grafts. Tissue Eng Part A. 2009; 15(9): 2665–2676, doi: 10.1089/ten.tea.2008.0526, indexed in Pubmed: 19207043.

13. Houlé JD, Reier PJ. Transplantation of fetal spinal cord tissue into the chronically injured adult rat spinal cord. J Comp Neurol. 1988; 269(4): 535–547, doi: 10.1002/cne.902690406, indexed in Pubmed: 2453536.

14. Hsieh JY, Wang HW, Chang SJ, et al. Mesenchymal stem cells from human umbilical cord express preferentially secreted factors related to neuroprotection, neurogenesis, and angiogenesis. PLoS One. 2013; 8(8): e72604, doi: 10.1371/journal.pone.0072604, indexed in Pubmed: 23991127.

15. Hunt SP, Mantyh PW. The molecular dynamics of pain control. Nat Rev Neurosci. 2001; 2(2): 83–91, doi: 10.1038/35053509, indexed in Pubmed: 11252998.

16. Iftimia-Mander A, Hourd P, Dainty R, et al. Mesenchymal stem cell isolation from human umbilical cord tissue: understanding and minimizing variability in cell yield for process optimization. Biopreserv Biobank. 2013; 11(5): 291–298, doi: 10.1089/bio.2013.0027, indexed in Pubmed: 24835260.

17. Irina A, Timur F, Evgeniya K, et al. Role of VEGF-A in angiogenesis promoted by umbilical cord-derived mesenchymal stromal/stem cells: in vitro study. Stem Cell Res Ther. 2016; 7: 46, doi: 10.1186/s13287-016-0305-4, indexed in Pubmed: 27001300.

18. Jadalannagari S, Converse G, McFall C, et al. Decellularized Wharton's Jelly from human umbilical cord as a novel 3D scaffolding material for tissue engineering applications. PLoS One. 2017; 12(2): e0172098, doi: 10.1371/journal.pone.0172098, indexed in Pubmed: 28222169.

19. Jung N, Park S, Choi Y, et al. Tonsil-derived mesenchymal stem cells differentiate into a Schwann cell phenotype and promote peripheral nerve regeneration. Int J Mol Sci. 2016; 17(11): 1867, doi: 10.3390/ijms17111867, indexed in Pubmed: 27834852.

20. Marinescu SA, Zărnescu O, Mihai IR, et al. An animal model of peripheral nerve regeneration after the application of a collagen-polyvinyl alcohol scaffold and mesenchymal stem cells. Rom J Morphol Embryol. 2014; 55(3): 891–903, indexed in Pubmed: 25329117.

21. Place ES, Evans ND, Stevens MM. Complexity in biomaterials for tissue engineering. Nat Mater. 2009; 8(6): 457–470, doi: 10.1038/nmat2441, indexed in Pubmed: 19458646.

22. Qian C, Zhang Z, Zhao R, et al. Effect of acellular nerve scaffold containing human umbilical cord-derived mesenchymal stem cells on nerve repair and regeneration in rats with sciatic nerve defect. Ann Transl Med. 2022; 10(8): 483, doi: 10.21037/atm-22-1578, indexed in Pubmed: 35571424.

23. Qiu Y, Yun MM, Han X, et al. Human umbilical cord mesenchymal stromal cells suppress MHC class II expression on rat vascular endothelium and prolong survival time of cardiac allograft. Int J Clin Exp Med. 2014; 7(7): 1760–1767, indexed in Pubmed: 25126177.

24. Ramesh B, Bishi DK, Rallapalli S, et al. Ischemic cardiac tissue conditioned media induced differentiation of human mesenchymal stem cells into early stage cardiomyocytes. Cytotechnology. 2012; 64(5): 563–575, doi: 10.1007/s10616-012-9440-7, indexed in Pubmed: 22395895.

25. Ramesh B, Chandrasekaran J, Jeevankumar S, et al. Hybrid amniotic membrane dressing with green silver nanoparticles as bioengineered skin for wounds and burns: a pilot studies. J Biotechnol Biomater. 2017; 07(03), doi: 10.4172/2155-952x.1000272.

26. Ramesh B, Kotturathu MC, Adegbenro OJ, et al. Fabrication and electrospinning of 3D biodegradable poly-l-lactic acid (PLLA) nanofibers for clinical application. Stem Cell Nanotechnology. 2020; 2125: 119–128, doi: 10.1007/7651_2019_213, indexed in Pubmed: 30771191.

27. Schiaveto de Souza A, da Silva CA, Del Bel EA. Methodological evaluation to analyze functional recovery after sciatic nerve injury. J Neurotrauma. 2004; 21(5): 627–635, doi: 10.1089/089771504774129955, indexed in Pubmed: 15165370.

28. Siddique R, Thakor N. Investigation of nerve injury through microfluidic devices. J R Soc Interface. 2014; 11(90): 20130676, doi: 10.1098/rsif.2013.0676, indexed in Pubmed: 24227311.

29. Smit Xander (2006). Struggle at the site of nerve injury: a rat sciatic nerve study on fundamental problems of peripheral nerve injury. https://repub.eur.nl/pub/8033/061013_Smit,%20Xander.pdf.

30. Taghizadeh RR, Cetrulo KJ, Cetrulo CL. Wharton's Jelly stem cells: future clinical applications. Placenta. 2011; 32 Suppl 4: S311–S315, doi: 10.1016/j.placenta.2011.06.010, indexed in Pubmed: 21733573.

31. Torch S, Usson Y, Saxod R. Automated morphometric study of human peripheral nerves by image analysis. Pathol Res Pract. 1989; 185(5): 567–571, doi: 10.1016/S0344-0338(89)80195-5, indexed in Pubmed: 2626366.

32. Varejão AS, Meek MF, Ferreira AJ, et al. Functional evaluation of peripheral nerve regeneration in the rat: walking track analysis. J Neurosci Methods. 2001; 108(1): 1–9, doi: 10.1016/s0165-0270(01)00378-8, indexed in Pubmed: 11459612.

33. Wang AY, Loh CY, Shen HH, et al. Topical application of human wharton's jelly mesenchymal stem cells accelerates mouse sciatic nerve recovery and is associated with upregulated neurotrophic factor expression. Cell Transplant. 2019; 28(12): 1560–1572, doi: 10.1177/0963689719880543, indexed in Pubmed: 31565957.

34. Zhao Z, Wang Yu, Peng J, et al. Repair of nerve defect with acellular nerve graft supplemented by bone marrow stromal cells in mice. Microsurgery. 2011; 31(5): 388–394, doi: 10.1002/micr.20882, indexed in Pubmed: 21503972.

VM VIA MEDICA

ORIGINAL ARTICLE

Morphological changes in striated muscle fibres caused by components of the Thiel embalming method

Dea Aaldijk*, Adrian Reusser*, Elisabeth Eppler, Eveline Yao, Valentin Djonov, Sebastian Halm

Institute of Anatomy, University of Bern, Switzerland

Background: Thiel-fixed body donors are highly valued for surgical training courses. The pronounced flexibility of Thiel-fixed tissue has been postulated to be caused by histologically visible fragmentation of striated muscle. The aim of this study was to analyse whether a specific ingredient, pH, decay, or autolysis could cause this fragmentation in order to modulate the Thiel solution to adapt specimen flexibility specifically to the needs of different courses.

Materials and methods: Striated muscle of the mouse was fixed for different time periods in formalin, Thiel solution, and its individual ingredients, and analysed by light microscopy. Further, pH-values of Thiel solution and its ingredients were measured. In addition, unfixed muscle tissue was histologically analysed including Gram staining to investigate a relationship between autolysis, decomposition, and fragmentation.

Results: Muscle fixed with Thiel solution for 3 months was slightly more fragmentated than muscle fixed for 1 day. Fragmentation was more pronounced after 1 year of immersion. Three individual salt ingredients showed slight fragmentation. Decay and autolysis had no effect on fragmentation, which occurred regardless of the pH of all solutions.

Conclusions: Fragmentation of Thiel-fixed muscle is dependent on fixation time and most likely occurs due to salts present in the Thiel solution. Adjustment of the salt composition in the Thiel solution with verification of the influence on the fixation effect, fragmentation and flexibility of the cadavers could be performed in further studies. (Folia Morphol 2024; 83, 1: 83–91)

Keywords: tissue fixation, skeletal muscle, light microscopy, fragmentation, saturated salt solution, formalin, boric acid, pH

INTRODUCTION

Walter Thiel's stated intention was to develop a fixation method where cadavers tissues should have the smallest possible alteration with respect to colour, consistency, shape and volume and therefore facilitate anatomy teaching [37]. Since then, many studies investigated the advantages of soft embalmed Thiel-fixed cadavers, such as joint pliability, tissue suppleness and appearance with realistic colour [2, 9, 13, 16, 23, 31, 46]. These characteristics are favourable for surgical training [5, 9, 14, 18, 20, 30, 32, 33, 40, 43, 44]. However, some less favourable aspects regarding

dissection, appearance or recognition of tissue, as compared to formalin-fixed cadavers, are reported [24, 42], particularly muscular disorganization and noticeable histological alterations [19, 32]. Although Thiel fixation has been in use for 30 years, and several studies have investigated the histological effects of Thiel fixation, there is still no sufficient explanation why cadavers retain such a high pliability. Benkhadra et al. [5] and McDougall et al. [27] specifically addressed this question in a histological investigation: Benkhadra et al. [5] studied Thiel-fixed muscle tissue from human body donors and demonstrated a "cut-up and minced" appearance of the striated muscle fibres (MF), while nuclei were not visible. They hypothesized boric acid to be the cause of this observed fragmentation, due to corrosive properties of acids on muscle tissue and its proteins [5]. Similarly, McDougall et al. [27] described "loss of nuclear staining, loss of definitive striation, cell structure integrity and considerable muscle fibre fragmentation". Interestingly, these findings were also detected in muscle tissue fixed in a modified Thiel solution without boric acid so that they proposed that, in addition to boric acid, salts in the Thiel solution might be responsible for fragmentation [27]. Other studies also described histological alterations of Thiel-fixed muscle tissue, but without focusing on potential reasons. In a study using human skeletal muscle fixed with a modified Thiel solution (i.e. no intrathecal, rectal, tracheal and gastral injection and minimum immersion time shortened from 3 to 2 months), washed-out appearance of the muscle, absence of cell membranes and nuclei were observed [16]. However, the MF were mainly cut transversely, and fragmentation was neither described nor visible. In another study in rats perfused immediately postmortem with Thiel solution, muscle tissue showed a blurred image, impaired integrity and poorly demarcated nuclei after immersion in Thiel solution for 2 months [4]. Images from this study can be interpreted to reveal muscle tissue that had been pulled apart, some showing fragmentation (described as an impairment of integrity) and missing nuclei. Notably, on images of saturated salt solution (SSS) preparations, individual fragmentations of striated MF were visible as well. A study on formalin-fixed bovine striated muscle [38] revealed impaired tissue after subsequent 7-month fixation in boric acid, but fragmentation in tissue stored in 0.9% NaCl. More recently, only few fragmentations were seen in Thiel-fixed rabbit muscle tissue, but more pronounced fragmentation in SSS--fixed tissue after 2 days [34]. So far, the effects of the

individual ingredients of the Thiel solution have not been investigated but could contribute to the understanding of the detailed morphological effect of Thiel solution on muscle tissues. This could open the possibility of adjusting the composition of the Thiel solution according to properties of individual ingredients to retain the advantages of Thiel fixation while reducing the disadvantages (consistency, dissection, hyperlaxity). Anatomical institutes might adapt the tissue pliability according to its use, either in dissection courses or for clinical courses depending on the surgical discipline, approach, or a specific technique. By identifying an ingredient responsible for fragmentation and pliability, cadavers could be used more purposefully. The suitability of Thiel muscle tissue for biomechanical studies is controversial [4, 10–12, 15, 17, 21, 25, 26, 28, 35, 39, 41, 43, 45, 47]. If the biomechanical properties could be normalized by adaptation of the ingredients, it would open new possibilities for scientists working biomechanically with Thiel muscle tissue. The aim of this study was to investigate the effect of the whole Thiel solution, as well as its individual ingredients, on skeletal muscle and to find a possible explanation for the histologically visible fragmentation. Since rodents are widely used for research on muscle morphology, striated muscle of the mouse was selected for this purpose [27]. We analysed the effect of Thiel solution and its individual components, i.e., formaldehyde, boric acid, ethylene glycol, p-chlorocresol, and the salts ammonium nitrate, potassium nitrate and sodium sulphite and the influence of pH as well as the time of autolysis and decay.

MATERIALS AND METHODS

Tissue sampling and muscle preparation

Muscles from 4 mice that were originally part of another experiment approved by the Canton of Bern (number: BE 61/18) were collected. In the original experiment, the mice were euthanized by intraperitoneal injection of pentobarbital (100 mg/kg). Once death was confirmed and tissues were collected for the original experiment, we immediately harvested muscles from the limbs and back for subsequent experiments (Fig. 1).

Fixation with formalin, Thiel solution and Thiel ingredients

Muscle tissue was immersed in the respective fixative, either Thiel's immersion solution (Supplementary material 1 — see journal website), 4% buffered for-
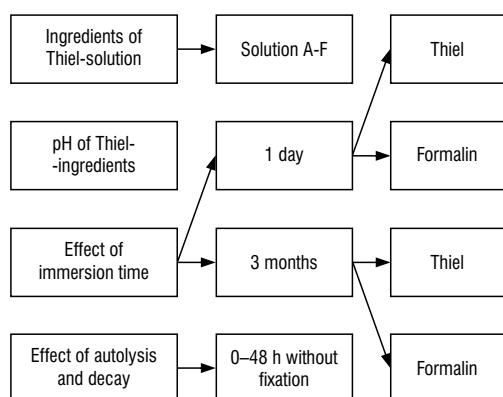
Figure 1. Flowchart of investigations using formalin solution, Thiel solution and its ingredients A–F (compare Table 1).

Table 1. Aqueous solutions of the Thiel-fixation ingredients

Solution A = Ammonium nitrate (10%)
Solution B = Boric acid (3%)
Solution C = Chlorocresol (0.18%)
Solution D = Ethylene glycol (10%)
Solution E = Potassium nitrate (5%)
Solution F = Sodium sulfite (7%)

Note: The concentrations are in line with the final concentration in the immersion solution.

malin solution, or a solution of the individual ingredients A-F of the Thiel immersion solution (Table 1). Tissue:liquid ratio was at least 1:10 (weight/volume). The Thiel solution and the solutions containing the ingredients (all purchased from Sigma-Aldrich, Buchs, Switzerland) were prepared in-house. Muscle tissue was fixed for 1 day or, according to the original protocol by Thiel [37], 3 months in Thiel immersion solution, or as a control in 4% formalin, at 8°C. To study long-term effects, we also used muscle tissue from Thiel-fixed body donors from our own Institute stored at least 1 year in Thiel immersion solution or Thiel soaked cloths. Since immersion of muscle in the solutions of the single Thiel ingredients A–F (Table 1) must be considered as insufficient fixation, these samples were stored for 20 hours at 4°C to prevent bacterial growth but ensure sufficient diffusion into the muscle to avoid manifestations of autolysis and cytoplasmic vacuolization [7, 36]. Thereafter, the muscles and solutions were stored at room temperature for another 4 hours to warm up and allow the ingredients to chemically interact with the tissue as recommended [3].

pH measurement

To study the effects of pH on the muscle pieces, we measured the pH of the Thiel solution, and of its ingredients, with an IKA KMO 2 basic (IKA Werke GmbH, Staufen, Germany).

Testing of autolysis and natural decay effects

In order to investigate decay and autolysis as a possible cause of fragmentation, some muscles were left unfixed in phosphate-buffered saline (PBS)-soaked cloths at room temperature. After 8, 16, 24 and 48 hours, respectively, the muscle was immersed in Thiel solution for 14 days and prepared for light microscopy following the same protocol. To objectify the presence of decay with bacterial growth, an additional Gram staining was performed with these sections.

Tissue embedding, haematoxylin-eosin and Gram staining and light microscopy analysis

All muscles were dissected, and pieces of 5 × 2 mm cut in longitudinal MF direction, rinsed, and dehydrated using a Tissue Processor Histokinette (Shandon Citadel 1000, Thermo Fisher Scientific, Basel, Switzerland). After 17 hours, the pieces were manually embedded in paraffin (Dr. Grogg Chemie AG, Stettlen-Deisswil, Switzerland). The paraffin blocks were cut with a microtome (Microm HM 355 S, Thermo Fisher Scientific) at a section thickness of 5 μm. Subsequently, sections were stained with haematoxylin-eosin. Gram staining was performed on sections of all autolysis time points. A positive control was used to verify the obtained results. Slides were analysed with a Zeiss Axio Imager M2 microscope (Carl Zeiss AG, Feldbach, Switzerland) equipped with an Olympus UC50 camera (Olympus, Wallisellen, Switzerland) by the following criteria: Cell integrity and appearance, presence and appearance of nuclei, skeletal muscle striation, recognition of surrounding tissue, alignment and fragmentation of MF, whereby fragmentation was defined as transverse interruption of a longitudinally cut MF bundle, with sharp edges, which did not correspond to a cutting artifact. For the Gram-stained slices, the presence and quantity of bacteria was assessed and documented.

RESULTS

Fixation solutions and individual Thiel ingredients

The muscle fixed in formalin for 1 day represented a control tissue with intact MF integrity and align-
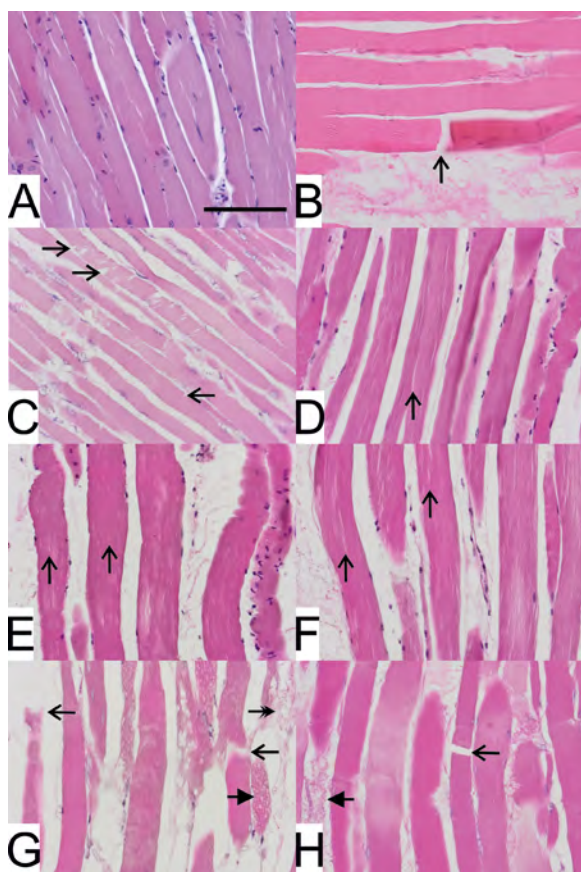
Figure 2. Histological analysis of muscle tissue fixed for 1 day stained with haematoxylin-eosin. **A.** formalin fixation; **B.** Thiel fixation. Arrow shows a fragmentation; **C.** Ammonium nitrate. Arrows show some indentations; **D.** Boric acid. Arrow shows a longitudinal tear; **E.** Chlorocresol solution. Arrows show the longitudinal and vacuole like alterations; **F.** Ethylene glycol. Arrows show longitudinal tears; **G.** Potassium nitrate. Open arrowhead points to shredded tears while the filled arrowhead shows a vacuolated muscle bundle. The double arrowhead points to amorphous surrounding tissue; **H.** Sodium sulfite. Open arrowhead shows a fragmentation, filled arrowhead shows amorphous surrounding tissue. Scale bar: 100 μm.

ment, correct staining, visible striations, intact nuclei, and demarcated and identifiable surrounding tissue (Fig. 2A). The muscle fixed in Thiel solution for 1 day showed few fragmentations, but with a well-preserved striation of MF (Fig. 2B). In general, the MF appeared slightly pale, loose and only moderately pulled apart. The architecture of the tissue appeared slightly disturbed and disintegrated. No indentations, which may be interpreted as beginning fragmentations, were visible. The nuclei appeared ballooned and pale. The surrounding tissue was generally well demarcated and intact, but with a slightly dissolved endomysium. In general, all MF bundles fixed in solutions of the Thiel ingredients A–F were

slightly pulled apart compared to the MF bundles of formalin-fixed muscle (Fig. 2C–H). In detail, the muscle fixed in solution A (ammonium nitrate, Fig. 2C) showed some perpendicular tears, the striation was preserved. Mainly at the sides of the MF bundle, there were small indentations at the level of the I zone, which were sporadically continuous throughout the MF bundle. The nuclei were ballooned and pale. The surrounding tissue was recognizable. Muscle from solution B (boric acid, Fig. 2D) showed a preserved striation. Dominant were longitudinal tears along the MF. The nuclei were present and regularly stained. The surrounding tissue was intact. Muscle fixed in solution C (chlorocresol, Fig. 2E) revealed slightly pulled apart MF with curly borders, intense staining, few tears, and a visible striation in some areas. Dominant were short and elongated tears along the MF, which appeared like long vacuoles, but no fragmentation. The MF appeared more pulled apart than in muscle from solution B. There was a normal shape and staining of the nuclei. Muscle from solution D (ethylene glycol, Fig. 2F) also showed a preserved striation. Dominant were elongated tears along the MF, but more pronounced than in muscle of solution B (Fig. 2D). There were fuzzy borders but only few transverse tears. The muscle showed normal nuclei. The surrounding tissue appeared partly amorphous. In muscle of solution E (potassium nitrate, Fig. 2G), striation was almost invisible with some blurred MF. The muscle showed tears, partially looking like shredded and partially like classic fragmentations. In some areas, the MF also possessed a lot of vacuoles so that the muscle structure was unrecognizable. Nuclei were mostly absent or ballooned and pale. The surrounding tissue was partly. In the muscle of solution F (sodium sulfite, Fig. 2H), the MF bundles were arranged more densely together. Striation was visible, and the borders appeared blurry. Some classical fragmentation was seen here (open arrowhead) with otherwise intact muscle. Unlike in the muscle from solution A, incipient indentations were rarely seen. Nuclei were present, but appeared slightly pale and ballooned, the surrounding tissue was mostly amorphous.

Duration of fixation

Muscle pieces immersed in formalin for 3 months (Fig. 3A) showed no notable difference to those stored for 1 day in formalin solution (Fig. 2A). Some areas appeared less dense with MF slightly pulled apart in the longitudinal direction, but for the most
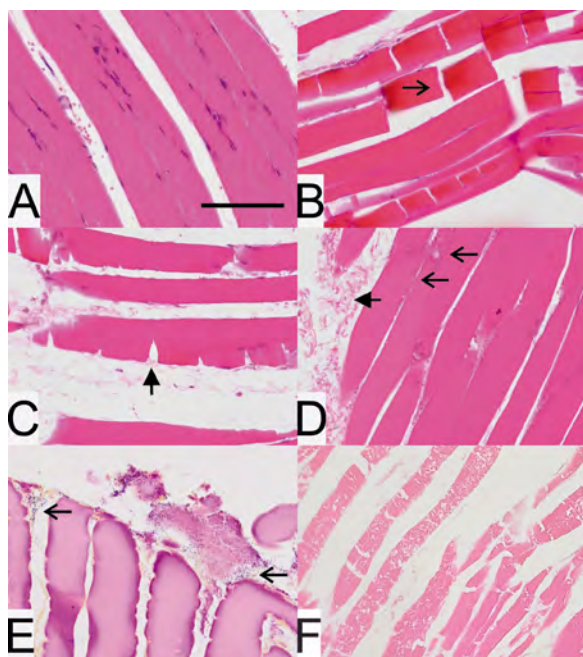
Figure 3. Histological analysis of muscle tissue stained with haematoxylin-eosin (**A–D, F**) and Gram stain (**E**); **A.** Formalin fixed, 3 months; **B.** Thiel fixed, 3 months. Arrow shows a fragmentation; **C.** Thiel fixed, 3 months. Arrow points to indentation (also visible in panel B); **D.** Muscle unfixed for 48 hours with signs of autolysis. The open arrowheads show vacuolization and the filled arrowhead amorphous tissue; **E.** Same muscle treated as in panel D, after Gram staining. The arrows point to gram-positive cocci; **F.** Muscle fixed for more than 1 year in Thiel-solution. In addition to fragmentation, the structure in the muscle fibres is considerably dissolved and the striation almost no longer recognizable. Scale bar: 100 μm.

part revealed intact tissue with single transverse tears, intact nuclei and visible striations, and intact surrounding tissue. On the contrary, the MF preserved in the Thiel solution for 3 months, were pulled apart and not dense with clear and classical fragmentations of the tissue (Fig. 3B). There were also indentations present (Fig. 3B, C). Striation was visible as well as the nuclei, which, however, were ballooned and pale. The surrounding tissue was moderately dissolved. Thiel tissues from body donors of our institute (Fig. 3F) fixed for more than 1 year showed a further increase in fragmentation and disintegration of the MF, looked like perforated, pale, and nuclei where missing.

pH-value

Table 2 summarizes the pH values of all solutions used. The pH value of the Thiel solution was 7.7 and therefore slightly within the basic range. While the pH of potassium nitrate, ethylene glycol and chlorocresol was slightly within the basic range, the pH of ammonium nitrate and boric acid was within the

Table 2. pH of Thiel and formalin solution and the solutions A–F

Solution	pH
Thiel solution	7.7
Formalin 4%	7.2
Ammonium nitrate 10% (A)	6.36
Boric acid 3% (B)	4.7
Chlorocresol 0.18% (C)	7.93
Ethylene glycol 10% (D)	7.87
Potassium nitrate 5% (E)	8.58
Sodium sulfite 7% (F)	8.73

acidic range. The boric acid solution (pH 4.7) was the solution with the lowest pH. The pH value of the formalin solution was 7.2.

Autolysis and natural decay effects

In general, there were no differences regarding fragmentation and nuclei between muscle pieces placed immediately in Thiel solution (Fig. 2B) and those stored up to 48 hours more before fixation (Fig. 3D), but there were differences in autolysis, condition of the surrounding tissue and bacterial growth. At all tested time points, unfixed tissue showed only few and diffusely formed tears, rather than fragmentations with the classic shape. The nuclei were present, but paleness and ballooning increased with the time before fixation. After remaining unfixed for 8 hours, signs of autolysis like vacuolization and disintegration, especially of the connective tissue around the muscle, were already visible (Fig. D). Signs of autolysis and disintegration increased with the duration the tissue remained unfixed. After 48 hours, the MF bundles appeared partly amorphous and with loss of striation, no classic fragmentations occurred. After 8 hours left unfixed, bacterial growth increased as compared to immediately fixed tissue. Bacteria appeared in clusters and were often present within the amorphous surrounding tissue (Fig. 3E). Progression of autolysis varied locally and over time, with the difference between 0–8 hours postmortem being greater than between 8–48 hours. Thus, fragmentation was not dependent on autolysis and decay.

Discussion and Conclusions

In this study, we investigated the influence of the Thiel solution and its individual ingredients on striated muscle fibres in the mouse. We used light microscopy to identify an ingredient responsible for

fragmentation and consequently the pliability of Thiel cadavers. For that purpose, we also ruled out autolysis and natural decay as a possible confounding factor.

While muscle fixed in formalin served as 1-day and 3-months control, and showed regular histology, muscle fixed in Thiel solution for one day already showed disintegrated and less dense MF with few fragmentations and some indentations, which we interpreted as beginning fragmentations. In muscles fixed according to Thiel [37], an increase in fragmentation and disintegration was visible after 3 months. In muscle tissue after Thiel fixation for more than 1 year, there was a further increase in fragmentation and strong disintegration, which looked like perforated muscle. This suggests both potentiation of the ingredients in the complete solution and progression of the effects over time. So far, Thiel-fixed muscle has been demonstrated to show a similar impairment of muscle tissue compared with other studies; however, in our study, the nuclei were still present, but paler than after formalin fixation [4, 16, 34, 38].

This time dependent effect on muscle histology, which presumably influences the cadaver pliability could be considered and adapted depending on the use of the cadavers by the institutes.

To specify the effect of each ingredient of the Thiel solution, we immersed muscle pieces in the single ingredients for 24 hours. Since this procedure corresponds to an incomplete fixation, we proceeded similar to the method of Cocariu et al. [7] and Baur et al. [3]. Striated muscle tissue was stored at 4°C for only 20 hours of immersion, in order to omit signs of decay and autolysis. Then the tissue was thawed until room temperature for another 4 hours to allow the chemicals to react. The histological effects were compared to those of muscle pieces fixed in 4% formalin and Thiel solution for 24 hours, respectively. Several ingredients of the Thiel solution could be identified to cause fragmentations in the muscle, predominantly sodium sulphite and potassium nitrate, and to a lesser extent ammonium nitrate, all belonging to the group of salts. This supports the hypothesis of McDougall et al. [27], that salts may play a role in tissue alteration. They had found fragmentation of tissue fixed in a modified Thiel solution without boric acid, which is supported by our finding that boric acid as a single component did not cause any fragmentation. In another study, boric acid exerted a slightly corrosive effect on striated muscle tissue at high concentration, but no classic fragmentation was

visible [38]. While low pH with its corrosive effect has been suggested as a possible cause of fragmentation [5], muscle pieces immersed in boric acid solution did not show any significant fragmentation, so that we do not consider boric acid or low pH to be the cause of fragmentation. Further, while our pH measurements showed that boric acid solution possessed the lowest pH of all ingredients, Liao postulated boric acid to be almost neutralized in Thiel solution [26].

Usually, fixation of body donors is not performed immediately, but 1 to 2 days postmortem after their arrival at an anatomical institute. As some studies used human muscle tissue from body donors, we also investigated the role of autolysis and decay on muscle histology and observed time-dependent morphological changes, which did not resemble fragmentations. Notably, these alterations were present from the beginning and did not increase after 48 hours, in contrast to bacterial growth and signs of decay and autolysis. This makes the influence of autolysis and decay on fragmentations unlikely. Therefore, we conclude that the fragmentations observed in Thiel-fixed muscle tissue can be attributed to the fixative itself, particularly the group of salts, i.e. sodium sulfite, potassium nitrate and to a lesser extent ammonium nitrate. While fragmentation was defined as disruption of the MF, it must be mentioned that in all individual ingredients, as well as in the Thiel tissue, the MF were also less dense, less contiguous and appeared pulled apart. There exist several histological studies, which have fixed muscle pieces in either sodium chloride or SSS [1, 4, 34, 38] and they showed similar tissue that was neither dense, nor contiguous and fragmented. In agreement with our findings, these studies showed a similar effect when muscle was fixed in solutions containing salts, as a possible reason for fragmentation [27]. We suggest a physiochemical process, which may underlie the principle of solvatization of salts. Anions and cations are enclosed in a hydration shell of water splitting them apart. The dissolved anions and cations, in our case mostly sodium and potassium, move around or into the myofibrils, due to the surrounding osmotic pressure or by directly binding the charged groups of the myofibrils. The bound and charged molecules lead to electrostatic repulsion, thus degrading the myofibrils and disturbing the spatial myofibrillar structure due to entropically driven forces.

Both physiochemical processes enable further water to enter in, as well as around the myofibrillar

structures, as a result of lattice changes [8, 22, 29]. These processes might well be the cause of indentations or, if increasing, fragmentation with less dense MF. Degradation and enhanced water retention pulls the MF apart, both longitudinally and perpendicularly as visible in light microscopy.

Another issue that leads to fragile tissue, and therefore presumably contributes to fragmentation, is the fact that, in Thiel solution, formalin concentration is significantly reduced. Methylene bridges crosslinking adjacent proteins, amines and related nucleophiles are missing [6, 16, 26]. We histologically noticed this fragility when the paraffin blocks were rotated during the cutting process on the microtome. Cutting the MF vertically instead of horizontally resulted in a significant increase of small tissue cracks and deformation in MF (data not shown). The lower formalin content and the effect of the salts might be a cumulative process. Adjusting the amount of salts in the Thiel solution, could be a possibility to decrease the amount of salt and water entering and binding to the MF, therefore reducing the lattice rearrangement. We assume that the reduced amount of formalin and the myofibrillar degradation due to salts could be the origin of the fragmentations in muscle tissue. This, in turn, reduces the muscle resistance while moving joints, described as pliability.

Limitations of the study

However, there are some limitations of the study. We tested the ingredients of the Thiel solution and their effects separately. Due to decay and autolysis, the long-term effect of the individual ingredients could not be investigated. Also, Thiel solution and potential effects due to altered properties of the solution were not analysed after 1 year. In addition, ingredients belonging to the same chemical group may have an amplifying effect.

Although this was not investigated, we consider the chemical effects to be similar to the effects of the complete Thiel solution. The chemical effect on muscle of mice and humans could be different. However, since they have basically the same histological structure, we assume that the effect of the chemicals is the same. In addition, similar images have been published in literature with fragmentations of human striated muscle. Nevertheless, further studies are needed to confirm our findings as well as the suitability of an adjusted solution as a fixative. The anticipated improved properties could then be evaluated for their potential applications to improve biomechanical properties for research and surgical training.

CONCLUSIONS

To conclude, we investigated the effects of Thiel solution on striated muscle to find an explanation for the observed fragmentation visible of Thiel-fixed tissue, which is proposed as reason of the cadaver joint pliability. The pH as well as autolysis and decay could be excluded. Fragmentations occurred after Thiel fixation and were time dependent. Ingredients belonging to the group of salts showed to cause fragmentations, disturbed myofibrillar lattice, likely by repulsion of actin and myosin as well as enhanced water binding. Adjustments of salt concentrations and altered tissue pliability might be advantageous for work with Thiel-cadavers.

REFERENCES

1. Astruc T, Desfrétières A, Vénien A. Histological study of ultrastructural changes in muscle exposed to various concentrations of nacl brine. J Food Sci. 2018; 83(5): 1221–1228, doi: 10.1111/1750-3841.14122, indexed in Pubmed: 29660824.
2. Balta JY, Lamb C, Soames RW. A pilot study comparing the use of Thiel- and formalin-embalmed cadavers in the teaching of human anatomy. Anat Sci Educ. 2015; 8(1): 86–91, doi: 10.1002/ase.1470, indexed in Pubmed: 24996059.
3. Bauer DR, Otter M, Chafin DR. A new paradigm for tissue diagnostics: tools and techniques to standardize tissue collection, transport, and fixation. Curr Pathobiol Rep. 2018; 6(2): 135–143, doi: 10.1007/s40139-018-0170-1, indexed in Pubmed: 29780664.
4. Beger O, Karagül Mİ, Koç T, et al. Effects of different cadaver preservation methods on muscles and tendons: a morphometric, biomechanical and histological study. Anat Sci Int. 2020; 95(2): 174–189, doi: 10.1007/s12565-019-00508-z, indexed in Pubmed: 31691180.
5. Benkhadra M, Bouchot A, Gérard J, et al. Flexibility of Thiel's embalmed cadavers: the explanation is probably in the muscles. Surg Radiol Anat. 2011; 33(4): 365–368, doi: 10.1007/s00276-010-0703-8, indexed in Pubmed: 20632174.
6. Brenner E. Human body preservation — old and new techniques. J Anat. 2014; 224(3): 316–344, doi: 10.1111/joa.12160, indexed in Pubmed: 24438435.

7. Cocariu EA, Mageriu V, Stăniceanu F, et al. Correlations between the autolytic changes and postmortem interval in refrigerated cadavers. Rom J Intern Med. 2016; 54(2): 105–112, doi: 10.1515/rjim-2016-0012, indexed in Pubmed: 27352439.

8. Desmond E. Reducing salt: A challenge for the meat industry. Meat Sci. 2006; 74(1): 188–196, doi: 10.1016/j.meatsci.2006.04.014, indexed in Pubmed: 22062728.

9. Eisma R, Wilkinson T. From "silent teachers" to models. PLoS Biol. 2014; 12(10): e1001971, doi: 10.1371/journal.pbio.1001971, indexed in Pubmed: 25333490.

10. Estermann SJ, Förster-Streffleur S, Hirtler L, et al. Comparison of Thiel preserved, fresh human, and animal liver tissue in terms of mechanical properties. Ann Anat. 2021; 236: 151717, doi: 10.1016/j.aanat.2021.151717, indexed in Pubmed: 33689839.

11. Fessel G, Frey K, Schweizer A, et al. Suitability of Thiel embalmed tendons for biomechanical investigation. Ann Anat. 2011; 193(3): 237–241, doi: 10.1016/j.aanat.2011.03.007, indexed in Pubmed: 21511447.

12. Gatt A, Schembri-Wismayer P, Chockalingam N, et al. Kinematic and kinetic comparison of fresh frozen and thiel-embalmed human feet for suitability for biomechanical educational and research settings. J Am Podiatr Med Assoc. 2019; 109(2): 113–121, doi: 10.7547/16-130, indexed in Pubmed: 31135207.

13. Giger U, Frésard I, Häfliger A, et al. Laparoscopic training on Thiel human cadavers: a model to teach advanced laparoscopic procedures. Surg Endosc. 2008; 22(4): 901–906, doi: 10.1007/s00464-007-9502-7, indexed in Pubmed: 17704868.

14. Groscurth P, Eggli P, Kapfhammer J, et al. Gross anatomy in the surgical curriculum in Switzerland: improved cadaver preservation, anatomical models, and course development. Anat Rec. 2001; 265(6): 254–256, doi: 10.1002/ar.10030, indexed in Pubmed: 11753916.

15. Halm S, Fairhurst PG, Tschanz S, et al. Effect of lateral sliding calcaneus osteotomy on tarsal tunnel pressure. Foot Ankle Orthop. 2020; 5(3): 2473011420931015, doi: 10.1177/2473011420931015, indexed in Pubmed: 35097388.

16. Hammer N, Löffler S, Bechmann I, et al. Comparison of modified Thiel embalming and ethanol-glycerin fixation in an anatomy environment: Potentials and limitations of two complementary techniques. Anat Sci Educ. 2015; 8(1): 74–85, doi: 10.1002/ase.1450, indexed in Pubmed: 24706536.

17. Hammer N, Schröder C, Schleifenbaum S. On the suitability of Thiel-fixed samples for biomechanical purposes: Critical considerations on the articles of Liao et al. "Elastic Properties of Thiel-Embalmed Human Ankle Tendon and Ligament" and Verstraete et al. "Impact of Drying and Thiel Embalming on Mechanical Properties of Achilles Tendons". Clin Anat. 2016; 29(4): 424–425, doi: 10.1002/ca.22679, indexed in Pubmed: 26679099.

18. Hassan S, Eisma R, Malhas A, et al. Surgical simulation flexor tendon repair using Thiel cadavers: a comparison with formalin embalmed cadavers and porcine models. J Hand Surg Eur Vol. 2015; 40(3): 246–249, doi: 10.1177/1753193413520281, indexed in Pubmed: 24436356.

19. Hayashi S, Naito M, Kawata S, et al. History and future of human cadaver preservation for surgical training: from formalin to saturated salt solution method. Anat Sci Int. 2016; 91(1): 1–7, doi: 10.1007/s12565-015-0299-5, indexed in Pubmed: 26670696.

20. Healy SE, Rai BP, Biyani CS, et al. Thiel embalming method for cadaver preservation: a review of new training model for urologic skills training. Urology. 2015; 85(3): 499–504, doi: 10.1016/j.urology.2014.11.009, indexed in Pubmed: 25582818.

21. Hohmann E, Keough N, Glatt V, et al. The mechanical properties of fresh versus fresh/frozen and preserved (Thiel and Formalin) long head of biceps tendons: A cadaveric investigation. Ann Anat. 2019; 221: 186–191, doi: 10.1016/j.aanat.2018.05.002, indexed in Pubmed: 29879483.

22. Huff-Lonergan E, Lonergan SM. Mechanisms of water--holding capacity of meat: The role of postmortem biochemical and structural changes. Meat Sci. 2005; 71(1): 194–204, doi: 10.1016/j.meatsci.2005.04.022, indexed in Pubmed: 22064064.

23. Jaung R, Cook P, Blyth P. A comparison of embalming fluids for use in surgical workshops. Clin Anat. 2011; 24(2): 155–161, doi: 10.1002/ca.21118, indexed in Pubmed: 21322038.

24. Kennel L, Martin DMA, Shaw H, et al. Learning anatomy through Thiel- vs. formalin-embalmed cadavers: Student perceptions of embalming methods and effect on functional anatomy knowledge. Anat Sci Educ. 2018; 11(2): 166–174, doi: 10.1002/ase.1715, indexed in Pubmed: 28719722.

25. Kerdok AE, Ottensmeyer MP, Howe RD. Effects of perfusion on the viscoelastic characteristics of liver. J Biomech. 2006; 39(12): 2221–2231, doi: 10.1016/j.jbiomech.2005.07.005, indexed in Pubmed: 16126215.

26. Liao X, Kemp S, Corner G, et al. Elastic properties of Thiel-embalmed human ankle tendon and ligament. Clin Anat. 2015; 28(7): 917–924, doi: 10.1002/ca.22512, indexed in Pubmed: 25707906.

27. McDougall S, Soames R, Felts P. Thiel embalming: Quantifying histological changes in skeletal muscle and tendon and investigating the role of boric acid. Clin Anat. 2020; 33(5): 696–704, doi: 10.1002/ca.23491, indexed in Pubmed: 31591790.

28. Nicolle S, Palierne JF. Dehydration effect on the mechanical behaviour of biological soft tissues: observations on kidney tissues. J Mech Behav Biomed Mater. 2010; 3(8): 630–635, doi: 10.1016/j.jmbbm.2010.07.010, indexed in Pubmed: 20826370.

29. Offer G, Knight P, Jeacocke R. The structural basis of the water-holding, appearance and toughness of meat and meat products. Food Structure. 1989; 8(1): Article 17.

30. Porzionato A, Polese L, Lezoche E, et al. On the suitability of Thiel cadavers for natural orifice transluminal endoscopic surgery (NOTES): surgical training, feasibility studies, and anatomical education. Surg Endosc. 2015; 29(3): 737–746, doi: 10.1007/s00464-014-3734-0, indexed in Pubmed: 25060684.

31. Prasad Rai B, Tang B, Eisma R, et al. A qualitative assessment of human cadavers embalmed by Thiel's method used in laparoscopic training for renal resection. Anat Sci Educ. 2012; 5(3): 182–186, doi: 10.1002/ase.1267, indexed in Pubmed: 22362548.

32. Rakuša M, Kocbek Šaherl L. Thiel embalming method used for anatomy dissection as an educational tool in teaching human anatomy, in research, and in training in comparison of different methods for long term preservation. Folia Morphol. 2023; 82(3): 449–456, doi: 10.5603/FM.a2022.0055, indexed in Pubmed: 35692115.

33. Ruiz-Tovar J, Prieto-Nieto I, García-Olmo D, et al. Training courses in laparoscopic bariatric surgery on cadaver Thiel: results of a satisfaction survey on students and professors. Obes Surg. 2019; 29(11): 3465–3470, doi: 10.1007/s11695-019-04003-2, indexed in Pubmed: 31168719.

34. Saetan J, Nopparat J, Tipbunjong C. Modified Thiel and saturated salt solutions for rabbit soft cadaveric embalming: a preliminary study. Sonklanakarin J Sci Technol. 2021; 43(5): 1435–1442.

35. Stouthandel MEJ, Vanhove C, Devriendt W, et al. Biomechanical comparison of Thiel embalmed and fresh frozen nerve tissue. Anat Sci Int. 2020; 95(3): 399–407, doi: 10.1007/s12565-020-00535-1, indexed in Pubmed: 32144646.

36. Tavichakorntrakool R, Prasongwattana V, Sriboonlue P, et al. Serial analyses of postmortem changes in human skeletal muscle: A case study of alterations in proteome profile, histology, electrolyte contents, water composition, and enzyme activity. Proteomics Clin Appl. 2008; 2(9): 1255–1264, doi: 10.1002/prca.200800051, indexed in Pubmed: 21136921.

37. Thiel W. The preservation of the whole corpse with natural color]. Ann Anat. 1992; 174(3): 185–195, indexed in Pubmed: 1503236.

38. Türkmen RD, Akarca G, Akosman MS. The investigation of potential preservative effect of boric acid on formalin fixed striated muscle tissues. Kocatepe Vet J. 2017; 10(4): 317–321.

39. Unger S, Blauth M, Schmoelz W. Effects of three different preservation methods on the mechanical properties of human and bovine cortical bone. Bone. 2010; 47(6): 1048–1053, doi: 10.1016/j.bone.2010.08.012, indexed in Pubmed: 20736094.

40. Usami T, Fujioka T, Yoshida A, et al. Assessment of laparoscopic training for gynecological malignancies using Thiel-embalmed human cadavers. Mol Clin Oncol. 2018; 9(5): 511–514, doi: 10.3892/mco.2018.1715, indexed in Pubmed: 30345045.

41. Verstraete MA, Van Der Straeten C, De Lepeleere B, et al. Impact of drying and thiel embalming on mechanical properties of achilles tendons. Clin Anat. 2015; 28(8): 994–1001, doi: 10.1002/ca.22624, indexed in Pubmed: 26378610.

42. Villacorta P, Hernando H, Abdulla A, et al. A comparative study of Thiel soft-embalmed and formalin preserved cadavers for anatomy dissection. Acta Med Philip. 2019; 53(1), doi: 10.47895/amp.v53i1.235.

43. Völlner F, Pilsl U, Craiovan B, et al. Stability of knee ligament complex of Thiel-embalmed cadaver compared to in vivo knee. J Mech Behav Biomed Mater. 2017; 71: 392–396, doi: 10.1016/j.jmbbm.2017.04.009, indexed in Pubmed: 28411549.

44. Waerlop F, Rashidian N, Marrannes S, et al. Thiel embalmed human cadavers in surgical education: Optimizing realism and long-term application. Am J Surg. 2021; 221(6): 1300–1302, doi: 10.1016/j.amjsurg.2020.10.007, indexed in Pubmed: 33070982.

45. Wilke HJ, Werner K, Häussler K, et al. Thiel-fixation preserves the non-linear load-deformation characteristic of spinal motion segments, but increases their flexibility. J Mech Behav Biomed Mater. 2011; 4(8): 2133–2137, doi: 10.1016/j.jmbbm.2011.07.013, indexed in Pubmed: 22098913.

46. Yiasemidou M, Roberts D, Glassman D, et al. A multispecialty evaluation of Thiel cadavers for surgical training: reply. World J Surg. 2017; 41(12): 3230–3231, doi: 10.1007/s00268-017-4251-9, indexed in Pubmed: 28936705.

47. Zwirner J, Scholze M, Ondruschka B, et al. Tissue biomechanics of the human head are altered by Thiel embalming, restricting its use for biomechanical validation. Clin Anat. 2019; 32(7): 903–913, doi: 10.1002/ca.23409, indexed in Pubmed: 31112307.

ORIGINAL ARTICLE

VIA MEDICA

TLN1 synergizes with ITGA5 to ameliorate cardiac microvascular endothelial cell dysfunction

Xianfeng Wang[1], Wenkai Mao[2], Xiaofeng Ma[3]

[1]Emergency Department, Qinghai Cardio-Cerebrovascular Specialty Hospital, Qinghai High Altitude Medical Research Institute, Xining, Qinghai, P.R. China
[2]Medical Department, Qinghai Cardio-Cerebrovascular Specialty Hospital, Qinghai High Altitude Medical Research Institute, Xining, Qinghai, P.R. China
[3]Personnel Department, Qinghai Cardio-Cerebrovascular Specialty Hospital, Qinghai High Altitude Medical Research Institute, Xining, Qinghai, P.R. China

Background: The complex process of atherosclerosis is thought to begin with endothelial cell dysfunction, and advanced atherosclerosis is the underlying cause of coronary artery disease (CAD). Uncovering the underlying mechanisms of CAD-related endothelial cell injury may contribute to the treatment.

Materials and methods: Cardiac microvascular endothelial cells (CMVECs) were treated with oxidised low-density lipoprotein (ox-LDL) to mimic an injury model. The involvement of Talin-1 (TLN1) and integrin alpha 5 (ITGA5) in the proliferation, apoptosis, angiogenesis, inflammatory response, and oxidative stress in CMVECs were assessed.

Results: TLN1 overexpression assisted CMVECs in resistance to ox-LDL stimulation, with alleviated cell proliferation and angiogenesis, reduced apoptosis, inflammatory response, and oxidative stress. TLN1 overexpression triggered increased ITGA5, and ITGA5 knockdown reversed the effects of TLN1 overexpression on the abovementioned aspects. Together, TLN1 synergized with ITGA5 to ameliorate the dysfunction in CMVECs.

Conclusions: This finding suggests their probable involvement in CAD, and increasing their levels is beneficial to disease relief. (Folia Morphol 2024; 83, 1: 92–101)

Key words: Talin-1, integrin, coronary artery disease, cardiac microvascular endothelial cells, atherosclerosis

INTRODUCTION

Coronary artery disease (CAD), a common cardiovascular disease, is one of the primary threats to human health worldwide [15]. Advanced atherosclerosis is the underlying cause of CAD and heritability estimates for CAD vary from 40% to 70%, indicating a strong contribution of genes to disease pathology [13]. Genome-wide association studies have revealed that approximately one-third of CAD-related loci are associated with traditional risk factors, such as lipids, blood pressure, body mass index, diabetes, and smoking behaviour. Genes at the remaining loci have been implicated in vascular wall-related risk mechanisms [1]. Cardiac microvascular endothelial cells (CMVECs), the most abundant cells in the myocardium [22], orchestrate cardiogenesis during development, regulate

adult cardiac function, and modulate the pathological processes in heart failure [31, 32, 36]. CAD is always accompanied by endothelial cell damage [21], and uncovering the underlying mechanisms of CAD-related endothelial cell injury may contribute to the treatment of the disease.

The protein encoded by the Talin-1 (TLN1) gene, a major component of the extracellular matrix (ECM), mediates the adhesion of integrins to the ECM [3, 18], and both bioinformatics and experimental analyses identified downregulated expression of TLN1 in CAD samples [9]. Overexpressed TLN1 may cooperate with β-oestradiol to stimulate endometrial stromal cell proliferation and neovascularisation in adenomyosis, synergistically promoting the growth and survival of ectopic lesions [24]. TLN1 expression was significantly downregulated in aortic dissection samples, and downregulation of TLN1 expression was associated with increased proliferation and migration of vascular smooth muscle cells in aortic dissection [26]. However, the specific role and regulatory mechanism of TLN1 in CAD have not been reported yet. According to the String website [19], TLN1 was found to have a potential interaction with integrin alpha 5 (ITGA5), and ITGA5 is involved in promoting endocardial differentiation and cardiac morphogenesis [17].

This study utilised oxidised low-density lipoprotein (ox-LDL) to induce CMVECs to mimic an injury model [29], with the intention of defining the association existing between TLN1 and ITGA5, and exploring their roles in CMVECs. Exploring the mechanism of endothelial cell injury is beneficial to the development of CAD treatment.

MATERIALS AND METHODS

Cell culture and treatment

Cardiac microvascular endothelial cells (Procell, Wuhan, China) were cultured in Dulbecco's modified eagle's medium (DMEM, Gibco) along with 10% fetal bovine serum (Gibco), 30 μg/mL endothelial cell growth supplement (ScienCell), 1 U/mL heparin, and penicillin-streptomycin mixture (Gibco) [4]. CMVECs were maintained at 37°C in a 5% CO_2 atmosphere. CMVECs were stimulated with ox-LDL (100 μg/mL, Yeasen, Shanghai, China) for 24 h to mimic CAD [29].

Cell transfection

Cells underwent transfection to promote TLN1 overexpression or ITGA5 knockdown. X-tremeGENE transfection reagent (Roche, Shanghai, China) mixed with plasmids or short hairpin RNAs (HanBio, Shanghai, China) were added to the CMVECs [23] and incubated at 37°C for 6 h before replacing with fresh medium. After 48 h, transfection efficacy was assessed.

Reverse transcription quantitative polymerase chain reaction (RT-qPCR)

Cardiac microvascular endothelial cells were added with TRIzol® Reagent (Invitrogen), followed by chloroform, and the lysate was centrifuged at 10,000×g for 15 min at 4°C. Isopropanol precipitated the RNA in the upper aqueous phase and then RNA was reverse transcribed to generate cDNA using Evo M-MLV RT Kit (Accurate, Changsha, China). QuantiTect SYBR Green PCR Kit (Qiagen, Shanghai, China) was used to perform quantitative polymerase chain reaction (qPCR) according to the instructions. Relative mRNA levels were measured using the ΔΔCt method after normalization to actin [37].

Western blotting

Proteins were isolated from CMVECs after treatment with RIPA lysis buffer (Solarbio, Beijing, China) and quantified using a Nano 3000 protein detector (YPH-Bio, Beijing, China). Proteins were then separated using SDS-polyacrylamide gel electrophoresis and transferred to PVDF membranes (Roche) [6]. Membranes were incubated sequentially with skimmed milk, primary antibodies, and HRP-conjugated secondary antibody. The antibodies involved in the study were all from Invitrogen or Abcam. Blots were visualised after ECL reagent (Millipore) treatment and semi-quantified using ImageJ software.

Cell counting Kit-8 (CCK8)

Transfected CMVECs were seeded in 96-well plates and treated with ox-LDL for 24 h. The incubation was continued for 2 h after CCK8 solution (Beyotime, Shanghai, China) was supplemented into each well [11]. Optical density was recorded at 450 nm using a microplate reader (Thermo Fisher Scientific).

5-ethynyl-2'-deoxyuridine (EdU) assay

Following the transfected CMVECs were treated with ox-LDL for 24 h, they were incubated with 100 μL EdU reagent (Ribobio, Guangzhou, China) for 4 h [12]. Then CMVECs were washed twice with phosphate buffered saline (PBS), fixed with 4% paraformaldehyde (Chemegen, Shanghai, China) for 15 min, and stained with DAPI (Beyotime) for 10 min.
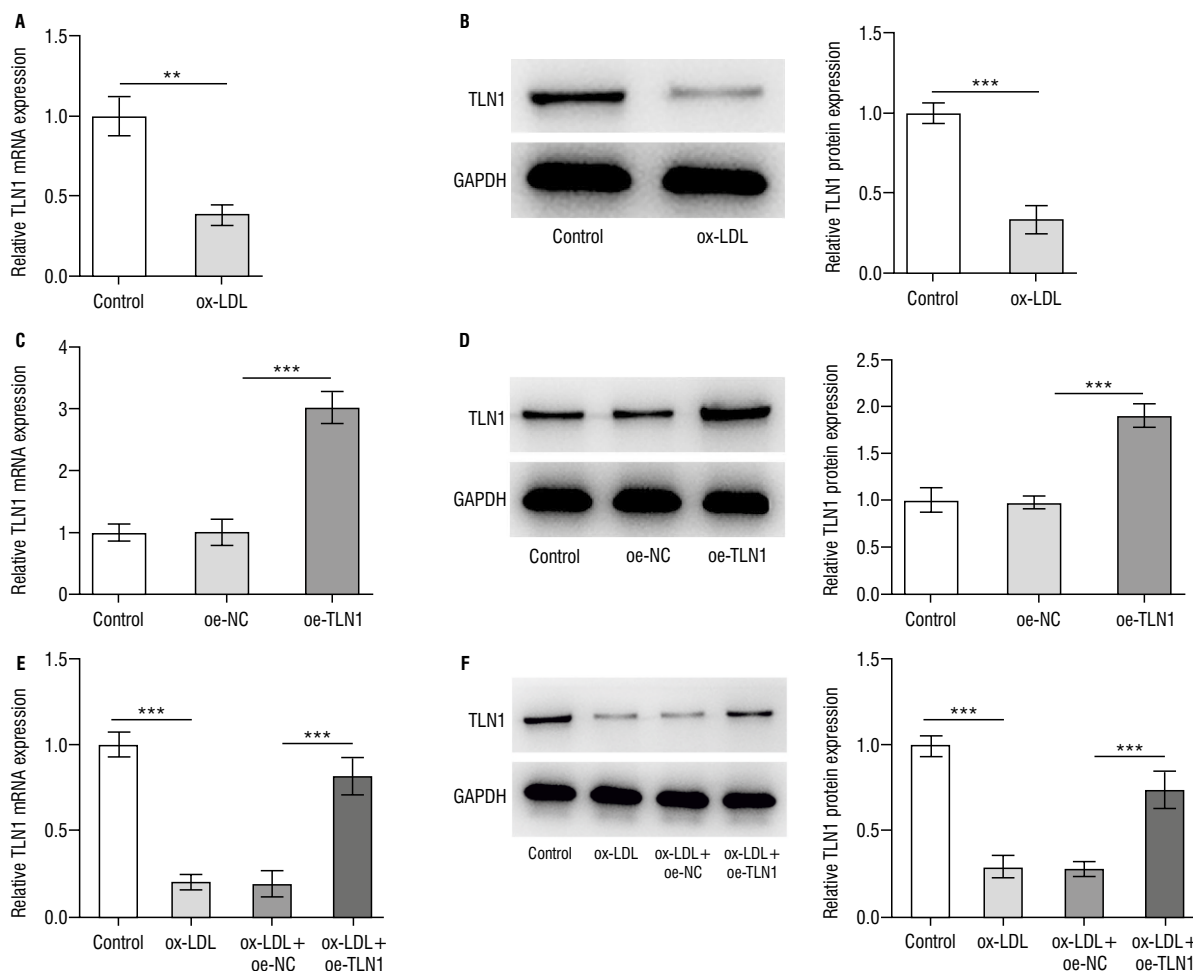
Figure 1. Talin-1 (TLN1) level in cardiac microvascular endothelial cells (CMVECs) (**A**) CMVECs were treated with oxidised low-density lipoprotein (ox-LDL) and the expression level of TLN1 was determined using reverse transcription quantitative polymerase chain reaction (RT-qPCR) and (**B**) western blotting; TLN1 overexpression in CMVECs by transfection was confirmed using RT-qPCR (**C**) and western blotting (**D**); Following ox-LDL treatment, TLN1 in the transfected CMVECs was confirmed using RT-qPCR (**E**) and western blotting (**F**); **p < 0.01, ***p < 0.001; oe — overexpression; NC — negative control.

Stained CMVECs were visualized and imaged under a fluorescent microscope (Olympus, Japan).

Flow cytometry

Cardiac microvascular endothelial cells were washed twice with cold PBS and suspended in binding buffer. 100 μL of cell suspension was transferred to culture tubes and incubated with Annexin V FITC and propidium iodide (Elabscience, Wuhan, China) for 15 min at room temperature in the dark [25]. Apoptosis was analysed using flow cytometry (BD FACSCanto, USA) and FlowJo software.

Angiogenesis assay

Matrigel (BD Biosciences) was diluted 1:1 with cold endothelial cell growth medium, starved CMVECs were seeded on Matrigel and incubated at 37°C for

6 h [35]. The structure of the capillary was observed using a microscope (Olympus).

ELISA

Secreted levels of tumour necrosis factor alpha (TNF-α), interleukin (IL)-6, and IL-1β [10] were determined in CMVECs using corresponding ELISA kits (Elabscience) according to the manufacturer's instructions. Optical density was recorded at 450 nm using a microplate reader.

Co-immunoprecipitation (Co-IP)

Cardiac microvascular endothelial cells were lysed on ice for 10 min, centrifuged at 13,000×g for 10 min at 4°C, and the supernatant was collected. 2.5 μg of TLN1 or ITGA5 antibody (Invitrogen) was added to the lysate (500 μg/IP) along with 10 μL of
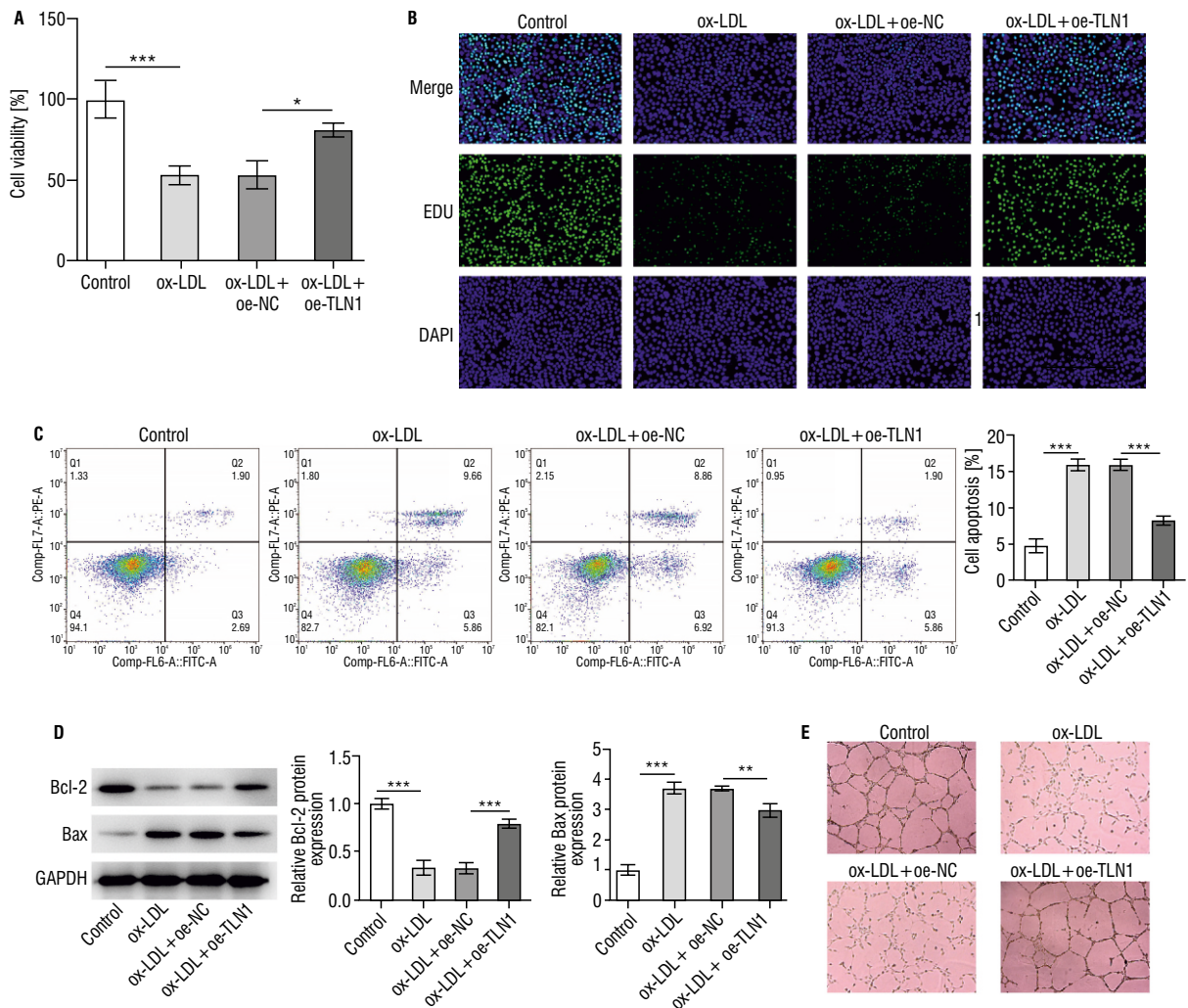
Figure 2. Talin-1 (TLN1) in apoptosis and angiogenesis. The viability and proliferation in each group was determined using cell counting Kit-8 (CCK8) (**A**) and 5-ethynyl-2'-deoxyuridine (EdU) assays (**B**). Cell apoptosis was determined using flow cytometry (**C**) and western blotting (**D**); **E.** The matrigel-based angiogenesis assay was used to detect the angiogenic capacity; *p < 0.05, **p < 0.01, ***p < 0.001; ox-LDL — oxidised low-density lipoprotein; oe — overexpression; NC — negative control.

protein A+G magnetic beads (Beyotime), followed by gentle rotation for 2 h at room temperature. The supernatant was removed magnetically and the beads together with SDS sample buffer were boiled at 95°C for 5 min prior to routine western blot analysis [37].

Statistical analysis

Statistical analysis was performed using SPSS 19.0. Data are presented as mean ± standard deviation, and statistical differences between groups were analysed using two tailed, unpaired Student's t-test (two groups), and one-way ANOVA followed by Tukey's post hoc test (multiple groups) [14]. P < 0.05 was considered a significant difference.

RESULTS

TLN1 in apoptosis and angiogenesis

In CMVECs, TLN1 mRNA and protein levels declined in response to the ox-LDL treatment (Fig. 1A, B). To discover the specific roles of TLN1, the overexpression of TLN1 in CMVECs was confirmed (Fig. 1C, D). Following ox-LDL treatment, TLN1 in the ox-LDL + oe-TLN1 group elevated compared with the ox-LDL + oe-NC group (Fig. 1E, F). Cell viability (Fig. 2A) and proliferation (Fig. 2B) were decreased upon ox-LDL treatment and TLN1 overexpression reversed these decline. Ox-LDL treatment increased the proportion of apoptotic cells, accompanied by a decline in Bcl-2 and an increase in Bax. Nevertheless, TLN1 overex-
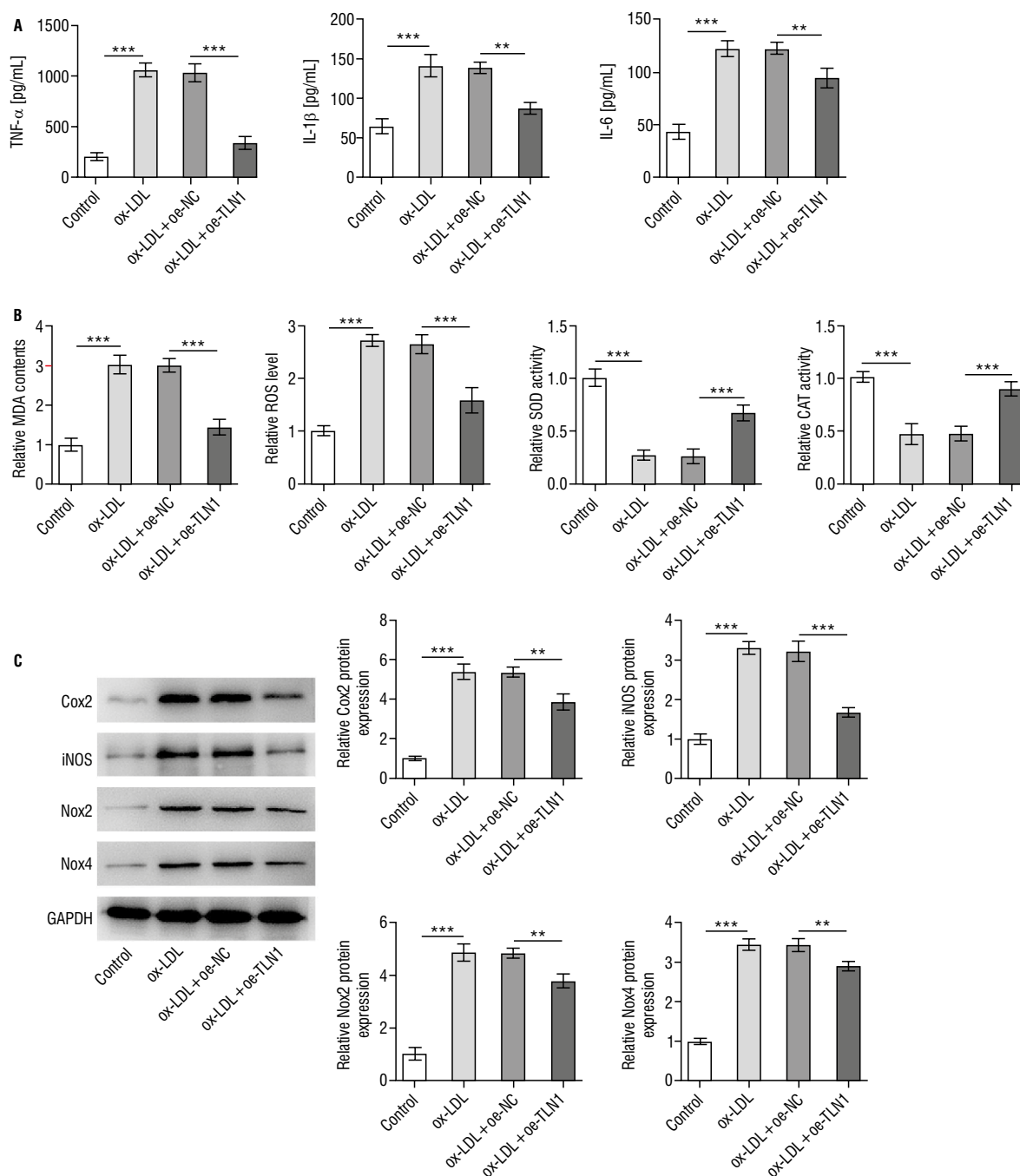
Figure 3. Talin-1 (TLN1) in inflammation and oxidative stress; **A.** ELISA kits were used to measure cellular inflammatory factor levels; **B.** Oxidative stress was evaluated based on the levels of malondialdehyde (MDA), reactive oxygen species (ROS), superoxide dismutase (SOD), and catalase (CAT); **C.** Western blotting was used to detect the enrichment of proteins associated with inflammation and oxidative stress; **p < 0.01; ***p < 0.001; ox-LDL — oxidised low-density lipoprotein; oe — overexpression; NC — negative control.

pression reduced ox-LDL-induced apoptosis (Fig. 2C, D). Moreover, ox-LDL treatment attenuated the angiogenic capacity of cells, whereas TLN1 overexpression alleviated this impact (Fig. 2E).

TLN1 in inflammation and oxidative stress

TNF-α, IL-1β, and IL-6 levels in CMVECs were increased upon ox-LDL treatment, and TLN1 overexpression reduced the impacts of ox-LDL on these
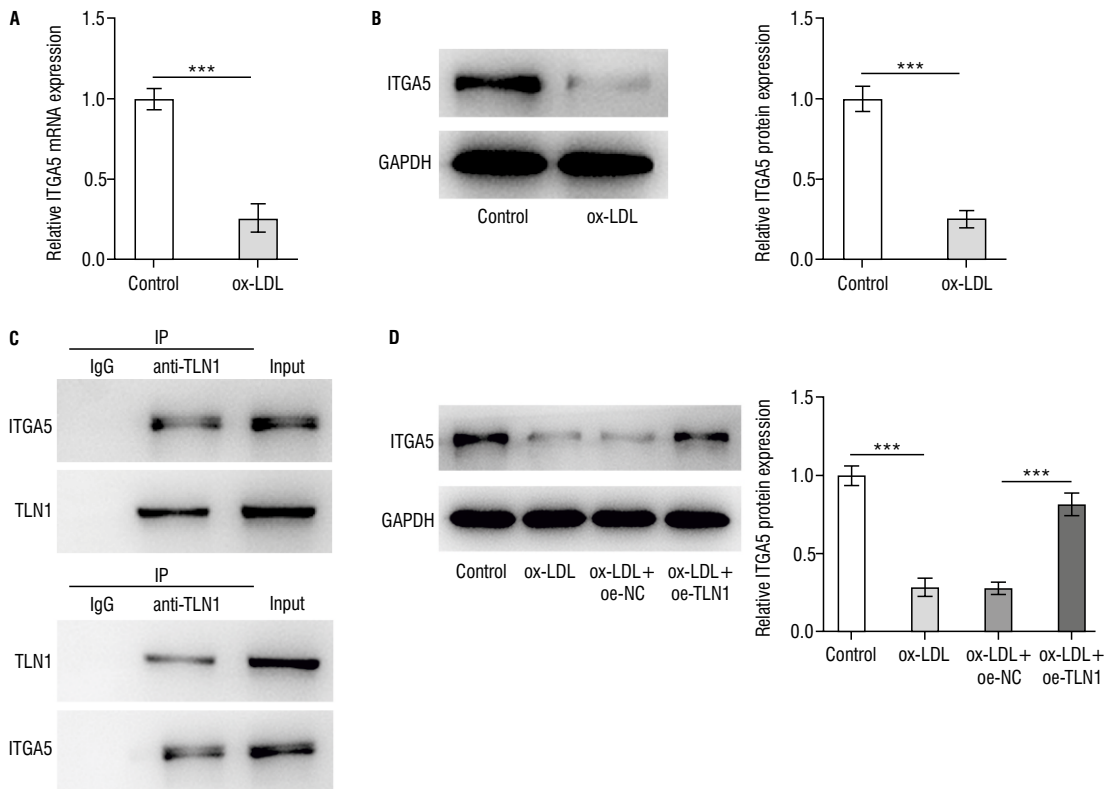
Figure 4. The interaction between talin-1 (TLN1) and integrin alpha 5 (ITGA5). Following oxidised low-density lipoprotein (ox-LDL) treatment, ITGA5 level in cardiac microvascular endothelial cells (CMVECs) was confirmed using reverse transcription quantitative polymerase chain reaction (RT-qPCR) (**A**) and western blotting (**B**). **C.** Co-immunoprecipitation (Co-IP) assay was used to verify the interaction between TLN1 and ITGA5; **D.** The level of ITGA5 upon TLN1 overexpression was determined using western blotting; ***$p < 0.001$; oe — overexpression; NC — negative control.

factors (Fig. 3A). In terms of oxidative stress, ox-LDL treatment triggered the increase in malondialdehyde (MDA) and reactive oxygen species (ROS), accompanied by the decrease in superoxide dismutase (SOD) and catalase (CAT). TLN1 overexpression likewise reduced the alterations in these indicators resulted from ox-LDL treatment (Fig. 3B). The enrichments of proteins associated with inflammation (Cox2 and iNOS) and oxidative stress (Nox2 and Nox4) were all elevated after ox-LDL treatment, and partially fell back due to TLN1 overexpression (Fig. 3C).

The interaction between TLN1 and ITGA5

The expression level of ITGA5 was found to be declined in response to the ox-LDL treatment (Fig. 4A, B). According to Co-IP results, ITGA5 protein enrichment could be detected in TLN1 antibody-bead complexes, vice versa (Fig. 4C). Moreover, TLN1 overexpression increased the level of ITGA5 (Fig. 4D).

Modulation of ITGA5

Following ITGA5 was identified to be knocked down (Fig. 5A, B), additional ITGA5 knockdown was found to reduce cell viability and proliferation, partly reversing the effects of TLN1 overexpression (Fig. 5C, D). ITGA5 knockdown likewise promoted the apoptosis of CMVECs, along with dropped Bcl-2 and elevated Bax protein expression (Fig. 5E, G). The angiogenesis of CMVECs was weakened by the influence of ITGA5 knockdown (Fig. 5H). In addition, ITGA5 knockdown enhanced the secretion of inflammatory factors and promoted oxidative stress (Fig. 6A–C).

DISCUSSION

Atherosclerotic plaque builds up in the blood vessels that supply the heart with oxygen and nutrients [20, 33]. The complex process of atherosclerosis begins early and is thought to begin with dysfunction of coronary endothelial cells [2]. To prevent CAD,
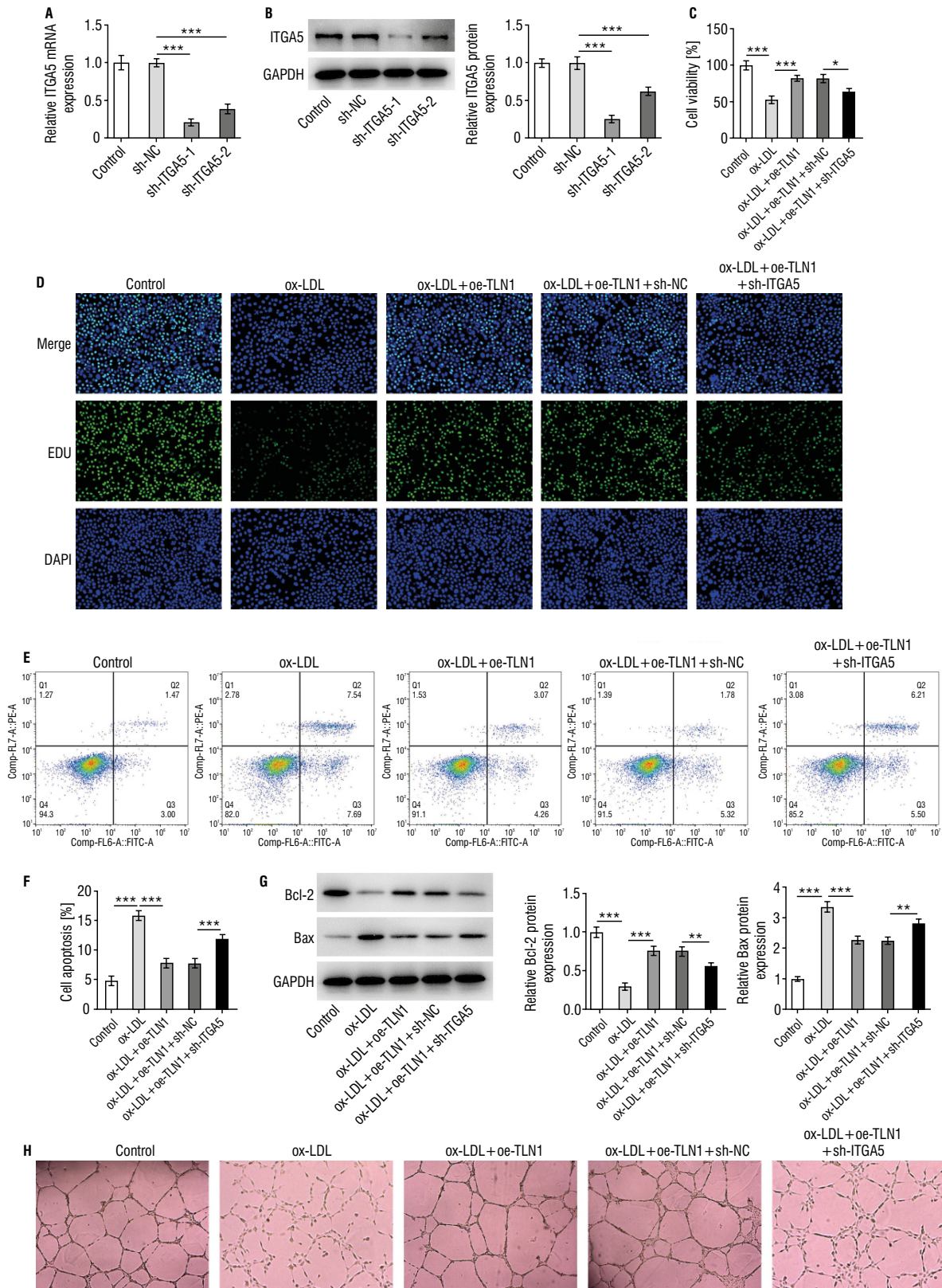
Figure 5. Modulation of integrin alpha 5 (ITGA5) in apoptosis. ITGA5 knockdown in CMVECs by transfection was confirmed using reverse transcription quantitative polymerase chain reaction (RT-qPCR) (**A**) and western blotting (**B**); The impacts of ITGA5 knockdown on the viability and proliferation of cardiac microvascular endothelial cells (CMVECs) was assessed using cell counting Kit-8 (CCK8) (**C**) and 5-ethynyl-2'--deoxyuridine (EdU) assays (**D**); The impact of ITGA5 knockdown on the apoptosis was determined using flow cytometry (**E**, **F**) and western blotting (**G**); **H.** The impact of ITGA5 knockdown on the angiogenesis was detected. **p < 0.01; ***p < 0.001; ox-LDL — oxidized low-density lipoprotein; sh — short hairpin RNA; oe — overexpression; NC — negative control.
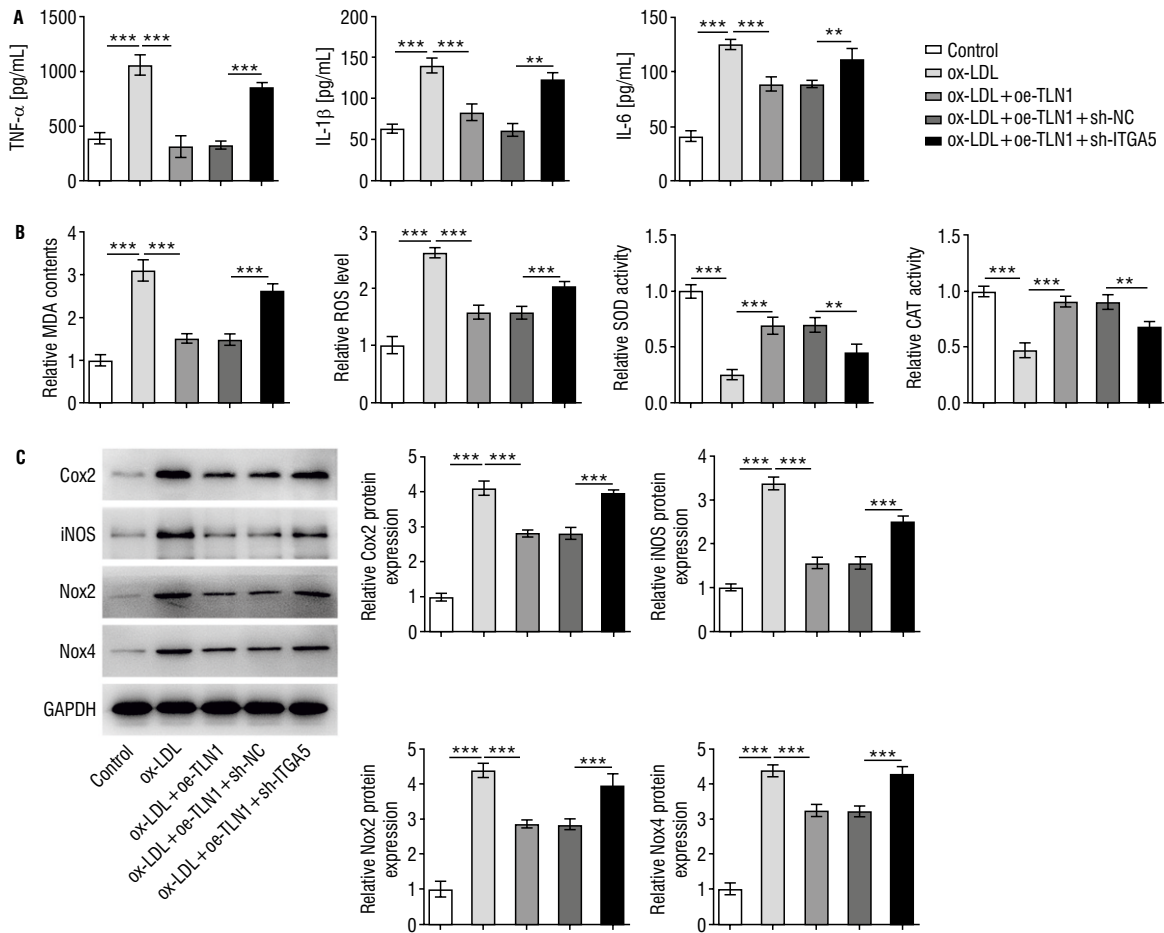
Figure 6. Modulation of integrin alpha 5 (ITGA5) in inflammation and oxidative stress; **A.** ELISA kits were used to measure cellular inflammatory factor levels; **B.** The impact of ITGA5 knockdown on oxidative stress was evaluated; **C.** The impact of ITGA5 knockdown on the enrichment of proteins associated with inflammation and oxidative stress were assessed using western blotting; **p < 0.01; ***p < 0.001; TLN1 — talin-1; ox-LDL — oxidised low-density lipoprotein; MDA — malondialdehyde; ROS — reactive oxygen species; SOD — superoxide dismutase; CAT — catalase; sh — short hairpin RNA; oe — overexpression; NC — negative control.

the population is encouraged to adhere to a healthy lifestyle, such as not smoking, avoiding obesity, eating a healthy diet, and exercising regularly [13]. High-risk groups benefit from drugs to lower LDL, blood pressure, or prevent blood clots [8, 28]. As with most complex diseases, an individual's risk for developing CAD is modulated by the interplay between genetic and lifestyle factors [15]. In this study, TLN1 was found to positively cooperate with ITGA5 to suppress ox-LDL-induced inflammation, oxidative stress, and enhance angiogenesis in CMVECs. The involvement of TLN1 in CAD has been revealed for the first time.

The integrin family to which ITGA5 belongs is closely related to the occurrence and development of atherosclerosis [5, 16]. Alterations in integrin signalling affect multiple aspects of atherosclerosis, from the earliest induction of inflammation to the develop-

ment of advanced fibrotic plaques [7]. In a previous study, the expression of miR-92a was upregulated in neointimal hyperplastic lesions after vein transplantation, and TGF-β1 induced a significant increase of microRNA-92a in human umbilical vein endothelial cells and induced endothelial-mesenchymal transition. ITGA5 is a potential target gene involved in the development of neointima formation in these vein grafts [34]. MicroRNA-92a was also elevated in LPS-induced pulmonary microvascular endothelial cells, and inhibition of miR-92a negatively regulated ITGA5 to improve LPS-induced (LPS, lipopolysaccharide) endothelial barrier dysfunction [27]. In view of the penetration of ITGA5 in the development of atherosclerosis [30], it is suggested that regulating ITGA5 can eradicate the occurrence of CAD from the early stage.

CONCLUSIONS

In summary, this study reveals for the first time that TLN1 and ITGA5 are involved in alleviating CMVECs injury, and suggests their probable involvement in CAD, and increasing their levels is beneficial to disease relief. It is hoped that the findings of the present study will provide a theoretical basis for further research.

Conflict of interest: None declared

REFERENCES

1. Aherrahrou R, Guo L, Nagraj VP, et al. Genetic regulation of atherosclerosis-relevant phenotypes in human vascular smooth muscle cells. Circ Res. 2020; 127(12): 1552–1565, doi: 10.1161/CIRCRESAHA.120.317415, indexed in Pubmed: 33040646.
2. Bidault G, Garcia M, Capeau J, et al. Progerin expression induces inflammation, oxidative stress and senescence in human coronary endothelial cells. Cells. 2020; 9(5), doi: 10.3390/cells9051201, indexed in Pubmed: 32408587.
3. Chakraborty S, Banerjee S, Raina M, et al. Force-Directed "mechanointeractome" of talin-integrin. Biochemistry. 2019; 58(47): 4677–4695, doi: 10.1021/acs.biochem.9b00442, indexed in Pubmed: 31393109.
4. Chen G, Xu C, Gillette TG, et al. Cardiomyocyte-derived small extracellular vesicles can signal eNOS activation in cardiac microvascular endothelial cells to protect against Ischemia/Reperfusion injury. Theranostics. 2020; 10(25): 11754–11774, doi: 10.7150/thno.43163, indexed in Pubmed: 33052245.
5. Demos C, Williams D, Jo H. Disturbed flow induces atherosclerosis by annexin A2-mediated integrin activation. Circ Res. 2020; 127(8): 1091–1093, doi: 10.1161/CIRCRESAHA.120.317909, indexed in Pubmed: 32970527.
6. Fan L, Zhou W, Zhang L, et al. Sitagliptin protects against hypoxia/reoxygenation (H/R)-induced cardiac microvascular endothelial cell injury. Am J Transl Res. 2019; 11(4): 2099–2107, indexed in Pubmed: 31105821.
7. Finney AC, Stokes KY, Pattillo CB, et al. Integrin signaling in atherosclerosis. Cell Mol Life Sci. 2017; 74(12): 2263–2282, doi: 10.1007/s00018-017-2490-4, indexed in Pubmed: 28246700.
8. Fukaya H, Ako J, Yasuda S, et al. Aspirin versus P2Y inhibitors with anticoagulation therapy for atrial fibrillation. Heart. 2021; 107(21): 1731–1738, doi: 10.1136/heartjnl-2021-319321, indexed in Pubmed: 34261738.
9. Gholipour A, Shakerian F, Zahedmehr A, et al. Downregulation of Talin-1 is associated with the increased expression of miR-182-5p and miR-9-5p in coronary artery disease. J Clin Lab Anal. 2022; 36(4): e24252, doi: 10.1002/jcla.24252, indexed in Pubmed: 35156729.
10. Guo X, Jiang H, Chen J, et al. RP105 ameliorates hypoxia/reoxygenation injury in cardiac microvascular endothelial cells by suppressing TLR4/MAPKs/NF-κB signaling. Int J Mol Med. 2018; 42(1): 505–513, doi: 10.3892/ijmm.2018.3621, indexed in Pubmed: 29693119.
11. Hu J, Zheng Z, Li X, et al. Metformin attenuates hypoxia-induced endothelial cell injury by activating the amp-activated protein kinase pathway. J Cardiovasc Pharmacol. 2021; 77(6): 862–874, doi: 10.1097/FJC.0000000000001028, indexed in Pubmed: 33929389.
12. Jin H, Zhu Yi, Li Y, et al. BDNF-mediated mitophagy alleviates high-glucose-induced brain microvascular endothelial cell injury. Apoptosis. 2019; 24(5-6): 511–528, doi: 10.1007/s10495-019-01535-x, indexed in Pubmed: 30877409.
13. Khera AV, Kathiresan S. Genetics of coronary artery disease: discovery, biology and clinical translation. Nat Rev Genet. 2017; 18(6): 331–344, doi: 10.1038/nrg.2016.160, indexed in Pubmed: 28286336.
14. Liu M, Solomon W, Cespedes JC, et al. Neuregulin-1 attenuates experimental cerebral malaria (ECM) pathogenesis by regulating ErbB4/AKT/STAT3 signaling. J Neuroinflammation. 2018; 15(1): 104, doi: 10.1186/s12974-018-1147-z, indexed in Pubmed: 29636063.
15. Malakar AKr, Choudhury D, Halder B, et al. A review on coronary artery disease, its risk factors, and therapeutics. J Cell Physiol. 2019; 234(10): 16812–16823, doi: 10.1002/jcp.28350, indexed in Pubmed: 30790284.
16. Marx C, Novotny J, Salbeck D, et al. Eosinophil-platelet interactions promote atherosclerosis and stabilize thrombosis with eosinophil extracellular traps. Blood. 2019; 134(21): 1859–1872, doi: 10.1182/blood.2019000518, indexed in Pubmed: 31481482.
17. Schumacher JA, Wright ZA, Owen ML, et al. Integrin α5 and Integrin α4 cooperate to promote endocardial differentiation and heart morphogenesis. Dev Biol. 2020; 465(1): 46–57, doi: 10.1016/j.ydbio.2020.06.006, indexed in Pubmed: 32628938.
18. Sun Z, Costell M, Fässler R. Integrin activation by talin, kindlin and mechanical forces. Nat Cell Biol. 2019; 21(1): 25–31, doi: 10.1038/s41556-018-0234-9, indexed in Pubmed: 30602766.
19. Szklarczyk D, Gable AL, Nastou KC, et al. The STRING database in 2021: customizable protein-protein networks, and functional characterization of user-uploaded gene//measurement sets. Nucleic Acids Res. 2021; 49(D1): D605–D612, doi: 10.1093/nar/gkaa1074, indexed in Pubmed: 33237311.
20. Timofeeva M, Ooi A, Poon EKW, et al. Numerical simulation of the blood flow through the coronary artery stenosis: Effects of varying eccentricity. Comput Biol Med. 2022; 146: 105672, doi: 10.1016/j.compbiomed.2022.105672, indexed in Pubmed: 35661622.
21. Tuso P, Stoll SR, Li WW. A plant-based diet, atherogenesis, and coronary artery disease prevention. Perm J. 2015; 19(1): 62–67, doi: 10.7812/TPP/14-036, indexed in Pubmed: 25431999.
22. Vermeulen Z, Mateiu L, Dugaucquier L, et al. Cardiac endothelial cell transcriptome in neonatal, adult, and remodeling hearts. Physiol Genomics. 2019; 51(6): 186–196, doi: 10.1152/physiolgenomics.00002.2019, indexed in Pubmed: 30978160.
23. Wang J, Zhang H, Du A, et al. DJ-1 alleviates anoxia and hypoglycemia injury in cardiac microvascular via AKT and GSH. Mol Cell Probes. 2020; 53: 101600, doi: 10.1016/j.mcp.2020.101600, indexed in Pubmed: 32445781.
24. Wang YY, Duan H, Wang S, et al. Upregulated Talin1 synergistically boosts β-estradiol-induced proliferation and pro-angiogenesis of eutopic and ectopic endometrial stro-

mal cells in adenomyosis. Reprod Biol Endocrinol. 2021; 19(1): 70, doi: 10.1186/s12958-021-00756-7, indexed in Pubmed: 33990206.

25. Wang Y, Zhang Yu, Li J, et al. Role of Mydgf in the regulation of hypoxia/reoxygenation-induced apoptosis in cardiac microvascular endothelial cells. In Vitro Cell Dev Biol Anim. 2022; 58(8): 669–678, doi: 10.1007/s11626-022-00709-3, indexed in Pubmed: 36006589.

26. Wei X, Sun Y, Wu Y, et al. Downregulation of Talin-1 expression associates with increased proliferation and migration of vascular smooth muscle cells in aortic dissection. BMC Cardiovasc Disord. 2017; 17(1): 162, doi: 10.1186/s12872-017-0588-0, indexed in Pubmed: 28637452.

27. Xu F, Zhou F. Inhibition of microRNA-92a ameliorates lipopolysaccharide-induced endothelial barrier dysfunction by targeting ITGA5 through the PI3K/Akt signaling pathway in human pulmonary microvascular endothelial cells. Int Immunopharmacol. 2020; 78: 106060, doi: 10.1016/j.intimp.2019.106060, indexed in Pubmed: 31841757.

28. Xu RX, Wu YJ. Lipid-Modifying drugs: pharmacology and perspectives. Adv Exp Med Biol. 2020; 1177: 133–148, doi: 10.1007/978-981-15-2517-9_5, indexed in Pubmed: 32246446.

29. Ye Q, Ju C, Ye Z, et al. Circ_ROBO2/miR-186-5p/TRIM14 axis regulates oxidized low-density lipoprotein-induced cardiac microvascular endothelial cell injury. Regen Ther. 2022; 20: 138–146, doi: 10.1016/j.reth.2022.04.005, indexed in Pubmed: 35620639.

30. Yun S, Hu R, Schwaemmle ME, et al. Integrin α5β1 regulates PP2A complex assembly through PDE4D in atherosclerosis. J Clin Invest. 2019; 129(11): 4863–4874, doi: 10.1172/JCI127692, indexed in Pubmed: 31408443.

31. Zhang Q, Cao Y, Liu Y, et al. Shear stress inhibits cardiac microvascular endothelial cells apoptosis to protect against myocardial ischemia reperfusion injury via YAP/miR-206//PDCD4 signaling pathway. Biochem Pharmacol. 2021; 186: 114466, doi: 10.1016/j.bcp.2021.114466, indexed in Pubmed: 33610591.

32. Zhang Z, Tang J, Song J, et al. Elabela alleviates ferroptosis, myocardial remodeling, fibrosis and heart dysfunction in hypertensive mice by modulating the IL-6/STAT3/GPX4 signaling. Free Radic Biol Med. 2022; 181: 130–142, doi: 10.1016/j.freeradbiomed.2022.01.020, indexed in Pubmed: 35122997.

33. Zhao BS, Belhoul-Fakir H, Jansen S, et al. Major gaps in human evidence for structure and function of the vasa vasora limit our understanding of the link with atherosclerosis. J Anat. 2021; 238(3): 785–793, doi: 10.1111/joa.13324, indexed in Pubmed: 33084089.

34. Zhong CM, Li S, Wang XW, et al. MicroRNA-92a -mediated endothelial to mesenchymal transition controls vein graft neointimal lesion formation. Exp Cell Res. 2021; 398(1): 112402, doi: 10.1016/j.yexcr.2020.112402, indexed in Pubmed: 33253710.

35. Zhou H, Wang S, Zhu P, et al. Empagliflozin rescues diabetic myocardial microvascular injury via AMPK-mediated inhibition of mitochondrial fission. Redox Biol. 2018; 15: 335–346, doi: 10.1016/j.redox.2017.12.019, indexed in Pubmed: 29306791.

36. Zhou H, Zhang Y, Hu S, et al. Melatonin protects cardiac microvasculature against ischemia/reperfusion injury via suppression of mitochondrial fission-VDAC1-HK2-mPTP-mitophagy axis. J Pineal Res. 2017; 63(1), doi: 10.1111/jpi.12413, indexed in Pubmed: 28398674.

37. Zou R, Shi W, Qiu J, et al. Empagliflozin attenuates cardiac microvascular ischemia/reperfusion injury through improving mitochondrial homeostasis. Cardiovasc Diabetol. 2022; 21(1): 106, doi: 10.1186/s12933-022-01532-6, indexed in Pubmed: 35705980.

VIA MEDICA

ORIGINAL ARTICLE

Mesenchymal stem cell-derived exosomes are beneficial to suppressing inflammation and promoting autophagy in intervertebral disc degeneration

Baicheng Yang[1]*, Xinming Yang[2]*

[1]Hebei North University, Zhangjiakou, Hebei, China
[2]Department of Orthopaedics, the First Affiliated Hospital of Hebei North University, Zhangjiakou, Hebei, China

Background: Intervertebral disc degenerative diseases is one the main causes of lumbago, and its main pathological mechanism is intervertebral disc degeneration (IDD). As shown in previous reports, mesenchymal stem cell (MSC)-exosomes can slow down or even reverse degenerated nucleus pulposus (NP) cells in IDD. Thus, we attempted to clarify the specific role of MSC-exosomes underlying IDD progression.

Materials and methods: In the present study, the harvested particles were identified as MSC-exosomes. MSC-exosomes facilitated activation of autophagy pathway in AGE-treated NP cells. MSC-exosomes repressed inflammatory response in AGE-treated NP cells. Autophagy pathway activation enhanced inflammatory response in AGE-stimulated NP cells.

Results: Mesenchymal stem cell-exosomes facilitated autophagy pathway activation and repressed inflammation in IDD rats. Autophagy inhibition exerted a protective role against inflammatory response in IDD rats.

Conclusions: In conclusion, MSC-exosomes represses inflammation via activating autophagy pathway, which provides a potential novel insight for seeking therapeutic plans of IDD. (Folia Morphol 2024; 83, 1: 102–112)

Keywords: intervertebral disc degeneration, mesenchymal stem cell, exosomes, autophagy, inflammation

INTRODUCTION

Lumbago is the most common spinal surgery symptom with high morbidity and disability rate, seriously affecting human health and quality of life and also bringing a heavy burden to individuals, families and the whole society [2]. One of the main causes of lumbago is intervertebral disc degener-ative diseases, of which main pathological mech-anism is intervertebral disc degeneration (IDD). Since most patients with early IDD have no obvious symptoms, they also miss the opportunity for early intervention and therapy [21, 34]. Currently, treat-ment methods for diseases caused by IDD include conservative therapy and surgery. Both of them can

relieve clinical symptoms to a certain extent, but the long-term effect is often unfavourable [33]. Thus, it is of great clinical significance to figure out molecular biology to prevent or even reverse IDD with less damage to patients.

The intervertebral disc (IVD) is the largest avascular structure in the human body [9]. The changes in the structure of IVD are caused by a combination of factors such as cellular aging, nutritional disorders, stress factors, inflammatory mediators, reduction of nucleus pulposus cells, abnormal metabolism of extracellular matrix (ECM), etc. [10]. To address IDD and related degenerative diseases, multiple studies have focused on maintaining the amount of nucleus pulposus (NP) cells [11, 25]. Thus, bone marrow mesenchymal stem cells (BMSCs), which have the advantages of easy access, multi-directional differentiation, low immunogenicity, and mature acquisition and identification, have been widely researched [14]. The inflammatory response mediated by pro-inflammatory cytokines can directly cause the loss of water in IVD and exacerbate IDD process [31]; mesenchymal stem cells (MSCs) are capable of migrating to damaged tissues and releasing cytokines, inflammatory regulators, extracellular matrix components, and antimicrobial proteins in this area to create a suitable microenvironment for tissue repair [23]. With the deepening of research, it has been demonstrated that biological information can be transmitted between non-contact cells through paracrine or in the form of exosomes [35]. MSC-exosomes can upregulate autophagy marker proteins LC3 and Beclin-1 and facilitate autophagosome formation [40]. Rat MSCs can produce positive trophic effects on degenerated NP cells by secreting exosomes, and NP degeneration degree can still be improved after non-contact co-culture of BMSCs and NP cells [28]. Moreover, MSC-exosomes are capable of attenuating NP cell apoptosis induced by proinflammatory cytokines [17]. These reports indicate that MSC-exosomes can slow down or even reverse degenerated NP cells in IDD.

Thus, we hypothesized that MSC-exosomes delayed or even reversed IDD via autophagy activation and inflammation inhibition. Herein, we clarified potential role of MSC-exosomes in IDD by establishing animal models and AGE-treated cell models, which may provide a novel insight for targeted therapy of IDD.

MATERIALS AND METHODS

Isolation and identification of MSCs

Human bone marrow specimens were collected from healthy donors. The institutional review board of our hospital approved this research with informed consent signed by patients. MSCs from bone marrow were separated using density gradient centrifugation and adherence to tissue culture plastic. MSCs amplification was performed in Dulbecco's modified Eagle medium (DMEM) supplemented with 15% fetal bovine serum (FBS; Gibco) and 1% penicillin-streptomycin (Invitrogen). MSCs were photographed through microscopy (Olympus, USA). For detecting cell surface markers, MSCs were characterized by CD73, CD90 and CD105 positive expression as well as CD34 and HLA-DR negative expression through flow cytometry (BD Biosciences, USA) under manufacturer's guidance. The surface antigens were provided by BD Biosciences.

Isolation and identification of exosomes

Mesenchymal stem cells were cultured in DMEM deprived of FBS for 2 days. Then the collected culture media were centrifuged at 500 g for 10 min, then 2000 g for 30 min to eliminate dead cells and debris, and finally 10000 g for 1 h to eliminate large vesicles. The supernatant containing cell-free culture media was transferred to a new tube without disturbing the pellet and the Total Exosome Isolation reagent (Invitrogen) was added, according to manufacturer's guidelines. After collection, morphology of isolated exosomes was observed through transmission electron microscopy (TEM) (Philips, NLD). The particles were characterized by exosomal markers including CD63, TSG101 and Alix via western blotting.

A cellular model of IDD

Human NP cells (cat no. CP-H097) provided by Procell (Wuhan, China) were cultured in DMEM containing 15% FBS and 1% penicillin-streptomycin. The culture medium was replaced twice every week and NP cells in the second or third passage were harvested for further use. NP cells under AGEs (200 μg/mL) stimulation were co-cultured with MSC-exosomes (cat no. CP-H166) at 10, 50, or 100 μg/mL for 24 h. The untreated NP cells were taken as negative controls. For rescue assays, AGE-stimulated NP cells co-cultured with MSC-exosomes were treated with 5 mM of 3-MA (Sigma-Aldrich), a specific autophagy inhibitor, for 24 h.

An animal model of IDD

The Animal Experimentation Committee of our hospital approved the animal experiments. A total of 24 three-month-old Sprague-Dawley rats were utilized in our research. After all rats were anaesthetized with 2% (w/v) pentobarbital (40 mg/kg), three IVDs (Co7/8, Co8/9 and Co9/10) in each rat were located by palpation on coccygeal vertebrae and validated using trial radiography. Moreover, three IVDs (Co7/8, Co8/9 and Co9/10) respectively received intradiscal injection of 2 μL of phosphate buffer saline (PBS), AGEs (200 μg/mL) or a mixture of AGEs (200 μg/mL) and exosomes (100 μg/mL) through a 33-gauge needle (Hamilton), termed Sham, Model or Model+exosomes group, with 6 rats in each group. The injections were performed every 2 weeks for 2 months. For rescue assays, IVDs in Model+exosomes group received intraperitoneal injection of 3-MA at 1.5 mg/100 g for 24 h.

MRI examination

Magnetic resonance imaging (MRI) was performed on all rats using a 7.0 T animal specific MRI system (Bruker Pharmascan, Germany). Pfirrmann classification was used to assess the degree of IVD degeneration [26]. The average score of punctured IVDs were calculated as degeneration grading of rats.

Histological analysis

After MRI examination, all rats were sacrificed through intraperitoneal administration with overdose pentobarbital sodium. The specimens were decalcified and fixed in formaldehyde, followed by dehydration, and were finally embedded in paraffin. The slides of each disc were stained with haematoxylin-eosin and observed through microscopy.

Immunofluorescence

Nucleus pulposus cells or tissues attached to slides were fixed with 4% paraformaldehyde and permeabilized with 0.2% Triton X-100 in PBS. After washed using PBS, slides were blocked with 2% bovine serum albumin (BSA) in PBS at 37°C for 2 h, followed by incubation with primary antibody against LC3B (ab48394, Abcam, Shanghai, China). After washed twice, slides underwent subsequent treatment with secondary goat anti-rabbit antibody at 37°C for 2 h. Nuclei were co-stained by DAPI (Beyotime) at 0.1 g/mL for 5 min. Images were obtained through microscopy.

Western blot

Total proteins were isolated from NP cells or mouse tissues through a protein extraction kit (Beyotime) according to manufacturer's guidelines. The primary antibodies including CD63, TSG101, Alix, LC3B, Beclin-1, ATG5, interleukin (IL)-6, IL-1β, tumour necrosis factor alpha (TNF-α) and β-actin as well as horseradish peroxidase (HRP)-conjugated secondary antibodies were obtained from Abcam. Protein bands visualization and detection through enhanced chemiluminescence.

Enzyme linked immunosorbent assay (ELISA)

The concentrations of proinflammatory cytokines were tested with corresponding ELISA kits (IL-6, IL-1β and TNF-α; ThermoFisher) under manufacturer's guidance.

Ethics approval and consent to participate

Animal procedures were approved by the First Affiliated Hospital of Hebei North University and this study was approved by the Ethics Committee of the First Affiliated Hospital of Hebei North University.

Statistical analysis

Data were expressed as the mean ± standard deviation of three independent assays. Statistical analysis was conducted using GraphPad Prism 7 software. Comparisons between two groups were assessed with Student's t-test and comparisons among multiple groups were assessed with one-way ANOVA followed by Tukey's post hoc test. A statistical significance was presented upon $p < 0.05$.

RESULTS

Identification of MSC and its derived exosomes

Mesenchymal stem cells, which have the advantages of easy access, multi-directional differentiation, low immunogenicity, and mature acquisition and identification, have been widely used in IDD-related reports [14]. Herein, human MSCs were harvested from bone marrow aspirates of donors. We observed characteristics of MSCs through microscopy. As a result, it appeared like a spindle with a 60–70% confluence (Fig. 1A). Flow cytometry demonstrated CD90, CD73 and CD105 positive expression as well as HLA-DR and CD34 negative expression in MSCs (Fig. 1B). Then, MSC-exosomes were isolated and purified from MSC culture medium and particle morphology was confirmed under TEM (Fig. 1C). Additionally,
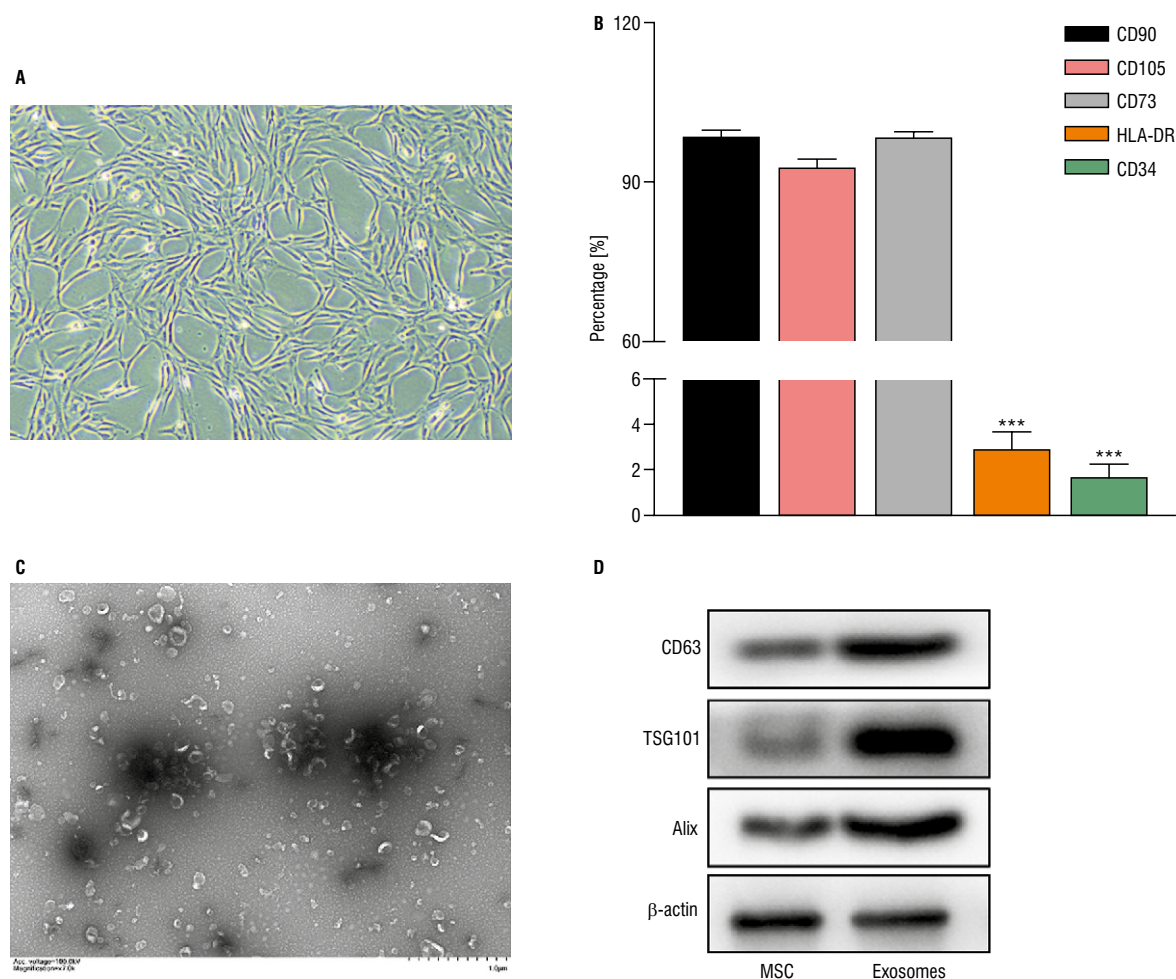
Figure 1. Characterization of mesenchymal stem cell (MSC) and its derived exosomes were identified; **A.** Characteristics of MSCs through microscopy; **B.** Characteristics of MSCs through flow cytometry; **C.** Characteristics of MSC-exosomes through transmission electron microscopy; **D.** Characteristics of MSC-exosomes through western blot; ***p < 0.001.

western blotting depicted that the level of exosomal marker proteins (CD63, TSG101 and Alix) presented a remarkable elevation in exosomes relative to MSCs (Fig. 1D). Collectively, these harvested particles were identified as MSC-exosomes.

MSC-exosomes facilitate autophagy in AGE-stimulated NP cells

Previously, AGEs accumulation exerted a pathogenic role in IDD [22]. Thus, we mimicked IDD characteristics in vitro through establishing a cellular model in NP cells under AGE treatment, termed AGEs group, and non-treated NP cells were taken as Control group. To clarify MSC-exosomes role in AGE-stimulated NP cells, AGEs group received additional exosomes treatment at different doses, termed Model+exosomes-10/50/100 group. Previously, MSC-exosomes

upregulated autophagy marker proteins LC3 and Beclin-1 and facilitated autophagosome formation [40]. We attempted to clarify impact of MSC-exosomes on autophagy pathway in NP cells. Detecting autophagosomal marker LC3 through immunofluorescence is a reliable means of monitoring autophagy [32]. Thus, we measured fluorescent intensity of LC3 using immunofluorescence. As a result, LC3-labeled NP cells presented depletion in AGEs group and showed a dose-dependent elevation under co-treatment with MSC-exosomes (Fig. 2A). Additionally, western blotting demonstrated the downregulation of LC3B-II, Beclin-1 and ATG5 in AGEs group and this effect was reversed by MSC-exosomes along with increase of concentration of MSC-exosomes (Fig. 2B). Collectively, MSC-exosomes facilitate activation of autophagy pathway in AGE-treated NP cells.
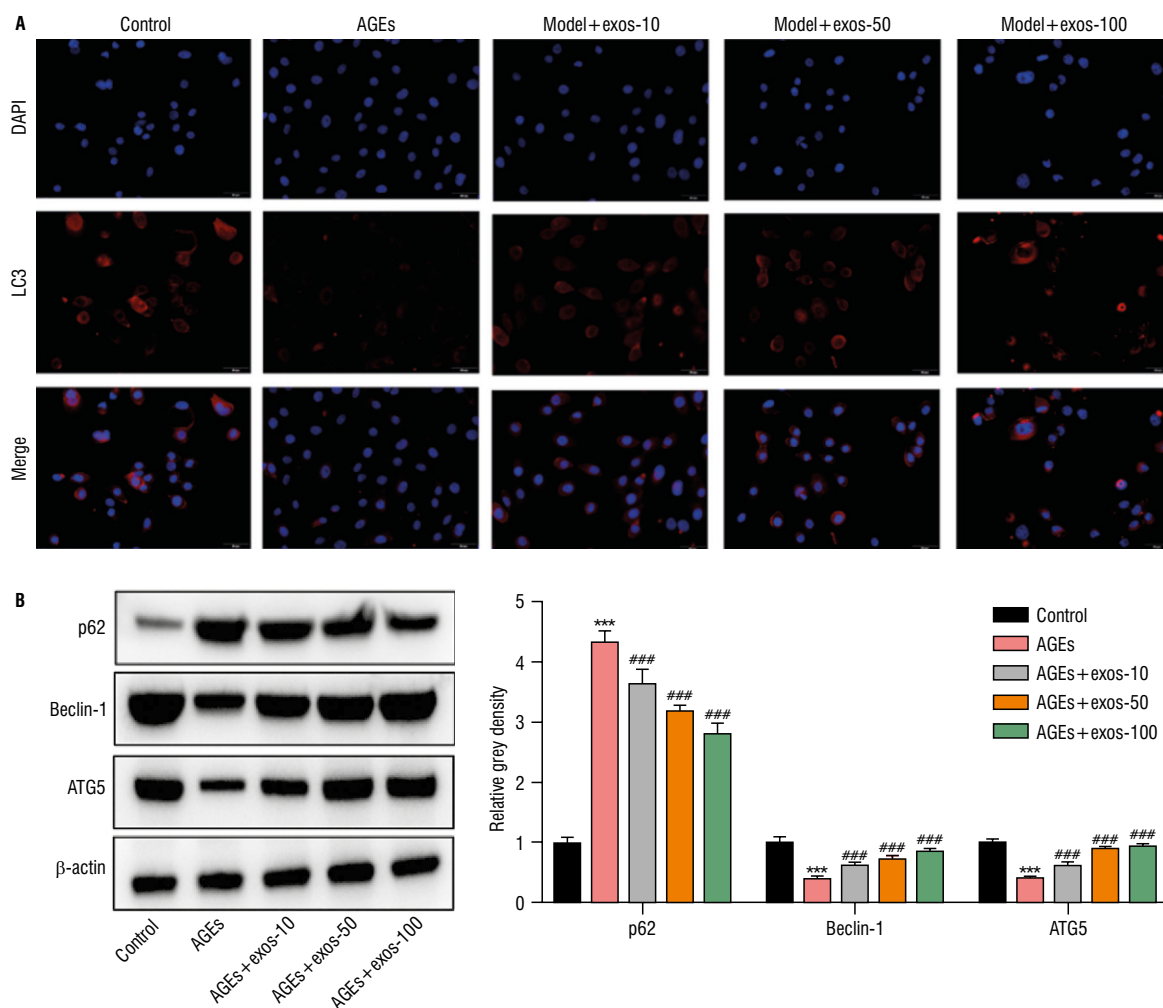
Figure 2. Mesenchymal stem cell-exosomes facilitated autophagy in AGE-stimulated nucleus pulposus (NP) cells; **A.** Immunofluorescence detected LC3 fluorescence in NP cells in Control/AGEs/Model+exos-10/Model+exos-50/Model+exos-100 group; **B.** Western blot detected levels of autophagy-related proteins in NP cells under different conditions; ***p < 0.001; ###p < 0.001.

MSC-exosomes suppress inflammation in AGE-stimulated NP cells

Mesenchymal stem cell-exosomes are capable of attenuating NP cell apoptosis induced by proinflammatory cytokines [17]. Thus, we attempted to clarify influence of MSC-exosomes on inflammatory response in NP cells. ELISA demonstrated that contents of proinflammatory cytokines (IL-6, IL-1β and TNF-α) presented elevation in AGEs group and showed a dose-dependent depletion under co-treatment with MSC-exosomes (Fig. 3A). Similarly, western blotting demonstrated the upregulation of IL-6, IL-1β and TNF-α in AGEs group and this effect was reversed by MSC-exosomes along with increase of concentration of MSC-exosomes (Fig. 3B). Collectively, MSC-exosomes repress inflammatory response in AGE-treated NP cells.

Inhibiting autophagy enhances inflammation in AGE-stimulated NP cells

We aimed to clarify whether autophagy pathway exerted a role in inflammatory response in NP cells. Thus, we performed rescue assays using 3-MA, a specific autophagy inhibitor [30], in cellular models under AGEs treatment. Immunofluorescence illustrated that LC3 fluorescence in AG-stimulated NP cells presented elevation under treatment with MSC-exosomes and showed depletion under co-treatment with 3-MA (Fig. 4A). Moreover, ELISA depicted that contents of IL-6, IL-1β and TNF-α in AG-stimulated NP cells presented depletion under treatment with MSC-exosomes and showed elevation under co-treatment with 3-MA (Fig. 4B). Western blotting showed a similar trend to ELISA results (Fig. 4C). Collectively, autophagy pathway activation enhances inflammatory response in AGE-stimulated NP cells.
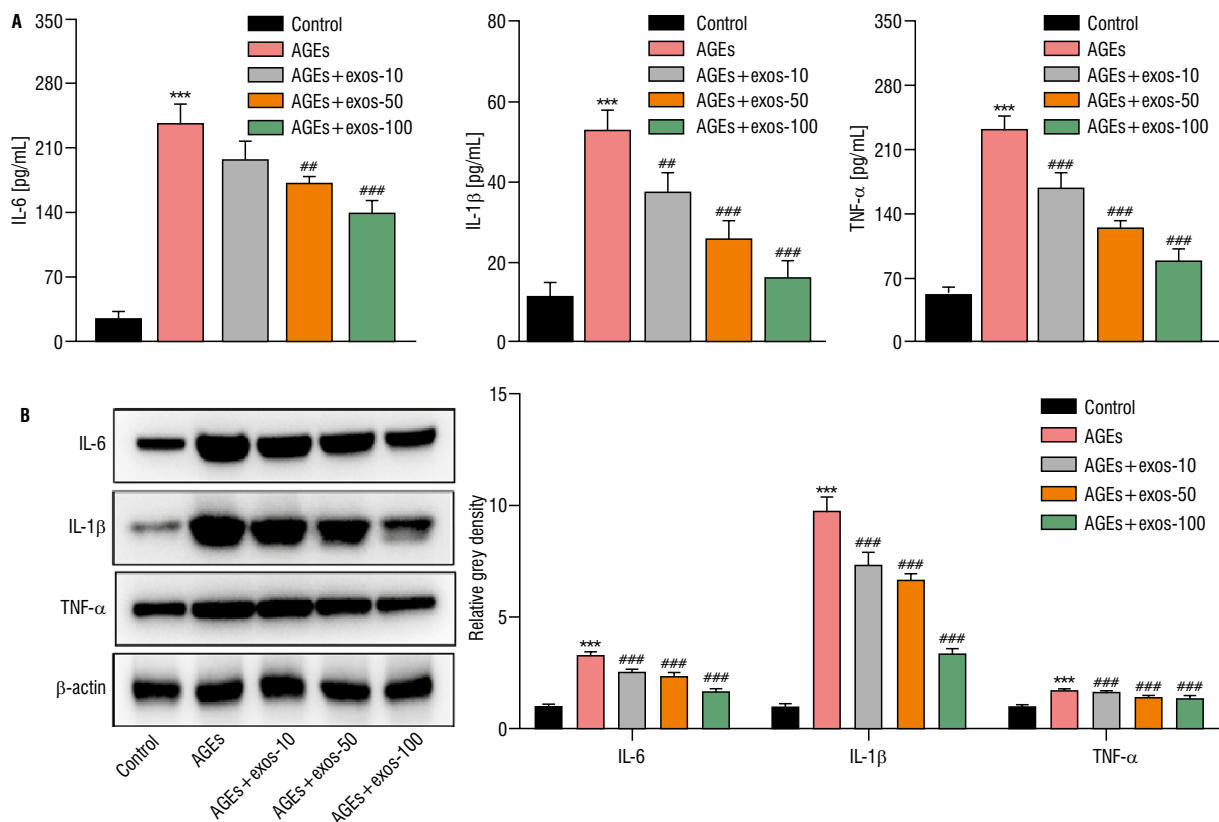
Figure 3. Mesenchymal stem cell-exosomes suppressed inflammation in AGE-stimulated nucleus pulposus (NP) cells; **A.** ELISA detected levels of proinflammatory cytokines in NP cells in Control/AGEs/Model+exos-10/Model+exos-50/Model+exos-100 group; **B.** Western blot detected levels of inflammation-related proteins in NP cells under different conditions; IL — interleukin; TNF-α — tumour necrosis factor alpha; ***p < 0.001; ###p < 0.001; ##p < 0.05.

MSC-exosomes induce autophagy and repress inflammation in a rat model of IDD

We attempted to further elucidate role of MSC-exosomes underlying IDD progression. Thus, we mimicked IDD characteristics in vivo through establishing IDD rat models. All rats were divided into Sham, Model or Model+exosomes group in a random manner. Three independent discs of each rat received intradiscal injection with PBS, AGEs, or AGEs+MSC-exosomes, respectively. We evaluated IDD degree through Pfirrmann MRI grading system [12]. As a result, Pfirrmann scores presented elevation in Model group and showed depletion under co-treatment with MSC-exosomes (Fig. 5A). Histology by haematoxylin-eosin staining indicated that MSC-exosomes reversed AGE-triggered IVD degradation during IDD (Fig. 5B). Moreover, immunofluorescence demonstrated that AGE-triggered depletion in LC3 fluorescence was rescued by MSC-exosomes (Fig. 5C). Western blotting also depicted that AGE-triggered depletion in LC3B-II, Beclin-1 and ATG5 protein abundances was rescued by MSC-exosomes (Fig. 5D), suggesting that autophagy

pathway is suppressed in IDD rats while activated by MSC-exosomes. Furthermore, AGE-triggered increase in IL-6, IL-1β and TNF-α concentrations was reversed by MSC-exosomes (Fig. 5E). Western blotting showed a similar trend to ELISA results (Fig. 5F). Collectively, MSC-exosomes facilitates autophagy pathway activation and repress inflammation in IDD rats.

Autophagy inhibition exerts a protective role against inflammation in a rat model of IDD

We aimed to clarify whether autophagy pathway exerted a role in inflammatory response in IDD progression. Thus, we performed rescue assays using 3-MA in IDD rat models. MSC-exosomes-triggered depletion in Pfirrmann scores in IDD rats was rescued by 3-MA treatment (Fig. 6A). Histology by haematoxylin-eosin staining indicated that 3-MA countervailed the inhibitory impact of MSC-exosomes on IVD degradation during IDD (Fig. 6B). Moreover, immunofluorescence demonstrated that MSC-exosomes-triggered elevation in LC3 fluorescence was rescued by 3-MA (Fig. 6C). Furthermore, MSC-exosomes-triggered de-
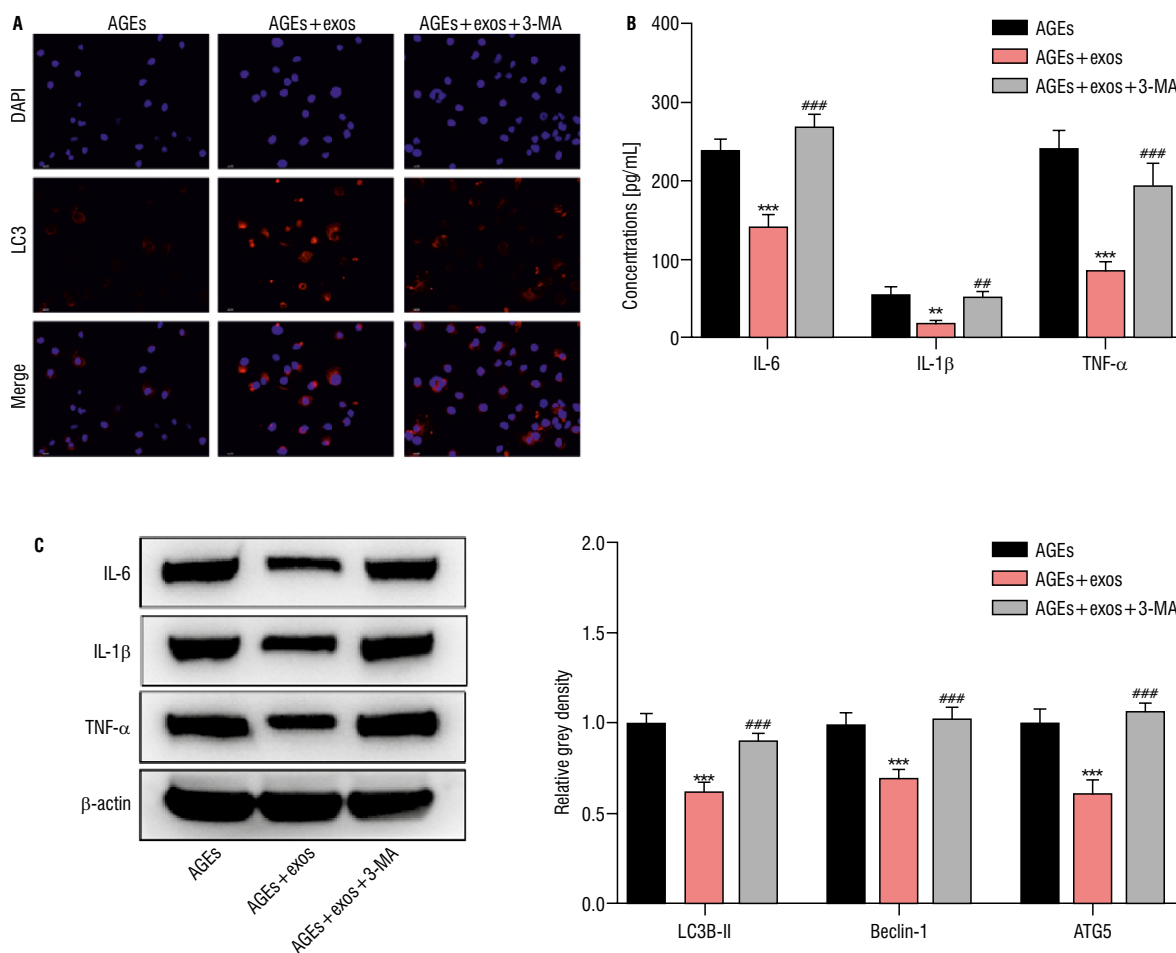
Figure 4. Inhibiting autophagy enhanced inflammation in AGE-stimulated nucleus pulposus (NP) cells; **A.** Immunofluorescence detected LC3 fluorescence in NP cells in AGEs/AGEs+exos/AGEs+exos+3-MA group; **B.** ELISA detected levels of proinflammatory cytokines in NP cells in NP cells under different conditions; **C.** Western blot detected levels of inflammation-related proteins in NP cells under different conditions; IL — interleukin; TNF-α — tumour necrosis factor alpha; ***p < 0.001; **p < 0.05; ###p < 0.001; ##p < 0.05.

crease in IL-6, IL-1β and TNF-α concentrations was reversed by MSC-exosomes (Fig. 6D). Western blotting showed a similar trend to ELISA results (Fig. 6E). Collectively, autophagy inhibition exerts a protective role against inflammatory response in IDD rats.

DISCUSSION

At the cellular level, IDD presents pathological characterization by decrease in NP cell amount and a metabolic imbalance of major products of the ECM (proteoglycan and collagen type II) [1, 3, 36]. Thus, finding a source of cells that can replenish degenerated NP cells can effectively improve IDD and simultaneously can achieve the purpose of early prevention and avoid further aggravation of IDD and serious consequences.

Autophagy is a crucial mechanism for cells to self-digest and recycle damaged components, espe-

cially under stressful conditions, and is a vital survival mechanism for cells under nutrient deprivation [8, 13]. Autophagy exerts a protective role in IVD cells [24]. Oxidative stress, pH, stress load, inflammatory cytokine stimulation, and hyperglycaemic hypertonic environment in IVD microenvironment can activate the autophagy activity of NP cells, while various extracellular environment stimuli, such as oxidative stress, can reduce ability of cells to proliferate [29, 37, 38]. Our research also validated that IDD degree can be remarkably improved through modulating autophagy level in NP cells. Biological information can be transmitted between cells that are not in contact with each other in the form of paracrine or exosomes, and MSCs can also treat IDD through secreting exosomes [41, 42]. MSC exosomes can alleviate endoplasmic reticulum stress-induced apoptosis by activating AKT and ERK signalling [19]. Herein, exosomes secreted
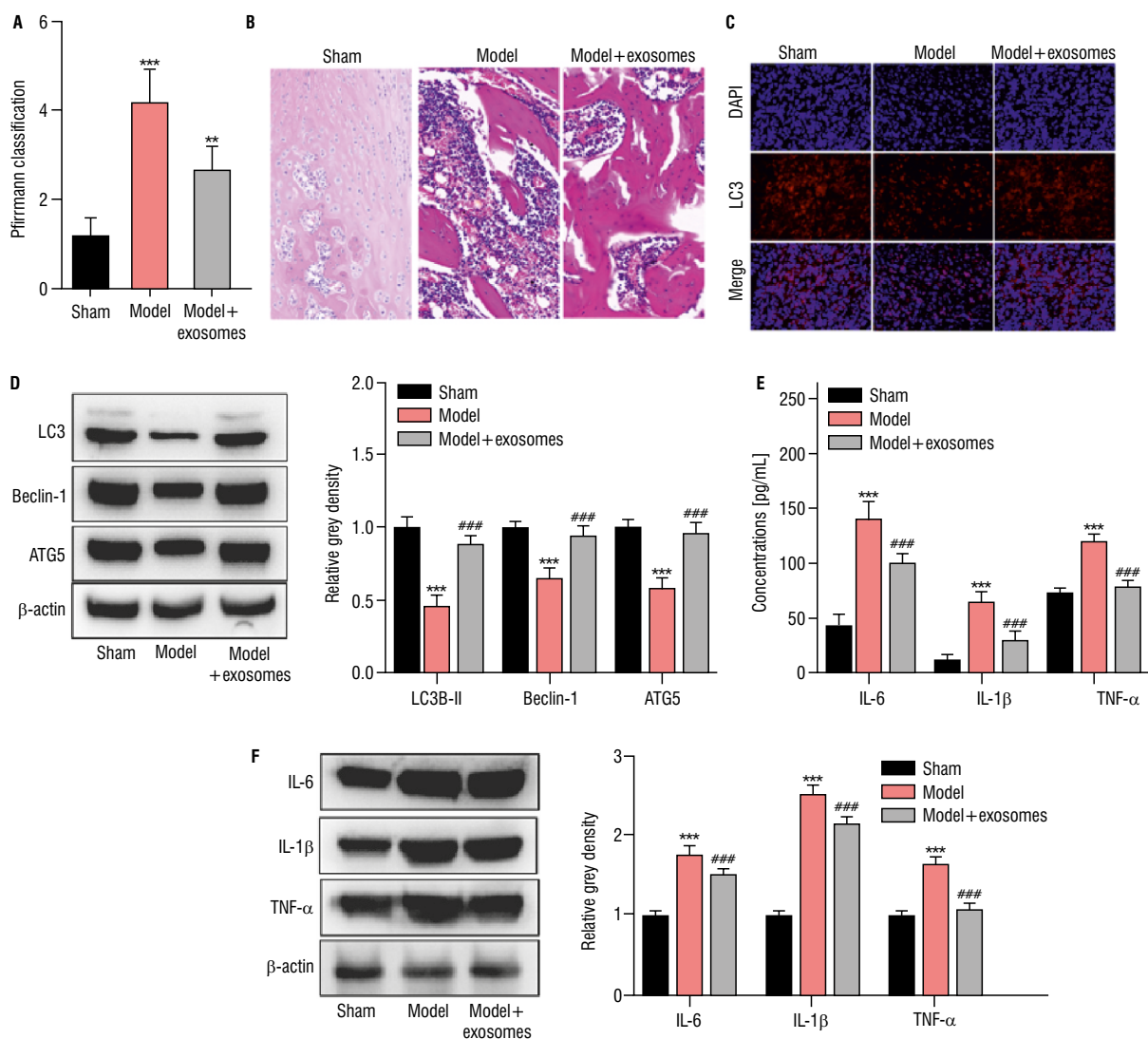
Figure 5. Mesenchymal stem cell-exosomes induced autophagy and repressed inflammation in a rat model of intervertebral disc degeneration; **A.** Pfirrmann magnetic resonance imaging grading system evaluated pathological changes in discs in Sham/Model/Model+exosomes group; **B.** Haematoxylin-eosin staining evaluated pathological changes in discs in each group; **C.** Immunofluorescence detected LC3 fluorescence in discs in each group; **D.** Western blot detected levels of autophagy-related proteins in discs in each group; **E.** ELISA detected levels of proinflammatory cytokines in discs in each group; **F.** Western blot detected levels of inflammation-related proteins in discs in each group; ***$p < 0.001$; **$p < 0.05$; ###$p < 0.001$.

by MSCs were successfully detected through TEM and immunoblot. By establishing a co-culture model, we discovered that in NP cellular model under AGEs stimulation, autophagy-related proteins in AGE-stimulated NP cells presented downregulation, while autophagy-related proteins in AGE-stimulated NP cells with MSC-exosome co-culture presented upregulation along with elevation of MSC-exosomes concentration, fully suggesting that MSCs enhances autophagy level in AGE-stimulated NP cells through MSC-secreted exosomes. Additionally, we established an IDD rat model and obtained similar results to a cellular model.

Inflammatory response mediated by pro-inflammatory cytokines can directly cause loss of water in IVD and exacerbate IDD process [20]. The enhanced "pro-inflammatory" role and insufficient "anti-inflammatory" role, that is, the imbalance of "inflammatory arm", may be a vital reason for aggravated inflammatory response in IDD [39]. Previously, pro-inflammatory cytokine IL-1 presented upregulation and its inhibitor IL-1a presented depletion in IDD [4]. Kritschil et al. [15] illustrated that insulin-like growth factor-1, which exerted an anti-inflammatory role, presented downregulation in IDD. Herein, in AGE-treated NP cellular model, pro-inflammatory
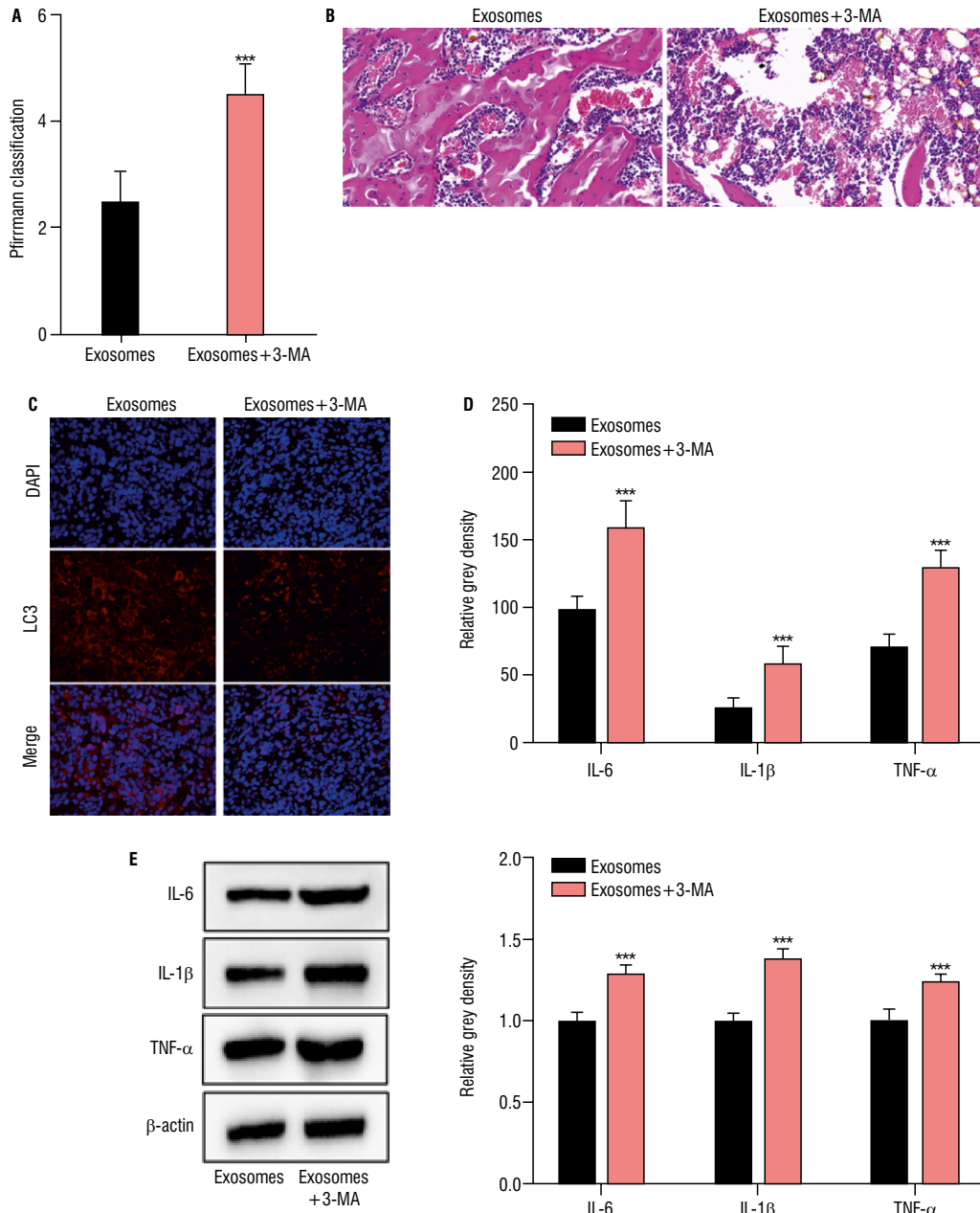
Figure 6. Autophagy inhibition exerted a protective role against inflammation in a rat model of intervertebral disc degeneration; **A.** Pfirrmann magnetic resonance imaging grading system evaluated pathological changes in discs in Exosomes/Exosomes+3-MA group; **B.** Haematoxylin--eosin staining evaluated pathological changes in discs in each group; **C.** Immunofluorescence detected LC3 fluorescence in discs in each group; **D.** ELISA detected levels of proinflammatory cytokines in discs in each group; **E.** Western blot detected levels of inflammation-related proteins in discs in each group; ***p < 0.001.

cytokines in AGEs-treated NP cells presented upregulation, while pro-inflammatory cytokines presented downregulation along with elevation of MSC-exosomes concentration, fully suggesting that MSCs repress inflammatory response of NP cells through MSC-secreted exosomes. Additionally, we established an IDD rat model and obtained similar results to a cellular model.

Autophagy is a widespread self-protection mechanism in eukaryotic cells [18]. Recent research has revealed that there is a close connection between autophagy and inflammation [7, 16]. Though inflammatory responses innately protect the body from infection or tissue damage, persistent or excessive inflammatory responses can result in irreversible damage to the body [5]. It has been demonstrated that

autophagy suppresses the inflammatory response possibly through directly repressing inflammatory complexes and indirectly through removing inflammatory stimuli such as damaged organelles or pathogenic microorganisms, thereby protecting cells from excessively persistent inflammation [6, 27]. Herein, in AGE-stimulated NP cellular model co-cultured with MSC-exosomes, 3-MA, an autophagy inhibitor, counteracted promoting influence of MSC exosomes on autophagy activation and reversed inhibitory impact of MSC-exosomes on inflammation, fully suggesting that MSC-exosomes suppresses AGE-induced NP cell inflammation via activating autophagy pathway. These results were also validated in animal models.

CONCLUSIONS

In conclusion, MSC-exosomes can improve degeneration of IDD via activating autophagy pathway to suppress inflammation, providing a potential novel insight for seeking therapeutic plans of IDD. However, due to complex and diverse components in exosomes, it remains elusive which component or cytokine in exosomes and which pathway exerts the main role, which will be addressed one by one in our future research.

Funding

Conflict of interest: None declared.

REFERENCES

1. Bai Z, Liu W, He D, et al. Protective effects of autophagy and NFE2L2 on reactive oxygen species-induced pyroptosis of human nucleus pulposus cells. Aging (Albany NY). 2020; 12(8): 7534–7548, doi: 10.18632/aging.103109, indexed in Pubmed: 32320383.
2. Buchbinder R, Tulder Mv, Öberg B, et al. Low back pain: a call for action. Lancet. 2018; 391(10137): 2384–2388, doi: 10.1016/s0140-6736(18)30488-4.
3. Chen J, Lin Z, Deng K, et al. Tension induces intervertebral disc degeneration via endoplasmic reticulum stress-mediated autophagy. Biosci Rep. 2019; 39(8), doi: 10.1042/BSR20190578, indexed in Pubmed: 31285389.
4. Chen Y, Ma H, Bi D, et al. Association of interleukin 1 gene polymorphism with intervertebral disc degeneration risk in the Chinese Han population. Biosci Rep. 2018; 38(4), doi: 10.1042/BSR20171627, indexed in Pubmed: 29884765.
5. Choudhary V, Griffith S, Chen X, et al. Pathogen-Associated molecular pattern-induced TLR2 and TLR4 activation increases keratinocyte production of inflammatory mediators and is inhibited by phosphatidylglycerol. Mol Pharmacol. 2020; 97(5): 324–335, doi: 10.1124/mol.119.118166, indexed in Pubmed: 32173651.
6. Chung C, Seo W, Silwal P, et al. Crosstalks between inflammasome and autophagy in cancer. J Hematol Oncol. 2020; 13(1), doi: 10.1186/s13045-020-00936-9.
7. Deretic V. Autophagy in inflammation, infection, and immunometabolism. Immunity. 2021; 54(3): 437–453, doi: 10.1016/j.immuni.2021.01.018, indexed in Pubmed: 33691134.
8. Feng Y, Ariosa AR, Yang Y, et al. Downregulation of autophagy by Met30-mediated Atg9 ubiquitination. Proc Natl Acad Sci USA. 2021; 118(1), doi: 10.1073/pnas.2005539118, indexed in Pubmed: 33443148.
9. Fournier DE, Kiser PK, Shoemaker JK, et al. Vascularization of the human intervertebral disc: A scoping review. JOR Spine. 2020; 3(4): e1123, doi: 10.1002/jsp2.1123, indexed in Pubmed: 33392458.
10. González Martínez E, García-Cosamalón J, Cosamalón-Gan I, et al. [Biology and mechanobiology of the intervertebral disc]. Neurocirugia (Astur). 2017; 28(3): 135–140, doi: 10.1016/j.neucir.2016.12.002, indexed in Pubmed: 28130014.
11. He R, Wang Z, Cui M, et al. HIF1A Alleviates compression-induced apoptosis of nucleus pulposus derived stem cells via upregulating autophagy. Autophagy. 2021; 17(11): 3338–3360, doi: 10.1080/15548627.2021.1872227, indexed in Pubmed: 33455530.
12. Hollenberg AM, Maqsoodi N, Phan A, et al. Bone morphogenic protein-2 signaling in human disc degeneration and correlation to the Pfirrmann MRI grading system. Spine J. 2021; 21(7): 1205–1216, doi: 10.1016/j.spinee.2021.03.002, indexed in Pubmed: 33677096.
13. Kim J, Lee S, Kim H, et al. Autophagic organelles in DNA damage response. Front Cell Dev Biol. 2021; 9, doi: 10.3389/fcell.2021.668735.
14. Kos N, Gradisnik L, Velnar T. A brief review of the degenerative intervertebral disc disease. Med Arch. 2019; 73(6): 421–424, doi: 10.5455/medarh.2019.73.421-424, indexed in Pubmed: 32082013.
15. Kritschil R, Zhang Z, Lei C, et al. Effects of suppressing bioavailability of insulin-like growth factor on age-associated intervertebral disc degeneration. JOR Spine. 2020; 3(4): e1112, doi: 10.1002/jsp2.1112, indexed in Pubmed: 33392450.
16. Levine B, Kroemer G. Biological functions of autophagy genes: a disease perspective. Cell. 2019; 176(1-2): 11–42, doi: 10.1016/j.cell.2018.09.048.
17. Li M, Li R, Yang S, et al. Exosomes derived from bone marrow mesenchymal stem cells prevent acidic pH-Induced damage in human nucleus pulposus cells. Med Sci Monit. 2020; 26: e922928, doi: 10.12659/MSM.922928, indexed in Pubmed: 32436493.
18. Li M, Liu DW. [Advances in the research of effects of regulation of cell autophagy on wound healing]. Zhonghua Shao Shang Za Zhi. 2017; 33(10): 625–628, doi: 10.3760/cma.j.issn.1009-2587.2017.10.009, indexed in Pubmed: 29056024.

19. Liao Z, Luo R, Li G, et al. Exosomes from mesenchymal stem cells modulate endoplasmic reticulum stress to protect against nucleus pulposus cell death and ameliorate intervertebral disc degeneration in vivo. Theranostics. 2019; 9(14): 4084–4100, doi: 10.7150/thno.33638, indexed in Pubmed: 31281533.

20. Liu ZM, Lu CC, Shen PC, et al. Suramin attenuates intervertebral disc degeneration by inhibiting NF-κB signalling pathway. Bone Joint Res. 2021; 10(8): 498–513, doi: 10.1302/2046-3758.108.BJR-2020-0041.R3, indexed in Pubmed: 34372688.

21. Loibl M, Wuertz-Kozak K, Vadala G, et al. Controversies in regenerative medicine: Should intervertebral disc degeneration be treated with mesenchymal stem cells? JOR Spine. 2019; 2(1): e1043, doi: 10.1002/jsp2.1043, indexed in Pubmed: 31463457.

22. Luo R, Li S, Li G, et al. FAM134B-Mediated ER-phagy upregulation attenuates ages-induced apoptosis and senescence in human nucleus pulposus cells. Oxid Med Cell Longev. 2021; 2021: 3843145, doi: 10.1155/2021/3843145, indexed in Pubmed: 34394825.

23. Luo Z, Lin J, Sun Y, et al. Bone marrow stromal cell-derived exosomes promote muscle healing following contusion through macrophage polarization. Stem Cells Dev. 2021; 30(3): 135–148, doi: 10.1089/scd.2020.0167, indexed in Pubmed: 33323007.

24. Madhu V, Guntur AR, Risbud MV. Role of autophagy in intervertebral disc and cartilage function: implications in health and disease. Matrix Biol. 2021; 100-101: 207–220, doi: 10.1016/j.matbio.2020.12.002, indexed in Pubmed: 33301899.

25. Ou X, Ying J, Bai X, et al. Activation of SIRT1 promotes cartilage differentiation and reduces apoptosis of nucleus pulposus mesenchymal stem cells via the MCP1/CCR2 axis in subjects with intervertebral disc degeneration. Int J Mol Med. 2020; 46(3): 1074–1084, doi: 10.3892/ijmm.2020.4668, indexed in Pubmed: 32705163.

26. Pfirrmann CW, Metzdorf A, Zanetti M, et al. Magnetic resonance classification of lumbar intervertebral disc degeneration. Spine (Phila Pa 1976). 2001; 26(17): 1873–1878, doi: 10.1097/00007632-200109010-00011, indexed in Pubmed: 11568697.

27. Ravanan P, Srikumar IF, Talwar P. Autophagy: the spotlight for cellular stress responses. Life Sci. 2017; 188: 53–67, doi: 10.1016/j.lfs.2017.08.029, indexed in Pubmed: 28866100.

28. Shi M, Zhao Y, Sun Y, et al. Therapeutic effect of co-culture of rat bone marrow mesenchymal stem cells and degenerated nucleus pulposus cells on intervertebral disc degeneration. Spine J. 2021; 21(9): 1567–1579, doi: 10.1016/j.spinee.2021.05.007, indexed in Pubmed: 34000376.

29. Shi PZ, Wang JW, Wang PC, et al. Urolithin a alleviates oxidative stress-induced senescence in nucleus pulposus-derived mesenchymal stem cells through SIRT1/PGC-1α pathway. World J Stem Cells. 2021; 13(12): 1928–1946, doi: 10.4252/wjsc.v13.i12.1928, indexed in Pubmed: 35069991.

30. Shi Y, Tao M, Ma X, et al. Delayed treatment with an autophagy inhibitor 3-MA alleviates the progression of hyperuricemic nephropathy. Cell Death Dis. 2020; 11(6): 467, doi: 10.1038/s41419-020-2673-z, indexed in Pubmed: 32555189.

31. Song XX, Jin LY, Li XF, et al. Substance P mediates estrogen modulation proinflammatory cytokines release in intervertebral disc. Inflammation. 2021; 44(2): 506–517, doi: 10.1007/s10753-020-01347-1, indexed in Pubmed: 32965648.

32. Tanida I, Ueno T, Kominami E. LC3 and autophagy. Methods Mol Biol. 2008; 445: 77–88, doi: 10.1007/978-1-59745-157-4_4, indexed in Pubmed: 18425443.

33. van den Berg R, Jongbloed EM, Kuchuk NO, et al. Association between self-reported spinal morning stiffness and radiographic evidence of lumbar disk degeneration in participants of the Cohort Hip and Cohort Knee (CHECK) study. Phys Ther. 2020; 100(2): 255–267, doi: 10.1093/ptj/pzz170, indexed in Pubmed: 31742363.

34. Wang Y, Che M, Xin J, et al. The role of IL-1β and TNF-α in intervertebral disc degeneration. Biomed Pharmacother. 2020; 131: 110660, doi: 10.1016/j.biopha.2020.110660, indexed in Pubmed: 32853910.

35. Webber JP, Spary LK, Sanders AJ, et al. Differentiation of tumour-promoting stromal myofibroblasts by cancer exosomes. Oncogene. 2015; 34(3): 290–302, doi: 10.1038/onc.2013.560, indexed in Pubmed: 24441045.

36. Wu X, Liao Z, Wang K, et al. Targeting the IL-1β/IL-1Ra pathways for the aggregation of human islet amyloid polypeptide in an ex vivo organ culture system of the intervertebral disc. Exp Mol Med. 2019; 51(9): 1–16, doi: 10.1038/s12276-019-0310-7, indexed in Pubmed: 31554783.

37. Xiang Q, Cheng Z, Wang J, et al. Allicin attenuated advanced oxidation protein product-induced oxidative stress and mitochondrial apoptosis in human nucleus pulposus cells. Oxid Med Cell Longev. 2020; 2020: 6685043, doi: 10.1155/2020/6685043, indexed in Pubmed: 33381267.

38. Yin H, Wang K, Das A, et al. The REDD1/TXNIP complex accelerates oxidative stress-induced apoptosis of nucleus pulposus cells through the mitochondrial pathway. Oxid Med Cell Longev. 2021; 2021: 7397516, doi: 10.1155/2021/7397516, indexed in Pubmed: 34603601.

39. Zhao F, Guo Z, Hou F, et al. Magnoflorine alleviates "M1" polarized macrophage-induced intervertebral disc degeneration through repressing the HMGB1/Myd88/NF-κB pathway and NLRP3 inflammasome. Front Pharmacol. 2021; 12: 701087, doi: 10.3389/fphar.2021.701087, indexed in Pubmed: 34366853.

40. Zhao S, Liu Y, Pu Z. Bone marrow mesenchymal stem cell-derived exosomes attenuate D-GaIN/LPS-induced hepatocyte apoptosis by activating autophagy in vitro. Drug Des Devel Ther. 2019: 2887–2897, doi: 10.2147/DDDT.S220190, indexed in Pubmed: 31695322.

41. Zhu G, Yang X, Peng C, et al. Exosomal miR-532-5p from bone marrow mesenchymal stem cells reduce intervertebral disc degeneration by targeting RASSF5. Exp Cell Res. 2020; 393(2): 112109, doi: 10.1016/j.yexcr.2020.112109, indexed in Pubmed: 32464126.

42. Zhu L, Shi Y, Liu L, et al. Mesenchymal stem cells-derived exosomes ameliorate nucleus pulposus cells apoptosis via delivering miR-142-3p: therapeutic potential for intervertebral disc degenerative diseases. Cell Cycle. 2020; 19(14): 1727–1739, doi: 10.1080/15384101.2020.1769301, indexed in Pubmed: 32635856.

Autophagy exerts a protective role in cervical spinal cord injury by microglia inhibition through the nuclear factor kappa-B pathway

Baicheng Yang[1]*, Xinming Yang[2]*

[1]Hebei North University, Zhangjiakou, Hebei, China
[2]Department of Orthopaedics, the First Affiliated Hospital of Hebei North University, Zhangjiakou, Hebei, China

Background: Spinal cord injury (SCI) is a serious trauma to the central nervous system. M1/M2 microglial polarization as well as the following neuroinflammatory response are crucial factors in SCI. Autophagy plays an important role in SCI, but its neuroprotective or neurodegenerative role remains controversial.
Materials and methods: Here, we majorly examined the properties of autophagy in SCI and uncovered the regulatory relationship between autophagy and microglial polarization in SCI.
Results: In our study, the Basso-Beattie-Bresnahan (BBB) score was declined in SCI. The cervical contusion SCI stimulated a sustaining neuropathic pain-linked phenotype characterized by thermal hyperalgesia as well as mechanical allodynia. It was revealed the structural damage to the spinal cord in SCI. Besides, the expression of microglia markers as well as inflammatory factor were promoted in SCI. Cervical contusion SCI induced autophagy inhibition and nuclear factor kappa-B (NF-κB) activation in mice. More importantly, enhanced autophagy induced by rapamycin suppressed the NF-κB pathway and alleviated cervical contusion SCI-induced neurological function damage in mice. Additionally, rapamycin promoted microglia M2 polarization and improved microglia-mediated inflammatory response.
Conclusions: In conclusion, our study demonstrated that autophagy played a protective role in cervical SCI by promoting microglia polarization toward M2 through the NF-κB pathway. Our study may provide a novel sight for SCI treatment. (Folia Morphol 2024; 83, 1: 113–124)

Keywords: spinal cord injury, microglia activation, NF-κB, autophagy

INTRODUCTION

Spinal cord injury (SCI) belongs to a serious disease resulting in specific neurological symptoms depending on the degree of injury, with high morbidity and mortality [4]. About 60% of SCI involves the cervical spinal cord, resulting in complete or incomplete quadriplegia, and the mortality rate is higher than that of thoracolumbar injuries [10]. Primary injury of the spinal cord is linked to the destruction of axons along with neurons, whereas secondary injury is resulted by neuroinflammation and can result in morphologic oedema, cavitation, as well as reactive gliosis [17]. Up to now, long-term treatment mainly targets the symptoms of secondary complications containing

severe neuroinflammation as well as poor adaptive plasticity after secondary injury [27]. Nevertheless, due to the existence of blood-brain barrier, few therapeutic drugs or other interventions have been proven to suppress the development of secondary injury after SCI and effectively facilitate functional recovery [34].

To the best of our knowledge, SCI induces inflammatory responses that include the release of cytokines and the activation of microglia [7]. Microglia belongs to a main resident cell in the central nervous system, and activates and modulates neuroinflammation after SCI [39]. Microglia are activated into two polarization states: the pro-inflammatory phenotype (M1) as well as the anti-inflammatory phenotype (M2) [25]. Microglia plays dual roles in neuroinflammation together with neurogenesis, which depends on its polarization: the classic M1 phenotype secrets proinflammatory cytokines that are detrimental to neurogenesis. The alternative type M2 secretes anti-inflammatory cytokines and is beneficial to neurogenesis [26]. Therefore, in the treatment of SCI, efforts should be made to explore therapeutic methods to convert microglia from M1 to M2 type and to inhibit harmful excessive neuroinflammation.

The neuroinflammatory responses stimulated by activation of microglia through the nuclear factor kappa-B (NF-κB) pathway is a key factor in SCI [2]. After necrotic or damaged cells are injured, the NF-κB signalling pathway is released, which activates microglia to secrete inflammatory cytokines [8]. NF-κB activation is started by IκB kinase, degrading IκB protein in the cytoplasm and causing release and nuclear translocation of NF-κB [29].

Autophagy, a catabolic process that protects cells from various stresses by degrading dysfunctional organelles and proteins, has been reported to be involved in SCI recovery [36]. Increasing evidence has suggested that autophagy exerts neuroprotection in SCI [30]. According to the location as well as severity of SCI, autophagic flow may increase or decrease. Thus, it remains unclear whether autophagy is beneficial or detrimental after injury [28]. However, restoring and increasing autophagic flow can improve functional recovery after injury by enhancing cell survival, which mirrored that autophagy is a possible therapeutic target for SCI treatment [44].

In this research, a mouse model of cervical spinal cord injury was established to explore the role of autophagy in cervical spinal cord injury and the relationship between autophagy and microglia activation.

MATERIALS AND METHODS

Establishment of the mouse model of cervical SCI

Animal procedures were approved by The First Affiliated Hospital of Hebei North University and this study was approved by the Ethics Committee of The First Affiliated Hospital of Hebei North University. To probe the property of autophagy in SCI and uncover the regulatory relationship between autophagy and microglial polarization in SCI, 10 male C57BL/6 mice (26–30 g) frequently used in the construction of SCI models [11, 14, 21] were anesthetized with 1% isoflurane. As described before, contusion SCI was performed (n = 5) [35]. C5/C6 right spinal cord contusion was generated using an Infinite Horizons impactor with 0.7 mm impactor tip, 40 nephron force, and 2-second dwell time. The sham group (n = 5), which underwent laminectomy only, underwent the same procedure but did not develop contusion. To explore the regulatory mechanism between autophagy and the polarization of microglia in SCI, 10 male C57BL/6 mice (26–30 g) were subjected to either rapamycin (RAP) administration, mice were intraperitoneally injected with RAP (1.5 mg/kg every day) after injury (SCI+RAP, n = 5) or sham surgery (sham+RAP, n = 5) [24]. All the mice were administrated by RAP for 6 weeks.

Behavioural testing

The recovery of general motor function was assessed by the Basso-Beattie-Bresnahan (BBB) scale, in accordance with the previous reports [40]. BBB scores ranged from 0 to 21. A total score of 0 suggested a serious neurological deficit and a total score of 21 represented normal function.

Assessment of mechanical allodynia

The von Frey filament test was implemented to measure mechanical allodynia [3]. Mice were kept in transparent boxes on a raised platform of barbed wire. The tactile stimulation device with a thin wire was placed below the midplantar surface of the left hind paw. With an automatic increase in force, the filaments are lifted to the plantar surface. Maximal force at which the animal retracted its paw was recorded. The 5 g dominant force within 20 s was used as the cut-off point.

Assessment of thermal hyperalgesia

The Hargreaves test (Ugo Basile, Italy) was implemented to measure thermal hyperalgesia [38]. Mice were permitted to acclimate in a transparent box

placed on a raised glass platform. A mobile infrared heat source was placed below the midsurface of the left hind foot of the mice. The time for mice to retract the paw against the heat source was recorded. The cutoff point was set to 20 s.

Tissue processing and haematoxylin and eosin staining

Six weeks after SCI, mice were sacrificed by given an overdose of ketamine (100 mg/kg) together with xylazine (5 mg/kg). 0.9% saline was then transcardially perfused, followed by 4% paraformaldehyde. The spinal cord was dissected to a thickness of 30 μm. Tissue was fixed and dehydration, and then embedded in paraffin wax. Finally, slices were cut to obtain paraffin sections (thickness: 4 μm). The paraffin sections were stained with haematoxylin (Solarbio, Beijing, China) solution for 5 min, and then dyed with Eosin (Solarbio, Beijing, China) for another 2 min. An optical microscope was utilized to observe the changes at the injury epicentre.

RT-qPCR

To evaluate the expression levels of pro-inflammatory cytokines including tumour necrosis factor alpha (TNF-α), interleukin (IL)-1β, and IL-6 and microglia markers including Iba-1, CD16 (M1 markers) and CD206 (M2 marker) in the SCI, total RNA from tissues was extracted with TRIzol reagent (Ambion, USA), Then, total RNA was implemented for reverse transcription to synthesize cDNA (Promega, USA), followed by reverse transcription quantitative polymerase chain reaction (RT-qPCR) using SYBR Green (Promega, USA). Gene expression was normalized to β-actin. Each sample was measured in triplicate using the $2^{-\Delta\Delta Ct}$ method. The following primers were used as follows:
— Iba-1: forward, 5'-ATGAGCCAGAGCAAGGATT-3' and reverse, 5'-GCATTCGCTTCAAGGACA-3';
— CD16: forward, 5'-CCACGGATGACCTGTGCTC-3' and reverse, 5'-TTTATGGTCCTTCCAGTCTCTTG-3';
— CD206: forward, 5'-CCACGGATGACCTGTGCTC-3' and reverse, 5'-CCACGGATGACCTGTGCTC-3';
— TNF-α: forward, 5'-ATGAGCCAGAGCAAGGATT-3' and reverse, 5'-GCATTCGCTTCAAGGACA-3';
— IL-6: forward, 5'-TGCCTTCTTGGGACTGAT-3' and reverse, 5'-TTGCCATTGCACAACTCT-3';
— IL-1β: forward, 5'-TGTGATGTTCCCATTAGAC-3' and reverse, 5'-AATACCACTTGTTGGCTTA-3';
— β-actin: forward, 5'-GTGACGTTGACATCCG-TAAAGA-3' and reverse, 5'-GCCGGACTCATCG-TACTCC-3'.

Western blot

Proteins were extracted from spinal cords tissues using the lysis buffer (Beyotime, Shanghai). The samples were separated using 10% SDS-PAGE and transferred onto nitrocellulose membranes (Life sciences, USA). The membranes were incubated with different primary antibodies for overnight at 4°C after blocking in 5% skim milk. Primary antibodies included Iba-1 (ab178846, 1/500), CD16 (ab246222, 1/1000), CD206 (ab252921, 1/1000), TNF-α (ab183218, 1/1000), IL-6 (ab233706, 1/1000), IL-1β (ab254360, 1/1000), LC3 (ab192890, 1/2000), Beclin-1 (ab207612, 1/2000), p62 (ab109012, 1/10000), p65 (ab32536, 1/1000), IKB-α (ab32518, 1/1000), p50 (ab32360, 1/1000), and β-actin (ab8227, 1/1000) were provided by Abcam. After washing, the blots were then treated with the secondary antibodies (Abcam, ab6728, 1/2000), followed by detection using the ECL detection kit (Bio-Rad, USA).

Immunofluorescence staining

Embedded sections (4-μm-thick) were deparaffinized with xylene and rehydrated in a graded series of alcohol before antigen repair. The sections were then hatched overnight at 4°C with primary antibody anti-LC3B (Abcam, ab63817, 1 μg/mL), followed by treating with secondary antibodies (Abcam, ab150077, 1:200) after washing. Next, the sections were labelled with Alexa Red fluorescent dye for 1 h, and then dyed with a fluorescent dye of DAPI to evidence the nucleus, followed by visualization under a fluorescence microscope.

NF-κB DNA-binding activity assay

NF-κB p65 DNA-binding activity was tested by a transcription factor binding assay colorimetric ELISA kit (Cayman Chemical, USA). The absorbance at 450 nm was determined by a microplate reader.

Ethics approval and consent to participate

Animal procedures were approved by the First Affiliated Hospital of Hebei North University and this study was approved by the Ethics Committee of the First Affiliated Hospital of Hebei North University.

Statistical analysis

The data was analysed with SPSS 19.0 software (SPSS Inc., Chicago, IL, USA). Data are expressed as the mean ± standard deviation. Comparisons were assessed by the unpaired Student's t test or one-way ANOVA. $P < 0.05$ was statistically significant.
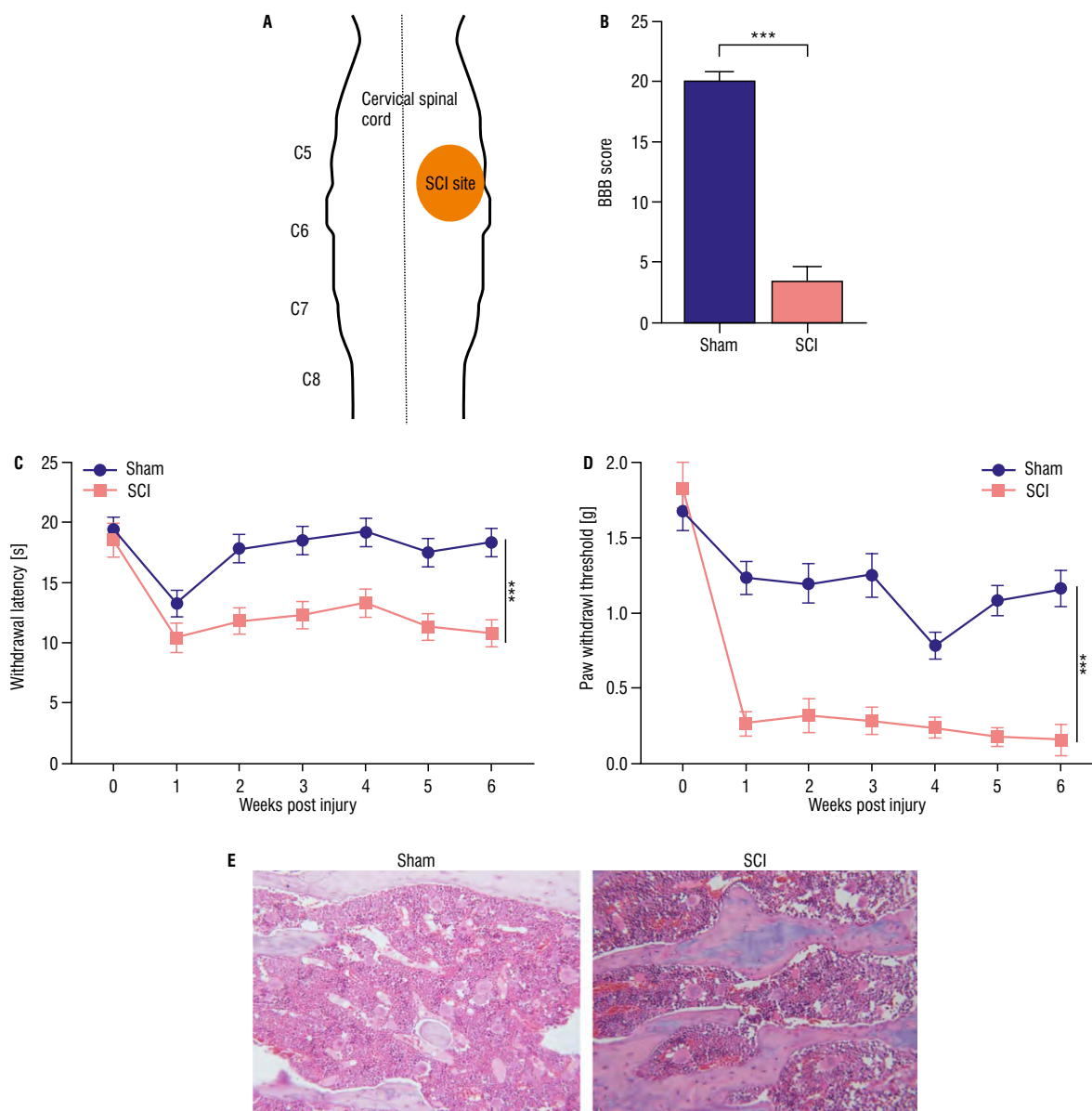
Figure 1. Successful establishment of the mouse model of cervical spinal cord injury (SCI); **A.** A cross-sectional view of the spinal cord in the region of analysis; **B.** Basso-Beattie-Bresnahan (BBB) score of mice in the sham group and SCI group, respectively; **C, D.** Thermal hyperalgesia and mechanical allodynia in the plantar surface of each forepaw in the sham group and SCI group were measured by Hargreaves test and von Frey filament test, respectively; **E.** Haematoxylin and eosin staining detected the histological changes at the injury epicentre in the sham and SCI groups; ***p < 0.001.

RESULTS

Successful establishment of the mouse model of cervical SCI

For the quantitative histological analysis carried out in the cervical spinal cord, the tissue sections caudal to the epicentre of the C5/C6 contusion were adopted. This area for histological assessment was accordance with the C6/C7 spinal cord, which was the site of the central projections of primary afferent sensory neurons innervating the plantar surface of the forepaw (Fig. 1A). The BBB score was implemented to evaluate the recovery of general motor function after SCI. The mice in the sham obtained the maximum BBB score (21 points). However, the BBB score was declined in SCI groups, indicating the neurological function of mice was severely impaired immediately after the SCI (Fig. 1B). Through Hargreaves test and von Frey filament test to assess thermal sensitivity and mechanical sensitivity in the plantar surface of each forepaw, respectively, we discovered that cervical contusion SCI at the C5/C6 spinal cord level stimulated a sustaining neuropathic pain-linked phenotype characterized by
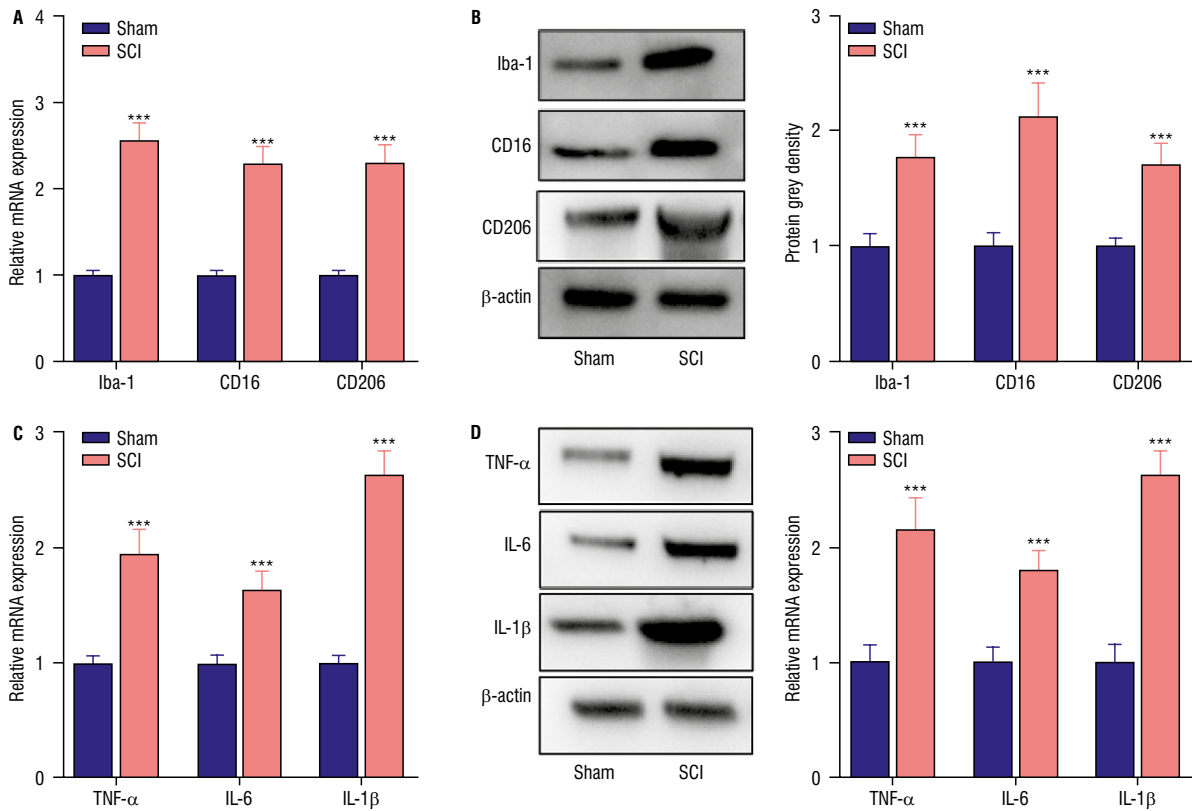
Figure 2. Microglia activation and inflammatory response in spinal cord of mice with cervical contusion spinal cord injury (SCI); **A, B.** Expression of Iba-1, CD16 and CD206 in the sham and SCI groups was detected by reverse transcription quantitative polymerase chain reaction (RT-qPCR) and western blot; **C, D.** Expression of tumour necrosis factor alpha (TNF-α), interleukin (IL)-6 and IL-1β in the sham and SCI groups was detected by RT-qPCR and western blot; ***p < 0.001.

thermal hyperalgesia (Fig. 1C) and mechanical allodynia (Fig. 1D). Haematoxylin and eosin staining demonstrated histological changes at the injury epicentre. The spinal cord was intact in the sham group. The SCI group showed the structural damage to the spinal cord, including neuronal nuclear fragmentation, pyknosis, neurocilia destruction, extracellular matrix degradation, interstitial oedema, cytoplasm reduction, as well as cavity formation (Fig. 1E).

Microglia activation and inflammatory response in spinal cord of mice with cervical contusion SCI

Based on qRT-PCR and western blot analysis, we observed that relative to the sham group, the mRNA and protein levels of microglia markers (Iba-1, CD16 and CD206), as well as inflammatory factor (TNF-α, IL-6 and IL-1β) were increased in the SCI group (Fig. 2A–D).

Cervical contusion SCI induces autophagy inhibition and NF-κB activation in mice

Consistently, in our study, the immunofluorescence staining results for LC3 expression showed

that the number of LC3 puncta was deceased in the SCI group compared with the sham group (Fig. 3A). Besides, western blot analysis revealed that LC3 II and Beclin-1 protein levels were declined, whereas p62 protein level was elevated in the SCI group relative to the sham group (Fig. 3B). Herein, we found that the activity of NF-κB p65 DNA-binding was enhanced in the SCI group relative to the sham group (Fig. 3C). At the same time, western blot analysis revealed that p65, IKB-α and p50 protein levels were significantly elevated in the SCI group relative to the sham group (Fig. 3D), suggesting that cervical contusion SCI could activate the NF-κB pathway.

Enhanced autophagy suppresses the NF-κB pathway in mice with cervical contusion SCI

Based on above results, we concluded that cervical contusion SCI induced autophagy inhibition and NF-κB activation in mice. Thus, a hypothesis that autophagy activation could regulate the NF-κB pathway in mice with cervical contusion SCI of our study was made. To verify our hypothesis, rapamycin (RAP) was
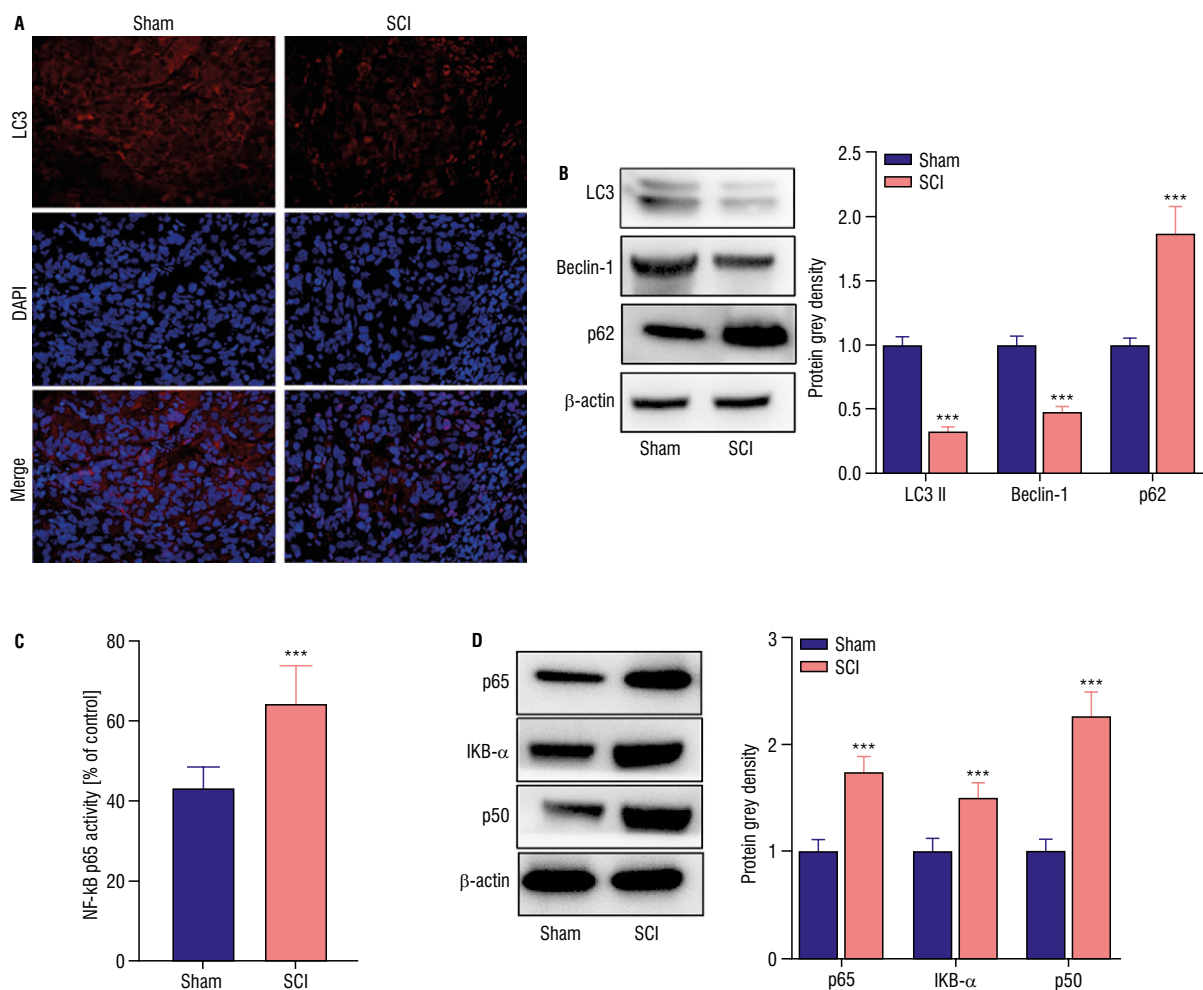
Figure 3. Cervical contusion spinal cord injury (SCI) induces autophagy inhibition and nuclear factor kappa-B (NF-κB) activation in mice; **A.** Immunofluorescence staining results for LC3 expression in the sham and SCI groups; **B.** Protein levels of LC3, Beclin-1 and p62 in the sham and SCI groups were examined by western blot; **C.** A transcription factor binding assay colorimetric ELISA kit was used to detect NF-κB p65 DNA-binding activity in the sham and SCI groups; **D.** Protein levels of p65, IKB-α and p50 in the sham and SCI groups were tested by western blot; ***p < 0.001.

firstly used to intraperitoneally inject into mice for 6 weeks after SCI. The outcomes displayed that RAP could obviously enhance the number of LC3 puncta in both sham and SCI groups, and the number of LC3 puncta in the SCI+RAP group was less than that in the sham+RAP group (Fig. 4A). Then, we detected the impacts of RAP on the transcriptional activity of NF-κB. We observed that the enhanced activity of NF-κB p65 DNA-binding caused by SCI was abolished after RAP treatment (Fig. 4B). Similarly, the elevated protein levels of p65, IKB-α and p50 in the SCI group were lessened after injection of RAP (Fig. 4C), which implied that activated autophagy could suppress the NF-κB pathway in mice with cervical contusion SCI.

RAP alleviates cervical contusion SCI-induced neurological function damage in mice

The effects of autophagy on cervical contusion SCI-induced neurological function damage in mice were further investigated. As shown in Figure 5A, the reduced BBB score in the SCI group was partly enhanced after RAP treatment. Besides, we found that SCI-caused the obvious decrease in both mechanical withdrawal thresholds as well as thermal withdrawal latencies of paw was partially reversed after RAP induction (Fig. 5B, C). Moreover, haematoxylin and eosin staining results demonstrated the structural damage to the spinal cord in the SCI group was partly improved after RAP treatment (Fig. 5D).
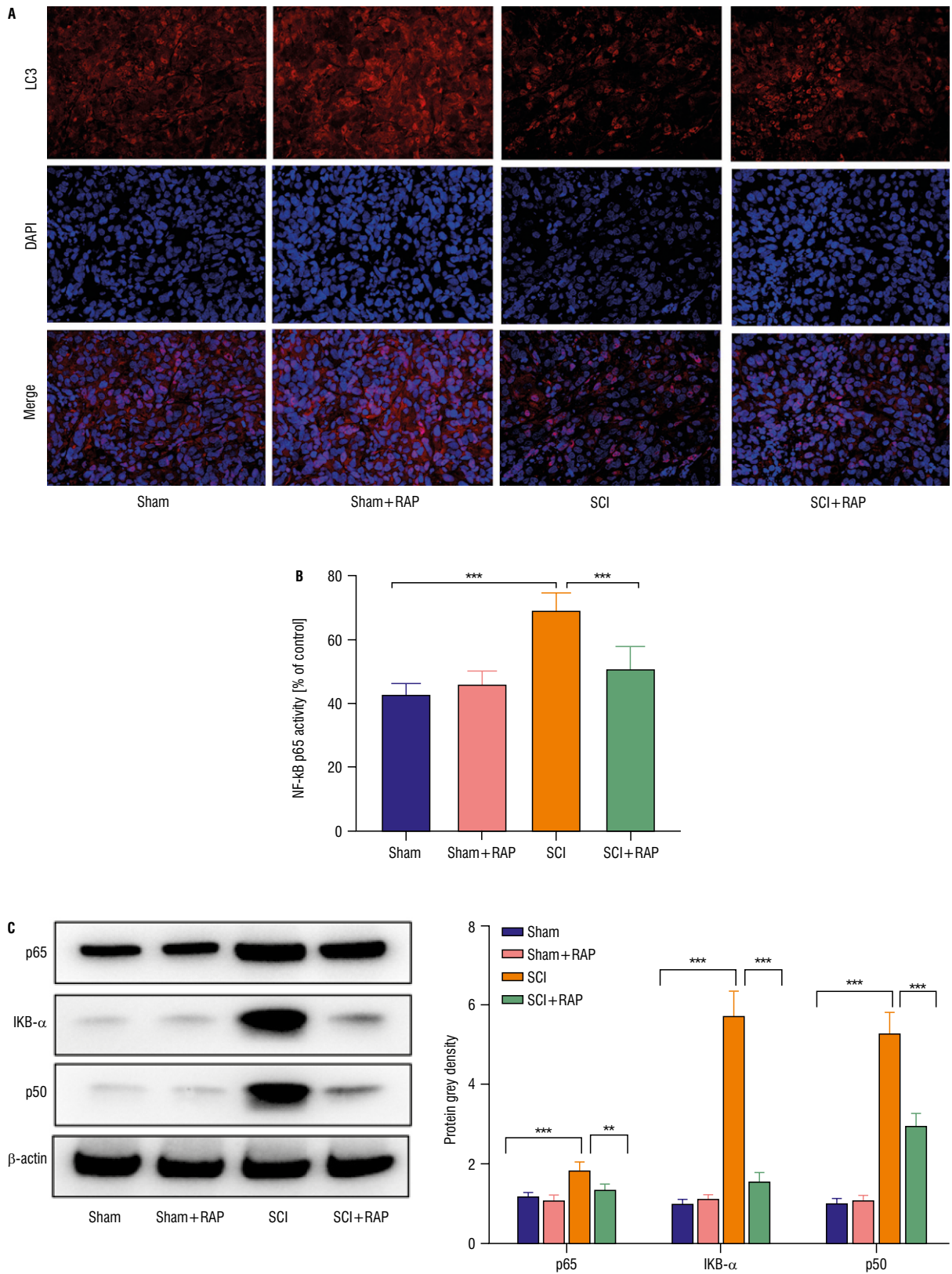
Figure 4. Enhanced autophagy suppresses the nuclear factor kappa-B (NF-κB) pathway in mice with cervical contusion spinal cord injury (SCI); **A.** Immunofluorescence staining results for LC3 expression in the sham, sham+rapamycin (RAP), SCI and SCI+RAP groups; **B.** A transcription factor binding assay colorimetric ELISA kit was used to detect NF-κB p65 DNA-binding activity in the sham, sham+RAP, SCI and SCI+RAP groups; **C.** Protein levels of p65, IKB-α and p50 in the sham, sham+RAP, SCI and SCI+RAP groups were tested by western blot; ***p < 0.001.
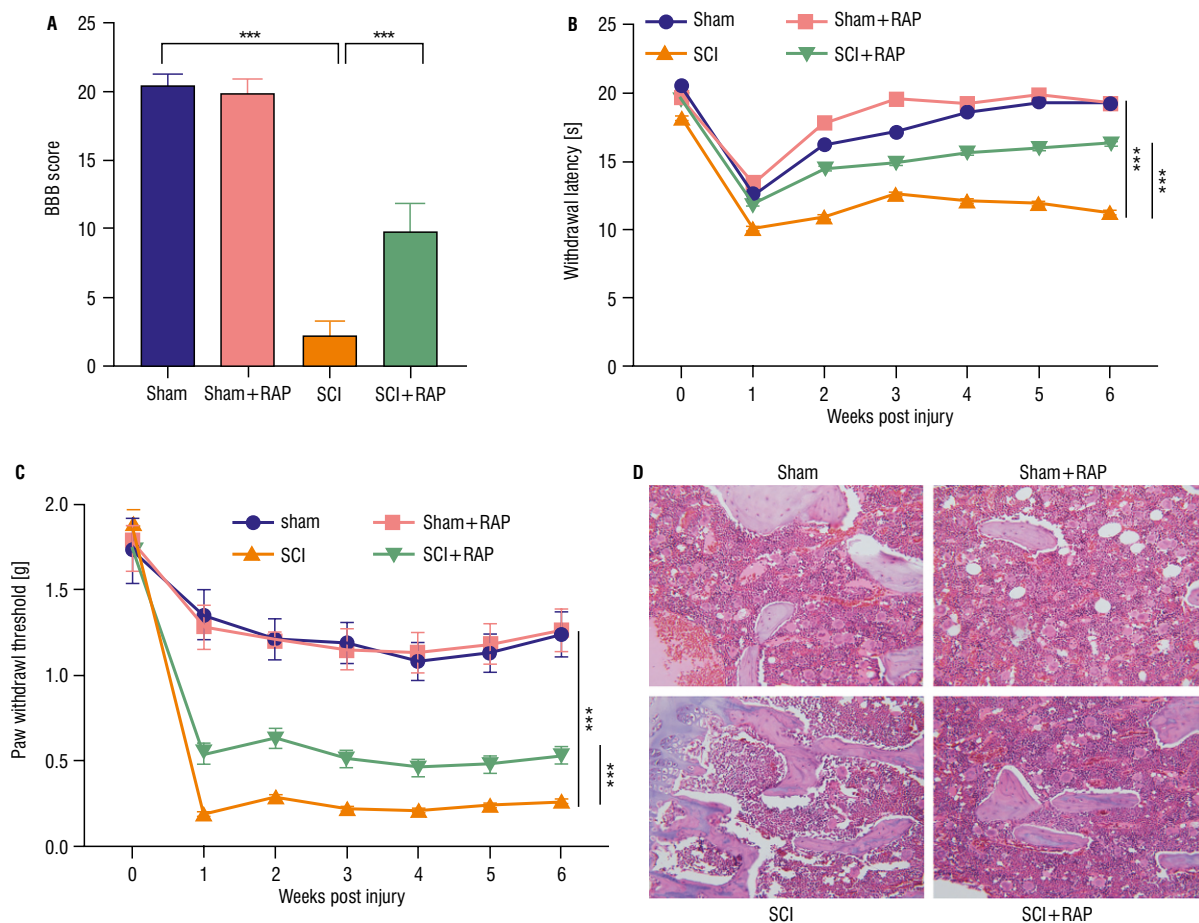
Figure 5. Rapamycin (RAP) alleviates cervical contusion spinal cord injury (SCI)-induced neurological function damage in mice; **A.** Basso-
-Beattie-Bresnahan (BBB) score of mice in the sham, sham+RAP, SCI and SCI+RAP groups, respectively; **B, C.** Thermal hyperalgesia and
mechanical allodynia in the plantar surface of each forepaw in the sham, sham+RAP, SCI and SCI+RAP groups were measured by Hargreaves
test and von Frey filament test, respectively; **D.** Haematoxylin and eosin staining detected the histological changes at the injury epicentre in
the sham, sham+RAP, SCI and SCI+RAP groups; ***p < 0.001.

RAP facilitates microglia M2 polarization and improves microglia-mediated inflammatory reaction

Here, the role of autophagy in microglia polarization and inflammatory response was assessed. Based on western blot analysis, we discovered that the elevated protein levels of M1 markers (Iba-1 and CD16) caused by SCI were offset after RAP treatment. However, the increased protein level of M2 marker (CD206) caused by SCI was further elevated after RAP treatment (Fig. 6A), indicating that RAP promoted microglia polarization toward M2. Accordingly, we discovered that the increased protein levels of TNF-α, IL-6 as well as IL-1β in the SCI group were counteracted after RAP treatment (Fig. 6B).

DISCUSSION

Spinal cord injury is a global problem and a heavy burden for society and families. In addition, the treat-
ment of SCI has always been a challenge [1]. Many biochemical events happen after SCI-mediated secondary injury, and microglia infiltration plays an important role in this process. The proinflammatory and anti-inflammatory potentials of microglia play a key role throughout the process of secondary injury [19]. Kwiecien et al. [16] elucidated a number of fundamental mechanisms in pathogenesis of SCI, and they confirmed the increased levels of TNF-α, IL-1β, interferon-gamma and other proinflammatory cytokines, chemokines and proteases decrease and anti-inflammatory cytokines increase in the late stage of SCI. Therefore, our study established the mouse model of cervical SCI and explored the influences of SCI on microglia activation as well as inflammatory factors. The results demonstrated the activated microglia and increased inflammatory response in spinal cord of mice with cervical contusion SCI, which was consistent with previous literatures [20].
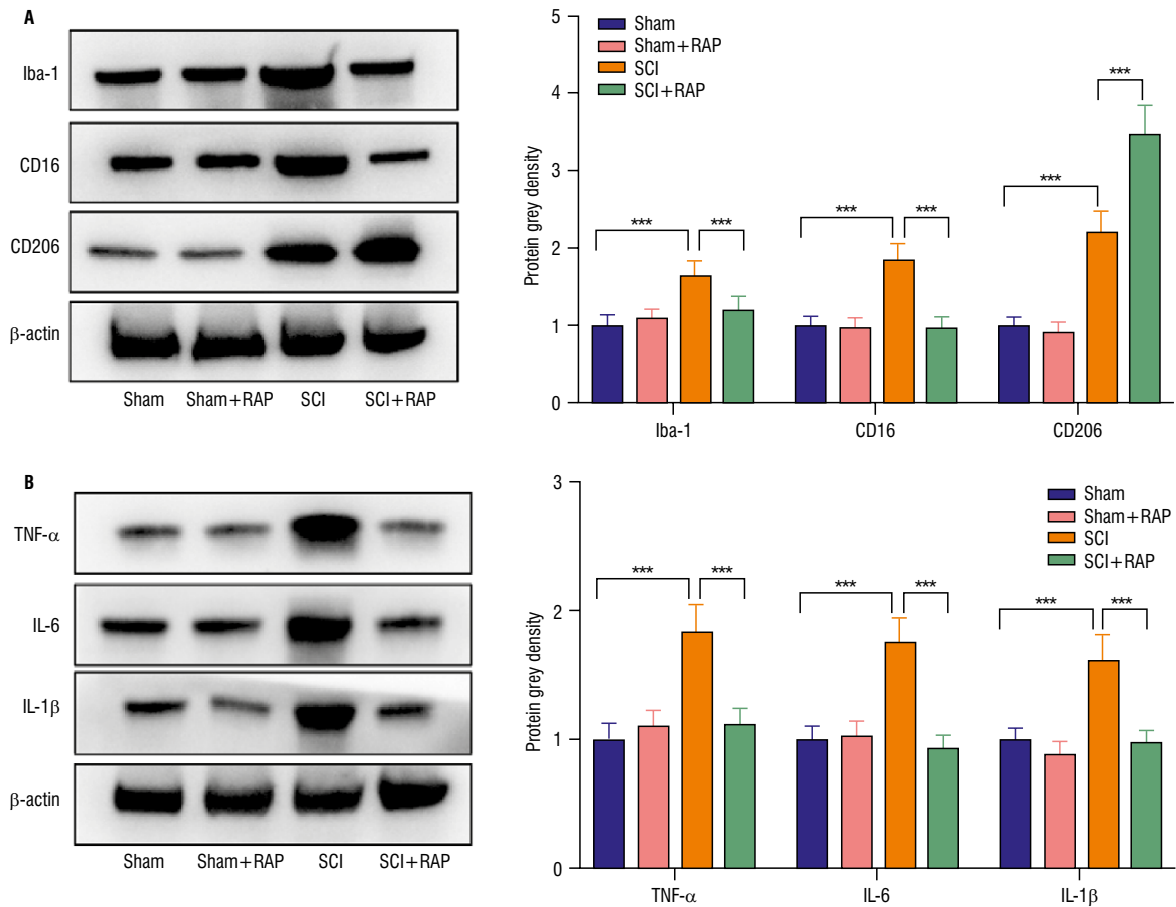
Figure 6. Rapamycin (RAP) promotes microglia polarization toward M2 and alleviates microglia-mediated inflammatory response; **A.** Expression of Iba-1, CD16 and CD206 in the sham, sham+RAP, spinal cord injury (SCI) and SCI+RAP groups was detected by western blot; **B.** Expression of tumour necrosis factor alpha (TNF-α), interleukin (IL)-6 and IL-1β in the sham, sham+RAP, SCI and SCI+RAP groups was detected by western blot; ***p < 0.001.

Autophagy is a lysosomal-dependent degradation pathway of intracellular proteins, which has a crucial part in human diseases [18]. Pathological situations or cellular stress can stimulate autophagy to be an adaptive as well as protective mechanism [15]. Reports have proved autophagy can mitigate cell damage in rat models of traumatic brain injury [41]. Furthermore, autophagy has been suggested to have a protective role in traumatic SCI [43]. Autophagy is a conserved activity controlling protein degradation and the clearance of damaged organelles. Regarding the autophagy-related signalling, LC3 is the marker for the formation of autophagosome, and the level of p62 protein reflects the activity of autophagic flux [13]. Beclin-1 is also a critical molecular participating in autophagy [42]. In our study, we discovered that the number of LC3 puncta was deceased in SCI. Moreover, western blot analysis demonstrated the protein levels of LC3 II and Beclin-1 were declined, whereas p62 protein level was

elevated in SCI. All these findings in our study supported the protective role of autophagy in SCI, which was in accordance with previous reports [32].

NF-κB is a core transcription factor of inflammatory response, and exerts a crucial potential in microglial activation [22]. Additionally, NF-κB signalling is implicated in the inflammatory response during SCI [23]. Former studies have also verified a modulatory cross-talk between autophagy and NF-κB signalling pathway in SCI, which demonstrates that activation of autophagy can hinder the NF-κB signalling pathway [9]. The most abundant form of NF-κB is a heterodimer of p50 and p65 subunits [31]. Consistent with the above studies, our research showed that the activity of NF-κB p65 DNA-binding was enhanced in SCI. Meanwhile, western blot analysis showed the protein levels of p65, IKB-α (NF-κB inhibitor alpha) and p50 were elevated in SCI, suggesting that cervical contusion SCI could activate the NF-κB pathway. More importantly, our

study proved that activated autophagy by RAP, a well-known autophagy activator [6], could repress the NF-κB signalling and alleviate cervical contusion SCI-induced neurological function damage in mice, which implied that autophagy is conductive to the context of SCI.

Increasing evidence has manifested that microglial activation in the central nervous system can be categorized into M1 phenotype and M2 phenotype [37]. Microglia M2 polarization is conducive to local anti-inflammatory response after SCI [5]. Besides, recent researches have shown that autophagy modulates microglia polarization to affect neurological diseases [12]. As mentioned by Shi et al. [33], granule protein precursor has an anti-inflammatory role by enhancing autophagy and inducing M2 microglial polarization, which relieves neurological function after acute SCI. In line with these evidences, our study indicated that activated autophagy by RAP promoted microglia M2 polarization toward and mitigated microglia-mediated inflammatory response. However, there are still some limitations in the current research. For example, we should conduct sufficient clinical observations to further consolidate the clinical significance of the article. In addition, the number of mice constructing SCI models is relatively small, and there are fewer independent duplicate data. In future research, we will further address these issues, making the data more sufficient and the results more reliable.

CONCLUSIONS

In conclusion, our study demonstrated that autophagy played a protective role in cervical SCI by promoting microglia M2 polarization through the NF-κB pathway. Our study may be provided a novel sight for SCI treatment.

Funding

Conflict of interest: None declared

REFERENCES

1. Anjum A, Yazid MD, Fauzi Daud M, et al. Spinal cord injury: pathophysiology, multimolecular interactions, and underlying recovery mechanisms. Int J Mol Sci. 2020; 21(20), doi: 10.3390/ijms21207533, indexed in Pubmed: 33066029.
2. Chen S, Ye J, Chen X, et al. Valproic acid attenuates traumatic spinal cord injury-induced inflammation via STAT1 and NF-κB pathway dependent of HDAC3. J Neuroinflammation. 2018; 15(1): 150, doi: 10.1186/s12974-018-1193-6, indexed in Pubmed: 29776446.
3. Ding HL, Chen JL, Su S, et al. BDNF promotes activation of astrocytes and microglia contributing to neuroinflammation and mechanical allodynia in cyclophosphamide-induced cystitis. J Neuroinflammation. 2020; 17(19): e1166, doi: 10.1016/s2666-1683(20)33365-6.
4. Eli I, Lerner DP, Ghogawala Z. Acute traumatic spinal cord injury. Neurol Clin. 2021; 39(2): 471–488, doi: 10.1016/j.ncl.2021.02.004, indexed in Pubmed: 33896529.
5. Fan L, Liu C, Chen X, et al. Exosomes-Loaded electroconductive hydrogel synergistically promotes tissue repair after spinal cord injury via immunoregulation and enhancement of myelinated axon growth. Adv Sci (Weinh). 2022; 9(13): e2105586, doi: 10.1002/advs.202105586, indexed in Pubmed: 35253394.
6. Gao G, Chen W, Yan M, et al. Rapamycin regulates the balance between cardiomyocyte apoptosis and autophagy in chronic heart failure by inhibiting mTOR signaling. Int J Mol Med. 2020; 45(1): 195–209, doi: 10.3892/ijmm.2019.4407, indexed in Pubmed: 31746373.
7. Gao J, Sun Z, Xiao Z, et al. Dexmedetomidine modulates neuroinflammation and improves outcome via alpha2-adrenergic receptor signaling after rat spinal cord injury. Br J Anaesth. 2019; 123(6): 827–838, doi: 10.1016/j.bja.2019.08.026, indexed in Pubmed: 31623841.
8. Gaojian T, Dingfei Q, Linwei Li, et al. Parthenolide promotes the repair of spinal cord injury by modulating M1/M2 polarization via the NF-κB and STAT 1/3 signaling pathway. Cell Death Discov. 2020; 6(1): 97, doi: 10.1038/s41420-020-00333-8, indexed in Pubmed: 33083018.
9. Gholaminejhad M, Jameie SB, Abdi M, et al. All-trans retinoic acid-preconditioned mesenchymal stem cells improve motor function and alleviate tissue damage after spinal cord injury by inhibition of Hmgb1/Nf-Kb/Nlrp3 pathway through autophagy activation. J Mol Neurosci. 2022; 72(5): 947–962, doi: 10.1007/s12031-022-01977-0, indexed in Pubmed: 35147911.
10. Gonzalez-Rothi EJ, Lee KZ. Intermittent hypoxia and respiratory recovery in pre-clinical rodent models of incomplete cervical spinal cord injury. Exp Neurol. 2021; 342: 113751, doi: 10.1016/j.expneurol.2021.113751, indexed in Pubmed: 33974878.
11. Hou Y, Luan J, Deng T, et al. Tauroursodeoxycholic acid alleviates secondary injury in spinal cord injury mice through reducing oxidative stress, apoptosis, and inflammatory response. J Neuroinflammation. 2021; 18: 216, doi: 10.21203/rs.3.rs-361252/v1.
12. Ji J, Xue TF, Guo XD, et al. Antagonizing peroxisome proliferator-activated receptor γ facilitates M1-to-M2 shift of microglia by enhancing autophagy via the LKB1-AMPK signaling pathway. Aging Cell. 2018; 17: e12774, doi: 10.1111/acel.12774, indexed in Pubmed: 29740932.
13. Jiang P, Mizushima N. LC3- and p62-based biochemical methods for the analysis of autophagy progression in mammalian cells. Methods. 2015; 75: 13–18, doi:

10.1016/j.ymeth.2014.11.021, indexed in Pubmed: 25484342.

14. Khan NZ, Cao T, He J, et al. Spinal cord injury alters microRNA and CD81+ exosome levels in plasma extracellular nanoparticles with neuroinflammatory potential. Brain Behav Immun. 2021; 92: 165–183, doi: 10.1016/j.bbi.2020.12.007, indexed in Pubmed: 33307173.

15. Klionsky D, Petroni G, Amaravadi R, et al. Autophagy in major human diseases. EMBO J. 2021; 40(19), doi: 10.15252/embj.2021108863.

16. Kwiecien JM, Dabrowski W, Dąbrowska-Bouta B, et al. Prolonged inflammation leads to ongoing damage after spinal cord injury. PLoS One. 2020; 15(3): e0226584, doi: 10.1371/journal.pone.0226584, indexed in Pubmed: 32191733.

17. Lee SY, Schmit BD, Kurpad SN, et al. Acute magnetic resonance imaging predictors of chronic motor function and tissue sparing in rat cervical spinal cord injury. J Neurotrauma. 2022; 39(23-24): 1727–1740, doi: 10.1089/neu.2022.0034, indexed in Pubmed: 35708112.

18. Levine B, Kroemer G. Biological functions of autophagy genes: a disease perspective. Cell. 2019; 176(1-2): 11–42, doi: 10.1016/j.cell.2018.09.048.

19. Li Yi, He X, Kawaguchi R, et al. Microglia-organized scar-free spinal cord repair in neonatal mice. Nature. 2020; 587(7835): 613–618, doi: 10.1038/s41586-020-2795-6, indexed in Pubmed: 33029008.

20. Li Y, Lei Z, Ritzel RM, et al. Impairment of autophagy after spinal cord injury potentiates neuroinflammation and motor function deficit in mice. Theranostics. 2022; 12(12): 5364–5388, doi: 10.7150/thno.72713, indexed in Pubmed: 35910787.

21. Li Y, Ritzel RM, Khan N, et al. Delayed microglial depletion after spinal cord injury reduces chronic inflammation and neurodegeneration in the brain and improves neurological recovery in male mice. Theranostics. 2020; 10(25): 11376–11403, doi: 10.7150/thno.49199, indexed in Pubmed: 33052221.

22. Liu G, Fan G, Guo G, et al. FK506 attenuates the inflammation in rat spinal cord injury by inhibiting the activation of NF-κB in microglia cells. Cell Mol Neurobiol. 2017; 37(5): 843–855, doi: 10.1007/s10571-016-0422-8, indexed in Pubmed: 27572744.

23. Liu H, Zhang J, Xu X, et al. SARM1 promotes neuroinflammation and inhibits neural regeneration after spinal cord injury through NF-κB signaling. Theranostics. 2021; 11(9): 4187–4206, doi: 10.7150/thno.49054, indexed in Pubmed: 33754056.

24. Liu J, Li R, Huang Z, et al. Rapamycin preserves neural tissue, promotes schwann cell myelination and reduces glial scar formation after hemi-contusion spinal cord injury in mice. Front Mol Neurosci. 2020; 13: 574041, doi: 10.3389/fnmol.2020.574041, indexed in Pubmed: 33551740.

25. Liu LR, Liu JC, Bao JS, et al. Interaction of microglia and astrocytes in the neurovascular unit. Front Immunol. 2020; 11: 1024, doi: 10.3389/fimmu.2020.01024, indexed in Pubmed: 32733433.

26. Liu W, Rong Y, Wang J, et al. Exosome-shuttled miR-216a-5p from hypoxic preconditioned mesenchymal stem cells repair traumatic spinal cord injury by shifting microglial M1/M2 polarization. J Neuroinflammation. 2020; 17(1):

47, doi: 10.1186/s12974-020-1726-7, indexed in Pubmed: 32019561.

27. Liu Z, Yao X, Jiang W, et al. Advanced oxidation protein products induce microglia-mediated neuroinflammation via MAPKs-NF-κB signaling pathway and pyroptosis after secondary spinal cord injury. J Neuroinflammation. 2020; 17(1): 90, doi: 10.1186/s12974-020-01751-2, indexed in Pubmed: 32192500.

28. Luo C, Tao L. The function and mechanisms of autophagy in spinal cord injury. Adv Exp Med Biol. 2020; 1207: 649–654, doi: 10.1007/978-981-15-4272-5_47, indexed in Pubmed: 32671782.

29. Mulero MC, Huxford T, Ghosh G. NF-κB, IκB, and IKK: integral components of immune system signaling. Adv Exp Med Biol. 2019; 1172: 207–226, doi: 10.1007/978-981-13-9367-9_10, indexed in Pubmed: 31628658.

30. Ray SK. Modulation of autophagy for neuroprotection and functional recovery in traumatic spinal cord injury. Neural Regen Res. 2020; 15(9): 1601–1612, doi: 10.4103/1673-5374.276322, indexed in Pubmed: 32209759.

31. Ren C, Han X, Lu C, et al. Ubiquitination of NF-κB p65 by FBXW2 suppresses breast cancer stemness, tumorigenesis, and paclitaxel resistance. Cell Death Differ. 2022; 29(2): 381–392, doi: 10.1038/s41418-021-00862-4, indexed in Pubmed: 34465889.

32. Rong Y, Liu W, Wang J, et al. Neural stem cell-derived small extracellular vesicles attenuate apoptosis and neuroinflammation after traumatic spinal cord injury by activating autophagy. Cell Death Dis. 2019; 10(5): 340, doi: 10.1038/s41419-019-1571-8, indexed in Pubmed: 31000697.

33. Shi Q, Wu Y, Zhang B, et al. Progranulin promotes functional recovery in rats with acute spinal cord injury via autophagy-induced anti-inflammatory microglial polarization. Mol Neurobiol. 2022; 59(7): 4304–4314, doi: 10.1007/s12035-022-02836-0, indexed in Pubmed: 35505051.

34. Sweeney MD, Zhao Z, Montagne A, et al. Blood-brain barrier: from physiology to disease and back. Physiol Rev. 2019; 99(1): 21–78, doi: 10.1152/physrev.00050.2017, indexed in Pubmed: 30280653.

35. Watson JL, Hala TJ, Putatunda R, et al. Persistent at-level thermal hyperalgesia and tactile allodynia accompany chronic neuronal and astrocyte activation in superficial dorsal horn following mouse cervical contusion spinal cord injury. PLoS One. 2014; 9(9): e109099, doi: 10.1371/journal.pone.0109099, indexed in Pubmed: 25268642.

36. Wu C, Chen H, Zhuang R, et al. Betulinic acid inhibits pyroptosis in spinal cord injury by augmenting autophagy via the AMPK-mTOR-TFEB signaling pathway. Int J Biol Sci. 2021; 17(4): 1138–1152, doi: 10.7150/ijbs.57825, indexed in Pubmed: 33867836.

37. Wu H, Zheng J, Xu S, et al. Mer regulates microglial M1/M2 polarization and alleviates neuroinflammation following traumatic brain injury. J Neuroinflammation. 2021; 18: 2, doi: 10.21203/rs.3.rs-29587/v1.

38. Xu Bo, Zhang Ws, Yang Jl, et al. Dexmedetomidine blocks thermal hyperalgesia and spinal glial activation in rat model of monoarthritis. Acta Pharmacol Sin. 2010; 31(5): 523–530, doi: 10.1038/aps.2010.32, indexed in Pubmed: 20364156.

39. Xu S, Shao M, Ma X, et al. CD73 alleviates GSDMD-mediated pyroptosis in spinal cord injury through PI3K/AKT/

/Foxo1 signaling. Clin Transl Med. 2021; 11: e269, doi: 10.21203/rs.2.18409/v1.

40. Zeng H, Liu N, Yang YY, et al. Lentivirus-mediated down-regulation of α-synuclein reduces neuroinflammation and promotes functional recovery in rats with spinal cord injury. J Neuroinflammation. 2019; 16(1): 283, doi: 10.1186/s12974-019-1658-2, indexed in Pubmed: 31888724.

41. Zeng Z, Zhang Y, Jiang W, et al. Modulation of autophagy in traumatic brain injury. J Cell Physiol. 2020; 235(3): 1973–1985, doi: 10.1002/jcp.29173, indexed in Pubmed: 31512236.

42. Zhang Y, Liu D, Hu H, et al. HIF-1α/BNIP3 signaling pathway-induced-autophagy plays protective role during myo-cardial ischemia-reperfusion injury. Biomed Pharmacother. 2019; 120: 109464, doi: 10.1016/j.biopha.2019.109464, indexed in Pubmed: 31590128.

43. Zhao H, Chen S, Gao K, et al. Resveratrol protects against spinal cord injury by activating autophagy and inhibiting apoptosis mediated by the SIRT1/AMPK signaling pathway. Neuroscience. 2017; 348: 241–251, doi: 10.1016/j.neuroscience.2017.02.027, indexed in Pubmed: 28238848.

44. Zhou K, Zheng Z, Li Y, et al. TFE3, a potential therapeutic target for spinal cord injury via augmenting autophagy flux and alleviating ER stress. Theranostics. 2020; 10(20): 9280–9302, doi: 10.7150/thno.46566, indexed in Pubmed: 32802192.

ORIGINAL ARTICLE

VM VIA MEDICA

FOXO6 transcription inhibition of CTRP3 promotes OGD/R-triggered cardiac microvascular endothelial barrier disruption via SIRT1/Nrf2 signalling

Sanfu Zheng[1], Yu Wang[2], Weixi Guo[3], Hongyu Tan[4]

[1]Department of Cardiology, The First Affiliated Hospital of Xiamen University, Xiamen, Fujian, China
[2]Department of Ultrasound, The First Affiliated Hospital of Xiamen University, Xiamen, Fujian, China
[3]Department of Thoracic Surgery, The First Affiliated Hospital of Xiamen University, Xiamen, Fujian, China
[4]Department of Internal Medicine, The First Affiliated Hospital of Xiamen University, Xiamen, Fujian, China

Background: *C1q/TNF-related protein 3 (CTRP3) has been clarified to display its protective roles in cardiac function. The current study is concentrated on exploring the impacts of CTRP3 on myocardial ischaemia.*

Materials and methods: *Oxygen and glucose hypoxia/reoxygenation (OGD/R) model was constructed in human cardiac microvascular endothelial cells (HCMECs). Reverse transcription-quantitative polymerase chain reaction and western blot analysis of CTRP3 expression were conducted. CCK-8 assay was to estimate cell activity and lactate dehydrogenase (LDH) assay kit was to test LDH release. TUNEL assay and western blot were to judge apoptosis. Endothelial barrier function was detected by in vitro vascular permeability assay kit. Zonula occludens-1 (ZO-1) expression was evaluated by immunofluorescence assay. The interaction between CTRP3 promoter and Forkhead Box O6 (FOXO6) was predicted by JASPAR database and verified by chromatin immunoprecipitation and luciferase reporter assays. After OGD/R-induced HCMECs were co-transfected with CTRP3 overexpression and FOXO6 overexpression plasmids, the above functional experiments above were conducted again. Lastly, the expression of sirtuin 1 (SIRT1)/nuclear factor erythroid 2-related factor 2 (Nrf2) signalling-related proteins was examined by western blot.*

Results: *CTRP3 was down-regulated in OGD/R-induced HCMECs. CTRP3 enhanced the viability and barrier integrity while reduced the apoptosis and permeability of OGD/R-insulted HCMECs. This process may be regulated by FOXO6 transcription. Also, FOXO6 inhibition-mediated CTRP3 up-regulation activated the SIRT1/Nrf2 signalling.*

Conclusions: *FOXO6 transcription inhibition of CTRP3 promotes OGD/R-triggered cardiac microvascular endothelial barrier disruption via SIRT1/Nrf2 signalling.* (Folia Morphol 2024; 83, 1: 125–138)

Keywords: myocardial ischaemia, cardiac microvascular endothelial cells, barrier disruption, CTRP3, FOXO6, SIRT1/Nrf2 signalling

---

Address for correspondence: Dr. Hongyu Tan, Department of Internal Medicine, The First Affiliated Hospital of Xiamen University,
55 Zhenhai Road, Siming District, Xiamen, Fujian, 361003, China, e-mail: tanhongyu02@163.com

INTRODUCTION

Cardiovascular disease (CVD) is recognized as a prevalent and threatening worldwide health problem accompanied with increasing morbidity and mortality [32]. Notably, myocardial ischaemia is a dominant contributor responsible for the high death rate of CVD patients and the incidence of myocardial ischaemia is increasingly elevated nowadays [25]. Myocardial ischaemia is referred to as a pathological condition of myocardial anoxia, metabolic changes, cardiac dysfunction as well as damaged myocardial structure due to reduced blood perfusion to the heart [1]. Moreover, cardiac microvascular endothelial cells (CMECs) injury represents an earlier and severer phenomenon during the process of myocardial ischaemia. Therefore, the protection for CMECs is indispensable for reducing the risk of myocardial ischaemia.

C1q/TNF-related protein (CTRP) family, which contains a group of adiponectin paralogous proteins, can regulate the proliferation, apoptosis and metabolism in malignant tumours as well as other human diseases [15]. CTRP3, a well-studied member of CTRP family, was initially identified as a secretory protein expressed in the cartilage and kidney of adult mice [23]. Notably, CTRP3 has been discovered to display abnormal expression in CVD [9]. It has reported that CTRP3 protects mesenchymal stem cells from hypoxia and serum deprivation induced apoptosis through PI3K/Akt pathway [11]. Moreover, CTRP3 alleviates ox-LDL-induced inflammatory response and endothelial dysfunction in mouse aortic endothelial cells by activating PI3K/Akt/eNOS pathway, thus improving atherosclerosis [2]. However, the study of CTRP3 on cardiac microvascular endothelial cells in myocardial ischaemia has not been reported so far.

JASPAR database predicts the binding of the transcription factor FOXO6 to the CTRP3 promoter. FOXO6 belongs to the Forkhead box O (FOXO) family of transcription factors that are implicated in multiple cellular pathways via posttranslational modifications [20, 24]. Previous study showed that FOXO6 is up-regulated in hypoxia-exposed cardiomyocytes and its silencing mitigates apoptosis and oxidative stress through elevating silent information regulator 2 homolog 6 (SIRT6) expression and activating nuclear factor E2-related factor (Nrf2) [14]. Nonetheless, whether FOXO6 exerts influence on CMECs remains obscure.

Silent information regulator 2 homolog 1 (SIRIT1), a histone deacetylase dependent on nicotinamide adenosine dinucleotide (NAD), has been supported to be related to a variety of cell metabolisms, such as inflammation, carcinogenesis, oxidative stress and so on [42]. The activation of SIRT1 signalling participates in endothelial barrier function [34]. Besides, elevation of SIRT1 reduces endothelial tight junction permeability to alleviate LPS-stimulated lung injury [7]. The regulation of SIRT1 signalling pathway can promote angiogenesis of rat brain microvascular endothelial cells after oxygen and glucose hypoxia/reoxygenation (OGD/R) injury [29].

Transcription factor Nrf2 is regarded as a decisive downstream target of SIRT1 signalling [37]. Intriguingly, it is also well documented that Nrf2 is involved in endothelial barrier function through mediating oxidative stress [19]. And activation of SIRT1/Nrf2 signalling pathway can inhibit oxidative stress and inflammatory response, and reduce OGD/R injury of human umbilical vein endothelial cells [18]. Moreover, CTRP3 can protect against doxorubicin-induced cardiac dysfunction, inflammation and cell death via activation of SIRT1 [40]. So we made a hypothesis that CTRP3 is regulated by FOXO6 transcription to affect the SIRT1/Nrf2 pathway, thus affecting the function of OGD/R-induced cardiac microvascular endothelial cells.

Herein, this paper is aimed at exploring the impacts of CTRP3 on OGD/R-treated CMECs and probing into the interaction among CTRP3, FOXO6 as well as SIRT1/Nrf2 signalling. Our study provides a theoretical basis for the pathogenesis and clinical treatment of myocardial ischaemia.

MATERIALS AND METHODS

Cell culture

The culture medium for human cardiac microvascular endothelial cells (HCMECs) purchased from ScienCell was endothelial cell medium (ECM; ScienCell). The medium was supplemented 10% fetal bovine serum (FBS; Atlanta Biologicals; Bio-Techne Corporation) and placed in a humid atmosphere at 37°C with 5% CO_2. To mimic cardiac ischaemia/reperfusion (I/R) injury *in vitro*, HCMECs were grown in serum/ /glucose-free ECM under the condition of 95% N_2 and 5% CO_2 at 37°C for 4 h. After that, the cells were subjected to re-oxygenation in the normoxic incubator (5% CO_2 at 37°C) for 24 h. Untreated HCMECs that cultured under normoxic conditions for 4 days were referred to the control group.

Reverse transcription-quantitative polymerase chain reaction (RT-qPCR)

With the aid of Omega Bio-tek E.Z.N.A. Total RNA kit (Doraville, GA, USA), total RNA was prepared from HCMECs and then subjected to reverse transcription using RevertAid First Strand cDNA Synthesis Kit (Fermentas, Shanghai, China). SYBR® Green PCR master mix (Bio-Rad Laboratories, Inc.) was adopted to perform PCR reactions on the MX3000p PCR system (Agilent, Santa Clara, CA). The calculation of relative gene expression was achieved by $2^{-\Delta\Delta Ct}$ method [30]. Glyceraldehyde 3-phosphate dehydrogenase (GAPDH) was adopted for normalization. Primer sequences were as follows: CTRP3 forward: 5'-ATGCTTTGGAGGCAGCT-CAT-3', reverse: 5'-TCACCTTTGTCGCCCTTCTC-3'; FOXO6 forward: 5'-TCTACGACTGGATGGTCCGT-3', reverse: 5'-GGGTCTTCCCTGTCTTTCCG-3'; GAPDH forward: 5'-AATGGGCAGCCGTTAGGAAA-3', reverse: 5'-GCGCCCAATACGACCAAATC-3'.

Western blot

Total proteins that extracted from HCMECs utilizing RIPA buffer (JRDUN Biotechnology) were ascertained with the application of BCA protein assay kit (CoWin, Beijing, China). Following, PVDF membranes were to shift protein samples that resolved by 10% SDS-PAGE. Non-specific interaction was ensured after the membranes were incubated with 5% non-fat milk. Afterwards, primary antibodies as well as goat anti-rabbit HRP antibody (cat. no. ab205718; 1/2000; Abcam) were respectively probed with the membranes overnight at 4°C and for 1 h. The blots were visualized by the ECL western blotting system (Amersham; Cytiva) and analysed by Image Quant LAS 500 (GE Healthcare) [36]. CTRP3 (cat. no. GTX85505; 1:1000; GeneTex), B cell lymphoma-2 (Bcl-2; cat. no. ab32124; 1/1000; Abcam), BCL-2-associated X (Bax; cat. no. ab32503; 1/1000; Abcam), cleaved caspase 3 (cat. no. ab2302; 1/1000; Abcam), cytochrome c (cyto-C; cat. no. ab133504; 1/5000; Abcam), zonula occludens-1 (ZO-1; cat. no. ab216880; 1/5000; Abcam), Occludin (cat. no. ab216327; 1/1000; Abcam), VE-cadherin (cat. no. ab33168; 1/1000; Abcam), Claudin-5 (cat. no. ab131259; 1/1000; Abcam), FOXO6 (cat. no. 19122-1-AP; 1/500; Proteintech), SIRT1 (cat. no. ab189494; 1/1000; Abcam), Nrf2 (cat. no. ab62352; 1/1000; Abcam), GAPDH (cat. no. ab9485; 1/2500; Abcam) antibodies were utilized here.

Plasmid transfection

PcDNA3.1 expression vector containing full-length human CTRP3 (pcDNA3.1-CTRP3) as well as corresponding negative control (pcDNA3.1-NC), pcDNA3.1(+) FOXO6 overexpression vector (Ov-FOXO6) and Ov-NC were all provided by GenePharma (Shanghai, China). OGD/R-induced cells overexpressing CTRP3 were divided into control, OGD/R, OGD/R+pcDNA3.1 and OGD//R+pcDNA3.1-CTRP3 groups. After both CTRP3 and FOXO6 were overexpressed, the cells were grouped into control, OGD/R, OGD/R+pcDNA3.1, OGD/R+p-cDNA3.1-CTRP3, OGD/R+pcDNA3.1-CTRP3+OV-NC and OGD/R+pcDNA3.1-CTRP3+OV-FOXO6 groups. Above plasmids were transduced into cells employing Lipofectamine™ 3000 (Takara, Kusatsu, Japan). Cells were obtained for ensue assays 48 h later.

CCK-8 assay

Human cardiac microvascular endothelial cells were inoculated into 96-well plates at a density of 3,000 cells/well and then cultivated overnight at 37°C. A total of 10 μL cell counting Kit-8 (CCK-8) solution (Beijing TransGen Biotech Co., Ltd.) was added into each well and the cells were cultivated at 37°C for another 2 h. The measurement of the absorbance at 450 nm was implemented with a microplate reader (Beckman Coulter, Inc.) [33].

Detection of LDH release

Briefly, lactate dehydrogenase (LDH) concentration in HCMECs was ascertained by means of LDH assay kit (cat. no. BC0685; Solarbio) in the light of the manufacturer's guidance. Before incubating with supernatant (60 μL) and LDH substrate solution (30 μL) for another 30 min, cell supernatant was obtained after centrifugation at 300 × g for 10 min. With the application of a microplate reader (Beckman Coulter, Inc.), at a wavelength of 440 nm, LDH activity was calculated [38].

TUNEL

Cell apoptosis was appraised applying a terminal-deoxynucleoitidyl transferase mediated nick end labelling (TUNEL) Apoptosis kit (cat. no. BA27A; Nanjing Biobox Biotech Co., Ltd.) in the light of the manufacturer's guidance. In short, 4% paraformaldehyde was added to HCMECs for immobilization, following which was the permeabilization with 0.1% Triton X-100. Subsequently, the cells were cultivated with TUNEL reaction reagent for 1 h and the nuclei were

labelled with 10 mg/mL DAPI for 10 min. Finally, the images were acquired under a fluorescence microscope (UltraVIEW VoX; PerkinElmer, Inc.) [12].

Detection of HCMECs permeability

The permeability of HCMECs was detected using a commercial *in vitro* permeability assay kit (Millipore, Billerica, MA, USA). In brief, a tight monolayer was formed after 1×10^3 HCMECs that plated onto collagen-coated inserts were incubated for 3 days. After indicated treatment, each receiver plate well was supplemented with 500 μL glucose-free ECM. To permeate the monolayers, 2.5% FITC (fluorescein isothiocyanate)-dextran (40 kDa) solution was added for 20 min. The medium in the receiver wells was then thoroughly mixed. The intensity of FITC fluorescence was captured under a fluorescence spectrometer (MV06744, MoleCular Devices, Shanghai, China). The excitation wavelength was 482 nm and the detection wavelength was 525 nm [16].

Immunofluorescence staining

Following OGD/R treatment, HCMECs were subjected to immobilization and then probed with 0.2% Triton X-100 for 20 min. 1% BSA was used for blocking after cells were rinsed in PBS. Then ZO-1 (Abcam, 1:100, cat. no. ab221547) antibody was supplemented overnight at 4°C, after which was the cultivation with goat anti-rabbit IgG/Alexa Fluor 555 (Beijing Biosynthesis Biotechnology Co., Ltd., 1:100, cat. no. bs-0295G-A555) was used. Nuclear staining with DAPI (OriGene Technologies, Inc.) was performed. A fluorescence microscope (UltraVIEW VoX; PerkinElmer, Inc.) was to monitor the images [3].

Chromatin immunoprecipitation

With the adoption of the Imprint chromatin immunoprecipitation (ChIP) kit (cat. no. CHP1; Sigma-Aldrich; Merck KGaA), ChIP assay was executed in with the light of the manufacturer's guidelines. For the purpose of crosslinking the protein and DNA, HCMECs were firstly treated by 1% formaldehyde. The chromatin fragments that acquired after sonicating of cell lysates were precipitated with FOXO6 antibody (Proteintech, cat. no. 19122-1-AP) or IgG antibody (Abcam, ab6715) overnight. The purified DNA fragments were subjected to PCR analysis [5].

Luciferase reporter assay

PGL3 vectors (Huada Genomics, Shenzheng, China) containing wild type (WT) binding sequences between FOXO6 and CTRP3 promoter and the corresponding mutant type named as CTRP3-MUT were co-transfected with Ov-FOXO6 and Ov-NC into cells employing Lipofectamine™ 3000 (Takara, Kusatsu, Japan). After 48 h, with the aid of the Dual-Glo® Luciferase Reagent (Promega Corporation), the luciferase activity was evaluated.

Statistical analyses

Statistical analyses were executed employing SPSS 22.0 (IBM, Armonk, NY, USA). All data that collected 3 parallel repeat experiments were denoted as the mean ± standard deviation. Statistical significances were measured using Student's t-test or one-way ANOVA along with Tukey's post hoc test. The significance level was p < 0.05.

Bioinformatics tools

The potential binding sites between FOXO6 and CTRP3 promoter were predicted by JASPAR database (https://jaspar.genereg.net/) [6].

RESULTS

Elevation of CTRP3 potentiates the viability of OGD/R-insulted HCMECs

To determine the role of CTRP3 in OGD/R-treated HCMECs, CTRP3 expression was examined. It was noted from RT-qPCR and western blot that CTRP3 expression was declined in HCMECs following OGD/R treatment (Fig. 1A, B). Before assessing the impacts of CTRP3 on the behaviours of OGD/R-treated HCMECs, the overexpression efficiency of CTRP3 was tested. As Figures 1C and D illuminated, CTRP3 expression was remarkably increased after the transfection with pcDNA3.1-CTRP3. Through CCK-8 assay, it was observed that the viability of HCMECs was prominently reduced under OGD/R conditions. When CTRP3 was up-regulated, the viability of OGD/R-insulted HCMECs was obviously enhanced relative to the OGD/R+pcDNA3.1 group (Fig. 1E). Similarly, LDH production was monitored to evaluate cell cytotoxicity. LDH release was found to be stimulated in OGD/R-treated HCMECs, which was then suppressed after CTRP3 was overexpressed (Fig. 1F).
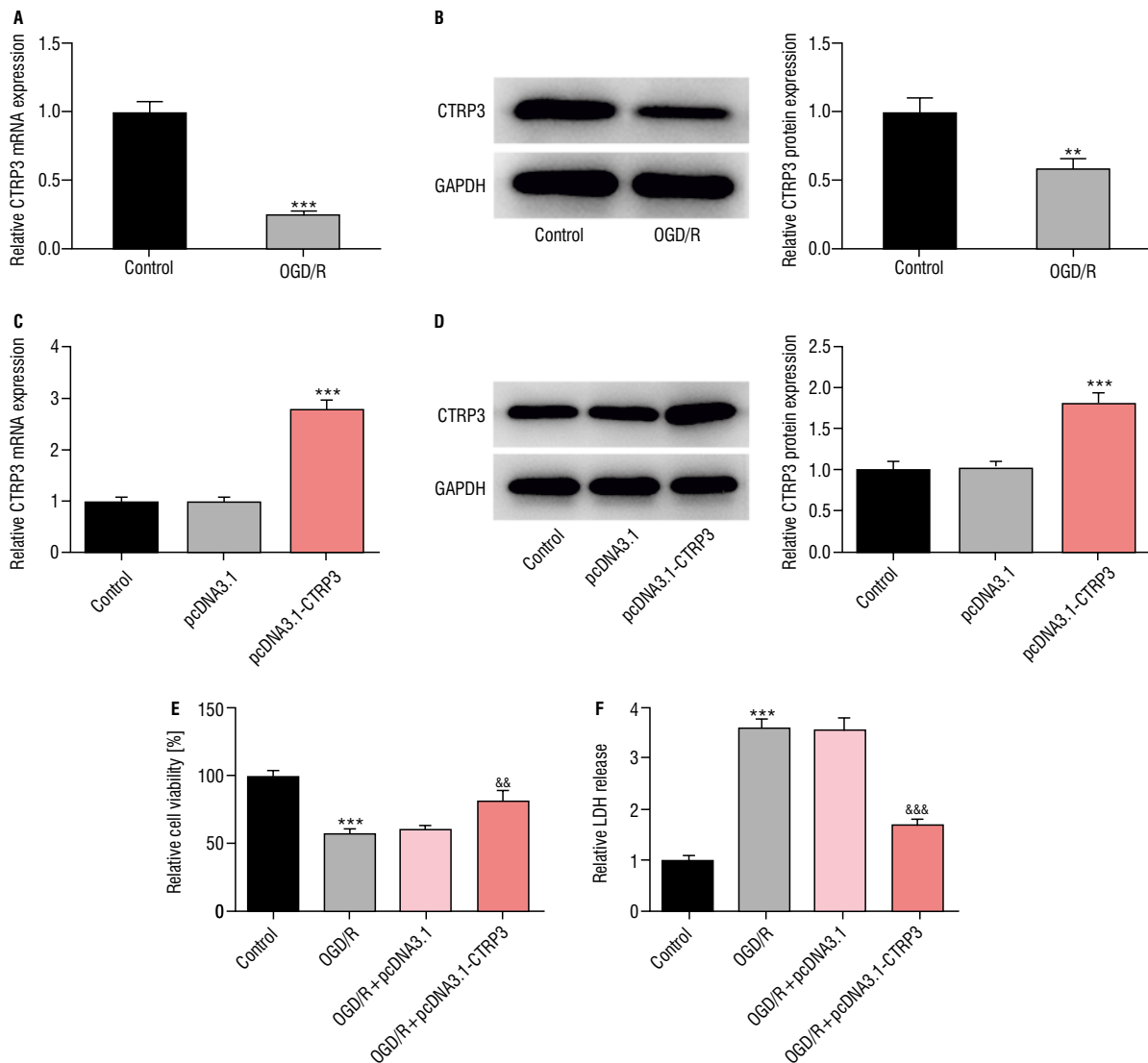
Figure 1. Elevation of C1q/TNF-related protein 3 (CTRP3) potentiates the viability of oxygen and glucose hypoxia/reoxygenation (OGD/R)-insulted human cardiac microvascular endothelial cells (HCMECs). Reverse transcription-quantitative polymerase chain reaction (RT-qPCR) (**A**) and western blot (**B**) ascertained CTRP3 expression in HCMECs with the absence or presence of OGD/R treatment; **p < 0.01, ***p < 0.001 vs. control; RT-qPCR (**C**) and western blot (**D**) analysis of the overexpression efficacy of pcDNA3.1-CTRP3 plasmid; ***p < 0.001 vs. pcDNA3.1. OGD/R-exposed HCMECs activity was judged via CCK-8 assay (**E**). Lactate dehydrogenase (LDH) production was examined with LDH assay kit (**F**); ***p < 0.001 vs. control; &&p < 0.01, &&&p < 0.001 vs. OGD/R+pc DNA3.1.

CTRP3 elevation attenuates OGD/R-elicited HCMECs apoptosis

On the contrary, the experimental results of TUNEL assay uncovered that OGD/R treatment-stimulated apoptosis of HCMECs was significantly suppressed by up-regulation of CTRP3 (Fig. 2A). In addition, western blot was to analyse the expression of apoptosis-associated factors. As expected, OGD/R treatment resulted in decreased Bcl-2 expression and increased Bax, cleaved caspase 3 and cyto-C expression, whereas these effects were offset by enhancive CTRP3 (Fig. 2B).

Up-regulation of CTRP3 reduces permeability and stabilizes tight junction in HCMECs following OGD/R treatment

Further, cell permeability was detected by *in vitro* permeability assay kit and the results indicated that the raised permeability of OGD/R-induced HCMECs was greatly decreased after the transfection with pcDNA3.1-CTRP3 (Fig. 3A). Besides, as analysed by immunofluorescence assay, the down-regulated expression of ZO-1 in OGD/R-insulted HCMECs was elevated again after CTRP3 was overexpressed (Fig.
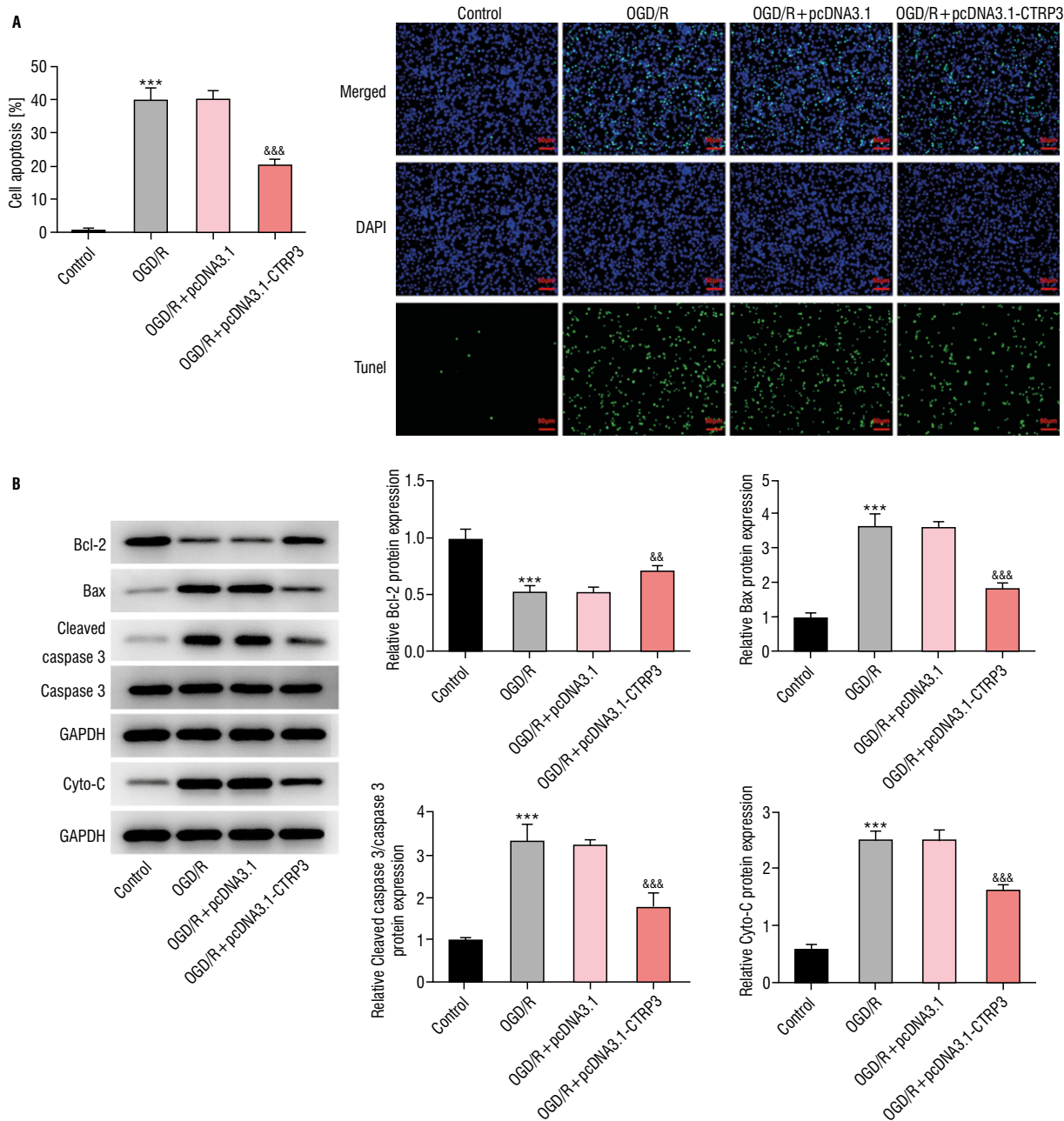
Figure 2. C1q/TNF-related protein 3 (CTRP3) elevation attenuates oxygen and glucose hypoxia/reoxygenation (OGD/R)-triggered human cardiac microvascular endothelial cells (HCMECs) apoptosis. The apoptotic ability of OGD/R-insulted HCMECs was evaluated by TUNEL assay (**A**); Western blot analysed the expression of apoptosis-associated factors (**B**); ***p < 0.001 vs. control; &&p < 0.01, &&&p < 0.001 vs. OGD//R + pc DNA3.1; Bcl-2 — B-cell lymphoma 2; Bax — BCL-2 associated X; Cyto-c — cytochrome c.

3B). Western blot also analysed that the expressions of tight junctions including ZO-1, Occludin, VE-cadherin, Claudin-5 were cut down by OGD/R treatment in HCMECs, which were then increased by CTRP3 up-regulation (Fig. 3C).

FOXO6 is a transcription inactivator of CTRP3

Interestingly, JASPAR database predicted that CTRP3 promoter had a potential binding with FOXO6

(Fig. 4A). Moreover, FOXO6 was discovered to display high expression in OGD/R-exposed HCMECs (Fig. 4B, C). After FOXO6 was overexpressed by transfection with Ov-FOXO6 (Fig. 4D, E), the experimental results from luciferase reporter assay elaborated that elevation of FOXO6 distinctly lessened the luciferase activity of CTRP3-WT instead of that of CTRP3-MUT (Fig. 4F). Further, ChIP assay testified the high enrichment of CTRP3 promoter in FOXO6 antibody (Fig. 4G). Also,
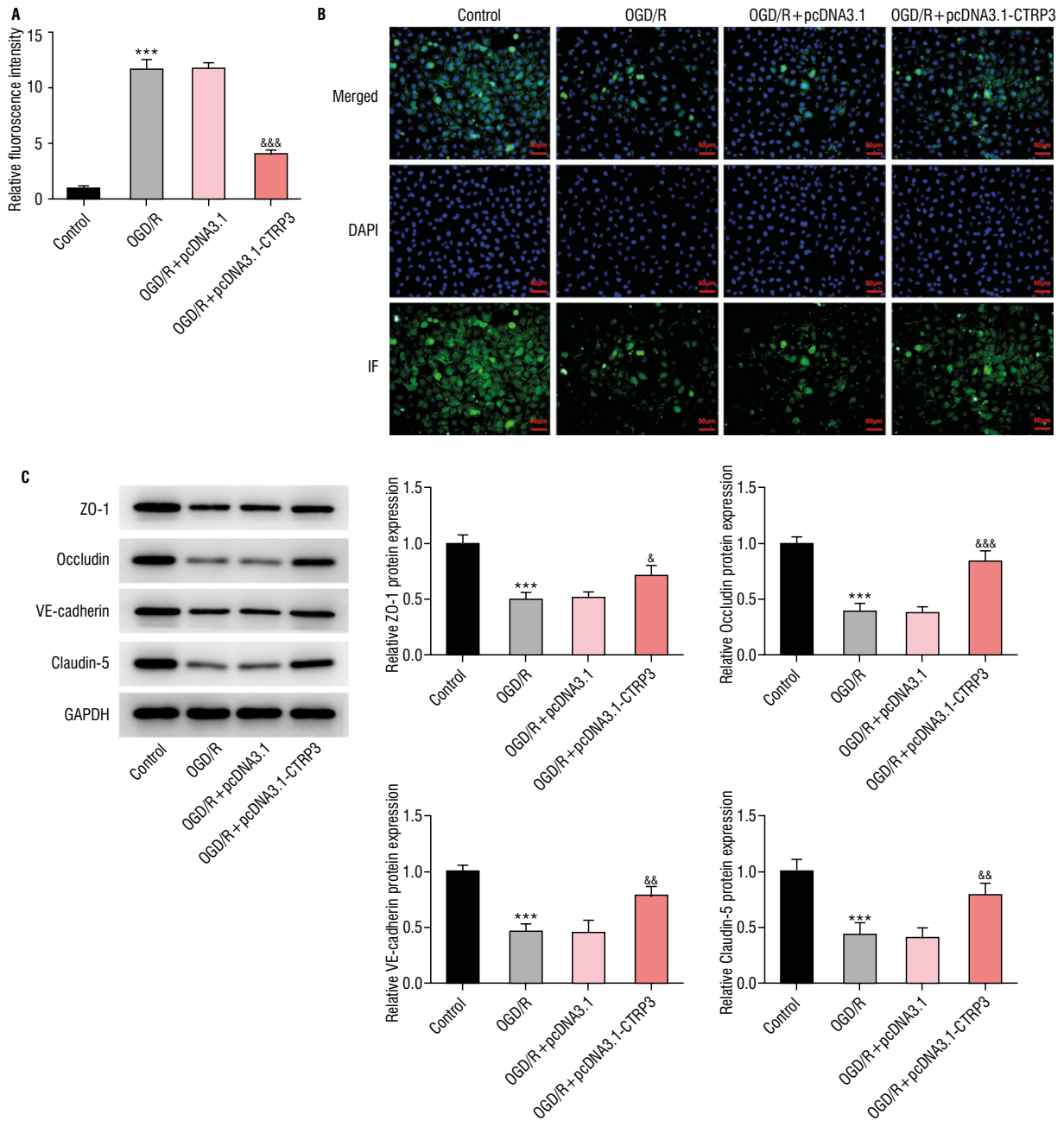
Figure 3. Up-regulation of C1q/TNF-related protein 3 (CTRP3) reduces permeability and stabilizes tight junction in human cardiac microvascular endothelial cells (HCMECs) following oxygen and glucose hypoxia/reoxygenation (OGD/R) treatment; **A.** *In vitro* permeability assay kit was to estimate the permeability of OGD/R-insulted HCMECs; **B.** Immunofluorescence (IF) assay was to examine zonula occludens-1 (ZO-1) expression; **C.** Western blot tested ZO-1, Occludin, VE-cadherin and Claudin-5 expression; ***p < 0.001 vs. control; &p < 0.05, &&p < 0.01, &&&p < 0.001 vs. OGD/R+pc DNA3.1.

RT-qPCR and western blot analysis indicated that the up-regulated CTRP3 expression in OGD/R-insulted HCMECs transfected with pcDNA3.1-CTRP3 was declined again when FOXO6 was up-regulated (Fig. 4H, I). In all, CTRP3 was transcriptionally suppressed by FOXO6.

FOXO6 overexpression reverses the protective role of CTRP3 in OGD/R-evoked HCMECs injury

To validate the mechanism mediated by FOXO6 and CTRP3 in OGD/R-induced cardiac microvascular endothelial barrier disruption, Ov-FOXO6 plasmid was
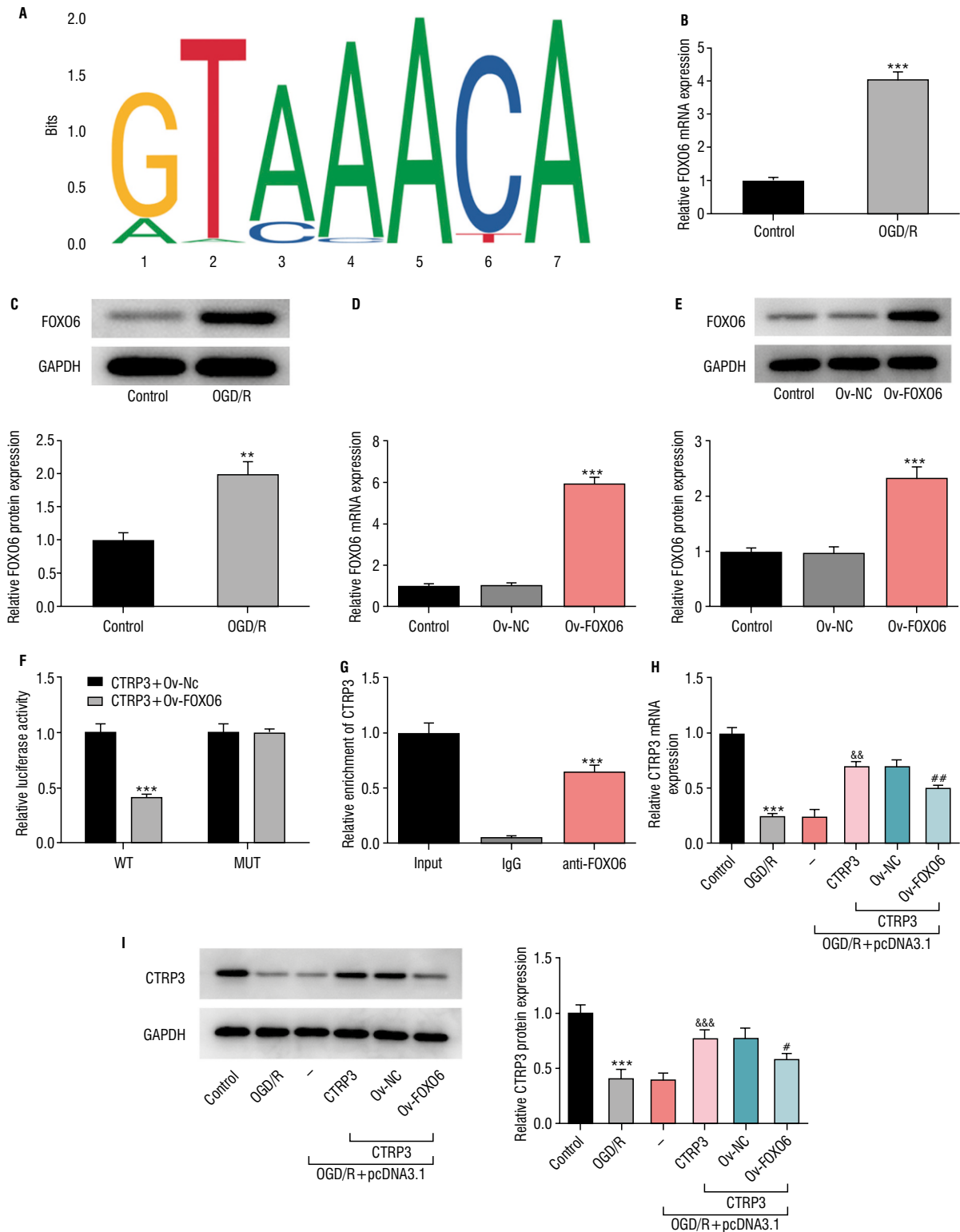
Figure 4. Forkhead Box O6 (FOXO6) is a transcription inactivator of C1q/TNF-related protein 3 (CTRP3); **A.** The potential binding sites between CTRP3 promoter and FOXO6 were predicted by JASPAR database; Reverse transcription-quantitative polymerase chain reaction (RT-qPCR) (**B**) and western blot (**C**) ascertained FOXO6 expression in human cardiac microvascular endothelial cells (HCMECs) with the absence or presence of oxygen and glucose hypoxia/reoxygenation (OGD/R) treatment; **p < 0.01, ***p < 0.001 vs. control. RT-qPCR (**D**) and western blot (**E**) analysis of the overexpression efficacy of Ov-FOXO6 plasmid; ***p < 0.001 vs. Ov-NC. Luciferase reporter assay verified the luciferase activity of CTRP3-WT and CTRP3-MUT (**F**); ***p < 0.001 vs. CTRP3+Ov-NC; Chromatin immunoprecipitation (ChIP) assay identified the abundance of CTRP3 promoter in FOXO6 antibody (**G**); ***p < 0.001 vs. IgG. RT-qPCR (**H**) and western blot (**I**) ascertained CTRP3 expression in OGD/R-induced HCMECs co-transfected with pcDNA3.1-CTRP3 and Ov-FOXO6 plasmids; ***p < 0.001 vs. control; &&p < 0.01, &&&p < 0.001 vs. OGD/R + pcDNA3.1; #p < 0.05, ##p < 0.01 vs OGD/R + pcDNA3.1-CTRP3 + Ov-NC.
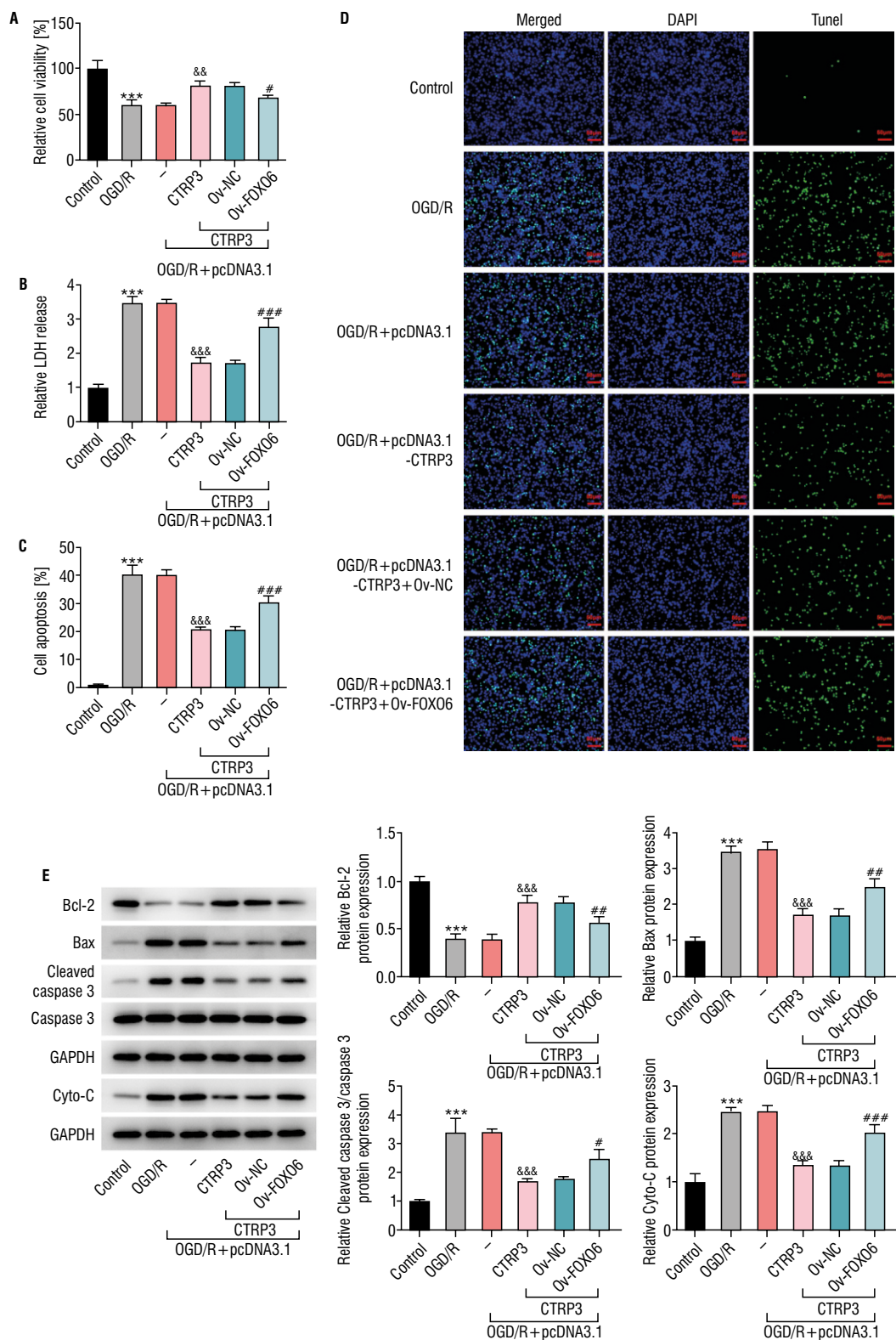
Figure 5. Forkhead Box O6 (FOXO6) overexpression reverses the impacts of C1q/TNF-related protein 3 (CTRP3) on oxygen and glucose hypoxia/reoxygenation (OGD/R)-evoked human cardiac microvascular endothelial cells (HCMECs) proliferation and apoptosis. OGD/R-exposed HCMECs activity was judged via CCK-8 assay (**A**). Lactate dehydrogenase (LDH) production was examined with LDH assay kit (**B**). The apoptotic ability of OGD/R-insulted HCMECs was evaluated by TUNEL assay (**C**, **D**). Western blot analysed the expression of apoptosis-associated factors (**E**); ***p < 0.001 vs. control; &&p < 0.01, &&&p < 0.001 vs. OGD/R+pcDNA3.1; #p < 0.05, ##p < 0.01, ###p < 0.001 vs. OGD//R+pcDNA3.1-CTRP3+Ov-NC; Bcl-2 — B-cell lymphoma 2; Bax — BCL-2 associated X; Cyto-c — cytochrome c.
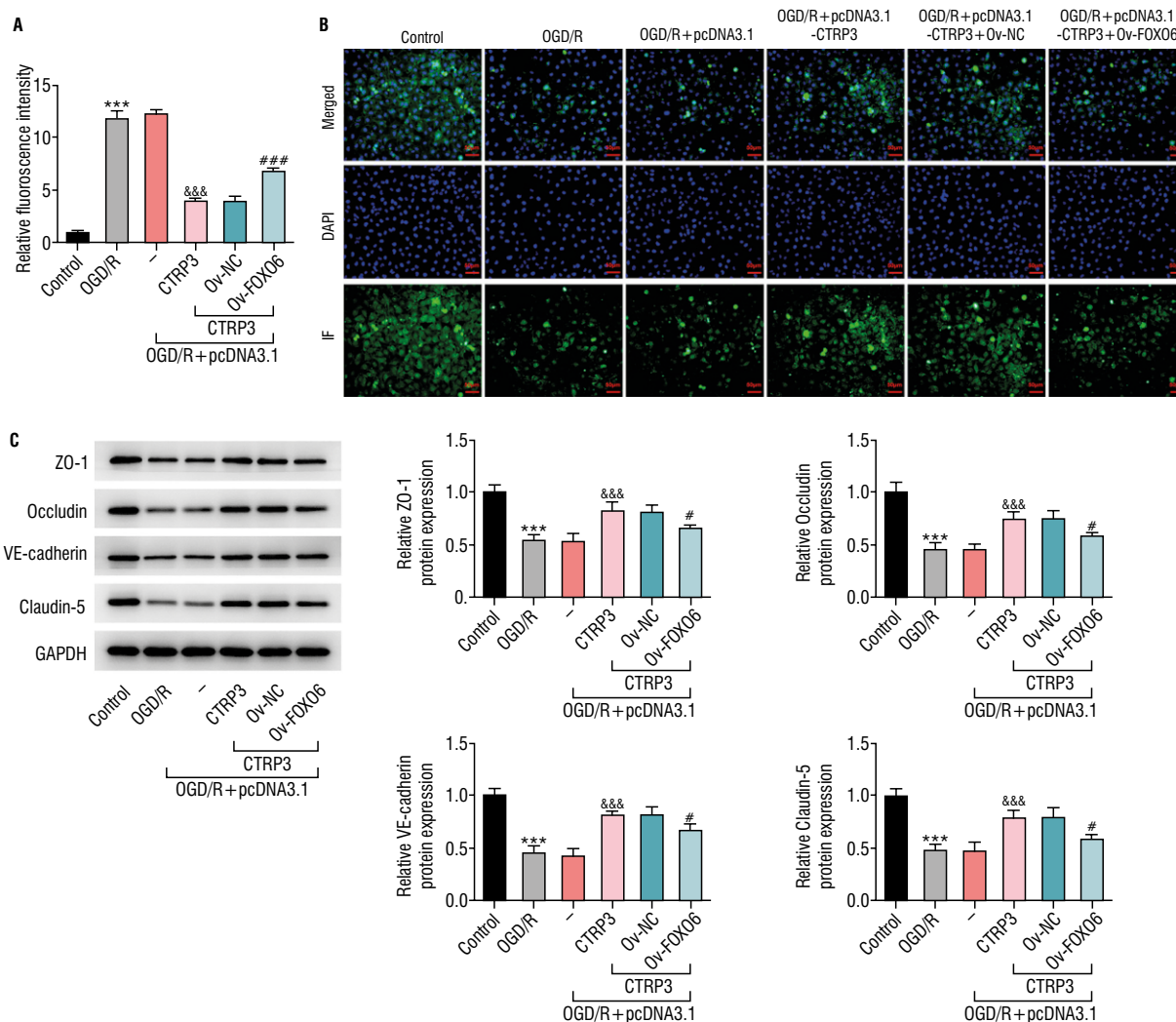
Figure 6. Forkhead Box O6 (FOXO6) overexpression reverses the protective role of C1q/TNF-related protein 3 (CTRP3) in glucose hypoxia/ /reoxygenation (OGD/R)-evoked cardiac microvascular endothelial barrier dysfunction; **A.** *In vitro* permeability assay kit was to estimate the permeability of oxygen and OGD/R-insulted human cardiac microvascular endothelial cells (HCMECs); **B.** Immunofluorescence (IF) assay was to examine zonula occludens-1 (ZO-1) expression; **C.** Western blot tested ZO-1, Occludin, VE-cadherin and Claudin-5 expression; ***p < 0.001 vs. control; &&&p < 0.001 vs. OGD/R+pcDNA3.1; #p < 0.05, ###p < 0.001 vs. OGD/R+pcDNA3.1-CTRP3+Ov-NC.

transfected into CTRP3-overexpressed HCMECs with OGD/R induction and then functional experiments were conducted again. The results of CCK-8 assay revealed that the stimulated viability of OGD/R-insulted HCMECs caused by CTRP3 was abrogated after FOXO6 was overexpressed (Fig. 5A). Also, the impeded LDH release caused by CTRP3 elevation was abated again when FOXO6 was up-regulated (Fig. 5B). Conversely, as Figures 5C and D depicted, FOXO6 strengthened the weakened apoptotic capacity of OGD/R-exposed HCMECs caused by CTRP3. Besides, the enhanced Bcl-2 protein level as well as declined Bax, cleaved caspase 3 and cyto-C protein levels caused by CTRP3 were also restored after upregulating FOXO6 (Fig. 5E). Additionally, CTRP3 led to decreased permeability of OGD/R-treated

HCMECs, whereas this effect was reversed by Ov-FOXO6 (Fig. 6A). Compared with OGD/R+pcDNA3.1 group, the higher expression of ZO-1 in OGD/R-exposed HCMECs transfected with pcDNA3.1-CTRP3 was diminished again after FOXO6 was overexpressed (Fig. 6B). In the same way, FOXO6 up-regulation cut down CTRP3-stimulated protein levels of ZO-1, Occludin, VE-cadherin and Claudin-5 (Fig. 6C). Taken together, the suppressive role of CTRP3 in OGD/R-induced injury in HCMECs was counteracted by FOXO6.

CTRP3 negatively regulated by FOXO6 transcription factor activates SIRT1/Nrf2 signalling

Notably, western blot analysed that overexpression of CTRP3 increased the protein levels of SIRT1
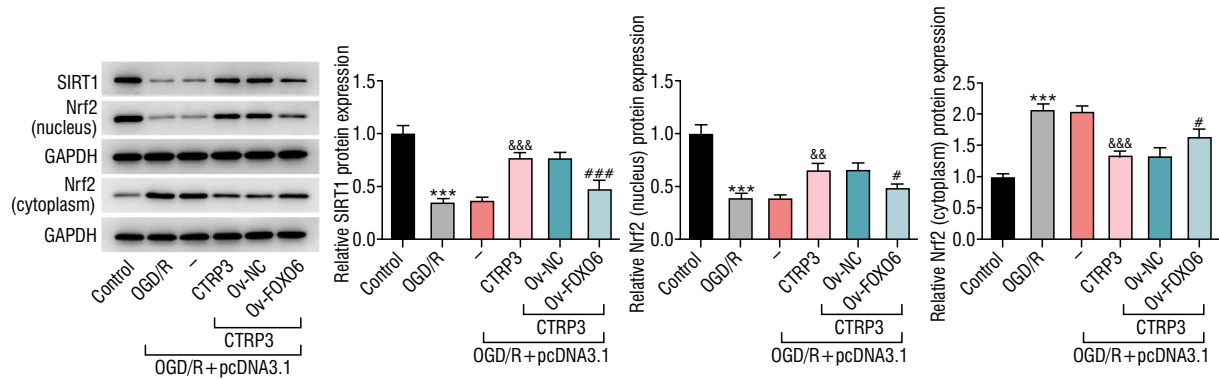
Figure 7. C1q/TNF-related protein 3 (CTRP3) negatively regulated by Forkhead Box O6 (FOXO6) transcription factor activates silent information regulator 2 homolog 1/nuclear factor E2-related factor (SIRT1/Nrf2) signalling. Western blot tested cytoplasmic Nrf2, nuclear Nrf2 and SIRT1 expression; ***p < 0.001 vs. control; &&p < 0.01, &&&p < 0.001 vs. OGD/R+pcDNA3.1; #p < 0.05, ###p < 0.001 vs. OGD/R+pcD-NA3.1-CTRP3+Ov-NC.

and nuclear Nrf2 but decreased the protein level of cytoplasmic Nrf2. However, the consequence was reversed when FOXO6 was up-regulated. Collectively, CTRP3 that mediated by FOXO6 silencing served as a transcription activator of SIRT1/Nrf2 signalling.

DISCUSSION

Cardiac microvascular endothelial cells, an element of coronary circulation microvessels, are some of the predominant cells prone to immediately suffer damage after myocardial ischaemia injury [28]. Disruption of epithelial barriers that mediated by CMECs injury is considered as an initiating factor of CVD [17], even heart failure [4]. During the process of myocardial ischaemia injury, endothelial barrier injury is commonly characterized by autoregulatory dysfunction, eventually bringing about increased endothelial permeability[27]. Hence, OGD/R was utilized in the present study to induce endothelial barrier breakdown model, aiming to explore the proliferation, apoptosis and permeability of HCMECs.

In recent years, the impact of CTRP3 on cardiac events has attracted much attention. CTRP3 alleviates pressure overload induced cardiac hypertrophy by inhibiting the P38/CREB pathway and endoplasmic reticulum stress induced by P38 [41]. CTRP3 also relieves inflammation and endothelial dysfunction in atherosclerosis [2]. Melatonin alleviates obesity-induced myocardial oxidative stress and apoptosis by promoting the secretion of CTRP3 in adipose tissue, while the loss of CTRP3 largely eliminates melatonin-mediated cardiac protection [22]. However, the effect of CTRP3 on HCMECs in myocardial ischaemia has not been reported so far.

In our experiment, it was found that the expression of CTRP3 in OGD/R-induced HCMECs decreased significantly, and the overexpression of CTRP3 could significantly improve the activity of OGD/R-induced HCMECs and inhibit cell apoptosis. The knockdown of endothelial barrier can be attributed to the altered cell junction protein levels; meanwhile, the unique property of tight junction in HCMECs is of great significance in controlling permeability [10]. As important mediators of endothelial adherence junction, the expressions of ZO-1, Occludin, VE-cadherin and Claudin-5 were also examined here. It was observed that OGD/R exposure led to decreased ZO-1, Occludin, VE-cadherin and Claudin-5 expressions, which were subsequently raised by overexpression of CTRP3.

JASPAR database and mechanism assays in this study predicted and verified the binding of FOXO6 to CTRP3 promoter. FOXO family transcription factors can affect microvascular endothelial cells, induce oxidative stress response pathways, and thus participate in cell injury and apoptosis [26]. FOXO6 is a member of the FOXO family. Previous study showed that FOXO6 contributes to hypoxia-exposed cardiomyocyte apoptosis and oxidative stress [14]. Therefore, we have reason to guess that FOXO6 can transcriptionally regulate CTRP3 and thus regulate the function of HCMECs. Our data suggested that FOXO6 was up-regulated in OGD/R-treated HCMECs. Moreover, the elevation of CTRP3 in CTRP3-overexpressed HCMECs following OGD/R injury was cut down after overexpressing FOXO6, implying that CTRP3 was transcriptionally inhibited by FOXO6. Further, functional experiments corroborated that the impacts of CTRP3

on the viability, apoptosis, permeability and tight junction of HCMECs upon exposure to OGD/R treatment were all reversed by overexpression of FOXO6.

Increasing previous studies have supported that the activation of SIRT1/Nrf2 signalling protects against myocardial ischaemia injury mainly through the regulation of apoptosis, inflammation, oxidative stress and endoplasmic reticulum stress [21, 35]. SIRT1/Nrf2 signalling mitigates intestinal barrier injury [39]. And targeting SIRT1 can inhibit apoptosis of rat retinal vascular endothelial cells and improve blood retinal vascular barrier permeability [13]. Moreover, FOXO6 contributes to hypoxia-exposed cardiomyocyte apoptosis and oxidative stress via inactivating Nrf2 [14]. CTRP3 inhibits OGD/R-induced hippocampal neuron injury through SIRT1 signalling pathway [8]. CTRP3 can protect against doxorubicin-induced cardiac dysfunction, inflammation and cell death via activation of SIRT1 [40]. However, in HCMECs of myocardial ischaemia, the regulation of FOXO6 transcriptional regulation of CTRP3 on SIRT1/Nrf2 has not been reported. Our study proved that OGD/R exposure down-regulated SIRT1 and nuclear Nrf2 protein levels but up-regulated cytoplasmic Nrf2 protein level. Meanwhile, in OGD/R-treated HCMECs, the stimulated SIRT1 expression and Nrf2 nuclear translocation imposed by CTRP3 were restored by FOXO6.

Limitations of the study

This article also has some limitations. The response of HCMECs to inflammatory response has not been covered and *in vivo* models of myocardial ischaemia induced by coronary ligation in mice also require further study. The research on the role of SIRT1/Nrf2 pathway in downstream pathway of CTRP3 is not in-depth enough. In future experiments, we will further explore the mechanism by adding SIRT1/Nrf2 pathway inhibitors or pathway activators.

CONCLUSIONS

In conclusion, CTRP3 was inhibited by FOXO6 transcription factor at posttranscriptional level. CTRP3 relieved OGD/R-evoked cardiac microvascular endothelial barrier disruption through activating SIRT1/Nrf2 signalling. This finding might provide a theoretical basis for the pathogenesis of myocardial ischaemia and provide substantial evidence for the efficacy of novel targeted therapy based on CTRP3-mediated molecular mechanism. At the same time, accumulating evidence has elucidated that endothelial barrier dysfunction is associated with inflammatory response and clinical outcomes [31].

Conflict of interest: None declared

REFERENCES

1. Barstow C, Barstow C, Rice M, et al. Acute coronary syndrome: diagnostic evaluation. Am Fam Physician. 2017; 95(3): 170–177, indexed in Pubmed: 28145667.
2. Chen L, Qin L, Liu X, et al. CTRP3 alleviates Ox-LDL-induced inflammatory response and endothelial dysfunction in mouse aortic endothelial cells by activating the PI3K/Akt//eNOS pathway. Inflammation. 2019; 42(4): 1350–1359, doi: 10.1007/s10753-019-00996-1, indexed in Pubmed: 30887395.
3. Deng F, Zhou R, Lin C, et al. Tumor-secreted dickkopf2 accelerates aerobic glycolysis and promotes angiogenesis in colorectal cancer. Theranostics. 2019; 9(4): 1001–1014, doi: 10.7150/thno.30056, indexed in Pubmed: 30867812.
4. Dong W, Zhang GN, Gao SH. Preliminary in vitro analysis of mechanism of cardiac microvascular endothelial barrier function. Genet Mol Res. 2016; 15(4), doi: 10.4238/gmr15048864, indexed in Pubmed: 27813591.
5. Dou R, Liu K, Yang C, et al. EMT-cancer cells-derived exosomal miR-27b-3p promotes circulating tumour cells-mediated metastasis by modulating vascular permeability in colorectal cancer. Clin Transl Med. 2021; 11(12): e595, doi: 10.1002/ctm2.595, indexed in Pubmed: 34936736.
6. Fornes O, Castro-Mondragon JA, Khan A, et al. JASPAR 2020: update of the open-access database of transcription factor binding profiles. Nucleic Acids Res. 2020; 48(D1): D87–D92, doi: 10.1093/nar/gkz1001, indexed in Pubmed: 31701148.
7. Fu C, Hao S, Xu X, et al. Activation of SIRT1 ameliorates LPS-induced lung injury in mice via decreasing endothelial tight junction permeability. Acta Pharmacol Sin. 2019; 40(5): 630–641, doi: 10.1038/s41401-018-0045-3, indexed in Pubmed: 30022154.
8. Gao J, Qian T, Wang W. CTRP3 activates the AMPK/SIRT1-PGC-1α pathway to protect mitochondrial biogenesis and functions in cerebral ischemic stroke. Neurochem Res. 2020; 45(12): 3045–3058, doi: 10.1007/s11064-020-03152-6, indexed in Pubmed: 33098065.
9. Guo B, Zhuang T, Xu F, et al. New insights into implications of CTRP3 in obesity, metabolic dysfunction, and cardiovascular diseases: potential of therapeutic interventions. Front Physiol. 2020; 11: 570270, doi: 10.3389/fphys.2020.570270, indexed in Pubmed: 33343381.
10. Hashimoto Y, Campbell M. Tight junction modulation at the blood-brain barrier: Current and future perspectives. Biochim Biophys Acta Biomembr. 2020; 1862(9): 183298, doi: 10.1016/j.bbamem.2020.183298, indexed in Pubmed: 32353377.
11. Hou M, Liu J, Liu F, et al. C1q tumor necrosis factor-related protein-3 protects mesenchymal stem cells against hypoxia- and serum deprivation-induced apoptosis through the phosphoinositide 3-kinase/Akt pathway. Int J Mol Med. 2014; 33(1): 97–104, doi: 10.3892/ijmm.2013.1550, indexed in Pubmed: 24212403.
12. Hu GF, Wang C, Hu GX, et al. AZD3463, an IGF-1R inhibitor, suppresses breast cancer metastasis to bone via modu-

lation of the PI3K-Akt pathway. Ann Transl Med. 2020; 8(6): 336, doi: 10.21037/atm.2020.02.110, indexed in Pubmed: 32355780.

13. Ji Q, Han J, Wang L, et al. MicroRNA-34a promotes apoptosis of retinal vascular endothelial cells by targeting SIRT1 in rats with diabetic retinopathy. Cell Cycle. 2020; 19(21): 2886–2896, doi: 10.1080/15384101.2020.1827509, indexed in Pubmed: 33064974.

14. Jin A, Zhang Q, Li S, et al. Downregulation of FOXO6 alleviates hypoxia-induced apoptosis and oxidative stress in cardiomyocytes by enhancing Nrf2 activation via upregulation of SIRT6. J Bioenerg Biomembr. 2020; 52(6): 409–419, doi: 10.1007/s10863-020-09856-2, indexed in Pubmed: 33123950.

15. Kong M, Gao Yu, Guo X, et al. Role of the CTRP family in tumor development and progression. Oncol Lett. 2021; 22(4): 723, doi: 10.3892/ol.2021.12984, indexed in Pubmed: 34429763.

16. Kunimura K, Miki S, Takashima M, et al. S-1-propenyl-cysteine improves TNF-α-induced vascular endothelial barrier dysfunction by suppressing the GEF-H1/RhoA/ /Rac pathway. Cell Commun Signal. 2021; 19(1): 17, doi: 10.1186/s12964-020-00692-w, indexed in Pubmed: 33588881.

17. Li B, Li Y, Liu K, et al. High glucose decreases claudins-5 and -11 in cardiac microvascular endothelial cells: Antagonistic effects of tongxinluo. Endocr Res. 2017; 42(1): 15–21, doi: 10.3109/07435800.2016.1163723, indexed in Pubmed: 27111519.

18. Li J, Yang C, Wang Y. miR126 overexpression attenuates oxygenglucose deprivation/reperfusion injury by inhibiting oxidative stress and inflammatory response via the activation of SIRT1/Nrf2 signaling pathway in human umbilical vein endothelial cells. Mol Med Rep. 2021; 23(2), doi: 10.3892/mmr.2020.11804, indexed in Pubmed: 33355373.

19. Li X, Zhang Q, Hou N, et al. Carnosol as a Nrf2 activator improves endothelial barrier function through antioxidative mechanisms. Int J Mol Sci. 2019; 20(4), doi: 10.3390/ ijms20040880, indexed in Pubmed: 30781644.

20. Link W. Introduction to FOXO Biology. Methods Mol Biol. 2019; 1890: 1–9, doi: 10.1007/978-1-4939-8900-3_1, indexed in Pubmed: 30414140.

21. Liu P, Li J, Liu M, et al. Hesperetin modulates the Sirt1/Nrf2 signaling pathway in counteracting myocardial ischemia through suppression of oxidative stress, inflammation, and apoptosis. Biomed Pharmacother. 2021; 139: 111552, doi: 10.1016/j.biopha.2021.111552, indexed in Pubmed: 33839495.

22. Liu Y, Li LN, Guo S, et al. Melatonin improves cardiac function in a mouse model of heart failure with preserved ejection fraction. Redox Biol. 2018; 18: 211–221, doi: 10.1016/j.redox.2018.07.007, indexed in Pubmed: 30031269.

23. Maeda T, Abe M, Kurisu K, et al. Molecular cloning and characterization of a novel gene, CORS26, encoding a putative secretory protein and its possible involvement in skeletal development. J Biol Chem. 2001; 276(5): 3628–3634, doi: 10.1074/jbc.M007898200, indexed in Pubmed: 11071891.

24. Murtaza G, Khan AK, Rashid R, et al. FOXO transcriptional factors and long-term living. Oxid Med Cell Longev. 2017; 2017: 3494289, doi: 10.1155/2017/3494289, indexed in Pubmed: 28894507.

25. Pagliaro BR, Cannata F, Stefanini GG, et al. Myocardial ischemia and coronary disease in heart failure. Heart Fail Rev. 2020; 25(1): 53–65, doi: 10.1007/s10741-019-09831-z, indexed in Pubmed: 31332663.

26. Ponugoti B, Dong G, Graves DT. Role of forkhead transcription factors in diabetes-induced oxidative stress. Exp Diabetes Res. 2012; 2012: 939751, doi: 10.1155/2012/939751, indexed in Pubmed: 22454632.

27. Qi K, Li X, Geng Y, et al. Tongxinluo attenuates reperfusion injury in diabetic hearts by angiopoietin-like 4-mediated protection of endothelial barrier integrity via PPAR-pathway. PLoS One. 2018; 13(6): e0198403, doi: 10.1371/ journal.pone.0198403, indexed in Pubmed: 29912977.

28. Qi XF, Li YJ, Chen ZY, et al. Involvement of the FoxO3a pathway in the ischemia/reperfusion injury of cardiac microvascular endothelial cells. Exp Mol Pathol. 2013; 95(2): 242–247, doi: 10.1016/j.yexmp.2013.08.003, indexed in Pubmed: 23948278.

29. Ruan J, Wang L, Dai J, et al. Hydroxysafflor yellow a promotes angiogenesis in rat brain microvascular endothelial cells injured by oxygen-glucose deprivation/reoxygenation(OGD/R) through SIRT1-HIF-1α-VEGFA signaling pathway. Curr Neurovasc Res. 2021; 18(4): 415–426, doi: 10.2174/1567202618666211109104419, indexed in Pubmed: 34751117.

30. Schmittgen TD, Livak KJ. Analyzing real-time PCR data by the comparative C(T) method. Nat Protoc. 2008; 3(6): 1101–1108, doi: 10.1038/nprot.2008.73, indexed in Pubmed: 18546601.

31. Skaria T, Bachli E, Schoedon G. RSPO3 impairs barrier function of human vascular endothelial monolayers and synergizes with pro-inflammatory IL-1. Mol Med. 2018; 24(1): 45, doi: 10.1186/s10020-018-0048-z, indexed in Pubmed: 30157748.

32. Stoney CM, Kaufmann PG, Czajkowski SM. Cardiovascular disease: Psychological, social, and behavioral influences: Introduction to the special issue. Am Psychol. 2018; 73(8): 949–954, doi: 10.1037/amp0000359, indexed in Pubmed: 30394774.

33. Sun X, Liu B. Donepezil ameliorates oxygen-glucose deprivation/reoxygenation-induced brain microvascular endothelial cell dysfunction via the SIRT1/FOXO3a/NF-κB pathways. Bioengineered. 2022; 13(3): 7760–7770, doi: 10.1080/21655979.2022.2045833, indexed in Pubmed: 35286233.

34. Wang K, Zhao J, Zhang W, et al. Resveratrol attenuates aortic dissection by increasing endothelial barrier function through the SIRT1 pathway. J Cardiovasc Pharmacol. 2020; 76(1): 86–93, doi: 10.1097/FJC.0000000000000837, indexed in Pubmed: 32324654.

35. Wang X, Yuan B, Cheng B, et al. Crocin alleviates myocardial ischemia/reperfusion-induced endoplasmic reticulum stress via regulation of miR-34a/Sirt1/ /Nrf2 pathway. Shock. 2019; 51(1): 123–130, doi: 10.1097/SHK.0000000000001116, indexed in Pubmed: 29424794.

36. Yan W, Ma X, Zhao X, et al. Baicalein induces apoptosis and autophagy of breast cancer cells via inhibiting PI3K//AKT pathway in vivo and vitro. Drug Des Devel Ther. 2018; 12: 3961–3972, doi: 10.2147/DDDT.S181939, indexed in Pubmed: 30510404.

37. Yang B, Xu B, Zhao H, et al. Dioscin protects against coronary heart disease by reducing oxidative stress and inflammation via Sirt1/Nrf2 and p38 MAPK pathways. Mol Med Rep. 2018; 18(1): 973–980, doi: 10.3892/mmr.2018.9024, indexed in Pubmed: 29845299.

38. Yang M, Lv H, Liu Qi, et al. Colchicine alleviates cholesterol crystal-induced endothelial cell pyroptosis through activating AMPK/SIRT1 pathway. Oxid Med Cell Longev. 2020; 2020: 9173530, doi: 10.1155/2020/9173530, indexed in Pubmed: 32733639.

39. Yao B, He J, Yin X, et al. The protective effect of lithocholic acid on the intestinal epithelial barrier is mediated by the vitamin D receptor via a SIRT1/Nrf2 and NF-κB dependent mechanism in Caco-2 cells. Toxicol Lett. 2019; 316: 109–118, doi: 10.1016/j.toxlet.2019.08.024, indexed in Pubmed: 31472180.

40. Yuan YP, Ma ZG, Zhang X, et al. CTRP3 protected against doxorubicin-induced cardiac dysfunction, inflammation and cell death via activation of Sirt1. J Mol Cell Cardiol. 2018; 114: 38–47, doi: 10.1016/j.yjmcc.2017.10.008, indexed in Pubmed: 29061338.

41. Zhang B, Zhang P, Tan Y, et al. C1q-TNF-related protein-3 attenuates pressure overload-induced cardiac hypertrophy by suppressing the p38/CREB pathway and p38-induced ER stress. Cell Death Dis. 2019; 10(7): 520, doi: 10.1038/s41419-019-1749-0, indexed in Pubmed: 31285424.

42. Zhao B, Li X, Zhou L, et al. SIRT1: a potential tumour biomarker and therapeutic target. J Drug Target. 2019; 27(10): 1046–1052, doi: 10.1080/1061186X.2019.1605519, indexed in Pubmed: 31056963.

O R I G I N A L   A R T I C L E

The association between body height and longevity: evidence from a national population sample

Piotr Paweł Chmielewski

Division of Anatomy, Department of Human Morphology and Embryology, Faculty of Medicine, Wroclaw Medical University, Wroclaw, Poland

Background: A wealth of research suggests that taller individuals are healthier and live longer than their shorter counterparts, although conflicting results have been reported. This study aims to investigate whether taller individuals in Poland exhibit greater longevity compared to their shorter counterparts.

Materials and methods: Data on declared height were collected from 848,860 adults who died in the years 2004–2008 in Poland. To eliminate the cohort effects, Z-values were computed. Pearson's correlation coefficients were calculated independently for males and females. Subsequently, one way ANOVA was performed.

Results: The correlation between adult height and longevity was negative and statistically significant in both men and women. After eliminating the effects of secular trends in height, the correlation was very weak (r = –0.0044 in men and r = –0.0038 in women) but significant (p = 0.023 and p = 0.022, respectively).

Conclusions: Despite the significant correlation observed between the two variables, it should be noted that the relationship between height and longevity is very weak and tenuous. Overall, these results do not support the hypothesis that taller individuals have a longevity advantage. Further research is warranted to identify the underlying biological mechanisms driving this phenomenon as well as to explore additional variables affecting human longevity. (Folia Morphol 2024; 83, 1: 139–145)

Keywords: adult height, body height, lifespan, longevity, stature, survival

INTRODUCTION

Human body height is a polygenic trait that is controlled by several genomic loci [35]. Stature is also one of the most conspicuous morphological traits that has important ecological and social consequences [17]. Historically, taller individuals were more privileged as they were the richest people who had significantly more resources to address own demands and who were able to lead a healthy lifestyle [12]. An abundance of studies have reported that body height correlates positively with educational attainment, socioeconomic status (SES), income, wealth, reproductive success, overall health and survival [4, 19, 25–27]. However, these links are often complex and may be obscured by various interactions. For example, women prefer taller men but men prefer shorter

women [25, 30, 31]. In general, body height and cardiovascular disease (CVD) mortality are inversely correlated [11]. Nonetheless, not all researchers agree that shorter people are more susceptible to CVD as individuals of similar body proportions, body mass index (BMI), educational attainment and SES should be compared with each other [29].

Several studies have revealed that taller people are healthier and have a longevity advantage over their shorter counterparts [11, 12, 15, 24, 26]. It is generally accepted that taller stature reflects better childhood nutrition and better environment and as such can be used as a genuine indicator of the health status and disease exposure in historical populations [11]. Furthermore, the hypothesis that taller individuals are healthier and live longer is widespread among physicians and anthropologists. This is because these early studies have long been interpreted as indicating that taller individuals have lower mortality rates and live longer. Nevertheless, the relationship between adult stature and longevity, which has recently been studied more intensively, remains unclear. For instance, compelling data from animal studies show that greater body size correlates with shorter lifespan within, but not between, mammalian species [1, 2, 6, 21]. Interestingly, recent findings indicate that greater body size, but especially body weight and BMI, is costly in terms of longevity, and smaller individuals outlive those that are larger. Moreover, a similar relationship has been shown in studies of various human populations [1, 2, 9, 13, 28, 29]. The aim of the current study is to explore the relationship between adult height and longevity in adults who died between 2004 and 2008 in Poland.

MATERIAL AND METHODS

For the purpose of the study, we collected data on all adult deaths in the years 2004–2008 in Poland from the national archives at the Ministry of the Interior and Administration in Warsaw. In total, records from 848,860 individuals, including 483,512 (57%) men and 365,348 (43%) women, were available. These data derive from two sources: (1) signalments in the census obtained from identity card offices (body height declared on the identity card) and (2) the Universal Electronic System for Registration of the Population 'PESEL' (sex and dates of birth and death).

The collected data have a number of advantages. Firstly, the sample is very large and representative for the whole population. It is generally agreed that the collection of large samples is a *sine qua non* prerequisite. Secondly, the study sample involves typical causes of death. Numerous studies were confined to the data that were derived from small geographic areas, e.g. a given city or district, obtained in a short period of time or from individuals who died of a specific disease, e.g. CVD or cancer. Although this approach is justified for practical reasons, this can be precarious. Our data are based on reliable documents, i.e. death certificates, which were issued by the authorities. Although it is true that respondents often overestimate their height, these effects are significant when people advertise for dating, and not when they provide information on their stature for legal or official purposes [16, 23]. Thus, it should be emphasised that the use of declared height instead of measured height is acceptable.

The normality of distribution was tested with the goodness-of-fit test χ^2 as well as coefficients of asymmetry (*As*) and kurtosis (*K*). Student's *t*-test and one-way analysis of variance (ANOVA) were performed. In this study, we use a statistical approach that takes into account the effects of secular changes in height. In order to control the cohort effect, the *Z*-value, i.e. standard deviation (SD)-normalized difference from the arithmetic mean of each individual, was calculated for the body height of each individual, according to the formula: $Z = (\text{actual height} - \text{mean height}) / \text{SD}$. Subsequently, Pearson's *r* coefficients of correlation were calculated separately for both sexes.

RESULTS

The distributions for height and lifespan in men and women did not differ from the normal distribution. Men were taller than women (arithmetic mean ± SD, 171.6 ± 6.6 cm and 159.6 ± 6.2 cm, respectively, *t*-test, p < 0.001) and they had a lower age at death (67.9 ± 13.8 years and 75.0 ± 12.7 years, respectively, *t*-test, p < 0.001). For individuals who died at the age of 50 years and above, these results were as follows: 171.1 ± 6.4 cm and 71.1 ± 10.8 years for men and 159.4 ± 6.1 cm and 76.5 ± 10.8 years for women, all differences were statistically significant (p < 0.001).

The analysis revealed that taller individuals had shorter lifespans compared with their shorter peers (Table 1). In individuals who lived for at least 50 years, longevity was inversely correlated with adult height in men (r = −0.27, p < 0.001) and women (r = −0.25, p < 0.001). For both sexes, the longest lifespan was

Table 1. Body height (arithmetic mean ± standard deviation [SD], in cm) in adults who died at a given age in the years 2004–2008 in Poland

Age at death	Men			Women		
	N	Mean	SD	N	Mean	SD
50	12305	174.3	6.5	4312	162.1	5.7
55	171622	173.4	6.3	7373	161.7	5.8
60	19335	172.5	6.1	9181	161.6	5.5
65	18301	171.6	6.1	9447	161.0	5.7
70	25826	171.0	6.0	14903	160.3	5.6
75	30493	170.5	6.1	22658	159.8	5.9
80	27263	170.0	6.3	29103	159.1	6.0
85	17186	169.5	6.6	25836	158.5	6.1
90	5443	168.7	6.8	10983	157.3	6.2
95	2266	167.5	6.9	6009	156.5	6.4
100	261	167.0	6.9	820	155.3	6.3

found for individuals born in December, and the shortest for those born in May. The amplitude of lifespan resulting from the month of birth effect was 16 months in men and 14 months in women. In the oldest old, i.e. people aged 85 years and above, there was an inverse relationship between body height and longevity (Figs. 1, 2).

When body height was plotted against lifespan, it turned out that smaller individuals, in general, had a longevity advantage. However, all of these effects waned after the calculation of the Z-values (Figs. 3, 4), when the influences of secular changes in body height were eliminated in the whole study sample. The coefficients of correlation were extremely low, i.e. r = −0.0044 for men and r = −0.0038 for women, but statistically significant (p = 0.023 and p = 0.022, respectively).
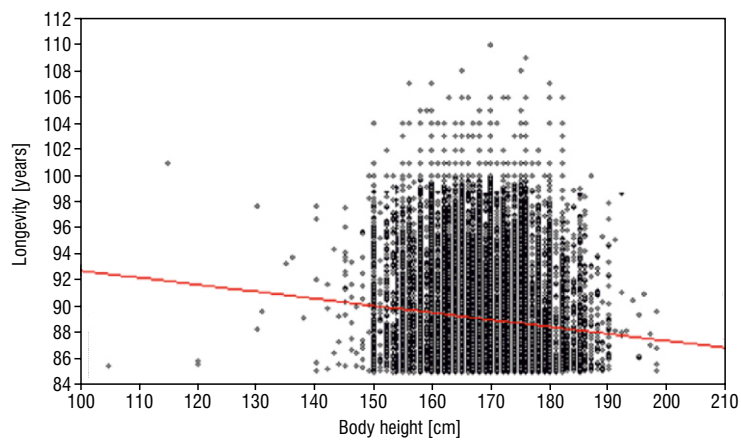
Figure 1. The relationship between actual height and longevity in men aged 85 and above (N = 39,191).
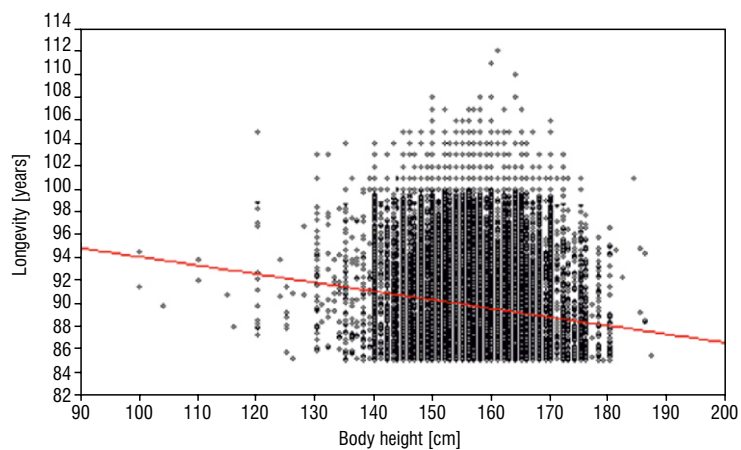
Figure 2. The relationship between actual height and longevity in women aged 85 and above (N = 75,405).

141
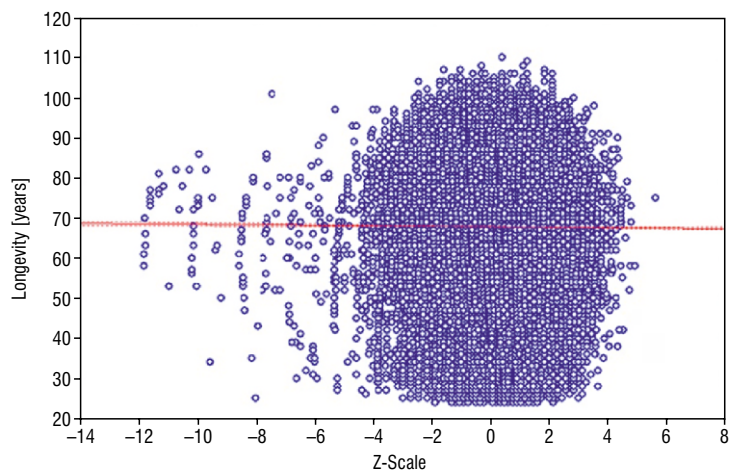
Figure 3. The relationship between normalised height and longevity in men ($N = 483{,}512$).
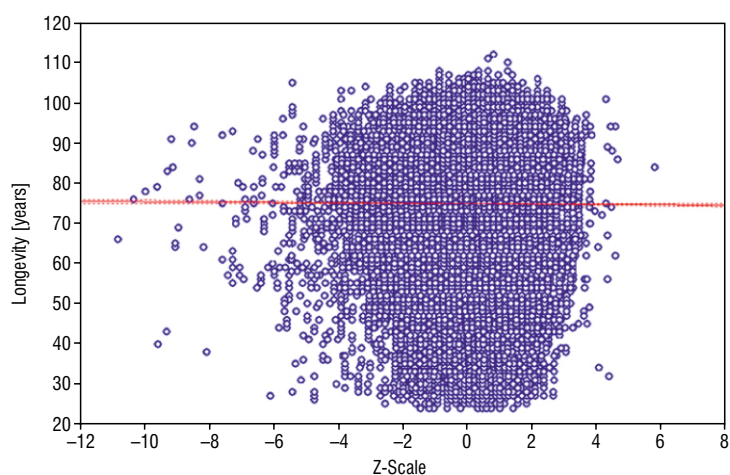
Figure 4. The relationship between normalised height and longevity in women ($N = 365{,}348$).

DISCUSSION

This research has revealed an inverse relationship between adult height and lifespan in both sexes, which is in agreement with several studies [9, 13, 28, 29, 32, 33]. Given that taller people have better nutrition and higher SES, including income and wealth [4, 19, 25–27], these findings convincingly demonstrate that taller stature is not associated with enhanced longevity in the studied population. Contrary to the popular belief that tallness is linked to better health and survival, these results strongly suggest that shorter people can outlive their taller counterparts. There are, however, both theoretical and empirical reasons for doubting that the observed relationship between stature and longevity is direct or causal. Probably, stature is just not a good predictor of longevity, and there are many other factors and processes at play.

It has been established that adult height represents the interactive effects of many processes [3], including the influences of genetic, epigenetic, nutritional, psychological, ecological and lifestyle-related factors such as pathogens, parasites, stress level, amount of sleep, diseases or disorders (Fig. 5). It should be remembered that not only environmental and lifestyle-related factors, such as an unhealthy diet and malnutrition, but also genetic disorders, such as Down syndrome, Russel-Silver syndrome, Noonan syndrome, Turner syndrome, Prader-Willi syndrome, dwarfism due to achondroplasia and other causes, as well as metabolic and developmental problems, such as diabetes, Cushing's syndrome, growth hormone deficiencies, renal dysfunctions, heart failure etc., can result in short stature.

Beard and Blaser [3] argued that infectious diseases in childhood can negatively affect adult stature.
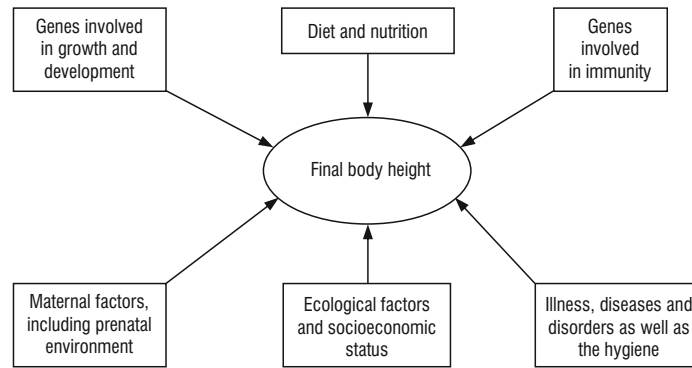
Figure 5. A constellation of factors that affect growth and development and are crucial for adult stature in humans.

Indeed, numerous studies have shown that children who suffered from diarrhoea and dehydration were significantly shorter as adults than those children who did not have these problems. For example, a study by Martorell and associates [20] demonstrated that in Guatemala children relatively free from diarrhoea during the first seven years of life would be around 4 cm taller than children more frequently ill with diarrhoea. Interestingly, it has been estimated that each episode of diarrhoea in childhood is associated with a decrease in adult height by roughly 0.6 cm [5]. Furthermore, several other studies confirm the hypothesis that infectious diseases in the first years of life are important factors affecting adult stature. Clinical observations suggest that other medical problems and conditions, such as chronic granulomatous disease, can also result in diminished final height.

Interestingly, taller stature might be associated with increased risk of cancer at different anatomic sites [14, 22, 28, 32, 34], even though it is unclear why taller and stouter people are more likely to develop cancer. However, tentative explanations can be offered. For example, taller and stockier individuals have significantly more cells in the body as opposed to their smaller and slimmer counterparts. It has recently been suggested that the sheer number of cells in the body can predict the relation between body size and cancer with no need to suggest additional factors [22]. Although cells are constantly repairing and maintaining themselves via the intake of energy from food, individuals within the same species that have a considerable amount of extra cells are more prone to DNA damage and cancer. This is because more cells in the body increase the risk factor for DNA damage and somatic mutations. Furthermore, an organism that accumulates extra senescent cells, a situation that can occur in those organisms that produce more cells and need more new cells to replace older ones, is more likely to reach higher levels of chronic low-grade systemic inflammation, which is detrimental to health and survival [8, 10]. It should be remembered that biological factors related to greater height, such as hormonal and genetic influences, can directly stimulate cancer development and progression. It is well known that growth is physiologically costly, and smaller individuals within mammalian species tend to have lower mortality rates. For example, dogs, cows, horses and mice have been studied for years, and smaller individuals live longer [1, 2, 6, 21]. The data showing that smaller individuals outlive their larger counterparts suggest a role of biological factors (Table 2). Interestingly, animal studies indicate that caloric restriction reduces body size and extends lifespan. Additionally, several studies have demonstrated that tall people are less likely to reach advanced ages [7, 9, 13, 28, 29, 32–34].

However, several confounders, such as BMI, somatotypes, SES, educational attainment, smoking, health care etc., may influence the relationship between body height and longevity. Furthermore, it can be argued that adjusting for risk factors is a crude and inexact process. In addition, poor medical care can also affect results. Another confounder is that in upper economic classes, those who have spent their lives in the upper class are taller and have lower mortality rates than upper class individuals who were born in lower classes and worked up to the upper class. For example, a number of insurance studies have reported that taller men had lower mortality rates than their shorter counterparts. According to Samaras [29], body height is an index for greater body weight and thus BMI. Although taller and slimmer individuals can live longer than shorter and overweight people, greater body weight and BMI are related to increased mortality and morbidity.

143

Table 2. Putative mechanisms providing smaller people with a longevity advantage

Biological factors	Explanation
The total number of cells in the body	Tall people have more somatic cells, thus allowing greater exposure to DNA damage and molecular entropy. The sheer number of cells in the body predicts the relationship between adult height and cancer risk with no need to suggest additional factors [22]
Longer telomeres and more cell replications	Although the results are inconclusive, most studies indicate that longer telomeres are related to greater longevity. Some studies suggest taller nonagenarians have shorter telomeres [18]. Taller individuals use up more cells in the initial production of a larger body and in the daily replacement of damaged or dead cells they are at a disadvantage as they continuously need more cells as opposed to smaller individuals
Lower levels of GH and reduced insulin/IGF-1 signalling	Insulin/IGF-1 signalling is an evolutionarily conserved pathway that participates in various molecular processes and regulates lifespan across species. Reduced GH/insulin/IGF-1 signalling seems beneficial in terms of longevity. Taller individuals have higher levels of GH and more active insulin/IGF-1 signalling [1, 2]
Less hyperactive mTOR, which is a central hub of nutrient signalling	mTOR is an important sensor for nutrient signals that is involved in the longevity pathway. Taller and stouter individuals eat more as opposed to their shorter counterparts, assuming that larger and stockier individuals have more active mTOR, this central hub of nutrient signalling can be involved in the link between body size and longevity [6]
Desirable levels of certain biochemical parameters	Shorter and slimmer individuals who follow a healthy diet tend to have lower levels of total cholesterol and CRP and higher levels of SHBG [13, 28]

CRP — C-reactive protein; GH — growth hormone; IGF-1 — insulin-like growth factor 1 (also referred to as somatomedin C); mTOR — mechanistic (mammalian) target of rapamycin; SHBG — sex hormone binding globulin

Limitations of the study

This study has limitations that should be acknowledged. Firstly, only declared body height was used. Secondly, the analysis did not consider potentially significant confounding factors, such as BMI, SES, educational attainment etc., as these data were not available. However, the relationship between adult height and longevity can be established based on the study sample used for the analysis. It should be stressed that shorter individuals score *worse* in terms of SES, income and wealth, and since taller individuals score *better*, the finding that taller individuals do not live longer than their shorter counterparts is even more intriguing.

CONCLUSIONS

On balance, these results do not confirm the view that taller people live longer. The inverse relationship between height and longevity was reported for both sexes. After allowing for secular trends in stature, these effects waned but remained statistically significant, thereby suggesting that longevity favours smaller individuals in the studied population.

Conflict of interest: None declared

REFERENCES

1. Bartke A. Healthy aging: is smaller better? — a mini-review. Gerontology. 2012; 58(4): 337–343, doi: 10.1159/000335166, indexed in Pubmed: 22261798.
2. Bartke A. Somatic growth, aging, and longevity. NPJ Aging Mech Dis. 2017; 3: 14, doi: 10.1038/s41514-017-0014-y, indexed in Pubmed: 28970944.
3. Beard AS, Blaser MJ. The ecology of height: the effect of microbial transmission on human height. Perspect Biol Med. 2002; 45(4): 475–498, doi: 10.1353/pbm.2002.0064, indexed in Pubmed: 12388882.
4. Bielicki T, Charzewski J. Body height and upward social mobility. Ann Hum Biol. 1983; 10(5): 403–408, doi: 10.1080/03014468300006591, indexed in Pubmed: 6638935.
5. Black RE, Brown KH, Becker S. Effects of diarrhea associated with specific enteropathogens on the growth of children in rural Bangladesh. Pediatrics. 1984; 73(6): 799–805, indexed in Pubmed: 6374599.
6. Blagosklonny MV. Big mice die young but large animals live longer. Aging (Albany NY). 2013; 5(4): 227–233, doi: 10.18632/aging.100551, indexed in Pubmed: 23603822.
7. Chmielewski P, Borysławski K. Understanding the links between month of birth, body height, and longevity: why some studies reveal that shorter people live longer – further evidence of seasonal programming from the Polish population. Anthropol Rev. 2016; 79(4): 375–395, doi: 10.1515/anre-2016-0028.
8. Chmielewski P. Leukocyte count, systemic inflammation, and health status in older adults: a narrative review. Anthropol Rev. 2018; 81(1): 81–101, doi: 10.2478/anre-2018-0007.
9. Chmielewski P. The relationship between adult stature and longevity: tall men are unlikely to outlive their short peers – evidence from a study of all adult deaths in Poland in the years 2004–2008. Anthropol Rev. 2016; 79(4): 439–460, doi: 10.1515/anre-2016-0032.
10. Chmielewski PP, Strzelec B. Elevated leukocyte count as a harbinger of systemic inflammation, disease progression, and poor prognosis: a review. Folia Morphol. 2018; 77(2): 171–178, doi: 10.5603/FM.a2017.0101, indexed in Pubmed: 29064542.
11. Finch CE, Crimmins EM. Inflammatory exposure and historical changes in human life-spans. Science. 2004; 305(5691): 1736–1739, doi: 10.1126/science.1092556, indexed in Pubmed: 15375259.

144

12. Gunnell D, Rogers J, Dieppe P. Height and health: predicting longevity from bone length in archaeological remains. J Epidemiol Community Health. 2001; 55(7): 505–507, doi: 10.1136/jech.55.7.505, indexed in Pubmed: 11413182.

13. He Q, Morris BJ, Grove JS, et al. Shorter men live longer: association of height with longevity and FOXO3 genotype in American men of Japanese ancestry. PLoS One. 2014; 9(5): e94385, doi: 10.1371/journal.pone.0094385, indexed in Pubmed: 24804734.

14. Kabat GC, Anderson ML, Heo M, et al. Adult stature and risk of cancer at different anatomic sites in a cohort of postmenopausal women. Cancer Epidemiol Biomarkers Prev. 2013; 22(8): 1353–1363, doi: 10.1158/1055-9965.EPI-13-0305, indexed in Pubmed: 23887996.

15. Kemkes-Grottenthaler A. The short die young: the interrelationship between stature and longevity-evidence from skeletal remains. Am J Phys Anthropol. 2005; 128(2): 340–347, doi: 10.1002/ajpa.20146, indexed in Pubmed: 15861421.

16. Krzyżanowska M, Umławska W. Measured versus self--reported body height. Int J Anthropol. 2002; 17(2): 113–120, doi: 10.1007/bf02447402.

17. Little MA. Evolutionary strategies for body size. Front Endocrinol (Lausanne). 2020; 11: 107, doi: 10.3389/fendo.2020.00107, indexed in Pubmed: 32210916.

18. Maier AB, van Heemst D, Westendorp RGJ. Relation between body height and replicative capacity of human fibroblasts in nonagenarians. J Gerontol A Biol Sci Med Sci. 2008; 63(1): 43–45, doi: 10.1093/gerona/63.1.43, indexed in Pubmed: 18245759.

19. Marco-Gracia FJ, Puche J. The association between male height and lifespan in rural Spain, birth cohorts 1835-1939. Econ Hum Biol. 2021; 43: 101022, doi: 10.1016/j.ehb.2021.101022, indexed in Pubmed: 34139454.

20. Martorell R, Habicht JP, Yarbrough C, et al. Acute morbidity and physical growth in rural Guatemalan children. Am J Dis Child. 1975; 129(11): 1296–1301, doi: 10.1001/archpedi.1975.02120480022007, indexed in Pubmed: 1190161.

21. Miller RA, Harper JM, Galecki A, et al. Big mice die young: early life body weight predicts longevity in genetically heterogeneous mice. Aging Cell. 2002; 1(1): 22–29, doi: 10.1046/j.1474-9728.2002.00006.x, indexed in Pubmed: 12882350.

22. Nunney L. Size matters: height, cell number and a person's risk of cancer. Proc Biol Sci. 2018; 285(1889), doi: 10.1098/rspb.2018.1743, indexed in Pubmed: 30355711.

23. Olfert MD, Barr ML, Charlier CM, et al. Self-Reported vs. measured height, weight, and BMI in young adults. Int J Environ Res Public Health. 2018; 15(10), doi: 10.3390/ijerph15102216, indexed in Pubmed: 30314261.

24. Paajanen TA, Oksala NKJ, Kuukasjärvi P, et al. Short stature is associated with coronary heart disease: a systematic review of the literature and a meta-analysis. Eur Heart J. 2010; 31(14): 1802–1809, doi: 10.1093/eurheartj/ehq155, indexed in Pubmed: 20530501.

25. Pawlowski B, Dunbar RI, Lipowicz A. Tall men have more reproductive success. Nature. 2000; 403(6766): 156, doi: 10.1038/35003107, indexed in Pubmed: 10646589.

26. Perkins JM, Subramanian SV, Davey Smith G, et al. Adult height, nutrition, and population health. Nutr Rev. 2016; 74(3): 149–165, doi: 10.1093/nutrit/nuv105, indexed in Pubmed: 26928678.

27. Rietveld CA, Hessels J, van der Zwan P. The stature of the self-employed and its relation with earnings and satisfaction. Econ Hum Biol. 2015; 17: 59–74, doi: 10.1016/j.ehb.2015.02.001, indexed in Pubmed: 25756317.

28. Salaris L, Poulain M, Samaras TT. Height and survival at older ages among men born in an inland village in Sardinia (Italy), 1866-2006. Biodemography Soc Biol. 2012; 58(1): 1–13, doi: 10.1080/19485565.2012.666118, indexed in Pubmed: 22582890.

29. Samaras TT. Shorter height is related to lower cardiovascular disease risk: a narrative review. Indian Heart J. 2013; 65(1): 66–71, doi: 10.1016/j.ihj.2012.12.016, indexed in Pubmed: 23438615.

30. Sear R, Marlowe FW. How universal are human mate choices? Size does not matter when Hadza foragers are choosing a mate. Biol Lett. 2009; 5(5): 606–609, doi: 10.1098/rsbl.2009.0342, indexed in Pubmed: 19570778.

31. Sear R. Height and reproductive success: How a Gambian population compares with the west. Hum Nat. 2006; 17(4): 405–418, doi: 10.1007/s12110-006-1003-1, indexed in Pubmed: 26181610.

32. Sohn K. Now, the taller die earlier: the curse of cancer. J Gerontol A Biol Sci Med Sci. 2016; 71(6): 713–719, doi: 10.1093/gerona/glv065, indexed in Pubmed: 25991828.

33. Wilhelmsen L, Svärdsudd K, Eriksson H, et al. Factors associated with reaching 90 years of age: a study of men born in 1913 in Gothenburg, Sweden. J Intern Med. 2011; 269(4): 441–451, doi: 10.1111/j.1365-2796.2010.02331.x, indexed in Pubmed: 21175902.

34. Wirén S, Häggström C, Ulmer H, et al. Pooled cohort study on height and risk of cancer and cancer death. Cancer Causes Control. 2014; 25(2): 151–159, doi: 10.1007/s10552-013-0317-7, indexed in Pubmed: 24173535.

35. You C, Zhou Z, Wen J, et al. Polygenic scores and parental predictors: an adult height study based on the United Kingdom biobank and the Framingham heart study. Front Genet. 2021; 12: 669441, doi: 10.3389/fgene.2021.669441, indexed in Pubmed: 34093660.

ORIGINAL ARTICLE

VIA MEDICA

Three-dimensional volumetric analyses of temporal bone pneumatization from early childhood to early adulthood in a South African population

Okikioluwa Stephen Aladeyelu[1], Samuel Oluwaseun Olojede[1], Sodiq Kolawole Lawal[1], Matome Nadab Matshipi[1], Andile Lindokuhle Sibiya[2, 3], Carmen Olivia Rennie[1], Wonder-Boy Eumane Mbatha[4, 5]

[1]Discipline of Clinical Anatomy, School of Laboratory Medicine and Medical Sciences, Nelson R. Mandela School of Medicine Campus, University of Kwazulu-Natal, South Africa
[2]Discipline of Otorhinolaryngology, Head and Neck Surgery, School of Clinical Medicine, Nelson R. Mandela School of Medicine Campus, University of Kwazulu-Natal, South Africa
[3]ENT Department, Inkosi Albert Luthuli Central Hospital, Durban, South Africa
[4]Radiology Department, Inkosi Albert Luthuli Central Hospital, Durban, South Africa
[5]Lake, Smit and Partners Inc., Durban, South Africa

Background: A debate exists on whether the size of temporal bone pneumatization is a cause or consequence of otitis media (a global disease burden). However, a normal middle-ear mucosa is a prerequisite for normal temporal bone pneumatization. This study investigated the size of temporal bone pneumatization with age and the normal distribution of air cell volume in different stages of human growth postnatally.

Materials and methods: A three-dimensional computer-based volumetric-rendering technique was performed bilaterally on 248 head/brain and internal acoustic meatus computed tomography images of slice thickness ≤ 0.6 mm consisting of 133 males and 115 females with age range 0–35 years.

Results: The average volume of infant (0–2 years) pneumatization was 1920 mm³ with an expected rapid increase to about 4510 mm³ in childhood (6–9 years). The result also showed a significant increase (p < 0.001) in the volume of air cells up to the young adult stage I (19–25 years), followed by a significant decline in young adult stage II (26–35 years). However, the females were observed to experience an earlier increase than males. Also, population differences were observed as the Black South African population group showed a higher increase in volume with age than the White and Indian South African population groups, though the volumes of the latter increased up to young adult stage II.

Conclusions: This study concludes that the pneumatization of a healthy temporal bone is expected to continue a linear increase up until at least adult stage I. Termination of temporal bone pneumatization in an individual before this stage could signify pathologic involvement of the middle ear during childhood. (Folia Morphol 2024; 83, 1: 146–156)

Keywords: pneumatization, temporal bone, air cells, three-dimensional

Address for correspondence: Dr. Okikioluwa Stephen Aladeyelu, Discipline of Clinical Anatomy, School of Laboratory Medicine and Medical Sciences, Nelson R. Mandela School of Medicine Campus, University of Kwazulu-Natal, South Africa, 719, Umbilo Road, Private Bag 7 Congella 4013, Durban, KwaZulu-Natal, South Africa, tel: +27656975373, e-mail: aladeyeluo@ukzn.ac.za

INTRODUCTION

Since the interest of science in the temporal bone and ear dating back to 'Hippocrates' (460 B.C.), studies regarding the development of temporal bone pneumatization or the size of air cells with age remain minimal [1, 15, 45]. Embryologically, the temporal bone pneumatization or air cell system begins between the 22nd and 24th week of intrauterine life, as the mastoid antrum (the only visible cell) begins to develop during this period [15, 45]. During late foetal life or at birth, the mastoid antrum (the large central air cell) is fully developed, either pneumatized or filled with embryonic connective tissue [8, 15]. After birth, temporal bone air cells become readily visible as hollowed-out spaces lined by flattened, non-ciliated squamous epithelium [27, 38, 40]. As postnatal development and growth continue, these air cells exhibit variability in size and extent, communicating with the middle ear via the mastoid antrum and the aditus ad antrum and extending variably to the petrous apex and around the inner ear [24, 39, 45]. However, a gradual reduction in air cells is expected throughout life as the individual continues growing older [48].

Although the prevalence of minimal pneumatization of temporal bones in connection with chronic inflammatory middle-ear disease is well known, controversy about the relationship between temporal bone pneumatization and chronic middle-ear disease still exists [12, 25, 42]. A common infection to the middle ear is otitis media (OM) which still exists as one of the global burdens of diseases and a predisposing factor to hearing loss with increasing prevalence in sub-Saharan Africa with South Africa inclusive [11, 31, 41, 46]. More so, studies in South Africa revealed an 8.2% prevalence rate of OM among children [9, 13, 32]. Recent studies have shown an increased incidence rate of OM among younger and older children, with 31.4% and 16.7% prevalence, respectively [6, 34]. It was also recorded as the major significant risk factor for the high prevalence of hearing loss (up to 19.88%) [20, 28].

Much as genetically determined hypo-cellularity predisposes to acute and chronic otitis, the concrete fact remains that a normal middle-ear mucosa is a prerequisite for normal pneumatization, which may be hampered throughout childhood by inflammation, infection, and poor tubal function [12, 25, 42]. Another substantiated fact is that the onset of middle--ear infection such as OM has been linked to the development of the temporal bone pneumatization and air cell system, which in turn tends to affect the size of the air cells with age [3, 25]. Evidence has demonstrated that a temporal bone pneumatization with larger air cells tends to improve functional results after surgery (e.g. *mastoidectomy*) than one with smaller air cells [25, 30]. Among major theories, the hereditary theory explains the factors determining an individual pneumatization. However, the normal size of air cells and growth rate within a population should not be disregarded since there is an established link between OM and the size of pneumatization. On this account, there is a paucity of information on the normal size of the air cells and growth rate concerning a particular population, especially in sub-Saharan Africa and South Africa.

Several reports have utilized different techniques to measure the size of the temporal bone or mastoid pneumatization quantitatively. These techniques include the water-weight, acoustic and pressurized transducer [2, 30]. Following the development of radiological tools, more accurate and easier methods have been developed and mostly employed in measuring the size of temporal bone pneumatization in area or volume.

Various studies have been identified to utilize different radiological tools in evaluating the size of temporal bone pneumatization with age [4, 7, 12, 15, 18, 21, 27, 35, 37]. These studies, however, have revealed changes in the size of air cells with age and discrepancies in growth rates. These reported discrepancies may be due to different methods or techniques used and the differences in age, sex, and population groups of the study populations, with the highest growth rate reported to be around the third decade of life among the Korean population [27] and age-related changes (beginning from infants; 0–2 years) in the bony organization of pneumatized spaces in various regions of the temporal bone reported in Missouri, Columbia [15].

Although both areas (2D sizes) and volumes (3D sizes) were used to measure the size of air cells in these studies, volumetric analysis, which likely gives the foremost comprehensive insight to appreciate the air cells estimate, was limited to 3 studies [15, 18, 27]. In addition, the slice thickness of computed tomography (CT) images used in those studies ranges between 1 mm to 2.5 mm. Precision in quantifying air cells requires very thin slices of about 0.6 mm and below, which brings about the limitations of these studies.

147

Table 1. Distribution of patients according to age groupings, sex and population groups

Age groupings [years]	Overall (n = 248)			Black South African (n = 202)			Indian South African (n = 28)			White South African (n = 18)		
	Male	Female	Total	Male	Female	Total	Male	Female	Total	Male	Female	Total
0–2	12	10	22	10	8	18	1	1	2	1	1	2
3–5	11	13	24	8	12	20	2	0	2	1	1	2
6–9	22	15	37	18	12	30	1	3	4	2	1	3
10–14	39	14	53	34	12	46	3	1	4	2	1	3
15–18	10	16	26	9	13	22	1	1	2	0	2	2
19–25	14	22	36	11	19	30	1	2	3	2	1	3
26–35	25	25	50	16	20	36	7	4	11	2	1	3

The present study focuses on the CT images of slice thickness ≤ 0.6 mm for precision in volumetric quantification of air cells utilizing a 3D computer-based volume rendering technique arriving at a more accurate volume as possible to achieve a normal distribution of air cells with age as well as the growth rate in other to ascertain the development of temporal bone pneumatization from early childhood to adulthood. In addition, this study also considered sex, laterality, and population groupings.

MATERIALS AND METHODS

Study design and population

Following ethical approval obtained from the University of KwaZulu-Natal Biomedical Research Ethics Committee (Protocol Ref. No.: BREC/00002263/2020) and ethical clearance obtained from the National Health Research Committee of the Kwazulu-Natal Department of Health (NHRD Ref.: KZ_202102_026), 248 head and neck/ /brain and internal acoustic meatus (IAM) CT images of South African patients (133 males, 115 females) from the radiology departments of public hospitals in Durban and Pietermaritzburg, Kwazulu-Natal, South Africa were retrospectively retrieved, reviewed and analysed bilaterally (giving a total of 496) from January 2011 to August 2021. These CT scans were selected because they meet the inclusion criteria, which are as follows; a) scans of patients between the age range 0–35 years; b) high-resolution multidetector CT images acquired with ≤ 0.6 mm collimation; c) images without observable signs of abnormal pathological processes in the temporal bone or compatible with chronic otitis and/or mastoiditis on CT; d) images of patients with no history of middle ear infection such as OM and any other pathology (by reviewing patients' medical history), and e) absence of bony destruction, fluid, or mass in any of the temporal bone air spaces.

The age range of 0 to 35 years was further conveniently subdivided into seven levels: 0–2 (infant); 3–5 (young child); 6–9 (middle child); 10–14 (early adolescent); 15–18 (middle adolescent); 19–25 (young adult stage I); 26–35 (young adult stage II). Age categorization was similar to that reported by Hill [15]: according to age-related changes in the bony organization of pneumatized spaces in various regions of the temporal bone. The distribution of patients in the age categorization used for this study is presented in Table 1.

The South African population groups included in this study were as follows; Black South African (202; 81.4%), Indian South African (28; 11.3%), and White South Africans (18; 7.3%) (Table 1). (Note: Generally, of the South African population, Black South Africans make up about 79.8%, White South Africans make up about 8.7%, while Asian/Indians make up about 2.5%) [22, 26].

Imaging protocol

The head and neck, and IAM CT images were taken using a multi-detector row computed tomography (MDCT) scanner (GE Revolution Evo 64 slice, 128 configuration, Milwaukee, Wisconsin, USA). The axial view was reconstructed parallel to the orbito-meatal line using a slice thickness of 0.625 mm, detector coverage of 20 mm, and a PITCH of 0.5. The scan was performed using 140 kV and modulated mAs ranging between 280–400 mA with 30% dose reduction and ASIR-V application in a bony algorithm with a window width of > 3000 hU and a window centre of 500 hU.

Calculation of 3D volume of air cells of the temporal bone

Continuous non-overlapping temporal bone CT scans with acquisition parameters of ≤ 0.6 mm slice thickness, 140 kV, and modulated mAs ranging between 280–400 mA were used for this study. The DICOM images stored in the PACS of these hospitals were transferred to a Workstation running IntelliSpace Portal (ISP) Version 11.1 (Philips Image and Information Management software, Nederland).

With a surface rendering algorithm of lowest limit window level of –1,024 hU and uppermost limit window level of –318 hU, the clip and 3D segmentation process were used to achieve 3D reconstruction and the volume of air cells of each temporal bone. The axial image was double-clicked in other to be enlarged. Next, 3D models were created using a smart segmentation process. The IntelliSpace Portal (ISP) Version 11.1 then provided a calculator that automatically calculates the volume of each 3D reconstructed temporal bone pneumatization from the mastoid process to the petrous apex, including the middle ear (Fig. 1).

Inter-observer reliability testing

The accuracy and repeatability of the volume calculation were determined by using 50 randomly selected temporal bone CT scans independently by two authors, and a third observer (Specialist Radiologist) verified the volumetric calculation for inter-observer reliability.

Statistical analysis

The statistical data analysis was conducted in R Statistical computing software of the R Core Team, 2020, version 3.6.3, and presented in the form of descriptive and inferential statistics. The continuous variables were non-normal and were presented in median (interquartile ranges). The median differences were assessed using Wilcoxon for two groups. The median differences across at least three categorical variable levels (in the case of population group) were assessed with the aid of Kruskal-Wallis. In the case of significant median difference, post-hoc tests were conducted using the Dunn test. All the inferential statistical analysis tests were conducted at 5% significance levels.

RESULTS

Data from 496 HRCT temporal bones (right and left side) of 248 patients' scans were presented as the median and interquartile range (IQR). The intraclass correlation was 89% for volumetric calculation for inter-observer reliability testing.

Average volume (mm³) of temporal bone pneumatization according to laterality, sex, and population group

The average volume of temporal bone pneumatization in this study population was 8300 mm³ (interquartile range of 4100–12200 mm³). The result presented in Table 2 showed no significant difference in the average volume of temporal bone pneumatization as regards laterality (p = 0.719), sex (p = 0.363), and population group (p = 0.416) using Ranksum and Kruskal-Wallis tests.

The volume of temporal bone pneumatization with age

From early childhood to adulthood, the average volumes of temporal bone pneumatization of infants (0–2 years), children (3–9 years), adolescents (10–18 years), and adults (19–35 years) were 1920 mm³, 6005 mm³, 11750 mm³, and 11550 mm³, respectively. In general, the Kruskal-Wallis test showed a significant difference (p < 0.001) in the volume of temporal bone pneumatization between age groups (Table 3), with a linear and rapid increase at an average of 2400 mm³ between age groups up to 19–25 years followed by a decrease (Fig. 2). However, the volume of temporal bone pneumatization was higher on the right side, as shown in Figure 2.

The volume of temporal bone pneumatization with age concerning sex

The Kruskal-Wallis test showed a significant difference (p < 0.001) in the volume of temporal bone pneumatization with age groups in males and females. In the distribution of the volume of air cells with age, a decrease in pneumatization was also observed after the age group 19–25 years, but the females showed a more rapid increase in pneumatization of the temporal bone earlier (6–9 years) than males (Table 4). However, pneumatization in males was observed to follow a rapid linear growth between the age groups 10–14 years and 19–25 years (Fig. 3).

The volume of temporal bone pneumatization with age concerning population groups

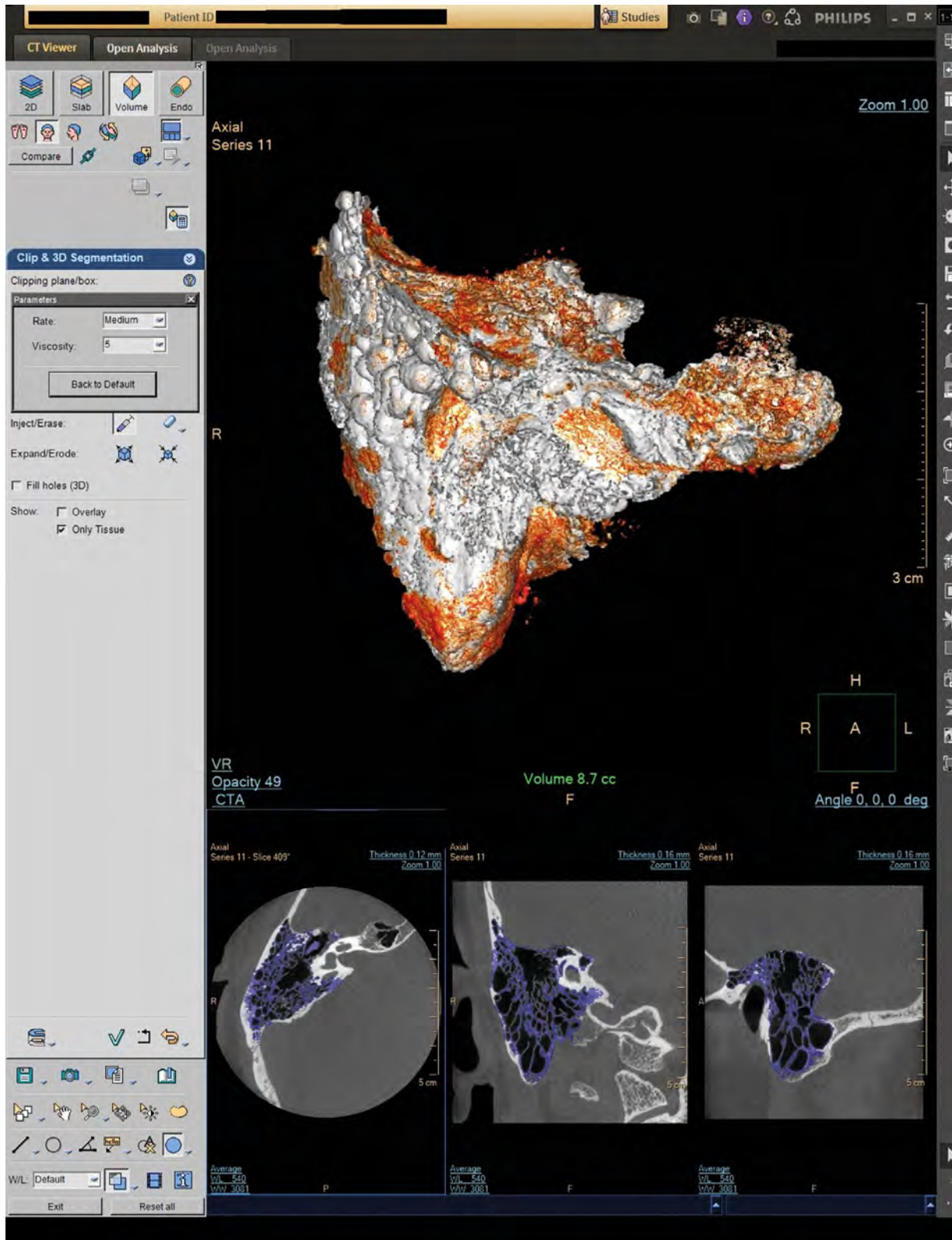The Kruskal-Wallis test showed a significant difference (p < 0.001) in the volume of temporal bone

Figure 1. Three-dimensional using computer-based volume rendering reconstruction technique. Pneumatization of the right temporal bone composing the middle ear, petrous, and mastoid air cells with a volume of 8.7 cc (cubic centimetre) (Conversion to cubic millimetres = 8700 mm³).

Table 2. Average volume (mm³) of temporal bone pneumatization according to laterality, sex, and population group

Laterality			Sex			Population group			
Left Median (IQR)	Right Median (IQR)	L vs. R	Male Median (IQR)	Female Median (IQR)	M vs. F	SA Black Median (IQR)	Indian Median (IQR)	White Median (IQR)	B vs. I vs. W
7830 mm³ (3860–12200)	8500 mm³ (4210–12200)	P = 0.719	8510 mm³ (4340–12100)	8900 mm³ (4550–12700)	P = 0.363	7580 mm³ (4010–12200)	9400 mm³ (4400–10800)	9900 mm³ (3060–10900)	P = 0.416

L — left; R — right; M — male; F— female; SA — South African; B — black; I — Indian; W — white; IQR — interquartile range
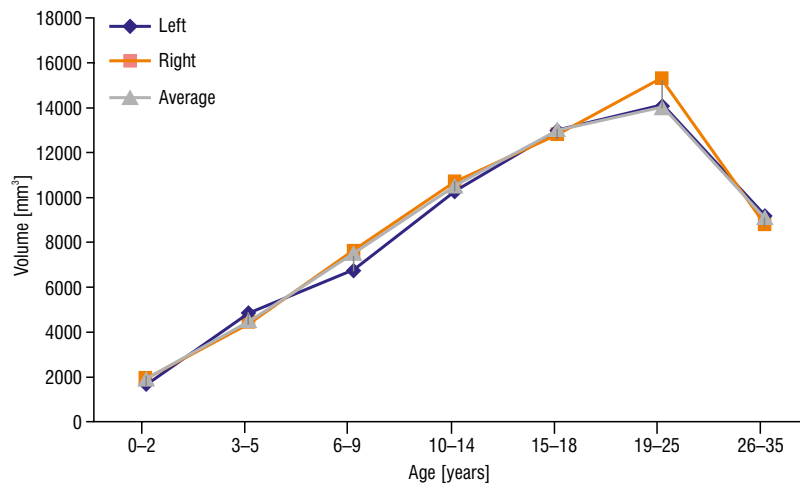
Figure 2. Distribution of volumes of temporal bone pneumatization of left and right sides according to human stages of development.

Table 3. Median volumes (mm³) and interquartile range of temporal bone pneumatization according to age groups of human stages of development (overall and laterality)

Laterality	Age groups [years]							P-value
	0–2 (n = 22)	3–5 (n = 24)	6–9 (n = 37)	10–14 (n = 53)	15–18 (n = 26)	19–25 (n = 36)	26–35 (n = 50)	
Left [mm³] Median (IQR)	1680 (1510–2910)	4880 (4990–9190)	6750 (4990–9190)	10300 (7000–11800)	13000 (9360–18600)	14100 (8230–14500)	9840 (3810–14500)	< 0.001*
Right [mm³] Median (IQR)	1950 (1450–2400)	4330 (3910–5450)	7600 (5300–8790)	10700 (7090–12400)	12800 (8120–15000)	15300 (11100––18900)	8800 (4750–12400)	< 0.001*
Both sides [mm³] (average) Median (IQR)	1920 (1450–2450)	4510 (4010–5450)	7500 (5080–8840)	10500 (6950–12100)	13000 (9420–18900)	14000 (7970–15000)	9100 (4240––113900)	< 0.001*

IQR — interquartile range

pneumatization with age groups among the Black South African population. Still, it showed no significant difference in the volume of temporal bone pneumatization with age groups among the Indians and Whites with p = 0.053 and p = 0.058, respectively (Table 5). In the distribution of the volume of air cells with age, a rapid linear increase in the volume of air cells was observed among South African Blacks from 0–2 years up to 19–25 years, afterward a decline. However, a slow increase in air cell volume was observed in the Indian and White population from 3–5 years, continuing up to 26–35 years (Fig. 4).

DISCUSSION

The interest in the size of temporal bone pneumatization and its importance arose from the association between mastoid air cells and OM either as a cause or a consequence. Concerning human development

Table 4. Median volume (mm³) and interquartile range of temporal bone pneumatization of males and females according to age groups of human stages of development

Male

Age range [years]	0–2 (n = 12)	3–5 (n = 11)	6–9 (n = 22)	10–14 (n = 39)	15–18 (n = 10)	19–25 (n = 14)	26–35 (n = 25)	P-value
Volume [mm³] Median (IQR)	1940 (1410–2480)	4320 (3550–4880)	5570 (3920–8300)	10600 (6930–12000)	13600 (10800–14100)	16700 (8830–20800)	9700 (5800–16100)	< 0.001*

Female

Age range [years]	0–2 (n = 10)	3–5 (n = 13)	(6–9 (n = 15)	10–14 (n = 14)	15–18 (n = 16)	19–25 (n = 22)	26–35 (n = 25)	P-value
Volume [mm³] Median (IQR)	1920 (1510–2450)	5230 (4170–5800)	8100 (6650–9880)	11500 (7300–12500)	13000 (10900–17100)	15000 (7900–15100)	9100 (3880–12300)	< 0.001*
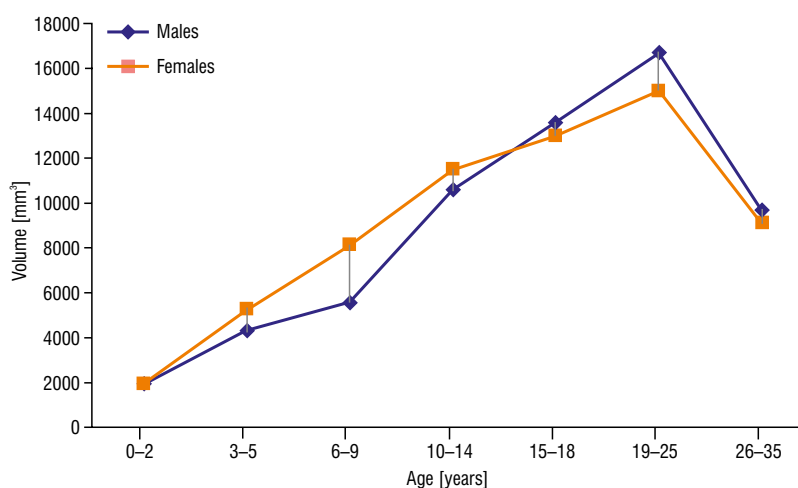
Figure 3. Distribution of volumes of temporal bone pneumatization of males and females according to human stages of development.
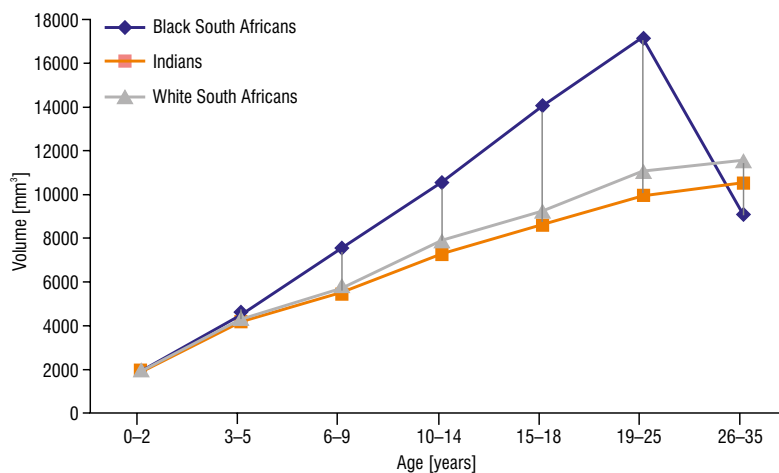
Figure 4. Distribution of volumes of temporal bone pneumatization of Black South Africans, South African Indians, and White South Africans according to human stages of growth.

and growth, Virapongse et al. [45] described changes in the size of temporal bone pneumatization to occur in three stages: "the infantile stage — occurring from birth to two years of age (air cells begin to appear and are readily visible by two years); transitional stage — from two to five years (squamomastoid/mastoid

Table 5. Population group distribution median volume (mm³) and interquartile range of temporal bone pneumatization according to age groups of human stages of growth

Black South African

Age range [years]	0–2 (n = 18)	3–5 (n = 20)	6–9 (n = 30)	10–14 (n = 46)	15–18 (n = 22)	19–25 (n = 30)	26–35 (n = 36)	P-value
Volume [mm³] Median (IQR)	1920 (1450–2450)	4470 (4010–5450)	7500 (5140–8790)	10500 (7010–15000)	14000 (7970–15000)	17100 (9200–19300)	9100 (4130–13700)	< 0.001*

Indian South African

Age range [years]	0–2 (n = 2)	3–5 (n = 2)	6–9 (n = 4)	10–14 (n = 4)	15–18 (n = 2)	19–25 (n = 3)	26–35 (n = 11)	P-value
Volume [mm³] Median (IQR)	1920 (1510–2450)	4210 (3100–4400)	5510 (5510–5510)	7270 (5860–9360)	8600 (7100–10200)	9900 (7680–10400)	10500 (8900–11800)	0.053

White South African

Age range [years]	0–2 (n = 2)	3–5 (n = 2)	6–9 (n = 3)	10–14 (n = 3)	15–18 (n = 2)	19–25 (n = 3)	26–35 (n = 3)	P-value
Volume [mm³] Median (IQR)	1950 (1510–2480)	4300 (3500–4850)	5700 (4250–5900)	7900 (5910–9600)	9200 (7200–10900)	11000 (7550–11500)	11500 (7840–11500)	0.053

undergoes gradual enlargement with the migration of air cells toward the periphery); and adult stage — age 6 and above (attainment of this stage result in cessation of pneumatization)". Cinamon [10] also supported this description and further identified that air cells continue to increase in size until puberty, while Aladeyelu et al. [1] identified a continuous increase in the size of air cells beyond puberty.

Two theories on pneumatization have been hypothesized: the first is that the size of air cells in temporal bone pneumatization is genetically determined [12]; while the second is that the size of air cells in temporal bone pneumatization is determined by the degree of pathologic involvement of the middle ear during childhood [14, 33, 44]. The second hypothesis validated this study as the degree of pathologic involvement during life may influence the size of mastoid pneumatization with age. Although considering the first theory, there may be a few limitations resulting from interindividual variation. However, to overcome these limitations, a longitudinal study needs to be employed, which would be a dilemma and seem impossible in practice as it would involve tracking all subjects daily for scanning and measurement and could take an entire career of these subjects to measure the size of their air cells. Hence, the second hypothesis appears to be widely used and generally accepted [4, 7, 15, 18, 21, 27, 35, 37, 43].

This study utilized a 3D computer-based volumetric-rendering technique on head/brain and inner ear CT images of slice thicknesses of ≤ 0.6 mm. The average volumes of infants, children, adolescents, and

adults' temporal bone pneumatization obtained in this study were quite higher than the previous reports [15, 17–19, 23, 25, 27, 29]. This discrepancy may be due to technical characteristics (e.g. 0.6 mm slice thickness which gives more detailed volumetric information) or population differences. It may also be due to the cranial size and shape of the study population. Hence, the average air cell volumetric size of temporal bone pneumatization in a South African population is higher than in other age-related studies reported in Japanese, Korean, and Colombian populations [15, 18, 27]. The temporal bone pneumatization with average volumes of 1920 mm³ in paediatrics and 4510 mm³ in young children indicates that pneumatization of the temporal bone is expected to follow a rapid growth during childhood development. This finding agrees with previous studies, which reported that air cells are readily visible after birth and immediately begin to increase in size and extent [24, 40].

In this study, various developmental stages were subdivided into the infant, young child, middle child, early adolescents, middle adolescents, young adult stage I, and young adult stage II to reflect human postnatal growth stages and understand the possible age when pneumatization ceases. An evident increase in the volume of temporal bone pneumatization relative with age until young adult stage I and reduction in the volume of air cells as well as cessation in pneumatization in young adult stage II observed in this study concurs with the previous study that linked aging-related changes to reduction in air cells [48]. In contrast, this finding contradicts the previous reports

about pneumatization terminating at puberty though these reports utilized planimetric measurements and were only to give information on the area of air cells, not volume [4, 12, 35].

Notably, a significant increase in pneumatization volumes in different age groups in relation to sex was observed in this study. But the females showed a much earlier rapid increase in the volume of temporal bone pneumatization before the onset of puberty (6–9 years) which is similar to the report of Diamant [12] that utilized surface area and Hill [15] that utilized both 2D and 3D methods. This may, however, be linked to early puberty in females [10]. However, the males were observed to have a larger pneumatization at late puberty up to the young adult stage I, which is similar to the previous study by Chatterjee et al. [7] that utilized 2D planimetric measurements of temporal bone pneumatization. This implies that the development of temporal bone pneumatization tends to be more rapid in adolescent females, with the females first attaining adult size before adolescent males.

Furthermore, differences were also observed among population groups within the study population. The present study considered three groups: Black South Africans (indigenous African origin or Native group), White South Africans (European descent), and Indians (Asian descent). Although the paediatric volume was about the same size with a rapid increase in volume during childhood development, the volume of temporal bone pneumatization was observed to increase significantly with age showing a rapid linear growth up to the young adult stage I among the Black South Africans. The significant increase in the volume of pneumatization observed from the young child to young adult stage I conforms with the increase in the volume of paranasal air sinus in the same stages of postnatal growth in a South African population as reported by Rennie et al. [36]. Kim et al. [23] also identified a correlation between pneumatization of mastoid air cells and paranasal air sinus.

However, among the South African White and Indians, the volume of temporal bone pneumatization follows a rapid increase from infant up to the young child (3–5 years), followed by a slow increase up to the young adult stage I; thereafter, a plateau with no significant difference. This could be attributed to the small skull sizes, especially among Indians, because the skull size influences the pneumatization of the temporal bone [5, 7, 16]. In addition, the early study

of Arora et al. [4] also identified this attribute while working with the population in the Northern part of the Indian subcontinent and found the size of the temporal bone air cell system to have a value much less than that of the Swedish population in the study of Diamant [12] and assumed that it could be due to the smaller sized cranial bones of Indians. Although, there were no significant differences in the volume of temporal bone pneumatization within age groups among Indians and White. However, the continuous increase in the pneumatization among these two population groups up to young adult stage II conforms with the previous study among the Korean population of Asian descent [27].

Although the two hypothesized theories of pneumatization (genetic and environmental) have described the relationship between temporal bone pneumatization and middle-ear diseases to be "a chicken and egg" tale [14, 44], a small pneumatization of the temporal bone could possibly permit normal ventilation of the ear. However, a small mastoid system predisposes to acute and chronic OM. Consequently, the degree of pathologic involvement of the middle ear during childhood, such as acute and chronic OM, is well known to be a determinant factor in temporal bone pneumatization. The present study has been able to analyse healthy temporal bones in order to know the expected size of normal temporal bone pneumatization at every stage of human growth, ascertaining its growth rate and completion stage in adult life. This study also utilized a method with high accuracy and hope that it will contribute to establishing general references of what is expected to be the size of temporal bone volume and size as regards to age and development, which could help give an understanding of the history of the middle-ear of any patient, most especially during childhood.

CONCLUSIONS

This study investigated the size of temporal bone pneumatization from early childhood to adulthood utilizing a 3D computer-based volumetric rendering technique of normal CT images of slice thickness of ≤ 0.6 mm. A rapid increase in the size of pneumatization was observed during childhood development, with females showing a more rapid increase. In addition, the volume of air cells was observed to increase at an average of 2400 mm^3 at every stage of human postnatal growth, with a higher volume of the right temporal bone up to the young adult stage I before

experiencing a decline. Population group differences were also observed in the distribution of air cells as the volume of temporal bone pneumatization of other population groups aside from Black South Africans increased up to adult stage II. The study concludes that the pneumatization of a healthy temporal bone is expected to continue linear increase up until at least adult stage I (19–25 years). This study hopes that its findings will contribute significantly to achieving a unanimous age landmark expected for the temporal bone pneumatization to be complete among otolaryngologists. Furthermore, it could also be useful in anatomical and forensic sciences for predicting age by evaluating the volume of temporal bone air cells of skulls.

Ethical approval

Acknowledgments

Conflict of interest: None declared

REFERENCES

1. Aladeyelu OS, Olaniyi KS, Olojede SO, et al. Temporal bone pneumatization: A scoping review on the growth and size of mastoid air cell system with age. PLoS One. 2022; 17(6): e0269360, doi: 10.1371/journal.pone.0269360, indexed in Pubmed: 35657972.
2. Andreasson L, Mortensson W. Comparison between the area and the volume of the air-filled ear space. Acta Radiol Diagn (Stockh). 1975; 16(4): 347–352, doi: 10.1177/028418517501600405, indexed in Pubmed: 1189960.
3. Aoki K, Esaki S, Honda Y, et al. Effect of middle ear infection on pneumatization and growth of the mastoid process. An experimental study in pigs. Acta Otolaryngol. 1990; 110(5-6): 399–409, doi: 10.3109/00016489009107461, indexed in Pubmed: 2284915.
4. Arora M, Sain U, Sodhi JS. Mastoid pneumatization in children — a roentgenographic planimetric study. Indian J Otolaryngol. 1973; 25(2): 87–90, doi: 10.1007/bf02993885.
5. Balzeau A, Girmaud-Herve D, Semah F. Characteristics and variation of the temporal bone pneumatization in Asian Homo errectus. EurASEAA, Bougon papers. 2006; 21–27.
6. Biagio L, Swanepoel DW, Laurent C, et al. Paediatric otitis media at a primary healthcare clinic in South Africa. S Afr Med J. 2014; 104(6): 431–435, doi: 10.7196/samj.7534, indexed in Pubmed: 25214254.
7. Chatterjee D, Ghosh TB, Ghosh BB. Size variation of mastoid air cell system in Indian people at different age groups: a radiographic planimetric study. J Laryngol Otol. 1990; 104(8): 603–605, doi: 10.1017/s0022215100113349, indexed in Pubmed: 2230550.
8. Cheatle AH. The infantile types of mastoid with ninety-six specimens. J Laryngol. 1907; 22: 56.
9. Cilliers NJ, Merwe AV, Hurter M, et al. The manifestation of middle ear pathology in an elderly group. S Afr J Commun Disord. 1988; 35(1), doi: 10.4102/sajcd.v35i1.304.
10. Cinamon U. The growth rate and size of the mastoid air cell system and mastoid bone: a review and reference. Eur Arch Otorhinolaryngol. 2009; 266(6): 781–786, doi: 10.1007/s00405-009-0941-8, indexed in Pubmed: 19283403.
11. DeAntonio R, Yarzabal JP, Cruz JP, et al. Epidemiology of otitis media in children from developing countries: A systematic review. Int J Pediatr Otorhinolaryngol. 2016; 85: 65–74, doi: 10.1016/j.ijporl.2016.03.032, indexed in Pubmed: 27240499.
12. Diamant M. Otitis and pneumatization of the mastoid bone. Acta Otolaryngol. 1940; 41.
13. Halama AR, Voogt GR, Musgrave GM. Prevalence of otitis media in children in a black rural community in Venda (South Africa). Int J Pediatr Otorhinolaryngol. 1986; 11(1): 73–77, doi: 10.1016/s0165-5876(86)80030-1, indexed in Pubmed: 3710702.
14. Han SJ, Song MH, Kim J, et al. Classification of temporal bone pneumatization based on sigmoid sinus using computed tomography. Clin Radiol. 2007; 62(11): 1110–1118, doi: 10.1016/j.crad.2007.04.019, indexed in Pubmed: 17920872.
15. Hill CA. Ontogenetic change in temporal bone pneumatization in humans. Anat Rec (Hoboken). 2011; 294(7): 1103–1115, doi: 10.1002/ar.21404, indexed in Pubmed: 21618436.
16. Inal M, Muluk N, Dağ E, et al. The pitfalls and important distances in temporal bones HRCT of the subjects with high jugular bulb - preliminary review. Adv Clin Exp Med. 2015; 24(2): 315–324, doi: 10.17219/acem/40472.
17. Isono M, Murata K, Azuma H, et al. Computerized assessment of the mastoid air cell system. Auris Nasus Larynx. 1999; 26(2): 139–145, doi: 10.1016/s0385-8146(98)00055-8, indexed in Pubmed: 10214891.
18. Isono M, Ito A, Nakayama K, et al. Computerized assessment of developmental changes in the mastoid air cell system. Int Congr Ser. 2003; 1254: 487–491, doi: 10.1016/s0531-5131(03)01061-6.
19. Jadhav AB, Fellows D, Hand AR, et al. Classification and volumetric analysis of temporal bone pneumatization using cone beam computed tomography. Oral Surg Oral Med Oral Pathol Oral Radiol. 2014; 117(3): 376–384, doi: 10.1016/j.oooo.2013.12.398, indexed in Pubmed: 24528795.
20. Joubert K, Botha D. Contributing factors to high prevalence of hearing impairment in the Elias Motsoaledi Local

Municipal area, South Africa: A rural perspective. S Afr J Commun Disord. 2019; 66(1): e1–e7, doi: 10.4102/sajcd.v66i1.611, indexed in Pubmed: 30843412.

21. Kawamura S, Okabe K, Mogi S, et al. [The normal development of the mastoid pneumatic cells]. J Otorhinolaryng Soc Jap. 1963; 66: 909–912, doi: 10.3950/jibiinko-ka.66.909, indexed in Pubmed: 14075498.

22. Khalfani A, Zuberi T. Racial classification and the modern census in South Africa, 1911–1996. Race Soc. 2001; 4(2): 161–176, doi: 10.1016/s1090-9524(03)00007-x.

23. Kim J, Song SW, Cho JH, et al. Comparative study of the pneumatization of the mastoid air cells and paranasal sinuses using three-dimensional reconstruction of computed tomography scans. Surg Radiol Anat. 2010; 32(6): 593–599, doi: 10.1007/s00276-009-0618-4, indexed in Pubmed: 20047049.

24. Knipe H, Hacking C. Mastoid air cells. Reference article, Radiopaedia.org. 2014 Mar 23. https://doi.org/10.53347/rID-28366 (revised 2021 Nov 19; accessed 2021 Dec 26).

25. Koç A, Ekinci G, Bilgili AM, et al. Evaluation of the mastoid air cell system by high resolution computed tomography: three-dimensional multiplanar volume rendering technique. J Laryngol Otol. 2003; 117(8): 595–598, doi: 10.1258/002221503768199906, indexed in Pubmed: 12956911.

26. L'Abbé EN, Rooyen CV, Nawrocki SP, et al. An evaluation of non-metric cranial traits used to estimate ancestry in a South African sample. Forensic Sc Int. 2011; 209(1-3): 195.e1–195.e7, doi: 10.1016/j.forsciint.2011.04.002.

27. Lee DH, Jun BC, Kim DG, et al. Volume variation of mastoid pneumatization in different age groups: a study by three-dimensional reconstruction based on computed tomography images. Surg Radiol Anat. 2005; 27(1): 37–42, doi: 10.1007/s00276-004-0274-7, indexed in Pubmed: 15349696.

28. Louw C, De Wet S, Eikelboom RH, et al. Prevalence of hearing loss at primary health care clinics in South Africa. Afr Health Sci. 2018; 18(2): 313–320, doi: 10.4314/ahs.v18i2.16, indexed in Pubmed: 30602958.

29. Luntz M, Malatskey S, Tan M, et al. Volume of mastoid pneumatization: three-dimensional reconstruction with ultrahigh-resolution computed tomography. Ann Otol Rhinol Laryngol. 2001; 110(5 Pt 1): 486–490, doi: 10.1177/000348940111000516, indexed in Pubmed: 11372935.

30. Molvaer OI, Vallersnes FM, Kringlebotn M. The size of the middle ear and the mastoid air cell. Acta Otolaryngol. 1978; 85(1-2): 24–32, doi: 10.3109/00016487809121419, indexed in Pubmed: 626053.

31. Morris PS, Leach AJ. Acute and chronic otitis media. Pediatr Clin North Am. 2009; 56(6): 1383–1399, doi: 10.1016/j.pcl.2009.09.007, indexed in Pubmed: 19962027.

32. Nel M, Odendall W, Hurter M, et al. The occurrence and nature of hearing problems and middle ear pathologies with a group of black African urban children. S Afr J Commun Disord. 1988; 35(1): 25–30.

33. Palva T, Palva A. Size of the human mastoid air cell system. Acta Otolaryngol. 1966; 62(3): 237–251, doi: 10.3109/00016486609119570, indexed in Pubmed: 5970742.

34. Phanguphangu MC. Otoscopic examinations reveal high prevalence of outer and middle ear pathologies in paediatrics in Limpopo, South Africa. Int J Audiol. 2017; 56(4): 215–218, doi: 10.1080/14992027.2016.1244868, indexed in Pubmed: 27783901.

35. Qvarnberg Y. Acute otitis media. A prospective clinical study of myringotomy and antimicrobial treatment. Acta Otolaryngol Suppl. 1981; 375: 1–157, indexed in Pubmed: 6274132.

36. Rennie CO, Haffajee MR, Satyapal KS. Development of the paranasal air sinuses in a South African Population utilising three dimensional (3D) reconstructed models. Eur J Anat. 2017; 21(3): 197–209.

37. Rubensohn G. Mastoid pneumatization in children at various ages. Acta Otolaryngol. 1965; 60: 11–14, doi: 10.3109/00016486509126983, indexed in Pubmed: 14337947.

38. Schillinger R. Pneumatization of the Mastoid. Radiology. 1939; 33(1): 54–67, doi: 10.1148/33.1.54.

39. Schmalfuss IM. Petrous Aex. In: Chong V (ed.). Skull Base Imaging. Elsevier, Missouri 2018: 233–245.

40. Sethi A, Singh I, Agarwal AK, et al. Pneumatization of mastoid air cells: role of acquired factors. Int J Morphol. 2006; 24(1): 35–38, doi: 10.4067/s0717-95022006000100007.

41. Tesfa T, Mitiku H, Sisay M, et al. Bacterial otitis media in sub-Saharan Africa: a systematic review and meta-analysis. BMC Infectious Diseases. 2020; 20(1), doi: 10.1186/s12879-020-4950-y.

42. Todd NW, Pitts RB, Braun IF, et al. Mastoid size determined with lateral radiographs and computerized tomography. Acta Otolaryngol. 1987; 103(5-6): 226–231, doi: 10.3109/00016488709107788, indexed in Pubmed: 21449646.

43. Tos M, Stangerup SE. The causes of asymmetry of the mastoid air cell system. Acta Otolaryngol. 1985; 99(5-6): 564–570, doi: 10.3109/00016488509182262, indexed in Pubmed: 4024906.

44. Turgut S, Tos M. Correlation between temporal bone pneumatization, location of lateral sinus and length of the mastoid process. J Laryngol Otol. 1992; 106(6): 485–489, doi: 10.1017/s0022215100119942, indexed in Pubmed: 1624879.

45. Virapongse C, Sarwar M, Bhimani S, et al. Computed tomographic anatomy of the temporal bone: Normal pattern and morphology. Am J Neuroradiol. 1985; 145: 473–481.

46. Vos T, Barber RM, Bell B, et al. Global, regional, and national incidence, prevalence, and years lived with disability for 301 acute and chronic disease and injuries in 188 countries, 1990–2013: a systemic analysis for the global burden of disease study. Lancet. 2015; 386(9995): 743–800, doi: 10.1016/S0140-6736(15)60692-4, indexed in Pubmed: 26063472.

47. World Health Organization. Deafness and hearing loss: Prevalence. World Health Organization, Health Topics 2022. https://www.who.int/health-topics/hear-ing-loss#tab=tab_2 (06.06.2022).

48. Wright A, Davis A, Bredberg G, et al. Hair cell distributions in the normal human cochlea. A report of a European working group. Acta Otolaryngol Suppl. 1987; 436: 15–24, doi: 10.3109/00016488709124972, indexed in Pubmed: 3478958.

VIA MEDICA

ORIGINAL ARTICLE

Anatomical assessment of the trabecular structure of the alveolar bone in periodontal disease by fractal analysis method

Semra Eser[1], Ebru Sarıbaş[2]

[1]Private Practice, Ankara, Turkey
[2]Department of Periodontology, Dicle University Faculty of Dentistry, Diyarbakır, Turkey

Background: Early diagnosis and treatment of periodontitis, which can cause loss of bone support of the teeth, is of great importance. The use of fractal analysis method is being investigated in order to differentiate periodontal disease radiographically. Fractal analysis presents the degree of complexity in the structure of fractal objects as a numerical data, and has been used to measure changes in trabecular bone. The aim of this study was to compare the trabecular bone fractal dimension (FD) values of patients with periodontitis and gingivitis using panoramic radiographs, and to evaluate the possible relationship between age and gender with fractal dimension.

Materials and methods: Panoramic radiographs of 64 patients with gingivitis and 64 patients with periodontitis were evaluated retrospectively in the study. Using the radiographs of the patients, FD values measured from the trabecular bone were calculated with the box-counting method in the Image J programme. The FD values of both groups were compared. In addition, the relationship between age and gender parameters and FD values was evaluated within the groups.

Results: According to the results of the study, the calculated average FD value of the patients in the gingivitis group was 1.195, while the calculated average FD value of the patients in the periodontitis group was 1.196. No statistically significant difference was observed between the FD values of the gingivitis group and the periodontitis group (p > 0.05). No statistically significant correlation was observed between FD values and age and gender (p > 0.05).

Conclusions: No statistically significant results were obtained for the calculated mean FD values of the patients in the gingivitis and periodontitis groups. (Folia Morphol 2024; 83, 1: 157–167)

Keywords: fractal analysis, periodontitis, gingivitis, panoramic radiography

INTRODUCTION

Periodontitis is a disease of the periodontium and therefore of many structures including the gums. It concerns the tissues lying around the periodontium. And the periodontium also includes the cementum of the tooth root and, therefore, the tooth tissue. Periodontal diseases, which are inflammatory lesions of the tissues surrounding the teeth, are among the

most common oral diseases in adults [39]. Gingivitis is a disease of the gums characterized by hyperaemia, oedema, and bleeding symptoms. It is also characterized by loss of attachment and alveolar bone loss [33]. Plaque tartar, periodontal pocket, inflammation, and reduced bone level are the findings that can be seen at this level. However, periodontal pocket depth differs between clinically healthy patients and patients with gingival disease. This depth detection with a periodontal probe is also important in determining the staging of periodontitis (Fig. 1) [8]. The stages of gingival disorders can start as gingivitis and progress to advanced periodontitis (Fig. 2) [4, 25, 35]. Periodontitis and osteoporosis are known to be common inflammation-related skeletal system disorders. Aging, accumulation of oxidative stress and cellular aging, vitamin D deficiency, smoking have been reported to be factors affecting the progression of osteoporosis and the formation of perio-

dontitis [51]. Particularly, the increasing relationship between aging and periodontist has been included in the studies. Diep et al. [10] reported that there is an important need for dental care associated with endodontic conditions in the future elderly.

Alveolar bones of the upper and lower jaws consist of cortical (compact) and cancellous (trabecular) bone parts. Trabecular bone is surrounded by cortical bone like an outer sheath. Cortical bone in our skeletal system is protected against external factors, and trabecular bone has undertaken the task of actively maintaining metabolic functions [6].

Radiographs are essential tools for the diagnosis and follow-up of periodontal diseases. It has been stated that the destruction in the bone can only be detected with conventional radiographs when it reaches 30–50% [32]. This may cause the initial stage of periodontitis to be overlooked. Nowadays, technology and artificial intelligence applications have been developed, and a non-invasive diagnostic method containing objective and quantitative data is tried to be developed in the radiographic analysis [38]).

Mandelbrot described the shapes of objects that can be found outside of the geometric shapes known in nature, different from the typical geometries taught in schools and complex, with the term 'fractal'. Fractal analysis has been used in the measurement of many objects existing in nature. The complexity of fractals comes from the endless repetition of details within details. Two features that characterize fractal geometry are the self-similarity property of each part of the figure viewed from separate scales, that is, the resemblance to the whole object, and the vari-
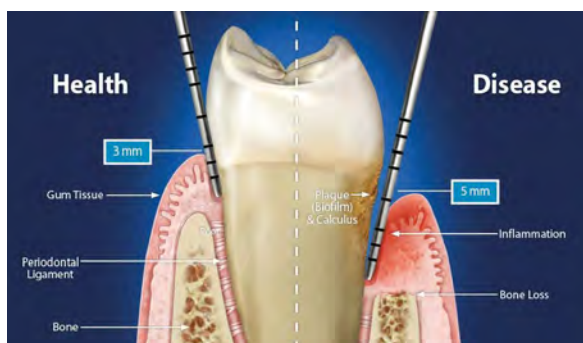
Figure 1. Morphological differences between healthy and diseased teeth and their appearance in terms of depth detection with a periodontal probe staging of periodontitis.
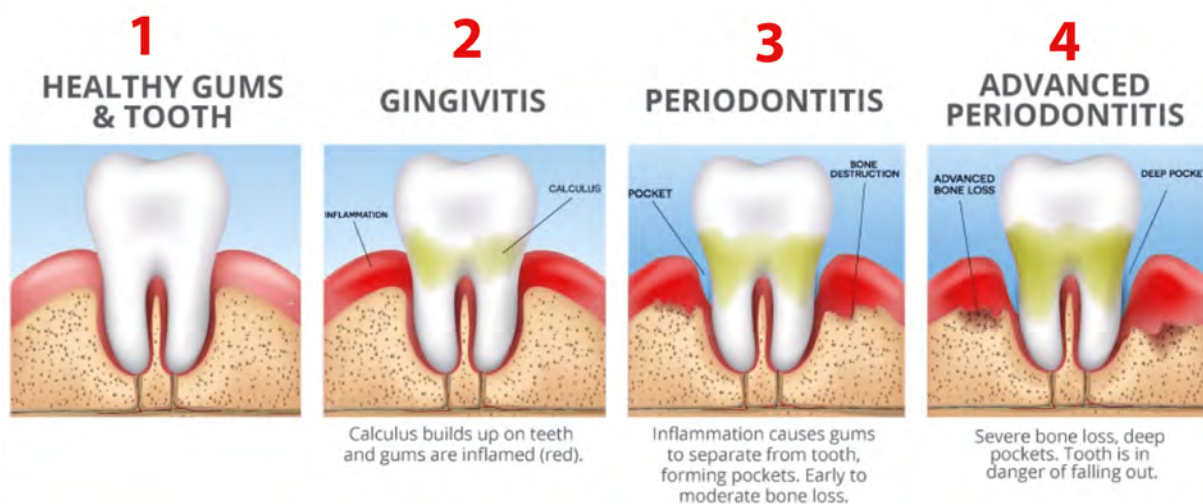
Figure 2. Stages of gum disease; 1— healthy gums and tooth; 2 — gingivitis; 3 — periodontitis; 4 — advanced periodontitis.

ation of a defined scale. That is when the examined area is enlarged or reduced by scale change; there is a similarity to the whole shape in each scale dimension [30]. An increase in the fractal dimension (FD) value is observed when the patterns have a more complex structure, while lower values indicate a simpler structure.

A special computer algorithm developed by White and Rudolph generates a number that gives the FD value representing the morphological features of the architecture, and this value gives us information about the complexity of the structure [49]. In addition to this programme called Image J, other software types that calculate fractal size such as NRecon, Scion Image CTAn, and TAS Plus have been produced.

When the trabecular structure of the cancellous bone was examined, it was observed that it showed fractal characteristics [15, 34, 50]. As a result of the studies, it was concluded that the fractal size of the bone and its biomechanical properties are related to predictors of the Young's modulus of equine cancellous bone [14]. It was found that the loss of minerals in the bone and the decrease in density decreased the FD value; likewise, a high FD has been shown to indicate fewer cavities in the more complex bone architecture [49].

It was investigated how the fractal dimensions of trabecular bone of the periapical bone showed a prospective morphological change after two different apexification treatments in teeth with apical periodontitis. The lesion area of the case was evaluated with the fractal analysis method on the periapical radiographs obtained before the treatment and 1 year after the treatment with the Image-J programme [17]. In addition, Tosun et al. [45] calculated the fractal size of abnormal tissue areas around the root apex on periapical radiographs taken before and after treatment in a retrospective study of 50 patients. And they mentioned a statistically significant difference in FD in the comparison of treated and untreated patient groups [45]. In another study, using the fractal analysis method, it was investigated whether it could distinguish the trabecular bone in this region between healthy peri-implant mucosa and individuals with peri-implant disease on periapical radiographs. They reported that the method used did not have any distinguishing features in terms of FD, but it could be useful in terms of probing depth, the presence or absence of bleeding on probing, and clinical attachment level [26].

The invisible details in the structure of the trabecular bone, which has been proven to have fractal

properties, can be evaluated by the fractal analysis method [36]. Studies are reporting that the trabecular morphology of the alveolar bone and changes in the trabeculae in case of disease can be detected by this method [21]. There are limited studies in the literature investigating the use of fractal analysis to support the radiographic diagnosis of periodontal disease.

We aimed to evaluate the fractal size of patients with periodontitis and gingivitis using panoramic radiographs, and to evaluate the possible contribution of fractal analysis method to radiographic diagnosis, as well as to evaluate the possible relationship of fractal size with gender and age.

MATERIALS AND METHODS

Patient selection

Our study was carried out retrospectively using the records of Dicle University Faculty of Dentistry, Department of Periodontology. This study, which was approved by Dicle University Clinical Research Ethics Committee on 24.02.2021 with protocol number 2021-15, was conducted by the ethical principles of the World Medical Association Declaration of Helsinki. The records of 562 patients who had periodontal treatments in the Dicle University Periodontology Department between 01.10.2017 and 31.12.2018 were scanned and the patients were selected by the inclusion criteria. Among the patients whose existing periodontal index records and radiographic records were evaluated together, a total of 128 patients, 64 patients with gingivitis and 64 patients with periodontitis, were included in the study.

Inclusion criteria

The inclusion criteria were as follows having been diagnosed with gingivitis or periodontitis according to the records of the Department of Periodontology and to have a panoramic radiograph that is registered in the system and has diagnostic value.

Exclusion criteria

The exclusion criteria were as follows: presence of any systemic disease affecting bone metabolism, use of drugs that affect bone metabolism, the number of existing teeth is less than 20, presence of overflow filling, root canal treatment, cyst, tumour, lesion in the relevant area, presence of bone fracture in the relevant region, extraction of tooth numbers 5, 6 or 7 in the relevant region, to have had periodontal treatment in the last 6 months, patients with panoramic

Figure 3. Region of interest selection in the Image J programme.

radiographs of no diagnostic value due to various artifacts or positioning errors.

Radiological evaluation

All the panoramic radiographs were taken with the Planmeca ProMax 2D panoramic X-ray device at Dicle University Faculty of Dentistry, Department of Oral and Maxillofacial Radiology, and the irradiation parameters were determined as 64 kVp, 7mA.

Radiographic images included in the study were opened and analysed in Meta Soft Pacs imaging system and saved in Digital Imaging and Communications in Medicine (DICOM) format, which has high image quality.

Fractal analysis

The panoramic image was opened in the Image J programme and the area to be examined, called region of interest (ROI), was selected (Fig. 3). The relevant area was selected to include first the mesial and then the distal of tooth 36, and two separate FDs were calculated and the average of the two measurements was taken. If tooth 36 was out of consideration, tooth 46 was used in the calculation. The ROI was chosen in a rectangular shape with a size of 23 × 51 pixels. Narrow interproximal areas that do not allow ROI selection at this site are adjusted to be in the closest pixel to it.

The image was rotated in the desired direction with the 'rotate' option and the relevant region was enlarged with the 'magnifying' feature so that the ROI selected in the posterior of the mandible can be selected in a rectangular shape and at the specified pixel.
— The ROI selected to include the interdental trabecular bone was clipped with the 'crop' feature.
— The cropped ROI was copied with the 'duplicate' feature.

— A 'Gaussian filter' set to 35 pixels was used to remove the density differences created by the soft tissue in the image and to make sharper differences more evident.
— The image filtered by the 'Subtraction' feature has been extracted from the original.
— It was set to 128 values with the 'add' property to reveal the density differences in the image.
— With the 'Binary' feature, the image was made black and white. Thus, the trabeculae became evident.
— The 'erode' and then 'dilate' features were used to eliminate noise and highlight the main lines.
— With the 'invert' feature, the image was inverted, and the desired features are brought into view.
— Using the 'skeletonized' feature, the trabecular structure in the bone was transformed into complex lines.

With the 'Box-counting' feature, the image was divided into squares of 2, 3, 4, 6, 8, 12, 16, 32, and 64 pixels (Fig. 4). Squares containing these complex lines representing trabeculae were counted. This calculation was done separately for each pixel size and the total number of frames was calculated. The number of counted plates was plotted against the total number of plates on a logarithmic scale. A line is drawn through the data points in the graph. The slope of the drawn line gives the FD value, which expresses the complexity of the analysed image (Fig. 3).

Statistical analysis

In this study, Shapiro Wilk's and/or Kolmogorov-Smirnov tests were used due to the number of units while investigating the normal distribution of the variables. While evaluating the results, 0.05 was used as the significance level. Chi-square analysis was applied while examining the relationships between groups of nominal variables.

FRACTAL ANALYSIS STEPS

Figure 4. Fractal analysis steps; a — cropped view of the relevant area; b — duplicated image; c — applying a Gaussian filter; d — image extracted from the original; e — grayscale adjustment; f — binarization; g — eroding; h — dilatation; i — reversal; j — skeletonization.

Table 1. Relationship between groups in terms of gender

Gender	Groups							
	Periodontitis		Gingivitis		Total			
	N	%	N	%	N	%	Chi-square	P-value
Male	31	48.44	32	50	63	49.22		
Female	33	51.56	32	50	65	50.78	0.031	0.86
Total	64	100	64	100	128	100		

Table 2. Differences between groups in terms of age

Groups	Age							
	N	Mean	Median	Minimum	Maximum	Standard deviation	Mean rank	z	P-value
Periodontitis	64	34.05	33	18	54	9.91	65.09		
Gingivitis	64	33.91	32	22	65	9.32	63.91	–0.181	0.856
Total	128	33.98	32.5	18	65	9.58			

Table 3. Differences between groups in terms of fractal dimension values

Groups	Fractal dimension value							
	N	Mean	Median	Minimum	Maximum	Standard deviation	Mean rank	z	P-value
Periodontitis	64	1.196	1.214	0.813	1.395	0.141	67.23		
Gingivitis	64	1.195	1.185	0.957	1.429	0.121	61.77	–0.832	0.406
Total	128	1.195	1.206	0.813	1.429	0.131			

Spearman's correlation coefficient was used while examining the relationships between variables that did not come from the normal distribution. While examining the differences between groups, if the variables did not come from a normal distribution, the Mann-Whitney U test was used for comparisons between groups.

RESULTS

Demographic findings

There was no statistically significant relationship between the groups in terms of gender (p > 0.05); 51.6% of the periodontitis group and 50% of the gin-givitis group were women. Table 1 shows the gender distribution and statistical relationship in the groups.

There was no statistically significant difference between the groups in terms of age (p > 0.05). The mean age of the periodontitis group was higher than the mean age of the gingivitis group, but the difference was not statistically significant. Table 2 shows the age and statistical relationship of the groups.

FD measurements

There was no statistically significant difference between the groups in terms of FD values (p > 0.05). Table 3 shows the FD values of the gin-

161

Table 4. Differences between genders in terms of fractal dimension values

		Fractal dimension value								
		N	Mean	Median	Minimum	Maximum	Standard deviation	Mean rank	z	P-value
Periodontitis	Male	31	1.201	1.199	0.885	1.395	0.109	30.68	–0.759	0.448
	Female	33	1.191	1.227	0.813	1.39	0.168	34.21		
	Total	64	1.196	1.214	0.813	1.395	0.141			
Gingivitis	Male	32	1.208	1.18	1.026	1.429	0.132	34.38	–0.806	0.42
	Female	32	1.181	1.193	0.957	1.367	0.108	30.63		
	Total	64	1.195	1.185	0.957	1.429	0.121			
Total	Male	63	1.204	1.192	0.885	1.429	0.12	65.16	–0.198	0.843
	Female	65	1.186	1.213	0.813	1.39	0.141	63.86		
	Total	128	1.195	1.206	0.813	1.429	0.131			

Table 5. The relationship between fractal dimension values and age

			Age
Periodontitis	Fractal dimension	r	0.055
		p	0.665
		n	64
Gingivitis	Fractal dimension	r	0.089
		p	0.483
		n	64
Total	Fractal dimension	r	0.08
		p	0.367
		n	128

givitis and periodontitis groups and their statistical relationship.

Although there was no statistically significant difference between the genders in terms of FD values measured from the radiographs of the patients in the periodontitis and gingivitis groups, the FD value measured from the radiographs of the men was higher (p > 0.05). Table 4 shows the relationship between FD and gender.

Although there was no statistically significant difference between the genders in terms of FD values measured from the radiographs of the individuals regardless of the group, the FD value calculated from the radiographs of the men was higher (p > 0.05; Table 4).

Although there was no statistically significant relationship between the FD values measured from the radiographs of the patients both gingivitis and periodontitis groups and the age values, the FD value increased as the age increased (p > 0.05). Table 5 shows the relationship between FD and age.

Regardless of the group, there was no statistically significant relationship between the FD values measured from the radiographs of the individuals and the age values, but the FD value increased as the age increased (p > 0.05; Table 5).

DISCUSSION

The clinical significance of the relationship between periodontitis and genetic factors is known. Based on recent research data, it has been reported that genetic and ethnic factors are considered the leading susceptibility or severity factors for devastating periodontitis. A family history of early-onset aggressive periodontitis has been known for a long time. Hereditary syndromes have often been associated with severe periodontitis. They reported that periodontal disease associated with systemic inherited syndromes mainly indicates Mendelian inheritance [12]. Shungin et al. [41] presented as a meta-analysis a genome-wide association study by identifying clinical findings, self-reported dental disease proxies with similar underlying genetic contributions, and then identifying 47 novel and conditionally independent risk loci for dental caries. Similarly, they reviewed the literature for gene polymorphisms associated with periodontitis and peri-implantitis susceptibility in the Iranian population[20]. In a study investigating epigenetic factors in periodontitis, these epigenetic changes have been reported to be associated with excess inflammatory cytokines, chemokines and matrix-degrading enzymes that can be suppressed by certain histone deacetylases (small molecule inhibitors of certain histone deacetylases) or by small molecule inhibitors of DNA methyltransferases. They noted the importance of providing critical information about

the therapeutic and diagnostic potential of epigenetics in periodontal disease [19]. For all that, they stated that periodontitis may be an individual risk factor for the development of oral cancer. They suggested that individuals with periodontal problems, especially those with severe periodontitis and coexisting lifestyle risk factors, should be followed closely. They concluded that maintaining periodontal health in at-risk patients can minimise their cancer risk [22]. In a genetic microbiological study, they reported that the correlation of mir155 with periodontal parameters and periodontal pathogens further strengthens the evidence for periodontal inflammation as a risk of preeclampsia in pregnant women, especially when associated with chronic periodontitis. They suggested that mir155 can be considered as one of the genetic biomarkers and is an important criterion for the early diagnosis of periodontitis [29].

The fractal analysis method, which is thought to contribute to the radiographic examination by examining the invisible details in the bone structure, has been used to understand objects in many fields such as astrophysics, genetic, economy, agriculture, medicine, and dentistry [11, 16, 27, 31].

It has been reported that the FD value calculated by the studies is not affected by variables such as irradiation time (mAs), kilovolt peak acceleration voltage (kVp), and projection angle, therefore fractal analysis can be performed with non-standardized radiographs during the filming of [7, 18, 46].

Considering this information, our study aimed to use fractal analysis to evaluate the trabecular bone morphology of patients with periodontitis and gingivitis, as well as to evaluate the possible relationship between fractal dimension, age, and gender.

There are a limited number of studies in the literature regarding the use of fractal analysis to support the radiographic diagnosis of periodontitis. Current studies used cone beam computed tomography (CBCT) and periapical radiography technique [1, 9, 37, 38, 40, 48]. Although there are many studies on FD calculation using panoramic radiographs in different fields in dentistry [15, 21, 42], no study has yet been conducted using panoramic radiographs in the evaluation of periodontal disease.

Periapical and bite-wing radiographs are imaging modalities with better resolution than panoramic radiographs. However, the disadvantages are that the number of films to be taken is higher when the whole mouth is evaluated and the radiation dose that the

patient will receive is higher than the dose that will be taken with panoramic radiographs [43].

The fact that panoramic radiographs are in widespread use with increasing frequency, the advantageous situation in their application and patient tolerance, and the fact that they allow imaging of larger areas with a lower radiation dose have prompted us to use panoramic radiography in this study.

It has been reported that the box-counting method is widely used and is currently in fractal analysis [21]. In this method, the process steps suggested by White and Rudolph are applied. For this purpose, the Image J image analysis programme was developed.

In our study, ROI was chosen within the borders of trabecular bone, not including cortical bone, tooth, or periodontal space. Like other studies [1, 38], In our study, two separate ROIs were selected from the mesial and distal interdental region of the mandible number 6 tooth, which is frequently affected by periodontitis, FD was calculated from these regions, and the average of the two values was taken.

In our study in which trabecular bone FD measurements of 64 gingivitis and 64 periodontitis patients were compared, it was observed that there was no statistically significant difference between the calculated FD values of the patients in the two groups.

In the study of Shrout et al. in 1998 [40], the FD values calculated from the periapical radiographs of the group with periodontitis and the healthy or another patient group with gingivitis were compared. As a result of this study, it was found that the FD value of the group with periodontitis was significantly lower [5]. In our study, digital panoramic radiographs were recorded and used in DICOM format with high image quality. We believe that this situation may have caused the difference between the results.

In the study of Şener et al. [38], in which they measured FD using the periapical radiographs of healthy and moderately severe periodontitis patients, a significant difference was found between the FD values of both groups. In the study of Bollen et al.[5], in which they compared periapical and panoramic radiographs, it was reported that FD values measured from periapical radiographs of the same patients were higher. This situation causes us to consider the possibility of different details and resolutions in imaging methods to change the results in diseases that cause local bone loss such as periodontitis.

Coşgunarslan et al. [9] calculated FD from CBCT images of healthy and periodontitis patients and re-

ported that there was no statistically significant difference between FD measurements of the two groups, like our study. They reported that the inconsistency of this result with some studies in the literature may be due to the difference in imaging methods [9]. In addition, Magat et al. suggested that CBCT has low image resolution for fractal analysis of trabecular bone [28]. Based on this, it can be thought that the results may vary when FD measurement is performed using periapical, panoramic, or CBCT imaging.

In the study of Updike and Nowzari [48], the FD values of healthy, moderate/severe, and severe periodontitis patients were compared. As a result of the study, there was a significant difference between the FD values of the periodontitis groups and the healthy group, but no significant difference was found between the FD values of the moderate/severe periodontitis and severe periodontitis groups [48]. We believe that the fact that the result of our study is not fully compatible with this study may be due to the difference in ROI position.

Region of interest selection is done manually. This leads to practitioner error and the inability to standardize the ROI position [28]. It is impossible to select an ROI from the same area in every patient, which may lead to differences in measurements. In the study by Shrout et al. [40], which compared the FD values of the periodontitis and healthy/gingivitis group, ROIs were determined in different sizes according to the shape and size of the interproximal bone. As a result of the study, it was reported that there was a significant difference between the FD values of the two groups. We think that the non-parallelism of our results may be due to the variation in the selected ROI sizes. For our study results to be of optimum accuracy, the gender and age distribution of the groups were determined to be homogeneous.

Studies have reported that there was no significant relationship between gender and FD [1, 47, 48]. The results of these studies support the findings of our study. Researchers reported that there was a significant difference between FD values in their studies [1, 48]. We think that the inconsistency of these results with our study may be due to the difference in age values between groups. Age distribution was determined to be homogeneous in the periodontitis and gingivitis groups so that our study results were not affected by age-related variability. Amer et al. [2]

reported that fractal size of trabecular bone was not associated with age.

Geraets and van der Stelt [13] mentioned that the conflicting results may be due to the anatomical differences of the examined region and the methods used to obtain the image. When utilizing the fractal analysis to study bone, it should be noted that all the steps in the analytical chain have an impact on the results.

It has been suggested that retrospective evaluation of the bone microstructure surrounding unerupted/impacted canines can provide analytical information on treatment prognosis and anchorage considerations. Bone surface area and bone marrow surface area can be measured by FD analysis of CBCT images, and bone density has been reported to be reliably estimated [3]. In addition, Köse et al. [23] observed a negative relationship between FDs in the mandibular mental region and total orthodontic treatment time. FD analysis has drawn attention to its importance for understanding the physiological properties of alveolar bone and predicting orthodontic tooth movement [23]. In a study of fractal analysis of periapical bone, it was stated that high resolution showed the least variation in FD values at all compression levels, making it the most reliable and consistent resolution for measuring FD values [44]. In a study in which implant evaluation was evaluated in terms of FD, they found that FD values of trabecular bone around the implants were significantly lower than the initial values 6 months after prosthetic loading. However, they reported that no significant decrease or increase was observed at 12 months, with results comparable to peri-implant alveolar bone at 6 months [52]. On the other hand, it has been suggested that fractal size of alveolar bone measured from intraoral digital radiographs alone may be an insufficient parameter to determine initial implant stability [24].

Many factors are likely to have an impact on the results, from patient selection in the study to imaging methods, the quality of these methods, sample size, gender and especially age distributions between groups, changes in ROI location and size, personal variations in ROI selection, and patients' anatomical variations. To standardize these variables as much as possible, the limitations of the method need to be developed and more studies with a larger sample size are needed.

CONCLUSIONS

In this study, trabecular bone fractal dimension values were compared using panoramic radiographs of patients with periodontitis and gingivitis, and the following results were obtained:

— there was no statistically significant difference between the groups in terms of FD values of trabecular bone calculated using panoramic radiographs of the patients in the periodontitis and gingivitis groups;

— in the periodontitis and gingivitis groups, there was no statistically significant difference between FD values, gender, and age values, according to the comparisons in the FD values of the trabecular bone, which were made within the group and without any group discrimination.

We believe that the inability to obtain a significant result is due to the wide age range of the population in this study. It is obvious that there is a need for prospective fractal analyses and follow-ups to be made between different age groups due to the degeneration of the anatomical structure in the trabecular structure with aging.

Conflict of interest: None declared

REFERENCES

1. Aktuna Belgin C, Serindere G. Evaluation of trabecular bone changes in patients with periodontitis using fractal analysis: A periapical radiography study. J Periodontol. 2020; 91(7): 933–937, doi: 10.1002/JPER.19-0452, indexed in Pubmed: 31850519.

2. Amer ME, Heo MS, Brooks SL, et al. Anatomical variations of trabecular bone structure in intraoral radiographs using fractal and particles count analyses. Imaging Sci Dent. 2012; 42(1): 5–12, doi: 10.5624/isd.2012.42.1.5, indexed in Pubmed: 22474642.

3. Arvind TR, Jain RK, Nagi R, et al. Evaluation of alveolar bone microstructure around impacted maxillary canines using fractal analysis in dravidian population: a retrospective CBCT study. J Contemp Dent Pract. 2022; 23(6): 593–600, indexed in Pubmed: 36259297.

4. Barsoum F, Prete BRJ, Ouanounou A. Drug-Induced gingival enlargement: a review of diagnosis and current treatment strategies. Compend Contin Educ Dent. 2022; 43(5): 276–286, indexed in Pubmed: 35589146.

5. Bollen AM, Taguchi A, Hujoel PP, et al. Fractal dimension on dental radiographs. Dentomaxillofac Radiol. 2001; 30(5): 270–275, doi: 10.1038/sj/dmfr/4600630, indexed in Pubmed: 11571547.

6. Bostrom M, Yang Xu, Koutras I. Biologics in bone healing. Curr Opin Orthop. 2000; 11(5): 403–412, doi: 10.1097/00001433-200010000-00013.

7. Buckland-Wright JC, Lynch JA, Rymer J, et al. Fractal signature analysis of macroradiographs measures trabecular

organization in lumbar vertebrae of postmenopausal women. Calcif Tissue Int. 1994; 54(2): 106–112, doi: 10.1007/BF00296060, indexed in Pubmed: 8012865.

8. Citterio F, Gualini G, Chang M, et al. Pocket closure and residual pockets after non-surgical periodontal therapy: a systematic review and meta-analysis. J Clin Periodontol. 2022; 49(1): 2–14, doi: 10.1111/jcpe.13547, indexed in Pubmed: 34517433.

9. Coşgunarslan A, Aşantoğrol F, Canger EM, et al. Use of fractal analysis to detect trabecular changes related to periodontitis. Selçuk Dent J. 2019: 341–345.

10. Diep MT, Hove LH, Ørstavik D, et al. Periapical and endodontic status among 65-year-old Oslo-citizens. BMC Oral Health. 2022; 22(1): 371, doi: 10.1186/s12903-022-02406-9, indexed in Pubmed: 36050662.

11. Elblbesy MA, Attia M. Optimization of fractal dimension and shape analysis as discriminators of erythrocyte abnormalities. A new approach to a reproducible diagnostic tool. Math Biosci Eng. 2020; 17(5): 4706–4717, doi: 10.3934/mbe.2020258, indexed in Pubmed: 33120525.

12. Gera I, Vári M. [Genetic background of periodontitis. Part I. Basic principles and inherited syndromes. Literature review]. Fogorv Sz. 2009; 102(3): 87–95, indexed in Pubmed: 19618776.

13. Geraets WG, van der Stelt PF. Fractal properties of bone. Dentomaxillofac Radiol. 2000; 29(3): 144–153, doi: 10.1038/sj/dmfr/4600524, indexed in Pubmed: 10849540.

14. Haire TJ, Hodgskinson R, Ganney PS, et al. A comparison of porosity, fabric and fractal dimension as predictors of the Young's modulus of equine cancellous bone. Med Eng Phys. 1998; 20(8): 588–593, doi: 10.1016/s1350-4533(98)00063-0, indexed in Pubmed: 9888237.

15. Heo MS, Park KS, Lee SS, et al. Fractal analysis of mandibular bony healing after orthognathic surgery. Oral Surg Oral Med Oral Pathol Oral Radiol Endod. 2002; 94(6): 763–767, doi: 10.1067/moe.2002.128972, indexed in Pubmed: 12464904.

16. Heymans O, Fissette J, Vico P, et al. Is fractal geometry useful in medicine and biomedical sciences? Med Hypotheses. 2000; 54(3): 360–366, doi: 10.1054/mehy.1999.0848, indexed in Pubmed: 10783467.

17. Ince Yusufoglu S, Ugur Aydin Z, Tulumbaci F, et al. Evaluation of different Apexification treatments of teeth with immature apices and apical periodontitis on the fractal dimensions of trabecular bone. Aust Endod J. 2021; 47(2): 163–169, doi: 10.1111/aej.12441, indexed in Pubmed: 32902092.

18. Jolley L, Majumdar S, Kapila S. Technical factors in fractal analysis of periapical radiographs. Dentomaxillofac Radiol. 2006; 35(6): 393–397, doi: 10.1259/dmfr/30969642, indexed in Pubmed: 17082328.

19. Jurdziński KT, Potempa J, Grabiec AM. Epigenetic regulation of inflammation in periodontitis: cellular mechanisms and therapeutic potential. Clin Epigenetics. 2020; 12(1): 186, doi: 10.1186/s13148-020-00982-7, indexed in Pubmed: 33256844.

20. Kadkhodazadeh M, Tabari ZA, Pourseyediyan T, et al. Relationship between Genetic Polymorphisms with Periodontitis and Peri-Implantitis in the Iranian Population: A Literature Review. J Long Term Eff Med Implants. 2016; 26(2): 183–190, doi: 10.1615/JLongTermEffMedImplants.2016015197, indexed in Pubmed: 28094743.

21. Kato CN, Barra SG, Tavares NPk, et al. Use of fractal analysis in dental images: a systematic review. Dentomaxillofac Radiol. 2020; 49(2): 20180457, doi: 10.1259/dmfr.20180457, indexed in Pubmed: 31429597.

22. Komlós G, Csurgay K, Horváth F, et al. Periodontitis as a risk for oral cancer: a case-control study. BMC Oral Health. 2021; 21(1): 640, doi: 10.1186/s12903-021-01998-y, indexed in Pubmed: 34911520.

23. Köse E, Ay Ünüvar Y, Uzun M. Assessment of the relationship between fractal analysis of mandibular bone and orthodontic treatment duration: a retrospective study. J Orofac Orthop. 2022; 83(Suppl 1): 102–110, doi: 10.1007/s00056-022-00406-6, indexed in Pubmed: 35776177.

24. Kulczyk T, Czajka-Jakubowska A, Przystańska A. A comparison between the implant stability quotient and the fractal dimension of alveolar bone at the implant site. Biomed Res Int. 2018; 2018: 4357627, doi: 10.1155/2018/4357627, indexed in Pubmed: 30410933.

25. Kuralt M, Cmok Kučič A, Gašperšič R, et al. Evaluation of gingival recessions with conventional versus digital methods. J Dent. 2022; 120: 104093, doi: 10.1016/j.jdent.2022.104093, indexed in Pubmed: 35301080.

26. Lang MS, Miyamoto T, Nunn ME. Validity of fractal analysis of implants in individuals with healthy and diseased peri-implant mucosa. Clin Oral Implants Res. 2020; 31(11): 1039–1046, doi: 10.1111/clr.13650, indexed in Pubmed: 32790884.

27. Lennon FE, Cianci GC, Cipriani NA, et al. Lung cancer-a fractal viewpoint. Nat Rev Clin Oncol. 2015; 12(11): 664–675, doi: 10.1038/nrclinonc.2015.108, indexed in Pubmed: 26169924.

28. Magat G, Ozcan Sener S. Evaluation of trabecular pattern of mandible using fractal dimension, bone area fraction, and gray scale value: comparison of cone-beam computed tomography and panoramic radiography. Oral Radiol. 2019; 35(1): 35–42, doi: 10.1007/s11282-018-0316-1, indexed in Pubmed: 30484179.

29. Mahendra J, Mahendra L, Mugri MH, et al. Role of periodontal bacteria, viruses, and placental mir155 in chronic periodontitis and preeclampsia: a genetic microbiological study. Curr Issues Mol Biol. 2021; 43(2): 831–844, doi: 10.3390/cimb43020060, indexed in Pubmed: 34449559.

30. Mandelbrot B. How long is the coast of britain? Statistical self-similarity and fractional dimension. Science. 1967; 156(3775): 636–638, doi: 10.1126/science.156.3775.636, indexed in Pubmed: 17837158.

31. Meyer HV, Dawes TJW, Serrani M, et al. Genetic and functional insights into the fractal structure of the heart. Nature. 2020; 584(7822): 589–594, doi: 10.1038/s41586-020-2635-8, indexed in Pubmed: 32814899.

32. Özer N, Baksı Şen BG. Third dimension in dental radiographic imaging: a literature update. J Dent Fac Atatürk Uni. 2021; 31(4): 652–661, doi: 10.17567/ataunidfd.821983.

33. Papapanou PN, Sanz M, Buduneli N, et al. Periodontitis: Consensus report of workgroup 2 of the 2017 World Workshop on the Classification of Periodontal and Peri-Implant Diseases and Conditions. J Periodontol. 2018; 89(Suppl 1): S173–S182, doi: 10.1002/JPER.17-0721, indexed in Pubmed: 29926951.

34. Prouteau S, Ducher G, Nanyan P, et al. Fractal analysis of bone texture: a screening tool for stress fracture risk? Eur J Clin Invest. 2004; 34(2): 137–142, doi: 10.1111/j.1365-2362.2004.01300.x, indexed in Pubmed: 14764077.

35. Revilla-León M, Gómez-Polo M, Barmak AB, et al. Artificial intelligence models for diagnosing gingivitis and periodontal disease: a systematic review. J Prosthet Dent. 2023; 130(6): 816–824, doi: 10.1016/j.prosdent.2022.01.026, indexed in Pubmed: 35300850.

36. Ruttimann UE, Webber RL, Hazelrig JB. Fractal dimension from radiographs of peridental alveolar bone. A possible diagnostic indicator of osteoporosis. Oral Surg Oral Med Oral Pathol. 1992; 74(1): 98–110, doi: 10.1016/0030-4220(92)90222-c, indexed in Pubmed: 1508517.

37. Sang-Yun C, Won Jeong H, Eun Kyung K. Usefulness of fractal analysis for the diagnosis of periodontitis. Korean J Oral Maxillofac Radiol. 2001; 31(1): 35–42.

38. Sener E, Cinarcik S, Baksi BG. Use of fractal analysis for the discrimination of trabecular changes between individuals with healthy gingiva or moderate periodontitis. J Periodontol. 2015; 86(12): 1364–1369, doi: 10.1902/jop.2015.150004, indexed in Pubmed: 26291294.

39. Ship JA, Crow HC. Diseases of periodontal tissues in the elderly. Description, epidemiology, aetiology and drug therapy. Drugs Aging. 1994; 5(5): 346–357, doi: 10.2165/00002512-199405050-00004, indexed in Pubmed: 7833588.

40. Shrout MK, Roberson B, Potter BJ, et al. A comparison of 2 patient populations using fractal analysis. J Periodontol. 1998; 69(1): 9–13, doi: 10.1902/jop.1998.69.1.9, indexed in Pubmed: 9527567.

41. Shungin D, Haworth S, Divaris K, et al. Genome-wide analysis of dental caries and periodontitis combining clinical and self-reported data. Nat Commun. 2019; 10(1): 2773, doi: 10.1038/s41467-019-10630-1, indexed in Pubmed: 31235808.

42. Suer BT, Yaman Z, Buyuksarac B. Correlation of fractal dimension values with implant insertion torque and resonance frequency values at implant recipient sites. Int J Oral Maxillofac Implants. 2016; 31(1): 55–62, doi: 10.11607/jomi.3965, indexed in Pubmed: 26478979.

43. Şener E, Baksı BG. Imaging Systems used for diagnosis of periodontal pathology. Part 1: Two or three dimensional imaging systems. EÜ Diş Hek Fak Derg. 2013; 34(2): 79–85.

44. Toghyani S, Nasseh I, Aoun G, et al. Effect of image resolution and compression on fractal analysis of the periapical bone. Acta Inform Med. 2019; 27(3): 167–170, doi: 10.5455/aim.2019.27.167-170, indexed in Pubmed: 31762572.

45. Tosun S, Karataslioglu E, Tulgar MM, et al. Fractal analysis and periapical index evaluation of multivisit nonsurgical endodontic retreatment: A retrospective study. Oral Surg Oral Med Oral Pathol Oral Radiol. 2022; 133(2): 245–251, doi: 10.1016/j.oooo.2021.08.016, indexed in Pubmed: 34556458.

46. Tosun S, Karataslioglu E, Tulgar MM, et al. Retrospective fractal analyses of one-year follow-up data obtained after single-visit nonsurgical endodontic retreatment on periapical radiographs. Clin Oral Investig. 2021; 25(11): 6465–6472, doi: 10.1007/s00784-021-04079-0, indexed in Pubmed: 34302217.

47. Uğur Aydın Z, Ocak MG, Bayrak S, et al. The effect of type 2 diabetes mellitus on changes in the fractal dimension of periapical lesion in teeth after root canal treatment: a fractal analysis study. Int Endod J. 2021; 54(2): 181–189, doi: 10.1111/iej.13409, indexed in Pubmed: 32931021.

48. Updike SX, Nowzari H. Fractal analysis of dental radiographs to detect periodontitis-induced trabecular changes. J Periodontal Res. 2008; 43(6): 658–664, doi: 10.1111/j.1600-0765.2007.01056.x, indexed in Pubmed: 18624949.

49. White SC, Rudolph DJ. Alterations of the trabecular pattern of the jaws in patients with osteoporosis. Oral Surg Oral Med Oral Pathol Oral Radiol Endod. 1999; 88(5): 628–635, doi: 10.1016/s1079-2104(99)70097-1, indexed in Pubmed: 10556761.

50. Yaşar F, Akgünlü F. The differences in panoramic mandibular indices and fractal dimension between patients with and without spinal osteoporosis. Dentomaxillofac Radiol. 2006; 35(1): 1–9, doi: 10.1259/dmfr/97652136, indexed in Pubmed: 16421256.

51. Yu Bo, Wang CY. Osteoporosis and periodontal diseases — An update on their association and mechanistic links. Periodontol 2000. 2022; 89(1): 99–113, doi: 10.1111/prd.12422, indexed in Pubmed: 35244945.

52. Zeytinoğlu M, İlhan B, Dündar N, et al. Fractal analysis for the assessment of trabecular peri-implant alveolar bone using panoramic radiographs. Clin Oral Investig. 2015; 19(2): 519–524, doi: 10.1007/s00784-014-1245-y, indexed in Pubmed: 24802628.

ORIGINAL ARTICLE

Topography of the mandibular canal in male human skulls originating from different time periods

Aleksandra Gawlikowska-Sroka[1], Łukasz Stocki[2], Jacek Szczurowski[3],
Wioletta Nowaczewska[4], Małgorzata Światłowska-Bajzert[5]

[1]Departament of Anatomy, Pomeranian Medical University, Szczecin, Poland
[2]Orion Dental Wawrzyniak & Stocki, Szczecin, Poland
[3]Department of Anthropology, Wroclaw University of Environmental and Life Sciences, Wroclaw, Poland
[4]Department of Human Biology, University of Wroclaw, Poland
[5]Department of Prosthetics, Pomeranian Medical University, Szczecin, Poland

Background: *Dynamic advances in dentistry, especially in implantology has inspired researchers to carry out many studies investigating the topography of the mandibular canal and its ethnic differences. The aim of the study was a comparative analysis of variations in the position and topography of the mandibular canal based on radiographic images of human mandibles originating from modern and medieval skulls.*

Materials and methods: *Morphometric examination of 126 radiographs of skulls (92 modern and 34 medieval skulls) was included. The age and sex of individuals were determined based on the morphology of the skull, the obliteration of cranial sutures, and the degree of tooth wear. To define the topography of the mandibular canal on X-ray images, we took 8 anthropometric measurements.*

Results: *We observed significant differences in several parameters. The distance between the base of the mandible and the bottom of the mandibular canal, the distance between the top of the mandibular canal and the crest of the alveolar arch, and the height of the mandibular body. Significant asymmetry was found for two parameters of mandibles from modern skulls: the distance between the top of the mandibular canal and the crest of the alveolar arch at the level of the second molar ($p < 0.05$), and the distance between the mandibular foramen and the margin of the anterior mandibular ramus ($p < 0.007$). There were no significant differences between measurements taken on the right and left sides of the medieval skulls.*

Conclusions: *Our study revealed differences in the position of the mandibular canal between modern and medieval skulls, confirming the presence of geographical and chronological differences between populations. Knowledge of variability in the position of the mandibular canal between different local populations is fundamental for the correct interpretation of findings from diagnostic radiological studies used in dental practice and in forensic odontology or analysis of archaeological bone materials.* (Folia Morphol 2024; 83, 1: 168–175)

Keywords: mandibular canal, palaeoanthropology, anatomy, mental foramen, asymmetry

Address for correspondence: Dr. Aleksandra Gawlikowska-Sroka, Department of Anatomy, Pomeranian Medical University, Al. Powstańców Wlkp. 72, 70–111 Szczecin, Poland, e-mail: aleksandra.gawlikowska.sroka@pum.edu.pl

INTRODUCTION

The mandibular canal, nowadays referred to as the inferior alveolar (nerve) canal [29, 36, 63], is located in the spongy bone of the mandible and is available for diagnosis only by imaging techniques using X-rays [1, 3, 8, 20–22, 29, 32, 66]. Panoramic images acquired with classical and digital techniques, or increasingly popular computed tomography are clinically relevant [3, 8, 43, 67]. Panoramic radiography is part of the standard dental diagnostics procedure performed before planning treatment. Acquired radiograms allow for the evaluation of dentition in terms of periapical inflammatory lesions, periodontitis, root position before tooth extraction, and the position of impacted teeth [3, 12, 57, 58, 64, 65]. They are also useful for the diagnosis of pathologies within the temporomandibular joint [48] or maxillary sinuses [16, 23, 25]. Radiographic evaluation is also necessary before treatment involving implant placement. It allows for the assessment of the volume and quality of the preserved bone of the maxillary alveolar process, the mandibular corpus, and the alveolar part of the mandible [32]. It visualises the position of important anatomical structures such as the bottom of the nasal cavity or maxillary sinus, and the topography of the mandibular canal with the position of the mental foramen [16, 17, 36, 43, 52, 57, 59, 64, 65]. Dynamic advances in dental implantology as well as prosthetics have inspired researchers to carry out many studies investigating the topography of the mandibular canal in terms of its position in relation to the base of the mandible and the apical parts of tooth roots [43, 57, 67]. Other studies have analysed the position of the mental foramen and the presence of the loop of the mental nerve [33, 50, 51, 57, 58], and the presence of the incisive canal [30] or bifid accessory canals [17, 41, 63, 62]. Studies in this area provide clinically relevant information which is extremely valuable for planning and performing treatments.

In the evolution leading to the emergence of *Homo sapiens*, the size and massiveness of the hominin facial skeleton has reduced, and its position in relation to the brain case has changed from the protruding face to retracted in the anterior region of the skull base [27, 38]. Archaeological studies have revealed certain trends that can be observed in the structure of the *Homo sapiens* skull, such as brachycephalization and gracilization combined with a reduction in the size of the facial skeleton attributed to the change in the life model of ancient human populations that shifted from hunting and gathering to a more sedentary lifestyle due to the development of agriculture [19, 31, 46, 47, 62].

The shape and size of the teeth over thousands of years of the existence of the human species did not change much, although the above-mentioned trends were accompanied by a slight reduction in the size of molars [5]. The formation of dentition in humans is generally regarded as very strongly determined by genetic factors, in contrast to the facial skeleton, which is characterized by high plasticity [34, 56]. This means that changing environmental conditions have a much stronger impact on the developing facial skeleton than on teeth formation [34, 56]. The aforementioned differences between the teeth and the facial skeleton in response to environmental factors can be interpreted as the main cause of tooth crowding, which is increasingly frequent in modern populations [62]. Thus, the reduction in the size of the maxilla and the mandible can lead to crowding of the teeth [66], especially in the anterior region. Another observed trend is the reduction in the number of teeth in the dental arch and impaction of teeth which mainly concerns third molars, also called wisdom teeth, within the alveolar process [24, 42], which is also important when planning dental treatment.

One reason for this is the development of civilization, which leads to changes in diet and the texture of ingested food. An increasing number of food products are processed and disintegrated, which influences the formation of the mandible [7, 26, 40, 68]. Studies carried out on the mandibles from different historical periods as well as modern ones have identified variability in the position of the mental foramen in different ethnic groups, which may be related to the differences in the topography of the mandibular canal [1, 4, 5, 15, 20, 22, 27, 31, 34, 37]. Information on the detailed anatomy and topography of the mandibular structures may be important not only in dental practice, but also for the analysis of archaeological material or in forensic medicine.

The aim of the study was to comparative analysis of variations in the position and topography of the mandibular canal based on radiographic images of human mandibles originating from modern and medieval skulls.

MATERIALS AND METHODS

Study material
— 92 modern human skulls dated to the beginning of the 20th century, kept in the museum collections

169
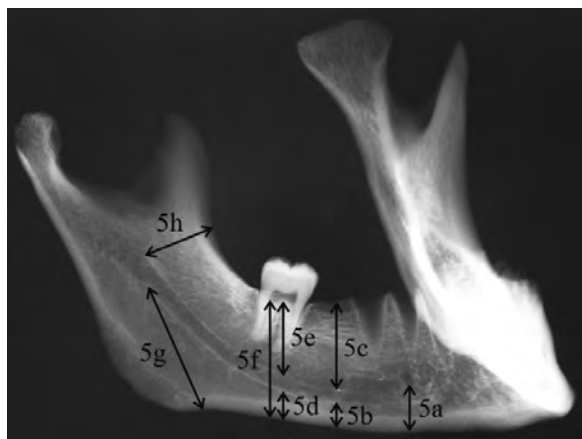
Figure 1. Selected anthropometric parameters describing the topography of the mandibular canal in a radiogram; 5a, 5b, 5c, 5d, 5e, 5f, 5g — abbreviation — see text.

of the Department of Anatomy of the Pomeranian Medical University in Szczecin, acquired during archaeological excavations in the cemetery near the church of St. Joseph in Szczecin in 1969–1970;

— 34 skulls from individuals living in the Middle Ages constituting a part of the collection kept at the Department of Human Biology, the University of Wroclaw, acquired during archaeological excavations carried out in 1959–1989 at the cemetery in Sypniewo (necropolis dated to the 11–13th centuries).

All skulls were from male individuals classified as adultus (age at death 30–35 years) or maturus (50–55 years) and represented European populations.

The age and sex of individuals were determined based on the morphology of the skull [9, 10, 18], the obliteration of cranial sutures [9, 10] and the degree of tooth wear according to the scoring system by Brothwell [9].

The criteria for inclusion in the study were as follows: adult age, male sex, good preservation of the bone material (i.e. standing teeth in the mandible); if the teeth were lost post-mortem and there was no alveolar atrophy related to the loss of dentition, the study also included the mandibles without the third molar erupted if the analysis of the bone material indicated its adult age.

The exclusion criteria were as follows: damage to the bone material preventing all measurements, and developmental anomalies of the mandible.

Radiograms of the analysed mandibles were acquired using X-ray machine Multa 320 type X-18 made by FARUM manufacturer with the following

parameters: the focal distance was 100 cm, exposure conditions: voltage 85 kV, current 125 mA, exposure time 0.8 s at the Department of Anatomy Pomeranian Medical University in Szczecin. Relevant measurements were taken on the radiograms using an electronic callipers (with accuracy to the nearest 0.01 mm) three times by one experienced observer. Measurement error was estimated.

To define the topography of the mandibular canal on X-ray images, we took the following anthropometric measurements (Fig. 1), also used by other researchers [8, 30, 43, 45, 50, 51, 52, 57, 61, 63, 67]:

— 5a. Distance between the base of the mandible and the inferior margin of the mental foramen — *Bas.Ma.-For.Me.*;

— 5b. Distance between the base of the mandible and the bottom of the mandibular canal at the level of the first molar — *Bas.Ma-Ca.Ma. I*;

— 5c. Distance between the top of the mandibular canal and the crest of the alveolar arch at the level of the first molar — *Ca.Ma.-Arc.Alv. I*;

— 5d. Distance between the base of the mandible and the bottom of the mandibular canal at the level of the second molar — *Bas.Ma-Ca.Ma. II*;

— 5e. Distance between the top of the mandibular canal and the crest of the alveolar arch at the level of the second molar — *Ca.Ma.-Arc.Alv. II*;

— 5f. The height of the mandibular body measured at the level of the second molar — *He.Ma.Bo.II*;

— 5g. Distance between the base of the mandible near the gonial angle and the inferior margin of the mental foramen (in the projection of the lowest point of the base of the uvula) — *Bas. Ma.-For.Ma.*;

— 5h. Distance between the mandibular foramen and the anterior margin of the mandibular ramus — *For.Ma.-Mar.Ant.*

Statistical analysis

Collected data were analysed with statistical methods using Statistica 7.1 software. The normality of distribution was verified with the Shapiro-Wilk test for two datasets (separately for the measurements taken on the left and right sides of the mandible). Metric features of modern mandibles from the beginning of the 20th century and those dated for the Middle Ages were compared using Student's t-test or its non-parametric equivalent, the Mann-Whitney U test (only in justified cases when the distribution of data was non-normal). Measurements taken on the left

Table 1. Basic statistics of the analysed anthropometric features and results of comparative analyses for the two series of mandibles

Parameter	Modern skulls (n = 92)				Medieval skulls (n = 34)					
	Mean ± SD	Median	Mini-mum	Maxi-mum	Mean ± SD	Median	Mini-mum	Maxi-mum	Student's t test	Mann-Whitney U test
Bas.Ma-For.Me. R	12.36 ± 1.85	12.35	8.64	18.05	11.65 ± 1.72	11.71	7.26	14.39	> 0.51	> 0.10
Bas.Ma-For.Me. L	12.05 ± 1.84	12.18	7.61	16.47	11.56 ± 1.67	11.30	7.94	15.08	> 0.17	> 0.15
Bas.Ma-Ca.Ma. I R	7.57 ± 1.52	7.38	3.75	12.33	6.93 ± 1.44	6.93	3.77	9.96	**< 0.04**	> 0.11
Bas.Ma-Ca.Ma. I L	7.44 ± 1.52	7.20	4.06	11.53	7.11 ± 1.58	7.17	3.22	10.85	> 0.38	> 0.54
Ca.Ma.-Arc.Alv. I R	13.98 ± 2.92	14.99	8.91	21.72	16.10 ± 3.97	16.25	4.45	21.98	> 0.08	> 0.06
Ca.Ma.-Arc.Alv. I L	15.19 ± 3.04	15.61	7.87	21.92	16.25 ± 3.63	15.87	6.69	23.58	> 0.10	> 0.09
Bas.Ma-Ca.Ma. II R	7.75 ± 1.83	7.66	2.95	13.90	7.05 ± 1.70	7.05	3.90	10.94	**< 0.05**	> 0.10
Bas.Ma-Ca.Ma. II L	7.72 ± 2.15	7.44	3.90	17.83	7.27 ± 1.51	7.04	4.16	11.27	> 0.19	> 0.2
Ca.Ma.-Arc.Alv. II R	13.06 ± 2.58	13.09	6.50	19.52	14.96 ± 3.56	15.51	5.21	21.54	**< 0.008**	**< 0.002**
Ca.Ma.-Arc.Alv. II L	13.53 ± 3.18	13.37	6.41	28.79	15.22 ± 3.74	15.82	4.90	23.13	**< 0.02**	**< 0.006**
He. Ma. Bo.II R	23.86 ± 3.15	23.63	16.35	31.38	24.79 ± 3.73	24.75	15.54	31.01	> 0.16	> 0.10
He. Ma. Bo.II L	23.98 ± 3.27	23.93	16.17	31.98	24.45 ± 4.14	25.98	13.92	32.26	**< 0.04**	**< 0.03**
Bas.Ma-For.Ma. R	34.09 ± 3.47	33.95	24.84	41.04	33.90 ± 3.34	34.41	25.32	39.92	> 0.77	> 0.83
Bas.Ma-For.Ma. L	34.17 ± 3.48	34.01	24.85	42.76	34.56 ± 3.64	34.93	27.38	42.76	> 0.57	> 0.54
For.Ma-B.P. R	12.33 ± 1.95	12.44	7.15	17.00	11.61 ± 2.37	11.72	7.76	17.42	> 0.08	> 0.058
For.Ma-B.P. L	11.97 ± 2.12	12.04	7.39	16.71	11.24 ± 1.62	11.15	7.91	15.08	> 0.07	> 0.06

All measurements in millimetres, SD — standard deviation; L — left; R — right; rest abbreviations — see text

and right sides of the mandible were compared using Student's t-test for paired samples or, in justified cases, its non-parametric counterpart, the Wilcoxon matched-pairs test [54].

The probability of type 1 error (level of statistical significance) was adopted at p = 0.05.

RESULTS

The basic statistics of the analysed anthropometric features of mandibles from two series of skulls (modern and medieval) as well as the results of statistical analyses carried out to identify significant differences between the compared features of mandibles are presented in Table 1.

The comparison of modern and medieval skulls for the topography of the mandibular canal revealed significant differences in several parameters (Table 1). The distance between the base of the mandible and the bottom of the mandibular canal at the level of the first and second molars on the right side in modern skulls was longer than in medieval skulls (p < 0.05). In medieval skulls, the distance between the top of the mandibular canal and the crest of the alveolar arch was longer on the right and left sides, p < 0.005. The height of the mandibular body on the left side was greater in the medieval skulls.

Statistics describing the symmetry in the mandibular anatomy for both analysed samples of skulls are presented in Table 2.

Significant differences were found for two parameters of mandibles from modern skulls: the distance between the top of the mandibular canal and the crest of the alveolar arch at the level of the second molar (p < 0.05), and the distance between the mandibular foramen and the margin of the anterior mandibular ramus (p < 0.007; Table 2). There were no significant differences between measurements taken on the right and left sides of the medieval skulls.

DISCUSSION

Knowledge of the topography of the mandibular canal and its foramina is necessary for every dentist or dental surgeon dealing with implantology, tooth extractions, surgical repair of mandibular fractures [3, 11, 13, 52, 64], or the transposition of the inferior alveolar nerve [60]. Today, it is difficult to imagine preoperative diagnostic procedures without performing an X-ray study, be it classical radiography or more advanced computed tomography [3, 64, 67]. The reason for this are known differences in the position and topography of the mandibular canal and, in some cases, the presence of accessory canals

Table 2. Comparison of measurements taken on the right and left sides in modern and medieval skulls

	Modern skulls (n = 92)		Medieval skulls (n = 34)	
	Student'	Wilcoxon matched-pairs test	Student'	Wilcoxon matched-pairs test
Bas.Ma-For.Me.	> 0.11	> 0.17	> 0.78	> 0.77
Bas.Ma-Ca.Ma. I	> 0.26	> 0.33	> 0.34	> 0.37
Ca.Ma.-Arc.Alv. I	> 0.43	> 0.21	> 0.79	> 0.62
Bas.Ma-Ca.Ma. II	> 0.90	> 0.62	> 0.43	> 0.31
Ca.Ma.-Arc.Alv. II	**< 0.05**	> 0.14	> 0.61	> 0.58
He. Ma. Bo.II	> 0.60	> 0.75	> 0.13	> 0.11
Bas.Ma-For.Ma.	> 0.78	> 0.58	> 0.08	> 0,07
For.Ma-B.P.	**< 0.007**	**< 0.006**	> 0.16	> 0.13

[41, 61]. Certain ethnic differences in the location of the mandibular canal and mental foramen have also been reported [1, 4, 5, 14, 15, 22, 39], and they are extremely important in anthropometric analyses performed during archaeological research or in forensic medicine [5, 15, 19, 37]. Our study investigating modern and medieval skulls revealed differences in the position of the mental foramen between the level of the first and second molars. The mandibular canal at the level of the second molar was ascending, while the position of the mandibular canal in relation to the base of the mandible was lowest under the alveolar arch of the first molar. These observations are consistent with reports by Kilic et al. [32] and Wychowański et al. [66], although values presented by these researchers were slightly lower. Wical and Swoope [65] reported that in skulls with complete dentition preserved, the mental foramen, which is the exit point of the mandibular canal, is most often located below the apex of the premolars' roots, i.e. in the lower third of the mandibular height. The observed trend is consistent with our findings. This rule was also confirmed in studies by Phillips et al. [45] and Al-Khateeb et al. [1]. Apinhasmit et al. [4] observed that the mental foramen was usually located in the middle of the mandible's height. Measurements of the bone height above the canal to the top of the alveolar arch of the mandible strongly depend on the presence of dentition or the time that elapsed since its loss. This distance depends on the degree of bone atrophy, which does not affect the distance between the base of the mandible and the mandibular canal [11, 13, 44, 52, 65]. Soikkonen et al. [52] and Wical et al. [65] argued that the distance between the base of the mandible and the mandibular canal and the mental foramen is reduced in edentulous mandibles with severe alveolar atrophy. The position of the mandibular foramen on radiograms was measured in relation to the base of the mandible and the margin of the anterior mandibular ramus. Values measured in our study were consistent with those reported by Wychowański et al. [66]. The location of the mandibular foramen does not depend on the alveolar atrophy or potential loss of dentition. In medieval mandibles, the mean values of measurements describing the position of the mental foramen and the topography of the mandibular canal in relation to the base of the mandible were lower than in modern mandibles. It should be noted, however, that significant differences were found only between the features describing the position of the mandibular canal in relation to the base of the mandible on the right side of the analysed mandibles. Thus, the position of the mandibular canal in medieval skulls is lower than in modern skulls. No accessory mandibular canals were observed, which also highlights ethnic homogeneity of analysed bone material. Al.-Siveedi et al. [2] reported a higher incidence of accessory mandibular canals among Malaysians compared to Chinese or Indian populations.

Analysis of face and skull asymmetry is extremely important due to the need for extensive diagnostics in orthodontic treatment [6, 12, 25, 28, 49] in paediatric surgery before the repair of cleft lip and palate [26, 35] and in forensic medicine and anthropology [6, 7, 20, 55]. In maxillofacial surgery, the analysis is performed before the surgical treatment of congenital asymmetrical distortions, such as hemifacial microsomia or plagiocephaly, surgeries of craniofacial tumours, facial clefts, severe craniofacial fractures or treatment of condylar hypoplasia [3, 11, 28, 53]. Our research revealed significant differences in the

symmetry of the mandible only in modern skulls. We found differences in the distance between the top of the mandibular canal and the crest of the alveolar arch at the level of the second molar, and the distance between the mandibular foramen and the margin of the anterior mandibular ramus. No statistically significant differences were found in medieval skulls.

CONCLUSIONS

Our study revealed differences in the position of the mandibular canal between modern and medieval skulls, but also findings reported in the literature, which confirms the presence of both geographical and chronological differences between populations.

Knowledge of variability in the position of the mandibular canal between different local populations is fundamental for the correct interpretation of findings from diagnostic radiological studies used in dental practice and for the planning and preparation of effective anaesthesia and implant placement, as well as in forensic odontology or analysis of archaeological bone materials.

Institutional Review Board Statement

The study protocol was approved by the Bioethics Committee, Pomeranian Medical University in Szczecin, Poland, decision no. KB-0012/161/17 of 18 December 2017. The study complies with the Declaration of Helsinki.

Acknowledgments

Conflict of interest: None declared

REFERENCES

1. Al-Khateeb T, Al-Hadi Hamasha A, Ababneh KT. Position of the mental foramen in a northern regional Jordanian population. Surg Radiol Anat. 2007; 29(3): 231–237, doi: 10.1007/s00276-007-0199-z, indexed in Pubmed: 17375258.
2. Al-Siweedi SYA, Ngeow WC, Nambiar P, et al. A new classification system of trifid mandibular canal derived from Malaysian population. Folia Morphol. 2023; 82(2): 315–324, doi: 10.5603/FM.a2022.0024, indexed in Pubmed: 35285511.
3. Angelopoulos C, Thomas SL, Hechler S, et al. Comparison between digital panoramic radiography and cone-beam computed tomography for the identification of the mandibular canal as part of presurgical dental implant assessment. J Oral Maxillofac Surg. 2008; 66(10): 2130–2135, doi: 10.1016/j.joms.2008.06.021, indexed in Pubmed: 18848113.
4. Apinhasmit W, Methathrathip D, Chompoopong S, et al. Mental foramen in Thais: an anatomical variation related to gender and side. Surg Radiol Anat. 2006; 28(5): 529–533, doi: 10.1007/s00276-006-0119-7, indexed in Pubmed: 16642278.
5. Bernal V, Perez SI, Gonzalez PN, et al. Ecological and evolutionary factors in dental morphological diversification among modern human populations from southern South America. Proc Biol Sci. 2010; 277(1684): 1107–1112, doi: 10.1098/rspb.2009.1823, indexed in Pubmed: 19955158.
6. Bishara SE, Burkey PS, Kharouf JG. Dental and facial asymmetries: a review. Angle Orthod. 1994; 64(2): 89–98, doi: 10.1043/0003-3219(1994)064<0089:DAFAAR>2.0.CO;2, indexed in Pubmed: 8010527.
7. Björk A, Björk L. Artificial deformation and crani-facial asymmetry in Ancient Peruvians. J Dent Res. 1964; 43(2): 356–362.
8. Borghesi A, Bondioni MP. Unilateral triple mandibular canal with double mandibular foramen: cone-beam computed tomography findings of an unexpected anatomical variant. Folia Morphol. 2021; 80(2): 471–475, doi: 10.5603/FM.a2020.0057, indexed in Pubmed: 32459362.
9. Brothwell DR. Digging up bones. Natural History Museum Publications, London 1981.
10. Buikstra J, Ubelaker DH. Standards for data collection from human skeletal remains. Arkansas Archeological Survey Research, 1994, Series 44.
11. Cawood JI, Howell RA. A classification of the edentulous jaws. Int J Oral Maxillofac Surg. 1988; 17(4): 232–236, doi: 10.1016/s0901-5027(88)80047-x, indexed in Pubmed: 3139793.
12. Cawood JI, Howell RA. Reconstructive preprosthetic surgery. I. Anatomical considerations. Int J Oral Maxillofac Surg. 1991; 20(2): 75–82, doi: 10.1016/s0901-5027(05)80711-8, indexed in Pubmed: 2051053.
13. Chrcanovic BR, Abreu MH, Custódio AL. Morphological variation in dentate and edentulous human mandibles. Surg Radiol Anat. 2011; 33(3): 203–213, doi: 10.1007/s00276-010-0731-4, indexed in Pubmed: 20878404.
14. Crawford JF. An interesting asymmetry in a mediaeval skull. Br Dent J. 1973; 134(11): 488–490, doi: 10.1038/sj.bdj.4803028, indexed in Pubmed: 4576905.
15. Cutright B, Quillopa N, Schubert W. An anthropometric analysis of the key foramina for maxillofacial surgery. J Oral Maxillofac Surg. 2003; 61(3): 354–357, doi: 10.1053/joms.2003.50070, indexed in Pubmed: 12618976.
16. El-Anwar MW, Khazbak AO, Hussein A, et al. Sphenopalatine foramen computed tomography landmarks. J Craniofac Surg. 2020; 31(1): 210–213, doi: 10.1097/SCS.0000000000005857, indexed in Pubmed: 31469730.
17. Eliades AN, Papadeli Ch, Tsirlis AT. Mandibular canal, foramina of the mandible and their variations: part II: the clinical relevance of the preoperative radiographic evaluation and report of five cases. Oral Surgery. 2015; 9(2): 85–93, doi: 10.1111/ors.12168.
18. Ferembach D, Schwindezky M, Stoukal M. Recommendations for age and sex diagnoses of skeletons.

J Hum Evol. 1980; 9(7): 517–549, doi: 10.1016/0047-2484(80)90061-5.

19. Galland M, Van Gerven DP, Von Cramon-Taubadel N, et al. 11,000 years of craniofacial and mandibular variation in Lower Nubia. Sci Rep. 2016; 6: 31040, doi: 10.1038/srep31040, indexed in Pubmed: 27503560.

20. Gawlikowska A, Szczurowski J, Czerwiński F, et al. Analysis of skull asymmetry in different historical periods using radiological examinations. Pol J Radiol. 2007; 72(4): 35–43.

21. Gawlikowska-Sroka A. [Methods for the assessment of skull asymmetry on radiograms]. Ann Acad Med Stetin. 2009; 55(3): 36–39, indexed in Pubmed: 20698176.

22. Gawlikowska-Sroka A, Stocki Ł, Dąbrowski P, et al. Topography of the mental foramen in human skulls originating from different time periods. Homo. 2013; 64(4): 286–295, doi: 10.1016/j.jchb.2013.03.009, indexed in Pubmed: 23726019.

23. Gawlikowska-Sroka A, Szczurowski J, Kwiatkowska B, et al. Concha bullosa in paleoanthropological material. Adv Exp Med Biol. 2016; 952: 65–73, doi: 10.1007/5584_2016_62, indexed in Pubmed: 27614624.

24. Gkantidis N, Tacchi M, Oeschger ES, et al. Third molar agenesis is associated with facial size. Biology (Basel). 2021; 10(7): doi: 10.3390/biology10070650, indexed in Pubmed: 34356505.

25. Grayson BH, McCarthy JG, Bookstein F. Analysis of craniofacial asymmetry by multiplane cephalometry. Am J Orthod. 1983; 84(3): 217–224, doi: 10.1016/0002-9416(83)90129-x, indexed in Pubmed: 6577794.

26. Holmes MA, Ruff CB. Dietary effects on development of the human mandibular corpus. Am J Phys Anthropol. 2011; 145(4): 615–628, doi: 10.1002/ajpa.21554, indexed in Pubmed: 21702003.

27. Hublin JJ, Ben-Ncer A, Bailey SE, et al. New fossils from Jebel Irhoud, Morocco and the pan-African origin of Homo sapiens. Nature. 2017; 546(7657): 289–292, doi: 10.1038/nature22336, indexed in Pubmed: 28593953.

28. Hwang HS, Youn IS, Lee KH, et al. Classification of facial asymmetry by cluster analysis. Am J Orthod Dentofacial Orthop. 2007; 132(3): 279.e1–279.e6, doi: 10.1016/j.ajodo.2007.01.017, indexed in Pubmed: 17826592.

29. Iwanaga J, Matsushita Y, Decater T, et al. Mandibular canal vs. inferior alveolar canal: Evidence-based terminology analysis. Clin Anat. 2021; 34(2): 209–217, doi: 10.1002/ca.23648, indexed in Pubmed: 32644203.

30. Jacobs R, Mraiwa N, vanSteenberghe D, et al. Appearance, location, course, and morphology of the mandibular incisive canal: an assessment on spiral CT scan. Dentomaxillofac Radiol. 2002; 31(5): 322–327, doi: 10.1038/sj.dmfr.4600719, indexed in Pubmed: 12203132.

31. Katz DC, Grote MN, Weaver TD. Changes in human skull morphology across the agricultural transition are consistent with softer diets in preindustrial farming groups. Proc Natl Acad Sci U S A. 2017; 114(34): 9050–9055, doi: 10.1073/pnas.1702586114, indexed in Pubmed: 28739900.

32. Kilic C, Kamburoğlu K, Ozen T, et al. The position of the mandibular canal and histologic feature of the inferior alveolar nerve. Clin Anat. 2010; 23(1): 34–42, doi: 10.1002/ca.20889, indexed in Pubmed: 19918867.

33. Kqiku L, Sivic E, Weiglein A, et al. Position of the mental foramen: an anatomical study. Wien Med Wochenschr.

2011; 161(9-10): 272–273, doi: 10.1007/s10354-011-0898-2, indexed in Pubmed: 21638218.

34. Lacruz RS, Stringer CB, Kimbel WH, et al. The evolutionary history of the human face. Nat Ecol Evol. 2019; 3(5): 726–736, doi: 10.1038/s41559-019-0865-7, indexed in Pubmed: 30988489.

35. Laspos CP, Kyrkanides S, Tallents RH, et al. Mandibular and maxillary asymmetry in individuals with unilateral cleft lip and palate. Cleft Palate Craniofac J. 1997; 34(3): 232–239, doi: 10.1597/1545-1569_1997_034_0232_mamaii_2.3.co_2, indexed in Pubmed: 9167074.

36. Levine MH, Goddard AL, Dodson TB. Inferior alveolar nerve canal position: a clinical and radiographic study. J Oral Maxillofac Surg. 2007; 65(3): 470–474, doi: 10.1016/j.joms.2006.05.056, indexed in Pubmed: 17307595.

37. Liang X, Jacobs R, Corpas LS, et al. Chronologic and geographic variability of neurovascular structures in the human mandible. Forensic Sci Int. 2009; 190(1-3): 24–32, doi: 10.1016/j.forsciint.2009.05.006, indexed in Pubmed: 19525074.

38. Lieberman D, McBratney B, Krovitz G. The evolution and development of cranial form in Homo sapiens. Proc Natl Acad Sci USA. 2002; 99(3): 1134–1139, doi: 10.1073/pnas.022440799.

39. Lundström A. Some asymmetries of the dental arches, jaws, and skull, and their etiological significance. Am J Orthodontics. 1961; 47(2): 81–106, doi: 10.1016/0002-9416(61)90205-6.

40. Malinowski A. Czynniki działające na rozwój i kształt czaszki. Auksologia a promocja zdrowia, Kielce 1997: 89–96.

41. Ngeow WC, Chai WL. The clinical significance of the retromolar canal and foramen in dentistry. Clin Anat. 2021; 34(4): 512–521, doi: 10.1002/ca.23577, indexed in Pubmed: 32020669.

42. Oeschger ES, Kanavakis G, Halazonetis DJ, et al. Number of teeth is associated with facial size in humans. Sci Rep. 2020; 10(1): 1820, doi: 10.1038/s41598-020-58565-8, indexed in Pubmed: 32019986.

43. Ozturk A, Potluri A, Vieira AR. Position and course of the mandibular canal in skulls. Oral Surg Oral Med Oral Pathol Oral Radiol. 2012; 113(4): 453–458, doi: 10.1016/j.tripleo.2011.03.038, indexed in Pubmed: 22676925.

44. Ozturk CN, Ozturk C, Bozkurt M, et al. Dentition, bone loss, and the aging of the mandible. Aesthet Surg J. 2013; 33(7): 967–974, doi: 10.1177/1090820X13503473, indexed in Pubmed: 24023258.

45. Phillips JL, Weller RN, Kulild JC. The mental foramen: Part 3. Size and position on panoramic radiographs. J Endod. 1992; 18(8): 383–386, doi: 10.1016/s0099-2399(06)81224-0, indexed in Pubmed: 1431694.

46. Pinhasi R, Eshed V, Shaw P. Evolutionary changes in the masticatory complex following the transition to farming in the southern Levant. Am J Phys Anthropol. 2008; 135(2): 136–148, doi: 10.1002/ajpa.20715, indexed in Pubmed: 18046779.

47. Pokhojaev A, Avni H, Sella-Tunis T, et al. Changes in human mandibular shape during the Terminal Pleistocene-Holocene Levant. Sci Rep. 2019; 9(1): 8799, doi: 10.1038/s41598-019-45279-9, indexed in Pubmed: 31217474.

48. Richards LC, Richards LC. Temporomandibular joint morphology in two Australian aboriginal popula-

tions. J Dent Res. 1987; 66(10): 1602–1607, doi: 10.1177/00220345870660101901, indexed in Pubmed: 3476561.

49. Rossi M, Ribeiro E, Smith R. Craniofacial asymmetry in development: an anatomical study. Angle Orthod. 2003; 73(4): 381–385, doi: 10.1043/0003-3219(2003)073<0381:CAIDAA>2.0.CO;2, indexed in Pubmed: 12940558.

50. Sankar DK, Bhanu SP, Susan PJ. Morphometrical and morphological study of mental foramen in dry dentulous mandibles of South Andhra population of India. Indian J Dent Res. 2011; 22(4): 542–546, doi: 10.4103/0970-9290.90290, indexed in Pubmed: 22124049.

51. Santini A, Alayan I. A comparative anthropometric study of the position of the mental foramen in three populations. Br Dent J. 2012; 212(4): E7, doi: 10.1038/sj.bdj.2012.143, indexed in Pubmed: 22349415.

52. Soikkonen K, Wolf J, Ainamo A, et al. Changes in the position of the mental foramen as a result of alveolar atrophy. J Oral Rehabil. 1995; 22(11): 831–833, doi: 10.1111/j.1365-2842.1995.tb00230.x, indexed in Pubmed: 8558356.

53. Souyris F, Moncarz V, Rey P. Facial asymmetry of developmental etiology. A report of nineteen case. Oral Surg Oral Med Oral Pathol. 1983; 56(2): 113–124, doi: 10.1016/0030-4220(83)90273-6, indexed in Pubmed: 6578470.

54. Stanisz A. Przystępny kurs statystyki z zastosowaniem STATISTICA PL na przykładach z medycyny. Tom 1. Statystyki podstawowe. StatSofft Polska Sp. z o o., Kraków 2006.

55. Teul I, Czerwiński F, Gawlikowska A, et al. Asymmetry of the ovale and spinous foramina in mediaeval and contemporary skulls in radiological examinations. Folia Morphol. 2002; 61(3): 147–152, indexed in Pubmed: 12416930.

56. Townsend G, Bockmann M, Hughes T, et al. Genetic, environmental and epigenetic influences on variation in human tooth number, size and shape. Odontology. 2012; 100(1): 1–9, doi: 10.1007/s10266-011-0052-z, indexed in Pubmed: 22139304.

57. Tsuji Y, Muto T, Kawakami J, et al. Computed tomographic analysis of the position and course of the mandibular canal: relevance to the sagittal split ramus osteotomy. Int J Oral Maxillofac Surg. 2005; 34(3): 243–246, doi: 10.1016/j.ijom.2004.06.001, indexed in Pubmed: 15741030.

58. Uchida Y, Noguchi N, Goto M, et al. Measurement of anterior loop length for the mandibular canal and diameter of the mandibular incisive canal to avoid nerve damage when installing endosseous implants in the interforaminal region: a second attempt introducing cone beam computed tomography. J Oral Maxillofac Surg. 2009; 67(4): 744–750, doi: 10.1016/j.joms.2008.05.352, indexed in Pubmed: 19304029.

59. Uchida Y, Noguchi N, Goto M, et al. Measurement of anterior loop length for the mandibular canal and diameter of the mandibular incisive canal to avoid nerve damage when installing endosseous implants in the interforaminal region. J Oral Maxillofac Surg. 2007; 65(9): 1772–1779, doi: 10.1016/j.joms.2006.10.015, indexed in Pubmed: 17719396.

60. Vasconcelos JA, Avila GB, Ribeiro JC, et al. Inferior alveolar nerve transposition with involvement of the mental foramen for implant placement. Med Oral Patol Oral Cir Bucal. 2008; 13(11): E722–E725, indexed in Pubmed: 18978714.

61. von Arx T, Bornstein MM. The bifid mandibular canal in three-dimensional radiography: morphologic and quantitative characteristics. Swiss Dent J. 2021; 131(1): 10–28.

62. Von Cramon-Taubadel N. Global human mandibular variation reflects differences in agricultural and hunter-gatherer subsistence strategies. Proc Natl Acad Sci USA. 2011; 108(49): 19546–19551, doi: 10.1073/pnas.1113050108, indexed in Pubmed: 22106280.

63. Wadu SG, Penhall B, Townsend GC. Morphological variability of the human inferior alveolar nerve. Clin Anat. 1997; 10(2): 82–87, doi: 10.1002/(SICI)1098-2353(1997)10:2<82::AID-CA2>3.0.CO;2-V, indexed in Pubmed: 9058013.

64. Watanabe H, Mohammad Abdul M, Kurabayashi T, et al. Mandible size and morphology determined with CT on a premise of dental implant operation. Surg Radiol Anat. 2010; 32(4): 343–349, doi: 10.1007/s00276-009-0570-3, indexed in Pubmed: 19812884.

65. Wical KE, Swoope CC. Studies of residual ridge resorption. I. Use of panoramic radiographs for evaluation and classification of mandibular resorption. J Prosthet Dent. 1974; 32(1): 7–12, doi: 10.1016/0022-3913(74)90093-6, indexed in Pubmed: 4525507.

66. Wychowański P, Nieckula P, Panek M, et al. Próba oceny położenia otworu żuchwowego i bródkowego na podstawie analizy cyfrowych zdjęć pantomograficznych. Dent Med Probl. 2008; 45(1): 21–28.

67. Yu IH, Wong YK. Evaluation of mandibular anatomy related to sagittal split ramus osteotomy using 3-dimensional computed tomography scan images. Int J Oral Maxillofac Surg. 2008; 37(6): 521–528, doi: 10.1016/j.ijom.2008.03.003, indexed in Pubmed: 18450425.

68. Ziółkiewicz T. Redukcja twarzoczaszki człowieka współczesnego. Czas Stomat. 1967; XX(4): 339–402.

ORIGINAL ARTICLE

Occurrence of the ossification of petrosphenoid ligament: a retrospective radiologic study from computed tomographic images

Bhagath Kumar Potu[1], Fatemah Hamad Al-Khamis[2],
Hebah Husain Taher[2], Abdulrahman Abdulreheim[3]

[1]Department of Anatomy, College of Medicine and Medical Sciences, Arabian Gulf University, Manama, Kingdom of Bahrain
[2]College of Medicine and Medical Sciences, Arabian Gulf University, Manama, Kingdom of Bahrain
[3]Medical Imaging Department, Mubarak Al-Kabeer Hospital, Jabriya, Kuwait

Background: Various ligaments present in the skull base are of clinical and surgical importance. One among them, is the petrosphenoid ligament (PSL). PSL may ossify either in a partial or complete form and forms the roof of Dorello's canal underneath which the abducens nerve passes. Studies argued both protective and adverse effects of the ossified PSL. Hence, the incidence of PSL ossification has become a relevant subject in clinical practice to radiologists, neurologists and neurosurgeons for understanding its potential role in abducens nerve compression.

Materials and methods: We have undertaken this study to investigate the incidence of PSL ossification from multidetector computed tomography (MDCT) images of the patients who had been referred to the Medical Imaging Department of Mubarak Al-Kabeer Hospital in Kuwait. We retrospectively assessed a total of 200 patients' head CT scans (400 petroclival regions) between January 2021 and June 2022 in which 59% were males (n = 118) and 41% were females (n = 82) aged between 18 and 91 years.

Results: A total of 37 patients (26 male, 11 female) aged between 18–84 years were presented with ossification of PSL. Among these 37 patients, 28 patients were presented with unilateral ossified PSL, and 9 patients were presented with bilateral ossified PSL, amounting to the total of 46 ossified PSL from 400 CT images of the petroclival regions (11.5%). The genderwise and sidewise occurrence of the PSL ossification seen in different age groups were not statistically significant (p > 0.05). Among all the ossified cases, there was no patient presented with abducens nerve palsy.

Conclusions: We believe our results provide baseline data in the region for understanding PSL ossification and its impact on the abducens nerve palsy. (Folia Morphol 2024; 83, 1: 176–181)

Keywords: petrosphenoid ligament, ossification, multidetector computed tomography, abducens nerve palsy

Address for correspondence: Dr. Bhagath Kumar Potu, Department of Anatomy, College of Medicine and Medical Sciences, Arabian Gulf University, Manama, Kingdom of Bahrain, e-mail: potubk@agu.edu.bh
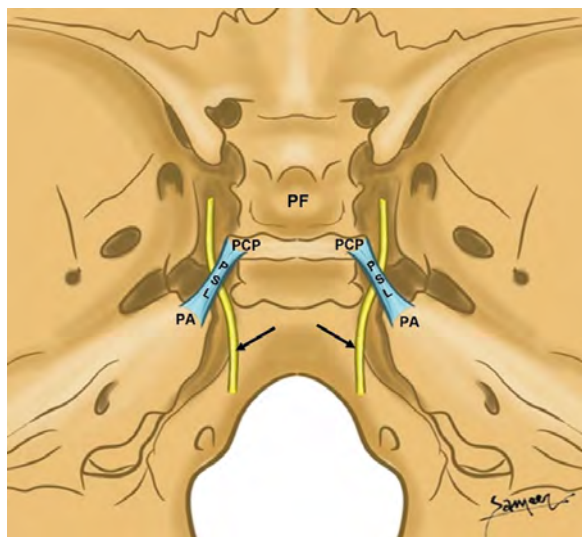
Figure 1. Schematic diagram showing the extent of petrosphenoid ligament (PSL); PF — pituitary fossa; PCP — posterior clinoid process; PA — petrous apex. Arrows showing the abducens nerve.

INTRODUCTION

Various ligaments present in the skull base are of clinical and surgical importance. One among them is the petrosphenoid ligament (PSL). As early as in the year 1859; Gruber [10] first described this ligament as a sphenopetrosal ligament that extends between the petrous apex and the accessory clinoid process of the sphenoid bone. Subsequently, in further studies, it is often referred to as the ligament of Gruber [18, 27]. Later on, Dorello [7] explored this region and found that the ligament constitutes the roof of the sphenopetrosal passageway to the abducens nerve as well as to the inferior petrosal sinus. This passage is named after Dorello as, Dorello's canal [7]. Several studies followed, reported that the abducens nerve usually [6, 8], but not in all the cases [21, 30], passes below the PSL, which is located between the petrous apex and the posterior clinoid process (Fig. 1) [12]. The available morphometric data on PSL length suggests that the average length may vary from 8–14 mm and its average width measured at the midsection ranges from 1–2 mm. The Dorello's canal, which is situated below the PSL, near the tip of petrous bone is as narrow as 5–6 mm in width with 1–2 mm height, respectively [12, 21, 25].

In some cases, the PSL may ossify either in a partial or complete form and form a bony bridge connecting the apex of the petrous bone with the sphenoid bone. Such bony bridge forms an osseous foramen, which is a normal feature seen in nonhuman primates, but

not in human beings. Up to date, the incidence of PSL ossification has been found to be in a range of 1–25% from the studies reported from various populations [12, 14, 16, 20, 28]. Studies argued both protective and adverse effects of the ossified PSL. A few studies have proposed that the ossified PSL might pose an increased risk of injury to the abducens nerve in the petroclival region causing abducens nerve palsy [21, 25, 28]. Contrary to these findings, a study also proposed the protective effects of PSL in guarding the abducens nerve [20]. Hence, the incidence of PSL ossification has become a relevant subject in clinical practice to radiologists, neurologists and neurosurgeons for understanding its potential role in abducens nerve compression. Although few anatomical studies determined the characteristic features of ossified PSL, radiological studies evaluating the incidence of PSL ossification are scarce in the available literature. To the best of our knowledge, no computed tomography (CT) imaging study has been performed in Kuwait region to assess the ossification of PSL. Therefore, we have undertaken this study to investigate the incidence of PSL ossification from the multidetector computed tomography (MDCT) images.

MATERIALS AND METHODS

Subjects

In this study, we retrospectively assessed a total of 200 patients' head CT scans (400 petroclival regions), who were referred to the Medical Imaging Department of Mubarak Al-Kabeer Hospital in Kuwait. Patients' CT scan data were reviewed using the "Centricity Universal Viewer" system at Mubarak Al-Kabeer Hospital from January 2021 till June 2022. The age of patients evaluated was in the range of 18–91 years. The mean age of the patient was 54.8 ± 18.3. CT images presenting artefacts and images with history of tumour and fractures of the petroclival region were excluded. This study was approved by the Ministry of Health, Kuwait (No: 1794/2021) as well as the Institutional Research and Ethics Committee, College of Medicine and Medical Sciences, Arabian Gulf University (Project number: E01-PI-10-21).

Assessment of PSL ossification from MDCT images

Scans were obtained using 64-row CT Scanner (GE Healthcare, Chicago, IL, USA). The image parameters were: rotation time = 1.0 s, slice thickness = 0.65 mm, effective mAs [Milli-Ampere seconds] = 150–300

Table 1. Genderwise distribution of petrosphenoid ligament ossification

Gender	Extent		Total
	Partial	Complete	
Male	24	2	26
Female	11	0	11
Total	35	2	37

Table 2. Sidewise distribution of petrosphenoid ligament ossification

	Side of ossification	Gender	
		Male	Female
Partial	Left	9	3
	Right	8	7
	Bilateral	7	1
Complete	Left	0	0
	Right	1	0
	Bilateral	1	0
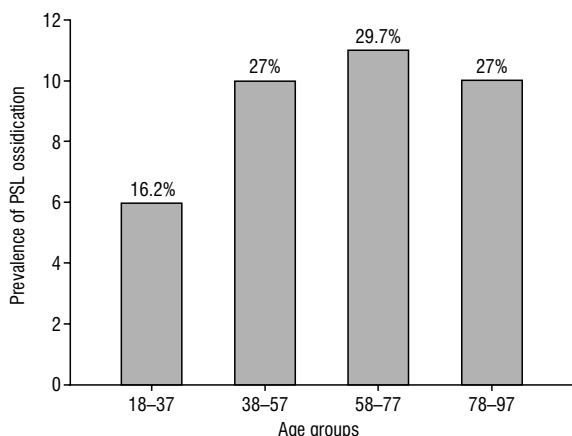
Figure 2. Age distribution of petrosphenoid ligament (PSL).

and 140 kV dose. The images were observed and assessed carefully on high-resolution monitors at bone window settings (W: 3077, C: 570). Axial slices of the skull base above the uppermost portion of the petroclival region were assessed in a craniocaudal direction to look for an ossification of the PSL. If PSL ossification was observed as an uninterrupted hyperdense extension from the petrous apex to posterior clinoid process, we defined it as a complete ossification. Any hyperdense, incomplete bony ridge in the course of PSL was noted, we defined it as a partial ossification. Age related demographics of the patients were recorded for detailed evaluation to see

whether there is any association between the age and frequency of the ossification. The medical records of patients with PSL ossification were also assessed to investigate whether the cases of PSL ossified cases are associated with abducens nerve palsy.

Statistical analysis

Data were analysed using IBM SPSS v.24 (IBM Corp., Armonk, NY, USA). Descriptive statistics were used to analyze the prevalence of PSL among age groups and sex. Data were presented as percentages. Chi-square test was performed to see whether any significant influence of sex and side on occurrence of the ossification of PSL and the significant association between the age and occurrence of the ossification of PSL. The level of significance was set at $p < 0.05$.

RESULTS

In our study of 200 patients, 59% were males (n = 118) and 41% were females (n = 82). Patients were divided into groups according to age with each group spanning 20 years. A total of 400 CT images of petroclival regions were assessed to analyze the extent of PSL ossification.

A total of 37 patients (26 male, 11 female) aged between 18–84 years were presented with ossification of the PSL. The overall prevalence of PSL ossification was 18.5% and it was seen in all age groups.

Among these 37 patients, 28 patients were presented with unilateral ossified PSL, and 9 patients were presented with bilateral ossified PSL, amounting to the total of 46 ossified PSL from 400 CT images of the petroclival regions assessed (11.5%) (Table 1). The genderwise, sidewise, and partial to complete occurrence of the PSL ossification were shown in Table 2. The age distribution of all subjects with occurrence of PSL ossification were presented in Figure 2. With regards to the extent of ossification, we found completely ossified PSL in 2 male patients (1 on the right side and 1 bilaterally) (Tables 1, 2; Fig. 3A). Of 35 partially ossified cases (24 male, 11 female), 15 were on the right side, 12 were on the left side and 8 were bilateral (Tables 1, 2; Fig. 3B). Figure 4A, B show the unilateral ossification of PSL on the right and left sides. Figure 5A, B are the volume rendered three-dimensional CT images showing bilateral partial and unilateral partial ossification of the PSL. There was no statistically significant association between gender, side, age groups and occurrence of the PSL ($p > 0.05$).
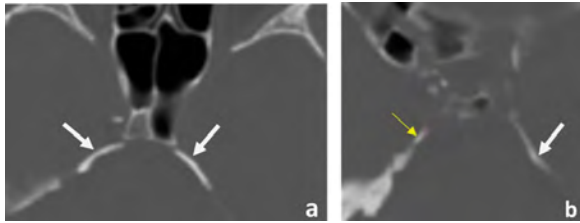
Figure 3. Bilateral ossification of petrosphenoid ligament (PSL); **A.** Axial computed tomography image showing bilateral complete ossification of PSL (white arrows) in a 52-year-old male; **B.** Axial computed tomography image showing partially ossified PSL on the right side (thin yellow arrow) and completely ossified PSL on the left side (thick white arrow) in a 68-year-old male.
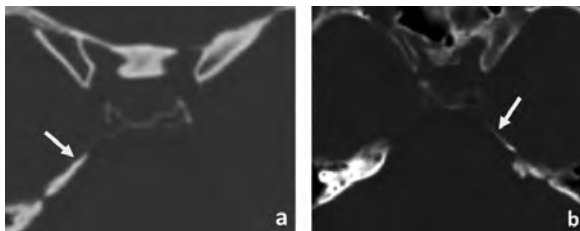
Figure 4. Unilateral partial ossification of petrosphenoid ligament (PSL); **A.** Axial computed tomography image showing unilateral ossification of PSL on the right side (white arrow) in a 26-year-old female; **B.** Axial computed tomography image showing unilateral ossification of PSL on the left side in a 59-year-old male (white arrow).
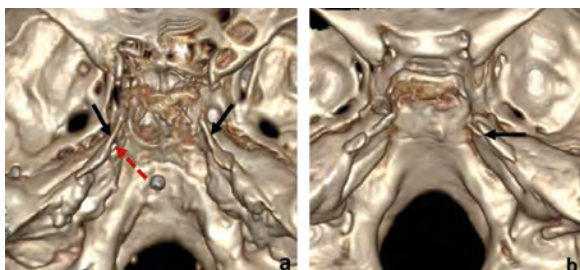
Figure 5. Volume rendered three-dimensional computed tomography images of ossified petrosphenoid ligament (PSL); **A.** Postero-superior view of the skull base showing bilateral partial ossification of PSL (black arrows) in a 68-year-old male. Dotted red arrow showing the petrous apex; **B.** Postero-superior view of the skull base showing partially ossified PSL on the right side (black arrow) in a 26-year-old female.

Based on the data reviewed, there was no patient registered with abducens nerve palsy among all the ossified cases.

DISCUSSION

To the best of our knowledge, this is the first study to report the prevalence of PSL ossification from CT scans of the skull bases in Kuwait region.

Our study found 46 ossified PSL from 400 CT images of the petroclival regions assessed (11.5%). The incidence of ossified PSL was found to range from 1 to 12% in different radiological and anatomical studies. However, in one study [14], results are different in which ossified PSL was found to be 25% (5 out of 20 specimens). A recent radiological study conducted on 240 CT images found 26 ossified PSL (19 unilateral, 7 bilateral) and identified that in bilateral cases, 14.3% were completely ossified and 85.7% were partially ossified. In unilateral cases, 26.3% were completely ossified and 73.7% were partially ossified [26]. A study by Tsitsopulos et al. [27] confirmed that PSL was ossified in 10% of cases. Ozgur and Esen [20] in their study from 523 CT images (1046 petroclival regions) found 61 ossified PSL (31 unilateral, 15 bilateral) of which 6.5% were on the right side and 5.1% were on the left side. They identified that 38 (3.6%) ligaments were partially ossified, whereas 23 (2.2%) ligaments were completely ossified. In addition to these radiological findings, very few gross anatomical studies are existing in the literature. A gross anatomical study conducted on 134 skulls observed 7 ossified PSL [1]. Peker et al. [22] in a sample of 80 subjects, reported these ossifications occurring at the incidence of 7.6% on the right side and 10.1% on the left side, respectively. A few anatomical studies have also reported a completely ossified bilateral PSL [1, 13, 19, 22, 29] and to a lesser extent, partially ossified unilateral PSL from their sample [24]. In addition to these, few reports have also discussed the atypical attachments of PSL to the posterior genu of the cavernous internal carotid artery in a male cadaver [31], and to the dorsum sellae in a fetal skull [5]. Ossification of the skull base ligaments could be attributed to factors, such as genetics, metabolic abnormalities and mechanical stress [26]. It is clear from our study results that the ossification of PSL is a common finding in all the age groups and the incidence of ossification is found to be increasing in all the age groups from 18–77 years.

Apart from ossification, partial to complete calcification of PSL is also described in the literature. Inal et al. [13] conducted a CT study on 130 skull bases and reported that the partial calcifications of the PSL were found to be 9.8% on both right and left sides and complete calcifications at the incidence of 2.3% on right and 2.9% on left sides, respectively. There were no statistically significant differences seen between PSL calcification in males and females on the right and left sides, respectively. In addition to these

radiological findings, a few anatomical studies were also conducted to assess the calcification of PSL. Icke et al. [12] have noted a small number of calcified PSL at the incidence of 5% in 2 of 40 cases studied, followed by Destrieux et al. [6] examined 16 human cadaver heads and found only 1 calcified PSL (6.25%).

The anatomical relationship of PSL with Dorello's canal has become an important aspect in clinical practice, particularly in skull base surgeries [8, 9], dealing with the pathologies of petroclival region [15]. The association of ossified PSL with hypoplasia of the Dorello´s canal [3, 4], has explained the mechanism of abducens nerve palsy in several pathological conditions caused by the infection and inflammation of the petrous apex [2]. Contrary to these adverse findings, studies also claimed that the ossified PSL may act as an important anatomical landmark, shielding the abducens nerve by limiting the petrous drilling in skull base surgeries [11] and may protect the structures passing through Dorello's canal as commonly seen in nonhuman primates [17, 23]. A study by Ozgur and Esen [20] supported this hypothesis and revealed that the complete or partial ossification of PSL was not associated with abducens nerve palsy as in our study.

Our results also suggest that the abducens nerve palsy may be mostly related to the hypoplastic Dorello's canal and the position of nerve within Dorello's canal, rather than the ossification of PSL alone. Studies confirmed that the passage of abducens nerve through Dorello's canal is not constant. It may travel in the lateral 1/3rd, middle 1/3rd or, rarely, medial 1/3rd of the canal [4, 20, 25]. In any of these cases, the abducens nerve can be entrapped when the narrow segment of the canal corresponds to the course of the abducens nerve.

CONCLUSIONS

In conclusion, our study confirms the efficiency of MDCT in identifying the ossification of PSL. We believe that these results provide baseline data in the region for understanding PSL ossification and its impact on the abducens nerve palsy. Our study has some limitations, are that: this study contained smaller samples and the complete clinical data on the radiological imaging and surgical correlation was not available. Although CT provides information about the ossified PSL, magnetic resonance imaging may be useful in future to determine the precise relationship between the ossified PSL and abducens nerve.

Conflict of interest: None declared

REFERENCES

1. Aggarwal B, Gupta M, Kumar H. Ossified ligaments of the skull. J Anat Soc India. 2012; 61(1): 37–40, doi: 10.1016/s0003-2778(12)80010-4.
2. Ambekar S, Sonig A, Nanda A. Dorello's canal and Gruber's ligament: historical perspective. J Neurol Surg B Skull Base. 2012; 73(6): 430–433, doi: 10.1055/s-0032-1329628, indexed in Pubmed: 24294562.
3. Barges-Coll J, Fernandez-Miranda JC, Prevedello DM, et al. Avoiding injury to the abducens nerve during expanded endonasal endoscopic surgery: anatomic and clinical case studies. Neurosurgery. 2010; 67(1): 144–154, doi: 10.1227/01.NEU.0000370892.11284.EA, indexed in Pubmed: 20559102.
4. Chua C, Cooper LL, Wei XC, et al. Recurrent sixth nerve palsy associated with a hypoplastic Dorello's canal. J AAPOS. 2011; 15(4): 392–394, doi: 10.1016/j.jaapos.2011.03.015, indexed in Pubmed: 21907125.
5. Clarke E, Golberg M, Smędra A, et al. Bilateral caroticoclinoid foramen and unilateral abducens nerve canal found on the fetal skull: case report. Transl Res Anat. 2022; 29: 100224, doi: 10.1016/j.tria.2022.100224.
6. Destrieux C, Velut S, Kakou M, et al. A new concept in Dorello's canal microanatomy: the petroclival venous confluence. J Neurosurg. 1997; 87(1): 67–72, doi: 10.3171/jns.1997.87.1.0067.
7. Dorello P. Considerazioni sopra la causa della paralisi transitoria dell' abducente nelle flogosi dell' orecchio medio. In: Ferrari G (ed.). Atti della Clinica Oto-Rino-Laringoiatrica. Tipografia del Campidoglio, Roma 1905: 209–217.
8. Duque PJ, Barco RJ, Mendoza ZJ. Dorello´s Canal or Abducens Nerve Canal: Constancy or Inconstancy? Int J Morphol. 2017; 35(1): 233–235, doi: 10.4067/s0717-95022017000100038.
9. Ezer H, Banerjee AD, Thakur JD, et al. Dorello's canal for laymen: a lego-like presentation. J Neurol Surg B Skull Base. 2012; 73(3): 183–189, doi: 10.1055/s-0032-1311753, indexed in Pubmed: 23730547.
10. Gruber W. Beitrage zur anatomie des keilbeins und schlafenbeins. In: Richter HE, Winter A (ed.). Schmidt's Jahrbucher der in-und Auslandischen. Gessamten Medicin, Anatomie und Physiologie. Verlag Von Otto Wigard, Leipzig 1859: 40–41.
11. Iaconetta G, Tessitore E, Samii M. Duplicated abducent nerve and its course: microanatomical study and surgery-related considerations. J Neurosurg. 2001; 95(5): 853–858, doi: 10.3171/jns.2001.95.5.0853.
12. Icke C, Ozer E, Arda N. Microanatomical characteristics of the petrosphenoidal ligament of gruber. Turk Neurosurg. 2010; 20(3): 323–327, doi: 10.5137/1019-5149.jtn.2921-10.0.
13. Inal M, Muluk NB, Burulday V, et al. Investigation of the calcification at the petroclival region through multi-slice computed tomography of the skull base. J Craniomaxillofac Surg. 2016; 44(4): 347–352, doi: 10.1016/j.jcms.2016.01.018, indexed in Pubmed: 26922483.
14. Joo W, Yoshioka F, Funaki T, et al. Microsurgical anatomy of the abducens nerve. Clin Anat. 2012; 25(8): 1030–1042, doi: 10.1002/ca.22047, indexed in Pubmed: 22334502.
15. Kshettry VR, Lee JH, Ammirati M. The Dorello canal: historical development, controversies in microsurgical

anatomy, and clinical implications. Neurosurg Focus. 2013; 34(3): E4, doi: 10.3171/2012.11.FOCUS12344, indexed in Pubmed: 23451716.

16. Liu XD, Xu QW, Che XM, et al. Anatomy of the petrosphenoidal and petrolingual ligaments at the petrous apex. Clin Anat. 2009; 22(3): 302–306, doi: 10.1002/ca.20771, indexed in Pubmed: 19173250.

17. Marom A. A new look at an old canal. Skull Base. 2011; 21(1): 53–58, doi: 10.1055/s-0030-1263282, indexed in Pubmed: 22451800.

18. Nathan H, Ouaknine G, Kosary IZ. The abducens nerve. Anatomical variations in its course. J Neurosurg. 1974; 41(5): 561–566, doi: 10.3171/jns.1974.41.5.0561, indexed in Pubmed: 4417502.

19. Ozer E, Icke C, Arda N. Microanatomical study of the intracranial abducens nerve: clinical interest and surgical perspective. Turk Neurosurg. 2010; 20(4): 449–456, doi: 10.5137/1019-5149.JTN.3303-10.1, indexed in Pubmed: 20963693.

20. Özgür A, Esen K. Ossification of the petrosphenoidal ligament: multidetector computed tomography findings of an unusual variation with a potential role in abducens nerve palsy. Jpn J Radiol. 2015; 33(5): 260–265, doi: 10.1007/s11604-015-0410-9, indexed in Pubmed: 25749833.

21. Ozveren MF, Erol FS, Alkan A, et al. Microanatomical architecture of Dorello's canal and its clinical implications. Neurosurgery. 2007; 60(2 Suppl 1): 1–7, doi: 10.1227/01.NEU.0000249229.89988.4D, indexed in Pubmed: 17297359.

22. Peker T, Anil A, Gülekon N, et al. The incidence and types of sella and sphenopetrous bridges. Neurosurg Rev. 2006; 29(3): 219–223, doi: 10.1007/s10143-006-0018-8, indexed in Pubmed: 16528575.

23. Rusu MC, Vrapciu AD, Rădoi PM, et al. Concomitant completely ossified trigeminal pore and Dorello's canal. Folia Morphol. 2023; 82(1): 187–189, doi: 10.5603/fm.a2022.0007, indexed in Pubmed: 35099042.

24. Skrzat J, Mróz I, Spulber A, et al. Ossification of the petrosphenoid ligament: a case study. Folia Med Cracov. 2017; 57(2): 87–94, indexed in Pubmed: 29121040.

25. Tomio R, Toda M, Sutiono AB, et al. Grüber's ligament as a useful landmark for the abducens nerve in the transnasal approach. J Neurosurg. 2015; 122(3): 499–503, doi: 10.3171/2014.10.JNS132437, indexed in Pubmed: 25380109.

26. Touska P, Hasso S, Oztek A, et al. Skull base ligamentous mineralisation: evaluation using computed tomography and a review of the clinical relevance. Insights Imaging. 2019; 10(1): 55, doi: 10.1186/s13244-019-0740-8, indexed in Pubmed: 31115710.

27. Tsitsopoulos PD, Tsonidis CA, Petsas GP, et al. Microsurgical study of the Dorello's canal. Skull Base Surg. 1996; 6(3): 181–185, doi: 10.1055/s-2008-1058643, indexed in Pubmed: 17170976.

28. Tubbs RS, Sharma A, Loukas M, et al. Ossification of the petrosphenoidal ligament: unusual variation with the potential for abducens nerve entrapment in Dorello's canal at the skull base. Surg Radiol Anat. 2014; 36(3): 303–305, doi: 10.1007/s00276-013-1171-8, indexed in Pubmed: 23877841.

29. Umansky F, Elidan J, Valarezo A. Dorello's canal: a microanatomical study. J Neurosurg. 1991; 75(2): 294–298, doi: 10.3171/jns.1991.75.2.0294, indexed in Pubmed: 2072168.

30. Wysiadecki G, Orkisz S, Gałązkiewicz-Stolarczyk M, et al. The abducens nerve: its topography and anatomical variations in intracranial course with clinical commentary. Folia Morphol. 2015; 74(2): 236–244, doi: 10.5603/FM.2015.0037, indexed in Pubmed: 26050813.

31. Żytkowski A, Clarke E, Musiał A, et al. Atypical attachment of the petrosphenoidal (petroclival) ligament to the posterior genu of the cavernous internal carotid artery: case report. Transl Res Anat. 2022; 27: 100185, doi: 10.1016/j.tria.2022.100185.

VIA MEDICA

ORIGINAL ARTICLE

Evaluation of congenital rib anomalies with multi-detector computed tomography in the Turkish population

Zulal Oner[1] , Serkan Oner[2] , Necati Emre Sahin[3] , Mahmut Cay[4]

[1]Department of Anatomy, Faculty of Medicine, İzmir Bakırçay University, İzmir, Turkey
[2]Department of Radiology, Faculty of Medicine, İzmir Bakırçay University, İzmir, Turkey
[3]Department of Anatomy, Faculty of Medicine, Karabük University, Karabük, Turkey
[4]Department of Anatomy, Faculty of Medicine, Uşak University, Uşak, Turkey

Background: This study aimed to evaluate the congenital anomalies of ribs in the Turkish population using multi-detector computed tomography (CT) and to reveal the prevalence and distribution of these anomalies according to sexes and body sides.

Materials and methods: This study included 1120 individuals (592 male, 528 female) over 18 who presented to our hospital with a suspicion of COVID-19 and who had thoracic CT. Anomalies such as a bifid rib, cervical rib, fused rib, Srb anomaly, foramen rib, hypoplastic rib, absent rib, supernumerary rib, pectus carinatum, and pectus excavatum, which were previously defined in the literature, were examined. Descriptive statistics were performed with the distribution of anomalies. Comparisons were made between the sexes and body sides.

Results: A prevalence of 18.57% rib variation was observed. Females had 1.3 times more variation than males. Although there was a significant difference in the distribution of anomalies by sex ($p = 0.000$), there was no difference in terms of body side of anomaly ($p > 0.05$). The most common anomaly was the hypoplastic rib, followed by the absence of a rib. While the incidence of the hypoplastic rib was similar in females and males, 79.07% of the absent ribs was seen in females ($p < 0.05$). The study also includes a rare case of bilateral first rib foramen. At the same time, this study includes a rare case of rib spurs extending from the left 11th rib to the 11th intercostal space.

Conclusions: This study demonstrates detailed information about congenital rib anomalies in the Turkish population, which may vary between people. Knowing these anomalies is essential for anatomy, radiology, anthropology, and forensic sciences. (Folia Morphol 2024; 83, 1: 182–191)

Keywords: rib, rib anomalies, thorax, multi-detector computed tomography (MDCT)

Address for correspondence: Dr. Zulal Oner, İzmir Bakırçay University, Faculty of Medicine, Department of Anatomy, İzmir, Turkey,
tel: +90 (532) 587 34 38, e-mail: zulal.oner@bakircay.edu.tr

INTRODUCTION

There are 12 pairs of ribs, and they consist of bone and cartilage. The ribs articulate with the sternum anteriorly and the thoracic vertebrae posteriorly to form the rib cage. The head, neck, and tubercle form the proximal part of the rib, while the shaft comprises the distal portion. The 11 pairs of intercostal spaces between the ribs have intercostal muscles, nerves, and veins [8]. Ribs are mobile and flexible structures that allow for inspiration and expiration to ensure gas exchange in the lungs, and they protect the heart, lungs, and great vessels in the chest cavity [18].

Congenital rib anomalies are significantly associated with rib development during embryogenesis [24]. The ribs consist of somites located on the dorsal side of the embryo and related to the level of the spine where it is located. One rib follows a pattern that includes the caudal and rostral halves of two adjacent somites. Each somite identity is determined under the control of the Hox gene family, leading to the formation of specific structures associated with its location [21, 24]. The segmentation process forms the somites, where the embryo starts from the cranial end and separates from the presomitic mesoderm towards the caudal end. The somites' segmental boundary is defined under mesoderm posterior protein 2 (MESP2 gene) [3].

Congenital anomalies of the ribs can be classified as numerical or structural anomalies. Numerical anomalies are classified as supernumerary if more than 12 pairs of ribs are present and absent ribs if less than 12. Structural anomalies include bifid, bifurcated, fused, bridging, and hypoplastic ribs [22]. Additional ribs, such as cervical ribs, are of interest to surgeons because of their clinical implications, such as thoracic outlet syndrome [16]. As a structural anomaly, the bifid rib is usually asymptomatic [4]. It may be an isolated anomaly or associated with pathological malformations [29, 31, 33].

Chest radiographs are commonly used as the initial diagnostic method to evaluate pathologies in this region, such as rib fractures. At the same time, they are known to have a lower sensitivity than computed tomography (CT) [12, 26, 32]. Therefore, the need for more sensitive imaging techniques has led to multi-detector computed tomography (MDCT) use for thoracic imaging [2]. MDCT provides a unique perspective on thoracic anatomy and the disease with shorter acquisition times, more extensive coverage, and superior image resolution [8, 20]. To avoid misdi-agnosis, radiologists and surgeons should be familiar with normal rib anatomy, normal rib variants, and the radiological appearance of ribs. In addition, this issue is essential for the correct analysis and identification of the bones found in terms of anthropologists and forensic medicine. Based on this, the present study was planned to evaluate congenital anomalies of ribs in the Turkish population using MDCT.

MATERIALS AND METHOD

This study was approved by 09.02.2022 dated 502 protocol numbered permission of (İzmir Bakırçay) University non-interventional ethics board. In this retrospective study, 1120 cases (592 male, 528 female) aged 18–94 who were referred to our hospital with a suspicion of COVID-19 and had thoracic CT between October 2021 and February 2022 were evaluated. Cases in which the images of all vertebrae between C6 and L1 and all existing ribs could be taken were included. The study did not include images of individuals with a history of surgery and trauma in the thorax and with artifacts on CT images. The presence of comorbid clinical findings was not examined.

Multi-detector computed tomography protocol

All MDCT applications were performed with a routine thoracic CT protocol using a 128-detector spiral CT scanner (GE Optimal CT660, USA). With a tube voltage of 130 kV and 20–300 mA smart dosing technology, images were obtained from axial slices of 5 mm thickness with 1.25 mm axial and 3 mm coronal-sagittal reconstructions.

Image analysis

All CT images transferred to the workstation (Horos, Version 3.3, USA) were evaluated by a specialist radiologist and two anatomists with consensus. All images were scanned from start to finish across the entire image series of axial, coronal, and sagittal planes at a standard bone dose (W/C: 500/2000). Previously defined bifid rib, cervical rib, fused rib, the fusion of the two uppermost ribs (Srb anomaly), foramen rib, hypoplastic rib, absent rib, supernumerary rib, pectus carinatum, and pectus excavatum anomalies were examined. Information about the age, sex, type, and location of the anomaly was recorded in patients with rib anomaly. The lengths (cm) of the 12th ribs, which were evaluated as hypoplastic, were measured.
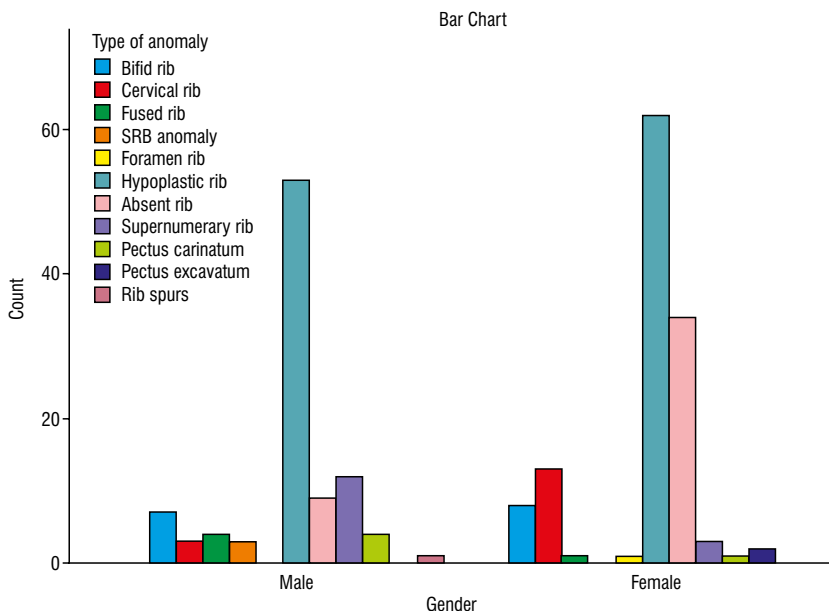
Figure 1. Distribution graph of all costal anomalies by gender.

Table 1. Distribution of anomalies by gender

Type of anomaly	Gender		Total (%)
	Male	**Female**	
Bifid rib	7 (3.17%)	8 (3.62%)	15 (6.79%)
Cervical rib	3 (1.36%)	13 (5.88%)	16 (7.24%)
Fused rib	4 (1.80%)	1 (0.45%)	5 (2.26%)
SRB anomaly	3 (1.36%)	–	3 (1.36%)
Foramen rib	–	1 (0.45%)	1 (0.45%)
Hypoplastic rib	53 (23.98%)	62 (28.05%)	115 (52.04%)
Absent rib	9 (4.07%)	34 (15.38%)	43 (19.46%)
Supernumerary rib	12 (5.43%)	3 (1.36%)	15 (6.79%)
Pectus carinatum	4 (1.80%)	1 (0.45%)	5 (2.26%)
Pectus excavatum	–	2 (0.90%)	2 (0.90%)
Rib spurs	1 (0.45%)	–	1 (0.45%)
Total	96 (43.44%)	125 (56.56%)	221 (100%)

Pearson chi-square test results: Value: 34.342[a], df: 10, p = 0.000 (a. 12 cells [54.5%] have expected count less than 5. The minimum expected count is 0.43).

Statistical analysis

The data were analysed by using SPSS 22.0 package programme. In defining the data, number and percentage were used for congenital rib anomalies, while mean ± standard deviation was used for hypoplastic 12th rib length. Descriptive statistics were performed, and distribution values were given as percentages. Differences between sexes and body sides were analysed with the Pearson chi-square test. A p-value less than 0.05 was considered statistically significant.

RESULTS

Rib anomaly was detected in 208 (18.57%) cases in 1120 thorax CT images. The mean age of subjects with variation was 53.68 (18–94). Thirteen cases were found to have more than one rib variation. The total number of variations was 221, 96 (43.44%) in males and 125 (56.56%) in females. Body side of rib anomalies by sex is shown in Table 1 and Figure 1. The most frequent anomaly was hypoplastic rib with 52.04%, followed by absent rib with 9.46%. There was statistical significance between sexes according to the distribution of anomalies (p = 0.000). In males, 17 (17.7%) of all anomalies were seen on the right, 12 (12.5%) on the left, and 67 (69.8%) bilateral. In females, these numbers were 15 (12%), 15 (12%), and 95 (76%), respectively. There was no statistically significant difference between the sexes on the side of the body for all anomalies (p > 0.05; Table 2).

Bifid rib prevalence was found as 1.34%. Fifteen (6.79%) cases were found to have bifid rib variation, and the mean age of these patients was 60.2. Seven of these cases were male, while 8 were female. The bifid rib was found unilateral in all cases, on the right side in 13 cases and on the left side in 2 cases. All bifid ribs were on ribs 3rd–5th (Fig. 2). The results of bifid rib variation did not differ between the sexes (p > 0.05; Table 3).

The fused rib prevalence was 0.45%. Nine fused ribs were found in 5 (2.26%) cases, and the mean age was 51. Five fusions were found in 1 of the cases (Fig. 3).

Table 2. Body side distribution of all anomalies by sex

Gender		Side			Total
		Right	Left	Bilateral	
Male	Count	17	12	67	96
	Expected count	13.9	11.7	70.4	96.0
	% within sex	17.7%	12.5%	69.8%	100.0%
	% within side	53.1%	44.4%	41.4%	43.4%
	% of total	7.7%	5.4%	30.3%	43.4%
Female	Count	15	15	95	125
	Expected count	18.1	15.3	91.6	125.0
	% within sex	12.0%	12.0%	76.0%	100.0%
	% within side	46.9%	55.6%	58.6%	56.6%
	% of total	6.8%	6.8%	43.0%	56.6%
Total	Count	32	27	162	221
	Expected count	32.0	27.0	162.0	221.0
	% within sex	14.5%	12.2%	73.3%	100.0%
	% within side	100.0%	100.0%	100.0%	100.0%
	% of total	14.5%	12.2%	73.3%	100.0%

Pearson chi-square test results: Value: 1.519[a], df: 2, p = 0.468 (a. 0 cells [0.0%] have expected count less than 5. The minimum expected count is 11.73).
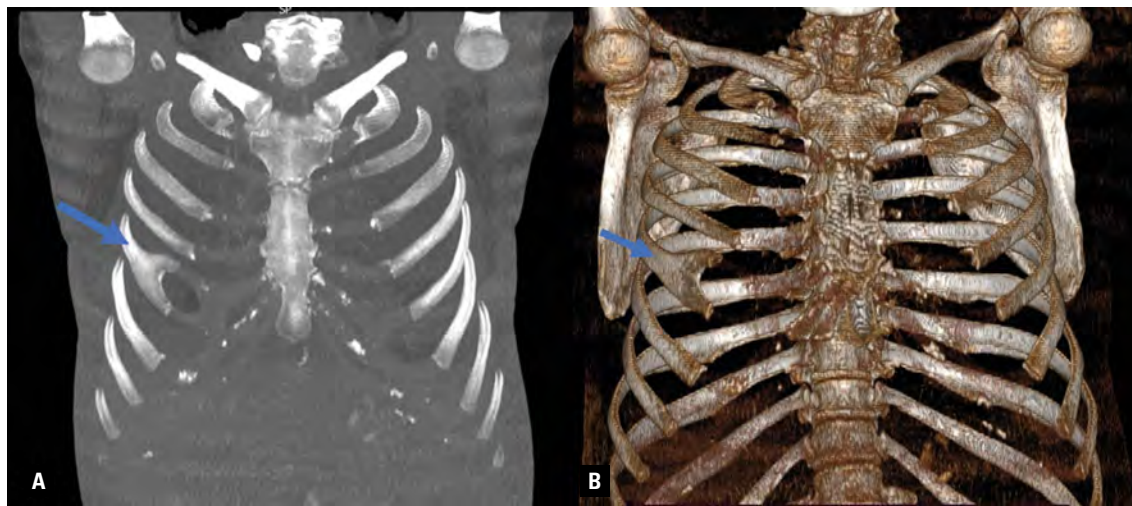
Figure 2. Bifid appearance on the right fifth rib on the coronal computer tomography image (**A**) and three-dimensional image (**B**).

Table 3. Results regarding the bifid rib variation

Gender	Anomaly location				Total
	Right side			Left side	
	3rd rib	4th rib	5th rib	3rd rib	
Male	3 (20%)	4 (26.7%)	–	–	7 (46.7%)
Female	2 (13.3%)	3 20%)	1 (6.7%)	2 (13.3%)	8 (53.3%)
Total	5 (33.3%)	7 (46.7%)	1 (6.7%)	2 (13.3%)	15 (100.0%)

Pearson chi-square test results: Value: 3.291[a], df: 3, p = 0.349 (a. 8 cells [100.0%] have expected count less than 5. The minimum expected count is 0.47).

Fused rib was observed in 4 males and 1 female. While 4 of the 9 fused ribs were on the right side, 5 were on the left. There was no difference between the sexes regarding fused rib variation (p > 0.05). Fusions were found between the 5th and 6th, 6th and 7th, and 7th and 8th ribs (Table 4).

Srb anomaly prevalence was found as 0.27%. Three (1.36%) cases had SRB anomaly, and the mean age 50.33. All the cases were male. All SRB anomalies
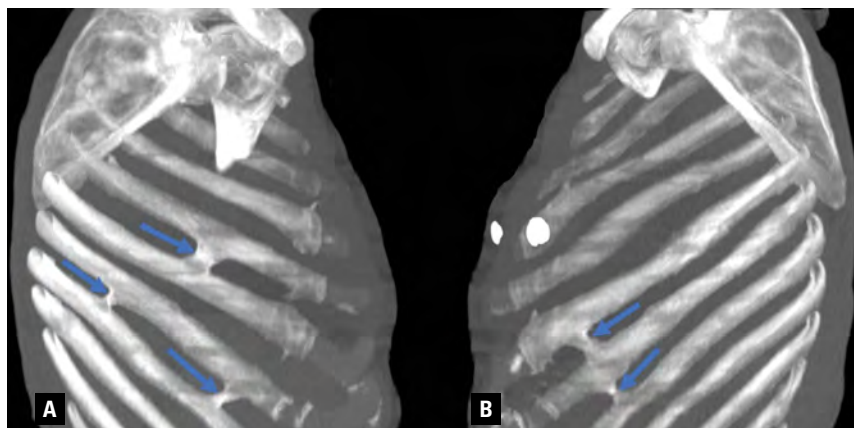
Figure 3. Right side (**A**) and left side (**B**) thoracic computer tomography images of 5 fusion centres in the same case.

Table 4. Results regarding fused rib variation

Sex		Anomaly location			Total
		5th and 6th rib	6th and 7th rib	7th and 8th rib	
Right side	Male	2	–	2	4
	Female	–	–	–	–
Left side	Male	1	2	1	4
	Female	1	–	–	1

Pearson chi-square test results: Value: 3.938ª, df: 4, p = 0.415 (a. 10 cells [100.0%] have expected count less than 5. The minimum expected count is 0.11).

were unilateral; 1 was on the right side, while 2 were on the left (Fig. 4).

Foramen rib prevalence was found as 0.09%. The only case (0.45%) with a foramen rib variation was a 26-year-old female. The foramen was located symmetrically on the first ribs (Fig. 5).

Cervical rib prevalence was found as 1.43%. There was cervical rib variation in 16 (7.24%) cases, and their mean age was 47.71 years. Thirteen of these cases were female, while 3 were male. Ten cases had bilateral cervical ribs. It was bilateral in all male cases. One of the unilateral cervical ribs was on the right side, while 5 were on the left (Table 5, Fig. 6).

Supernumerary rib prevalence was found as 1.34%. Fifteen (6.79%) cases had supernumerary ribs, and their mean age was 55.33. Three of the cases were female, while 12 were male. Bilateral 13 ribs were seen in 10 cases and unilateral in 5 (3 on the right, 2 on the left) cases (Table 5).

Hypoplastic rib prevalence was found as 10.27%. There were hypoplastic ribs in 115 (52.04%) cases, and their mean age was 52.67. In 2 cases, the first rib was hypoplastic; both were male and on the left side. In 113 cases (51 male, 62 female), the 12th ribs were hypoplastic. Ninety-eight cases had bilateral hypoplastic 12th rib, while 15 (7 on the right, 8 on the left) had unilateral (Table 5). The mean length of all hypoplastic 12th ribs was found to be 3.98 ± 1.58 cm on the left side and 4.00 ± 1.35 cm on the right (p > 0.05; Fig. 7).

Absent rib prevalence was found as 3.84%. There were missing ribs in 43 (19.46%) cases (9 male, 34 female), and their mean age was 54.9. Eleven ribs were observed bilaterally in 36 cases and unilaterally in 7 (3 on the right, 4 on the left). The absent rib in all males was bilateral (Table 5).

Pectus carinatum prevalence was found as 0.45%, while pectus excavatum was found as 0.18%. There were 5 (2.26%) cases (4 male, 1 female) with pectus carinatum, and their mean age was 56.6. There were 2 (0.90%) cases (0 male, 2 female) with pectus excavatum, and their mean age was 48.

Rib spurs extending from the left 11th rib to the 11th intercostal space were observed in 1 (0.45%) case. The case was a 61-year-old male (Fig. 7). The same subject had a comorbidity of fusion anomaly between the 5th and 6th ribs and between the 7th and 8th ribs.

DISCUSSION

In this study, which was conducted to discover congenital rib anomalies in the Turkish population using MDCT, 18.57% rib variation was observed in 1120 subjects. Although there was a significant difference in the distribution of anomalies by sex, there was no difference in terms of body side of anomaly. Females were found to have more variations (1.3x) than males. The most frequent anomaly was hypoplastic rib, followed by absent rib anomaly. While the
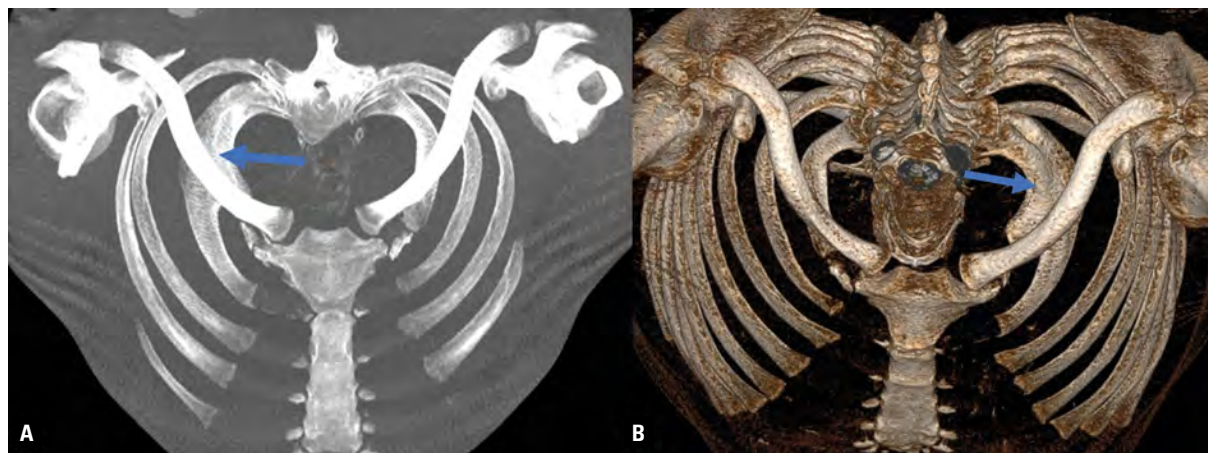
Figure 4. Cases with the right (**A**) and left (**B**) Srb anomaly.
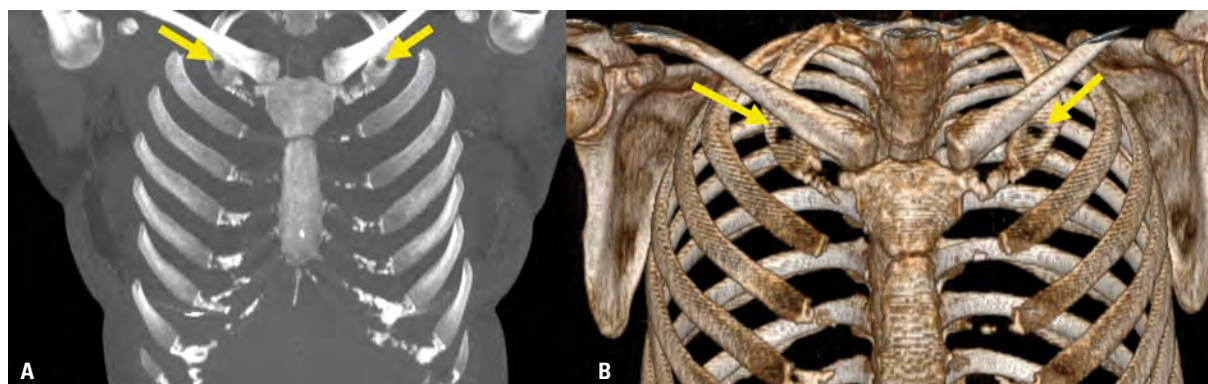
Figure 5. Presence of a single foramen on the first rib on both sides on the coronal computed tomography image (**A**) and three-dimensional image (**B**).

Table 5. Results regarding cases with cervical rib, supernumerary rib, hypoplastic 12th rib, and absent rib

Anomaly type	Anomaly location			
	Gender	Bilateral	Right side	Left side
Cervical rib	Male (19%)	3 (19%)	–	–
	Female (81%)	7 (44%)	1 (6%)	5 (31%)
	Total (100%)	10 (63%)	1 (6%)	5 (31%)
Supernumerary rib	Male (80%)	8 (53%)	2 (13%)	2 (13%)
	Female (20%)	2 (13%)	1 (7%)	–
	Total (100%)	10 (67%)	3 (20%)	2 (13%)
Hypoplastic 12th rib	Male (45%)	43 (38%)	3 (3%)	5 (4%)
	Female (55%)	55 (49%)	4 (3%)	3 (3%)
	Total (100%)	98 (87%)	7 (6%)	8 (7%)
Absent rib	Male (21%)	9 (21%)	–	–
	Female (79%)	27 (63%)	3 (7%)	4 (9%)
	Total (100%)	36 (84%)	3 (7%)	4 (9%)

Pearson chi-square test results: Value: 25.316[a], df: 11, $p = 0.008$ (a. 18 cells [75.0%] have expected count less than 5. The minimum expected count is 0.40).

Figure 6. Left cervical rib on the coronal computed tomography image.
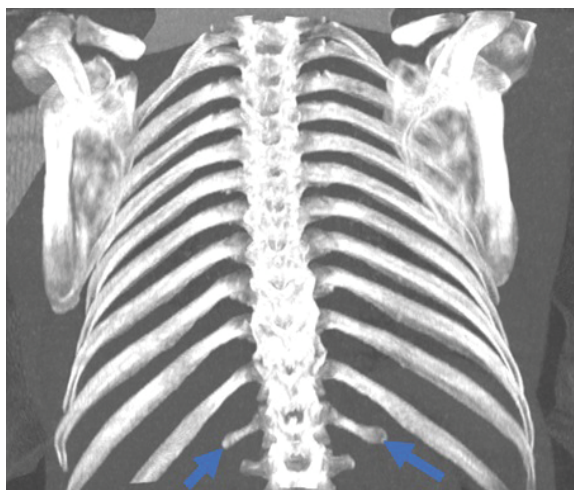
Figure 7. Bilateral hypoplastic 12th rib.
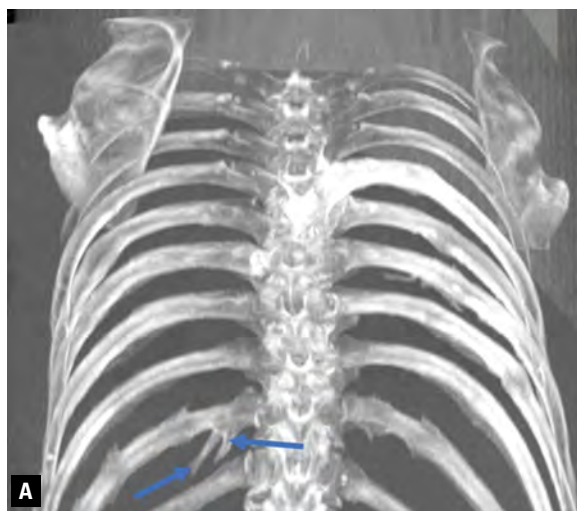
Figure 8. Spurs on the left 11th rib on the coronal computed tomography image (**A**) and three-dimensional image (**B**).

prevalence of hypoplastic rib was similar in females and males, absent rib anomaly was seen about four times more in females.

In a study conducted by Davran et al. [8], congenital rib anomalies were investigated in 650 individuals (231 female, 419 male) with MDCT, and 54 bifid rib anomaly was found in 44 (6.76%). 82% of bifid ribs were in males, and in unilateral ones, both sides were equal [8]. In the present study we conducted with a higher number of cases in the same population, a lower rate of bifid rib variation (1.34%) was found. Unlike the previous study, more bifid rib was found in females and on the right side (6.5x). The most common location of bifid rib variation was 3–5th ribs, similar to previous studies [8, 9, 11, 27].

The cervical rib is a congenital anomaly clinically associated with thoracic outlet syndrome (TOS). A meta-analysis showed that 30% of patients with TOS consist of individuals with cervical ribs [20]. In vascular TOS, compression of the cervical rib to the subclavian artery and vein may cause stenosis or aneurism [21]. As a result of neurological TOS, paraesthesia in the upper extremity or atrophy in intrinsic muscles of the hand may occur. For this reason, resection of the cervical rib, which has been found to cause TOS, is frequently used in treatment [20].

Gülekon et al. [13] found 200 (3%) cervical rib anomalies in the Turkish population on 6630 X-ray images. In a study Brewin et al. [6] conducted to find out the incidence of cervical rib in the London population,

the anomaly was found in 10 (0.74%) individuals in 1352 X-ray images and reported that variations were more common in females. In 5 of the 10 cases with cervical rib, variation was on the left side, on the right side in 3 cases, and it was bilateral in 2 cases [6]. According to a study conducted by Bokhari et al. [5] with 1000 chest X-rays, cervical rib rate was found as 3.4%, and two times higher variation rate was reported in females. In the same study, bilateral cervical rib was reported as 41%, 32.3% on the right, and 26.7% on the left [5]. Unlike these studies in literature, in the present study, we conducted with MDCT images of 1120 individuals, the rate of cervical rib variation was found as 1.4%. 63% of these variations were bilateral, 6% on the right, and 31% on the left. In addition, in our study, the cervical rib was 4.3 times more common in females and only bilaterally in males. Similar to other studies, more cervical ribs in females can be used to predict sex in bones with unknown identities. Population-based differences can be seen regarding the rate and side of the anomaly. The high number of cases and sample selection can explain the difference in the results of studies conducted on similar populations. However, this study stands out because some anomalies are difficult to detect by radiography due to the superposition disadvantage.

Rib fusion is a rare condition with a rate of 0.3% in society. It refers to the partial or complete fusion of ribs seen in the anterior or posterior ribs. It is most commonly seen between the first and second ribs. It is thought to be associated with a developmental segmentation defect since vertebral segmentation anomalies can also accompany it [14]. Similarly, fused rib prevalence was found as 0.45% in our study, and it was four times higher in males. However, in our study, the fused rib was seen on ribs 5, 6, 7, and 8, unlike the general appearance.

Srb anomaly is the formation of a solid bone layer with the incomplete fusion of the first and second rib due to one or both of the first ribs being short. The intercostal space between the first and second rib is not seen radiologically [34]. In our study, SRB anomaly was observed with a rate of 0.27%, which was unilaterally similar to other studies.

Foramen rib development is a very rare condition and has been reported to be clinically insignificant [34]. Our literature review found no incidence data or images about this anomaly. The bilateral first rib foramen we found in a female case in our study will contribute to the literature as a scarce variation. The foramen rib should be kept in mind in the differential diagnosis of bone lesions. In addition, the rib spurs we found on the left 11th rib of a male case is a different variation not reported before. This appearance may be related to incomplete rib fusion.

One of the anomalies with the higher prevalence in the society reported in the literature is hypoplastic 12th rib anomalies [19]. A rudimentary 12th rib and asymmetry in the size of this rib are often seen in the lower part of the rib cage. However, this is not clinically significant. Davran et al. [8] found a rudimentary 12th rib with a rate of 9.62%. Our study found the hypoplastic rib rate as 10.27%, similar to the literature. Unlike other studies, hypoplasia was found on the left side first rib in two of the cases.

The supernumerary rib is a rare condition that most commonly presents as a cervical rib originating from C7 or a lumbar rib originating from L1. Supernumerary rib can be a normal variation or seen in some syndromes (Turner syndrome, trisomy 8) [11]. In line with the literature, supernumerary rib was seen in a small number, and its prevalence was 1.34%. In addition, this variation was four times greater in males. The prevalence of absent rib (11 pairs of ribs) in various populations has been reported as between 5% and 8% [11, 34]. In our study, the prevalence of absence of rib was found as 3.84%, and it was 3.8 times higher in females.

Pectus carinatum is a convex forward protrusion of the sternum and costochondral joints, resulting in a pigeon-like appearance. This anomaly is the most common second deformity of the chest wall. This anomaly, seen at a rate of 0.1%, is more common in males [7, 17, 23]. In our study, pectus carinatum prevalence was 0.45%. Pectus excavatum is characterized by varying degrees of depression in the sternum and lower rib cartilage. It is the most common chest wall deformity. According to the literature, it is an anomaly with a rate of 0.4%, and it is more common in males [7, 10, 17, 30]. In our study, the prevalence of pectus excavatum was 0.18%. This difference can be interpreted as environmental or genetic reasons.

Aignătoaei et al. [1] classified the congenital anomalies of ribs according to defects in the period of embryological development. There are three main classes in this classification: results of homeotic transformation, segmentation errors, and anomalies of resegmentation.

The result of homeotic transformation is a condition in which the abnormal state of the homeobox

(Hox) genes causes an increase or decrease in the number of ribs due to the formation of false ribs, especially in the passages in the cervicothoracic and thoracolumbar borders [24]. It has been noted that the abnormal state of the Hoxa-4 and Hoxa-5 genes causes the formation of the cervical rib, while the abnormal state of the Hoxa-10 genes causes the formation of the lumbar rib [21, 33]. In this study we conducted in the Turkish population, cervical rib, supernumerary rib, absent rib, and hypoplastic 12th rib anomalies are included in this group, and results of homeotic transformation anomalies constitute the cause of 88.3% of all anomalies.

The segmentation errors are a class of rib anomalies thought to occur during somitogenesis [1]. It is thought to result from an abnormal condition in the Mesp2 transcription factor [25]. This class has been referred to as costal fusion and costal bridges [1]. Since the SRB anomaly is also a fusion in the first and second ribs, this anomaly should also be specified in this developmental error class. In addition, we thought that the rib spur anomaly in our study could be an incomplete costal bridge and included it in this group. According to the current study, 4.2% of the rib variations are due to segmentation errors.

Anomalies of resegmentation are bifid ribs that result from abnormalities in the union of two adjacent somites whose class will form the same condition [1]. We consider the foramen rib in our study should also be in this class. According to this information, 7.5% of the anomalies in our study are caused by anomalies of resegmentation.

Although our study, which had a sufficient sample size, was conducted on a specific population, the results may not be generalized since the data belong to a single hospital. This can explain why studies conducted with similar populations have different results in the literature. In addition, since the study was planned retrospectively, the presence of comorbid clinical findings was not examined. The fact that the findings of the study are based on CT images rather than radiograph can be considered as an advantage as it provides more detailed data. More comprehensive and multi-centre studies are needed to eliminate these conditions, which constitute the limitations of our study.

In addition to our study's mentioned limitations, we think it will be interesting for anatomy, radiology, anthropology, forensics, and some clinical sciences. According to the study's results, some variations showing significant sex differences may be helpful for identity analysis in bones found. Rib spurs observed in the left 11th rib in one patient and foramen rib anomalies in the bilateral first rib observed in another patient will be the first cases of these anomalies in the literature. The foramen rib, which can be found in individuals as a congenital anomaly, should not be confused with other bone lesions or injuries. Also, such anomalies can help identify unidentified individuals if previous radiographs are available.

CONCLUSIONS

In conclusion, recognizing rib variations with a wide variational range, which may be symptomatic in some cases, such as the cervical rib, will strengthen the clinician's hand. Numerical anomalies of the ribs, the most common variations in our study, should be considered because they may cause errors in determining vertebral levels in radiological imaging.

Conflict of interest: None declared

REFERENCES

1. Aignătoaei AM, Moldoveanu CE, Căruntu ID, et al. Incidental imaging findings of congenital rib abnormalities: a case series and review of developmental concepts. Folia Morphol. 2018; 77(2): 386–392, doi: 10.5603/FM.a2017.0080, indexed in Pubmed: 28868608.
2. Alkadhi H, Wildermuth S, Marincek B, et al. Accuracy and time efficiency for the detection of thoracic cage fractures: volume rendering compared with transverse computed tomography images. J Comput Assist Tomogr. 2004; 28(3): 378–385, doi: 10.1097/00004728-200405000-00013, indexed in Pubmed: 15100544.
3. Aulehla A, Pourquié O. Signaling gradients during paraxial mesoderm development. Cold Spring Harb Perspect Biol. 2010; 2(2): a000869, doi: 10.1101/cshperspect.a000869, indexed in Pubmed: 20182616.
4. Batra D, Lawner BJ. Bifid fifth rib in a 9-year-old girl with chest pain. J Am Osteopath Assoc. 2006; 106(6): 359–360, indexed in Pubmed: 16790544.
5. Bokhari RF, Al-Sayyad MJ, Baeesa SS. Prevalence of cervical ribs and elongated transverse processes in Saudi Arabia. Saudi Med J. 2012; 33(1): 66–69, indexed in Pubmed: 22273651.
6. Brewin J, Hill M, Ellis H. The prevalence of cervical ribs in a London population. Clin Anat. 2009; 22(3): 331–336, doi: 10.1002/ca.20774, indexed in Pubmed: 19280652.
7. Celik A, Kutlay H. Chest wall pectus deformities. Turkiye Klinikleri J Thor Surg-Special Topics. 2009; 2: 13–15.
8. Davran R, Bayarogullari H, Atci N, et al. Congenital abnormalities of the ribs: evaluation with multidetector computed tomography. J Pak Med Assoc. 2017; 67(2): 178–186, indexed in Pubmed: 28138167.
9. Etter L. Osseous abnormalities of the thoracic cage seen in forty thousand consecutive chest photoroentogenograms. Am J Roentgenol. 1944; 51: 359–363.

10. Fokin AA, Steuerwald NM, Ahrens WA, et al. Anatomical, histologic, and genetic characteristics of congenital chest wall deformities. Semin Thorac Cardiovasc Surg. 2009; 21(1): 44–57, doi: 10.1053/j.semtcvs.2009.03.001, indexed in Pubmed: 19632563.

11. Glass RBJ, Norton KI, Mitre SA, et al. Pediatric ribs: a spectrum of abnormalities. Radiographics. 2002; 22(1): 87–104, doi: 10.1148/radiographics.22.1.g02ja1287, indexed in Pubmed: 11796901.

12. Griffith JF, Rainer TH, Ching AS, et al. Sonography compared with radiography in revealing acute rib fracture. Am J Roentgenol. 1999; 173(6): 1603–1609, doi: 10.2214/ajr.173.6.10584808.

13. Gulekon I, Barut C, Turgut H. The prevalence of cervical rib in Turkish population. Gazi Med J. 1999; 10: 149–152.

14. Guttentag AR, Salwen JK. Keep your eyes on the ribs: the spectrum of normal variants and diseases that involve the ribs. Radiographics. 1999; 19(5): 1125–1142, doi: 10.1148/radiographics.19.5.g99se011125, indexed in Pubmed: 10489169.

15. Henry BM, Vikse J, Sanna B, et al. Cervical rib prevalence and its association with thoracic outlet syndrome: a meta-analysis of 141 studies with surgical considerations. World Neurosurg. 2018; 110: e965–e978, doi: 10.1016/j.wneu.2017.11.148, indexed in Pubmed: 29203316.

16. Huang JH, Zager EL. Thoracic outlet syndrome. Neurosurgery. 2004; 55(4): 897–902, doi: 10.1227/01.neu.0000137333.04342.4d, indexed in Pubmed: 15458598.

17. Jeung MY, Gangi A, Gasser B, et al. Imaging of chest wall disorders. Radiographics. 1999; 19(3): 617–637, doi: 10.1148/radiographics.19.3.g99ma02617, indexed in Pubmed: 10336192.

18. Kumar N, Guru A, Patil J, et al. Additional circular intercostal space created by bifurcation of the left 3rd rib and its costal cartilage: a case report. J Med Case Rep. 2013; 7: 6, doi: 10.1186/1752-1947-7-6, indexed in Pubmed: 23298541.

19. Kurihara Y, Yakushiji YK, Matsumoto J, et al. The ribs: anatomic and radiologic considerations. Radiographics. 1999; 19(1): 105–119; quiz 151, doi: 10.1148/radiographics.19.1.g99ja02105, indexed in Pubmed: 9925395.

20. Lawler LP, Fishman EK. Multi-detector row CT of thoracic disease with emphasis on 3D volume rendering and CT angiography. Radiographics. 2001; 21(5): 1257–1273, doi: 10.1148/radiographics.21.5.g01se021257, indexed in Pubmed: 11553832.

21. Li Z, Kawasumi M, Zhao B, et al. Transgenic over-expression of growth differentiation factor 11 propeptide in skeleton results in transformation of the seventh cervical vertebra into a thoracic vertebra. Mol Reprod Dev. 2010; 77(11): 990–997, doi: 10.1002/mrd.21252, indexed in Pubmed: 21049546.

22. Lim CY, Lee KW, Bin JC, et al. Congenital anomalies of the ribs. J Korean Radiol Society. 1982; 18(3): 487–495, doi: 10.3348/jkrs.1982.18.3.487.

23. Mak SM, Bhaludin BN, Naaseri S, et al. Imaging of congenital chest wall deformities. Br J Radiol. 2016; 89(1061): 20150595, doi: 10.1259/bjr.20150595, indexed in Pubmed: 26916279.

24. Mallo M, Vinagre T, Carapuo M. The road to the vertebral formula. Int J Develop Biol. 2009; 53(8-9-10): 1469–1481, doi: 10.1387/ijdb.072276mm.

25. Morimoto M, Kiso M, Sasaki N, et al. Cooperative Mesp activity is required for normal somitogenesis along the anterior-posterior axis. Dev Biol. 2006; 300(2): 687–698, doi: 10.1016/j.ydbio.2006.08.043, indexed in Pubmed: 16996494.

26. Omert L, Yeaney W, Protetch J. Efficacy of thoracic computerized tomography in blunt chest trauma. Am Surg. 2022; 67(7): 660–664, doi: 10.1177/000313480106700715.

27. Osawa T, Sasaki T, Matsumoto Y, et al. Bifid ribs observed in the third and the fourth ribs. Kaibogaku Zasshi J Anat. 1998; 73(6): 633–635.

28. Sanders RJ, Hammond SL. Management of cervical ribs and anomalous first ribs causing neurogenic thoracic outlet syndrome. J Vasc Surg. 2002; 36(1): 51–56, doi: 10.1067/mva.2002.123750, indexed in Pubmed: 12096257.

29. Schumacher R, Mai A, Gutjahr P. Association of rib anomalies and malignancy in childhood. Eur J Pediatr. 1992; 151(6): 432–434, doi: 10.1007/BF01959357, indexed in Pubmed: 1628671.

30. Semionov A, Kosiuk J, Ajlan A, et al. Imaging of thoracic wall abnormalities. Korean J Radiol. 2019; 20(10): 1441––1453, doi: 10.3348/kjr.2019.0181, indexed in Pubmed: 31544369.

31. Song WC, Kim SH, Park DK, et al. Bifid rib: anatomical considerations in three cases. Yonsei Med J. 2009; 50(2): 300–303, doi: 10.3349/ymj.2009.50.2.300, indexed in Pubmed: 19430569.

32. Thompson B, Finger W, Tonsfeldt D, et al. Rib radiographs for trauma: Useful or wasteful? Ann Emerg Med. 1986; 15(3): 261–265, doi: 10.1016/s0196-0644(86)80561-3.

33. Wattanasirichaigoon D, Prasad C, Schneider G, et al. Rib defects in patterns of multiple malformations: A retrospective review and phenotypic analysis of 47 cases. Am J Med Genet A. 2003; 122A(1): 63–69, doi: 10.1002/ajmg.a.20241.

34. Yochum T, Rowe L. Essentials of skeletal radiology. 2nd ed. Williams et Wilkins, Baltimore, USA 1996.

ORIGINAL ARTICLE

A retrospective evaluation of condylar morphology using panoramic radiography in a sample of Turkish population

Hilal Peker Öztürk[1] , Hakan Avsever İsmail[1, 2] , Buğra Şenel[1, 2] , Hatice Seda Özgedik[1] , Mehmet Hakan Kurt[3]

[1]Department of Dentomaxillofacial Radiology, Gulhane Dentistry Faculty, University of Health Sciences, Ankara, Turkey
[2]Department of Dentomaxillofacial Radiology, Faculty of Dentistry, University of East Mediterranean, Gazi Mağusa, Cyprus
[3]Department of Dentomaxillofacial Radiology, Faculty of Dentistry, Ankara University, Ankara, Turkey

Background: *The temporomandibular joint is one of the most complex anatomic structures. It takes a great role in masticatory system and helps to make possible some functions such as speaking, chewing and swallowing. Clinicians should have sufficient anatomical knowledge to assess relationships of the hard and soft tissues, including the mandibular condyle, glenoid fossa, articular eminence of the temporal bone, the articular disc and its attachments. The aim of this study was to evaluate the frequency of different types of mandibular condyles and its distribution according to the age and gender. It was also evaluated whether the condyle types were bilaterally symmetrical or not.*

Materials and methods: *A total of 1315 digital panoramic images which obtained from the patients suffering from the dental problems were assessed. Demographic data, condylar morphology were noted. All obtained data were analysed by using descriptive statistics. Morphology of mandibular condyles were classified into four shapes as identified in other studies, namely: type I — oval shape, type II — diamond shape, type III — bird beak shape, type IV — crooked finger shape. Two independent examiners, who have 19 and 7 years of experience in oral and dentomaxillofacial radiology, made a consensus and evaluated all images.*

Results: *A total of 1315 digital panoramic images were assessed. Seven hundred sixty-seven [58.3%] the patients were female and 548 [41.6%] were male. The age range of patients was from 18 to 84 years. Right-left condyle types were found to be symmetrical in the range of 67% of the subpopulation examined in the study. For the consensus, 'oval' condyle was common on both the right and left, while 'crooked finger' condyle was the rarest.*

Conclusions: *The temporomandibular joint is the most important structure for all jaw functions such as speech, swallowing. In order for all these functions to continue in a healthy way, the anatomical structure should be known very well down to the finest detail. Identification of anatomical structures and their variations can play an important role in implant dentistry. Clinicians commonly prefer conventional radiologic methods to evaluate dentomaxillofacial region. Although the most of the variations are asymptomatic and require no treatment,*

Address for correspondence: Assistant Professor Hilal Peker Öztürk, Health Sciences University, Gulhane Dentistry Faculty, Department of Dentomaxillofacial Radiology, Ankara, Turkey, tel-1: +90 3123046063, tel-2: +90 5054463628, e-mail: hpozturk0@gmail.com

correct identification of these findings will reduce unnecessary further diagnostic assessments and will provide more appropriate treatment plans. (Folia Morphol 2024; 83, 1: 192–199)

Keywords: mandibular condyle, anatomy, radiographic interpretation

INTRODUCTION

The temporomandibular joint (TMJ) is one of the most complex anatomic structures. It takes a great role in masticatory system and helps to make possible some functions such as speaking, chewing and swallowing [29]. Although TMJ has some common features with other joints, it has some differences such as anatomic complexity and close anatomical relationships make it specific among others in the body. TMJ has bony articular surfaces, articular capsule, synovial membrane, ligaments and also an articular disc [25]. Clinicians should have sufficient anatomical knowledge to assess relationships of the hard and soft tissues, including the mandibular condyle, glenoid fossa, articular eminence of the temporal bone, the articular disc and its attachments [11, 18, 20].

Improving the knowledge of dentomaxillofacial anatomy and the features of imaging modalities will lead practitioners to avoid misinterpretations and misdiagnosis. In this context, radiographic examination is necessary to evaluate TMJ structures, abnormalities, growth and bony changes. Choosing the most appropriate imaging technique is precious. Over the years, radiologists have used different oblique projections to overcome the limitations of standard conventional radiographic techniques. Recently, there are several imaging modalities available including conventional radiographic techniques, computerized tomography (CT) scanning, cone-beam CT (CBCT), arthrography, magnetic resonance imaging (MRI), computerized axiography, and ultrasonography [20].

Considering the advantages of the panoramic imaging technique, it is often used for dental reasons in the evaluation of the dentomaxillofacial area. Although panoramic imaging is one of the most common imaging techniques in dental practice, there are some limitations. These limitations including; magnifications, distortions and superimpositions make difficult to interpret the anatomical structures such as TMJ [21]. Despite these limitations some anatomical structures can be evaluated. One of these is condyle shape. A number of studies which were made in different populations by using panoramic imaging technique are available in literature about the shape of the mandibular condyle. Some differences between several populations were found in prevalence [2, 5, 10, 26, 27, 31].

Condyle is a special part of TMJ, because it stimulates the growth of the mandible. Shape of mandibular condyle can differ among some individuals. Simple developmental variability, remodelling to accommodate developmental variations, malocclusion, trauma and other developmental abnormalities can cause morphological changes on the mandibular condyle [3, 8]. Additionally, the form and function can be considered closely linked. Due to this situation, morphology of TMJ may be related to functional forces [12]. Full understanding of the anatomy and the morphology of the TMJ is crucial to detect the normal and the abnormal condition [8]. Normal condylar head is assumed to have convex structure and to be of the same shape bilaterally in the same person [23]. Morphological changes of mandibular condyle are most commonly observed in elderly people due to the degeneration of TMJ [17]. Based on all these, the detection of changes in the condyle is important for the diagnosis of TMJ diseases and reduces misinterpretation [3].

The aim of this study was to examine the morphologies of the mandibular condyle and evaluate the frequency of different types of mandibular condyles and their distribution according to age and gender in a Turkish subpopulation. It is also revealed the frequency of the difference of bilateral occurrence if available.

Therefore the current study's hypothesis was that the right and left mandibular condyles in a person mostly would be in different types and age and gender does not affect condyle types.

MATERIALS AND METHODS

Study design

This study was authorized by the Local Research Ethics Committee (Protocol: 2021/278). The retrospective cross-sectional study was performed on digital panoramic images of 10287 patients who were
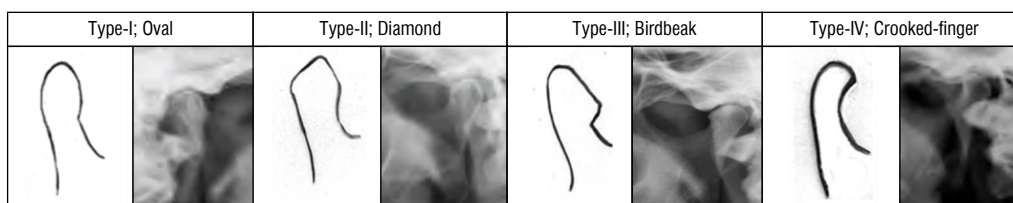
Figure 1. Four types of condyle shapes.

Table 1. Comparing the symmetry status of right and left condyles between both genders

	Symmetrical condyle types	Asymmetrical condyle types	Total	Does symmetricity differ subject to gender? (no)
Female	526 (40%)	241 (18%)	767 (58%)	P = 0.789
Male	537 (28%)	176 (14%)	548 (42%)	

referred to the Department of Dentomaxillofacial Radiology at Gulhane Dentistry Faculty, University of Health Sciences, Ankara, Turkey, between 2021 and 2022. The panoramic images were performed using a Planmeca Promax digital panoramic system at 66 kVp, 8 mA and 15.8 s exposure settings (Planmeca, Helsinki, Finland).

All images were made with the same radiographic equipment (Planmeca, Helsinki, Finland) with the maximum KVP of 66, mA = 8. All radiography were carried out by the same technician. All of the images were evaluated on the same monitor (HP Compaq LE1711 LCD Monitor, Palo Alto, CA, USA).

The panoramic images which were obtained for dentomaxillofacial problems such as impacted teeth, pathological lesions, orthognathic problems, dental implant procedures, endodontic lesions, etc were evaluated in this study. Inclusion criterion consisted of individuals over 18 years of age undergoing a panoramic radiographic examination with adequate diagnostic quality. The images of patients who were under the age of 18 or had a history of surgery, trauma, or developmental deficiencies in the dentomaxillofacial region and that were with low quality were excluded from the study. The images were evaluated to have adequate diagnostic quality, with all examined anatomical structures being visualized correctly, without any artifacts such as blurring, streaking, or ghosting, and with suitable contrast and density. A total of 1315 images were evaluated, 767 (58.3%) of the patients were female and 548 (41.6%) were male.

Image evaluation

The images were evaluated by consensus by two radiologists who have experience over 10 years,

with ClearCanvas DICOM Viewer, version 1.0.0.0v4 (ClearCanvas Inc., Toronto, Ontario, Canada) on a standard computer with calibrated monitor (HP Compaq LE1711 LCD Monitor, Palo Alto, CA, USA). The contrast and brightness level of the images and zooming were left to the examiner's choices.

Morphology of mandibular condyles were classified into four shapes as identified in other studies [2, 26]: type I — oval shape, type II — diamond shape, type III — bird beak shape, type IV — crooked finger shape shown in Figure 1.

Statistical analysis

Obtained data were analysed by descriptive statistics. The frequency of the condylar morphology types were calculated. All categorical variables were shown as number (%). The Pearson's chi-square test was used to compare categorical variables. All statistical analyses were carried out using IBM SPSS Statistics 21.0 (IBM Corp., Armonk, NY, USA) and MS Excel 2007.

RESULTS

Total of 2630 condyles from 1315 panoramic radiographs were evaluated; 767 of panoramic radiographs were female's and 548 of them were male's. In the study, there were 784 patients over the age of 40 and 531 patients under the age of 40. The average age of the included individuals was 43.93 years, with an age range between 15 and 89 years.

According to the consensus, the condyles were highly symmetrical (Table 1). Oval condyles were detected at a rate of 66% of the patients whose condyle type was symmetrical in the panoramic images (Fig. 2). However, crooked finger condyles were in symmetry
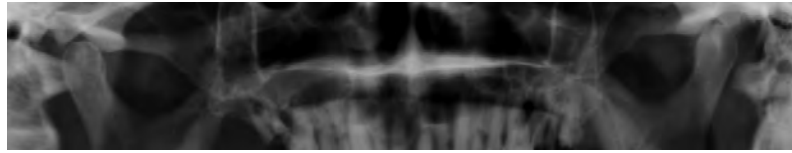
Figure 2. A panoramic radiograph which shows symmetry on right and left condyles as oval (type 1)-oval (type 1).

Figure 3. The most common asymmetrical combination seen in the study was bird-beak (type 3)-oval (type 1) for the right and left condyle.
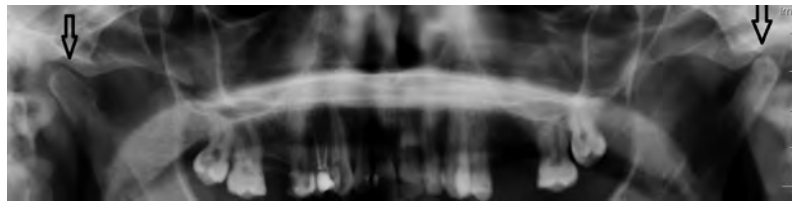
Figure 4. The rarest asymmetrical combination seen in the study was bird-beak (type 3)-crooked finger (type 4) for the right and left condyle.

Table 2. Comparing the symmetry status of right and left condyles between age groups

	Symmetrical condyle types	Asymmetrical condyle types	Total	Does symmetricity differ subject to age? (no)
Under the age of 40	361 (28%)	170 (13%)	531 (41%)	P = 0.677
Over the age of 40	372 (40%)	247 (19%)	784 (59%)	

with the lowest level at a rate of approximately 10%. Most of the patients who exhibited asymmetry had a right condyle type 3 (diamond)-left condyle type 1 (oval) form (Fig. 3). The rarest combination of asymmetry was found to be either a right condyle type 3 (diamond)-left condyle type 4 (crooked finger), or a right condylar type 4 (crooked finger)-left condylar type 3 (diamond) (Fig. 4).

At first, symmetrical or asymmetrical status of condyles were evaluated. In the study conducted on panoramic images, the probabilistic value was 0.789 (Table 1). Therefore Pearson chi-square test results concluded that symmetry/asymmetry appearance was independent of gender for the consensus in 5% confidence interval. Similar to gender results, age group indicator had no impact on symmetry/asymmetry appearance with p-value of consensus 0.677 (Table 2). Although there was no significant relationship, the

study divided the data into two age groups: under and over 40 years of age. In study groups symmetry was observed in 68% of individuals over the age of 40 and 69% of individuals under the age of 40.

Type of condyles were studied with age groups and gender. The distribution of condyles with respect to age groups was interpreted. For the consensus, oval type of condyle was seen as the most common type and the crooked finger as the rarest one in both right and left condyles.

According to the results, a strongly significant relationship was found between the type of condyles and the age group (p = 0.05; Table 3). Moreover, a strongly significant relationship was found between gender and condyle types (p = 0.00; Table 4). For the consensus at right condyles, 54% of women had oval condyle, while the lowest proportion (13%) of women had crooked finger condyles, whereas in male

195

Table 3. Distribution of condyle types according to age

	Condyle type 1	Condyle type 2	Condyle type 3	Condyle type 4	Total	Does condyle type differ subject to age group? (no)
Under age of 40	609 (23.2%)	164 (6.2%)	155 (5.9%)	134 (5.1%)	1062 (40.4%)	P = 0.05
Over age of 40	915 (34.7%)	260 (9.9%)	256 (9.8%)	137 (5.2%)	1568 (59.6%)	
Total	1524 (57.9%)	424 (16.1%)	411 (15.6%)	271 (10.3%)	2630 (100%)	

Table 4. Distribution of condyle types according to gender

	Condyle type 1	Condyle type 2	Condyle type 3	Condyle type 4	Total	Does condyle type differ subject to gender? (no)
Female	848 (32.2%)	288 (10.9%)	202 (7.7%)	196 (7.5%)	1534 (58.3%)	P = 0.00
Male	676 (25.7%)	136 (5.2%)	209 (8%)	75 (2.8%)	1096 (41.7%)	
Total	1524 (57.9%)	424 (16.1%)	411 (15.6%)	271 (10.3%)	2630 (100%)	

patients, 62% of the patients had oval condyle and 7% had crooked finger condyle. In both genders, oval condyle was observed with a significant frequency on the right and crooked finger condyle was the rarest. Left condyles were similar to the right side; oval condyles were seen in 57% of women and 61% of men and crooked finger condyles were observed most rarely in both genders.

According to consensus, oval condyle was observed at the highest rate among all types when both sides were evaluated separately within themselves: 57% oval on right side, 59% oval on left side and when both sides were evaluated together, oval type was found at a rate of 58%. Type of crooked finger was found at a rate of ten percentage on both sides as the rarest.

DISCUSSION

The study was performed on percentages and quantitative data of mandibular condyle shapes according to gender or age like the similar ones. This is useful because it provides to compare different populations or subgroups within a population.

The morphological view of the mandibular condyle may vary significantly between different age groups and different individuals [9, 26, 30]. Condyle findings in panoramic radiographs need to be interpreted with extreme caution. It is necessary to know the limitations of panoramic radiography when describing condyle morphology [19].

Research on condyle shape goes back to the 1960's. Yale et al. [31–33] performed the first research on this subject within the scope of 4 basic shapes of condyle head. In the present study the condyle clas-

sification is based on the studies of Anussizuman et al. [2] and Shaikh et al. [26].

This research aimed to reveal the rate of condyle types in a Turkish subpopulation. Condyle types and their rate were assessed in relation to age and gender. The study findings about the most common condyle type were oval type (in the range of 57%) on both the right and the left side. Besides, condyle types differed significantly according to gender. Proportionally, the oval type was detected as more intense in males (61%). The most common combination of symmetry was seen as oval-oval.

The null hypothesis that the right and left mandibular condyles in a person mostly would be asymmetrical was rejected. The rate of asymmetry was found as 32%. This outcome may be due to the group of patients studied or the number of patients who didn't use the right and left sides of the jaw equally was less than expected.

Honda et al. [9] performed a study and reported that the panoramic radiography technique is beneficial on assessment of TMJ pathologies. It's an evidence that about 20 years ago the panoramic radiograph's competence about TMJ pathologies was proved.

In a similar study it was conducted in a different population, type of oval was the most common condyle type, while crooked finger was the least common like the current study. This prevalence was seen in all age groups and in both genders. In the same study it was found 74.2% of condyles as symmetrical with oval-oval type and it was the most commonly occurring among the other combinations. All the results of our study were consistent with the results of the study of Al-Saedi et al. [1].

Similar to present study, another one was carried out by Sonal et al. [28]; the highest proportion in a population at 60% was the oval type condyle and crooked finger type was the least common at 2%. In a study conducted in Bangladesh population the 'oval' was the most common type with 68%, and the 'crooked finger' was the rarest type. The most common combination both in male and female was 'oval-oval', the less common one was 'crooked finger-crooked finger' [2]. Consistent with literature, Shaikh et al. [26] found that oval type condyle was the most common. In the current study, the oval condyle type was the most common and the crooked finger type was the rarest. It was seen that despite different populations and countries, it turns out that usually the common condyle type is the oval type. Shaikh et al. [26], Choudhary et al. [6] and Ribeiro et al. [22], in their studies in different country populations, each showed that round-round combination was the most common in both genders. They used a different classification as 'flat', 'pointed', 'angled' and 'round' condyle types. 'Round' type express the same type as the oval type in the classification used in the present study.

In Ashwinirani's study [4], the most common condyle type was 'round' in female, but 'angled' in male, different results were observed in male and female. Ashwinirani [4] used a different classification. In another study round type of condyle was again found to be the most common [24]. Similarly Maqbool et al. [13], Al Saedi et al. [1] and Gindha et al. [7] revealed highly significant difference in condylar type between right and left sides in females and males.

Similar to this one, a significant relation was found between gender and condyle types in the current study. Thus the second hypothesis that there would be no correlation between condyle types and age and gender was also rejected. According to the consensus, for both sides (right and left) condyle type of oval was the most common in both genders. The rarest type was the crooked finger in both genders and sides.

Al Saedi et al. [1], Nagaraj et al. [15], and Ashwinirani et al. [1] found no significant difference between age groups and condyle types. Contrary to these studies, in the present study it was observed that there was a significant relationship between age groups and condyle types. The study was performed by Nalla et al. [16] revealed that toughness of bones decreases by approximately 40% from 40 to 100 years. Another study reported that morphological change of condyle is commonly seen in patients over the age of 40 (90%) compared to under the age of 40 (64%) [14]. Based on present results, in this study, the patients were classified into two age groups: over the age of 40 and under the age of 40. According to the consensus, the most common oval condyle and the rarest crooked finger condyle were found both on the right and the left in examined patients. Similarly, Shaikh et al. [26] found a significant relation between condyle morphology and age; they revealed that diamond shape was more frequent in the 56 and older age group.

Al Saedi et al. [1] reported 64.8% of radiographs had bilateral occurrence of same type and most common combination was oval-oval (46%). Similar to Al-Saedi et al. [1], in another study, approximately two-thirds of the panoramic radiographs had the same type of condyles bilaterally [19]. In the current study, in line with the results of previous studies, most of the patients had a symmetrical condylar shape with most common oval-oval combination.

However in Oliveira-Santos's et al. [19] study, a more equal distribution between types is observed in older individuals, while a clear predominance of the 'round' type is observed among younger individuals. In the present study, condyle type of oval was seen distinctly more often in both age groups and the other types were seen approximately at the same rates in both age groups.

During the study, no evaluation was made according to the dentition and edentulous status. The fact that the edentulous state was not included in the study evaluation can be seen as a limitation of the study.

CONCLUSIONS

This study has demonstrated that evaluation of mandibular condyle shapes can be achieved through panoramic radiography.

According to the findings of this research, it has been concluded that there was no significant difference between bilateral occurrence of the same condyle shape depending on gender and age. However, it has also been found that age and gender do affect the types of condyles.

The oval shape of the condyle was most common for both genders and both age groups. The most common combination of symmetry was seen as oval-oval.

In future studies regarding this topic, clinical and radiological findings should be combined. By increas-

ing the study sample and including clinical parameters such as dentition or edentulism status of patients, how long this condition has been going on in the study, more reliable information about populations will be provided.

Acknowledgements

Conflict of interest: None declared

REFERENCES

1. Al-Saedi IL, Taee RA, asim NHA, et al. A panoramic study of the ogy of mandibular condyle in a sample of population from Basrah City. Int J Morphol. 2020; 38(6): 1707–1712.

2. Anisuzzaman MMd, Khan S, Khan M, et al. Evaluation of mandibular condylar morphology by orthopantomogram in Bangladeshi population. Update Dental Coll J. 2019; 9(1): 29–31, doi: 10.3329/updcj.v9i1.41203.

3. Arayapisit T, Ngamsom S, Duangthip P, et al. Understanding the mandibular condyle morphology on panoramic images: A cone beam computed tomography comparison study. Cranio. 2023; 41(4): 354–361, doi: 10.1080/08869634.2020.1857627, indexed in Pubmed: 33297888.

4. Ashwinirani SR, Patil ST, Nair B, et al. Morphological variations of condylar process and sigmoid notch using orthopantomograms in western part of Maharashtra population. Int J Appl Dent Sci. 2018; 4(1): 160–163.

5. Chaudhary S, Srivastava D, Jaetli V, et al. Evaluation of condylar morphology using panoramic radiography in normal adult population. Int J Sci Stud. 2015; 2(11): 164–168.

6. Choudhary A, Ahuja U, Rathore A, et al. Association of temporomandibular joint morphology in patients with and without temporomandibular joint dysfunction: A cone-beam computed tomography based study. Dent Res J. 2020; 17(5): 338–346, doi: 10.4103/1735-3327.294334, indexed in Pubmed: 33343841.

7. Gindha GS, Singh TP, Sood KS, et al. Amorphometric study of condyloid process of dry human mandible for sexing from its shape. MOJ Anat Physiol. 2017; 3(2): 58–62.

8. Hegde S, Praveen BN, Shetty SR. Morphological and radiological variations of mandibular condyles in health and diseases: a systematic review. Dentistry. 2013; 03(01), doi: 10.4172/2161-1122.1000154.

9. Honda E, Yoshino N, Sasaki T. Condylar appearance in panoramic radiograms of asymptomatic subjects and patients with temporomandibular disorders. Oral Radiol. 1994; 10(2): 43–53, doi: 10.1007/bf02390715.

10. Kanjani V, Kalyani P, Patwa N, et al. Morphometric variations in sigmoid notch and condyle of the mandible: A retrospective forensic digital analysis in North Indian population. Arch Med Health Sci. 2020; 8(1): 31–34, doi: 10.4103/amhs.amhs_37_20.

11. Kaplan AS. Plain, tomographic, and panoramic radiography and radionuclide imaging. In: Kaplan AS, Assael LA (ed.). Temporomandibular disorders, diagnosis and treatment. WB Saunders, Philadelphia 1991: 312–336.

12. Katsavrias EG, Halazonetis DJ. Condyle and fossa shape in Class II and Class III skeletal patterns: a morphometric tomographic study. Am J Orthod Dentofacial Orthop. 2005; 128(3): 337–346, doi: 10.1016/j.ajodo.2004.05.024, indexed in Pubmed: 16168330.

13. Maqbool S, Wani BA, Chalkoo AH, et al. Morphological Assessment of Variations of Condylar Head And Sigmoid Notch on Orthopantomograms of Kashmiri Population. Int J Recent Sci Res. 2018; 9(10): 29162–29165.

14. Mathew AL, Sholapurkar AA, Pai KM. Condylar changes and its association with age, TMD, and dentition status: a cross-sectional study. Int J Dent. 2011; 2011: 413639, doi: 10.1155/2011/413639, indexed in Pubmed: 22114595.

15. Nagaraj T, Nigam H, Santosh HN, et al. Morphological variations of the coronoid process, condyle and sigmoid notch as an adjunct in personal identification. J Med Radiol Pathol Surg. 2017; 4(2): 1–5, doi: 10.15713/ins.jmrps.86.

16. Nalla RK, Kruzic JJ, Kinney JH, et al. Effect of aging on the toughness of human cortical bone: evaluation by R-curves. Bone. 2004; 35(6): 1240–1246, doi: 10.1016/j.bone.2004.07.016, indexed in Pubmed: 15589205.

17. Neto JV, Estrela C, Bueno M, et al. Mandibular condyle dimensional changes in subjects from 3 to 20 years of age using cone-beam computed tomography: a preliminary study. Dental Press J Orthod. 2010; 15(5): 172–181, doi: 10.1590/s2176-94512010000500021.

18. Okeson JP. History and examination for temporomandibular disorders. In: Okeson JP (ed.). Management of temporomandibular disorders and occlusion. 4th ed. Mosby, St Louis 1998: 234–309.

19. Oliveira-Santos C, Bernardo RT, Capelozza ALA. Mandibular condyle morphology on panoramic radiographs of asymptomatic temporomandibular joints. IJD Int J Dent (Recife. 2009; 8(3): 114–118.

20. Orhan K. Introduction to TMJ imaging. In: Rozylo-Kalinowzka I, Orhan K (ed). Imaging of the temporomandibular joint. Springer, Switzerland 2019: 1–9.

21. Ozgedik S, Karacayli U, Ozarslanturk S, et al. Trifid mandibular canal and lingual accessory mental foramen: a case of two rare anatomical variations. Dentistry Adv Res. 2017; 2: 136, doi: 10.29011/2574-7347.100036.

22. Ribeiro E, Sanches M, Alonso L, et al. Shape and Symmetry of Human Condyle and Mandibular Fossa. Int J Odontostomatol. 2015; 9(1): 65–72, doi: 10.4067/s0718-381x2015000100010.

23. Ross BR, Johnston MC. Developmental anomalies and dysfunction. In: Zarb GA, Carlsson GE, Sessle BJ, Mohl ND (eds). Temporomandibular joint and masticatory muscle disorders. Mosby 1994: 221–222.

24. Sahithi D, Reddy S, Teja Divya DV, et al. Reveal the concealed – morphological variations of the coronoid process, condyle and sigmoid notch in personal identification. Egyp J Forensic Sci. 2016; 6(2): 108–113, doi: 10.1016/j.ejfs.2015.11.003.

25. Sakul BU, Bilecenoglu B, Ocak M. Anatomy of the temporomandibular joint. In: Rozylo-Kalinowzka I, Orhan K. (ed). Imaging of the temporomandibular joint. Springer, Switzerland 2019: 9–12.

26. Shaikh AH, Ahmed S, Ahmed AR, et al. Assessment of radiographic morphology of mandibular condyles: a radiographic study. Folia Morphol. 2022; 81(2): 481–486, doi: 10.5603/FM.a2021.0049, indexed in Pubmed: 34018177.

27. Singh B, Kumar NR, Balan A, et al. Evaluation of normal morphology of mandibular condyle: a radiographic survey. J Clin Imaging Sci. 2020; 10: 51, doi: 10.25259/JCIS_84_2020, indexed in Pubmed: 32874756.

28. Sonal V, Sandeep P, Kapil G, et al. Evaluation of condylar morphology using panoramic radiography. J Adv Clin Res Insights. 2016; 3: 5–8, doi: 10.15713/ins.jcri.94.

29. Ulhuq A. Management of temporomandibular disorders and occlusion (6th edition). Br Dent J. 2008; 204(9): 535, doi: 10.1038/sj.bdj.2008.369.

30. Yalcin E, Ararat E. Cone-Beam computed tomography study of mandibular condylar morphology. J Craniofac Surg. 2019; 30(8): 2621–2624, doi: 10.1097/scs.0000000000005699, indexed in Pubmed: 31261335.

31. Yale SH, Allison BD, Hauptfuehrer JD. An epidemiological assessment of mandibular condyle morphology. Oral Surg Oral Med Oral Pathol. 1966; 21(2): 169–177, doi: 10.1016/0030-4220(66)90238-6, indexed in Pubmed: 5215976.

32. Yale SH, Ceballos M, Kresnoff CS, et al. Some observations on the classification of mandibular condyle types. Oral Surg Oral Med Oral Pathol. 1963; 16: 572–577, doi: 10.1016/0030-4220(63)90146-4, indexed in Pubmed: 14002216.

33. Yale SH, Rosenberg HM, Ceballos M, et al. Laminagraphic cephalometry in the analysis of mandibular condyle morphology. A preliminary report. Oral Surg Oral Med Oral Pathol. 1961; 14: 793–805, doi: 10.1016/s0030-4220(61)80008-x, indexed in Pubmed: 13787074.

C A S E   R E P O R T

The axillary artery high bifurcation: coexisting variants and clinical significance

George Tsakotos[1], Konstantinos Natsis[2], George Triantafyllou[1], Trifon Totlis[2],
Dimitrios Chytas[3], Georgia Kostare[1], Vasilios Karampelias[1], Athina Tousia[4], Maria Piagkou[1]

[1]Department of Anatomy, School of Medicine, National and Kapodistrian University of Athens, Greece
[2]Department of Anatomy and Surgical Anatomy, Faculty of Health Sciences, Aristotle University of Thessaloniki, Greece
[3]Basic Sciences Laboratory, Department of Physiotherapy, University of Peloponnese, Sparta, Greece
[4]Department of Forensics and Toxicology, National and Kapodistrian University of Athens, Greece

Several branching patterns of the axillary artery (AA) have been described. Unusually, the brachial artery (BA) follows a course in front of the median nerve (MN), the so-called superficial brachial artery (SBA). The SBA may result in MN entrapment. The current cadaveric report highlights a high AA bifurcation, its continuation as SBA and the coexistence of muscular, neural, and vascular asymmetric aberrations. At the right side, the coracobrachialis muscle (CB) had a single head, and the ipsilateral musculocutaneous nerve (MCN) followed a medial course. The AA was highly divided into superficial and deep stems (SAS and DAS), at the 2nd rib lower border. Between two stems, the brachial plexus (BP) lateral and medial cords were identified. The MN originated from the BP lateral cord. The SAS, continued as SBA with a tortuous course. The DAS coursed posterior to the BP medial and lateral cords and gave off the subscapular artery. A bilateral 3rd head of the biceps brachii was identified. The MN atypically originated from the BP lateral cord. At the left side, the two-headed CB was typically penetrated by the MCN. A common trunk of the circumflex humeral arteries was identified in coexistence with an interconnection of the BP lateral cord with the MN medial root. The rare coexistence of muscular, neural, and arterial variants in axillary and brachial region is emphasized, taking into consideration the AA high division and related branching pattern. Documentation of such rare vascular variants is important in aneurysm and trauma surgery, and angiography, where all therapeutic manipulations must be accurately performed due to the possibility of complications. (Folia Morphol 2024; 83, 1: 200–206)

Keywords: superficial brachial artery, high origin, variation, accessory head, axilla, brachial plexus, entrapment

INTRODUCTION

The axillary artery (AA), the subclavian artery's continuation at the 1st rib lower border, gives rise to the brachial artery (BA) at the teres major muscle lower border. The AA typically is divided by the pectoralis minor into three parts, giving off the superior thoracic artery (STA) (1st part), the thoracoacromial and lateral thoracic artery (TAA and LTA, 2nd part) and the subscapular artery (SBSA, 3rd part) [1]. Several AA branching variants have been described, some of them rarely be identified (concerning the branches' origin and course) [13]. Unusually (3.6–9.6%) [31], the BA could follow a course in front of the median nerve (MN) [31]. Adachi [1] defined this type of artery as superficial brachial artery (SBA). When present, the SBA may completely replace the BA or may be accompanied by a BA trunk running posterior to the MN. This altered course may result in MN entrapment [25]. AA and BA variability is of paramount importance for surgeons and interventionists [23]. The current cadaveric report highlights a high AA bifurcation and its continuation as SBA and coexistence of asymmetric muscular, neural, and vascular aberrations.

MATERIALS AND METHODS

An 81-year-old donated male cadaver was bilaterally dissected at the axillary and brachial area. The body was donated before death, after a written informed consent.

RESULTS

At the right side, the coracobrachialis muscle (CB) had a single head, and the ipsilateral musculocutaneous nerve (MCN) didn't penetrate it but followed a medial course. An AA of anterior course in relation to the ansa pectoralis was identified. The vessel was highly divided into superficial and deep stems (SAS and DAS), at the 2nd rib lower border. Between two stems, the brachial plexus (BP) lateral and medial cords were identified (Fig. 1). The AA before bifurcation, gave off an aberrant suprascapular artery (coursing between the anterior and posterior branch of the C7 root, posterior to the BP upper trunk) (Fig. 2), the STA, the 1st LTA, and the TAA, 1.1 cm distally. The MN originated from the BP lateral cord (Fig. 3). The SAS, anterior to the BP lateral and medial cords gave off the 2nd LTA (Fig. 1) and continued as SBA with a tortuous course, anterior to the MN. The

Figure 1. High bifurcation of the right-sided (R) axillary artery (AA) into superficial and deep axillary stems (SAS and DAS); STA — superior thoracic artery; LTA1 — 1st lateral thoracic artery; TAA — thoracoacromial artery; LTA2 — 2nd lateral thoracic artery bifurcation (1, 2); UN — ulnar nerve; Pm — pectoralis minor retracted tendon; ICBN — intercostobrachial nerve; LC — lateral cord of the brachial plexus; MC — medial cord of the brachial plexus.

SBA was accompanied by two brachial veins that anastomosed with the basilic vein and drained into the axillary vein. At the bicipital tendon insertion, the SBA divided into radial and ulnar arteries, that were slightly tortuous in the distal forearm. The DAS coursed posterior to the BP medial and lateral cords and 5 cm distally gave off the upper subscapular artery and the SBSA that divided into a lateral and a medial trunk. The lateral trunk gave off the anterior and posterior circumflex humeral arteries (ACHA and PCHA), the profunda brachii artery (PBA) and a muscular branch for the teres minor upper part and the latissimus dorsi muscles. The medial trunk divided into the circumflex scapular artery, a muscular branch for the latissimus dorsi muscle and the thoracodorsal artery (Fig. 4). A 3rd head of the biceps brachii (BB) was bilaterally identified, originating from the CB insertion, and inserting at the radial tuberosity, after joining the bicipital tendon (Figs. 3B, 5). The MN atypically originated from the BP lateral cord and the MCN had a medial course related to the CB and innervated the BB and brachialis muscle. CB innervated by the MCN neural filaments. The BP posterior cord was located posterior to the DAS. At the level of the posterior cord formation, the upper
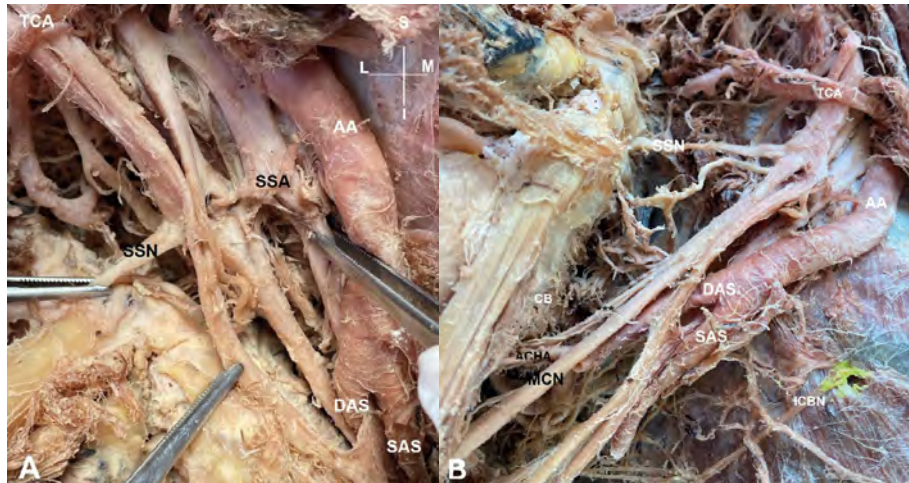
Figure 2. A. B. Ectopic origin of the right-sided suprascapular artery (SSA) from the 1st part of the axillary artery (AA); SSN —suprascapular nerve; TCA — transverse cervical artery; SAS — superficial axillary stem; DAS — deep axillary stem; MCN — musculocutaneous nerve; *** accessory MCN; ACHA — anterior circumflex humeral artery; ICBN — intercostobrachial nerve.
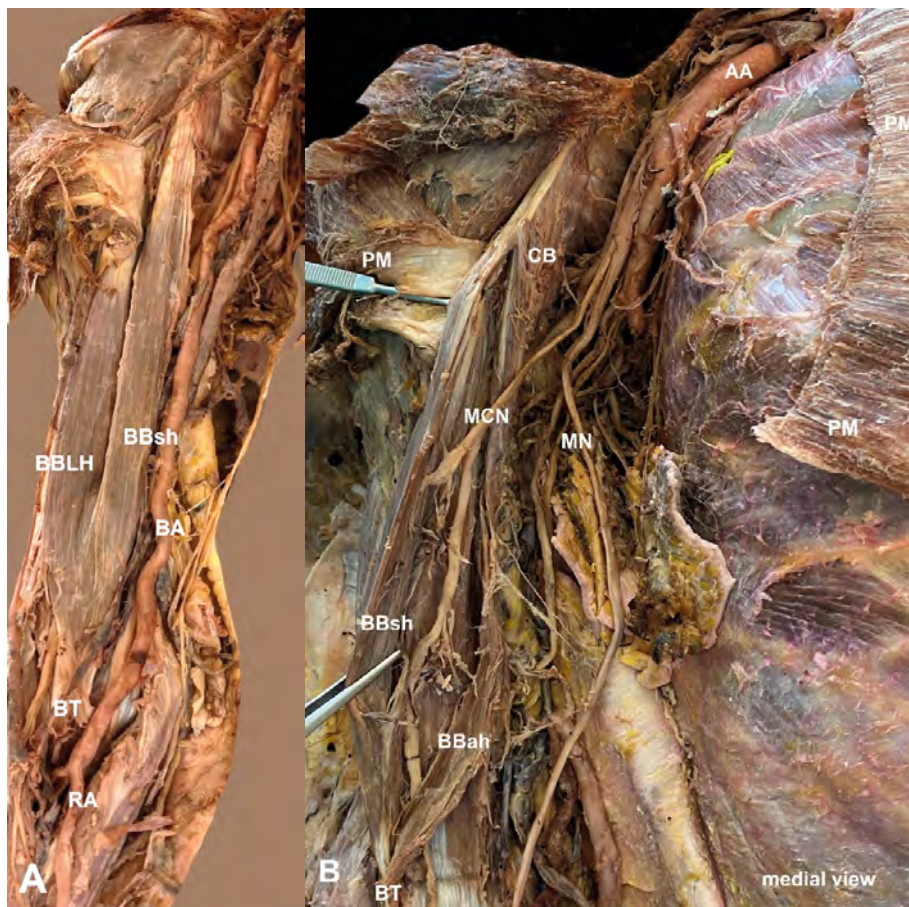
Figure 3. A, B. Right side views — variant biceps brachii with a 3rd (accessory) head, short head (BBsh), long head (BBLH) and accessory head (BBah) joining the bicipital tendon (BT) and inserting into the radial tuberosity. **A.** Brachial artery (BA) of tortuous course; **B.** Musculocutaneous nerve (MCN) of medial course and its division, median nerve (MN) of atypical origin exclusively from the lateral cord; CB — coracobrachialis muscle; AA — axillary artery; RA — radial artery; PM — pectoralis minor.

Figure 4. A. Right side — the branching pattern of the deep axillary stem into the subscapular artery (SBSA); SBA — superficial brachial artery; MT — medial trunk divided into the circumflex scapular artery (CSA) and the thoracodorsal artery (TDA); RN — radial nerve; AN — axillary nerve; MN — median nerve; **B.** Right side — PBA* [posterior brachii artery (the missing vessel)]. The lateral trunk giving off the PBA, the anterior circumflex humeral artery (ACHA) and the posterior circumflex humeral artery (PCHA); **muscular branches for the latissimus dorsi and teres major muscles.

Figure 5. The left-sided variant biceps brachii muscle with a short (BBsh), a long head (BBlh) and a 3rd head (BBah) joining the bicipital tendon (BT), the typical coracobrachialis muscle (CB), the musculocutaneous nerve (MCN), the axillary artery (AA), the brachial artery (BA), and the median nerve (MN).

subscapular nerve originated, followed by the lower subscapular nerve, 5.4 cm distally to the lower border of the 1st rib, the thoracodorsal nerve, and muscular branches for the teres major and minor muscles, and

the axillary, and the radial nerve. At the left side, the two-headed CB was typically penetrated by the MCN. The AA gave off the superior thoracic artery and the 1st LTA. The TAA originated 0.5cm distally to the 1st

Figure 6. Left-side — the double lateral root (LR1, LR2) of the median nerve (MN); MR — medial root; MCN — musculocutaneous nerve penetration to coracobrachialis muscle (CB); UN — ulnar nerve.

LTA origin, at the same level with a muscular branch for the subscapularis muscle upper part. The 2nd LTA originated 1.8 cm distally to the TAA origin, and 5 cm distally, originated the SBSA originated that further divided into a branch for the upper part of the latissimus dorsi, the circumflex scapular artery, muscular branches for the teres minor and major, branch for the subscapularis lower part and the thoracodorsal artery. A common trunk of ACHA-PCHA was identified, 1.3 cm distally and laterally to the SBSA origin. The AA continued its course as BA, with an evident tortuosity, and 3.4 cm distally to the lateral humeral epicondyle, bifurcated into radial and ulnar artery. An interconnection of the BP lateral cord with the MN medial root was identified (Fig. 6).

DISCUSSION

The current report highlights an AA high bifurcation similarly to other reports [4, 19, 23, 40]. The AA high bifurcation is more commonly identified in African Americans (13.4%) than in Caucasians (4.6%) [6]. In the current case, the AA highly bifurcated into

a SAS and a DAS, at the AA 2nd part. Many authors described a lower bifurcation (AA 3rd part) [4, 7, 14, 28, 37], while the extreme high origin (AA 1st part) is quite rare [13]. The current report highlights the rarity of the AA variants' coexistence compared to the wide variability of the isolated AA branching pattern variants [39]. In the current case, the bilateral coexistence of a 3rd head of the BB was identified. The presence of such an accessory head has a wide variability (0.18–21.5%) among populations [9, 16], with the Africans having the higher prevalence (9–21.5%) [9, 24]. Other reports [35] described the coexistence of an SBA of axillary origin with the absence of the BP lateral cord and the cephalic vein. The coexistence of anomalies in BP arrangement with the axillary and brachial arteries' variability was emphasized [30] and additionally the coexistence of SBA of axillary origin with an atypical MN formed by three roots was underlined. Caroll et al. [3] described the coexistence of a unilateral SBA with a contralateral single-corded BP posterolateral to the AA. No MN roots were identified, similarly to the current case. In the current report, the high bifurcated AA, continued partially as SBA. The SBA was identified from 0.12% to 19.7% among several studies [17]. The current case highlighted the SBA unilateral presence, that was identified in 5–12.2% [14, 29, 39], while Jurjus et al. [13] and Yang et al. [39] referred to the SBA occasional bilateral existence. The SBA presence is more commonly in males at the right side [31], as in our case. In cases in which the SBA did not gave branches, the PBA supplied the upper limb [4, 37]. In the current case, similarly to Natsis et al. [23], the SBA divided into radial and ulnar artery, while in other studies it terminated as superficial radial [4, 15, 21, 31] or superficial ulnar artery [15, 22, 31]. Jayakumari et al. [12] described the SBA bifurcation into radial and common interosseous artery. In the current study, similarly to Natsis et al. [23], the DAS terminated as PBA, while previously divided into the SBSA branching pattern. The SBA and the level of its axillary origin has clinical significance [23]. BA variations in the branching pattern may cause difficulties in conducting flap harvesting during reconstructive surgeries and in arteriography [10]. The BA tortuosity (presence of curves, angulations, or loops) may affect the trans-radial coronary angiography time, leading to perforation [34]. Degradation of elastin in the vessel wall results in aneurysm and vessel's elongation leading to tortuosity [8]. Entrapment of the MN

between SBA and AA could explain the idiopathic MN neuropathy. Nicomozepis et al. [25] presented three cases of unilateral presence of the SBA.

Many theories have been developed concerning the complexity of the embryological development of the upper limb arteries. Rodríguez-Niedenführ et al. [31] after a systematic study on fetuses' upper limbs, they concluded that the upper limb arterial system is developed after the selective enlargement or regression of a capillary plexus and not after the vessels' multiplication around a main arterial trunk that is closely connected with the bones' development. The arterial variants are an aberration from the typical vascularization's pattern [18, 33]. Specifically, the SBA presence is derived after the persistence of one or more intersegmental cervical arteries, that they enlarged [13]. Miller [20] explained the BP arrangement and relationship with the AA as a combination of embryological and evolutionary processes.

As various interventional procedures are performed in the upper limb, knowledge of the regional arterial variants is of paramount importance to avoid injury. Although the AA superficial course and its continuation as SBA facilitates the vascular graft reception and the vessels' catheterization, the AA high bifurcation may confuse interventionist during angiography, leading to misinterpretation. The SBA and its atypical origin increase the risk of iatrogenic injury due to its incorrect consideration as a vein, resulting in severe bleeding [13] or in a pseudoaneurysm formation [38]. Intraarterial injection can cause severe thrombosis, ischaemia, and upper extremity necrosis [5, 27]. Inappropriate cannulation due to the aberrant location and course of the arteries' branches may result in gangrene, and in limb loss [36]. Especially in axillary approaches, for the shoulder instability treatment, the performance of transverse incision can lead to injury the AA atypical branches. Thus, it is of the utmost necessity, the preoperative imaging of the area with ultrasound or computed tomography angiography, especially in urgent cases where thoracic wall reconstruction is required, such as in Poland syndrome [32] or in breast surgery and in axillary lymph node dissection, where surgeons should identify and protect the axillary vessels [13]. Vessels' branching pattern variants of the upper arm usually coexist with BP variations, resulting in an incomplete block [14]. Furthermore, BA pattern variants may implicate planning and conducting flap harvesting during reconstructive surgeries and arteriography [15].

CONCLUSIONS

The current interesting, rare report emphasizes on the coexistence of muscular, neural, and arterial variants of the axillary and brachial region providing detailed information of the AA branching pattern and distribution in the case of its high division. Documentation of such rare vascular variants in the axilla is important in aneurysm and trauma surgery, and angiography, where all therapeutic manipulations must be accurately performed due to the possibility of complications.

REFERENCES

1. Adachi B. Das Arterien System der Japaner. Maruzen, Kyoto 1928: 210–296.
2. Agrawal D, Singh N, Mohanty BB, et al. Variation in the branching pattern of axillary artery–a case report. Int J Anat Var. 2013; 6: 31–33.
3. Carroll MA, Blandino J, Flynn A, et al. Neurovascular axillary variations: superficial brachial artery and single-corded brachial plexus. Anat Sci Int. 2021; 96(1): 161–167, doi: 10.1007/s12565-020-00563-x, indexed in Pubmed: 32785843.
4. Cavdar S, Zeybek A, Bayramiçli M. Rare variation of the axillary artery. Clin Anat. 2000; 13(1): 66–68, doi: 10.1002/(SICI)1098-2353(2000)13:1<66::AID-CA8>3.0.CO;2-M, indexed in Pubmed: 10617889.
5. Cohen SM. Accidental intra-arterial injection of drugs. Lancet. 1948; 2(6523): 361–417, indexed in Pubmed: 18881545.
6. De Garis CF, Swartley WB. The axillary artery in white and negro stocks. Am J Anat. 2005; 41(2): 353–397, doi: 10.1002/aja.1000410208.
7. Desai SD, Sreepadma S, Rathnakar P. Anomalous division of axillary artery: a case report. Anat Karnataka. 2011; 5: 57–60.
8. Dobrin PB, Schwarcz TH, Baker WH. Mechanisms of arterial and aneurysmal tortuosity. Surgery. 1988; 104(3): 568–571, indexed in Pubmed: 3413685.
9. Greig HW, Anson BJ, Budinger JM. Variations in the form and attachments of the biceps brachii muscle. Q Bull Northwest Univ Med Sch. 1952; 26(3): 241–244, indexed in Pubmed: 14957982.
10. Hansdak R, Arora J, Sharma M, et al. Unusual branching pattern of brachial artery - Embryological basis and clinicoanatomical insight. Clin Ter. 2015; 166(2): 65–67, doi: 10.7417/CT.2015.1817, indexed in Pubmed: 25945432.
11. Huelke D. Variation in the origins of the branches of the axillary artery. Anat Rec. 2005; 135(1): 33–41, doi: 10.1002/ar.1091350105.

12. Jayakumari S, Rath G, Arora J. Unilateral double axillary and double brachial arteries: embryological basis and clinical implications. Int J Morphol. 2006; 24(3), doi: 10.4067/s0717-95022006000400027.

13. Jurjus AR, Correa-De-Aruaujo R, Bohn RC. Bilateral double axillary artery: embryological basis and clinical implications. Clin Anat. 1999; 12(2): 135–140, doi: 10.1002/(SICI)1098-2353(1999)12:2<135::AID-CA10>3.0.CO;2-M, indexed in Pubmed: 10089041.

14. Kachlik D, Konarik M, Baca V. Vascular patterns of upper limb: an anatomical study with accent on superficial brachial artery. Bosn J Basic Med Sci. 2011; 11(1): 4–10, doi: 10.17305/bjbms.2011.2615, indexed in Pubmed: 21342134.

15. Keen JA. A study of the arterial variations in the limbs, with special reference to symmetry of vascular patterns. Am J Anat. 1961; 108: 245–261, doi: 10.1002/aja.1001080303, indexed in Pubmed: 14454801.

16. Khaledpour C. [Anomalies of the biceps muscle of the arm]. Anat Anz. 1985; 158(1): 79–85, indexed in Pubmed: 3993969.

17. Khullar M. Superficial brachial artery: its embryological and clinical significance. Indian J Clin Pract. 2014; 24: 925–928.

18. Konarik M, Knize J, Baca V, et al. Superficial brachioradial artery (radial artery originating from the axillary artery): a case-report and its embryological background. Folia Morphol. 2009; 68(3): 174–178, indexed in Pubmed: 19722162.

19. Maraspin LE. A report of an anomalous bifurcation of the right axillary artery in man. Vasc Surg. 1971; 5(3): 133–136, doi: 10.1177/153857447100500303, indexed in Pubmed: 5122531.

20. Miller R. Observations upon the arrangement of the axillary artery and brachial plexus. Am J Anat. 2005; 64(1): 143–163, doi: 10.1002/aja.1000640107.

21. Natsis K, Papadopoulou AL, Papathanasiou E, et al. Study of two cases of high-origin radial artery in humans. Eur J Anat. 2009; 13(2): 97–103.

22. Natsis K, Papadopoulou AL, Paraskevas G, et al. High origin of a superficial ulnar artery arising from the axillary artery: anatomy, embryology, clinical significance and a review of the literature. Folia Morphol. 2006; 65(4): 400–405, indexed in Pubmed: 17171623.

23. Natsis K, Piagkou M, Panagiotopoulos NA, et al. An unusual high bifurcation and variable branching of the axillary artery in a Greek male cadaver. Springerplus. 2014; 3: 640, doi: 10.1186/2193-1801-3-640, indexed in Pubmed: 25392808.

24. Neto SH, Camilli JA, Andrade JC, et al. On the incidence of the biceps brachii third head in Brazilian white and blacks. Ann Anat. 1998; 180(1): 69–71, doi: 10.1016/s0940-9602(98)80137-4, indexed in Pubmed: 9488908.

25. Nkomozepi P, Xhakaza N, Swanepoel E. Superficial brachial artery: a possible cause for idiopathic median nerve entrapment neuropathy. Folia Morphol. 2017; 76(3): 527–531, doi: 10.5603/FM.a2017.0013, indexed in Pubmed: 28198531.

26. Panagouli E, Anagnostopoulou S, Venieratos D. Bilateral asymmetry of the highly bifurcated brachial artery variation. Rom J Morphol Embryol. 2014; 55(2): 469–472, indexed in Pubmed: 24970004.

27. Pandey SK, Gangopadhyay AN, Tripathi SK, et al. Anatomical variations in termination of the axillary artery and its clinical implications. Med Sci Law. 2004; 44(1): 61–66, doi: 10.1258/rsmmsl.44.1.61, indexed in Pubmed: 14984216.

28. Patnaik VVG, Kalsey G, Singla RK. Bifurcation of axillary artery in its 3rd part-a case report. J Anat Soc India. 2001; 50(2): 166–169.

29. Patnaik VVG, Kasley G, Singla Ra. Anomalous course of radial artery and a variant of deep palmar arch: a case report. Anat Soc India. 2000; 49(1): 54–57.

30. Piagkou M, Totlis T, Panagiotopoulos NA, et al. An arterial island pattern of the axillary and brachial arteries: a case report with clinical implications. Surg Radiol Anat. 2016; 38(8): 975–978, doi: 10.1007/s00276-016-1631-z, indexed in Pubmed: 26831326.

31. Rodríguez-Niedenführ M, Burton GJ, Deu J, et al. Development of the arterial pattern in the upper limb of staged human embryos: normal development and anatomic variations. J Anat. 2001; 199(Pt 4): 407–417, doi: 10.1046/j.1469-7580.2001.19940407.x, indexed in Pubmed: 11693301.

32. Shipkov Kh, Anastasov Iu, Mikhailov T. [Surgical reconstruction options in Poland's syndrome]. Khirurgiia (Sofiia). 2000; 56(2): 26–29, indexed in Pubmed: 11484283.

33. Singer E. Embryological pattern persisting in the arteries of the arm. Anat Rec. 2005; 55(4): 403–409, doi: 10.1002/ar.1090550407.

34. Sirisha V, Udaya KP, Suseelamma D, et al. study on tortuous course of peripheral arteries of upper extremity and its embryological, histological and clinical significance. IJAR. 2015; 3(10): 567–571.

35. Troupis TG, Michalinos A, Manou V, et al. Report of an unusual combination of arterial, venous and neural variations in a cadaveric upper limb. J Brachial Plex Peripher Nerve Inj. 2014; 9: 2, doi: 10.1186/1749-7221-9-2, indexed in Pubmed: 24495850.

36. Tsoucalas G, Eleftheriou A, Panagouli E. High bifurcation of the brachial artery: an embryological overview. Cureus. 2020; 12(2): e7097, doi: 10.7759/cureus.7097, indexed in Pubmed: 32231893.

37. VijayaBhaskar P, Ritesh R, Shankar PR. Anomalous branching of the axillary artery: a case report. Kathmandu Univ Med J (KUMJ). 2006; 4(4): 517–519, indexed in Pubmed: 18603967.

38. Yagain VK, Dave MR, Anadkat S. Unilateral high origin of radial artery from axillary artery. Folia Morphol. 2012; 71(2): 121–124, indexed in Pubmed: 22648593.

39. Yang HJ, Gil YC, Jung WS, et al. Variations of the superficial brachial artery in Korean cadavers. J Korean Med Sci. 2008; 23(5): 884–887, doi: 10.3346/jkms.2008.23.5.884, indexed in Pubmed: 18955798.

40. Yotova N, Novakov S. Unilateral double axillary artery. Clin Anat. 2004; 17(2): 149–151, doi: 10.1002/ca.10241, indexed in Pubmed: 14974104.

CASE REPORT

VIA MEDICA

Unique case of vascularization: superficial brachial artery and radial persistent median artery

Megan K. Kalinowski[1], Jeffery M. Bettag[1], Julian A. Giakas[1], Ankita Joshi[1],
Minh N. Pham[1], James C. Yang[1], Maurice N. Maglasang[1], Yun Tan[2], Daniel Daly[2]

[1]Saint Louis University School of Medicine, Saint Louis, MO, United States
[2]Center for Anatomical Science and Education, Department of Surgery,
Saint Louis University School of Medicine, Saint Louis, MO, United States

During a routine cadaveric dissection of a 93-year-old male donor, unique arterial variations were observed in the right upper extremity. This rare arterial branching pattern began at the third part of the axillary artery (AA), where it gave off a large superficial brachial artery (SBA) before bifurcating into the subscapular artery and a common stem. The common stem then gave off a division for the anterior and posterior circumflex humeral arteries, before continuing as a small brachial artery (BA). The BA terminated as a muscular branch to the brachialis muscle. The SBA bifurcated into a large radial artery (RA) and small ulnar artery (UA) in the cubital fossa. The UA branching pattern was atypical, giving off only muscular branches in the forearm and a deep UA before contributing to the superficial palmar arch (SPA). The RA provided the radial recurrent artery and a common trunk (CT) proximally before continuing its course to the hand. The CT from the RA gave off a branch that divided into anterior and posterior ulnar recurrent arteries, as well as muscular branches, before it bifurcated into the persistent median artery (PMA) and the common interosseous artery. The PMA anastomosed with the UA before entering the carpal tunnel and contributed to the SPA. This case presents a unique combination of arterial variations in the upper extremity and is clinically and pathologically relevant. (Folia Morphol 2024; 83, 1: 207–214)

Keywords: persistent median artery, superficial brachial artery, brachial arterial variation

INTRODUCTION

Typically, post-gestational anatomy displays the radial and ulnar arteries stemming from the brachial artery (BA), a continuation of the axillary artery (AA) at the lower border of the teres major muscle. The AA is the primary source of vascularization to the arm and forearm as described in anatomical texts. In some cases, the AA divides into two major branches (a superficial brachial artery [SBA] and a BA) to supply the upper limb. This variation of the SBA arising from the AA was found in 12.2% of cadaveric arms in a study of Korean cadavers. The SBA often continues distally and divides into the ulnar and brachial arteries [38].

In most cases, the median artery (MA) of the forearm, a branch of the ulnar artery (UA), regresses during the 8th week of gestation. The MA serves as the primary source of blood to the hand during intrauterine growth. In rare cases, the MA remains as an embryological remnant called the persistent median artery (PMA) with a prevalence ranging from 4.2% to 6.6% [13, 31, 36].

The most common forms of the PMA are either the antebrachial type, in which the artery provides blood supply to the median nerve but does not reach the hand, or palmar type, in which the PMA passes through the carpal tunnel and is involved in the formation of the superficial palmar arch (SPA) [16, 19, 28]. The palmar type is the direct remnant of the embryonic form and contributes to the arterial supply of the hand, whereas the antebrachial type is due to a partial regression [13, 16, 28]. The prevalence of each type is variable and inconsistent in literature. Some reports show the palmar type has a prevalence of 0.9–50% and the antebrachial type is reported to have a prevalence of 70–76% in individuals with PMAs [15, 18, 19, 34]. Most cases present with the PMA arising from the UA as an accessory branch while others report the PMA coming from the common interosseous artery [13, 16, 25, 36]. Both variations travel through the forearm as a main source of blood supply to the median nerve before either stopping at the wrist or crossing it to contribute to the SPA [11].

The presence of a PMA can have a variety of clinical implications that primarily impact surgical cases in the wrist region, especially with carpal tunnel release procedures [30]. The PMA can be associated with compression of the median nerve resulting in carpal tunnel syndrome type signs and symptoms [21]. Other clinical manifestations include calcification, thromboses, atherosclerosis and anterior interosseous nerve compression [5, 11, 12, 22, 23, 37].

Although the PMA itself is not a novel discovery, the origin and relationship with other vasculature in this case created a unique presentation that has not been described in the literature. This case presents an entirely unique branching pattern from the AA to arterial termination in the hand with the most notable variation being the PMA arising from a common trunk (CT) from the radial artery (RA).

CASE REPORT

The donor was received through the Saint Louis University Gift of Body Programme of the Center for Anatomical Science and Education (CASE) with signed informed consent from the donor. The CASE gift body program abides by the rules set forth by the Uniform Anatomical Gift Act.

During a routine anatomy laboratory dissection, an unusual vasculature pattern was identified in the right upper limb of a 93-year-old male cadaver. The initial variation was observed as an SBA branching from the third part of the AA. After giving off a large SBA, the AA bifurcated into the subscapular artery and a common stem. The common stem travelled deep to the lateral cord's contribution to the median nerve, before it gave off the anterior and posterior circumflex humeral arteries and continued as a smaller BA (Figs. 1, 2).

The BA, which was 24.6 cm in length and had a diameter of approximately 3.8 mm, continued into the arm giving off numerous muscular branches as well as the deep BA, which travelled with the radial nerve to the posterior compartment of the arm in the typical fashion (Fig. 2). The BA continued distally, giving off the superior and inferior ulnar collateral arteries before terminating as a muscular branch to the brachialis muscle in the cubital fossa deep and lateral to both the median nerve and the SBA (Figs. 3, 4).

The SBA crossed over the medial cord's contributions to the median nerve and ran laterally to the nerve (Fig. 2). It was 25.8 cm in length, had a diameter of approximately 5.4 mm, and bifurcated 1.08 cm proximal to the base of the cubital fossa as a small UA and a large RA (Fig. 4).

The UA had an atypical branching pattern. It did not give off the anterior and posterior ulnar recurrent arteries or the common interosseous as normally seen. Rather, the UA provided only muscular branches along its course to contribute to the SPA after giving off the deep ulnar branch as it entered the hand. (Figs. 4, 5).

The RA also presented an atypical branching pattern. The RA travelled deep to the pronator teres muscle after first giving off the radial recurrent artery which anastomosed with the radial collateral artery as expected. While between the two heads of the pronator teres it then gave off a CT that gave a branch for a common trunk for the anterior and posterior ulnar recurrent arteries, anastomosing with typical ulnar collateral arteries (Figs. 4, 6). The CT then provided muscular branching before bifurcating into the PMA medially and the common interosseous artery laterally. The common interosseous artery gave rise to the anterior and posterior interosseous arteries as expected
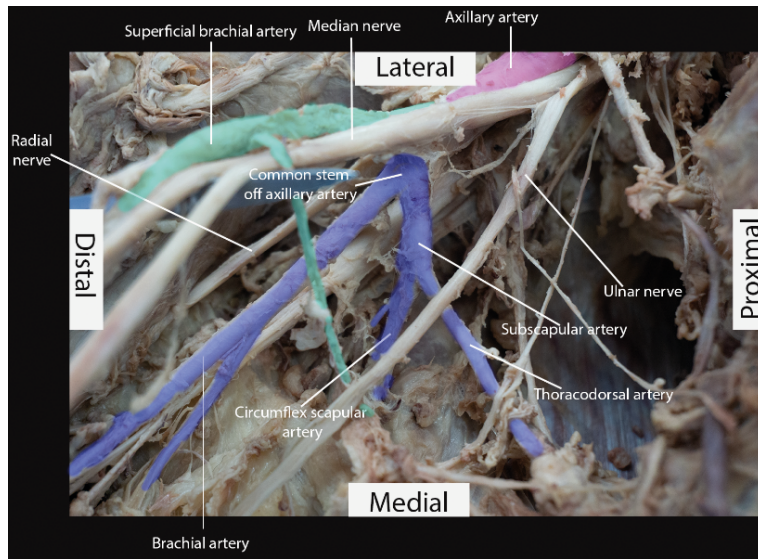
Figure 1. Medial view of the axillary region. The third part of the axillary artery (pink) gave off the superficial brachial artery (green), subscapular artery (purple) and a common stem for one of the branches, the brachial artery (purple). The superficial brachial artery with muscular branches visible, traveling superficially to the lateral contribution of the median nerve and running lateral to the median nerve.
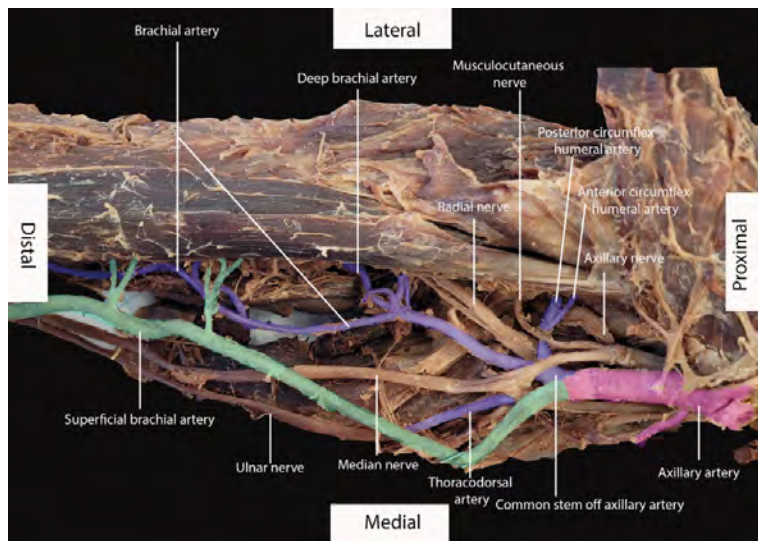
Figure 2. Axillary regions with additional views of the common stem off the axillary artery. The third of the axillary artery (pink) giving off the superficial brachial artery (green) with muscular branches in the biceps brachii. The common stem off the axillary (purple) gives off a division for the anterior and posterior humeral circumflex arteries, the subscapular artery traveling deep to the median nerve, and the brachial artery and deep brachial arteries.

while the PMA initially travelled lateral to the median nerve before crossing it anteriorly and coursed medially to the nerve, giving off many muscular branches in the forearm. The diameter of the PMA was 2.8 mm. The PMA anastomosed with the UA just before entering the carpal tunnel (Fig. 5). In the hand, together with RA, the PMA contributed to the SPA.

The subscapular artery and the humeral circumflex arteries travelled in a typical fashion after branching from the AA and common stem, respectively.

DISCUSSION

The MA of the forearm is an embryological structure that delivers blood to the fetal hands during the
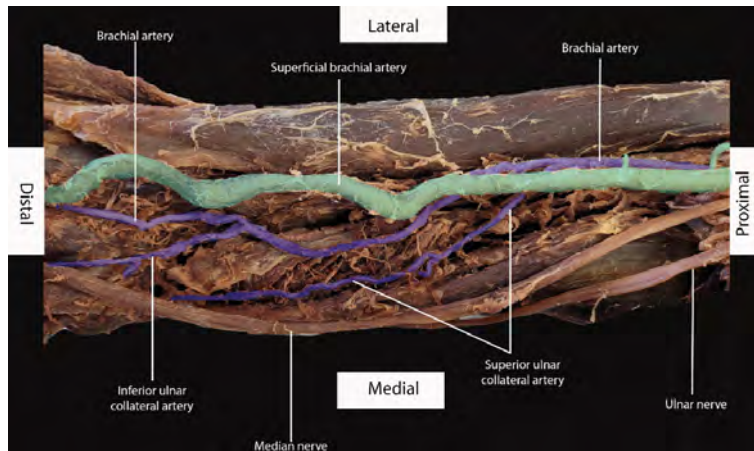
Figure 3. View of the arm proximally to the elbow joint. The superficial brachial artery (green) travels superficially to the neurovasculature of the arm, giving off muscular branches. The brachial artery (purple) travels distally with superior and inferior ulnar collateral arteries branches.
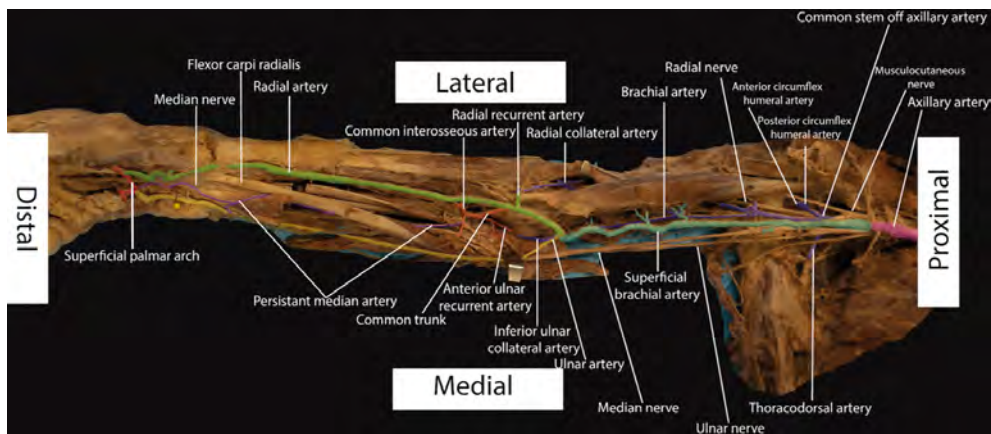
Figure 4. Overview of unique vascularization of the case. The axillary artery (pink) gives off the superficial brachial artery (aqua) traveling superficially to the brachial plexus before bifurcating into the radial artery (green) and ulnar artery (yellow). The common stem with branching (purple) becomes the brachial artery, giving off branches of the superior and inferior ulnar collateral arteries, radial collateral artery and muscular branches. It terminates in the brachialis muscle.
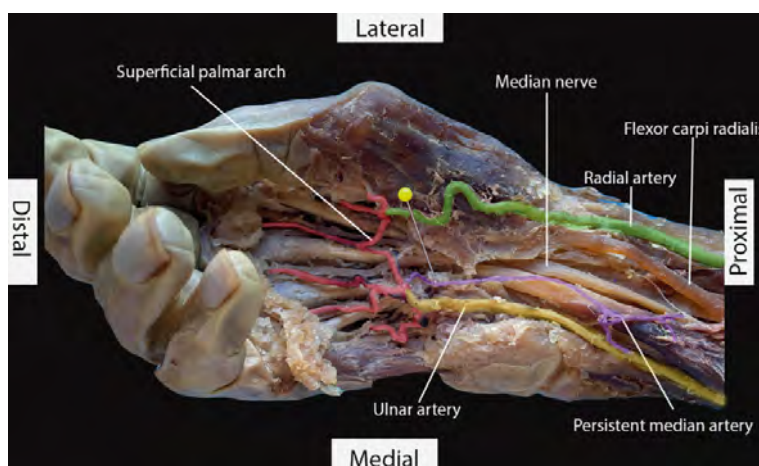
Figure 5. View of the superficial palmar arch containing the contributions of the ulnar artery (yellow) and radial artery (green). The persistent median artery (purple) is shown, anastomosing with the ulnar artery and entering the wrist.
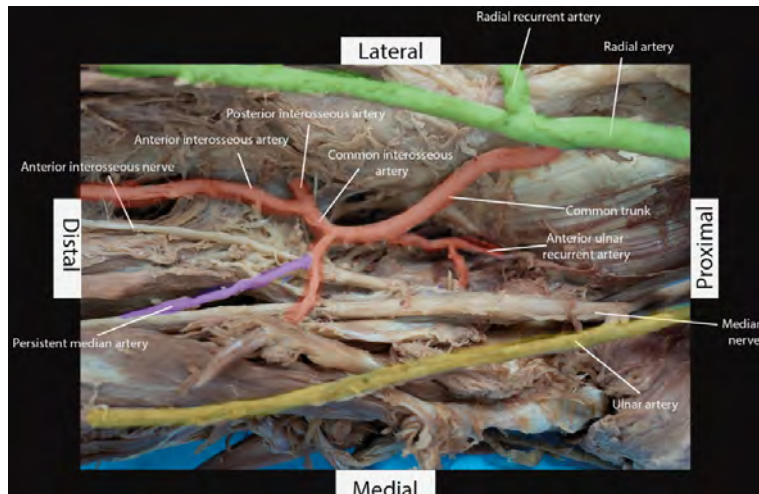
Figure 6. View of the unique branching of the radial artery (green). The common trunk arises from the radial artery, giving a branch for a common trunk for the anterior and posterior ulnar recurrent arteries. It continues to give the common interosseous artery and the persistent median artery (purple).

first trimester of gestation. One hypothesis states that the MA arises from a plexus of capillaries that supply blood to the upper limb very early during gestation [35]. These capillaries progressively differentiate and mature from the proximal to distal parts of the upper limb over time, forming the MA as well as other arteries. The MA typically undergoes regression and becomes an unnamed small artery that travels with the median nerve in the carpal tunnel, often supplying the nerve [35]. Thus, the blood supply of the hand is typically replaced by the ulnar and radial arteries, as seen in children and adults. However, there is some debate about the exact timing of regression. Some sources claim the MA regresses at 8 weeks of gestation, while others argue that it regresses during the 28th to 52nd days (4 to 7 weeks) of gestation when the embryo is approximately 23 mm long. Yet, other sources claim that the MA regresses during the perinatal stage and early infancy [24, 34]. Regardless, if the MA fails to regress altogether, it remains as the PMA.

It has recently been noted that the prevalence of PMA is approximately 4%, though it is more commonly reported in individuals of South African descent, where the frequency was 27.1% [17]. When discussing the presentation of PMAs in the general population, there is no difference in prevalence when comparing sexes or unilaterality/bilaterality [1, 13, 17].

The PMA is often an important source of blood supply for the hand not only during gestation, but also during childhood and adulthood in populations

with a PMA and a partial or complete absence of an SPA [31]. Thus, it is important to note the presence and location of the PMA via ultrasound before performing wrist surgery on these patients to avoid injury to this important blood source.

The presence of a PMA is generally asymptomatic if the diameter is between 1 and 1.5 mm, but, more often, it can be a source of pain and paraesthesia when a thrombus or aneurysm increases the diameter to greater than 2 mm [3, 9, 20, 23]. Altered median nerve function through thrombosis, aneurysm, rupturing, or physical impingement by the PMA can cause sudden onset of carpal tunnel symptoms. Sometimes, identifying the PMA as the cause of carpal tunnel can be difficult, especially if symptoms mimic tenosynovitis [14]. This highlights the importance of utilizing ultrasound imaging during diagnosis.

In a Polish study involving open carpal tunnel release surgery, a PMA was found in 2.8% of cases intraoperatively. Three of these PMAs contained thromboses, and all three required surgical resections [30]. Thus, there are a variety of suitable approaches to treating a PMA thrombus.

The presence of a PMA has been implicated in various entrapment neuropathies. For example, proximal median nerve neuropathies have been described in cases where the PMA pierces or splits the median nerve [21]. Additionally, the presence of a PMA can contribute to pronator teres syndrome or anterior interosseous syndrome. Pronator teres syndrome may be caused by a PMA that perforates the median nerve and gives rise to anomalous vascular leash and

fibrous bands to the flexor muscles, which compresses the nerve [10, 33]. Although compression of the anterior interosseous nerve occurs most frequently by the head of the pronator teres muscle, anterior interosseous syndrome was noted in a patient whose PMA pierced the anterior interosseous nerve below the elbow [33].

The PMA could be considered as an alternate source of graft tissue for coronary artery bypass grafts (CABG) [2, 6]. Use of the RA may result in symptoms such as paraesthesia, pain, and occasionally hypoperfusion at harvest sites [4]. The UA can be ligated when harvesting the RA for CABG, but this can result in severe ischaemia, especially when both the UA and RA contribute to the SPA [32]. The absence of the UA was responsible for hand ischaemia after RA graft for CABG in a recently reported clinical case [29]. When there are multiple contributions to the SPA, the PMA may serve as a potential graft for a CABG without jeopardizing blood supply to the hand and may serve to minimise adverse postoperative symptoms.

The SBA is important in fetuses to support or replace the BA [7]. The current case presents a unique variation in the branching pattern of the SBA. This is a relatively rare variation of the SBA, found in 0.1–12.2% of patients [7]. In the early embryo, the superficial and deep brachial arteries anastomose at various levels of the arm, including a more proximal level and a more distal level [35, 39]. Normally, these anastomoses will regress along with the SBA, while the deep BA will persist. However, if these anastomoses persist, the SBA will also persist, and its course of direction will depend on which anastomosis persists. For example, if the proximal anastomosis persists, the SBA will persist and course medial to the ulnar nerve. If the distal anastomosis persists, the SBA will persist and course lateral to the ulnar nerve; this is consistent with the variation found in the present case [35].

This SBA variation may or may not present with any pathology [7]. For unknown reasons, the SBA is more prone to injury and severe bleeding than the BA [8, 27]. Awareness of this variant is especially important during orthopaedic procedures such as repair of a fractured or dislocated humerus; as such, imaging before beginning a procedure would be prudent. The SBA in this case is found more superficially, making it more prone to injury.

CONCLUSIONS

The current case presents a novel set of vascular variations in the upper limb that includes an SBA and a PMA with a unique branching pattern that had not been previously reported in the literature. Awareness of such variations is important for healthcare providers due to the complications and pathology related to persistence of embryological arterial structures.

Conflict of interest: None declared

REFERENCES

1. Acarturk TO, Tuncer U, Aydogan LB, et al. Median artery arising from the radial artery: its significance during harvest of a radial forearm free flap. J Plast Reconstr Aesthet Surg. 2008; 61(10): e5–e8, doi: 10.1016/j. bjps.2007.10.026, indexed in Pubmed: 18023628.
2. Adnan G, Yandrapalli S. Radial artery coronary bypass. StatPearls. 2022, indexed in Pubmed: 33085397.
3. Barfred T, Højlund AP, Bertheussen K. Median artery in carpal tunnel syndrome. J Hand Surg Am. 1985; 10(6 Pt 1): 864–867, doi: 10.1016/s0363-5023(85)80163-5, indexed in Pubmed: 4078270.
4. Barner HB. Conduits for coronary bypass: strategies. Korean J Thorac Cardiovasc Surg. 2013; 46(5): 319–327, doi: 10.5090/kjtcs.2013.46.5.319, indexed in Pubmed: 24175266.
5. Beran SJ, Friedman RM, Kassir M. Recurrent digital ischemia due to thrombosis of the persistent median artery. Plast Reconstr Surg. 1997; 99(4): 1169–1171, doi: 10.1097/00006534-199704000-00042, indexed in Pubmed: 9091922.
6. Buch C, Devora CM, Johnson LY, et al. Incomplete superficial palmar arch and bilateral persistent median artery. Int J Surg Case Rep. 2019; 58: 205–207, doi: 10.1016/j. ijscr.2019.04.035, indexed in Pubmed: 31078992.
7. Carroll MA, Blandino J, Flynn A, et al. Neurovascular axillary variations: superficial brachial artery and single-corded brachial plexus. Anat Sci Int. 2021; 96(1): 161–167, doi: 10.1007/s12565-020-00563-x, indexed in Pubmed: 32785843.
8. Chakravarthi KK, Ks S, Venumadhav N, et al. Anatomical variations of brachial artery - its morphology, embryo-

genesis and clinical implications. J Clin Diagn Res. 2014; 8(12): AC17–AC20, doi: 10.7860/JCDR/2014/10418.5308, indexed in Pubmed: 25653931.

9. Chen Li, Chen J, Hu B, et al. Sonographic findings of the bifid median nerve and persistent median artery in carpal tunnel: a preliminary study in chinese individuals. Clinics (Sao Paulo). 2017; 72(6): 358–362, doi: 10.6061/clinics/2017(06)05, indexed in Pubmed: 28658435.

10. Claassen H, Schmitt O, Wree A. Large patent median arteries and their relation to the superficial palmar arch with respect to history, size consideration and clinic consequences. Surg Radiol Anat. 2008; 30(1): 57–63, doi: 10.1007/s00276-007-0290-5, indexed in Pubmed: 18071622.

11. D'Costa S, Narayana K, Narayan P, et al. Occurrence and fate of palmar type of median artery. ANZ J Surg. 2006; 76(6): 484–487, doi: 10.1111/j.1445-2197.2006.03758.x, indexed in Pubmed: 16768774.

12. Dickinson JC, Kleinert JM. Acute carpal-tunnel syndrome caused by a calcified median artery. A case report. J Bone Joint Surg. 1991; 73(4): 610–611, doi: 10.2106/00004623-199173040-00020, indexed in Pubmed: 2013602.

13. Eid N, Ito Y, Shibata MA, et al. Persistent median artery: cadaveric study and review of the literature. Clin Anat. 2011; 24(5): 627–633, doi: 10.1002/ca.21127, indexed in Pubmed: 21647963.

14. Fricker R, Fuhr P, Pippert H, et al. Acute median nerve compression at the distal forearm caused by a thrombosed aneurysm of an epineural vessel: case report. Neurosurgery. 1996; 38(1): 194–196, doi: 10.1097/00006123-199601000-00044, indexed in Pubmed: 8747970.

15. George BJ, Henneberg M. High frequency of the median artery of the forearm in South African newborns and infants. S Afr Med J. 1996; 86(2): 175–176, indexed in Pubmed: 8619148.

16. Haładaj R, Wysiadecki G, Dudkiewicz Z, et al. Persistent median artery as an unusual finding in the carpal tunnel: its contribution to the blood supply of the hand and clinical significance. Med Sci Monit. 2019; 25: 32–39, doi: 10.12659/MSM.912269, indexed in Pubmed: 30600313.

17. Henneberg M, George BJ. A further study of the high incidence of the median artery of the forearm in Southern Africa. J Anat. 1992; 181(Pt 1): 151–154, indexed in Pubmed: 1294564.

18. Huelin JG, Barreiro FJ, Barcia EC. Radio-anatomic study of the median artery. Acta Anat (Basel). 1979; 105(3): 250–255, indexed in Pubmed: 539363.

19. Ikeda A, Ugawa A, Kazihara Y, et al. Arterial patterns in the hand based on a three-dimensional analysis of 220 cadaver hands. J Hand Surg Am. 1988; 13(4): 501–509, doi: 10.1016/s0363-5023(88)80085-6, indexed in Pubmed: 3418051.

20. Jeon SY, Lee K, Yang WJ. Carpal tunnel syndrome caused by thrombosed persistent median artery - A case report. Anesth Pain Med (Seoul). 2020; 15(2): 193–198, doi: 10.17085/apm.2020.15.2.193, indexed in Pubmed: 33329813.

21. Jones NF, Ming NL. Persistent median artery as a cause of pronator syndrome. J Hand Surg Am. 1988; 13(5): 728–732, doi: 10.1016/s0363-5023(88)80135-7, indexed in Pubmed: 3241046.

22. Kele H, Verheggen R, Reimers CD. Carpal tunnel syndrome caused by thrombosis of the median artery: the importance of high-resolution ultrasonography for diagnosis. Case report. J Neurosurg. 2002; 97(2): 471–473, doi: 10.3171/jns.2002.97.2.0471, indexed in Pubmed: 12186479.

23. Khashaba A. Carpal tunnel syndrome from thrombosed persistent median artery. J Emerg Med. 2002; 22(1): 55–57, doi: 10.1016/s0736-4679(01)00436-x, indexed in Pubmed: 11809556.

24. Kopuz C, Gülman B, Bariş S. Persistent median artery: an anatomical study in neonatal and adult cadavers. Kaibogaku Zasshi. 1995; 70(6): 577–580, indexed in Pubmed: 8721812.

25. Muratore T, Ozer K. Persistent median artery in a pediatric trauma patient: case report. J Hand Surg Am. 2011; 36(4): 658–660, doi: 10.1016/j.jhsa.2011.01.020, indexed in Pubmed: 21463728.

26. Natsis K, Iordache G, Gigis I, et al. Persistent median artery in the carpal tunnel: anatomy, embryology, clinical significance, and review of the literature. Folia Morphol. 2009; 68(4): 193–200, indexed in Pubmed: 19950066.

27. Natsis K, Piagkou M, Panagiotopoulos NA, et al. An unusual high bifurcation and variable branching of the axillary artery in a Greek male cadaver. Springerplus. 2014; 3: 640, doi: 10.1186/2193-1801-3-640, indexed in Pubmed: 25392808.

28. Nayak SR, Krishnamurthy A, Kumar SjM, et al. Palmar type of median artery as a source of superficial palmar arch: a cadaveric study with its clinical significance. Hand (N Y). 2010; 5(1): 31–36, doi: 10.1007/s11552-009-9197-4, indexed in Pubmed: 19384461.

29. Nunoo-Mensah J. An unexpected complication after harvesting of the radial artery for coronary artery bypass grafting. Ann Thorac Surg. 1998; 66(3): 929–931, doi: 10.1016/s0003-4975(98)00559-1, indexed in Pubmed: 9768955.

30. Osiak K, Elnazir P, Mazurek A, et al. Prevalence of the persistent median artery in patients undergoing surgical open carpal tunnel release: A case series. Transl Res Anat. 2021; 23: 100113, doi: 10.1016/j.tria.2021.100113.

31. Patnaik M, Paul S. Persistent median artery of the forearm and palm: a cadaver study into its origin, course, fate and clinical significance. Ital J Anat Embryol. 2016; 121(1): 88–95, indexed in Pubmed: 28872801.

32. Patnaik VVG, Kalsey G, Singla Rajan K. Palmar arterial arches-A morphological study. J Anat Soc India. 2002; 51: 187–193.

33. Proudman TW, Menz PJ. An anomaly of the median artery associated with the anterior interosseous nerve syndrome. J Hand Surg Br. 1992; 17(5): 507–509, doi: 10.1016/s0266-7681(05)80231-1, indexed in Pubmed: 1479240.

34. Rodríguez-Niedenführ M, Sañudo JR, Vázquez T, et al. Median artery revisited. J Anat. 2002; 195(1): 57–63, doi: 10.1046/j.1469-7580.1999.19510057.x.

35. Singer E. Embryological pattern persisting in the arteries of the arm. Anat Rec. 2005; 55(4): 403–409, doi: 10.1002/ar.1090550407.

36. Singla RK, Kaur N, Dhiraj GS. Prevalence of the persistant median artery. J Clin Diagn Res. 2012; 6(9): 1454–1457, doi: 10.7860/JCDR/2012/4218.2531, indexed in Pubmed: 23285428.

37. Tsagarakis M, Tarabe M, Minoyiannis N, et al. Management of traumatic complete laceration of the median artery at the carpal tunnel: repair or ligate? Plast Reconstr Surg. 2004; 114(4): 1014–1015, doi: 10.1097/01.prs.0000138708.90798.2c, indexed in Pubmed: 15468423.

38. Yang HJ, Gil YC, Jung WS, et al. Variations of the superficial brachial artery in Korean cadavers. J Korean Med Sci. 2008; 23(5): 884–887, doi: 10.3346/jkms.2008.23.5.884, indexed in Pubmed: 18955798.

39. Yoshinaga K, Tanii I, Kodama K. Superficial brachial artery crossing over the ulnar and median nerves from posterior to anterior: embryological significance. Anat Sci Int. 2003; 78(3): 177–180, doi: 10.1046/j.0022-7722.2003.00053.x, indexed in Pubmed: 14527132.

V M
VIA MEDICA

C A S E   R E P O R T

Rare high branching pattern from the first part of the right axillary artery

Ahmad O. Odeh[1], Shivika Ahuja[1], Sania V. Karir[1], Felicia D. Lee[1], Young T. Lee[1],
Zoe I. Henkes[1], Larry F. Yang[1], Dane A. Meyer[1], Daniel T. Daly[1–3], Yun Tan[1–3]

[1]Saint Louis University School of Medicine, Saint Louis, MO, United States
[2]Center for Anatomical Science and Education, Saint Louis University School of Medicine, Saint Louis, MO, United States
[3]Department of Surgery, Saint Louis University School of Medicine, Saint Louis, MO, United States

A 77-year-old female cadaver was observed to have a rare branching pattern of the right axillary artery (AA). The first part of the AA typically gives off only a superior thoracic artery (STA) but was observed to give off three branches in the case: a lateral thoracic artery (LTA), a thoracoacromial trunk, and a large common trunk (CT). The LTA travelled to provide a variant STA to the 1st and 2nd intercostal spaces. The CT provided an accessory LTA and accessory thoracodorsal artery before bifurcating into a subscapular artery (SA) and posterior humeral circumflex artery. As expected, the SA further divided into the circumflex scapular artery and thoracodorsal artery. A pectoral artery and the anterior humeral circumflex artery originated directly from the second and third parts of the AA, respectively. Knowledge of AA branching variations is of great clinical significance to anatomists, radiologists, and surgeons due to the high rate of injury to this artery. (Folia Morphol 2024; 83, 1: 215–220)

Keywords: artery, upper limb vasculature, axillary artery, variation

INTRODUCTION

The subclavian artery continues lateral to the first rib as the axillary artery (AA) where it is divided into three distinct parts as it relates to the pectoralis minor muscle. The first part of the AA is proximal to the pectoralis minor and typically gives off only one branch, the superior thoracic artery (STA). As the AA travels in its second part, posterior to the pectoralis minor, it normally provides two branches: the thoracoacromial trunk (TAT) and the lateral thoracic artery (LTA). Finally, distal to the pectoralis minor muscle, the third part of the AA typically gives three branches: the anterior humeral circumflex artery (AHCA), posterior humeral circumflex artery (PHCA), and subscapular artery (SA). The SA then typically quickly bifurcates into the cir-

cumflex scapular artery (CSA) and the thoracodorsal artery (TDA). As the AA passes the inferior border of teres major its name changes to brachial artery which continues in the arm.

While the muscles of the shoulder girdle can receive collateral circulation from numerous sources, the study of arterial branching remains important because these major arteries maintain close anatomical relationships with the brachial plexus. The cords of the brachial plexus are named based on their relationship to the second part of the AA; their close proximity suggests that arterial variation in this region can pose a risk for neuropathy as seen by previous anatomical and clinical case studies [16, 22]. An understanding of

---

Table 1. Summary of axillary artery (AA) variations that differ from the current case, with brief descriptions of the AA variations identified in other individual case studies. This table compares other AA variations similar to the current case while highlighting differences based on reports in the literature. For comparison, note also the branches that typically arise from each part of the AA

AA parts	Typical branching pattern	Current variation branching pattern	Reported variants branching patterns
First	STA	LTA TAT CT: aLTA, aTDA, PHCA, SA	TAT and SA (described in the Discussion) [14]
Second	TAT LTA	Pectoral artery	SA gave the LTA and PHCA [20] CT for the SA and LTA [18]
Third	SA: CSA and TDA PHCA AHCA	AHCA	Common subscapular trunk was the origin for the SA, AHCA and PHCA [22] CT bifurcated into the PHCA and S [19] A common subscapular trunk provided the CSA, TDA, PHCA, LTA, TAT [3] A CT divided into the deep brachial artery, AHCA, PHCA, SA [1] A CT divided into the SA and a common stem for the AHCA, PHCA and the deep brachial artery [2]

AHCA — anterior humeral circumflex artery; aLTA — accessory lateral thoracic artery; aTDA — accessory thoracodorsal artery; CSA — circumflex scapular artery; CT — common trunk; LTA — lateral thoracic artery; PHCA — posterior humeral circumflex artery; SA —subscapular artery; STA — superior thoracic artery; TDA — thoracodorsal artery

possible anatomical variations can help guide surgical and therapeutic procedures.

While AA variations are not uncommon, the current case discusses a rare variation in which the first part of the right AA provides a novel common trunk (CT). This aberrant CT gave origin to the following branches: an accessory LTA (aLTA), an accessory (aTDA), the SA and the PHCA (Table 1) [1–3, 14, 18–20, 22]. The aim of this case study is to provide a detailed case presentation of this unique branching pattern of the AA while outlining possible clinical implications of this variant.

CASE REPORT

The body of a 77-year-old female was received by the Saint Louis University Gift Body Programme of the Center for Anatomical Science and Education (CASE) with the informed consent of the donor. The death certificate listed hepatic carcinoma as the cause of death. No other pathologies were noted.

Dissection of the right axilla was completed according to instructions outlined in Grant's dissector, 16th Edition [7]. After the right axillary vein was cleaned and studied, it was removed to better study the AA branching pattern. One unique variation observed in the right AA included the absence of a traditional STA originating from the first part of the AA. Instead, from proximal to distal, the first part of the AA gave three branches: the LTA, the TAT, and a large CT. After providing these three branches, the AA continued distally, deep to the pectoralis minor

and surrounded by the lateral, posterior, and medial cords of the brachial plexus. Proximally, the LTA provided the STA to the first and second intercostal spaces before continuing with the long thoracic nerve to supply the serratus anterior muscle (Fig. 1).

The large CT branched into an aLTA to the serratus anterior muscle and a large aTDA to the latissimus dorsi muscle. These named branches were identified based on the muscles they supply but are described as accessories because they originate from an atypical source. The CT then bifurcated into the PHCA and the SA. The PHCA travelled with the axillary nerve, while the SA bifurcated into a CSA and a small TDA (Fig. 2).

The second part of the AA provided one pectoral artery to the pectoralis minor. The third part of the AA supplied the AHCA artery before continuing as the brachial artery (Fig. 3). Normally, the AA is closely approximated by the three cords of the brachial plexus. However, in this unique case, the AA and CT surrounded the medial cord and the medial antebrachial cutaneous nerve (Fig. 3). The branching pattern of this variant AA is summarized in a sketch depicting the branches from each part of the AA (Fig. 4). The left AA and upper extremity venous drainage were anatomically typical.

DISCUSSION

Previously documented AA variations

A wide variety of AA variations have been documented in the literature, including the presence of common arterial trunks which give rise to branches that normally originate directly from the AA [5, 6].
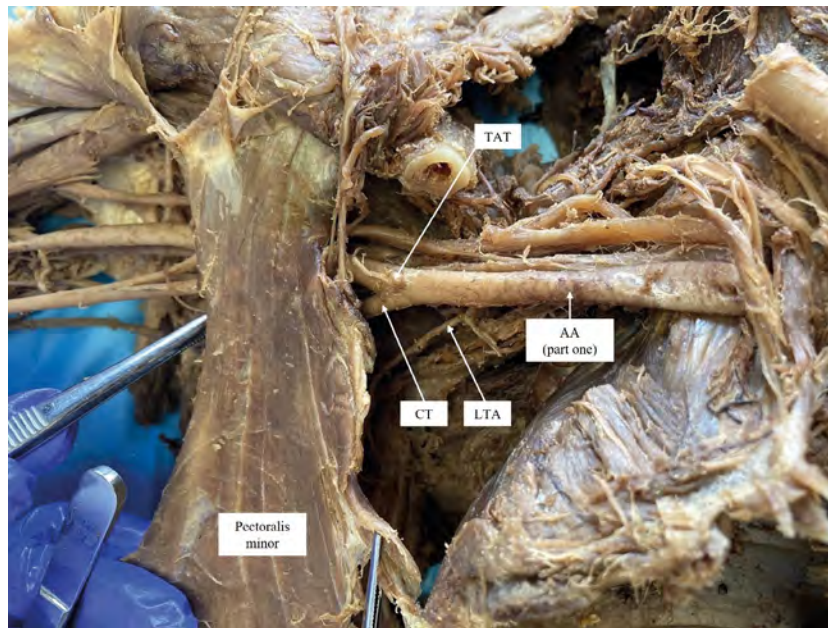
Figure 1. Arterial branching from the first part of the axillary artery (AA). The pectoralis minor muscle has been detached from its origin along the anterior aspect of the upper ribs and the arm has been abducted and extended to best show the three branches originating from the first part of the AA. The lateral thoracic artery (LTA) branches first, followed by the thoracoacromial trunk (TAT) and common trunk (CT). Both the CT and the AA continue deep to the pectoralis minor.
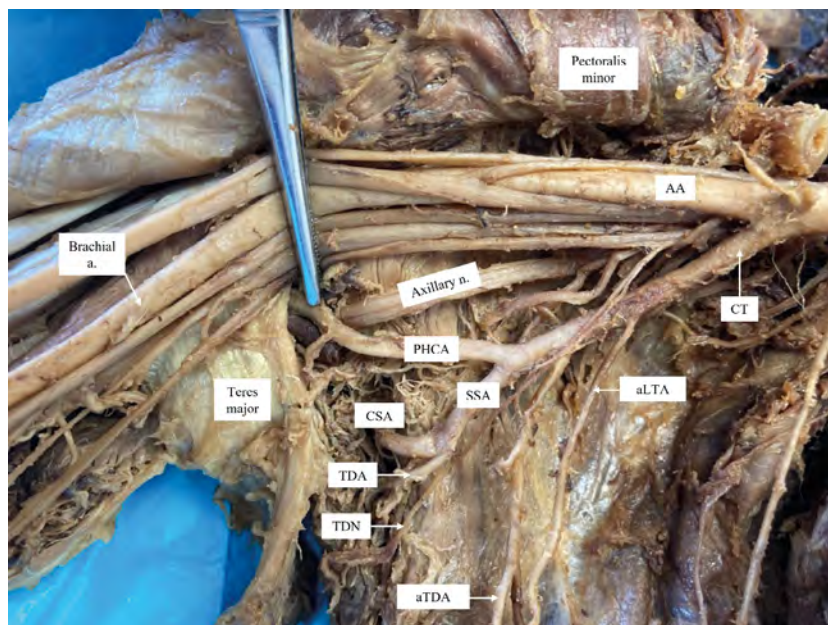
Figure 2. Common trunk from the first part of the axillary artery (AA). The common trunk (CT) provides the accessory lateral thoracic artery (aLTA) and accessory thoracodorsal artery (aTDA) before terminating as the subscapular artery (which bifurcates into the circumflex scapular artery [CSA] and thoracodorsal artery [TDA]) and the posterior humeral circumflex artery (PHCA) artery. The TDA travels with the thoracodorsal nerve (TDN) and the PHCA travels with the axillary nerve. The AA was observed continuing as the brachial artery distal to the teres major muscle; SSA — subscapular artery.

In addition to the typical origin of the SA and PHCA from the third part of the AA, these two vessels have been observed arising from a CT from either the first or second part of the AA [11]. The current case adds another distinct finding to this description with the higher origin of a CT from the first part of the AA.
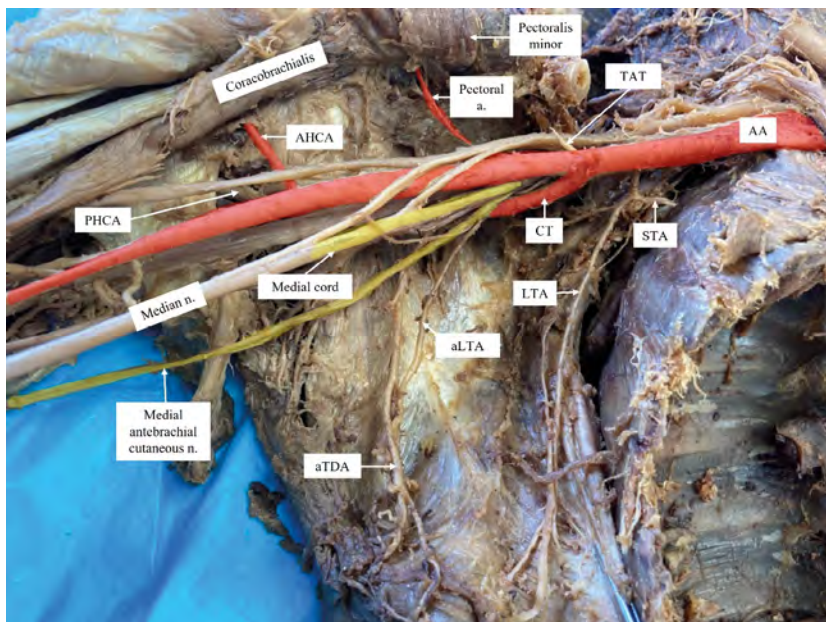
Figure 3. Unique neurovascular relationship between brachial plexus and axillary artery (AA). The pectoral artery and anterior humeral circumflex artery (AHCA) can be observed branching from the second and third parts of the AA, respectively. Arterial structures have been shaded in red to emphasize the unique anatomical relationship of the AA and the common trunk (CT) with two neural structures, the medial cord and the medial antebrachial cutaneous nerve, that are shaded yellow. The two branches from the second and third parts of the AA are also in red. This image also allows one to appreciate the lateral thoracic artery (LTA) supplying the superior thoracic artery (STA); aLTA — accessory lateral thoracic artery; aTDA — accessory thoracodorsal artery); PHCA — posterior humeral circumflex artery; TAT — thoracoacromial trunk.
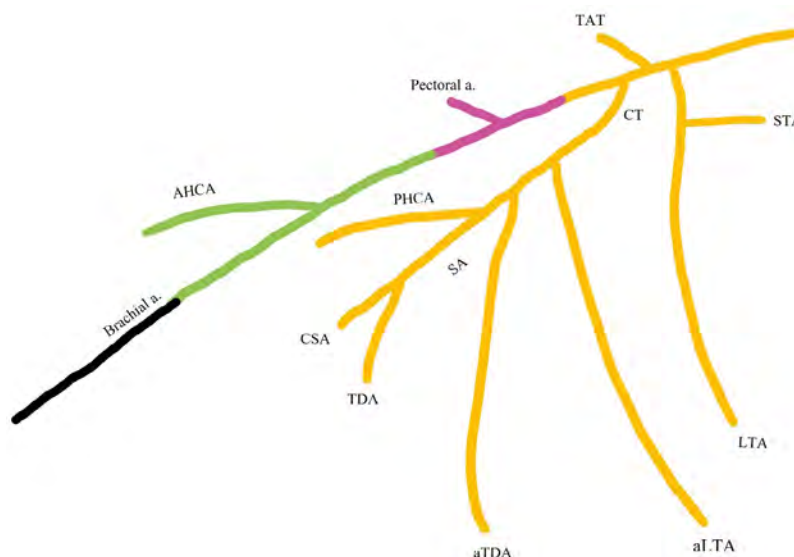
Figure 4. Representation of the axillary artery (AA) branching variation in the current case. This sketch (not drawn to scale) summarizes the AA branching in the current case. The branches are coloured based on the part of the AA from which they originate (orange — first part, pink — second part, green — third part). Notice that he lateral thoracic artery (LTA), the thoracoacromial trunk (TAT), and the common trunk (CT) all have a high origin from the AA. The CT continues distally and provides two accessory branches before bifurcating as the posterior humeral circumflex artery (PHCA) and subscapular artery (SA). The AA second part continues posterior to the pectoralis minor and gives an isolated pectoral artery before providing its final branch, the anterior humeral circumflex artery (AHCA), from the third part of the AA. The AA then continues as the brachial artery (black); aLTA — accessory lateral thoracic artery; aTDA — accessory thoracodorsal artery; CSA — circumflex scapular artery; STA — superior thoracic artery; TDA — thoracodorsal artery.

A study of 166 axillae described the branching pattern of the LTA, SA, and PHCA finding that the LTA gave rise to both the TDA and the SA in about 10% of the cases while the PHCA was observed to

variably originate from either the SA or the deep brachial artery in about 20% of the cases [15]. The current case adds to the description of the possible origins of the SA and PHCA as arising from a CT from the first part of the AA. Another case study describes two branches, the TAT and SA, arising from the first part of the AA, with the SA providing the LTA before terminating as the TDA and PHCA [14]. However, the current case has three branches originating from the first part of the AA. The CT in our report provided both an aLTA and an aTDA before bifurcating into the SA and PHCA artery.

Furthermore, the current case includes an LTA that quickly provides the STA, a branching pattern which is rarely seen. The current literature regarding reported anomalous STA origins and trajectories includes one case study in which the STA originates from the first part of the AA but travels between components of the brachial plexus to reach the lateral thoracic wall [1]. A second case report includes two cadaveric dissections where the LTA originated cephalad to the STA along the first part of the AA [25].

The presence of a large CT from the first part of the AA that supplies an aLTA and an aTDA, before bifurcating into the PHCA and SA, has not been reported in the literature. Table 1 [1–3, 14, 18–20, 22] outlines descriptions of documented AA branching patterns as they compare to the current case.

Clinical significance

It has been reported that the AA has the highest rate of arterial injury after the popliteal artery, so it is of great clinical significance for radiologists and surgeons to be aware of its possible variations [1, 3, 13, 15, 17–20, 22, 24]. Carotid-axillary bypass is an alternative to carotid-subclavian bypass due to the significant lymphatic risks that can occur in the latter procedure, but variations in the AA branching pattern can introduce new risks [4]. Furthermore, the current case reveals the PHCA artery originating from a CT rather than from the most distal portion of the AA. Both the AHCA and PHCA (as well as the deep brachial artery) are significant when repairing rotator cuff and proximal humeral injuries as the arteries anastomose around the surgical neck of the humerus [8, 9, 21].

Brachial plexus injuries account for 35% of surgical complications in the axillary region and have the most significant long-term morbidity and mortality [10]. In the present case, the medial cord of the brachial plexus and the medial antebrachial cutaneous nerve

travelled between the AA and the CT. This atypical relationship of the medial cord with an arterial variation may complicate peripheral nerve blocks or, in general, increase the risk of nerve damage during any procedure within the axilla [12].

The right axillary vein was not anatomically unique in this case, but the course of the venous tributaries may be altered in such arterial variation and can complicate procedures like central venous line placements, arteriovenous fistulas, or impede venous flow and cause swelling [23]. Aside from venous procedures, AA variations such as the one presented in this case may also complicate axillary lymph node dissection, breast augmentation, reconstructive surgery and tumour resections [23].

CONCLUSIONS

While AA variations are common, it is unreported in the literature to see a CT originating from the first segment of the AA. This CT is unique as it provided accessory arteries to the serratus anterior and latissimus dorsi muscles before terminating as the PHCA and SA. The first part of the AA also atypically provided the LTA and TAT. Knowledge of unique arterial variations can impact a wide range of procedures performed by radiologists as well as orthopaedic, vascular, oncology, and plastic surgeons.

REFERENCES

1. Aastha A, Jain A, Kumar MS. An unusual variation of axillary artery: a case report. J Clin Diagn Res. 2015; 9(1): AD05–AD07, doi: 10.7860/JCDR/2015/11680.5477, indexed in Pubmed: 25737968.
2. Armstrong A, Dangberg C, Vest L, et al. A unique lpsilateral axillary artery variation. Int J Anat Var. 2021; 14(1): 47–50.
3. Bagoji IB, Hadimani GA, Bannur BM, et al. A unique branching pattern of the axillary artery: a case report. J Clin Diagn Res. 2013; 7(12): 2939–2940, doi: 10.7860/JCDR/2013/5883.3795, indexed in Pubmed: 24551680.
4. Barakat TI, Kenny L, Khout H, et al. Carotid axillary bypass in a patient with blocked subclavian stents: a case report. J Med Case Rep. 2011; 5: 237, doi: 10.1186/1752-1947-5-237, indexed in Pubmed: 21703034.

5. Berezovsky DR, Bordoni B. Anatomy, shoulder and upper limb, forearm arteries. StatPearls Publishing LLC, Treasure Island (FL) 2021.

6. Bozlar U, Ogur T, Norton PT, et al. CT angiography of the upper extremity arterial system: Part 1-Anatomy, technique, and use in trauma patients. AJR Am J Roentgenol. 2013; 201(4): 745–752, doi: 10.2214/AJR.13.11207, indexed in Pubmed: 24059363.

7. Detton AJ, Tank PW. Grant's dissector. 2017.

8. Gilbert GM, Nelson R. Anatomy, shoulder and upper limb, anterior humeral circumflex artery. StatPearls Publishing LLC, Treasure Island (FL) 2021.

9. Gorthi V, Moon YL, Jo SH, et al. Life-threatening posterior circumflex humeral artery injury secondary to fracture-dislocation of the proximal humerus. Orthopedics. 2010; 33(3), doi: 10.3928/01477447-20100129-29, indexed in Pubmed: 20349876.

10. Graham JM, Mattox KL, Feliciano DV, et al. Vascular injuries of the axilla. Ann Surg. 1982; 195(2): 232–238, doi: 10.1097/00000658-198202000-00020, indexed in Pubmed: 7055402.

11. Hattori Y, Doi K, Sakamoto S, et al. Anatomic variations in branching patterns of the axillary artery: a multidetector-row computed tomography angiography study. J Reconstr Microsurg. 2013; 29(8): 531–536, doi: 10.1055/s-0033-1351354, indexed in Pubmed: 23884880.

12. Janjua MS, Pak A. Axillary block. StatPearls Publishing LCC, Treasure Island (FL) 2022.

13. Khaki AA, Shoja MA, Khaki A. A rare case report of subscapular artery. Ital J Anat Embryol. 2011; 116(1): 56–59.

14. Lee JH, Kim DK. Bilateral variations in the origin and branches of the subscapular artery. Clin Anat. 2008; 21(8): 783–785, doi: 10.1002/ca.20591, indexed in Pubmed: 18220282.

15. Olinger A, Benninger B. Branching patterns of the lateral thoracic, subscapular, and posterior circumflex humeral arteries and their relationship to the posterior cord of the brachial plexus. Clin Anat. 2010; 23(4): 407–412, doi: 10.1002/ca.20958, indexed in Pubmed: 20235185.

16. Ortiz-Pomales Y, Smith J, Weiss J, et al. Tortuous axillary artery aneurysm causing median nerve compression. Ann Vasc Surg. 2014; 28(1): 122.e1–122.e3, doi: 10.1016/j.avsg.2013.07.004, indexed in Pubmed: 24189011.

17. Patnaik VV, Singla Rajan K. Branching pattern of brachial artery: a morphological study. J Anat Soc India. 2002; 51(2): 176–186.

18. Shantakumar SR, Mohandas Rao KG. Variant branching pattern of axillary artery: a case report. Case Rep Vasc Med. 2012; 2012: 976968, doi: 10.1155/2012/976968, indexed in Pubmed: 23094192.

19. Singh R. Abnormal origin of posterior circumflex humeral artery and subscapular artery: case report and review of the literature. J Vasc Bras. 2017; 16(3): 248–251, doi: 10.1590/1677-5449.001917, indexed in Pubmed: 29930655.

20. Swamy R, Rao M, Kumar N, et al. Unusual branching pattern of axillary artery associated with the high origin of ulnar artery. Ann Med Health Sci Res. 2013; 3(2): 265–267, doi: 10.4103/2141-9248.113674, indexed in Pubmed: 23919202.

21. Tang A, Varacallo M. Anatomy, head and neck, posterior humeral circumflex artery. StatPearls Publishing LLC, Treasure Island (FL) 2021.

22. Venieratos D, Lolis ED. [Abnormal ramification of the axillary artery: sub-scapular common trunk]. Morphologie. 2001; 85(270): 23–24.

23. Yang HJ, Gil YC, Jin JD, et al. Novel findings of the anatomy and variations of the axillary vein and its tributaries. Clin Anat. 2012; 25(7): 893–902, doi: 10.1002/ca.22086, indexed in Pubmed: 22623347.

24. Yang HJ, Gil YC, Jung WS, et al. Variations of the superficial brachial artery in Korean cadavers. J Korean Med Sci. 2008; 23(5): 884–887, doi: 10.3346/jkms.2008.23.5.884, indexed in Pubmed: 18955798.

25. Yuksel M, Yuksel E. Anomalous branching order of the superior and lateral thoracic arteries. Clin Anat. 1997; 10(6): 394–396, doi: 10.1002/(sici)1098-2353(1997)10:6<394::aid-ca4>3.0.co;2-p.

CASE REPORT

VIA MEDICA

Aberrant accessory abductor digiti minimi manus muscle: a rare anatomical variation

Ioannis Antonopoulos[1], Georgios Tsikouris[1], Dimosthenis Chrysikos[1], Irene Asouhidou[2], George Paraskevas[2], Theodore Troupis[1]

[1]Department of Anatomy, School of Medicine, National and Kapodistrian University of Athens, Greece
[2]Department of Anatomy, Medical School, Aristotle University of Thessaloniki, Greece

The hypothenar muscle with the greatest frequency of variations is the abductor digiti minimi manus. Except for morphological variations of this muscle, have also been reported cases of an extra wrist muscle, the accessory abductor digiti minimi manus muscle. This case report presents a rare case of an accessory abductor digiti minimi muscle characterized by an unusual origin from the tendons of the flexor digitorum superficialis. This anatomical variation was identified on a formalin — fixed male cadaver of Greek origin during routine dissection. This anatomical variation, which may result in Guyon's canal syndrome or complicate common wrist and hand surgical procedures such as the carpal tunnel release, should be known to orthopaedic surgeons and hand surgeons in particular. (Folia Morphol 2024; 83, 1: 221–225)

Keywords: wrist muscles, hypothenar muscles variations, abductor digiti minimi

INTRODUCTION

The hypothenar eminence is formed by four muscles; the abductor digiti minimi muscle, the flexor digiti minimi brevis muscle, the opponens digiti minimi muscle, and the palmaris brevis muscle [10]. Many researchers have described abnormalities of the hypothenar muscles focusing mainly on their morphology and topography [1, 4, 6, 13, 17, 22]. The hypothenar muscle with the greatest frequency of variations appears to be the abductor digiti minimi manus and the second more variable muscle is the flexor digiti minimi manus [6]. Contrarywise, the opponens digiti minimi muscle mostly lacks anatomical variations [6]. To the best of our knowledge, the first description of an accessory abductor digiti minimi manus (AADM) was done by Wood in 1868 [23].

This small aberrant muscle usually originates either from the tendon of palmaris longus muscle [2, 7, 20, 21] or the tendon of flexor carpi radialis [1]. In addition, AADM origins may extend to the flexor retinaculum [3]. As for its insertion, the most common point is the proximal phalanx of the 5th finger [12].

The aim of this article is to present a rare case of an AADM muscle with an unusual origin, and further highlight the potential clinical implications regarding ulnar nerve and artery compression.

CASE REPORT

The reported case was identified during the dissection of the right wrist and hand of a male formalin-fixed (10% v/v solution) cadaver. The dissection was held for both educational and research purposes at the Dissection's Hall of our Anatomy Department.

Address for correspondence: Prof. Theodore G. Troupis, Department of Anatomy, School of Medicine, Faculty of Health Sciences, National and Kapodistrian University of Athens, 75 Mikras Asias str., Goudi, 11527, Athens, Greece, tel: +30 2107462388, e-mail: ttroupis@med.uoa.gr
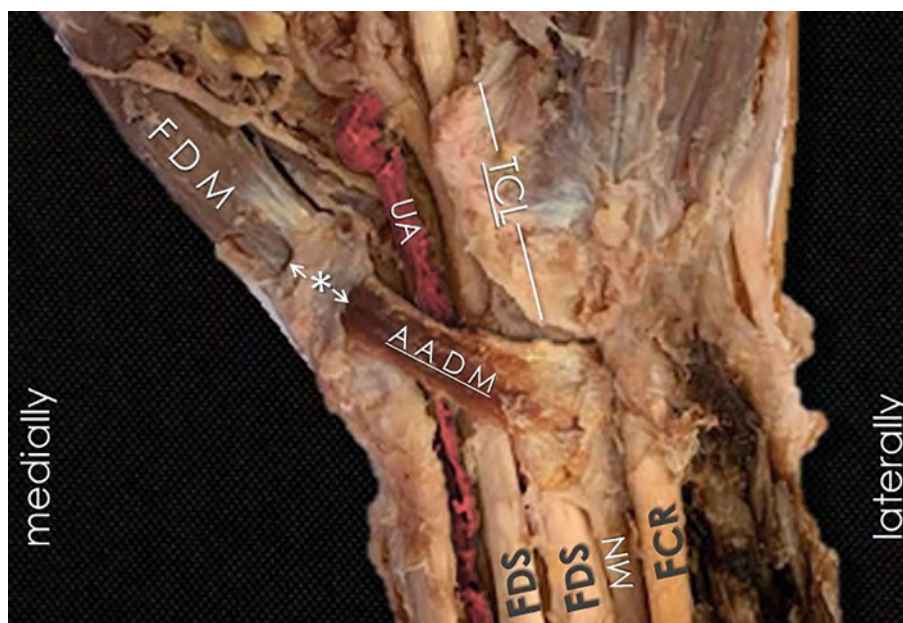
Figure 1. The accessory abductor digiti minimi manus (AADM) as first identified during the wrist dissection. It originates from the tendons of the flexor digitorum superficialis (FDS) and seems to stop under the pisohamate ligament (*); TCL — transverse carpal ligament; FDM — flexor digiti minimi; FCR — flexor carpi radialis; FCU — flexor carpi ulnaris.

The cadaver was of Greek origin and derived from body donation with the written and informed consent of the donor, according to the relevant legislation [16]. The specimen was properly cleaned and photographed. A Würth™ digital Vernier calliper (0.01 mm, accuracy) was used for the measurements of the distances and nerves' diameters.

The case described refers to the existence of an AADM muscle identified in the right wrist of a male adult. The muscle originated from the tendons of the flexor digitorum superficialis and after following a course under the pisohamate ligament (Fig. 1) its tendon inserted with the tendon of AADM into the base of the 5th proximal phalanx beneath the flexor digiti minimi muscle (Fig. 2). The ulnar artery and ulnar nerve passed beneath the AADM.

The length (L) of the AADM was 53.54 mm. The width of the muscle was 7.98 mm at its origin (w_1), 2.14 mm at its insertion (w_2) and its belly was of maximum thickness 0.96 mm (Fig. 3). The muscle was innervated by minor motor branches arising from the ulnar nerve. This was a unilateral finding.

DISCUSSION

Supernumerary hypothenar muscles mostly involve the abductor and flexor digiti minimi muscles [6]. The existence of an AADM muscle has been pre-viously described and May [15] recently proposed the use of term "long abductor digiti minimi" for this category of aberrant muscles. However, we describe a unique case of an AADM that originates from the tendons of the flexor digitorum superficialis and insert to the head of the 5th metacarpal.

Embryology

The development of the hand muscles has been thoroughly studied by Cihák back in 1970's [5]. According to his study, there are six embryonic origins for these muscles. The surface layer differentiates first, resulting in the formation of three blastemas. The radial, middle, and ulnar blastemas are responsible for the development of the abductor pollicis brevis, flexor digitorum superficialis, and abductor digiti minimi muscles (in that order) [5]. Thus, the flexor digitorum superficialis originates in the carpal area, but its blastema migrates proximally [9], and the abductor digiti minimi and abductor pollicis brevis originate from where their blastema started [15].

Frequency

The existence of an AADM muscle is considered among the most common variations of the hypothenar muscles. Its frequency varies between 22% and 35%. [18].
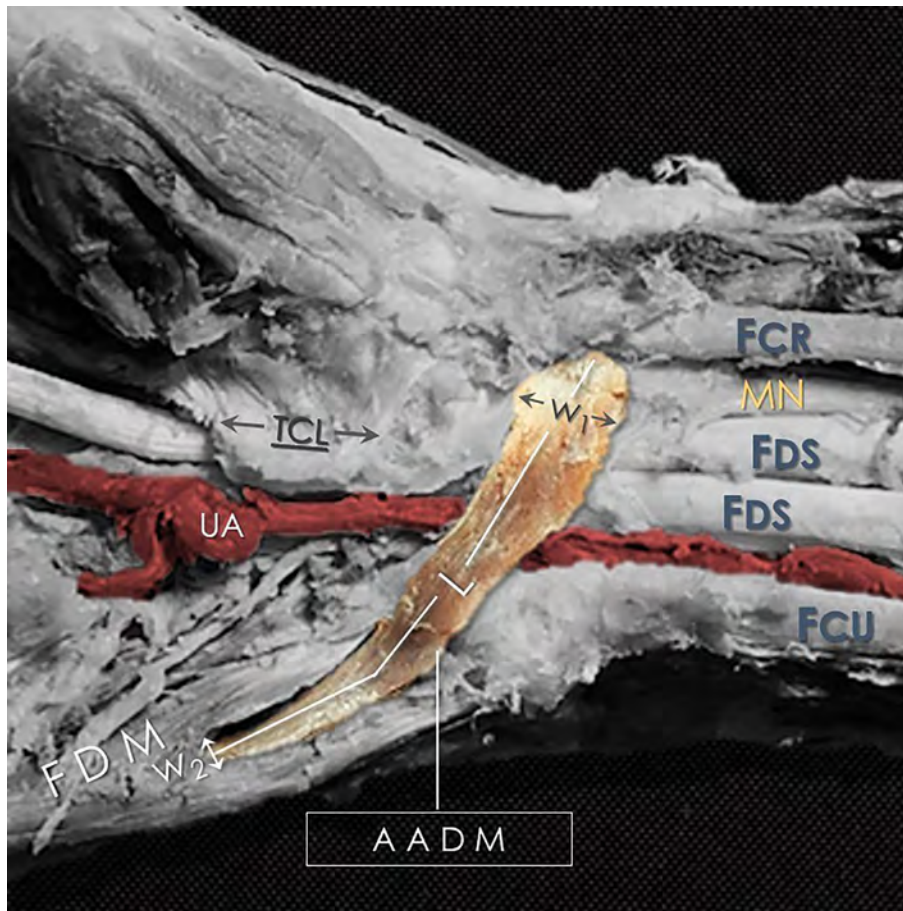
Figure 2. The length (L) of the accessory abductor digiti minimi (AADM) was 53.54 mm. The width of the muscle was 7.98 mm at its origin (w1) and 2.14 mm at its insertion (w2). Beneath the aberrant muscle passed the ulnar artery (UA — red) and the ulnar nerve; TCL — transverse carpal ligament; FDM — flexor digiti minimi; FCR — flexor carpi radialis; FCU — flexor carpi ulnaris; FDS — flexor digitorum superficialis; MN — median nerve.

Clinical considerations

Generally, the existence of an AADM muscle has been implicated with ulnar nerve compression at the wrist [6, 15]. Dimitriou and Natsis (2007) [8] reported a case of intraoperative identification of an AADM that was covering Guyon's canal and creating apparent undue pressure on the ulnar nerve proximal to its bifurcation. In that case the neurological symptoms were relieved by the resection of the AADM. Moreover, AADM's course via Guyon's canal may induce compression of the deep branch of the ulnar nerve and the ulnar vessels, which consists a major structural cause of Guyon's canal syndrome [14, 17]. Therefore, hand surgeons and orthopaedic surgeons in general, should consider the potential existence of an AADM muscle when diagnosing Guyon's canal syndrome. Worth mentioning is that, when passing through the Guyon's canal or in cases like the one we described, the AADM may compress not only the ulnar nerve but also the ulnar artery. In addition, the presence of an AADM muscle may complicate other common surgical procedures in hand, for instance during a surgical decompression of the carpal tunnel [19].

CONCLUSIONS

It is described a case of an aberrant AADM muscle found during routine dissection in the right hand of a male cadaver. This muscle took its origin from the tendons of the flexor digitorum superficialis and inserted into the head of the 5th metacarpal. Orthopaedic surgeons and especially hand surgeons should be aware of this anatomical variation that may cause Guyon's canal syndrome or complicate common wrist and hand surgical procedures, for instance the carpal tunnel release.
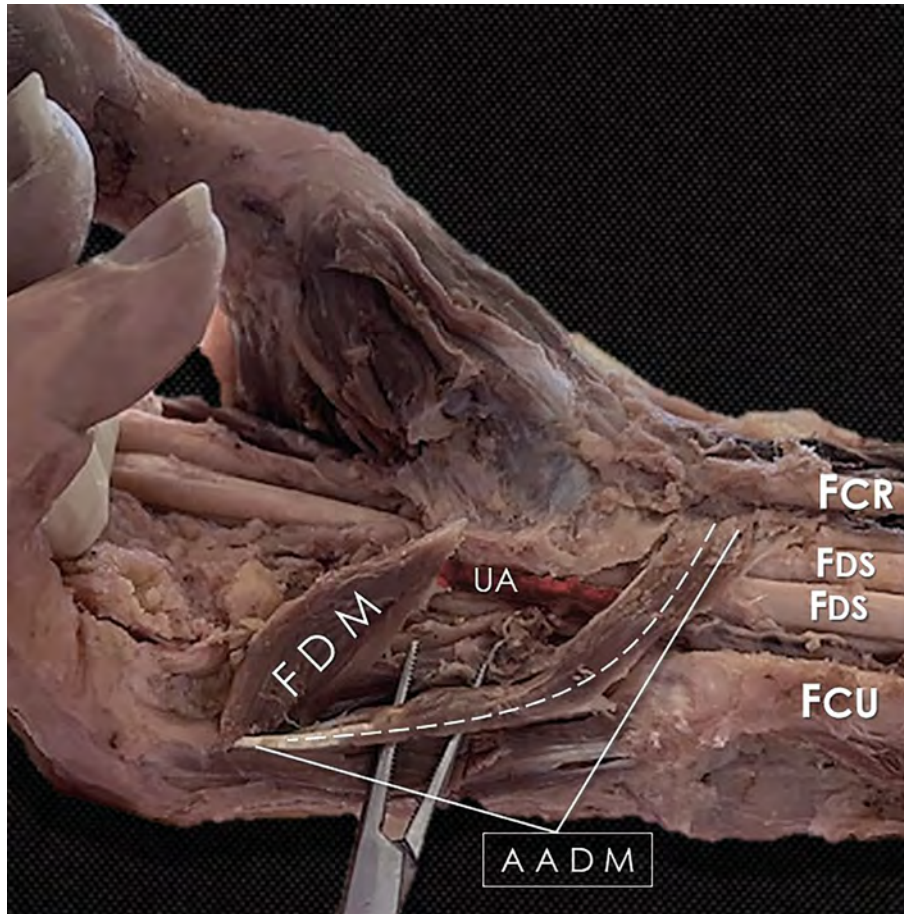
Figure 3. The full accessory abductor digiti minimi muscle (AADM) visualized by retraction of the flexor digiti minimi (FDM) muscle; UA — ulnar artery; FCR — flexor carpi radialis; FDS — flexor digitorum superficialis; FCU — flexor carpi ulnaris.

The authors also, sincerely thank those who donated their bodies to science so that anatomical research could be performed. Results from such research can potentially increase mankind's overall knowledge that can then improve patient care. Therefore, these donors and their families deserve our highest gratitude [11].

Conflict of interest: None declared

REFERENCES

1. Bakinde N, Yotovski P, Voigt T, et al. Accessory muscle in the hypothenar region: a functional approach. Ann Anat. 2005; 187(2): 149–152, doi: 10.1016/j.aanat.2004.10.002, indexed in Pubmed: 15900700.
2. Ballesteros LE, Ramirez LM. Possible implications of an accessory abductor digiti minimi muscle: a case report. J Brachial Plex Peripher Nerve Inj. 2007; 2: 22, doi: 10.1186/1749-7221-2-22, indexed in Pubmed: 18053190.
3. Bozkurt MC, Tagil SM, Ersoy M, et al. Muscle variations and abnormal branching and course of the ulnar nerve in the forearm and hand. Clin Anat. 2004; 17(1): 64–66, doi: 10.1002/ca.10094, indexed in Pubmed: 14695591.
4. Bucher O. Über die Varietäten des M. abductor digiti quinti. Anat Anz. 1943; 943: 17–324.
5. Cihák R. Ontogenesis of the skeleton and intrinsic muscles of the human hand and foot. Ergeb Anat Entwicklungsgesch. 1972; 46(1): 5–194, doi: 10.1007/978-3-662-09081-7, indexed in Pubmed: 5043313.
6. Claassen H, Schmitt O, Schulze M, et al. Variation in the hypothenar muscles and its impact on ulnar tunnel syndrome. Surg Radiol Anat. 2013; 35(10): 893–899, doi: 10.1007/s00276-013-1113-5, indexed in Pubmed: 23558800.
7. Curry B, Kuz J. A new variation of abductor digiti minimi accessorius. J Hand Surg Am. 2000; 25(3): 585–587, doi: 10.1053/jhsu.2000.6004, indexed in Pubmed: 10811767.
8. Dimitriou C, Natsis K. Accessory abductor digiti minimi muscle causing ulnar nerve entrapment at the Guyon's canal: a case report. Clin Anat. 2007; 20(8): 974–975, doi: 10.1002/ca.20518, indexed in Pubmed: 17583589.
9. Dylevsky I. Contribution to the ontogenesis of the flexor digitorum superficialis and the flexor digitorum profundus in man. Folia Morphol. 1967; 15(3): 330–335, indexed in Pubmed: 6056246.
10. Gray H, Howden R, Pick T. Gray's anatomy. 15th ed. Barnes & Noble, New York 2010: 745–753.

11. Iwanaga J, Singh V, Ohtsuka A, et al. Acknowledging the use of human cadaveric tissues in research papers: Recommendations from anatomical journal editors. Clin Anat. 2021; 34(1): 2–4, doi: 10.1002/ca.23671, indexed in Pubmed: 32808702.

12. Kanaya K, Wada T, Isogai S, et al. Variation in insertion of the abductor digiti minimi: an anatomic study. J Hand Surg Am. 2002; 27(2): 325–328, doi: 10.1053/jhsu.2002.31155, indexed in Pubmed: 11901393.

13. King TS, O'Rahilly R. M. palmaris accessories and duplication of M. palmaris longus. Acta Anat (Basel). 1950; 10(3): 327–331, doi: 10.1159/000140477, indexed in Pubmed: 14777258.

14. Lal RA, Raj S. Guyons canal syndrome due to accessory palmaris longus muscle: aetiological classification: a case report. Cases J. 2009; 2: 9146, doi: 10.1186/1757-1626-2-9146, indexed in Pubmed: 20062663.

15. May CA. Long abductor digiti minimi muscle: variation of the hypothenar muscles and clinical consequences. Clin Anat. 2020; 33(5): 643–645, doi: 10.1002/ca.23472, indexed in Pubmed: 31573103.

16. McHanwell S, Brenner E, Chirculescu ARM, et al. The legal and ethical framework governing Body Donation in Europe: a review of current practice and recommendations for good practice. Eur J Anat. 2008; 12: 1–24.

17. Nam Y, Hwang S, Eo S, et al. An aberrant abductor digiti minimi muscle crossing Guyon's canal. J Wrist Surg. 2017; 6(3): 235–237, doi: 10.1055/s-0036-1597682, indexed in Pubmed: 28725506.

18. Rixey A, Wenger D, Baffour F, et al. Accessory abductor digiti minimi muscle, less muscular than thought: an update on prevalence, morphology, and review of the literature. Skeletal Radiol. 2021; 50(8): 1687–1695, doi: 10.1007/s00256-021-03728-5, indexed in Pubmed: 33533963.

19. Slavchev S, Georgiev G. Aberrant abductor digiti minimi muscle found during open surgical decompression of the carpal tunnel: case report. Rev Argen Anat Clín. 2016; 5(2): 88–91, doi: 10.31051/1852.8023.v5.n2.14063.

20. Soldado-Carrera F, Vilar-Coromina N, Rodríguez-Baeza A. An accessory belly of the abductor digiti minimi muscle: a case report and embryologic aspects. Surg Radiol Anat. 2000; 22(1): 51–54, doi: 10.1007/s00276-000-0051-1, indexed in Pubmed: 10863748.

21. Uzel AP, Bulla A, Joye ML, et al. Variation of the proximal insertion of the abductor digiti minimi muscle: correlation with Guyon's canal syndrome? Case report and literature review. Morphologie. 2012; 96(313): 44–50, doi: 10.1016/j.morpho.2012.07.001, indexed in Pubmed: 23021108.

22. Wahba MY, Singh GD, Lozanoff S. An anomalous accessory flexor digiti minimi profundus muscle: a case study. Clin Anat. 1998; 11(1): 55–59, doi: 10.1002/(SICI)1098-2353(1998)11:1<55::AID-CA9>3.0.CO;2-R, indexed in Pubmed: 9445099.

23. Wood J. XVII. Variations in human myology observed during the winter session of 1867-68 at King's College, London. Proceedings of the Royal Society of London. 1868; 16: 483–525, doi: 10.1098/rspl.1867.0110.

V M

VIA MEDICA

C A S E   R E P O R T

Accessory part of the deltoid muscle

Łukasz Olewnik[1], Nicol Zielinska[1], Krzysztof Koptas[1], Krystian Maślanka[1], Kacper Ruzik[1], Georgi P. Georgiev[2], Richard Shane Tubbs[3–8]

[1]Department of Anatomical Dissection and Donation, Medical University of Lodz, Poland
[2]Department of Orthopaedics and Traumatology, University Hospital Queen Giovanna – ISUL, Medical University of Sofia, Bulgaria
[3]Department of Anatomical Sciences, St. George's University, Grenada, West Indies
[4]Department of Neurosurgery, Tulane University School of Medicine, New Orleans, Louisiana, United States
[5]Department of Neurology, Tulane University School of Medicine, New Orleans, Louisiana, United States
[6]Department of Structural and Cellular Biology, Tulane University School of Medicine, New Orleans, Louisiana, United States
[7]Department of Surgery, Tulane University School of Medicine, New Orleans, Louisiana, United States
[8]Department of Neurosurgery, Ochsner Medical Centre, New Orleans, Louisiana, United States

The shoulder and arm region has numerous morphological variations. The deltoid muscle usually consists of three parts: anterior, middle and posterior. This case report describes a very rare deltoid muscle variant, an addition to the spinal part that is attached proximally at the infraspinatus fascia and the spine of the scapula. The distal attachment transforms directly into the brachialis muscle. Additional parts can affect the biomechanics and function of the joints significantly. (Folia Morphol 2024; 83, 1: 226–230)

Keywords: deltoid muscle, deltoid tendon, anatomical variation, shoulder

INTRODUCTION

The deltoid region of the shoulder is important functionally because of its powerful abductor mechanism. It has a triangular shape due to the outline of the deltoid muscle (DM). The DM arises from an extensive V-shaped attachment from the anterior margin of the lateral third of the clavicle (clavicular or anterior part), the lateral border of the acromion (acromial or middle part) and from almost the whole of the spine of the scapula (spinal or posterior part). All fibres of the DM converge to insert into the deltoid tuberosity of the lateral surface of the shaft of the humerus [17]. The DM is innervated by the axillary nerve [17].

It continues and maintains the abduction of the humerus initiated by the supraspinatus muscle. At complete abduction, the arm is raised to an angle about 180 degrees, the first 15 degrees of which are affected by the supraspinatus muscle and the next 75 by the DM. The clavicular part comprises the flexors and mesial rotators of the arm. The posterior fibres have the opposite action.

The DM demonstrates variations with regard to the number of its segments and parts, its proximal attachment, distal attachment, fusion with surrounding muscles and innervation [2, 12, 14, 27, 31].

The different variants of the deltoid muscle are not only interesting from an anatomical point of view, but also from a clinical one, especially for orthopaedic surgeons. These variations could impede approaches to the proximal humerus, and allow the use of the deltoid in treating irreparable rotator cuffs,
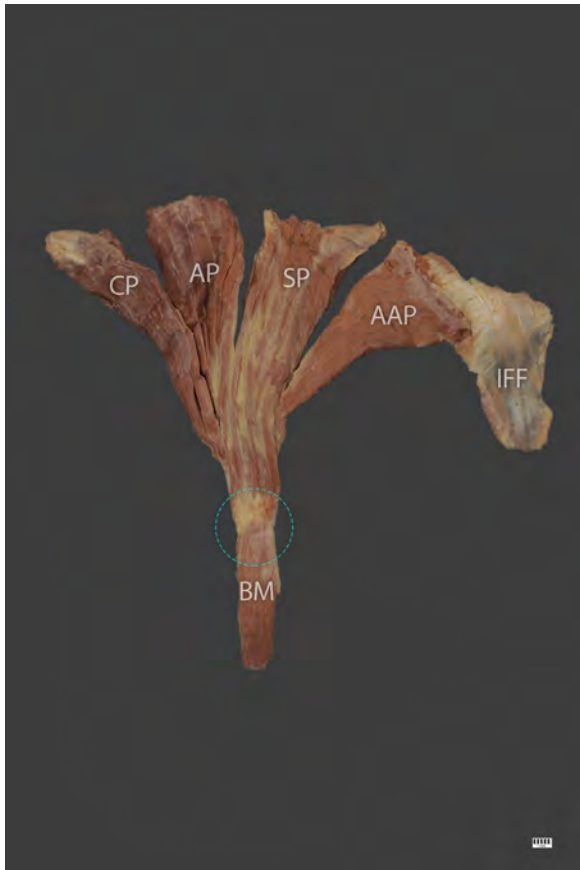
Figure 1. Anterior view of the deltoid muscle; CP — clavicular part; AP — acromial part; SP — spinal part; AAP — accessory spinal part; IFF — infraspinatus fascia; BM — brachialis muscle; turquoise circle show fusion between deltoid muscle and brachialis muscle.
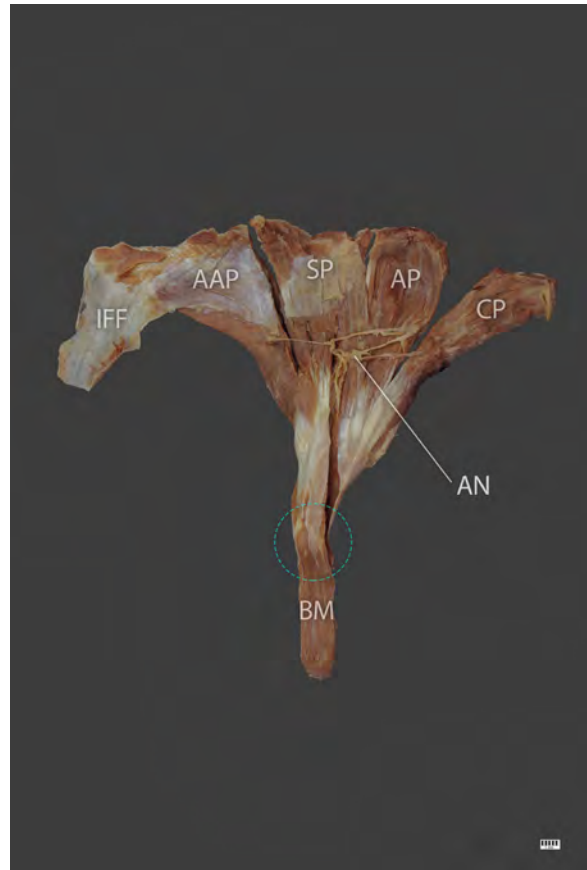
Figure 2. Posterior view of the deltoid muscle; CP — clavicular part; AP — acromial part; SP — spinal part; AAP — accessory spinal part; IFF — infraspinatus fascia; BM — brachialis muscle; AN — axillary nerve; turquoise circle show fusion between deltoid muscle and brachialis muscle.

Table 1. Morphometric measurements of parts of the deltoid muscle [mm]

	Clavicular part	Acromial part	Spinal part	Accessory part
Proximal attachment — width	26.96	50.32	70.40	69.14
Proximal attachment — thickness	5.91	6.23	7.84	4.67
The belly length up to the point where all parts connect and pass into the tendon	164.29	139.35	107.94	121.46

with or without acromioplasty or acromionectomy, or facilitate posterior deltoid-to-triceps tendon transfer [6, 15, 26].

This case report focuses on a very rare variant of the DM with an accessory segment (accessory spinal part), and the distal part passes directly into the brachialis muscle (BM) (fusion).

CASE REPORT

A male cadaver, 79 years old at death, was subjected to routine anatomical dissection for research and teaching purposes at the Department of Anatomical Dissection and Donation, Medical University of Lodz,

Poland. The right upper limb underwent traditional anatomical dissection and a morphological variant of the DM was found [25, 34]. This structure was subjected to a detailed assessment. The DM consisted of four parts (clavicular, acromial, spinal and accessory spinal; Figs. 1, 2). The clavicular part originated from the lateral third of the clavicle; the acromial part originated from the lateral border of the acromion; the spinal part originated from part of the spine of the scapula. The accessory spinal part originated from the other part of the spine and from the infraspinatus fascia (Figs. 1, 2). The measurements of the individual parts are shown in Table 1.

All the parts then interconnect to form a common muscle mass 48.54 mm wide and 13.45 mm thick. The length of this common muscle mass to the myotendinous junction point is 38.98 mm. The width of the myotendinous junction is 24.56 mm and its thickness is 4.16 mm.

The tendon is 18.97 mm long; it is attached to the deltoid tuberosity and provides an origin for the BM. At the site of transition of the tendon into the muscular part of the brachialis, it is 23.73 mm wide and 4.19 mm thick (Figs. 1, 2).

In the other upper limb, the DM comprised three segments (anterior, middle and posterior) and the BM demonstrated standard proximal and distal attachments.

DISCUSSION

The area of the shoulder girdle and the arm has numerous morphological variations. Older publications show only the numerous morphological variants within the biceps or triceps brachii [28], while newer scientific studies also show many variants in the shoulder area [13, 22, 23, 32–34].

In order to understand such morphological variations, one needs to know their embryological basis. The DM, teres minor, infraspinatus and supraspinatus muscles arise from a common premuscle mass continuous with the pectoral mass and the common arm sheath. In an 11 mm embryo the DM has partially split off from this mass towards its origin from the acromion and clavicula. In 14 to 16 mm embryos it has much of the adult form, with usually a distinct slip arising from the fascia over the infraspinatus muscle. In a 20 mm embryo, it has practically the adult form and attachments.

Many articles have examined the morphological variability of the musculoskeletal system in recent years [19–21, 24]. Previously, vascular variations seemed to be the most widespread, although muscle and tendon variations are also relatively common.

The DM has been classically divided into clavicular, acromial and spinal parts [17]. It also has morphological variants, which have been the focus of many studies over the years. Familiarity with them is a challenge for both scientists and clinicians. MacAlister [16] noted that the acromial part of the DM can be absent, and that its spinal part can be separated from both the acromial and clavicular parts. Mori [18] also described the possibility of separating the individual parts and analysed the types of separation.

For the acromial part of the DM, complete separation was observed in 24% of tested shoulders, incomplete separation in 38%, and no separation in 38% [18]. For the clavicular part, there was complete separation in 4%, incomplete separation in 4%, and no separation in 92% [18].

Fusion between the clavicular part of the DM and the pectoralis major (clavicular part) has often been reported [7, 8, 16, 28, 31]. Other possible fusions are between the DM and the trapezius, infraspinatus and teres minor or latissimus dorsi muscles [5, 16]. Calori [7] described another head, the 'costodeltoideus', which can originate from the lateral edge of the scapula between the teres minor and infraspinatus, or between the teres major and minor. Gruber [9] described an 'acromioclavicularis lateralis', which originates from the acromion and inserts into the clavicular head of the deltoideus.

Calori [7] report the presence of accessory slips of the DM originating from the spine of the scapula or the infraspinatus fascia and inserting into the humerus between the deltoid and triceps or into the fascia of the arm, while MacAlister [16] found a small muscle arising from the infraspinatus fascia near the inferior angle of the scapula, forming a small second head. The present case report differs in that a complete independent part, herein labelled the accessory spinal part, originates from the other part of the spine and from the infraspinatus fascia. This accessory part was completely separated from the second spinal part. Interestingly, each part was also separately innervated by branches of the axillary nerve.

Improved understanding of the origin and parts of the DM can help to optimise procedures and minimize functional deltoid comorbidity. The scapular spinal fibres of the DM act with the latissimus dorsi to generate extension of the arm during ambulation. These fibres also assist in external (or lateral) rotation of the humerus [1]. This is functionally important because strengthening the posterior fibres of the DM can help to offset the tendency of the shoulder to become internally rotated owing to poor posture [1].

Hence, having an accessory spinal part can result in better prevention of poor posture. Biomechanical research will be needed to confirm this thesis. Furthermore, the reported accessory spinal part could also impede posterior deltoid transfer to allow restoration of elbow extension in patients with tetraplegia and posterior approach to the shoulder [6]. In addition,

a portion of the BM can become interposed between the fragments, thus causing nonunion in fracture of the shaft of the humerus; this would represent another variation in the distal part of the deltoid.

Another variation observed herein involved a connection between the DM and the BM (proximal attachment of the BM) after all the parts had joined to became a tendon. Although this has been previously noted by MacAlister [16] on one male limb, it has not been identified in any other study [8, 18, 28–30]; only fusion of the acromial portion with the brachioradialis has been reported [5]. This type of fusion could seriously affect function because the BM is the 'workhorse' of the elbow. It is a major flexor of the forearm at the elbow joint, flexing the elbow in all positions. It is the only pure flexor of the elbow joint, producing most of the force during flexion. As such, it is unclear whether this type of fusion increases or decreases the bending strength of the elbow joint.

Such variation in anatomical spaces or the reference points for incisions is an important consideration in surgical interventions as it can be a source of complications [19, 24] . For example, neurovascular structures are particularly vulnerable to iatrogenic injury. Therefore, correct diagnosis and surgical treatment of the shoulder requires an accurate understanding of its anatomy in situ, and the presence of anatomical variations can hinder surgery.

CONCLUSIONS

The deltoid muscle is characterized by complex morphological variations. Additional parts of the DM can have a significant effect on the biomechanics, function of the joints and surgery.

REFERENCES

1. Anson BJMC. Surgical anatomy. Saunders Comp., Philadelphia, London, Toronto 1971.
2. Audenaert E, Barbaix E. Separate segments within the deltoid muscle: Anatomical variants or wishful thinking? Int J Shoulder Surg. 2008; 2(3): 69–70, doi: 10.4103/0973-6042.42583, indexed in Pubmed: 20300320.
3. Bardeen C. Studies of the development of the human skeleton. Am J Anat. 1905: 265–302.
4. Bardeen C. Development and variation of the nerves and the musculature of the inferior extremity and of the neighboring regions of the trunk in man. Am J Anat. 2005; 6(1): 259–390, doi: 10.1002/aja.1000060108.
5. Bergman R, Afifi A, Miyauchi R. Illustrated Encyclopedia of Human Anatomic Variations. Anatomy Atlases 2017.
6. Bonds CW, James MA. Posterior deltoid-to-triceps tendon transfer to restore active elbow extension in patients with tetraplegia. Tech Hand Up Extrem Surg. 2009; 13(2): 94–97, doi: 10.1097/BTH.0b013e318196c92d, indexed in Pubmed: 19516135.
7. Calori L. Memorie Della Academia Della Scienze Dell'Instituto Di Bologna. Tipografia Gamberini E Parmeggiani, Bologna 1866.
8. Le Double A. Traité Des Variations Du Système Musculaire de l'homme et de Leur Signification Au Point de Vue de l'anthropologie Zoologique. Schleicher frères, Paris 1897.
9. Gruber W. Über die varietäten des musculus extensor hallucis longus. Arch Anat Physiol Wissen Med. 1875; 1875: 565–589.
10. Iwanaga J, Singh V, Ohtsuka A, et al. Acknowledging the use of human cadaveric tissues in research papers: Recommendations from anatomical journal editors. Clin Anat. 2020; 34(1): 2–4, doi: 10.1002/ca.23671, indexed in Pubmed: 32808702.
11. Iwanaga J, Singh V, Takeda S, et al. Standardized statement for the ethical use of human cadaveric tissues in anatomy research papers: Recommendations from Anatomical Journal Editors-in-Chief. Clin Anat. 2022; 35(4): 526–528, doi: 10.1002/ca.23849, indexed in Pubmed: 35218594.
12. Kamburoğlu HO, Boran OF, Sargon MF, et al. An unusual variation of deltoid muscle. Int J Shoulder Surg. 2008; 2(3): 62–63, doi: 10.4103/0973-6042.42201, indexed in Pubmed: 20300317.
13. Koptas K, Zielinska N, Tubbs RS, et al. A newly reported muscle: an accessory infraspinatus or a deep layer of the latissimus dorsi. Surg Radiol Anat. 2022; 44(4): 617–620, doi: 10.1007/s00276-022-02917-8, indexed in Pubmed: 35266030.
14. Leijnse JN, Han SH, Kwon YH. Morphology of deltoid origin and end tendons--a generic model. J Anat. 2008; 213(6): 733–742, doi: 10.1111/j.1469-7580.2008.01000.x, indexed in Pubmed: 19094189.
15. Lim WAJ, Bin Abd Razak HR, Lim LW, et al. Outcomes are favorable in Asian patients undergoing deltoid-on open rotator cuff repair without acromioplasty. J Orthop. 2015; 12(3): 126–129, doi: 10.1016/j.jor.2015.01.019, indexed in Pubmed: 26236114.
16. MacAlister A. Observations on the mucular variations in the human anatomy. Third series with a catalogue of the

principal muscular variations hitherto published. Trans Rov Irish Acad Sci. 1875; 25: 1–134.

17. Moore K, Arthur F, Dalley I, Anne M. Agur. Clinically Oriented Anatomy. 7th ed. Lippincott Williams & Wilkins 2013.

18. Mori M. Statistics on the musculature of the Japanese. Okajimas Folia Anat Jpn. 1964; 40: 195–300, doi: 10.2535/ofaj1936.40.3_195, indexed in Pubmed: 14213705.

19. Olewnik Ł, Gonera B, Podgórski M, et al. A proposal for a new classification of pes anserinus morphology. Knee Surg Sports Traumatol Arthrosc. 2019; 27(9): 2984–2993, doi: 10.1007/s00167-018-5318-3, indexed in Pubmed: 30535546.

20. Olewnik Ł, Karauda P, Gonera B, et al. Impact of plantaris ligamentous tendon. Sci Rep. 2021; 11(1): 4550, doi: 10.1038/s41598-021-84186-w, indexed in Pubmed: 33633305.

21. Olewnik Ł, Łabętowicz P, Podgórski M, et al. Variations in terminal branches of the popliteal artery: cadaveric study. Surg Radiol Anat. 2019; 41(12): 1473–1482, doi: 10.1007/s00276-019-02262-3, indexed in Pubmed: 31134299.

22. Olewnik Ł, Zielinska N, Gołek Ł, et al. Is it the coracobrachialis superior muscle, or is it an unidentified rare variant of coracobrachialis muscle? Surg Radiol Anat. 2021; 43(10): 1581–1586, doi: 10.1007/s00276-021-02773-y.

23. Olewnik Ł, Zielinska N, Karauda P, et al. The co-occurrence of a four-headed coracobrachialis muscle, split coracoid process and tunnel for the median and musculocutaneous nerves: the potential clinical relevance of a very rare variation. Surg Radiol Anat. 2021; 43(5): 661–669, doi: 10.1007/s00276-020-02580-x, indexed in Pubmed: 32979058.

24. Olewnik L, Zielinska N, Ruzik K, et al. A new look at quadriceps tendon - is it really composed of three layers? SSRN Electronic J. 2022, doi: 10.2139/ssrn.4172665.

25. Olewnik Ł, Paulsen F, Tubbs RS, et al. Potential compression of the musculocutaneous, median and ulnar nerves by a very rare variant of the coracobrachialis longus muscle.

Folia Morphol. 2021; 80(3): 707–713, doi: 10.5603/FM.a2020.0085, indexed in Pubmed: 32844391.

26. Rasmussen JF, Wing DW, Steiner ME. Near-Normal shoulder function 10 years after complete acromionectomy: a case report. Orthop J Sports Med. 2017; 5(9): 2325967117726072, doi: 10.1177/2325967117726072, indexed in Pubmed: 28959696.

27. Sakoma Y, Sano H, Shinozaki N, et al. Anatomical and functional segments of the deltoid muscle. J Anat. 2011; 218(2): 185–190, doi: 10.1111/j.1469-7580.2010.01325.x, indexed in Pubmed: 21118198.

28. Testut L. Les Anomalies Musculaires Chez l'homme: Expliquées Par l'anatomie Comparée Leur Importance En Anthropologie. G Masson, Paris 1884.

29. Theile F. Traité de Myologie. Baillière, Paris 1843.

30. Tubbs RS, Radcliff V, Shoja MM, et al. Dorello canal revisited: an observation that potentially explains the frequency of abducens nerve injury after head injury. World Neurosurg. 2012; 77(1): 119–121, doi: 10.1016/j.wneu.2011.03.046, indexed in Pubmed: 22130113.

31. Wysiadecki G, Polguj M, Krasucki K, et al. Morphology and a proposed model of innervation of the human deltoid muscle: a pilot study. Folia Morphol. 2014; 73(2): 216–223, doi: 10.5603/FM.2014.0032, indexed in Pubmed: 24902102.

32. Zielinska N, Olewnik Ł. Six-headed coracobrachialis muscle. Folia Morphol. 2022; 81(3): 809–813, doi: 10.5603/FM.a2021.0082, indexed in Pubmed: 34608984.

33. Zielinska N, Olewnik Ł, Karauda P, et al. A very rare case of an accessory subscapularis muscle and its potential clinical significance. Surg Radiol Anat. 2021; 43(1): 19–25, doi: 10.1007/s00276-020-02531-6, indexed in Pubmed: 32656573.

34. Zielinska N, Tubbs RS, Podgórski M, et al. The subscapularis tendon: A proposed classification system. Ann Anat. 2021; 233: 151615, doi: 10.1016/j.aanat.2020.151615, indexed in Pubmed: 33068734.

V M

VIA MEDICA

C A S E   R E P O R T

Two-headed extensor digitorum longus with coexisting additional tendinous slips

Andrzej Węgiel, Nicol Zielinska, Łukasz Gołek, Łukasz Olewnik

Department of Anatomical Dissection and Donation, Medical University of Lodz, Poland

The extensor digitorum longus is a source of much anatomic variation, mostly related with extra tendinous slips or their unusual insertions. This report describes a new configuration of the extensor digitorum longus with two heads and two main tendons which bifurcate into five slips. These slips undergo further divisions and establish connections between the each other. Our findings provide a greater insight into the intricacies of human morphology. (Folia Morphol 2024; 83, 1: 231–234)

Keywords: extensor digitorum longus, double-head, variation, variant, tendinous slip, additional tendon, muscle belly

INTRODUCTION

Together with the extensor hallucis longus (EHL), tibialis anterior and fibularis tertius muscles, the extensor digitorum longus (EDL) is a muscle that constitutes the anterior compartment of the leg. It takes its origins at the inferior surface of the tibial lateral condyle and the proximomedial part of the fibula and three membranes: the anterior interosseous membrane, the deep fascia of the leg and the anterior intermuscular septum. The course of the EDL to the distal part of the lower limb takes it under the superior extensor then inside the inferior extensor retinaculum alongside the fibularis tertius. As it passes under the superior extensor retinaculum, the EDL typically splits into the two tendons, both of which subsequently divide into two final slips which reach the second and the third phalanges of the second, third, fourth and fifth toes. The tendons to the third, fourth and fifth toes fuse on their lateral side with the slips from the extensor digitorum brevis [7].

The EDL is supplied by the anterior tibial artery, and its distal part by branches deriving from the fibular artery. The innervation is provided by the deep fibular nerve. The main functions of the muscle are to extend the toes and allow dorsiflexion of the foot.

The present case illustrates a constellation of different morphological variants of the EDL, in which the presence of an atypical muscle belly is accompanied by fusions between the EDL tendons after their bifurcation.

CASE REPORT

A female body donor was admitted to the Department of Anatomical Dissection and Donation, Medical University of Lodz, Poland for scientific and didactic purposes. A routine anatomical dissection of the right lower limb was performed. It revealed a two-headed variant of the EDL with the tendinous connections in its distal part. The further steps of the case assessment include detailed measurements, characterization and photography.

The EDL originated in a typical manner from the anterolateral aspect of the proximal tibia and consisted of upper and lower bellies. The length of the upper belly was 127.59 mm. The width of its myotendinous junction was 6.85 mm and the thickness 1.3 mm. The length of the tendon from the point of junction

Figure 1. The lower limb before the distal dissection; TA — tibialis anterior; EHL — extensor hallucis longus; UH — upper head of the extensor digitorum longus; LH — lower head of the extensor digitorum longus.

to its bifurcation was 232.94 mm. After bifurcation, the tendons reached the second and the third digits with respective lengths of 74.95 mm and 69.92 mm.

The length of the lower belly was 140.90 mm. Its myotendinous junction was 4.97 mm wide and 1.91 mm thick. The tendon was found to be 153.86 mm long at its division, which split it into the three parts. The first slip was the most medial part. It was 35.62 mm in length. It divided into its two terminal parts, i.e. medial and lateral, which both fused with the tendinous slip to the third digit of the upper head's tendon. The medial part was 32.65 mm long and the lateral part 66.66 mm long. The length of the common part after the fusion of the three tendons was 40.31 mm, and it reached the third digit.

The second slip from the lower head's tendon reached the fourth digit and was 124.62 mm in length. Similarly, the third and the most lateral slip was 100.74 mm long and inserted the fifth digit (Figs. 1–3).

Ethical approval and consent to participate

The study protocol was accepted by the Bioethics Committee of the Medical University of Lodz. The cadavers were the property of the Department of Anatomical Dissection and Donation, Medical University of Lodz. Informed consent was obtained from all participants before they died.

DISCUSSION

The typical anatomical variations related to the EDL are present in its slips, which demonstrate variable numbers, points of insertion and fusions within the EDL or with the surrounding structures. The duplicated slip may reach the corresponding toe, creating a bifid tendon, or contribute to the adjacent toe. In some cases, it was found to insert to nearby muscles, such as the EHL, the fibularis tertius or the extensor digitorum brevis [9].

The tendinous division of the EDL may extend sufficiently proximally to divide it into the smaller, separate muscles. In the most pronounced form, the toes from the second to the fifth are all supplied by individual small muscles instead of a large, singular extensor [2].

The EDL has been reported to receive a contribution from the other muscles but also to give off its own accessory slips. Węgiel et al. [10] describe an accessory, tendinous band of the EDL which originated from its proximal part and fused with the distal part of the EHL; this was accompanied by the presence of an additional tendon deriving from the EHL and inserting the dorsal surface of the first proximal phalanx.

Tezer and Cicekcibasi [8] reported a case of an extensor digiti secundus muscle which originated from the EHL and bifurcated into two slips. The smaller,
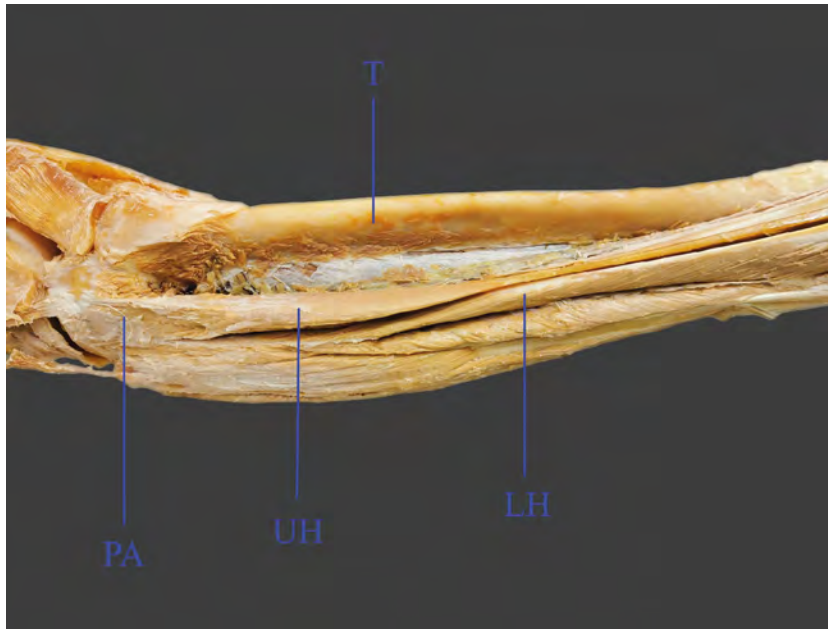
Figure 2. The proximal part of the lower limb; T — tibial shaft; PA — proximal attachment of the extensor digitorum longus; UH — upper head of the extensor digitorum longus; LH — lower head of the extensor digitorum longus.

Figure 3. The distal part of the lower limb; UT — upper tendon of the extensor digitorum longus; EHL — extensor hallucis longus; MSL — medial slip of the lower tendon; LSL — lateral slip of the lower tendon; MSU — medial slip of the upper tendon; LSU — lateral slip of the upper tendon; LT — lower tendon of the extensor digitorum longus; FS — first slip; SS — second slip; TS — third slip.

medial slip fused with the tendon of the EHL, while the lateral slip merged with the second toe tendon of the EDL.

Typically, the EDL reaches the phalanges from the second to the fifth toe. However, it is possible that one of the tendons may be absent [6], in which case, the role of the toe extensor can be performed singularly by the extensor digitorum brevis. If the absence refers only to the fifth digit, the missing tendon can be replaced by the accessory muscle, the peroneus quinti digiti, which arises with the fibularis tertius from the common muscle belly [9].

Table 1. The measurements of the presented case

Structure	Value
The upper head of the EDL	
Belly	127.59
Myotendinous junction width	6.85
Myotendinous junction thickness	1.3
Tendon	232.94
The medial slip	74.95
The lateral slip	69.92
The lower head of the EDL	
Belly	140.90
Myotendinous junction width	4.97
Myotendinous junction thickness	1.91
Tendon	153.86
The first slip	35.62
The medial slip	32.65
The lateral slip	66.66
The common tendon	40.31
The second slip	124.62
The third slip	100.74

EDL — extensor digitorum longus

The presence of an additional muscle belly is an unusual finding among the muscles of the anterior compartment of the leg; however, it is not limited only to the EDL. Ruzik et al. [5] present an EHL muscle with two heads (upper and lower), each of which with its own innervating branch: the tendon from the main belly inserted the distal phalanx of the hallux while the accessory tendon was located medially and reached the proximal phalanx of the same toe.

The muscles of the anterior compartment can be sometimes accompanied by supernumerary accessory muscles. Plochocki and Bodeen [4] reported the presence of an accessory fibularis tertius which originated from the shaft of fibula and inserted to the fibular diaphysis and the anterior interosseous membrane. This muscle is also known as the fibularis (peroneus) quartus. Its occurrence varies from 3% up to 21.7% of specimens [1].

Typically, the fibularis tertius takes its origin at the distal half of the fibula and the intermuscular septum, or at their distal third. However, in some cases, the muscular fibres of the fibularis tertius merge with the EDL belly, and it arises directly from the tendon of the EDL as an independent tendon with no separate muscle belly. This variant was found in 11% of the lower limbs and can be classified as type 3 according to Olewnik [3].

CONCLUSIONS

Despite the many years of refinement of anatomical classifications, the results of dissection still have the potential to surprise. The presented variant is a rare finding which expands our knowledge about the structure of the lower limb and is an important example of a complex pattern of the tendons and their connections within the same muscle.

Conflict of interest: None declared

REFERENCES

1. Chaney DM, Lee MS, Khan MA, et al. Study of ten anatomical variants of the foot and ankle. J Am Podiatr Med Assoc. 1996; 86(11): 532–537, doi: 10.7547/87507315-86-11-532, indexed in Pubmed: 8961655.
2. Kelikian AS, Sarrafian SK. Sarrafian's anatomy of the foot and ankle: descriptive, topographic, functional. Lippincott Williams & Wilkins 2011.
3. Olewnik Ł. Fibularis tertius: anatomical study and review of the literature. Clin Anat. 2019; 32(8): 1082–1093, doi: 10.1002/ca.23449, indexed in Pubmed: 31408221.
4. Plochocki JH, Bodeen M. Unusual supernumerary muscle in the anterior compartment of the leg. Clin Anat. 2010; 23(1): 104–105, doi: 10.1002/ca.20802, indexed in Pubmed: 19418447.
5. Ruzik K, Westrych K, Tubbs RS, et al. Case report of the double-headed extensor hallucis longus. Folia Morphol. 2023; 82(2): 429–433, doi: 10.5603/FM.a2022.0018, indexed in Pubmed: 35187631.
6. Sakuma E, Kato H, Honda N, et al. A rare anomaly of the extensor digitorum longus. Anat Sci Int. 2004; 79(4): 235–238, doi: 10.1111/j.1447-073x.2004.00082.x, indexed in Pubmed: 15633462.
7. Standring S. Gray's anatomy: the anatomical basis of clinical practice. . Elsevier Health Sciences 2021.
8. Tezer M, Cicekcibasi AE. A variation of the extensor hallucis longus muscle (accessory extensor digiti secundus muscle). Anat Sci Int. 2012; 87(2): 111–114, doi: 10.1007/s12565-011-0108-8, indexed in Pubmed: 21559883.
9. Tubbs RS, Shoja MM, Loukas M. Bergman's comprehensive encyclopedia of human anatomic variation. John Wiley & Sons 2016.
10. Węgiel A, Zielinska N, Tubbs RS, et al. Coexistence of accessory band with the second type of extensor hallucis longus. Surg Radiol Anat. 2022; 44(6): 845–849, doi: 10.1007/s00276-022-02966-z, indexed in Pubmed: 35729436.

V M
VIA MEDICA

CASE REPORT

Two variant muscles in the gluteal region

Nicol Zielinska[1], Richard Shane Tubbs[2–7], Piotr Łabętowicz[1], Łukasz Olewnik[1]

[1]Department of Anatomical Dissection and Donation, Medical University of Lodz, Poland
[2]Department of Anatomical Sciences, St. George's University, Grenada, West Indies
[3]Department of Neurosurgery, Tulane University School of Medicine, New Orleans, Louisiana, United States
[4]Department of Neurology, Tulane University School of Medicine, New Orleans, Louisiana, United States
[5]Department of Structural and Cellular Biology, Tulane University School of Medicine, New Orleans, United States
[6]Department of Surgery, Tulane University School of Medicine, New Orleans, Louisiana, United States
[7]Department of Neurosurgery, Ochsner Medical Centre, New Orleans, Louisiana, United States

The short lateral rotators of the thigh found in the gluteal region can have morphological variations. During anatomical dissection of a right lower limb, two variant structures were found in this region. The first of these accessory muscles originated from the external surface of the ramus of the ischium. Distally, it was fused with the gemellus inferior muscle. The second structure comprised tendinous and muscular parts. The proximal part originated from the external part of the ischiopubic ramus. It inserted on the trochanteric fossa. Both structures were innervated by small branches of the obturator nerve. The blood supply was via branches of the inferior gluteal artery. There was also a connection between the quadratus femoris and the superior part of the adductor magnus. These morphological variants could be clinically important. (Folia Morphol 2024; 83, 1: 235–238)

Keywords: pelvic region, morphological variations, gluteus inferior, gluteus superior, quadratus femoris, sciatic nerve, adductor minimus, adductor magnus

INTRODUCTION

The lateral rotator muscles of the thigh include the piriformis (PM), gemellus superior (GS) and inferior (GI), obturator externus (OE) and internus (OI), and quadratus femoris (QF) muscles [17]. These muscles can be morphologically variable. For example, the GS or GI can be absent (very rarely, both the GS and GI are lacking) [2, 8, 16]. These muscles can be also doubled [15]. Cases have been reported in which the GS is fused with the PM or gluteus minimus, or the GI is fused with the QF [12]. The OI is not as variable, though it can be divided into two distinct parts [9].

The PM, in contrast, is morphologically highly variable. For example, it can be fused with the GS, or OI, or gluteus medius [3].

Morphological variations in this region can have clinical implications. For example, additional structures such as an accessory head of the PM can compress nearby nerves or arteries. In cases of a three-headed PM, with the common fibular nerve passing between the first and second heads and the tibial nerves passing between the second and the third, there can be paraesthesia, loss of sensation, or lack or weakened function of the muscles [13].

Here, we report an unusual muscle found in the gluteal region during dissection and discuss the potential clinical ramifications.

CASE REPORT

An 84-year-old at death female cadaver donated to science was subjected to routine anatomical dissection for research and teaching purposes at the Department of Anatomical Dissection and Donation Medical University of Lodz, Poland. The left lower limb and its gluteal region were dissected traditionally and two interesting structures were found.

The next stage of the investigation involved detailed assessment of these variant muscles. The first muscle had only a muscular part, originating from the external surface of the ramus of the ischium (near the ischiopubic ramus). At the proximal attachment it was 7.46 mm wide and 2.17 mm thick. It was 79.90 mm long. Distally, this accessory muscle was fused with the GI, attached to the trochanteric fossa. At the point of fusion the width was 3.97 mm and the thickness 1.11 mm.

The second structure comprised tendinous and muscular parts. The proximal part originated from the external part of the ischiopubic ramus. At this point was 3.36 mm wide and 1.08 mm thick. The muscular part was 89.00 mm long, after which it passed into the tendinous part. The width at the myotendinous junction was 2.97 mm and the thickness was 1.64 mm. The tendon of this variant structure was 25.91 mm long, and it inserted on the trochanteric fossa. At this point it was 2.62 mm wide and 1.18 mm thick. Both structures were innervated by small branches of the obturator nerve. Blood was supplied by branches of the inferior gluteal artery (Fig. 1).

An electronic calliper (Mitutoyo Corporation, Kawasaki-shi, Kanagawa, Japan) was used for these measurements. Each measurement was repeated twice with an accuracy of up to 0.1 mm. No other morphological variants were found during dissection of the lower limb. Table 1 shows the morphometric measurements of the present case.

DISCUSSION

Muscles of pelvic region are morphologically variable. Sometimes there is no GS, or no GI, and in rare cases, both are lacking [2, 8, 16]. The QF can also be absent, and in most such cases there is an associated increase in the volume of the GI [16].
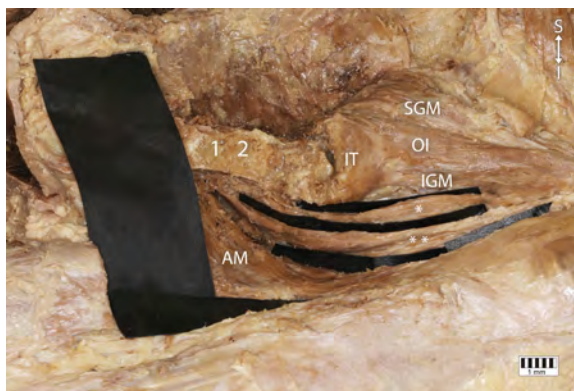
Figure 1. Anatomical variations of pelvic girdle; 1 — external part of the ischiopubic ramus; 2 — external surface of the ramus of the ischium; 3 — superior gemellus muscle (SGM); OI — obturator internus; IGM — inferior gemellus muscle; IT — ischial tuberosity; AM — adductor magnus; *first accessory muscle; **second accessory muscle.

Table 1. Morphometric measurements of the present case.

	1st	2nd
LENGTH	79.90 mm	114.91 mm (89.00 mm — muscular part 25.91 mm — tendinous part)
WIDTH		
PP	7.46 mm	3.36 mm
MJ	–	2.97 mm
PK	3.97 mm	2.62 mm
THICKNESS		
PP	2.17 mm	1.08 mm
MJ	–	1.34 mm
PK	1.11 mm	1.18 mm

MJ — myotendinosus junction; PP — proximal attachment; PK — distal attachment.

Some fusions have also been described in this region. For example, the GI can be fused with the QF. Leal et al. [12] also described fusion between the GS and the gluteus minimus. Charpy and Nicolas [5] found a muscular connection between the QF and the GI, and between the QF and the adductor magnus [5].

Macalister [10] reported that the QF can have two or three distinct parts. It is not known whether this was a divided muscle belly or duplication [13], though there are more detailed descriptions in the literature. For example, Natsis et al. [14] found two-headed PMs in 12 (4.1%) cases. Curiously, these two heads showed different arrangements. In five cases the first belly was not located superiorly to the second (as it is in most cases); it was positioned superficially and the other one more deeply [14]. Cassidy et al. [4] found cases in which the superior belly was partially superposed

on the inferior belly [4]. Such arrangements of two bellies can also occur in morphological variants of other pelvic muscles.

Tanyeli et al. [15] described an interesting case with a double PM, double GS, double GI, and double QF. The superior part of the PM originated from the anterior surface of the sacrum and the inferior part from the sacrotuberous ligament. Their common distal attachment was on the greater trochanter. The upper head of the GS was proximally attached on the body of the ischium and the lower head was attached to the ischial spine. The first head of the GI was proximally attached to the ischiadic spine and the second head to the ischial tuberosity. These four structures were inserted on to the greater trochanter. The final variation was the double QF, both parts originating from the ischial tuberosity and attaching distally on the intertrochanteric crest [15].

Analysing the attachments described above, we excluded the possibility that the present case involved an additional head of the PM or GS. However, a double GI and double QF seemed possible. We found two accessory structures. The first (superior) was fused with the GI, so it could either be an additional head of the GI or something never previously described in the literature. However, the second structure (inferior) was not connected to either the superior variant structure or the QF, so we cannot call it an accessory head of the QF or GI.

Interestingly, the volume of the QF was smaller than normal. In most cases, when the QF is absent, the volume of the GI is increased [16]. We can therefore infer that the additional structures described herein could be associated with incomplete development of the QF.

Moreover, the QF can be fused with the adductor magnus or adductor minimus, as it was in the present case. It is hard to say with which muscle it was fused because the adductor minimus is controversial in the literature. Some authors describe it as only a part of the adductor magnus [6], some as partially separate from the adductor magnus [14], and some as a completely separate accessory muscle. In our opinion, there was fusion between the superior part of the adductor magnus and the QF [7].

To assess the clinical significance of these variant structures, we should consider their position and morphological features. Usually, accessory structures are connected with some kind of neurovascular compression. For example, Arifoglu et al. [1] described

a case with double GS and double PF. The sciatic nerve passed between the two heads of the PF. In such variants there is a risk of piriformis syndrome, represented by chronic pain in the buttocks and hip with sporadic referred pain along the sciatic nerve distribution, external tenderness over the greater sciatic notch, aggravation of the pain through sitting, augmentation of it with manoeuvres that increase PM tension, and sometimes dyspareunia [10].

However, in the present case, the PM was anatomically normal and the sciatic nerve passed under it. Because the sciatic nerve was located under the described structures, the risk of PM syndrome was not high.

Taking everything into consideration, it is hard to say whether we should describe the superior variant muscle as an additional head of the GI or as something not previously described. In view of its course and morphological characteristics, the other variant muscle does not look like an accessory head of any pelvic muscle; it looks like a separate structure that is not a feature of normal anatomy.

CONCLUSIONS

The pelvic region shows several morphological variations. Accessory muscles can be associated with compression of nerves or vessels, and knowledge of them can therefore be important for clinicians, especially orthopaedists, neurologists, and physiotherapists. However, neurovascular compression depends on the arrangement and morphological characteristics of the variant muscles.

REFERENCES

1. Arifoglu Y, Sürücü HS, Sargon MF, et al. Double superior ge-mellus together with double piriformis and high division of the sciatic nerve. Surg Radiol Anat. 1997; 19(6): 407–408, doi: 10.1007/BF01628510, indexed in Pubmed: 9479716.

2. Bajka M, Manestar M, Hug J, et al. Detailed anatomy of the abdomen and pelvis of the visible human female. Clin Anat. 2004; 17(3): 252–260, doi: 10.1002/ca.10215, indexed in Pubmed: 15042575.

3. Bergman R, Afifi A, Miyauchi R. Illustrated Encyclopedia of Human Anatomic Variations. Anatomy Atlases 2017.

4. Cassidy L, Walters A, Bubb K, et al. Piriformis syndrome: implications of anatomical variations, diagnostic tech-niques, and treatment options. Surg Radiol Anat. 2012; 34(6): 479–486, doi: 10.1007/s00276-012-0940-0, in-dexed in Pubmed: 22327640.

5. Charpy A, Nicolas A. Traite d'Anatomie Humaine. In: Masson et Cie, Paris 1912: 238.

6. Clemente C. Anatomy. A regional atlas of the human body. Urban&Scha, Baltimire 1981.

7. Le Do. Traité Des Variations Du Système Musculaire de l'homme et de Leur Signification Au Point de Vue de l'anthropologie Zoologique. Schleicher frères, Paris 1897.

8. Duda GN, Brand D, Freitag S, et al. Variability of femoral muscle attachments. J Biomech. 1996; 29(9): 1185–1190, doi: 10.1016/0021-9290(96)00025-5, indexed in Pubmed: 8872275.

9. Gruber W. Die Musculi Subscapulares (Major et Minor) Und Die Neuen Supernumären Schultermuskel Des Men-schen. Máemoires de I'Acadáemie Impáeriale Des Sciences de Saint Páetersbourg Par Divers Savans et Lus Dans Ses Assembláees. 4th ed. Sankt Petersburg 1859.

10. Hopayian K, Song F, Riera R, et al. The clinical features of the piriformis syndrome: a systematic review. Eur Spine J. 2010; 19(12): 2095–2109, doi: 10.1007/s00586-010-1504-9, indexed in Pubmed: 20596735.

11. Iwanaga J, Singh V, Ohtsuka A, et al. Acknowledging the use of human cadaveric tissues in research papers: Recommendations from anatomical journal editors. Clin Anat. 2020; 34(1): 2–4, doi: 10.1002/ca.23671, indexed in Pubmed: 32808702.

12. Leal MC, Alexander JG, Beber EH, et al. The absence of piriformis muscle, combined muscular fusion, and neuro-vascular variation in the gluteal region. Autops Case Rep. 2021; 11: e2020239, doi: 10.4322/acr.2020.239, indexed in Pubmed: 34307211.

13. Macalister A. Observations on muscular anomalies in the human anatomy. Third series with a catalogue of the principal muscular variations hitherto published. Trans Roy Irish Acad Sci. 1875: 1–130.

14. Natsis K, Totlis T, Konstantinidis GA, et al. Anatomical variations between the sciatic nerve and the piriformis muscle: a contribution to surgical anatomy in piriformis syndrome. Surg Radiol Anat. 2014; 36(3): 273–280, doi: 10.1007/s00276-013-1180-7, indexed in Pubmed: 23900507.

15. Tanyeli E, Pestemalci T, Uzel M, et al. The double deep glu-teal muscles. Saudi Med J. 2006; 27(3): 385–386, indexed in Pubmed: 16532103.

16. Testut L. Les Anomalies Musculaires Chez l'homme Ex-pliquées Par Anatomie Comparée, Importance En Anthro-pologie. Masson, Paris 1884.

17. Yoo S, Dedova I, Pather N. An appraisal of the short lateral rotators of the hip joint. Clin Anat. 2015; 28(6): 800–812, doi: 10.1002/ca.22568, indexed in Pubmed: 26032283.

V M
VIA MEDICA

CASE REPORT

Very rare arrangement of the pes anserinus: potential clinical significance

Nicol Zielinska[1], Richard Shane Tubbs[2–7], Piotr Karauda[1], Teresa Vazquez[8], Łukasz Olewnik[1]

[1]Department of Anatomical Dissection and Donation, Medical University of Lodz, Poland
[2]Department of Anatomical Sciences, St. George's University, Grenada, West Indies
[3]Department of Neurosurgery, Tulane University School of Medicine, New Orleans, Louisiana, United States
[4]Department of Neurology, Tulane University School of Medicine, New Orleans, Louisiana, United States
[5]Department of Structural and Cellular Biology, Tulane University School of Medicine, New Orleans, Louisiana, United States
[6]Department of Surgery, Tulane University School of Medicine, New Orleans, Louisiana, United States
[7]Department of Neurosurgery, Ochsner Medical Centre, New Orleans, Louisiana, United States
[8]Department of Anatomy and Embryology, School of Medicine, Complutense University of Madrid, Spain

The pes anserinus superficialis is composed of the semitendinosus, gracilis and sartorius tendons. Normally, they all insert to the medial side of the tibial tuberosity, and the first two are attached superiorly and medially to the tendon of the sartorius muscle. During anatomical dissection, a new pattern of arrangement of tendons creating the pes anserinus was found. The pes anserinus comprised three tendons; the semitendinosus tendon was located superiorly to the gracilis tendon, and they both had distal attachments on the medial side of the tibial tuberosity. This seemed like the normal type, but the tendon of the sartorius muscle created an additional superficial layer, its proximal part lying just below the gracilis tendon and covering the semitendinosus tendon and a small part of the gracilis tendon. After crossing the semitendinosus tendon it is attached to the crural fascia significantly below the tibial tuberosity. Good knowledge of the morphological variations of the pes anserinus superficialis is necessary during surgical procedures in the knee region, especially anterior ligament reconstruction. (Folia Morphol 2024; 83, 1: 239–243)

Keywords: pes anserinus, superficialis, semitendinosus, gracilis, sartorius, autograft, anterior cruciate ligament reconstruction, hamstring tendon graft, patellar tendon graft

INTRODUCTION

The pes anserinus comprises two parts, the pes anserinus superficialis (PAS) and the pes anserinus profundus. The PAS is created by tendons of the sartorius (ST), gracilis (GT), and semitendinosus (STT) muscles. Normally, the STT and GT are located inferiorly and medially to the ST, but they all have distal attachments on the medial side of the tibial tuberosity [12].

The main function of the muscles constituting the PAS is flexion and external rotation of the knee joint. Moreover, this structure is responsible for stabilizing the knee, especially during rotatory movements [10].
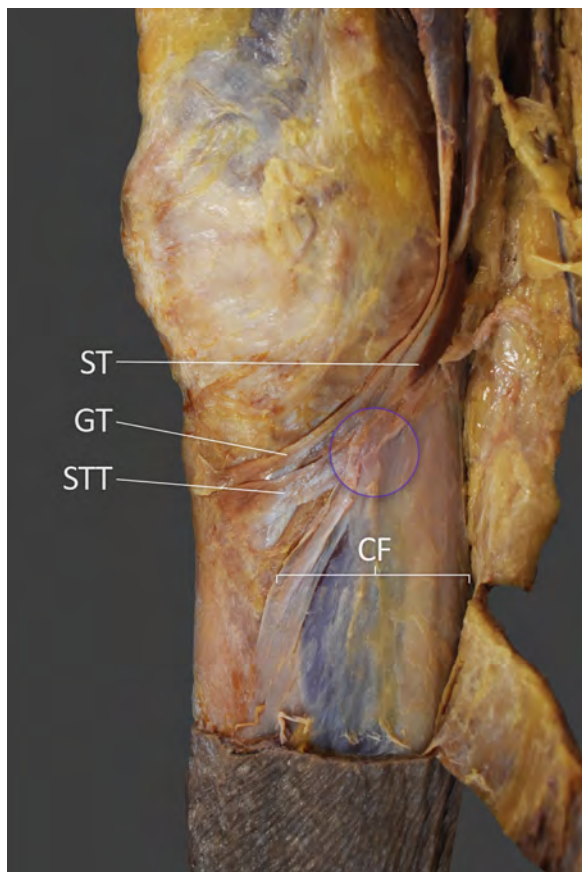
Figure 1. A very rare case of the sartorius muscle; ST — sartorius tendon; GT — gracilis tendon; STT — semitendinous tendon; CF — crural fascia (deep fascia of the leg). The purple circle indicate connection between the ST and CF.

The PAS shows several morphological variations. The literature contains descriptions of PASs with one or two accessory bands from the STT, or one accessory band from the GT, or one accessory band from the ST, in different combinations. The shape and location of insertion of the PAS can also vary [12].

The PAS can be used as a graft during reconstruction of the anterior cruciate ligament (ACL) [3]. Good knowledge of its morphological characteristics and variability is therefore useful during this procedure [12]. The tibial tuberosity helps to locate the PAS clearly [11]. However, the accessory tendons seem to be a major problem during operations [11].

During anatomical dissection a new pattern of arrangement of tendons constituting the PAS was found. This PAS comprised three tendons; the GT was located superiorly to the STT and the distal attachments of both were located on the medial side of the tibial tuberosity. This seemed like the normal arrangement, but the sartorius muscle tendon created

an additional superficial layer in its proximal part, just below the GT and covering the STT and small part of the GT. After crossing the STT, the ST was distally attached to the crural fascia significantly below the tibial tuberosity.

CASE REPORT

An 83-year-old female cadaver was dissected routinely for research and teaching purposes at the Department of Anatomical Dissection and Donation, Medical University of Lodz, Poland. The right lower limb was subjected to traditional anatomical dissection [11, 12] and a morphological variant of the PAS was found. The proximal course of the sartorius, semitendinosus, and gracilis muscles was normal. The sartorius originated from the anterior superior iliac spine, the gracilis from the pubis and ischium, and the semitendinosus from the ischial tuberosity. The interesting morphological variation was in their distal attachment (pes anserinus).

The ST created a superficial layer of which the proximal part was located just below the GT and covering the STT and a small part of the GT. The myotendinous junction of the sartorius was 5.32 mm wide and 0.43 mm thick. The ST was 79.92 mm long. After crossing the STT, the ST was distally attached to the crural fascia significantly below tibial tuberosity. At the point of the insertion it was 3.47 mm wide and 0.23 mm thick.

The GT was attached, as normal, to the medial part of the tibial tuberosity. At this point the tendon was 6.13 mm wide and 0.52 mm thick. The STT was attached to the same location, but just below the insertion of the GT, and it was covered by the ST. In its distal attachment the STT was 9.12 mm wide and 0.81 mm thick (Fig. 1).

An electronic calliper (Mitutoyo Corporation, Kawasaki-shi, Kanagawa, Japan) was used for these measurements. Each measurement was repeated twice with an accuracy of up to 0.1 mm.

No other morphological variabilities were found during dissection of the lower limb. Table 1 shows the morphometric measurements.

DISCUSSION

The PAS shows several morphological variations. Normally, it is composed of three tendons: the ST (which is located laterally and superiorly to the rest), the GT (inserting medially to the ST and superiorly to the STT), and the STT (the element of the PAS located

Table 1. Morphometric measurements

	Sartorius tendon	Gracilis tendon	Semitendinosus tendon
INSERTION	Crural fascia	Medial part of the TT	Medial part of the TT
WIDTH (DA)	3.47 mm	6.13 mm	9.12 mm
THICKNESS (DA)	0.23 mm	0.52 mm	0.81 mm

DA — distal attachment; TT — tibial tuberosity

most inferiorly). However, this arrangement can vary among the population [12].

Olewnik et al. [12] distinguished six types of PAS on the basis of the distribution of tendons. The first type showed the standard arrangement and occurred in 52.9%. In the second type the ST and GT were normal and one additional tendon arose from the STT. The frequency of this type was 31.4%. The third type (8.8%) had normal ST and GT with two accessory tendons from the STT. There was also a PAS with normal ST, one additional tendon from the GT and two from the STT, but this variation was the rarest (1% of the studied population). Another type (2% of studied population) had normal ST and GT, but one additional tendon from the STT. The final type, with frequency 3.9%, had one additional tendinous structure arising from both the GT and the ST, and two accessory tendons from the STT [12].

Olewnik et al. [12] also analysed the shape and insertion of the PAS and distinguished three types. In the first, the PAS had a short tendinous extension of the elongated muscle belly. In the second, called 'band-shaped', there was a distal attachment less than twice as wide as the tendon above. The last type, 'fan-shaped', had an insertion at least twice as wide as the tendon above [12].

There are alternative accounts of PAS variations. For example, there was an interesting case [11] with a normal PAS inserted to the tibia but an accessory slip arising from the STT. This structure was divided into two small tendons, the first attached to the tibia and the second to the fascia of the soleus muscle [2]. Rivizi et al. [13] found a case with an additional attachment of the STT and GT to the crural fascia. La Prade et al. [8] found a PAS divided into two layers; the ST was located superficially to the deep layer created by both the GT and the STT. A similar type was described by Lee et al. [9].

Snoeck et al. [14] carried out a study about GT and STT paratenons and other surrounding fascial connections. What is interesting GT and STT expansions were connected with the crural fascia in 100% of studied lower limbs. Moreover, these expansions were the edges of the paratenon tunnel. GT and STT paratenons were attached to the sartorius fascia, to the semimembranosus and the fascia lata. GT and STT are surrounded by a fascial structure whose edges diverge from the direction of the tendon to overlap. After that they are attached to the crural fascia [14].

The present case describes the new PAS variant. Although there were no additional tendons, the structures were arranged totally differently from those described earlier. The distal attachment of the ST had long tendon, the proximal part of the first layer being located just below the GT and covering the STT and a small part of the GT. After crossing the STT it inserted to the crural fascia, significantly below the GT and STT insertion. Normally, the ST attaches to the tibia, superiorly and medially to the other structures constituting the PAS.

Good knowledge of such morphological variations can be useful during surgery in the knee region, especially when the PAS is used for autografts [12]. The ST and GT are commonly grafted not only for the reconstructing the ACL, but also for the posterior cruciate, medial patellofemoral, and fibular collateral ligaments [12], medial knee reinforcement, and reconstruction of the patellar retinaculum (after patellar subluxation) [1]. Moreover, if the patellar tendon ruptures, these two tendons can also be used to repair the injury.

Patients after such a procedure report decreased anterior knee pain and better stabilization [4]. Recovery after a hamstring tendon graft (using STT and GT) is faster than after a bone-patellar tendon-bone graft [2]. However, the method seems more difficult because accessory tendons of the SM, the GT, or the STT, and morphological variations of their arrangement, are all common [12].

The present case, which has not been described previously, exemplifies this point. Even the latest classification created by Olewnik et al. [12] did not include a similar type of PAS. An interesting course of the ST (superficial layer with distal attachment to the

crural fascia) could cause confusion among surgeons or orthopedists during operations, increasing the operation time and making side effects more likely.

When there are such variants, most of the ST should be removed before the GT harvest. Only then is it possible to use GT and STT grafts during, for example, ACL reconstruction. There is also another option, which seems easier and could facilitate this procedure. In the present case, only the ST (rather than the GT) and STT should be used for reconstructing some knee ligaments. This method avoids the additional step or removing the ST, potentially shortening the duration of surgery.

Interestingly, the PAS regenerates after harvesting, though with altered anatomical and histological features that are not normally clinically visible [3]. Although the PAS is regenerated and normalized on magnetic resonance imaging images, histological examination reveals an irregular course of collagen fibres, increased angiogenesis, and proliferation of fibroblasts. This could explain why the PAS is more susceptible to injury after it is used for ACL reconstruction [3]. However, it is important to remember that the PAS will not regenerate in some cases; this is one of the disadvantages or risks of such a procedure [7].

CONCLUSIONS

The PAS is morphologically variable, and various types have already been classified. However, the present case shows a totally new and undescribed type of the PAS arrangement. Good knowledge of the morphological variations of this structure is useful during surgical procedures, not only in ACL reconstruction, but also during reconstruction of the posterior cruciate, medial patellofemoral, or fibular collateral ligament.

REFERENCES

1. Ashaolu JO, Osinuga TS, Ukwenya VO, et al. Pes anserinus structural framework and constituting tendons are grossly aberrant in Nigerian population. Anat Res Int. 2015; 2015: 483186, doi: 10.1155/2015/483186, indexed in Pubmed: 26246910.

2. Bernicker JP, Haddad JL, Lintner DM, et al. Patellar tendon defect during the first year after anterior cruciate ligament reconstruction: appearance on serial magnetic resonance imaging. Arthroscopy. 1998; 14(8): 804–809, doi: 10.1016/s0749-8063(98)70014-3, indexed in Pubmed: 9848589.

3. Curtis BR, Huang BK, Pathria MN, et al. Pes anserinus: anatomy and pathology of native and harvested tendons. Am J Roentgenol. 2019; 213(5): 1107–1116, doi: 10.2214/AJR.19.21315, indexed in Pubmed: 31361527.

4. Freedman KB, D'Amato MJ, Nedeff DD, et al. Arthroscopic anterior cruciate ligament reconstruction: a metaanalysis comparing patellar tendon and hamstring tendon autografts. Am J Sports Med. 2003; 31(1): 2–11, doi: 10.1177/03635465030310011501, indexed in Pubmed: 12531750.

5. Iwanaga J, Singh V, Ohtsuka A, et al. Acknowledging the use of human cadaveric tissues in research papers: Recommendations from anatomical journal editors. Clin Anat. 2020; 34(1): 2–4, doi: 10.1002/ca.23671, indexed in Pubmed: 32808702.

6. Iwanaga J, Singh V, Takeda S, et al. Standardized statement for the ethical use of human cadaveric tissues in anatomy research papers: Recommendations from Anatomical Journal Editors-in-Chief. Clin Anat. 2022; 35(4): 526–528, doi: 10.1002/ca.23849, indexed in Pubmed: 35218594.

7. Järvinen TLN, Järvinen TAH, Penttilä T, et al. Failed regrowth of the harvested semitendinosus tendon: a rare complication of tendon harvest after anterior cruciate ligament reconstruction. Arthroscopy. 2003; 19(4): E31, doi: 10.1053/jars.2003.50120, indexed in Pubmed: 12671606.

8. LaPrade RF, Engebretsen AH, Ly TV, et al. The anatomy of the medial part of the knee. J Bone Joint Surg Am. 2007; 89(9): 2000–2010, doi: 10.2106/JBJS.F.01176, indexed in Pubmed: 17768198.

9. Lee JH, Kim KJ, Jeong YG, et al. Pes anserinus and anserine bursa: anatomical study. Anat Cell Biol. 2014; 47(2): 127–131, doi: 10.5115/acb.2014.47.2.127, indexed in Pubmed: 24987549.

10. Mochizuki T, Akita K, Muneta T, et al. Pes anserinus: layered supportive structure on the medial side of the knee. Clin Anat. 2004; 17(1): 50–54, doi: 10.1002/ca.10142, indexed in Pubmed: 14695588.

11. Olewnik Ł, Podgórski M, Polguj M. An unusual insertion of an accessory band of the semitendinosus tendon: case report and review of the literature. Folia Morphol. 2020; 79(3): 645–648, doi: 10.5603/FM.a2019.0105, indexed in Pubmed: 31565787.

12. Olewnik Ł, Gonera B, Podgórski M, et al. A proposal for a new classification of pes anserinus morphology. Knee Surg Sports Traumatol Arthrosc. 2019; 27(9): 2984–2993, doi: 10.1007/s00167-018-5318-3, indexed in Pubmed: 30535546.

13. Rizvi A, Iwanaga J, Oskouian RJ, et al. Additional attachment of the semitendinosus and gracilis muscles to the crural fascia: a review and case illustration. Cureus. 2018; 10(8): e3116, doi: 10.7759/cureus.3116, indexed in Pubmed: 30338191.

14. Snoeck O, Beyer B, Rooze M, et al. Anatomical study of paratenons and fascia lata connections in the posteromedial knee region. Surg Radiol Anat. 2022; 44(6): 821–827, doi: 10.1007/s00276-022-02927-6, indexed in Pubmed: 35316382.

VIA MEDICA

C A S E   R E P O R T

A very rare case report: accessory head of the sartorius muscle

Nicol Zielinska[1], Richard Shane Tubbs[2–7], Adrian Balcerzak[1], Łukasz Olewnik[1]

[1]Department of Anatomical Dissection and Donation, Medical University of Lodz, Poland
[2]Department of Anatomical Sciences, St. George's University, Grenada, West Indies
[3]Department of Neurosurgery, Tulane University School of Medicine, New Orleans, Louisiana, United States
[4]Department of Neurology, Tulane University School of Medicine, New Orleans, Louisiana, United States
[5]Department of Structural and Cellular Biology, Tulane University School of Medicine, New Orleans, Louisiana, United States
[6]Department of Surgery, Tulane University School of Medicine, New Orleans, Louisiana, United States
[7]Department of Neurosurgery, Ochsner Medical Centre, New Orleans, Louisiana, United States

The sartorius muscle belongs to the anterior compartment of the thigh. Morphological variations of this muscle are very rare, few cases being described in the literature. An 88-year-old female cadaver was dissected routinely for research and teaching purposes. However, an interesting variation was found during anatomical dissection. The proximal part of the sartorius muscle had the normal course, but the distal part bifurcated into two muscle bellies. The additional head passed medially to the standard head; thereafter, there was a muscular connection between them. This connection then passed into the tendinous distal attachment. It created a pes anserinus superficialis, which was located superficially to the distal attachments of the semitendinosus and gracilis muscles. This superficial layer was very wide and attached to the medial part of the tibial tuberosity and to the crural fascia. Importantly, two cutaneous branches of the saphenous nerve passed between the two heads. The two heads were innervated by separate muscular branches of the femoral nerve. Such morphological variability could be clinically important.
(Folia Morphol 2024; 83, 1: 244–249)

Keywords: sartorius muscle, accessory head, morphological variation, case report, saphenous nerve entrapment syndrome, compression

INTRODUCTION

The sartorius muscle (SM) belongs to the anterior compartment of the thigh. It is proximally attached to the anterior superior iliac spine (ASIS) and distally attached on the medial side of the proximal part of the tibia at the pes anserine. Its blood supply is provided by muscular branches of the femoral artery. It is innervated by the femoral neve (L2–L4) [15]. Because of its specific attachment points, this muscle is responsible for movements in both the hip and knee joints: hip flexion, abduction, and external rotation, and knee flexion [15].

Morphological variations of the SM are very rare, and few instances have been described in the literature. However, absence of this muscle has been reported [12]. There are also descriptions of a doubled SM. When there is an additional head in the proximal attachment it can originate from the pectineal line,
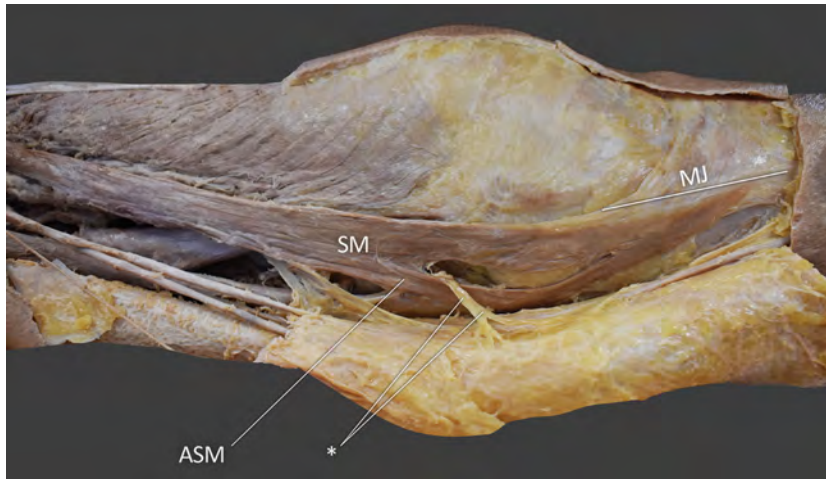
Figure 1. A very rare case of accessory part of the sartorius muscle; SM — sartorius muscle; ASM — accessory sartorius muscle; MJ — myotendinous junction; *cutaneous branches of the saphenous nerve.

the iliopectineal eminence, the femoral sheath, the inguinal ligament, or the pubic symphysis [2, 3]. The distal part of the SM can also bifurcate [10]. Its insertion can be located, for example, on the medial aspect of the patella [10].

Accessory structures can be associated with some kind of neurovascular compression [24]. If the additional head of the SM is located over the femoral nerve, then femoral nerve compression is a strong possibility [8]. For example, lateral femoral cutaneous entrapment could occur, also called meralgia paraesthetica, which can result in pain, paraesthesia, and sensory loss within the distribution of the lateral cutaneous nerve of the thigh [7].

During anatomical dissection, an interesting variant of the SM was found. Proximally, there was one short tendon attached to the ASIS. It then passed into the muscle belly, the distal part of which bifurcated into two muscular parts. The first had a normal course, the additional one passing medially to it; after that there was a muscular connection between the two, which passed into the tendinous distal attachment. This created a pes anserinus superficialis, located superficially to the distal attachment of the semitendinosus and gracilis muscles. This superficial layer was very wide and attached to the medial part of the tibial tuberosity and to the crural fascia. Importantly, cutaneous branches of the saphenous nerve passed between the two heads, which were innervated by separate muscular branches of the femoral nerve.

CASE REPORT

An 88-year-old female cadaver was dissected routinely for research and teaching purposes at the Department of Anatomical Dissection and Donation, Medical University of Lodz, Poland. The left lower limb was subjected to traditional anatomical dissection [17–20] and the skin, subcutaneous tissue, and deep fascia were dissected. Each muscle was then carefully examined and an anomalous SM was found.

Proximally, there was one short tendon attached to the ASIS. At the origin it was 15.86 mm wide and 3.41 mm thick. It then passed into the muscle belly. Distally, it bifurcated into two muscular parts. The distance from the origin to the bifurcation was 355.70 mm. The first part had normal course and was 83.68 mm long, and the additional muscle belly (92.36 mm long) passed medially to it. After that there was a muscular connection between these two structures, which was 67.03 mm long.

This connection passed into the tendinous distal attachment. At the myotendinous junction the width was 68.45 mm and the thickness 0.34 mm. It created a pes anserinus superficialis, which was located superficially to the distal attachment of the semitendinosus and gracilis muscles. This superficial layer was very wide and attached to the medial part of the tibial tuberosity and to the crural fascia. Its insertion was 36.16 wide and 0.41 mm thick (Fig. 1).

Importantly, two cutaneous branches of the saphenous nerve passed between the two heads. The
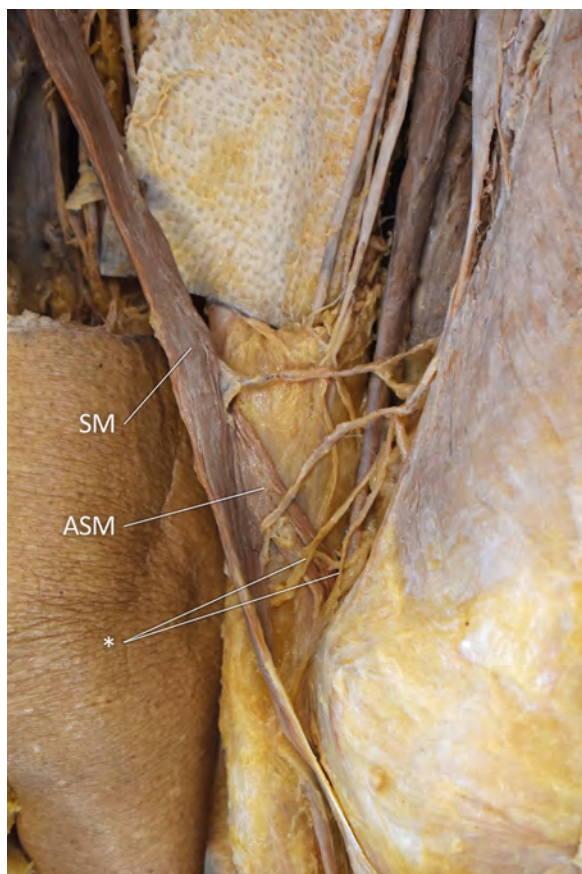
Figure 2. A very rare case of accessory part of the sartorius muscle and loop for the cutaneous branches of the saphenous nerve; SM — sartorius muscle; ASM — accessory sartorius muscle; *cutaneous branches of the saphenous nerve.
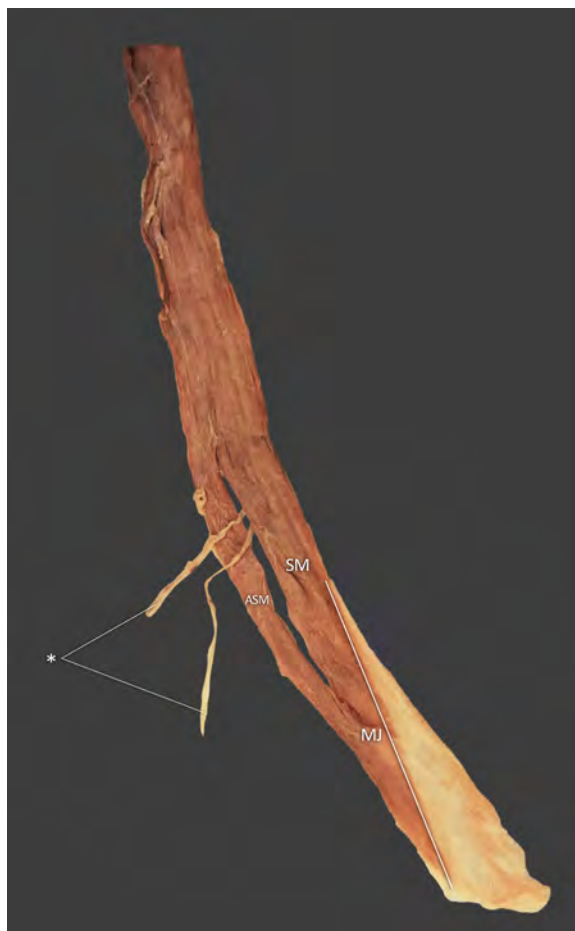
Figure 3. Excised sartorius muscle and loop for the cutaneous branches of the saphenous nerve; SM — sartorius muscle; ASM — accessory sartorius muscle; *cutaneous branches of the saphenous nerve.

Table 1. Morphometric measurements of the present case

ORIGIN	ASIS
Width	15.81 mm
Thickness	3.41 mm
LENGTH	
To the bifurcation	355.70 mm
To the connection	**The SM (normal):** 83.68 mm; **The accessory head:** 92.36 mm
To the MJ	67.03 mm
MJ	
Width	68.45 mm
Thickness	0.34 mm
INSERTION	To the medial part of the tibial tuberosity and to the crural fascia
Width	36.16 mm
Thickness	0.41 mm

ASIS — anterior superior iliac spine; MJ — myotendinous junction; SM — sartorius muscle

diameter of the first was 1.90 mm and that of the second was 2.19 mm (Figs. 2, 3).

An electronic calliper (Mitutoyo Corporation, Kawasaki-shi, Kanagawa, Japan) was used for the measurements. Each measurement was repeated twice with an accuracy of up to 0.1 mm. No other morphological variabilities were found during dissection of the lower limb. Table 1 shows the morphometric measurements.

DISCUSSION

There are some descriptions of morphological variations of the SM in the literature but these are very rare. One variation of the lower limb is absence of the SM [1]. The SM can also be doubled, with complete longitudinal division into two elements [1].

The proximal attachment of this muscle can have additional heads. Kumar et al. [11] found two heads of the SM, one following a normal course while the second (the accessory head) originated from the

inguinal ligament. This additional muscle belly was connected to the main SM between the upper one-third and lower two-thirds of the thigh. Importantly, the femoral nerve was located under the accessory head [11].

However, the inguinal ligament is not the only structure from which an accessory head of the SM can originate. Brock et al. [3] reported that it can also be attached to the pectineal line, or the iliopectineal eminence [3]. There are also cases in which an additional head originated from the ASIS, the femoral sheath, or the pubic symphysis [1].

The SM can also vary in its distal attachment. The tendinous attachment can bifurcate and insert to the anteromedial aspect of the patella, the medial condyle of the femur, the capsule of the knee joint, or the fascia of the leg [1]. However, this bifurcation can be more proximal and the muscular structure then ends in a tendon. Sometimes, a variation of this kind is called a musculus sartorius bicaudatus. Mailing and Zweymiillerb [11] found only one case of this variation in their study population (1.14%); this structure was attached to the medial meniscus anteromedially [18].

An interesting case was found by Kim and Lee [10]. The proximal attachment of the SM was normal, but in the proximal one third of this muscle there was a bifurcation into medial and lateral parts. The lateral part was distally attached by a tendon on to the medial aspect of the patella. We found the course of the medial part more interesting because it gave off a small muscular structure to the vastus medialis, and below this it connected with an accessory SM. This additional muscle was proximally attached to the inguinal ligament. The common junction inserted on the medial aspect of the proximal tibia (pes anserinus) [10].

Another anomalous presentation of the SM was described by el-Badawi [6]. The SM was distally divided into two parts. The first one located laterally had an insertion into the medial epicondyle of the femur. The medial part was distally attached to the medial surface of the tibia [6]. Mailing and Zweymiillerb [14] also found a distal division of the SM. The larger part (posteromedial) presented normal course. The smaller part (anterolateral) was attached to the medial meniscus and was pushing the synovial membrane into the joint [14].

Dziedzic et al. [5] carried out a study about anatomy of this muscle. It turned out that in most cases

the initial part of the SM was represented by the shortest width. In turn, the widest part was variable — in 10% it was the proximal part of the belly, in 30% it was the middle one, and in 50% the distal part. There was also a situation in which middle and distal parts were bigger than the proximal part, and its frequency was 10% [5].

Dudek et al. [4] carried out a study on human fetuses. It turned out that there was a statistically significant sexual dimorphism of thigh length and the SM's length — smaller sizes were observed in male fetuses. In turn, there were no significant differences in crown-rump length and total length. The SM's length rate was constant and amounted to 1.2 mm per week. They also distinguished two types of the SM — the rectangular and cone-shaped. Other observed morphological variations were: an accessory tendon, the start of muscle duplication in the form of a hollow, partial duplication of the distal part of the SM and discontinuous muscle [4].

In the present case, the normal proximal part originated from the ASIS by a short tendon, which passed into the muscular part. The additional muscular structure arising from the muscle belly of the SM was then observed. The first muscle belly had a normal course and the additional muscle belly passed medially to it. After that there was a muscular connection between these two structures, which passed into the tendinous distal attachment. This created a pes anserinus superficialis, which was located superficially to the distal attachment of the semitendinosus and gracilis muscles. This superficial layer was very wide and was attached to the medial part of the tibial tuberosity and to the crural fascia.

Analysing this course, we thought it could an example of the musculus sartorius bicaudatus, but in the present case there was an additional connection between the muscle bellies. However, the most interesting feature of our case was the specific course of saphenous nerve branches. Two cutaneous neural branches passed between the normal and additional bellies. Next to these there were small arteries arising from the femoral artery.

Additional structures are usually associated with some kind of neurovascular compression [25]. In the present case, the cutaneous branches of the saphenous nerve could have been trapped between the two heads of the SM and saphenous nerve entrapment syndrome could have resulted [21]. Patients with this pathology usually complain of pain along the

saphenous nerve. The pain can be located at the knee joint level, radiating superiorly to the medial aspect of thigh and inferiorly to the medial part of the foot. Symptoms can be aggravated when the knee is extended [15].

Sometimes, neuropathy in the foot can result from such a syndrome. Because of the pain, the knee is usually kept in a protective position (slight flexion). This results in shortening of the limb and there can be compensatory hypertrophy of the phalangeal muscles in the foot region, resulting in compression or nerve irritation.

Unrecognized saphenous neuritis can confuse the patient's clinical picture. For example, permanent pain in the knee region, without warming and reddening, can give a suspicion of rheumatoid arthritis, a long-term autoimmune disorder [23]. It can also be confused with injury or osteoarthritis of the knee. Permanent pain in one area should also draw attention to the possibility of bone metastases [13].

After diagnosis of saphenous nerve entrapment syndrome, appropriate treatment should be instituted. Treatment can be surgical or non-surgical. Non-surgical treatment involves different physiotherapy techniques and corticosteroid injections. If this does not succeed, invasive methods could help [22]. These depend on debridement of any fibrous tissue surrounding the compressed part of the nerve; so in the present case, removing part or all of the additional head of the SM could have been the best solution.

Good knowledge of morphological variations in various regions of the human body can help during diagnosis, especially when there is permanent paraesthesia or pain in one region with no apparent reason.

CONCLUSIONS

Morphological variations of the SM are very rare. An additional muscular band can be associated with some kind of neurovascular compression. Knowledge of the possibility of such variants can be important for clinicians, especially for orthopaedists, neurologists and rheumatologists, when entrapment syndrome and its symptoms need to be differentiated from other diseases.

Ethical approval and consent to participate

Acknowledgements

Conflict of interest: None declared

REFERENCES

1. Bergman R, Afifi A, Miyauchi R. Illustrated Encyclopedia of Human Anatomic Variations. Anatomy Atlases 2017.
2. Bergman R, Thompson S, Afifi A, Saadeh F. Compendium of human anatomic variation. Urban & Schwarzenberg, Baltimore 2018.
3. Brock GS. A two-headed sartorius. J Anat Physiol. 1879; 13(Pt 4): 578, indexed in Pubmed: 17231291.
4. Dudek K, Kędzia W, Kędzia E, et al. Mathematical modelling of the growth of human fetus anatomical structures. Anat Sci Int. 2017; 92(4): 521–529, doi: 10.1007/s12565-016-0353-y, indexed in Pubmed: 27393150.
5. Dziedzic D, Bogacka U, Ciszek B. Anatomy of sartorius muscle. Folia Morphol (Warsz). 2014; 73(3): 359–362, doi: 10.5603/FM.2014.0037, indexed in Pubmed: 25242250.
6. el-Badawi MG. An anomalous bifurcation of the sartorius muscle. Anat Anz. 1987; 163(1): 79–82, indexed in Pubmed: 3565790.
7. Grossman MG, Ducey SA, Nadler SS, et al. Meralgia paresthetica: diagnosis and treatment. J Am Acad Orthop Surg. 2001; 9(5): 336–344, doi: 10.5435/00124635-200109000-00007, indexed in Pubmed: 11575913.
8. Iwanaga J, Singh V, Ohtsuka A, et al. Acknowledging the use of human cadaveric tissues in research papers: Recommendations from anatomical journal editors. Clin Anat. 2020; 34(1): 2–4, doi: 10.1002/ca.23671, indexed in Pubmed: 32808702.
9. Iwanaga J, Singh V, Takeda S, et al. Standardized statement for the ethical use of human cadaveric tissues in anatomy research papers: Recommendations from Anatomical Journal Editors-in-Chief. Clin Anat. 2022; 35(4): 526–528, doi: 10.1002/ca.23849, indexed in Pubmed: 35218594.
10. Kim J, Lee JH. A unique case of an accessory sartorius muscle. Surg Radiol Anat. 2019; 41(3): 323–325, doi: 10.1007/s00276-018-2155-5, indexed in Pubmed: 30539207.
11. Kumar N, Swamy R, Guru A, et al. Unilateral accessory Sartorius muscle: A case report on its functional and clinical implications. Saudi J Sport Med. 2015; 15(3): 285, doi: 10.4103/1319-6308.164317.
12. Lin SE, Auyong DB, Dahl AB, et al. Successful continuous adductor canal block placement in a patient with absent

sartorius muscle: a case report. A A Case Rep. 2017; 9(4): 101–104, doi: 10.1213/XAA.0000000000000538, indexed in Pubmed: 28410261.

13. Macedo F, Ladeira K, Pinho F, et al. Bone metastases: an overview. Oncol Rev. 2017; 11(1): 321, doi: 10.4081/oncol.2017.321, indexed in Pubmed: 28584570.

14. Mailing M, Zweymiillerb K. Musculus sartorius bicaudatus. Cells Tissues Organs. 1996; 155: 215–218.

15. Moore KL, Dalley AF. Clinical Oriented Anatomy. 4th ed. Lippincott Williams & Wilkins, Philadeplphia 1999.

16. Morganti CM, McFarland EG, Cosgarea AJ. Saphenous neuritis: a poorly understood cause of medial knee pain. J Am Acad Orthop Surg. 2002; 10(2): 130–137, doi: 10.5435/00124635-200203000-00008, indexed in Pubmed: 11929207.

17. Olewnik Ł, Kurtys K, Gonera B, et al. Proposal for a new classification of plantaris muscle origin and its potential effect on the knee joint. Ann Anat. 2020; 231: 151506, doi: 10.1016/j.aanat.2020.151506, indexed in Pubmed: 32173563.

18. Olewnik Ł, Gonera B, Podgórski M, et al. A proposal for a new classification of pes anserinus morphology. Knee Surg Sports Traumatol Arthrosc. 2019; 27(9): 2984–2993, doi: 10.1007/s00167-018-5318-3, indexed in Pubmed: 30535546.

19. Olewnik Ł, Karauda P, Gonera B, et al. Impact of plantaris ligamentous tendon. Sci Rep. 2021; 11(1): 4550,

doi: 10.1038/s41598-021-84186-w, indexed in Pubmed: 33633305.

20. Olewnik Ł, LaPrade RF, Paulsen F, et al. A proposal for a new morphological classification of the popliteus muscle tendon with potential clinical and biomechanical significance. Sci Rep. 2021; 11(1): 14434, doi: 10.1038/s41598-021-93778-5, indexed in Pubmed: 34262097.

21. Romanoff ME, Cory PC, Kalenak A, et al. Saphenous nerve entrapment at the adductor canal. Am J Sports Med. 1989; 17(4): 478–481, doi: 10.1177/036354658901700405, indexed in Pubmed: 2782531.

22. Settergren R. Conservative management of a saphenous nerve entrapment in a female ultra-marathon runner. J Bodyw Mov Ther. 2013; 17(3): 297–301, doi: 10.1016/j.jbmt.2012.10.005, indexed in Pubmed: 23768272.

23. Sparks JA. Rheumatoid arthritis. Ann Int Med. 2019; 170(1): ITC1–ITC15, doi: 10.7326/aitc201901010.

24. Zielinska N, Olewnik Ł, Karauda P, et al. A very rare case of an accessory subscapularis muscle and its potential clinical significance. Surg Radiol Anat. 2021; 43(1): 19–25, doi: 10.1007/s00276-020-02531-6, indexed in Pubmed: 32656573.

25. Zielinska N, Olewnik Ł, Karauda P, et al. A very rare case of an accessory subscapularis muscle and its potential clinical significance. Surg Radiol Anat. 2021; 43(1): 19–25, doi: 10.1007/s00276-020-02531-6, indexed in Pubmed: 32656573.

LETTER TO THE EDITOR

Before assessing a novel muscle in the hand, please be very careful

Georgi P. Georgiev

Department of Orthopaedics and Traumatology, University Hospital Queen Giovanna – ISUL, Medical University of Sofia, Bulgaria

I read with interest the article of Antonopoulos et al. [1] on the study of a variant hypothenar muscle: "Aberrant accessory abductor digiti minimi manus muscle: a rare anatomical variation", which the authors accept as unique.

However, I want to apply my modest comments to this article. 1) In the abstract, the authors state that except for morphological variations of the accessory abductor digiti minimi manus (AADM), have been described other cases of an extra wrist muscle, as the accessory ADMM. Such an opinion at the start of the manuscript could mislead the readers; in the discussion most of the text is directed to the accessory ADMM, as hypothenar muscle variation, and its role in compression syndromes at the wrist. Moreover, all of the reported examples are different variants of the ADMM, not a cases of extra wrist muscles. 2) Antonopoulos et al. [1] reported that the presented accessory ADMM originated from the tendons of the flexor digitorum superficialis (FDS). Firstly, I would like to point out not so representative dissection and fixation of the upper extremity. Secondly, it is clearly visible that the origin of the presented muscle is from the antebrachial fascia, which is widely known [2]. 3) In the case report section the authors report an origin from the tendons of the FDS and insertion to the base of the fifth proximal phalanx. However, at the start of the discussion they present the described case as unique with origin from FDS and insertion to the head of the fifth metacarpal. Moreover, the same description is also included in the conclusion. Thus, it could be not clearly understood the correct attachment of unique accessory ADMM. This raised my forth comment. 4) About quality and clearness of the figures;

no clear insertion of the accessory muscle to the head of the fifth metacarpal bone or to the base of the fifth proximal phalanx is presented. I would like to point out that when the authors pretend to describe something unique nowadays, they need to present it in clear and informative dissection, excellent photographs and no misdescriptions in the text. 5) In the discussion the authors state that the existence of an accessory AADM muscle has been previously described [4]. According to this consideration and to the description in the case report section, Antonopoulos et al. [1] accept the described unique muscle as a hypothenar variation; this is in contrast to their previous assessment for an extra wrist muscle in the abstract. However, if they accepted an insertion to the fifth metacarpal, as they present in the start of discussion and conclusion, thus an extra wrist muscle which might involve the wrist function should be accepted. 6) In the discussion, at the start of section Clinical considerations, the authors report that generally, the existence of an accessory ADMM has been involved in ulnar nerve compression. However, the cited articles to this statement are cadaver cases, not some surgical ones. Therefore, to my opinion, presented in that way this statement is very speculative. It should be noted that the existing anatomical variation near the nerve generally does not mean entrapment [3]. To accept nerve compression by the variant muscle, hypertrophy of the muscle should exist, and thus narrowing the canal through which the nerve passes. Muscle variation should be considered as a predisposing factor that could provoke nerve compression [2, 3]. Moreover, in the presented cadaver case, no medical history was proven. To my opinion, the authors need to point out the medical

Address for correspondence: Georgi P. Georgiev, MD, PhD, DSc, Department of Orthopaedics and Traumatology, University Hospital Queen Giovanna – ISUL, Medical University of Sofia, 8, Bialo More Str., BG 1527 Sofia, Bulgaria, tel: +359884 493523, e-mail: georgievgp@yahoo.com

history of the anatomical specimen if existed or report that such an information is missed, especially in cases of possible neurovascular entrapment.

Conflict of interest: None declared

REFERENCES

1. Antonopoulos I, Tsikouris G, Chrysikos D, et al. Aberrant accessory abductor digiti minimi manus muscle: a rare anatomical variation. Folia Morphol. 2024; 83(1): 221–225, doi: 10.5603/FM.a2023.0015, indexed in Pubmed: 36811135.

2. Georgiev GP, Jelev L, Surchev L. Undescribed variant muscle: "deep abductor-flexor" of the little finger, in relation to ulnar nerve compression at the wrist. Ann Anat. 2007; 189(3): 276–282, doi: 10.1016/j.aanat.2006.11.003, indexed in Pubmed: 17534035.

3. Georgiev GP. Re: Wang CK, Ng CY. Accessory flexor carpi ulnaris: a rare cause of distal ulnar nerve compression. J Hand Surg Eur. 2021, 46: 197-9. J Hand Surg Eur Vol. 2021; 46(9): 1014–1015, doi: 10.1177/17531934211003791, indexed in Pubmed: 34720001.

4. May CA. Long abductor digiti minimi muscle: variation of the hypothenar muscles and clinical consequences. Clin Anat. 2020; 33(5): 643–645, doi: 10.1002/ca.23472, indexed in Pubmed: 31573103.

E R R A T U M

VIA MEDICA

To the article: **Paratenon of the cruciate ligaments of the knee: a macroscopic and histological study of human fetuses**

To the Editor,

I am writing this mail with the error in our published article.

In the article by Kim JH, Sugai N, Suzuki D, Murakami G, Abe H, Rodríguez-Vázquez JF, Yamamoto M. Paratenon of the cruciate ligaments of the knee: a macroscopic and histological study of human fetuses. Folia Morphol 2022;81(1):134–143 (DOI: 10.5603/FM.a2021.0003), the following errors should be corrected: in the legends and figure letterings to figures 1–6 should be added and changed because of a misinterpretation of figures. Throughout the legends and figures letterings of Fig. 1A–D, Fig. 2B, C, Fig. 3, Fig. 4A, B, D–F, Fig. 5C–E and Fig. 6, the ACL (anterior cruciate ligament) and PCL (posterior cruciate ligament) for identification of the cruciate ligaments should be reversed. And, in the figure legend and figure lettering of Fig. 1E, lateral condyle should change to medial condyle.

However, these errors are not relevant to the major contents of this paper. The authors apologize for the errors and inconveniences.

After our communication with the Editors, we have reanalyzed the data and have published Erratum (Folia Morphol 2024; DOI: 10.5603/fm.99214).

Article available online:

https://journals.viamedica.pl/folia_morphologica/article/view/72197 is correct.

FOLIA MORPHOLOGICA

C O N T E N T S

←

Cover picture: Anatomical variations of pelvic girdle; 1 — external part of the ischiopubic ramus; 2 — external surface of the ramus of the ischium; 3 — superior gemellus muscle (SGM); OI — obturator internus; IGM — inferior gemellus muscle; IT — ischial tuberosity; AM — adductor magnus; *first accessory muscle; **second accessory muscle. For details see: Nicol Zielinska et al., Folia Morphol 2024; 83, 1: 235–238.